Technische Universität München
TUM School of Natural Sciences

Organometallic Pillarplexes as Building Blocks for Supramolecular and Porous Solid-State Materials

Alexandra Annabella Heidecker

Vollständiger Abdruck der von der TUM School of Natural Sciences der Technischen Universität München zur Erlangung einer

Doktorin der Naturwissenschaften (Dr. rer. nat.)

genehmigten Dissertation.

Vorsitz: Prof. Dr. Torben Gädt

Prüfer*innen der Dissertation:

1. Priv.-Doz. Dr. Alexander Pöthig
2. Prof. Dr. Job Boekhoven

Die Dissertation wurde am 28.09.2023 bei der Technischen Universität München eingereicht und durch die TUM School of Natural Sciences am 19.10.2023 angenommen.

But in the end it`s only a passing thing, this shadow.

Even darkness must pass.

J. R. R. Tolkien

Acknowledgement

Zu Beginn möchte ich **PD Dr. Alexander Pöthig** danken, dass er mir die Möglichkeit gegeben hat meine Promotion auf einem solch spannenden und vielfältigen Thema durchzuführen und ich dabei einen tiefen Einblick in die Einkristallographie erhalten habe. Danke, dass ich die Möglichkeit hatte meine Forschung auch auf internationalen Konferenzen zu präsentieren und wichtige Erfahrungen bei meinem Auslandsaufenthalt in Berkeley sammeln konnte. Danke für die regen Diskussionen und das offene Ohr bei fachlichen und persönlichen Problemen. Auch die außeruniversitären Aktivitäten, wie Biergartenbesuch, Radeltour oder Konferenzen, mit der Untergruppe „Supramolecular Organometallics“ waren eine Freude und haben eine angenehme Arbeitsatmosphäre geschaffen.

Ich möchte mich bei **Prof. Dr. Torben Gädt** für die Übernahme des Prüfungsvorsitzes und **Prof. Dr. Job Boekhoven** für die Übernahme des Zweitprüfers bedanken.

Ein großer Dank gilt auch **Prof. Dr. Roland A. Fischer**, welcher zu Beginn meiner Promotion die Betreuung meiner Promotion übernahm, in den Gruppenseminaren stets Interesse für mein Thema gezeigt hat und mir dabei hilfreiche Tipps zur MOF-Chemie gegeben hat.

Natürlich möchte ich mich auch bei **Dr. Philipp Altmann** für die Übernahme meines Mentorings danken. Neben viel fachlichem Input hat er mich auch immer persönlich unterstützt und hatte bei aufgetretenen Problemen immer ein offenes Ohr.

Ich möchte mich bei **Dr. Christian Jandl** für SC-XRD und micro-ED Messungen, sowie die Einarbeitung in die Einkristall-Diffraktometrie bedanken und natürlich für die Unterstützung mit seinem großen Wissen bei so manch komplexer Strukturaufklärung. Zusätzlich möchte ich **Dr. Stefan Burger** für das Vertrauen danken, dass ich bei ihm die ein oder andere SC-XRD Messungen durchführen durfte und für die vielen Tipps, die mir die spätere Anwendung deutlich erleichtert haben. Ich möchte mich bei **Dr. Andreas Schneemann** für die Kooperation im Bereich der Gasadsorption Studien bedanken. Dann möchte ich mich bei **Dr. Jan Berger**, **Johanna Haimerl** und **Lena Schröck** für die BET-Messungen und die Hilfe bei der Auswertung und Diskussion dieser Ergebnisse bedanken. Bei **Dr. Gabriele Raudaschl-Sieber** möchte ich mich für die gute Betreuung der Praktika, die Einarbeitung in das NMR, das viele Hintergrundwissen, die solid-state NMR-Messungen und natürlich für die vielen netten Gespräche bedanken. Ich danke **Jürgen Kudermann** für Hilfestellungen bei allerlei Problemen, **Ulrike Ammari** und **Bircan Dilki** für Elementaranalysen, **Katja Rodewald** für SEM-Messungen und **Dr. Sebastian Weishäupl** für UV-vis-, Fluoreszenzmessungen und die ein oder andere hirnrisse Forschungsidee. I thank **Michele Stasi** for the ITC measurements and the expert view on the evaluation and discussion of the obtained results.

I would like to thank **Prof. Dr. Polly Arnold** for the opportunity and organisation of my short research stay at the UC Berkeley and her students for welcoming me at their chair.

Ich möchte mich hauptsächlich bei meinen Masterstudenten **Julian Zuber** und **Tom Calmus** sowie auch meinem Bachelorstudent **Felix Suttor** und meinen weiteren Forschungspraktikanten **Tom Calmus**, **Moritz Bohn**, **Alexander Spears**, **Markus Plagmann**, **Hümeyra Hikmet Yanar**, **Elisabeth Springl** und **Lukas Sippach** bedanke, dass sie mir das Vertrauen geschenkt haben ihre Arbeiten bei mir durchzuführen und für ihre tatkräftige Unterstützung im Labor.

Ein großes Dankeschön geht an den gesamte **AMC-Lehrstuhl** für die angenehme Arbeitsatmosphäre im Labor und in den Schreibräumen, für die täglichen Mensagänge, Kaffeepausen und natürlich auch die ein oder andere außerfachliche Aktivität (Lasertag, Oktoberfestbesuch, Gruppenausflüge, …).

Besonders möchte ich mich bei der **Neufahrn Gang Pati**+**Sebi**, **Margit**+**Lukas**, **Karina**+**Philip**, **Fabi**+**Meli**, **Stefan**+**Sylvia** und **Lena**+**Simon** für die vielen gemeinsamen Unternehmungen wie zum Beispiel das stets Corona-konforme Glühwein trinken am Neufahrner Marktplatz, den ein oder anderen Bachelorabend, Hungerbaumaufstellfestigkeiten und Hüttenwochenende … bedanken. Insbesondere **Margit** und **Pati** möchte ich danken. Ihr seid mir in der Zeit immer zur Seite gestanden und wir haben so viele gemeinsame Mittagessen / Kaffeepausen und Abende miteinander verbracht. Ohne euch wäre meine Promotion nicht so verlaufen wie sie es ist und ich möchte euch nicht mehr aus meinem Leben missen wollen.

Meinen **Ulmer Spatzen Angelika**, **Lena**, **Daniela**, **Robin** und **Michi** möchte ich danken. Ohne euch wäre das mit meinem Chemiestudium nichts geworden. Ihr habt mich immer unterstützt auch in meinen tiefsten Tiefs und auch wenn wir weite Distanzen zurücklegen mussten, haben wir doch immer wieder zusammengefunden. Ihr seid meine Wohlfühloase und ich freu mich auf viele weitere gemeinsame Ausflüge, Urlaube und Erlebnisse mit euch!

Natürlich gilt all meinen Freunden ein riesiges Dankeschön, dass ihr mich immer unterstützt habt und mir nicht nachtragend wart, wenn ich mich in stressigen Zeiten weniger oft bei euch gemeldet habe!

Der größte Dank geht an meine Familie! Danke **Cornelie**, **Uwe**, **Christoph** und **Vanessa,** für das Stärken meines frühen Interesses an der Wissenschaft, jegliche Unterstützungen auch während meines Studiums und meiner Promotion. Und vielen Dank, dass ihr stets für mich da wart, meine Gefühlsausbrüche ertragen habt und mir alles ermöglicht, was ich mir in den Kopf setze, wie zum Beispiel ein Praktikum in Neuseeland oder ein Semester in Finnland. Ich möchte auch meiner Schwiegerfamilie **Cornelia**, **Peter**, **Leonie** und **Dorothee** danken, dass ihr mich so herzlich in eure Familie aufgenommen habt!

Zu guter Letzt danke ich **Philip** aus tiefstem Herzen, du bist mein größter Unterstützer, hast stets an mich geglaubt, mich in allen Lebenslagen ermutigt und du hast mir wahnsinnig viel Kraft gegeben. Meinen geliebten Samtpfoten **Cleo** und **Freya** danke ich für die Geduld, die bedingungslose Liebe, ihre Persönlichkeiten und ihre Fähigkeit mich von einem auf den anderen Moment allen Stress und alle Sorgen vergessen zu lassen.

Abstract

For the design of smart materials with specific properties deep knowledge of the building units, the driving forces and the (non-)covalent interactions forming the assemblies is needed. By choosing supramolecules with an intrinsic functionality, cavity and properties as building units, the in-built functionalities are implemented into materials.

Pillarplexes $[M_8L_2](X)_4$ are organometallic complexes, which exhibit a hydrophobic, tubular cavity. These supramolecules are built up by two macrocyclic ligands linearly connected through eight metal(I) ions and are characteristic for their tuneable solubility dependent on the counter anion, intrinsic luminescence dependent on the metal ions and shape-selective guest encapsulation of linear alkyl chains over sterically branched aromatic systems. To utilise such pillarplex salts as building units, both the behaviour in the solid-state and synthetic modifications of the systems were evaluated.

The literature-known pillarplex salts $[Ag_8L^{Me}_2](PF_6)_4$, $[Au_8L^{Me}_2](PF_6)_4$, $[Ag_8L^{Me}_2](OAc)_4$ and $[Au_8L^{Me}_2](OAc)_4$ were analysed by SC-XRD measurements, which revealed particularly interesting crystal arrangement dependent on the metal ions and the occurring non-covalent interactions with counter anions or solvent molecules. To test the potential of these pillarplex salts concerning their guest uptake in the solid-state, gas adsorption of bulk material was investigated towards N_2 and CO_2. In general, the Au(I) congeners exhibited lower guest uptake and for the respective $[M_8L^{Me}_2](OAc)_4$ salts a lower resulting gas uptake was monitored probably due to the partial encapsulation of the acetate anions. Remarkably, different affinity of $[M_8L^{Me}_2](PF_6)_4$ to C_4 hydrocarbons (*n*-butane, *trans*-2-butene, *iso*-butylene, 1,3-butadiene) was observed with the highest uptake for 1,3-butadiene and decreasing uptakes of *trans*-2-butene to *iso*-butylene to butane most probably resulted by kinetic diameter and polarisability. The library of pillarplex salt $[M_8L^{Me}_2](X)_4$ with X as counter anion was expanded by anion exchange reactions using precipitation or anion exchange resins. The successfully synthesised salts, $[Ag_8L^{Me}_2](F)_4$, $[Ag_8L^{Me}_2](Cl)_4$, $[Ag_8L^{Me}_2](Br)_4$, $[Ag_8L^{Me}_2](I)_4$, $[Au_8L^{Me}_2](Cl)_4$, $[Au_8L^{Me}_2](Br)_4$, $[Ag_8L^{Me}_2](SCN)_4$, $[Ag_8L^{Me}_2](NO_3)_4$, $[Ag_8L^{Me}_2](ClO_4)_4$ and $[Ag_8L^{Me}_2](BF_4)_4$ were analysed towards their chemical composition by NMR spectroscopy, elemental analysis, mass spectrometry, and further methods. Additionally, crystallisation attempts were performed to determine the arrangement in the solid-state, however no single crystals were obtained. For $[Ag_8L^{Me}_2](BF_4)_4$ microcrystalline powder was subjected to electron diffraction, which revealed a highly symmetrical arrangement in the solid-state with a chain and pore alignment of the pillarplex cations and hence the formation of a quasi-continuous channelled cavity. All pillarplex salts were analysed towards their gas adsorption towards N_2 and CO_2, where high dependency of the gas uptake on the counter anion was observed. The potential to synthesise mixed anion pillarplex salts was discovered as structure determination by X-Ray diffraction revealed the mixed salts $[Au_8L^{Me}_2](PF_6)_{2.5}(AuCl_2)_{1.5}$ and $[Ag_8L^{t}_2]_2(PF_6)_5(OTf)_3$. Aromatic counter anions were implemented in the pillarplex system using a pseudorotaxane, which contained a 1,12-diammonium guest molecule and terephthalate units as counter anions. These aromatic counter anions displayed a strong influence of the π-interactions towards the crystal packing.

First steps using the pillarplex as a building unit to implement into materials were tested by introducing a bromide group at the pyrazole unit of the organic ligand. This late-stage modification at the macrocyclic ligand yielded the brominated ligand $L^{Br}(PF_6)_4$ and further conversion to the respective $[M_8L^{Br}_2](PF_6)_4$ pillarplexes was accomplished. The brominated compounds were fully characterised by common analytical methods, and the influence of the bromide group was investigated by X-Ray diffraction measurements. Here, the bromide groups

dictated the arrangement by non-classical hydrogen bonding with the hydrogen atoms and by metal coordination with the Ag(I) metal ions of neighbouring $[M_8L^{Br}_2]^{4+}$ cations. Even tough further modifications towards functionalised groups, such as dicarboxylic acids or pyridine units, were attempted, so far no positive results were obtained.

Another method for the implementation of pillarplexes into network materials was achieved using the host-guest chemistry of pillarplexes. By encapsulation of alkyl chains with functionalised end groups, such as carboxylic acids, so-called pseudorotaxanes are formed. The encapsulation of α,ω-dicarboxylic acids with different lengths of the alkyl chains was investigated towards their formation, their chemical composition, their crystal arrangement and their thermal stability. The binding affinities of the respective host-guest complexes was determined by NMR and isothermal calorimetry titration experiments. Various attempts were tried to coordinate the carboxylate units with either metal precursors or by organic polymerisation reactions. While the guest molecules bearing small end groups can slip of the ring component, introduction of sterically demanding stopper motifs form mechanically interlocked molecules, known as rotaxanes. According to a literature-known procedure, the synthesis of the rotaxane $[M_8L^{Me}_2][Py](PF_6)_4$, which are bearing a pyridine unit as stopper motif, was achieved and characterised in term of its chemical composition. Until now, no single crystals suitable for SC-XRD analysis could be obtained, nor was it possible to coordinate the pyridine units to a metal precursor.

Besides the investigation of $[M_8L_2](X)_4$ as building unit, $[Au_8L^{Me}_2](PF_6)_4$ was photophysical examined to understand quenching of emission due to guest encapsulation in solution or the occurrence of aggregation-induced emission at different solvent ratios. The synthesis of rotaxanes containing chromophores as stopper motifs for potential communication between the stopper motif and the pillarplex rim was tested by the introduction of *N*-naphthalimide building units. Additionally, the lability of the Ag(I)-pillarplex was used to achieve the formation of further supramolecular architectures, where a complex bearing three macrocyclic ligands and twelve Ag(I) ions was observed and called trillarplex due to a triangular arrangement of inner Ag(I) ions and a S-shaped complex with a partially protonated macrocyclic ligand and six Ag(I) ions was discovered. The pillarplex $[Ag_8L^{Me}_2](PF_6)_4$ was further tested towards the encapsulation of perfluorinated substances into the cavity to potentially use the non-water soluble pillarplex salt in the solid-state as sponge material to selectively adsorb perfluorinated compounds. Only partial encapsulation of the tested compounds PFOA and GenX was detected by NMR spectroscopy. The scope of guest molecules was expanded to five-membered heterocycles by the encapsulation of THF into $[Ag_8L^{Me}_2](PF_6)_4$.

Zusammenfassung

Für die Entwicklung intelligenter Materialien mit spezifischen Eigenschaften ist eine genaue Kenntnis der Bausteine, der treibenden Kräfte und der (nicht-)kovalenten Wechselwirkungen, die die Baueinheiten bilden, erforderlich. Durch die Auswahl von Supramolekülen mit einer intrinsischen Funktionalität, einem Hohlraum und Eigenschaften als Bauelemente werden die eingebauten Funktionalitäten in Materialien implementiert.

Die Pillarplexe $[M_8L_2](X)_4$ sind metallorganische Komplexe, die einen hydrophoben, röhrenförmigen Hohlraum aufweisen. Diese Supramoleküle bestehen aus zwei makrozyklischen Liganden, die über acht Metall(I)-Ionen linear verbunden sind und zeigen eine einstellbare Löslichkeit in Abhängigkeit vom Gegenanion, eine von den Metallionen abhängige intrinsische Lumineszenz und einen formselektiven Gasteineinschluss von linearen Alkylketten gegenüber sterisch verzweigten aromatischen Systemen. Um diese Pillarplexsalze als Bausteine zu nutzen, wird ihr Verhalten im festen Zustand und die synthetische Modifikation der Systeme untersucht.

Die literaturbekannten Pillarplexsalze $[Ag_8L^{Me}_2](PF_6)_4$, $[Au_8L^{Me}_2](PF_6)_4$, $[Ag_8L^{Me}_2](OAc)_4$ und $[Au_8L^{Me}_2](OAc)_4$ wurden durch SC-XRD-Messungen analysiert, welche besonders interessante Anordnung im Kristall in Abhängigkeit von den Metallionen und den auftretenden nicht-kovalenten Wechselwirkungen mit Gegenanionen oder Lösungsmittelmolekülen ergaben. Um das Potenzial dieser Pillarplexsalze hinsichtlich ihrer Gasaufnahme im festen Zustand zu testen, wurde die Gasadsorption des Bulkmaterials gegenüber N_2 und CO_2 untersucht. Im Allgemeinen wiesen die Au(I)-Spezies eine geringere Gastaufnahme auf und für die entsprechenden $[M_8L^{Me}_2](OAc)_4$ Salze wurde eine geringere Gasaufnahme beobachtet, welcher wahrscheinlich auf den teilweisen Einschlusses der Acetatanionen zurückzuführen ist. Interessanterweise wurde eine unterschiedliche Affinität von $[M_8L^{Me}_2](PF_6)_4$ zu C_4-Kohlenwasserstoffen (*n*-butan, *trans*-2-buten, *iso*-butylen, 1,3-butadien) beobachtet, wobei die höchsten Aufnahme für 1,3-Butadien und eine abnehmende Aufnahme von *trans*-2-Buten über *iso*-Butylen bis hin zu Butan zu verzeichnen war. Dies kann auf den kinetischen Durchmesser und die Polarisierbarkeit zurückgeführt werden. Die Bibliothek der Pillarplexsalze $[M_8L^{Me}_2](X)_4$ mit X als Gegenanion wurde durch Anionenaustauschreaktionen mittels Fällung oder Anionenaustauscherharzen erweitert. Die erfolgreich synthetisierten Salze $[Ag_8L^{Me}_2](F)_4$, $[Ag_8L^{Me}_2](Cl)_4$, $[Ag_8L^{Me}_2](Br)_4$, $[Ag_8L^{Me}_2](I)_4$, $[Au_8L^{Me}_2](Cl)_4$, $[Au_8L^{Me}_2](Br)_4$, $[Ag_8L^{Me}_2](SCN)_4$, $[Ag_8L^{Me}_2](NO_3)_4$, $[Ag_8L^{Me}_2](ClO_4)_4$ und $[Ag_8L^{Me}_2](BF_4)_4$ wurden mittels NMR-Spektroskopie, Elementaranalyse, Massenspektrometrie und weiteren Methoden auf ihre chemische Zusammensetzung untersucht. Zusätzlich wurden Kristallisationsversuche durchgeführt, um die Anordnung im festen Zustand zu bestimmen, jedoch wurden keine Einkristalle ausreichender Größe erhalten. Für $[Ag_8L^{Me}_2](BF_4)_4$ wurde mikrokristallines Pulver einer Elektronenbeugung unterzogen, die eine hochsymmetrische Anordnung im Festkörper mit einer Ketten- und Porenausrichtung der Pillarplex-Kationen und damit die Bildung eines quasi-kontinuierlichen kanalförmigen Hohlraums ergab. Alle Pillarplexsalze wurden auf ihre Gasadsorption an N_2 und CO_2 untersucht, wobei erneut eine starke Abhängigkeit der Gasaufnahme von der Wahl des Gegenanions festgestellt wurde. Das Potential zur Synthese von Pillarplexsalzen mit gemischten Anionen zeigte sich, als die Strukturbestimmung mittels Röntgenbeugung die gemischten Salze $[Au_8L^{Me}_2](PF_6)_{2.5}(AuCl_2)_{1.5}$ und $[Ag_8L^{t}_2]_2(PF_6)_5(OTf)_3$ ergab. Aromatische Gegenanionen wurden in das Pillarplex-System mit Hilfe eines Pseudorotaxanes implementiert, welches ein 1,12-Diammonium Gastmolekül und

Terephthalat-Einheiten als Gegenanionen enthielt. Diese aromatischen Gegenanionen zeigten einen starken Einfluss der π-Wechselwirkungen auf die Kristallpackung.

Erste Schritte zur Verwendung des Pillarplexes als Baustein für die Implementierung in Materialien wurden durch die Einführung einer Bromgruppe an der Pyrazol-Einheit des organischen Liganden getestet. Diese späte Modifikation am makrozyklischen Liganden ergab den bromierten Liganden $L^{Br}(PF_6)_4$, und die weitere Umwandlung in die entsprechenden $[M_8L^{Br}_2](PF_6)_4$ Pillarplexe wurde durchgeführt. Die bromierten Verbindungen wurden mit gängigen Analysemethoden vollständig charakterisiert und der Einfluss der Bromgruppe wurde durch Röntgenbeugungsmessungen untersucht. Dabei diktieren die Bromgruppen die Anordnung durch nicht-klassische Wasserstoffbrückenbindungen mit den Wasserstoffatomen und durch Metallkoordination mit den Ag(I)-Metallionen der benachbarten $[M_8L^{Br}_2]^{4+}$ Kationen. Auch wenn weitere Modifikationen in Richtung funktionalisierter Gruppen, wie Dicarbonsäuren oder Pyridin-Einheiten, versucht wurden, wurden bisher keine positiven Ergebnisse erzielt.

Eine weitere Methode zur Implementierung von Pillarplexen in Netzwerkmaterialien wurde mit Hilfe der Wirt-Gast-Chemie von Pillarplexen erreicht. Durch den Einschluss von Alkylketten mit funktionalisierten Endgruppen, wie z.B. Carbonsäuren, entstehen sogenannte Pseudorotaxane. Der Einschluss von α,ω-Dicarbonsäuren mit unterschiedlich langen Alkylketten wurde im Hinblick auf ihre Bildung, ihre chemische Zusammensetzung, ihre Kristallanordnung und ihre thermische Stabilität untersucht. Die Bindungsaffinitäten der jeweiligen Wirt-Gast-Komplexe wurden durch NMR- und isothermische Kalorimetrie-Titrationsversuche bestimmt. Es wurden diverse Versuche unternommen, die Carboxylat-Einheit entweder mit Metallpräkursor oder durch organische Polymerisationsreaktionen zu koordinieren. Während die Gastmoleküle, die kleine Endgruppen tragen, von der Ringkomponente abrutschen können, bildet die Einführung von sterisch anspruchsvollen Stoppermolekülen mechanisch verzahnte Moleküle, die als Rotaxane bezeichnet werden. Nach einem literaturbekannten Verfahren wurde die Synthese des Rotaxans $[M_8L^{Me}_2][Py](PF_6)_4$, welches eine Pyridin-Einheit als Stoppermolekül trägt, erreicht und hinsichtlich seiner chemischen Zusammensetzung charakterisiert. Bisher konnten weder für die SC-XRD Analyse geeignete Einkristalle erhalten werden, noch war es möglich, die Pyridin-Einheiten mit einem Metallpräkursor zu koordinieren.

Neben der Untersuchung von $[M_8L_2](X)_4$ als Baustein wurde $[Au_8L^{Me}_2](PF_6)_4$ photophysikalisch untersucht, um das Quenching der Emission aufgrund des Einschlusses von Gästen in Lösung oder das Auftreten von aggregationsinduzierter Emission bei unterschiedlichen Lösungsmittelverhältnissen zu verstehen. Die Synthese von Rotaxanen, welche Chromophore als Stopper Motive erhalten, um eine mögliche Kommunikation zwischen dem Stoppermolekül und dem Pillarplex-Rand zu erzielen, wurde durch die Einführung von *N*-Naphthalimid Einheiten getestet. Zusätzlich wurde die Labilität des Ag(I)-Pillarplexes genutzt, um die Bildung weiterer supramolekularer Architekturen zu erreichen, wobei ein Komplex mit drei makrozyklischen Liganden und zwölf Ag(I)-Ionen beobachtet und aufgrund der dreieckigen Anordnung der inneren Ag(I)-Ionen als Trillarplex bezeichnet wurde, sowie ein S-förmiger Komplet mit einem teilweise protonierten makrozyklischen Liganden und sechs Ag(I)-Ionen entdeckt wurde. $[Ag_8L^{Me}_2](PF_6)_4$ wurde des Weiteren im Hinblick auf den Einschluss perfluorierter Substanzen in den Hohlraum getestet, um das nicht wasserlösliche Pillarplex-Salz im festen Zustand als Schwammmaterial zur selektiven Adsorption perfluorierter Verbindungen zu nutzen. Durch NMR-Spektroskopie wurde nur ein teilweiser Einschluss der Verbindungen PFOA und GenX nachgewiesen. Der Umfang von Gastmolekülen wurde durch den Einschluss von THF in $[Ag_8L^{Me}_2](PF_6)_4$ auf fünfgliedrige Heterozyklen ausgeweitet.

List of Abbreviations

Å	Ångström (10^{-10} m)
a	pore opening
A	additive
AcOH	acetic acid
act	activated
ADP	atomic displacement parameter
as	as synthesised
ATR	attenuated
b	inner pore diameter
BDC	benzene-1,4-dicarboxylic acid
BET	Brunauer-Emmett-Teller
BJ	Becke-Johnson
bq	2,5-dihydroxy-1,4-benzoquinone
ca.	about (lat. circa)
cal.	calculated
CB[n]	cucurbit[n]uril
CD	cyclodextrin
COF	covalent organic framework
COP	covalent organic polymer
COSY	correlated spectroscopy
CP	coordination polymer
CSD	Cambridge Structural Database
Cy	cyclohexyl
d	distance
D	dimensional
DA	dodecyl diammonium
DAniF	*N*,*N*`-di-p-anisylformamidine
DCC	*N*,*N*`-dicyclohexylcarbodiimid
DCM	dichloromethane

DFT	density functional theory
DIPEA	diisopropylethylamine
DLS	dynamic light scattering
DMF	*N*,*N*-dimethylformamide
2,6-DMP	2,6-dimethylpyridine
DMSO	dimethyl sulfoxide
DNA	deoxyribonucleic acid
DOSY	diffused-ordered spectroscopy
DPEA	dipropyl ethylamine
EA	elemental analysis
EB	ethylbenzene
ED	electron diffraction
em	emission
eq.	equivalent
ESI	electron spray ionisation
Et_2O	diethyl ether
EtOH	ethanol
EtP[n]	ethylated pillar[n]arene
ex	excitation
FT IR	Fourier transformation infrared spectroscopy
G	guest
GenX	ammonium perfluoro(2-methyl-3-oxahexanoate)
GPC	gel permeation chromatography
h	height
H	host
HepG2	human liver cancer cell line (epithelial-like)
HG	host-guest complex
HKUST	Hong Kong University of Science and Technology
HSQC	heteronuclear single quantum coherence
HT	high temperature
i.e.	that is (lat. id est)

ITC	isothermal titration calorimetry
*i*Pr	*iso*propyl
IUPAC	International Union of Pure and Applied Chemistry
K_a	association constant
K_d	dissociation constant
L	variable ligand
lat.	latin
L^{Br}	brominated ligand
L^{Me}	methylene bridged ligand
L^{t}	triazole ligand
L^{X}	substituted ligand
M	variable metal
MD	molecular dynamics
MeCN	acetonitrile
MeOH	methanol
MHz	megahertz
MIC	mesoionic carbene
MIM	mechanically interlocked molecule
MMF	metal-macrocyclic framework
MOF	metal-organic framework
MOP	metal-organic polyhedra
MORF	metal-organic rotaxane framework
MP	metal precursor
MS	mass spectrometry
*m*X	*meta*-xylene
m / z	mass-to-charge ratio
NAC	non-porous adaptive crystal
NaOH	sodium hydroxide
NBS	*N*-bromo succinimide
NHS	*N*-hydroxy succinimide
NIR	near-infrared

NOESY	nuclear Overhauser enhancement spectroscopy
NHC	*N*-heterocyclic carbene
NDI	naphthalene diimide
NMI	naphthalene monoimide
*N*MMI	*N*-methyl naphthalene monoimide
NMR	nuclear magnetic resonance
*N*ONI	*N*-octyl naphthalimide
OAc	acetate anion
OR	variable alkoxy substituent
OTf	triflate anion
ox	oxalic acid / ethanedioic acid
*o*X	*ortho*-xylene
P[n]	pillar[n]arene
PAH	polyaromatic hydrocarbon
PBE	Perdew-Burke-Ernzerhof
PCP	porous coordination polymer
PFC	perfluorinated compound
PFOA	perfluorooctanoic acid
Ph	phenyl
PMC	porous molecular crystal
ppm	parts per million
PR	pseudorotaxane
*p*X	*para*-xylene
PXRD	powder X-Ray diffraction
Py	Pyridine
R	variable substituent
rt	room temperature
SCC	supramolecular coordination complex
SC-XRD	single crystal-X-ray diffraction
SEM	scanning electron microscope
SOC	supramolecular organometallic complex

SPhos	dicyclohexyl(2′,6′-dimethoxy[1,1′-biphenyl]-2-yl)phosphane
SPN	supramolecular polymer network
SPS	solvent purification system
sq	squaric acid
St	styrene
Stoic.	stoichiometry
SVP	split valence polarisation
TBA	tetrabutyl ammonium
TE	template
t-Bu	*tert*-butyl
TfOH	trifluoromethanesulfonic acid
TGA	thermogravimetric analysis
THF	tetrahydrofuran
thp	tetrahydropyran-2-yl
THT	tetrahydrothiophene
TM	transition metal
UV-vis	ultraviolet visible
viz.	namely (lat. videlicet)
vs.	versus
VT	variable temperature
X	variable anion
XantPhos	(9,9-Dimethyl-9*H*-xanthene-4,5-diyl)bis(diphenylphosphane)
XPhos	dicyclohexyl[2′,4′,6′-tris(propan-2-yl)[1,1′-biphenyl]-2-yl]phosphane

Table of Content

1. Introduction

For the development of new materials with specific physical properties a fundamental understanding of the self-assembly and the structure-function relationships is crucial and predictive design principles must be created.[1-5] Porous materials gained more interest from industry and academia due to their outstanding structural diversity / versatility[6-8] and their applicability towards uptake of guest molecules, gas adsorption / separation[9-15] and sensing, catalysis.[16-22]

Through the introduction of pre-defined motifs by using supramolecular host systems with an intrinsic porosity, a certain control over the structure and composition of the obtained porous material is gained.[23-28] However, while using pre-defined building units, the better the understanding of the properties and the reactivity of the building blocks is, the better predictions of the properties and the reactivity of the interconnected assemblies in the solid-sate and their applicability can be made.[29-34] The underlaying principle is called crystal engineering[5,35-38], where synthetic chemistry is applied to crystallisation processes. Design and control of structure and properties of the produced materials is achieved by knowledge concerning the optimal intermolecular interactions along with topology, shape, electronic and chemical properties. Especially the presence of cavities allows pore engineering by a functionalisation of the ligand or anchoring of substituents inside the pore, which for example exhibit catalytic sites.[39-41]

1.1 Supramolecular Chemistry and Mechanostereochemistry

Supramolecular chemistry described as the “chemistry beyond the molecule” deals with the (self-)assembly of two or more molecular species and their (non-)covalent interactions.[42-44] By applying principles obtained from nature to molecular systems, Charles J. Pedersen, Donald J. Cram and Jean-Marie Lehn were awarded the Nobel price 1987 “for their development and use of molecules with structure-specific interactions of high selectivity”. Due to common working principles of supramolecular chemistry and biological systems, artificial supramolecular systems mimicking biological systems are designed for a broad variety of applications.[44-47]

The intermolecular interactions are of non-covalent nature such as ion-ion, ion-dipole, dipole-dipole, hydrogen bonding, cation-π, anion-π , π-π interactions, induced dipolar interactions, polarisability, van der Waals forces, solvation effects , hydrophobic effects, halogen bonding and metallophilic interactions within a defined molecular architecture (size, geometry), which is capable of recognising anions, cations and neutral species in a strong and selective way and forming supramolecular entities.[36,42,45,48-49] The binding of one molecule with another one by non-covalent interactions produces a host-guest complex or supramolecule, where the host exhibits convergent binding sites inside a cavity and the guest exhibits divergent binding sites.

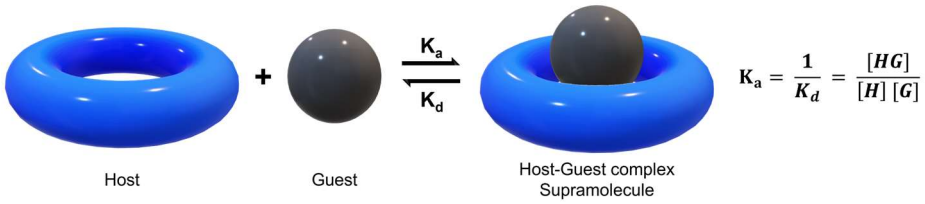

$$K_a = \frac{1}{K_d} = \frac{[HG]}{[H]\,[G]}$$

Figure 1: Schematic representation of the equilibrium between host and guest and the host-guest complex with the formula for the binding constant K_a.

Key focus of the supramolecular chemistry is the investigation of the thermodynamic stability of host-guest interactions in solution, which is described by the binding constant K in a specific solvent at a given temperature (Figure 1). In biochemistry the concentrations [H], [G] and [HG] can be determined by e.g., electrophoresis[50-51], however for most host-guest equilibria no direct determination of the concentration [HG] is possible and the binding constants are determined by titrations experiments.[52] First, an appropriate binding model based on the stoichiometry of host to guest must be applied followed by a suitable titration method, such as NMR titration, fluorescence titration, UV-vis spectrophotometric titration, potentiometric titration, calorimetric titration or isothermal titration calorimetry (ITC).[52-53] Several factors (e.g., solvation or desolvation effects[54]) can influence the formation of a host-guest complex and hence the binding constant. The pore opening of a host molecule is predefined by the structural configuration, however taking binding site cooperativity, multivalency, chelating effects, pre-organisation and complementarity into account stable host-guest complexes can be designed. The host systems can either be synthesised bearing in-built properties or can be post-synthetically modified to introduce specific functionalities to exhibit specific guest binding (Figure 2A).[55]

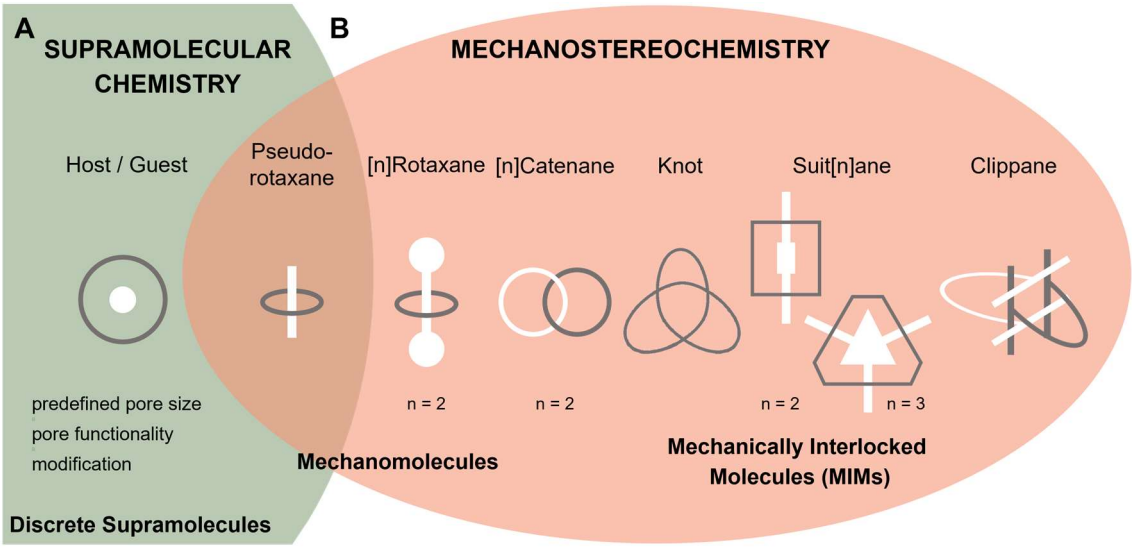

Figure 2: Schematic representation of (A) supramolecular chemistry dealing with discrete host-guest complexes exhibiting a predefined pore size, functionality, and the possibility for modification; (B) mechanostereochemistry dealing with the stereochemistry of mechanomolecules, which are connected by a mechanical bond and mechanically interlocked molecules (MIMs), where the two or more components cannot be separated without breaking a covalent bond. Exemplary the mechanomolecule as pseudorotaxane is displayed and the following exemplary MIMs are displayed: [n]rotaxanes, [n]catenanes with n interlocked architectures, molecular knots with foiled chains, suit[n]anes with a suit as host molecule and a guest molecule consisting of a body with n limbs pointing

outwards of the pore opening of the host molecule and clippanes with interconnected metallo-tweezers by sterically demanding side groups. Varied and taken from [56].

By the encapsulation of a linear guest molecule into a ring-shaped host molecule a pseudorotaxane is formed. Pseudorotaxanes are a class of rotaxanes where the two components can dissociate without breaking a covalent bond[57] and the further introduction of bulky sterically demanding stopper motifs can convert the pseudorotaxane into a rotaxane (Figure 2B).[58-59] The entanglement of two or more components in space is defined as a mechanical bond, when no separation of the units without breaking or distorting a covalent bond is possible.[56,60-61] Thus, molecules exhibiting at least one mechanical bond are called mechanomolecules and their stability is defined by the weakest covalent bond. When handling the structure, the spatial arrangement of atoms in molecules and the overall topology of such mechanomolecules, the term mechanostereochemistry is applied.[56,60] Such entangled molecules are also called mechanically interlocked molecules (MIMs) with the typical structural motifs of rotaxanes and catenanes (Figure 2B).[58,62] As MIMs can carry more than one mechanical bond, high-ordered entanglement opens up the possibility of divers topologies with the famous example of the olympiadane, where five interlocked macrocycles form a topology similar to the Olympic rings[63] or the molecular knots (Figure 2B)[64-66], which are mainly folded with the templating effect of metal ions.[67] The more recently introduced suitanes (Figure 2B)[68-70] are two-component MIMs with the host molecule acting as a suite fitting around the guest molecule, which can be described as a body with limbs pointing outwards of the pore openings of the host molecules. The number of limbs defines the nomenclature and hence the presence of two limbs leads to the name suit[2]ane. Recently, the synthetic approach by slippage was achieved for a suit[4]ane, where the host molecule opens up the pore opening at high temperatures with a following uptake of the guest molecule forming the locked topology at lower temperatures.[69] Synthesised by a similar slippage procedure, two metallo-tweezer can be combined to a so-called clippane (Figure 2B).[71] Here, a sterically demanding *tert*-butyl (*t*-Bu) group is introduced, which hinders the dissociation of the two metallo-tweezers and only through breakage of a covalent bond a disassembly would be possible, which defines the clippanes as MIM.[71] As seen in the mentioned examples, the mechostereochemistry results in mechanomolecules with unique properties, unique topologies and functionality.[60,72] These properties are the combined result of the coordinative, non-covalent and dynamic covalent bonding interactions that exists between the compounds of the MIMs. Such architectures can be responsive towards external stimuli, which makes them suitable for the manufacture of molecular switches and machines undergoing large-amplitude motions in a controlled and reversible way. In this area of research, the Nobel price in 2016 was awarded to Jean-Pierre Sauvage, Sir J. F. Stoddart and B. L. Feringa for the “design and synthesis of molecular machines”. Here, F. Stoddart examined the field of rotaxanes and their incorporation into molecular shuttles, switches and lifts.[61,73-76]

An important part is the synthetic accessibility, which is challenging since the formation of MIMs is intrinsically entropically unfavoured and hence, synthesis strategies have to be developed.[77] By only involving the random probability of interpenetration of cyclic and acyclic components with sufficient size, the statistical synthesis was used for first synthetic attempts (Figure 3A).[60] As expected, the formed MIMs were isolated in low yields and were difficult to separate from the residual reagents. To address these disadvantages of the statistical synthesis, the pre-organisation of the components around a covalent template with cleavage after synthesis, the direct synthesis was established (Figure 3B).[77] Although the direct synthesis exhibits higher efficiency, numerous synthetic steps still must be performed to yield

the MIM. Hence, the template-directed synthesis (Figure 3C+D) was established as the most successful synthetical strategy, where MIMs are formed by the presence of templates through occurring non-covalent bonding interactions.[78-79] An active template (e.g., metal ions) serves not only as the template but acts additionally as a catalyst driving the reaction towards the formation of the MIM.[60,77-79]

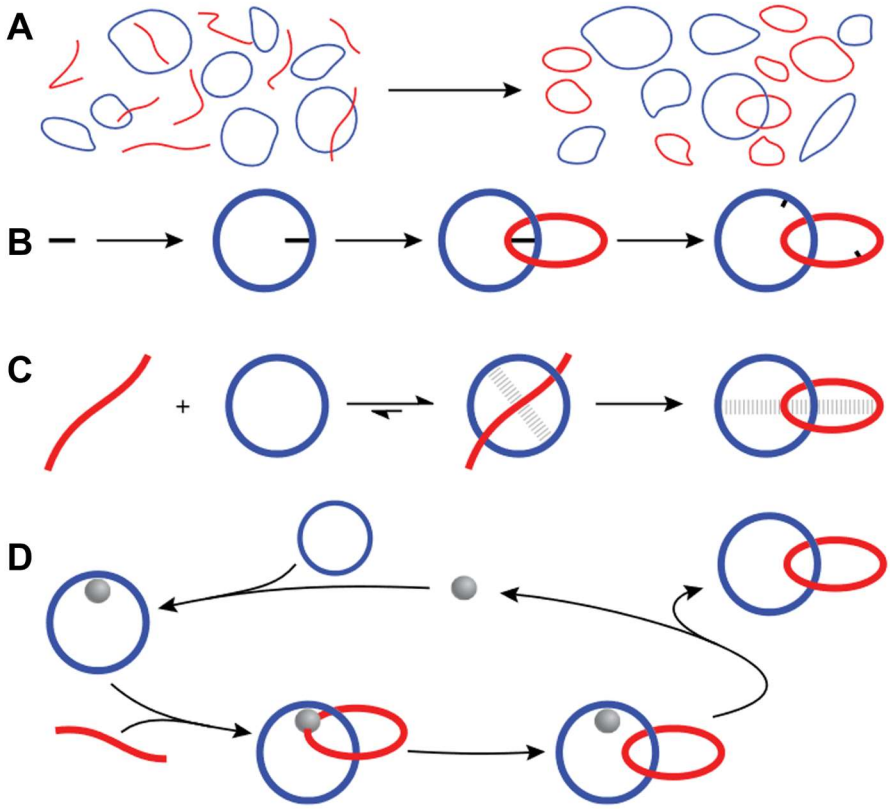

Figure 3: Schematic representation of synthesis strategies for the formation of MIMs shown exemplary for catenanes: (A) Statistical synthesis; (B) direct synthesis by a covalent template (black); (C) passive template-directed synthesis by non-covalent interaction (grey) and (D) active template-directed synthesis by a catalyst (grey sphere). Slightly varied and taken from [77].

By introducing metal ions into the synthesis of MIMs a great platform of template strategies *via* coordination chemistry is provided with high functionality.[59,80-83] However, the introduction of metal ions can increase the platform of structural architectures, properties (e.g., catalytic activity, sensing) and the modifiability of the synthesised supramolecules.[84]

1.2 Metallosupramolecular Chemistry

To overcome the limited post-synthetical modifiability and the design of elaborated molecular architectures, hosts featuring a metal-organic coordination were introduced. The molecular hosts were defined as metallocavitands, which are multi metallic complexes, where the metal coordination is necessary to form the cavity, and can be fine-tuned by the metal node or the multidental ligands.[48,84] Functionalities can be introduced by these ligand molecules, while their binding abilities determine the size, shape, geometry and functionality of the cavity. With a huge flexibility of metal and ligand the coordination self-assembly yields architectures in huge

dimensions which show possible applicability in molecular encapsulation, stabilisation of reactive species, supramolecular catalysis and drug delivery.[10,16,85]

By geometrically divergent combination of metal node and ligand so-called coordination polymers (CPs) or coordination networks such as metal-organic frameworks (MOFs) are formed (Figure 4A).[85] A CP exhibits the characteristics of a bridging ligand (organic or inorganic) between metal nodes forming 1D chains, which can be cross-linked and extended into 2D and 3D materials.[86] The presence of a measurable, permanent porosity can expand the materials into the porous coordination polymers (PCPs).[87] The specific combination of an organic bridging ligand in a 2D or 3D coordinated network with the potential for void space, is considered a metal-organic frameworks (MOFs).[86] However, no direct porosity must be displayed and dependent on the topology, the frameworks exhibit structural robustness and can be designed by assortment of ligand and metal node or post-synthetical modification. Although by combination of ligand and metal node, the pore of a MOF can be tuned, unwanted side-effects, such as the interpenetration can occur. Smart selection of ligand and metal node can assemble polymeric structures with high symmetry and an infinite porosity.

When mentioned in the following text, the abbreviations CPs, PCPs and MOFs will be used according to the aforementioned definitions.

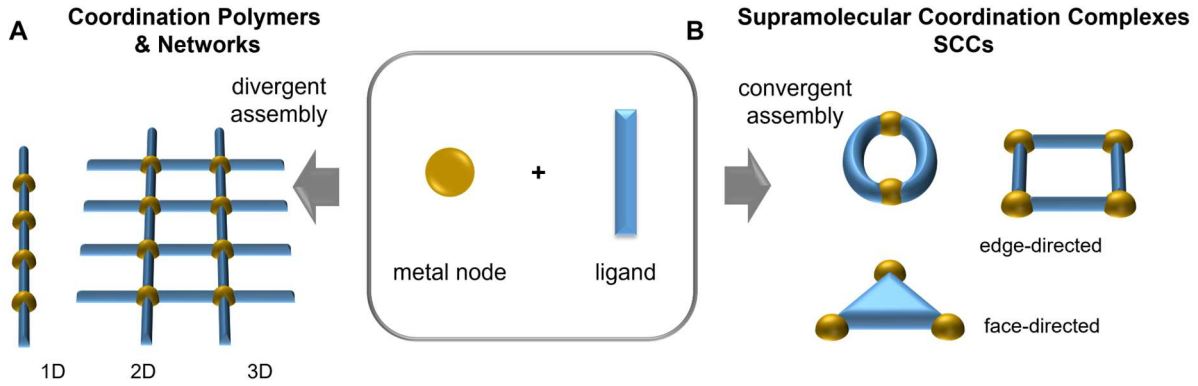

Figure 4: Schematic representation for the outcome of combining a metal node and a ligand motif: (A) Formation of coordination polymers or network materials by divergent assembly into more dimensional materials and (B) Formation of supramolecular coordination complexes by convergent assembly into discrete structures. Varied and taken from [85].

On the other hand, by convergent combination of metal node and ligand the discrete and well-defined supramolecular coordination complexes (SCCs) with either edge-directed or face-directed coordination are formed (Figure 4B).[88-91] These discrete organometallic assemblies can be formed by the node directionality (e.g., carbon metal bond in the metal node) or by the ligand properties, where a metal to carbon bond is implemented in the ligand. A dynamic SCCs, which can be reversibly assembled and disassembled, exhibits labile metal to ligand coordination, which allows the formation of the thermodynamical most stable complex.

Such molecular coordination complexes with a discrete composition and an internal pore can be referred to as metallacages[88,90], metal-organic cages[92-93] or metal-organic polyhedra[94-98] and in the following text the term metal-organic polyhedra (MOP) will be applied. The broad

parameter space of the ligand and the metal node geometries yields architectures such as cycles[88,99-100], tetrahedra[101-102] or helicates[103] (Figure 5).

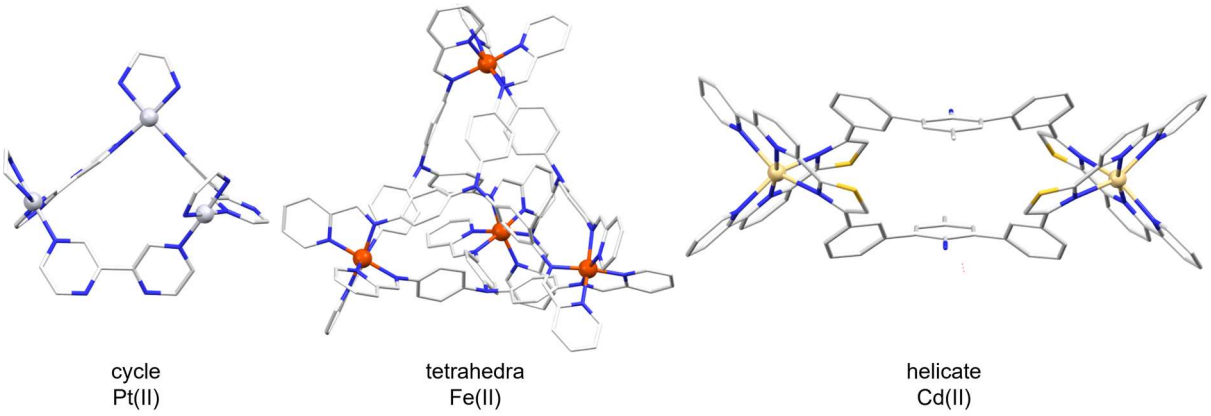

Figure 5: Examples of MOPs: Pt(II) cycle [(enPt(bpz-N4,N4`))$_3$](NO$_3$)$_2$(ClO$_4$)$_4$ · 2 H$_2$O with en = ethylenediamine, bpz = 2,2`-bipyrazine[99]; Fe(II) tetrahedra [Fe$_4$L$_4$](OTf)$_8$ with L containing triamine and pyridine units[104]; Cd(II) helicate [Cd$_2$(L^2)$_2$](ClO$_4$)$_5$ with L^2 containing thiazole-pyridyl donor units separated by a triphenylene unit with a amine group[105].

The microporous metal-organic polyhedra (MOPs) can be highlighted as building units for the synthesis of novel materials[95,97] since during the preparation of MOPs, the coordinative metal-to-ligand bond can be exploited to achieve discrete architectures, which can exhibit a permanent porosity in solution and in the solid-state.[94-97,106] Due to their discrete architecture, the number, nature and location of functional groups at the surface is known and hence, MOPs show orthogonal surface reactivity, meaning that one component of a MOP can react with a reagent without the other components reacting with the same reagent.[107-108] However, the functional pendant groups of the organic ligand, the open metal sites and the presence of counter-ions[93] provide great possibilities for covalent or coordinative post-synthetic modifications, which can tailor the solubility, stability and (surface) reactivity.[109-112] By the combination of intrinsic porosity and well-defined surface reactivity of MOPs, design strategies for the (hierarchical) self-assembly or polymerisation achieve the formation of controlled metal-organic porous materials by variation of stoichiometry, stability and solubility of the building units.[34,113-115]

Excursus: Organic Cavitands

Host molecules bear a cavity in solution and in the solid-state, allowing the host to engage with a guest molecule by versatile interactions and show a broad vary of size, shape and properties. Starting with purely organic compounds, such as the simple structure motive of the crown[n]ether and [n.n.n]cryptand (Figure 6A), where specific alkali metal ions can be encapsulated, led to more complex organic macrocyclic cavitands, which are container-shaped molecules. Trough introducing a tuneable cavity by varying the number and nature of included monomers (n), macrocyclic cavitands such as calix[n]arenes, n-cyclodextrins, pillar[n]arenes or cucurbit[n]urils were investigated (Figure 6B).[116-123] Defined by the monomer unit, the height of the cavitands is described by the parameter h, the large pore opening of the cavitands is defined as parameter a and the small pore opening is defined as parameter b. For the cucurbit[n]uril the parameter c is introduced for the inner pore diameter. The enforced cavity is usually a concave bowl or ring shape engaging with guest molecules based on matching size,

hydrophobic effect and electrostatic interactions. These supramolecules exhibit limited synthetical manipulation at the rim and by introducing a functionality, an improvement of solubility, an increase in cavity size or the alternation of non-covalent interactions can be achieved.[124-129]

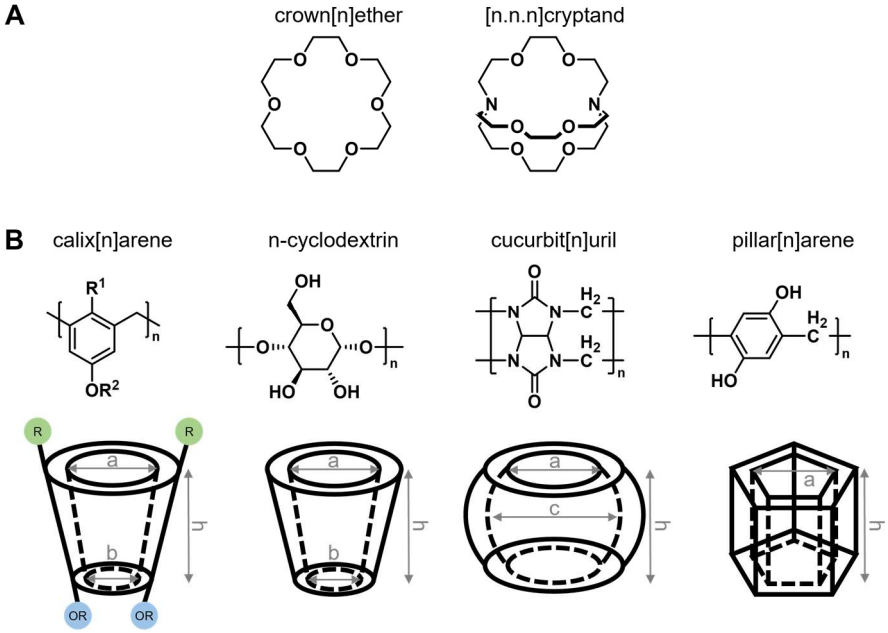

Figure 6: Chemical formula of exemplary organic cavitands: crown[n]ether, [n.n.n.]cryptand, calix[n]arene, n-cyclodextrin, pillar[n]arene and cucurbit[n]uril displayed concerning shape with selected parameters: h describes the height of the cavitand, a describes the (large) pore opening, b describes the (smaller) pore opening and c describes the inner pore diameter.

The calix[n]arene[116] are formed by the combination of *para*-substituted phenol units with formaldehyde exhibiting a cone-shaped hydrophobic π-binding cavity. On one side, a wider rim with substituents (R) and on the other side a narrow rim with the ether substituents exhibits a cone conformation due to the cyclic hydrogen bonding of the ether groups (OR). Upon guest encapsulation, conformational changes can occur due to breakage of the cyclic hydrogen bonding network and hence in solution a rotation around the aryl-methylene bridges is possible. Typical guest molecules are metal ions; for example, the calix[4]arene with a pore opening of a = 7.3 Å and b = 5.3 Å (h = 2.8 Å) (R^1 = -CH_3, R^2 = H) can selectively interact with Li^+ or Na^+ cation.[130]

By introducing rigidity in the conformation of host systems, the preorganisation effect yields an enhanced guest encapsulation of more complex organic species in solution. Through intramolecular hydrogen bonding and the sharp radius of n-cyclodextrins (n = 6, α-cyclodextrin; 7, β-cyclodextrin; 8, γ-cyclodextrin) a more rigid structural conformation of truncated funnels with a height of h = 7.8 Å is achieved.[117,119,131] The cyclic oligosaccharides can be divided into two rims, where the primary hydroxyl groups (-CH_2OH) form the narrow end of the funnel and the hydroxyl groups, directly attached at the six-membered rings, form the wider end of the funnel. With an edge-to-edge linkage of the six-membered rings and the faces pointing towards the inside a hydrophobic cavity is formed. Due to the hydrophilic alcohol groups cyclodextrins are soluble in water and guest encapsulation in aqueous environment is widely investigated. With a pore opening of a = 5.7 Å (b = 5.0 Å) for α-CD, the encapsulation of benzene or phenols (e.g., K = 758.58 for phenol in H_2O) is possible, while for β-CD already (substituted) naphthalene motifs can enter the cavity through the pore opening of a = 6.5 Å (b = 6.2 Å).[119]

The barrel-shaped cucurbit[n]urils (n = 5-14)[120,132] – named after pumpkins (lat. cucurbita) due to their similar shape – are host systems synthesised by the condensation of glycoluril and formaldehyde. During the synthesis a templating effect of oxonium ions (H_3O^+) through interactive coordination with the carbonyl atoms on both sides of the monomers takes place.[133] Interestingly, the uneven numbered supramolecules show solubility in water, while the even numbered supramolecules are less soluble in water. With a pore opening of a = 3.9 Å, an inner cavity c = 5.8 Å and a height of h = 9.1 Å, cucurbit[6]uril or CB[6] is an effective host for the encapsulation of polyamines and metal ions (e.g., Li^+, Mg^{2+}, Al^{3+})[134] in aqueous solutions and in the solid-state, where the host-guest complex is stabilised by a coordination with carbonyl functions of the rim.

With a similar shape, the pillar[n]arenes (n = 6-8(-14))[135] are synthesised from *para*-methylene-bridged hydroquinone derivatives and exhibit a height of h = 7.8 Å. However, these supramolecules exhibit a rigid hexagonal shape by extensive intramolecular hydrogen bonding with a planar chirality dictated by the orientation of the hydroquinone oxygens and show solubility in organic solvent. The most common ones are the pillar[5]arene (P[5]) with a pore opening of a = 4.7 Å, P[6] with a pore opening of a = 6.7 Å and P[7] with a pore opening of a = 8.7 Å. In the solid-state the mentioned derivatives enable microporous uptake of small molecules (e.g., N_2, CO_2), but in solution P[6] can also encapsulate aromatic systems, such as substituted xylene.[136] Interestingly, these organic host systems can be easily functionalised for example by the alkylation of the hydroxyl groups, which yields a lower rigidity due to the breakage of the hydrogen bond network.

Supramolecular Organometallic Complexes (SOCs)

Discrete organometallic assemblies of metal node and ligand, where the carbon metal bond is implemented in between metal node and ligand are called supramolecular organometallic complexes (SOCs).[85] In these SOCs the carbon-metal bond is structural decisive and hence crucial for the assembly and suitable ligand molecules include alkynyl, arenes or *N*-heterocyclic carbene (NHC) units with extended π-conjugated systems (Figure 7A). In the following, the term SOC will be used for complexes featuring a metal to carbon bond with typically NHC ligands and a cavity as previously defined. In general, these ligand motifs are very stable “spectator” ligands, which exhibit strong σ-donor and weak π-acceptor properties and have the possibility for finetuning of the electronic / steric properties or the solubility. The electronic and steric properties can be modified by synthetic modification; e.g. NHC ligands can be tuned by alternation of the wingtip and backbone positions without a huge impact onto the carbon metal bond.[137-138] Polyconjugated macrocyclic ligand motifs allow the synthesis of a broad variety of structural architectures with different pore sizes, influencing the host-guest chemistry by shape selectivity towards guest molecules. Most examples of SOCs contain metal nodes of group 11[139-140] – Ag(I), Au(I), Cu(I) – and NHC ligands with a linear coordination of the metal nodes facilitating a trans coordination of two NHC motifs, however other metals (Ni^{2+}, Ir^{2+}, Pd^{2+}, Pt^{2+}) have already been implemented into SOC architectures.[141-146] Strong NHC to metal bonds with late-stage metal complexes exhibit a static structure, which is strengthened by a synergistic effect of kinetic and thermodynamic stabilisation due to presence of macrocycles, and hence the reversible dissociation of SOCs is hindered.[140,147-148] Interestingly, for the self-assembly of Ag(I) with a bis-NHC ligand, which is built by the combination of a freely rotating imidazolylidene donor and a benzimidazolylidene unit, an equilibrium of tri- and tetranuclear complexes in solution on the NMR timescale was detected.

While the self-assembled tetranuclear Au(I)-complex shows a slow conversion in solution towards the respective trinuclear Au(I)-complex, which is boosted by the exposure to higher temperatures, no such conversion for the tetranuclear Cu(I)-complex was identified.[149-150]

By smart ligand design, various shapes can be achieved ranging from metallo-cylinders or metallo-cages[139,151-159], metallo-triangles or metallo-rectangles[144,149,160-162], metallo-folders to metallo-tweezer.[163-165] In Figure 7B-F various of these structure motifs are presented in a simplified manner.

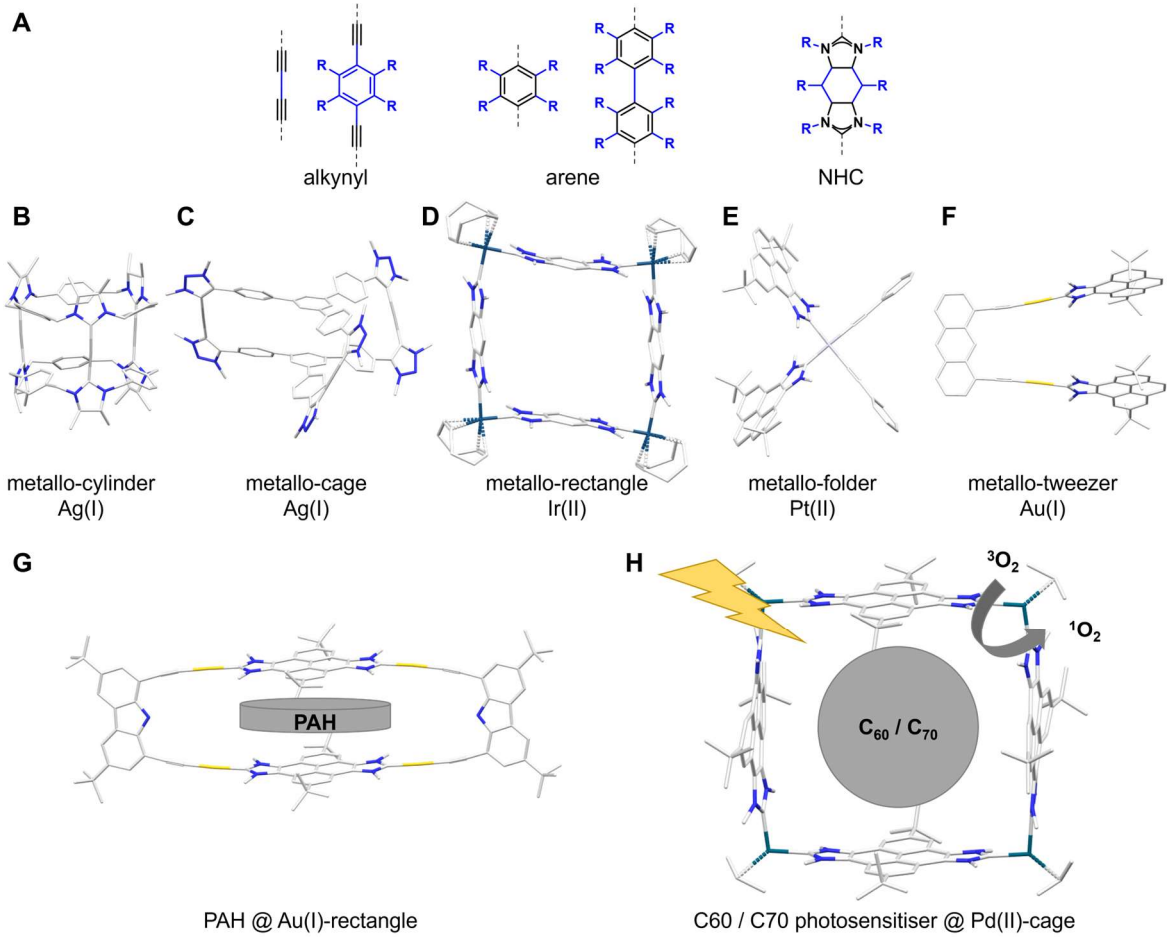

Figure 7: (A) Chemical structures of the ligand motifs with marked residues for modification; NHC-based SOCs including (B) metallo-cylinders, (C) cages, (D) rectangles, (E) folder and (F) tweezer; Exemplary schematic representation of host-guest complexes of (G) an Au(I)-rectangle examined towards selective encapsulation of polyaromatic hydrocarbons (PAH) and (H) a Pd(II)-cage with encapsulated fullerenes (C_{60} / C_{70}), which can act as efficient and photochemically stable photosensitiser to produce singlet oxygen for the oxidation of cyclic and acyclic alkanes.[140]

The metallo-cylinder $[Ag_3(CNHC)_2](BF_4)_3$ (Figure 7B) was synthesised *via* self-assembly at room temperature of the macrocyclic imidazoline salt with metal precursor Ag_2O in a "weak-base" approach.[166] Further testing the chiral Ag(I)-cylinder towards the enantioselective catalytic properties yielded a size-selective catalytic performance.[154] In a similar synthetic approach, metallo-cage $[Ag_3(L\text{-}MIC)_2](PF_6)_3$ (Figure 7C) was achieved, where the NHC motifs were exchanged by mesoionic carbenes (MICs) and transmetalation reactions with a Au(I) source yielded the respective $[Au_3(L\text{-}MIC)_2](PF_6)_3$ complex. Interestingly, by combination of $[Ag_3(L\text{-}NHC)_2](PF_6)_3$ and $[Au_3(L\text{-}MIC)_2](PF_6)_3$ a re-arrangement of the ligands towards the heteroleptic Ag(I) complex was noticed, indicating the lability of Ag(I) complexes in solution.[159]

The group of Hahn synthesised various metallo-rectangles by exploiting the linear coordination properties of NHC ligands to various metals including Ni(II), Ir(II), Pd(II) and Pt(II) (Figure 7D).[142,145-146] The implementation of mono-NHC ligands yields architectures such as the metallo-folder (Figure 7E) and the metallo-tweezer (Figure 7F). To synthesise the Pt(II) metallo-folder a *cis*-Pt(II) precursor and an imidazolium salt in the presence of a base formed a void space between the polyaromatic ligands, where electron-deficient aromatic compound can be trapped selectively by π-π stacking interactions.[167] However a relatively low affinity for guest encapsulation was explained by the orthogonal arrangement of the polyaromatic folders. Hence, the introduction of a ”connector” placed between the two flat, polyaromatic motifs in a parallel manner in a self-assembly reaction of Au(I)-NHC complexes with 1,8-diethynylanthracene was tested. This metallo-tweezer is stabilised by π- and aurophilic interactions and formed a dimer in the solid-state.[168] Taking the potential of π-π stacking and metallophilic interactions into account, the guest encapsulation of substituted polycyclic aromatic hydrocarbons was tested with an Au(I)-based rectangle (Figure 7G).[142,151,162,169-170] The size and nature of the obtained rectangle exhibited large binding affinity towards planar polyaromatic hydrocarbons (PAH), such as anthracene, pyrene or perylene, in DCM with an increasing binding affinity for PAHs with increasing numbers of π-electrons. Upon encapsulation of non-planar PAHs (e.g., corannulene) a loss in the binding energy was detected due to the straining effect.[162] The Pd(II) metallo-square displayed in Figure 7H exhibited strong guest encapsulation of the fullerenes C_{60} and C_{70} and showed good solubility and stability in organic solvents.[143,171] Due to the spin transfer properties of fullerenes, C60@Pd(II)-cage and C70@Pd(II)-cage were tested towards their applicability as photosensitiser to generate singlet oxygen.[172] This efficient and photochemically stable photosensitiser was able to generate singlet oxygen from air, which was used to oxidise cyclic and acyclic alkanes at room temperature and at atmospheric pressure.[172] Besides the described catalytic activity, SOCs were already investigated towards their potential as nano-vessels for size and shape constrained reactions[173], their potential for photo-induced cycloaddition[174] and photo- or redox-induced structural transformations by a change in the bond orientation.[158,164,175]

These structures are intriguing candidates for porous materials since their properties concerning porosity, such as pore size and shape in the solid-state, are highly dependent on the occurring non-covalent interactions and host-guest chemistry. The investigations of these structure-property relationships can be investigated by crystal engineering to tailor-make unique architectural landscapes, which can be altered by applying small changes. This makes crystal engineering an important tool to achieve functional porous materials by target-oriented design.

1.3 Supramolecules in Porous (Solid-State) Network Materials

The porosity of supramolecules can be exploited to either achieve porosity in liquids or solid-state materials. Porous liquids are at hand (Figure 8A), when the used solvent is not adsorbed by the supramolecules and leaves the pore vacant for the adsorption of smaller substrates.[176-178] This was presented by the group of *Cooper*, where rigid organic cages with an approximate pore diameter of 5 Å and approximate pore opening of 4 Å were dissolved in crown ether

(15-crown-5), which is liquid at room temperature and exhibits low surface curvature and which was not able to enter the pore of the cage. The organic cages were functionalized with crown ether groups for enhances solubility and showed the ability to uptake methane into the pore while being dissolved in the crown ether.[176] Very recently, the liquid-liquid extractions of substituted *ortho*- (*o*), *meta*- (*m*) or *para*-benzenes (*p*) was achieved by dissolution of organic cavitand in water. Although all isomers can enter the pore of CB[7] in an aqueous solution, a selective stronger binding affinity for *o*-xylene (*o*X), *o*-dichlorobenzene, *o*-dibromobenzene and *o*-chlorotoluene was accomplished.[179] By utilising the hydrophobic pore of a modified and hence water-soluble P[5], a liquid-liquid extraction of *m*-substituted benzene isomers with an approximate selectivity of 86 % for *m*-xylene (*m*X) and *m*-chlorotoluene up to a selectivity of 95 % for *m*-bromotoluene was achieved.[180]

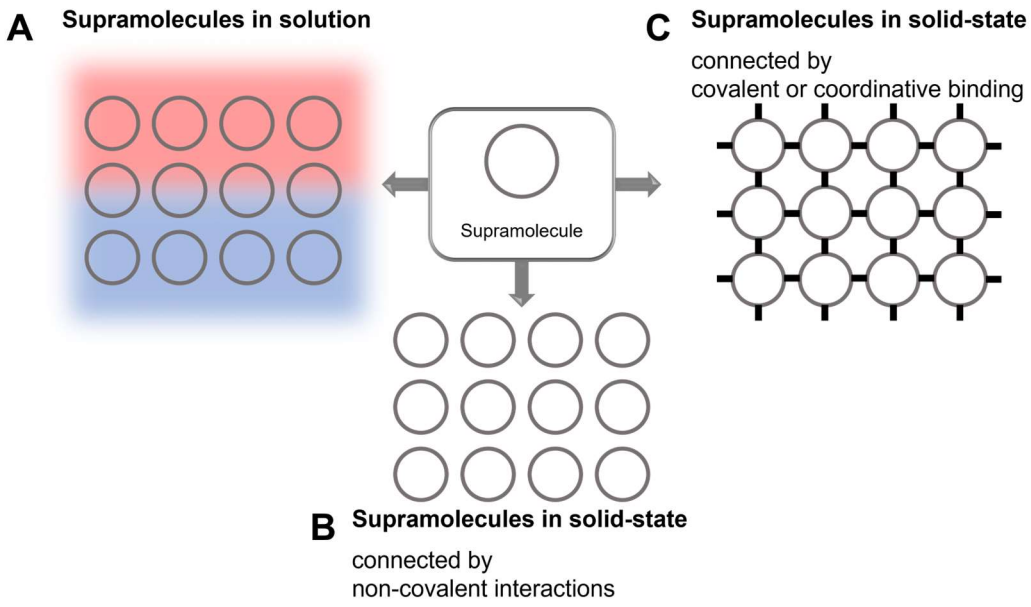

Figure 8: Overview of the implementation of supramolecules in porous materials: (A) in solution; (B) in solid-state connected by non-covalent interactions and (C) in solid-state connected by covalent or coordinative binding yielding more dimensional materials.

To establish the prediction of structure-property relationship for supramolecular building units in porous materials, assemblies of supramolecules in the solid-state driven by non-covalent interactions have to be investigated (Figure 8B). However, enhanced guest binding sites by pre- or post-synthetic modification and the retention of porosity by stabilising non-covalent interactions must be achieved.[87,181] The implementation of supramolecules into the solid-state can be attempted by crystallisation of the molecular host systems forming networks, which are cross-linked by weak non-covalent interactions. The structure and properties of these so-called supramolecular polymeric networks (SPNs)[89-90,182] are strongly dependent on the non-covalent interactions between the molecular components. The assemblies can either be in an equilibrium or in a non-equilibrium and hence the dynamic nature of the structure-dictating non-covalent interactions exhibit properties such as responsivity, experimental adaptability, ability to undergo self-healing[182]. Although functional materials can be achieved by design of the molecular component, the arrangement of the molecular components in the solid-state can lead to limitations in the pore accessibility. A distinction must be made between intrinsic and extrinsic porosity.[181] The intrinsic porosity is accompanied by a molecule bearing an internal pore, typically a central pore of a shape-persistent supramolecule, and the arrangement in the solid-state is highly dependent on the non-covalent interactions, which can lead to lability

towards solvents or reagents.[55,114] An extrinsic porosity is formed by the inefficient solid-state packing of molecules, which are not necessarily bearing an internal pore, and can lead to polymorphism.[181]

When dealing with the arrangement of nanoporous, discrete organic molecules, which are held together by non-covalent interactions, the term porous molecular crystals (PMCs) is introduced.[181] By synergistically combining the individual weak interactions, a robust and practical material is formed, which is solvent and vapour processable and hence allows the applicability for gas capture or separation.[183] This has been investigated by the group of *Khashab*, where molecular cages with triangular shaped pore opening were tested towards their solid- vapor adsorption for xylene isomers and a matching pore geometry and preferred encapsulation for *m*X and mesitylene but not for *p*-xylene (*p*X) was identified.[184] Additionally, the separation of styrene (St) and ethylbenzene (EB) was achieved with a trianglimine macrocycle.[185]

By the introduction of metal ions, the so-called metal-macrocycle frameworks (MMFs) were established by *Shionoya*, consisting of $PdCl_2$ units and a macrocyclic hexaamine ligand L yielding four different stereoisomers of $[Pd_3LCl_6]$, which are co-crystallising in a particular manner.[186-187] Within the four co-crystallised stereoisomers, nanochannels are formed by intermolecular hydrogen bonding and Pd-Pd interactions and the crystal arrangement possesses multiple binding sites, which allows for site selective adsorption of different guest molecules (e.g., pinene, serine, limonene) giving this material the ability for molecular recognition.[188-189] Additionally, this site-selective recognition could further be utilised for catalytic applications, where a specific reaction, such as the size-specific deprotection of tritylated substrates, was promoted by the MMF, while simultaneously inhibiting other possible conversion.[190-193]

Another approach for the implementation of supramolecules in the solid-state is by co-crystallisation with variable stoichiometry of guest molecules, which allows the studying of structure-properties relationships for the obtained self-assemblies. The co-crystallisation of perethylated (Et) EtP[5] and EtP[6] with tetracyanobenzene yielded different solid-state structures including the co-existence of two different host-guest complexes.[194]

Nonporous Adaptive Crystals

Materials, which exhibit no porosity at a supramolecular level in the initial crystalline state are called nonporous adaptive crystals (NACs).[195-201] Upon guest uptake by either solid-liquid or solid-gas phase reaction, intrinsic or extrinsic porosity is introduced in combination with a structural transformation of the arrangement in the solid-sate material (Figure 9). A re-arrangement into the initial state is occurring upon removal of guest molecules. This behaviour was observed for organic cavitands, which were able to separate hexane isomers or distinguish between benzene and cyclohexane[202-204] and for cages, which could separate xylene isomers.[205-206] The sorption and desorption of guest molecules combined with structural transformation was already extensively studied for pillar[n]arene-based NACs.[136,197-198,207-212] EtP[5] or EtP[6] display polymorphism in the solid-state, which was dependent on the temperature. While crystallisation at room temperature yielded a honeycomb-like 1D channel structure, the crystallisation at elevated temperatures yielded the thermodynamically stable and guest free phase EtP[6]*β*, where no alignment of the aromatic pillars was obtained. The

accompanied loss of porosity was determined by gas sorption experiments with N_2 in CO_2.[195,197-200]

Due to their similar molecular size, the separation of St and EB is difficult. However, exposure of crystalline EtP[6]*β* to vapourised St and EB yielded St@EtP[6] and EB@EtP[6]. While St was located in the extrinsic pores between distorted EtP[6] molecules, EB was located inside the intrinsic 1D channel of EtP[6]. Due to the higher stability after settling the reaction equilibrium, only St@EtP[6] was obtained. After subjection to heat the desorption of St yielded the crystal phase EtP[6]*β* and the cycle of sorption could be repeated (Figure 9A).[210] Similar behaviour was obtained for the separation of a mixture of *o*X, *m*X and *p*X. Adsorption into the EtP[6]*β* phase yielded *o*X@EtP[6] with a honeycomb 1D channel, aligned pillars and disordered *o*X guest molecules, *m*X@EtP[6] with a distorted pillar structure and guest *m*X located outside of the cavity, and *p*X@EtP[6] with 1D channels of aligned pillars to maximise the π-π interactions. However, exposure of EtP[6]*β* to a mixture of *o*X, *m*X and *p*X revealed the selective encapsulation of *p*X in combination with structural transformation (Figure 9B). Through heating, the release of *p*X transformed the solid-state phase back to EtP[6]*β*.[136,213]

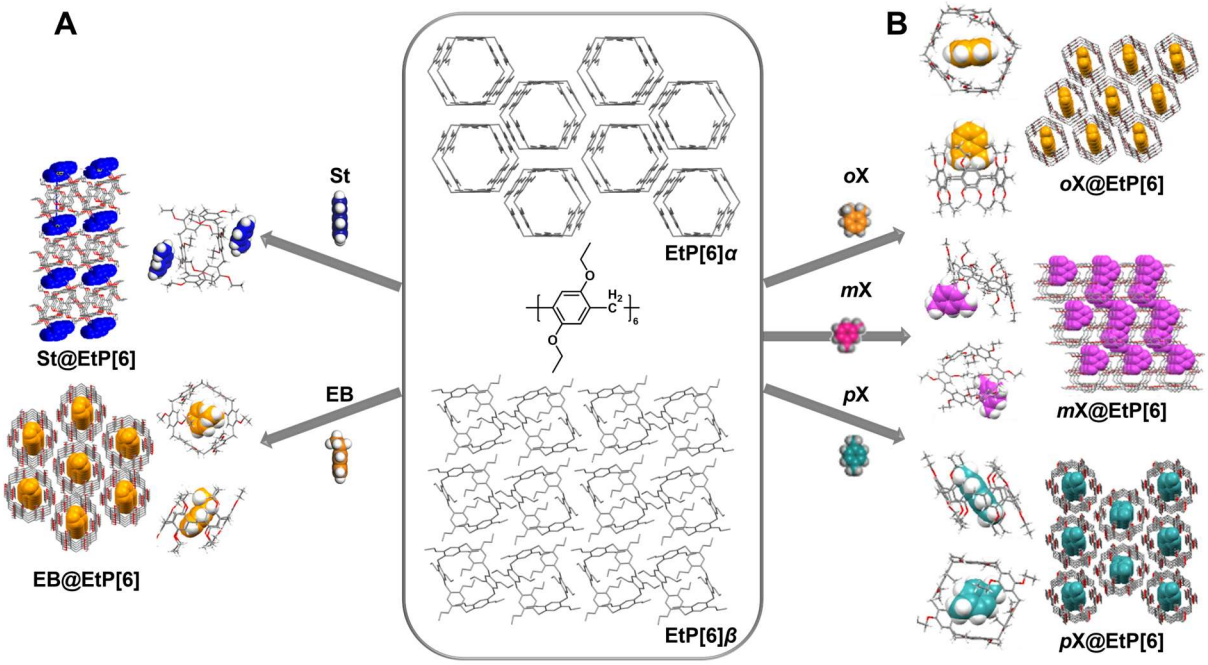

Figure 9: Schematic representation for the interconversion of non-porous adaptive crystals of perethylated pillar[6]arene (EtP[6]) with (A) Styrene (St) vs. ethylbenzene (EB) and (B) Xylene mixtures containing oX, mX and pX. Partially taken from [136,210].

The advantages of pillar[n]arene-based NACs is the simple preparation in a large-scale synthesis, their chemical / thermal stability, their solubility in common organic solvents and the recyclability of the whole sorption / desorption process.

The implementation of supramolecular character into the solid-state can also be achieved by the formation of infinite networks, which are either connected by covalent bonds or by coordinative bonds between ligand motifs and metal nodes (Figure 8C). The typically known porous materials are for example covalent organic frameworks (COFs)[214], which are more

dimensional structures connected by strong covalent bonds, or MOFs, which exhibit a complex structure and the implementation of porosity during the arrangement in the solid-state. These network materials show multiple domains, which can range from micro-, meso- to macro-pores dependent on the order in the dimensional space and the interpenetration of the building units.[10,16,215-217]

Network Materials with Ligand featuring Supramolecules

To overcome the problem of interpenetrated architectures, porous network materials can be tailored by the introduction of various supramolecular building units containing pre-defined and intrinsic porosity[39-41,218-219] and can form multi-pore frameworks.[220-221] By designing a ligand molecule, which is a simple supramolecule, control over the arrangement in the solid-state and tailoring the functionality of the pore portal can be achieved.

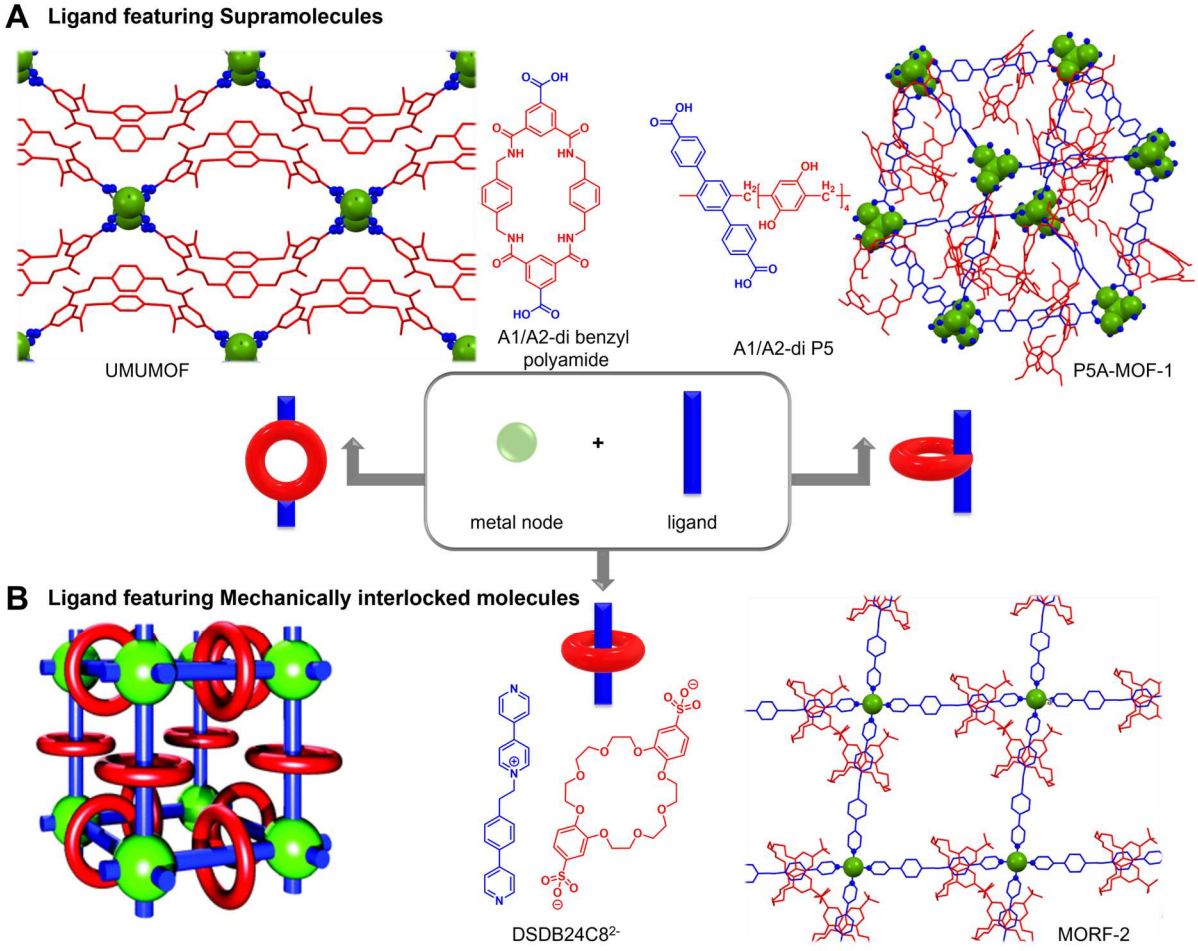

Figure 10: Schematic representation for network materials with implemented supramolecular motifs: (A) MOFs with ligands featuring supramolecules where either functionalised flexible benzyl amide macrocycle are combined with Cu(II), Zn(II) as metal node or difunctionalised pillar[5]arenes are combined with Zn(II) as metal node; (B) MOFs with ligands featuring MIMs where the difunctionalised axle of a rotaxane is combined with a metal node.[220,222-223]

To implement supramolecule as ligands, possibly either a macrocycle could directly be functionalised or a difunctionalised ligand could be used as one monomer unit for the macrocycle (Figure 10A). When using difunctionalised flexible benzyl amide macrocycles, which exhibit large and well-ordered cavities, a direct functionalised macrocyclic was obtained.

Dictated by the supramolecular nature of the macrocycle, guest encapsulation by specific non-covalent interactions is possible, which in this case would be hydrogen bonding or π-π stacking interactions. Combination with Cu(II) or Zn(II) metal nodes yielded the UMUMOF revealing a 1D linear polymer with bent ligand motifs. Oval channels with a height of 11.55 Å and a width of 16.59 Å were investigated towards the encapsulation of fullerene, where a size selective encapsulation of C60 driven by π-π stacking was achieved.[222] Various other macrocycles show the potential to be used as ligand motifs for the implementation into frameworks, which was utilised by the group of Stoddart for the implementation of cyclodextrins in highly biocompatible MOFs.[219,224] For the pillar[n]arenes the exchange of one monomer unit by a difunctionalised ligand motif was achieved and hence the multi-porous framework P[5]A-MOF-1 was obtained. Due to the rotational freedom and the random distribution of “enantiomeric” P[5] in the network structure, the structure of P[5]A-MOF-1 was modelled based on the similar network structure without the embedded supramolecular ligand molecules.[220]

Network Materials with Ligand featuring Mechanically Interlocked Molecules

The design principles inherent in mechanically interlocked molecules have already been integrated into the development of network materials. First introduced by Loeb the so-called Metal-Organic Rotaxane Frameworks (MORFs)[223,225-227] are network materials with rotaxane (or catenane) molecules as ligands (Figure 10B). One of the first examples was the MORF-2, which is built by the combination of a Zn(II) metal node and a [2]pseudorotaxane with a single charged pyridinium axle component and a crown[8]ether derivative as ring component. With a octahedral coordination sphere of Zn(II), 2D layers of square grids are formed, which are stacked in an alternating manner due to hydrogen bonding of the additional two water molecules coordinated to the Zn(II) nodes.[223]

The idea of implementing functionality of MIMs, which are individually address- and controllable is called `robust dynamics`.[228] The term `robust dynamic` describes constructs with repeated dynamics of one entity, which is not affecting the integrity of any other entity. By applying this concept to dynamic molecules with random motion 3D extended structures are established with significantly enhancing their order, coherence, and performance. After facing the challenges of ligand design and synthetic concepts, the formed mechanically interlocked network materials display the advantages of in-built properties, tunability of the internal properties and are individually address- & controllable upon exposure to an external stimulus.[229-230] A combination of these advantages was recently employed by MORFs with cucurbit[8]uril motifs demonstrating the selective detection of antibiotics.[231] MORFs combine the rigidity of a framework with the dynamic molecular motion by the added flexibility and functionality of the implemented MIM.[232]

1.4 Pillarplex – A Supramolecular Organometallic Complex

Based on the idea, that NHC ligands, where electronic and steric properties can be tailored by the modification of the substituents, lead to `static` supramolecular structures with no reversibility of the assembly, the pillarplexes $[M_8L_2](X)_4$ (with M = Ag(I), Au(I); X = PF_6^-, OTf^-, OAc^-), were introduced.[233-234] This organometallocavitand bears macrocyclic ligands with NHC and pyrazole units bridged by methylene units, while two of these ligands are connected by a relatively strong, linear NHC-M bond with eight coinage-based metal ions forming a tubular hydrophobic cavity.

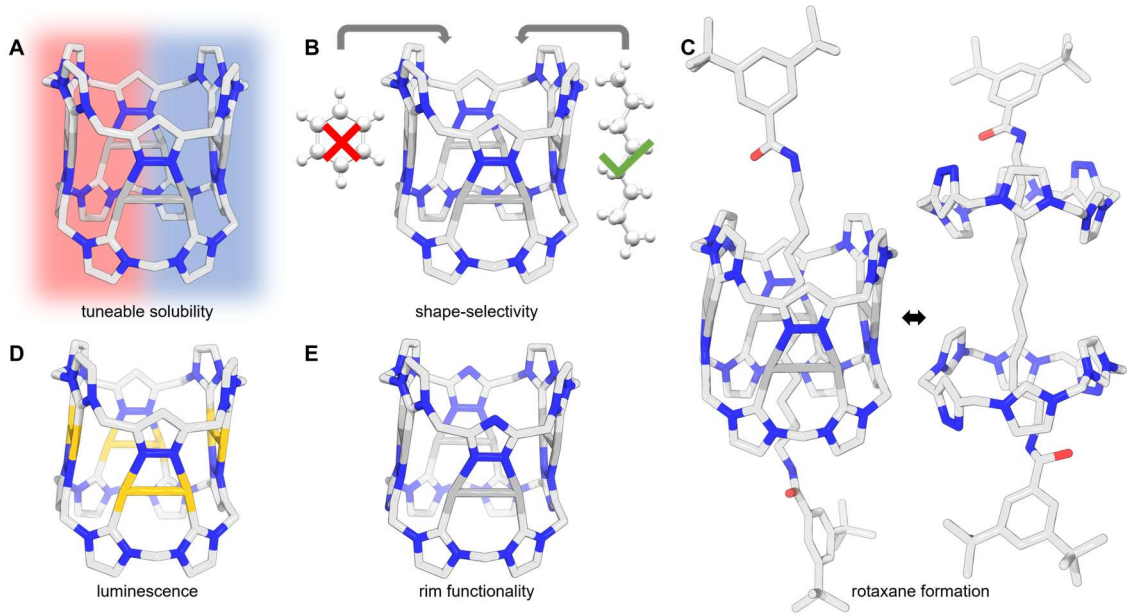

Figure 11: Schematic representation of the pillarplex cation $[M_8L_2]^{4+}$ and the properties (A) tuneable solubility by anion exchange reactions, (B) shape-selective guest encapsulation, (C) rotaxane formation by trapping 1,12-diamino dodecane with sterically demanding stopper motifs, (D) intrinsic luminescence of $[Au_8L_2]^{4+}$ and (E) possibility of rim functionalisation by exchanging the pyrazole unit with a triazole unit.

Due to the charged nature of $[M_8L_2](X)_4$ the solubility of the pillarplex salt can be tuned by simple anion exchange reactions. For example $[Ag_8L_2](PF_6)_4$ is soluble in organic solvents (MeCN, DMF), while $[Ag_8L_2](OAc)_4$ is soluble in aqueous solvents (H_2O, DMSO) (Figure 11A). The tubular cation $[M_8L^{Me}{}_2]^{4+}$ exhibits a pore opening of 4.3 Å and a pore height of 11.7 Å and hence showed excellent host properties for linear molecules (Figure 11B).[234-237] The dissociation constant K_d of the host-guest complex with 1,8-diaminooctane could already be determined by ^1H NMR (K_d = 24.0 ± 5.4 µM for $[Ag_8L^{Me}{}_2](PF_6)_4$ in MeCN) and ITC titration experiments (K_d = 7.45 ± 0.36 µM for $[Au_8L^{Me}{}_2](OAc)_4$ in H_2O) indicating relatively weak guest binding[238], however similar K_d values were observed for the encapsulation of respective guest molecule in functionalised pillar[5]arene (1:1 ratio of MeCN:H_2O).[125]

The stoichiometry of 1:1 for these host-guest complexes was calculated by Job-Plot analysis. Prolonging the guest molecule to 1,12-diamino dodecane led to a host-guest complex or pseudorotaxane, where the -NH_2 groups stick out of the cavity on both sides. By *in-situ* stoppering of these linear molecules with sterically high demanding aromatic rings (e.g., 1,3-di-*tert*-butylphenyl), the formation of a pillarplex rotaxane was achieved (Figure 11C).[235] This $[M_8L_2][2]Rot(X)_4$ can undergo a transformation of the inorganic rotaxane into a purely organic rotaxane $(H_6L)_2[3]Rot(X)_8$ with the metal ions in solution by simply lowering the pH

value. The pH reversibility and switch ability were examined and confirmed the re-assembly of the inorganic [2]rotaxane at higher pH values. It was also tested if the re-assembly of the inorganic pillarplex-rotaxane was possible with different metal ions and an exchange of Ag(I) with Au(I) ions was achieved. The gold congeners displayed intrinsic luminescence (Figure 11D). The emission was solvent dependent and quenching by guest encapsulation was observed. For example, MeCN can be encapsulated into the cavity of $[Au_8L^{Me}_2](PF_6)_4$ and hence no emission in solution was detected, but no encapsulation of H_2O into $[Au_8L^{Me}_2](OAc)_4$ occurred and hence the emission was not quenched.[239] Different methods were already investigated towards a rim-functionalisation of the pillarplex cation (Figure 11E). Here, a lone pair of electrons could be introduced by exchanging the pyrazole unit with a triazole unit (L^T).[236] The connectivity and the overall shape are similar to the pyrazole-based pillarplex. However, a structural distortion and hence a structural flexibility of the portal opening, and the cation was observed dependent on the counter anion resulted by intermolecular hydrogen bonding of PF_6^- with the hydrogen atoms of the organic rim.

Additionally, the potential for applications of the pillarplex salts in medicine were already investigated and revealed promising results. The activity of $[Ag_8L^{Me}_2](PF_6)_4$, $[Au_8L^{Me}_2](PF_6)_4$, $[Ag_8L^{Me}_2](OAc)_4$ and $[Au_8L^{Me}_2](OAc)_4$ towards bacterial strains, fungus and human cell line was investigated and all compounds exhibited bioactivity dependent on the incorporated metal. While the Ag(I)-pillarplex salts showed higher toxicity towards bacteria, fungus and the human cell line HepG2, the Au(I)-pillarplex salts displayed no toxicity towards bacteria and fungus and only demonstrated a low toxicity towards the human cell line. With the low or non-toxic properties of the Au(I) based pillarplex salts could be used as drug delivery systems for the slow release of active drug from inside of the pillarplex cavity.[240] Very recently, experimental results suggested the implementation of the $[Au_8L^{Me}_2](OAc)_4$ pillarplex into a 3-way junction with DNA, which was confirmed by MD calculations[241] and further investigation of applicability of the pillarplex salts in biological systems is on the way.

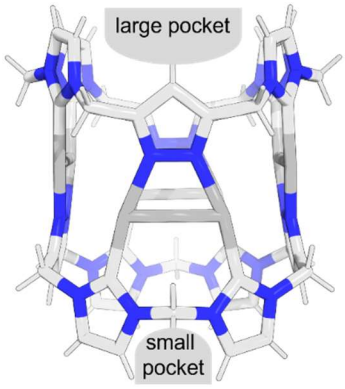

Figure 12: Representation of the division of $[M_8L^{Me}_2]^{4+}$ into the large pocket between two imidazolylidene units bridged by a methylene bridged pyrazole unit and the small pocket between two imidazolylidene units bridged by methylene units.

In general, the pillarplex rim can be divided into two pockets (Figure 12) containing aromatic C-H hydrogen atoms. The small pocket is defined as the space between two imidazolylidene units, which are bridged by a methylene unit and the larger pocket is defined as the space between two imidazolylidene units, which are bridged by two methylene units and the pyrazole unit.[237]

1.5 References for Chapter 1

1 C. E. Wilmer, O. K. Farha, Y.-S. Bae, J. T. Hupp, R. Q. Snurr, *Energy Environ. Sci.,* **2012**, *5*, 9849.
2 S. Bi, H. Banda, M. Chen, L. Niu, M. Chen, T. Wu, J. Wang, R. Wang, J. Feng, T. Chen, M. Dincă, A. A. Kornyshev, G. Feng, *Nat. Mater.,* **2020**, *19*, 552.
3 T. Liu, G. Liu, *Nat. Commun.,* **2020**, *11*, 4984.
4 A. G. Slater, A. I. Cooper, *Science,* **2015**, *348*, 1.
5 M. K. Mishra, U. Ramamurty, G. R. Desiraju, *Curr. Opin. Solid State Mater. Sci.,* **2016**, *20*, 361.
6 W. Deng, Q. Fang, H. Huang, X. Zhou, J. Ma, Z. Liu, *Small,* **2017**, *13*, 1701231.
7 M. Dincă, J. R. Long, *Chem. Rev.,* **2020**, *120*, 8037.
8 D. Taylor, S. J. Dalgarno, Z. Xu, F. Vilela, *Chem. Soc. Rev.,* **2020**, *49*, 3981.
9 G. Zhang, O. Presly, F. White, I. M. Oppel, M. Mastalerz, *Angew. Chem. Int. Ed.,* **2014**, *53*, 1516.
10 M. Safaei, M. M. Foroughi, N. Ebrahimpoor, S. Jahani, A. Omidi, M. Khatami, *TrAC, Trends Anal. Chem.,* **2019**, *118*, 401.
11 H. Wang, X. Dong, E. Velasco, D. H. Olson, Y. Han, J. Li, *Energy Environ. Sci.,* **2018**, *11*, 1226.
12 X. Cui, K. Chen, H. Xing, Q. Yang, R. Krishna, Z. Bao, H. Wu, W. Zhou, X. Dong, Y. Han, B. Li, Q. Ren, M. J. Zaworotko, B. Chen, *Science,* **2016**, *353*, 141.
13 R. L. Siegelman, E. J. Kim, J. R. Long, *Nat. Mater.,* **2021**, *20*, 1060.
14 Y. Wu, B. M. Weckhuysen, *Angew. Chem. Int. Ed.,* **2021**, *60*, 18930.
15 A. Ahmed, S. Seth, J. Purewal, A. G. Wong-Foy, M. Veenstra, A. J. Matzger, D. J. Siegel, *Nat. Commun.,* **2019**, *10*, 1568.
16 H. Furukawa, K. E. Cordova, M. O'Keeffe, O. M. Yaghi, *Science,* **2013**, *341*, 1230444.
17 J. Yang, J. Wang, B. Hou, X. Huang, T. Wang, Y. Bao, H. Hao, *Chem. Eng. J.,* **2020**, *399*, 125873.
18 C. Perego, R. Millini, *Chem. Soc. Rev.,* **2013**, *42*, 3956.
19 S. Horike, M. Dincă, K. Tamaki, J. R. Long, *J. Am. Chem. Soc.,* **2008**, *130*, 5854.
20 P. Peng, X.-H. Gao, Z.-F. Yan, S. Mintova, *Natl. Sci. Rev.,* **2020**, *7*, 1726.
21 P. Samanta, A. V. Desai, S. Let, S. K. Ghosh, *ACS Sustain. Chem. Eng.,* **2019**, *7*, 7456.
22 S. Wu, Y. Lin, J. Liu, W. Shi, G. Yang, P. Cheng, *Adv. Funct. Mater.,* **2018**, *28*, 1707169.
23 J. Aríñez-Soriano, J. Albalad, J. Pérez-Carvajal, I. Imaz, F. Busqué, J. Juanhuix, D. Maspoch, *Cryst. Eng. Comm.,* **2016**, *18*, 4196.
24 H. Xu, S. Rodríguez-Hermida, J. Pérez-Carvajal, J. Juanhuix, I. Imaz, D. Maspoch, *Cryst. Growth Des.,* **2016**, *16*, 5598.
25 B. H. Wilson, H. S. Scott, O. T. Qazvini, S. G. Telfer, C. Mathonière, R. Clérac, P. E. Kruger, *Chem. Commun.,* **2018**, *54*, 13391.
26 B. Li, D. Ma, Y. Li, Y. Zhang, G. Li, Z. Shi, S. Feng, M. J. Zaworotko, S. Ma, *Chem. Mater.,* **2016**, *28*, 4781.
27 A. M. Fracaroli, P. Siman, D. A. Nagib, M. Suzuki, H. Furukawa, F. D. Toste, O. M. Yaghi, *J. Am. Chem. Soc.,* **2016**, *138*, 8352.
28 O. M. Yaghi, *J. Am. Chem. Soc.,* **2016**, *138*, 15507.
29 P. J. Stang, B. Olenyuk, *Acc. Chem. Res.,* **1997**, *30*, 502.
30 Y. Kim, J. Koo, I.-C. Hwang, R. D. Mukhopadhyay, S. Hong, J. Yoo, A. A. Dar, I. Kim, D. Moon, T. J. Shin, Y. H. Ko, K. Kim, *J. Am. Chem. Soc.,* **2018**, *140*, 14547.
31 H. Li, M. Eddaoudi, M. O'Keeffe, O. M. Yaghi, *Nature,* **1999**, *402*, 276.
32 Mark V. de Ruiter, R. Mejia-Ariza, Jeroen J. L. M. Cornelissen, J. Huskens, *Chem,* **2016**, *1*, 29.
33 L. Bu, M. R. Nimlos, D. J. Robichaud, S. Kim, *Catal. Today,* **2018**, *312*, 73.
34 S. Yuan, L. Zou, J.-S. Qin, J. Li, L. Huang, L. Feng, X. Wang, M. Bosch, A. Alsalme, T. Cagin, H.-C. Zhou, *Nat. Commun.,* **2017**, *8*, 15356.
35 C. M. Reddy, G. Rama Krishna, S. Ghosh, *Cryst. Eng. Comm.,* **2010**, *12*, 2296.

36 A. J. Edwards, C. F. Mackenzie, P. R. Spackman, D. Jayatilaka, M. A. Spackman, *Faraday Discuss.,* **2017**, *203*, 93.
37 A. K. Nangia, G. R. Desiraju, *Angew. Chem. Int. Ed.,* **2019**, *58*, 4100.
38 S. Mukherjee, D. Sensharma, K.-J. Chen, M. J. Zaworotko, *Chem. Commun.,* **2020**, *56*, 10419.
39 S. Jeoung, S. Kim, M. Kim, H. R. Moon, *Coord. Chem. Rev.,* **2020**, *420*, 213377.
40 S. Kitagawa, S.-i. Noro, T. Nakamura, *Chem. Commun.,* **2006**, 701.
41 Y. Kim, S. Huh, *Cryst. Eng. Comm.,* **2016**, *18*, 3524.
42 J.-M. Lehn, *Science,* **1985**, *227*, 849.
43 J.-M. Lehn, *Science,* **1993**, *260*, 1762.
44 G. R. Desiraju, *Nature,* **2001**, *412*, 397.
45 H.-W. Schmidt, F. Würthner, *Angew. Chem. Int. Ed.,* **2020**, *59*, 8766.
46 J.-M. Lehn, *Angew. Chem. Int. Ed.,* **1990**, *29*, 1304.
47 J. Zhou, L. Rao, G. Yu, T. R. Cook, X. Chen, F. Huang, *Chem. Soc. Rev.,* **2021**, *50*, 2839.
48 J. T. Lenthall, J. W. Steed, *Coord. Chem. Rev.,* **2007**, *251*, 1747.
49 I. Alkorta, J. Elguero, A. Frontera, *Cryst.,* **2020**, *10*, 180.
50 J. A. K. Goodrich, Jennifer F.: *Binding and Kinetics for Molecular Biologists,* 1, Cold Spring Harbor Laboratory Press, Cold Spring Harbor, New York, USA, **2007**.
51 F. Yu, Q. Zhao, D. Zhang, Z. Yuan, H. Wang, *Anal. Chem.,* **2019**, *91*, 372.
52 P. Thordarson, *Chem. Soc. Rev.,* **2011**, *40*, 1305.
53 I. Jarmoskaite, I. AlSadhan, P. P. Vaidyanathan, D. Herschlag, *eLife,* **2020**, *9*, e57264.
54 G. Klebe, H. J. Böhm, *J Recept Signal Transduct Res,* **1997**, *17*, 459.
55 H. Wang, Y. Jin, N. Sun, W. Zhang, J. Jiang, *Chem. Soc. Rev.,* **2021**, *50*, 8874.
56 C. J. Bruns, J. F. Stoddart: *An Introduction to the Mechanical Bond* in *The Nature of the Mechanical Bond: From Molecules to Machines*, John Wiley & Sons, Hoboken, New Jersey, USA, **2016**.
57 T.-R. Tero, M. Nissinen, *Tetrahedron,* **2014**, *70*, 1111.
58 S. Mena-Hernando, E. M. Pérez, *Chem. Soc. Rev.,* **2019**, *48*, 5016.
59 P. R. Ashton, I. Baxter, M. C. T. Fyfe, F. M. Raymo, N. Spencer, J. F. Stoddart, A. J. P. White, D. J. Williams, *J. Am. Chem. Soc.,* **1998**, *120*, 2297.
60 G. Barin, R. S. Forgan, J. F. Stoddart, *Proc. Math. Phys. Eng. Sci.,* **2012**, *468*, 2849.
61 J. F. Stoddart, *Angew. Chem. Int. Ed.,* **2017**, *56*, 11094.
62 G. Gil-Ramírez, D. A. Leigh, A. J. Stephens, *Angew. Chem. Int. Ed.,* **2015**, *54*, 6110.
63 D. B. Amabilino, P. R. Ashton, A. S. Reder, N. Spencer, J. F. Stoddart, *Angew. Chem. Int. Ed.,* **1994**, *33*, 1286.
64 O. Safarowsky, M. Nieger, R. Fröhlich, F. Vögtle, *Angew. Chem. Int. Ed.,* **2000**, *39*, 1616.
65 S. D. P. Fielden, D. A. Leigh, S. L. Woltering, *Angew. Chem. Int. Ed.,* **2017**, *56*, 11166.
66 C. O. Dietrich-Buchecker, J.-P. Sauvage, *Angew. Chem. Int. Ed.,* **1989**, *28*, 189.
67 J. J. Danon, A. Krüger, D. A. Leigh, J.-F. Lemonnier, A. J. Stephens, I. J. Vitorica-Yrezabal, S. L. Woltering, *Science,* **2017**, *355*, 159.
68 X.-Y. Chen, D. Shen, K. Cai, Y. Jiao, H. Wu, B. Song, L. Zhang, Y. Tan, Y. Wang, Y. Feng, C. L. Stern, J. F. Stoddart, *J. Am. Chem. Soc.,* **2020**, *142*, 20152.
69 W. Liu, C. L. Stern, J. F. Stoddart, *J. Am. Chem. Soc.,* **2020**, *142*, 10273.
70 A. R. Williams, B. H. Northrop, T. Chang, J. F. Stoddart, A. J. P. White, D. J. Williams, *Angew. Chem. Int. Ed.,* **2006**, *45*, 6665.
71 S. Ibáñez, C. Vicent, E. Peris, *Angew. Chem. Int. Ed.,* **2022**, *61*, e202112513.
72 M. A. Olson, Y. Y. Botros, J. F. Stoddart, *Pure Appl. Chem.,* **2010**, *82*, 1569.
73 J. F. Stoddart, *Nano Lett.,* **2020**, *20*, 5597.
74 J. D. Badjic, C. M. Ronconi, J. F. Stoddart, V. Balzani, S. Silvi, A. Credi, *J. Am. Chem. Soc.,* **2006**, *128*, 1489.
75 P. L. Anelli, N. Spencer, J. F. Stoddart, *J. Am. Chem. Soc.,* **1991**, *113*, 5131.

76 P. R. Ashton, T. T. Goodnow, A. E. Kaifer, M. V. Reddington, A. M. Z. Slawin, N. Spencer, J. F. Stoddart, C. Vicent, D. J. Williams, *Angew. Chem. Int. Ed.,* **1989**, *28*, 1396.
77 C. J. Bruns, J. F. Stoddart: *The Fundamentals of Making Mechanical Bonds* in *The Nature of the Mechanical Bond: From Molecules to Machines*, John Wiley & Sons, Hoboken, New Jersey, USA, **2016**.
78 P. S. Bols, H. L. Anderson, *Acc. Chem. Res.,* **2018**, *51*, 2083.
79 Z. Zhang, M. J. Zaworotko, *Chem. Soc. Rev.,* **2014**, *43*, 5444.
80 J.-P. Sauvage, *Angew. Chem. Int. Ed.,* **2017**, *56*, 11080.
81 M. Xue, Y. Yang, X. Chi, X. Yan, F. Huang, *Chem. Rev.,* **2015**, *115*, 7398.
82 S. J. Rowan, S. J. Cantrill, G. R. L. Cousins, J. K. M. Sanders, J. F. Stoddart, *Angew. Chem. Int. Ed.,* **2002**, *41*, 898.
83 G. Schill, W. Beckmann, W. Vetter, *Chem. Ber.,* **1980**, *113*, 941.
84 P. D. Frischmann, M. J. MacLachlan, *Chem. Soc. Rev.,* **2013**, *42*, 871.
85 A. Pöthig, A. Casini, *Theranostics,* **2019**, *9*, 3150.
86 S. R. Batten, N. R. Champness, X.-M. Chen, J. Garcia-Martinez, S. Kitagawa, L. Öhrström, M. O'Keeffe, M. P. Suh, J. Reedijk, *Cryst. Eng. Comm.,* **2012**, *14*, 3001.
87 S. Kitagawa, R. Kitaura, S.-i. Noro, *Angew. Chem. Int. Ed.,* **2004**, *43*, 2334.
88 T. R. Cook, P. J. Stang, *Chem. Rev.,* **2015**, *115*, 7001.
89 R. Chakrabarty, P. S. Mukherjee, P. J. Stang, *Chem. Rev.,* **2011**, *111*, 6810.
90 M. Fujita, K. Ogura, *Bull. Chem. Soc. Jpn,* **1996**, *69*, 1471.
91 S. R. Seidel, P. J. Stang, *Acc. Chem. Res.,* **2002**, *35*, 972.
92 E. Sánchez-González, M. Y. Tsang, J. Troyano, G. A. Craig, S. Furukawa, *Chem. Soc. Rev.,* **2022**, *51*, 4876.
93 A. J. Gosselin, G. E. Decker, A. M. Antonio, G. R. Lorzing, G. P. A. Yap, E. D. Bloch, *J. Am. Chem. Soc.,* **2020**, *142*, 9594.
94 M. J. Prakash, M. S. Lah, *Chem. Commun.,* **2009**, 3326.
95 A. J. Gosselin, C. A. Rowland, E. D. Bloch, *Chem. Rev.,* **2020**, *120*, 8987.
96 M. Eddaoudi, J. Kim, J. B. Wachter, H. K. Chae, M. O'Keeffe, O. M. Yaghi, *J. Am. Chem. Soc.,* **2001**, *123*, 4368.
97 A. Khobotov-Bakishev, L. Hernández-López, C. von Baeckmann, J. Albalad, A. Carné-Sánchez, D. Maspoch, *Adv. Sci.,* **2022**, *9*, 2104753.
98 B. S. Pilgrim, N. R. Champness, *ChemPlusChem,* **2020**, *85*, 1842.
99 R.-D. Schnebeck, E. Freisinger, F. Glahé, B. Lippert, *J. Am. Chem. Soc.,* **2000**, *122*, 1381.
100 Y. Sun, P. J. Stang, *Aggregate,* **2021**, *2*, e94.
101 D. L. Caulder, R. E. Powers, T. N. Parac, K. N. Raymond, *Angew. Chem. Int. Ed.,* **1998**, *37*, 1840.
102 D. Nam, J. Huh, J. Lee, J. H. Kwak, H. Y. Jeong, K. Choi, W. Choe, *Chem. Sci.,* **2017**, *8*, 7765.
103 M. J. Hannon, L. J. Childs, *Supramol. Chem.,* **2004**, *16*, 7.
104 R. A. Bilbeisi, J. K. Clegg, N. Elgrishi, X. de Hatten, M. Devillard, B. Breiner, P. Mal, J. R. Nitschke, *J. Am. Chem. Soc.,* **2012**, *134*, 5110.
105 J. M. Cross, R. V. Fennessy, L. P. Harding, C. R. Rice, M. J. Hardie, C. Slater, *Chem. Commun.,* **2013**, *49*, 11290.
106 D. J. Tranchemontagne, Z. Ni, M. O'Keeffe, O. M. Yaghi, *Angew. Chem. Int. Ed.,* **2008**, *47*, 5136.
107 J. Albalad, L. Hernández-López, A. Carné-Sánchez, D. Maspoch, *Chem. Commun.,* **2022**, *58*, 2443.
108 B. M. Leonard, M. E. Anderson, K. D. Oyler, T. H. Phan, R. E. Schaak, *ACS Nano,* **2009**, *3*, 940.
109 A. Carné-Sánchez, J. Albalad, T. Grancha, I. Imaz, J. Juanhuix, P. Larpent, S. Furukawa, D. Maspoch, *J. Am. Chem. Soc.,* **2019**, *141*, 4094.
110 A. Legrand, L.-H. Liu, P. Royla, T. Aoyama, G. A. Craig, A. Carné-Sánchez, K. Urayama, J. J. Weigand, C.-H. Lin, S. Furukawa, *J. Am. Chem. Soc.,* **2021**, *143*, 3562.

111 A. Legrand, G. A. Craig, M. Bonneau, S. Minami, K. Urayama, S. Furukawa, *Chem. Sci.,* **2019**, *10*, 10833.
112 V. Guillerm, M. Eddaoudi, *Acc. Chem. Res.,* **2021**, *54*, 3298.
113 X.-Y. Yang, L.-H. Chen, Y. Li, J. C. Rooke, C. Sanchez, B.-L. Su, *Chem. Soc. Rev.,* **2017**, *46*, 481.
114 S. Yu, G.-L. Xing, L.-H. Chen, T. Ben, B.-L. Su, *Adv. Mater.,* **2020**, *32*, 2003270.
115 S. Lee, H. Jeong, D. Nam, M. S. Lah, W. Choe, *Chem. Soc. Rev.,* **2021**, *50*, 528.
116 E. v. Dienst, W. I. I. Bakker, J. F. J. Engbersen, W. Verboom, D. N. Reinhoudt, *Pure Appl. Chem.,* **1993**, *65*, 387.
117 E. M. M. Del Valle, *Process Biochem.,* **2004**, *39*, 1033.
118 D. N. Reinhoudt: *Supramolecular Chemistry and Heterocycles, Reference Module in Chemistry, Molecular Sciences and Chemical Engineering*, Academic Press, Elsevier, London, UK, **2013**.
119 J. Szejtli, *Chem. Rev.,* **1998**, *98*, 1743.
120 J. Lagona, P. Mukhopadhyay, S. Chakrabarti, L. Isaacs, *Angew. Chem. Int. Ed.,* **2005**, *44*, 4844.
121 M. Xue, Y. Yang, X. Chi, Z. Zhang, F. Huang, *Acc. Chem. Res.,* **2012**, *45*, 1294.
122 P. J. Cragg, K. Sharma, *Chem. Soc. Rev.,* **2012**, *41*, 597.
123 H. Zhang, Y. Zhao, *Chem. Eur. J.,* **2013**, *19*, 16862.
124 T. Ogoshi, S. Kanai, S. Fujinami, T.-a. Yamagishi, Y. Nakamoto, *J. Am. Chem. Soc.,* **2008**, *130*, 5022.
125 N. L. Strutt, R. S. Forgan, J. M. Spruell, Y. Y. Botros, J. F. Stoddart, *J. Am. Chem. Soc.,* **2011**, *133*, 5668.
126 T. Ogoshi, N. Ueshima, F. Sakakibara, T.-a. Yamagishi, T. Haino, *Org. Lett.,* **2014**, *16*, 2896.
127 X.-Y. Lou, Y.-W. Yang, *J. Am. Chem. Soc.,* **2021**.
128 Y. Chao, T. U. Thikekar, W. Fang, R. Chang, J. Xu, N. Ouyang, J. Xu, Y. Gao, M. Guo, H. Zuilhof, A. C.-H. Sue, *Angew. Chem. Int. Ed.,* **2022**, *61*, e202204589.
129 X. Wan, S. Li, Y. Tian, J. Xu, L.-C. Shen, H. Zuilhof, M. Zhang, A. C.-H. Sue, *Chem,* **2022**, *8*, 2136.
130 S. G. Bott, A. W. Coleman, J. L. Atwood, *J. Am. Chem. Soc.,* **1986**, *108*, 1709.
131 G. Crini, *Chem. Rev.,* **2014**, *114*, 10940.
132 J. W. Lee, S. Samal, N. Selvapalam, H.-J. Kim, K. Kim, *Acc. Chem. Res.,* **2003**, *36*, 621.
133 S. J. Barrow, S. Kasera, M. J. Rowland, J. del Barrio, O. A. Scherman, *Chem. Rev.,* **2016**, *116*, 12651.
134 S. Zhang, L. Grimm, Z. Miskolczy, L. Biczók, F. Biedermann, W. M. Nau, *Chem. Commun.,* **2019**, *55*, 14131.
135 T. Ogoshi, T.-a. Yamagishi, Y. Nakamoto, *Chem. Rev.,* **2016**, *116*, 7937.
136 K. Jie, M. Liu, Y. Zhou, M. A. Little, A. Pulido, S. Y. Chong, A. Stephenson, A. R. Hughes, F. Sakakibara, T. Ogoshi, F. Blanc, G. M. Day, F. Huang, A. I. Cooper, *J. Am. Chem. Soc.,* **2018**, *140*, 6921.
137 T. Dröge, F. Glorius, *Angew. Chem. Int. Ed.,* **2010**, *49*, 6940.
138 P. G. Edwards, F. E. Hahn, *Dalton Trans.,* **2011**, *40*, 10278.
139 C. Radloff, H.-Y. Gong, C. Schulte to Brinke, T. Pape, V. M. Lynch, J. L. Sessler, F. E. Hahn, *Chem. Eur. J.,* **2010**, *16*, 13077.
140 S. Ibáñez, M. Poyatos, E. Peris, *Acc. Chem. Res.,* **2020**, *53*, 1401.
141 C. Radloff, F. E. Hahn, T. Pape, R. Fröhlich, *Dalton Trans.,* **2009**, 7215.
142 V. Martínez-Agramunt, S. Ruiz-Botella, E. Peris, *Chem. Eur. J.,* **2017**, *23*, 6675.
143 V. Martínez-Agramunt, D. G. Gusev, E. Peris, *Chem. Eur. J.,* **2018**, *24*, 14802.
144 M. Schmidtendorf, C. Schulte to Brinke, F. E. Hahn, *J. Organomet. Chem.,* **2014**, *751*, 620.
145 N. Sinha, F. Roelfes, A. Hepp, F. E. Hahn, *Chem. Eur. J.,* **2017**, *23*, 5939.
146 M. Schmidtendorf, T. Pape, F. E. Hahn, *Dalton Trans.,* **2013**, *42*, 16128.

147 M.-M. Gan, J.-Q. Liu, L. Zhang, Y.-Y. Wang, F. E. Hahn, Y.-F. Han, *Chem. Rev.,* **2018**, *118*, 9587.
148 N. Sinha, F. E. Hahn, *Acc. Chem. Res.,* **2017**, *50*, 2167.
149 R. C. Nishad, S. Kumar, A. Rit, *Angew. Chem. Int. Ed.,* **2022**, *61*, e202206788.
150 B.-C. Tzeng, C.-L. Wu, J.-W. Hung, S.-Y. Chien, G.-H. Lee, *Dalton Trans.,* **2022**, *51*, 16973.
151 S. Ibáñez, E. Peris, *Angew. Chem. Int. Ed.,* **2019**, *58*, 6693.
152 A. Rit, T. Pape, F. E. Hahn, *J. Am. Chem. Soc.,* **2010**, *132*, 4572.
153 A. Rit, T. Pape, A. Hepp, F. E. Hahn, *Organometallics,* **2011**, *30*, 334.
154 D. Wang, B. Zhang, C. He, P. Wu, C. Duan, *Chem. Commun.,* **2010**, *46*, 4728.
155 C. Segarra, G. Guisado-Barrios, F. E. Hahn, E. Peris, *Organometallics,* **2014**, *33*, 5077.
156 N. Sinha, F. Roelfes, A. Hepp, C. Mejuto, E. Peris, F. E. Hahn, *Organometallics,* **2014**, *33*, 6898.
157 N. Sinha, L. Stegemann, T. T. Y. Tan, N. L. Doltsinis, C. A. Strassert, F. E. Hahn, *Angew. Chem. Int. Ed.,* **2017**, *56*, 2785.
158 Y. Li, Y.-Y. An, J.-Z. Fan, X.-X. Liu, X. Li, F. E. Hahn, Y.-Y. Wang, Y.-F. Han, *Angew. Chem. Int. Ed.,* **2020**, *59*, 10073.
159 C. Mejuto, G. Guisado-Barrios, D. Gusev, E. Peris, *Chem. Commun.,* **2015**, *51*, 13914.
160 F. M. Conrady, R. Fröhlich, C. Schulte to Brinke, T. Pape, F. E. Hahn, *J. Am. Chem. Soc.,* **2011**, *133*, 11496.
161 M. Schmidtendorf, T. Pape, F. E. Hahn, *Angew. Chem. Int. Ed.,* **2012**, *51*, 2195.
162 S. Ibáñez, E. Peris, *Angew. Chem. Int. Ed.,* **2020**, *59*, 6860.
163 C. Biz, S. Ibáñez, M. Poyatos, D. Gusev, E. Peris, *Chem. Eur. J.,* **2017**, *23*, 14439.
164 S. Ibáñez, E. Peris, *Chem. Eur. J.,* **2021**, *27*, 9661.
165 A. Gutiérrez-Blanco, C. Dobbe, A. Hepp, C. G. Daniliuc, M. Poyatos, F. E. Hahn, E. Peris, *Eur. J. Inorg. Chem.,* **2021**, *2021*, 2442.
166 E. A. Martynova, N. V. Tzouras, G. Pisanò, C. S. J. Cazin, S. P. Nolan, *Chem. Commun.,* **2021**, *57*, 3836.
167 D. Nuevo, S. Gonell, M. Poyatos, E. Peris, *Chem. Eur. J.,* **2017**, *23*, 7272.
168 S. Ibáñez, M. Poyatos, E. Peris, *Angew. Chem. Int. Ed.,* **2017**, *56*, 9786.
169 A. Gutiérrez-Blanco, S. Ibáñez, F. E. Hahn, M. Poyatos, E. Peris, *Organometallics,* **2019**, *38*, 4565.
170 S. Ibáñez, D. G. Gusev, E. Peris, *Organometallics,* **2020**, *39*, 4078.
171 V. Martínez-Agramunt, T. Eder, H. Darmandeh, G. Guisado-Barrios, E. Peris, *Angew. Chem. Int. Ed.,* **2019**, *58*, 5682.
172 V. Martínez-Agramunt, E. Peris, *Inorg. Chem.,* **2019**, *58*, 11836.
173 X.-X. Gou, T. Liu, Y.-Y. Wang, Y.-F. Han, *Angew. Chem. Int. Ed.,* **2020**, *59*, 16683.
174 L.-Y. Sun, T. Feng, R. Das, F. E. Hahn, Y.-F. Han, *Chem. Eur. J.,* **2019**, *25*, 9764.
175 D. Fink, A. Staiger, N. Orth, M. Linseis, I. Ivanović-Burmazović, R. F. Winter, *Inorg. Chem.,* **2020**, *59*, 16703.
176 N. Giri, M. G. Del Pópolo, G. Melaugh, R. L. Greenaway, K. Rätzke, T. Koschine, L. Pison, M. F. C. Gomes, A. I. Cooper, S. L. James, *Nature,* **2015**, *527*, 216.
177 N. O'Reilly, N. Giri, S. L. James, *Chem. Eur. J.,* **2007**, *13*, 3020.
178 B. D. Egleston, A. Mroz, K. E. Jelfs, R. L. Greenaway, *Chem. Sci.,* **2022**, *13*, 5042.
179 G. Zhang, A.-H. Emwas, U. F. Shahul Hameed, S. T. Arold, P. Yang, A. Chen, J.-F. Xiang, N. M. Khashab, *Chem,* **2020**, *6*, 1082.
180 G. Zhang, B. Moosa, A. Chen, N. M. Khashab, *ChemPlusChem,* **2020**, *85*, 1244.
181 A. Robles, O. Š. Miljanić, *ACS Appl. Nano Mater.,* **2023**.
182 D. Xia, P. Wang, X. Ji, N. M. Khashab, J. L. Sessler, F. Huang, *Chem. Rev.,* **2020**, *120*, 6070.
183 G. Zhang, W. Lin, F. Huang, J. Sessler, N. M. Khashab, *J. Am. Chem. Soc.,* **2023**.
184 T. Mitra, K. E. Jelfs, M. Schmidtmann, A. Ahmed, S. Y. Chong, D. J. Adams, A. I. Cooper, *Nat. Chem.,* **2013**, *5*, 276.
185 A. Dey, S. Chand, B. Maity, P. M. Bhatt, M. Ghosh, L. Cavallo, M. Eddaoudi, N. M. Khashab, *J. Am. Chem. Soc.,* **2021**, *143*, 4090.

186 S. Tashiro, M. Shionoya, *Acc. Chem. Res.,* **2020**, *53*, 632.
187 S. Tashiro, R. Kubota, M. Shionoya, *J. Am. Chem. Soc.,* **2012**, *134*, 2461.
188 S. Tashiro, T. Umeki, R. Kubota, M. Shionoya, *Angew. Chem. Int. Ed.,* **2014**, *53*, 8310.
189 S. Tashiro, K. Nakata, R. Hayashi, M. Shionoya, *Small,* **2021**, *17*, 2005803.
190 M. Han, S. Tashiro, T. Shiraogawa, M. Ehara, M. Shionoya, *Bull. Chem. Soc. Jpn,* **2022**, *95*, 1303.
191 S. Tashiro, W. He, R. Hayashi, Y. Lin, M. Shionoya, *Org. Chem. Front.,* **2021**, *8*, 4071.
192 S. Tashiro, H. Yonezawa, R. Kubota, T. Umeki, M. Shionoya, *Chem. Commun.,* **2016**, *52*, 7657.
193 W. He, S. Tashiro, M. Shionoya, *Chem. Sci.,* **2022**, *13*, 8752.
194 M. Li, Y. Liu, L. Shao, B. Hua, M. Wang, H. Liang, N. M. Khashab, J. L. Sessler, F. Huang, *J. Am. Chem. Soc.,* **2023**, *145*, 667.
195 J.-R. Wu, Y.-W. Yang, *Angew. Chem. Int. Ed.,* **2021**, *60*, 1690.
196 L.-P. Yang, S.-B. Lu, A. Valkonen, F. Pan, K. Rissanen, W. Jiang, *Beilstein J. Org. Chem.,* **2018**, *14*, 1570.
197 K. Jie, Y. Zhou, E. Li, F. Huang, *Acc. Chem. Res.,* **2018**, *51*, 2064.
198 K. Jie, Y. Zhou, E. Li, R. Zhao, F. Huang, *Angew. Chem. Int. Ed.,* **2018**, *57*, 12845.
199 E. Li, K. Jie, Y. Zhou, R. Zhao, F. Huang, *J. Am. Chem. Soc.,* **2018**, *140*, 15070.
200 M. Wang, J. Zhou, E. Li, Y. Zhou, Q. Li, F. Huang, *J. Am. Chem. Soc.,* **2019**, *141*, 17102.
201 M. Wang, S. Fang, S. Yang, Q. Li, N. M. Khashab, J. Zhou, F. Huang, *Mater. Today Chem.,* **2022**, *24*, 100919.
202 M. Yamada, F. Uemura, U. M. R. Kunda, T. Tanno, H. Katagiri, F. Hamada, *Chem. Eur. J.,* **2020**, *26*, 8393.
203 J. Zhou, G. Yu, Q. Li, M. Wang, F. Huang, *J. Am. Chem. Soc.,* **2020**, *142*, 2228.
204 J.-R. Wu, Y.-W. Yang, *J. Am. Chem. Soc.,* **2019**, *141*, 12280.
205 B. Moosa, L. O. Alimi, A. Shkurenko, A. Fakim, P. M. Bhatt, G. Zhang, M. Eddaoudi, N. M. Khashab, *Angew. Chem. Int. Ed.,* **2020**, *59*, 21367.
206 X. Li, W. Lin, V. Sharma, R. Gorecki, M. Ghosh, B. A. Moosa, S. Aristizabal, S. Hong, N. M. Khashab, S. P. Nunes, *Nat. Commun.,* **2023**, *14*, 3112.
207 K. Jie, Y. Zhou, E. Li, R. Zhao, M. Liu, F. Huang, *J. Am. Chem. Soc.,* **2018**, *140*, 3190.
208 Y. Zhou, K. Jie, R. Zhao, E. Li, F. Huang, *J. Am. Chem. Soc.,* **2020**, *142*, 6957.
209 Y. Zhou, K. Jie, R. Zhao, F. Huang, *J. Am. Chem. Soc.,* **2019**, *141*, 11847.
210 K. Jie, M. Liu, Y. Zhou, M. A. Little, S. Bonakala, S. Y. Chong, A. Stephenson, L. Chen, F. Huang, A. I. Cooper, *J. Am. Chem. Soc.,* **2017**, *139*, 2908.
211 T. Ogoshi, K. Saito, R. Sueto, R. Kojima, Y. Hamada, S. Akine, A. M. P. Moeljadi, H. Hirao, T. Kakuta, T.-a. Yamagishi, *Angew. Chem. Int. Ed.,* **2018**, *57*, 1592.
212 T. Ogoshi, R. Sueto, K. Yoshikoshi, Y. Sakata, S. Akine, T.-a. Yamagishi, *Angew. Chem. Int. Ed.,* **2015**, *54*, 9849.
213 H. Yan, J. Quan, H. Qu, F. Zhu, Y. Wang, M. K. Dhinakaran, T. Han, H. Li, *ACS Appl. Nano Mater.,* **2022**, *5*, 18637.
214 K. T. Tan, S. Ghosh, Z. Wang, F. Wen, D. Rodríguez-San-Miguel, J. Feng, N. Huang, W. Wang, F. Zamora, X. Feng, A. Thomas, D. Jiang, *Nat. Rev. Methods Primers,* **2023**, *3*, 1.
215 F. ZareKarizi, M. Joharian, A. Morsali, *J. Mater. Chem. A,* **2018**, *6*, 19288.
216 S. L. James, *Chem. Soc. Rev.,* **2003**, *32*, 276.
217 C. G. P. Taylor, J. S. Train, M. D. Ward, *Chemistry,* **2020**, *2*, 510.
218 A. Carné-Sánchez, G. A. Craig, P. Larpent, T. Hirose, M. Higuchi, S. Kitagawa, K. Matsuda, K. Urayama, S. Furukawa, *Nat. Commun.,* **2018**, *9*, 2506.
219 R. A. Smaldone, R. S. Forgan, H. Furukawa, J. J. Gassensmith, A. M. Z. Slawin, O. M. Yaghi, J. F. Stoddart, *Angew. Chem. Int. Ed.,* **2010**, *49*, 8630.
220 N. L. Strutt, D. Fairen-Jimenez, J. Iehl, M. B. Lalonde, R. Q. Snurr, O. K. Farha, J. T. Hupp, J. F. Stoddart, *J. Am. Chem. Soc.,* **2012**, *134*, 17436.
221 Q. Li, W. Zhang, O. S. Miljanić, C. H. Sue, Y. L. Zhao, L. Liu, C. B. Knobler, J. F. Stoddart, O. M. Yaghi, *Sci.,* **2009**, *325*, 855.

222 A. Saura-Sanmartin, A. Martinez-Cuezva, M. Marin-Luna, D. Bautista, J. Berna, *Angew. Chem. Int. Ed.,* **2021**, *133*, 10909.
223 V. N. Vukotic, S. J. Loeb, *Chem. Eur. J.,* **2010**, *16*, 13630.
224 I. Roy, J. F. Stoddart, *Acc. Chem. Res.,* **2021**, *54*, 1440.
225 S. J. Loeb, *Chem. Commun.,* **2005**, 1511.
226 D. J. Hoffart, S. J. Loeb, *Supramol. Chem.,* **2007**, *19*, 89.
227 N. C. Frank, D. J. Mercer, S. J. Loeb, *Chemistry,* **2013**, *19*, 14076.
228 H. Deng, M. A. Olson, J. F. Stoddart, O. M. Yaghi, *Nat. Chem.,* **2010**, *2*, 439.
229 B. H. Wilson, L. M. Abdulla, R. W. Schurko, S. J. Loeb, *Chem. Sci.,* **2021**, *12*, 3944.
230 H. T. B. Pham, J. Y. Choi, S. Huang, X. Wang, A. Claman, M. Stodolka, S. Yazdi, S. Sharma, W. Zhang, J. Park, *J. Am. Chem. Soc.,* **2022**, *144*, 10615.
231 W. Wu, Y. Xu, S. Wang, Q. Pang, S. Liu, *Chem. Commun.,* **2023**, *59*, 5890.
232 V. N. Vukotic, K. J. Harris, K. Zhu, R. W. Schurko, S. J. Loeb, *Nat. Chem.,* **2012**, *4*, 456.
233 P. J. Altmann, C. Jandl, A. Pöthig, *Dalton Trans.,* **2015**, *44*, 11278.
234 P. J. Altmann, A. Pöthig, *J. Am. Chem. Soc.,* **2016**, *138*, 13171.
235 P. J. Altmann, A. Pöthig, *Angew. Chem. Int. Ed.,* **2017**, *56*, 15733.
236 S. Guan, T. Pickl, C. Jandl, L. Schuchmann, X. Zhou, P. J. Altmann, A. Pöthig, *Org. Chem. Front.,* **2021**, *8*, 4061.
237 A. A. Heidecker, M. Bohn, A. Pöthig, *Z. Krist. - Cryst. Mater.,* **2022**, *237*, 167.
238 M. M. J. Smulders, S. Zarra, J. R. Nitschke, *J. Am. Chem. Soc.,* **2013**, *135*, 7039.
239 M. Rojas-Poblete, P. L. Rodríguez-Kessler, R. Guajardo Maturana, A. Muñoz-Castro, *Phys. Chem. Chem. Phys.,* **2021**, *23*, 15917.
240 A. Pöthig, S. Ahmed, H. C. Winther-Larsen, S. Guan, P. J. Altmann, J. Kudermann, A. M. Santos Andresen, T. Gjøen, O. A. Høgmoen Åstrand, *Front. Chem.,* **2018**, *6*.
241 J. S. Craig, L. Melidis, H. D. Williams, S. J. Dettmer, A. A. Heidecker, P. J. Altmann, S. Guan, C. Campbell, D. F. Browning, R. K. O. Sigel, S. Johannsen, R. T. Egan, B. Aikman, A. Casini, A. Pöthig, M. J. Hannon, *J. Am. Chem. Soc.,* **2023**, *145*, 13570.

2. Motivation

The overall aim of this thesis is to investigate the characteristics and interactions of the cationic pillarplex as building block in the solid-state. In the process, an enhanced understanding of the behaviour of porous pillarplexes in solution is aimed. Hence, the driving forces for a particular crystal arrangement and the influence or dependence of this arrangement on various parameters must be evaluated. By applying this fundamental knowledge of the pillarplex as a porous building block in the solid-state, further implementation as supramolecular organometallic ligand moieties in network materials can be achieved. The research carried out for this thesis can be divided into the following questions:

I How is the self-assembly of pillarplex salts and their properties in the solid-state influenced by the counter anion? Which (non-)covalent interactions are occurring and which of these demonstrate structure-decisive character?

The discrete supramolecular pillarplexes $[M_8L_2](X)_4$ with a predefined pore functionality and pore size is investigated towards the behaviour in the solid-state to gain a deeper understanding of the principles of self-assembly. While the pillarplex provides a broad range of parameters to vary within the metal ion, the ligands or the counter anions, the focus is put on the shape, size and charge of the counter anions and their interactions with the anisotropic pillarplex cation. Firstly, methodological tools to analyse the occurring (non-)covalent interactions were tested and their applicability towards an organometallocavitand was evaluated. Then, anion exchange reactions were performed to yield a library of pillarplex salts, which were analysed towards behaviour in the solid-state regarding the location and influence of solvent molecules, guest molecules and counter anions. The preservation of intrinsic porosity was investigated by adsorption experiments.

II Can a functionalisation be implemented into the pillarplex cation to achieve potential building blocks for the formation of network materials?

With the synthesis of the rim-modified triazole-based pillarplex $[M_8L^t_2]^{4+}$ an additional *N*-donor functionality was already introduced at the rim. Therefore, the -CH position at the pyrazole unit seems to be a fitting point for further introduction of functionality. To implement typical ligand units (e.g., carboxylates, pyridines) at this position, the first step could be the bromination followed by cross-coupling reactions to achieve suitable ligand moieties.

The functionalised pillarplexes will then be tested towards their implementation into network materials following literature-known synthetic procedures (e.g., solvothermal synthesis, diffusion, layering). The geometry of the metal precursors, the metal ions, solvent mixtures, temperature and additives can be varied to find a suitable method to form more dimensional materials, which will be analysed towards their chemical and structural composition and their properties (e.g., crystallinity, porosity, luminescence, thermal stability).

III Can mechanically interlocked pillarplex systems, which are bearing functional groups be achieve as potential building blocks for the formation of network materials?

The shape-selective encapsulation of linear alkyl chains into the pillarplex cavity and the formation of a pillarplex rotaxane by the addition of stopper units can be used to introduce a functional group for further coordination into network materials either through guest encapsulation or through smart design of the stopper units.

The encapsulation of difunctionalised alkyl chains (e.g., diamines, dicarboxylic acids) yields dynamic pseudorotaxanes already bearing ligand moieties (e.g., -NH_2, -COOH), which can be tested towards the implementation into network materials. Combining the pseudorotaxanes with stopper units yields the mechanically interlocked rotaxanes, which are bearing the functionality in the aromatic stopper unit.

These functionalised pillarplex (pseudo)rotaxanes will be tested towards their implementation into network materials. Investigation of suitable reactants (e.g., metal precursors, geometry, additives) and synthetic conditions (e.g., solvothermal synthesis, diffusion, deposition) must be performed to form 1D, 2D or 3D network materials, which will be analysed towards their chemical composition, structural arrangement, and their properties (e.g., responsivity).

3. Results and Discussion

3.1 Adsorption Studies of $[M_8L^{Me}_2](PF_6)_4$ and $[M_8L^{Me}_2](OAc)_4$

This chapter is based on work by this author, Philipp J. Altmann, Shengyang Guan, Yuh Hijikata, Shin-ichiro Noro, Jack D. Evans and Andreas Schneemann; manuscript in preparation.

3.1.1 Introduction

Porosity or porous materials are highly interesting topics, which influence several industrial processes, such as catalysis or separation of hydrocarbons.[1-12] Nevertheless, one porous material cannot fit all purposes and hence, further optimisation of the pore or the material itself is required to achieve a more accurate, miniaturised and efficient material.[13] Applying a (post-) synthetic modification approach leads to an improvement of the material properties by controlling the functionality in porous solids and their structure-property relationship.[14-16] In another approach crystal engineering[17-20] or pore engineering[21] is considered to form porous structures with the targeted properties. Besides the porosity of these materials, their chemical and mechanical stability, sorption kinetics, processability, mechanical properties, and thermal properties influence their applicability.[14] Most porous materials are extended networks, including porous coordination polymers, MOFs, zeolites, gels or clay, where the cavity is either formed upon material formation or by connection of porous subunits through intermolecular bonds.[22] In contrast, porous molecular materials are discrete molecules with a defined pore resulting in a high porosity, chemical stability and structural flexibility. The porous molecular materials exhibit solubility in (organic) solvents, which enables them to be processed into various forms (e.g, thin-films, membranes) and allows post-synthetic modification. Additionally, the porous units can undergo re-arrangement (e.g., NACs) as no interconnection is present.[23-26]

To generate reasonable predictions of the structure-property relationships, a detailed understanding of the inter- and intramolecular interactions between the porous host system and the guest is needed. This achieved knowledge of the host-guest system and their (non-)covalent interactions at a molecular level can be used to tailor the desired assemblies or porous material for specific applications. The influences of ions[20] – either metal ions or anions/cations – with their possible interactions (e.g., coulombic forces, metal coordination, (non-)classical hydrogen bonding) must be taken into account. In particular, a large internal cavity, ordered and well-defined pore dimensions, functionalised pore surfaces, adjustable pore dimensions and high tunability can be achieved in case of porous salts.[13,24,27] Additionally, due to the influence of a counter-ion, the structural flexibility and a certain sensitivity towards external stimuli was discovered.[20] By introducing metal sites and varying their number, the capacity of the obtained porous materials can be altered.[20,28]

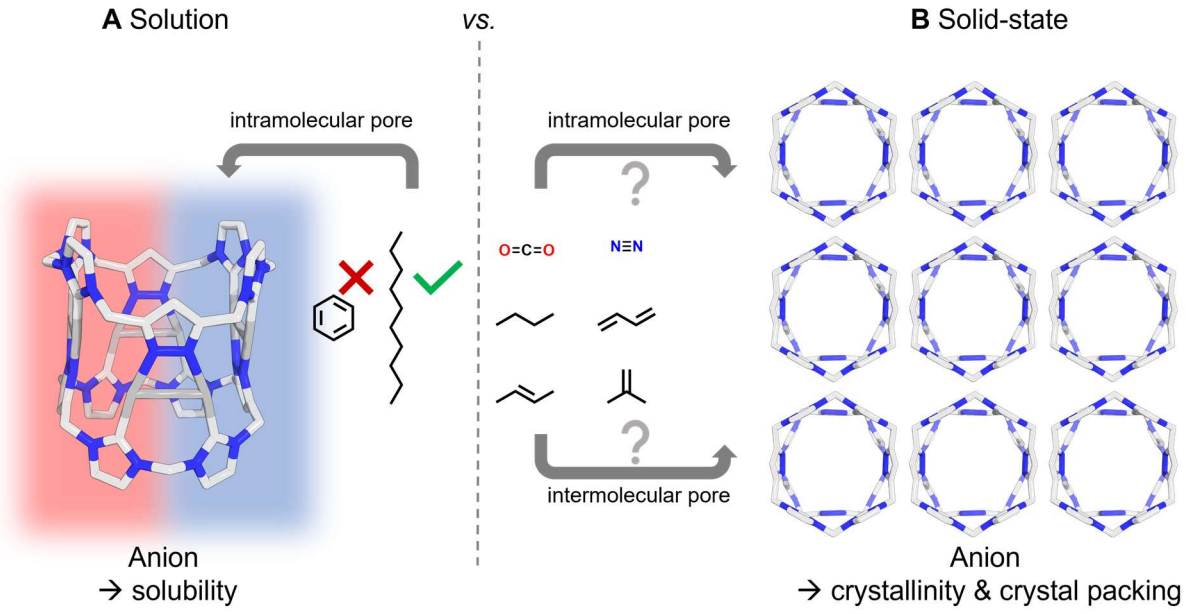

Figure 13: Schematic representation of pillarplex salts (A) in solution (red indicates aqueous solutions, blue indicates organic solutions), where encapsulation of linear guest molecules is preferred instead of branched aromatic molecules in the intramolecular pore of the pillarplex cation vs. (B) in solid-state with specific crystal arrangement of the pillarplex cations, where intramolecular pores inside the pillarplex cavity and intermolecular pores between the pillarplex cations are observed. The solid-state materials can be tested to the gas uptake of CO_2, N_2 and C_4 hydrocarbons n-butane, trans-2-butene, isobutylene and 1,3-butadiene.

Although the pillarplex salts $[M_8L^{Me}{}_2]X_4$ (M = Ag(I), Au(I); X=PF_6^-, OAc^-) with hexafluoro phosphate and acetate as counter anion were already analysed towards their properties in solution (Figure 13A)[29], no systematic studies for their behaviour in the solid-state were conducted. The investigations in solution revealed a strong influence of the anion towards the solubility. In particular, the PF_6^- salt provides solubility in organic solvent (e.g., acetonitrile, DMF), while the OAc^- salt is mainly soluble in aqueous solutions. Additionally, these organometallic complexes[30] provide a hydrophobic cavity with an approximate pore opening of 4.3 Å.[29] In solution, this pore size allows the shape-selective uptake of linear hydrocarbons, e.g., dodecyl diamines, while branched or aromatic hydrocarbons cannot enter the cavity. As the influence of the anions and the host-guest chemistry of the pillarplex salts $[M_8L^{Me}{}_2](X)_4$ are already partially studied in solution, the question arises about the performance of pillarplex salts in the solid-state (Figure 13B). This ionic supramolecule provides numerous parameters, such as a wide variety of size, shape and charge of anions, metal ions (M = Ag, Au) as well as the occurring (non-)covalent interactions (e.g., (non-)classical hydrogen bonding, metal coordination), with which can influence the solid-state structure.[31-32] Thus, the positions of different counter anions, their intra- or intermolecular (non-)covalent interactions and subsequently the influence of the selected anions on the crystal packing in the solid-state are investigated in detail.

3.1.2 Synthesis and Characterisation of $[M_8L^{Me}_2](PF_6)_4$ and $[M_8L^{Me}_2](OAc)_4$

The four pillarplex salts **1** $[Ag_8L^{Me}_2](PF_6)_4$, **2** $[Au_8L^{Me}_2](PF_6)_4$, **3** $[Ag_8L^{Me}_2](OAc)_4$ and **4** $[Au_8L^{Me}_2](OAc)_4$ (Figure 14) were synthesised according to literature[29] to conduct adsorption experiments on these salts in the solid-state. After synthesis and purification, **1**-**4** were analysed by ^{1}H NMR spectroscopy revealing the typical signal set for the organic residues in the range of 5-9 ppm, which verified the successful formation.

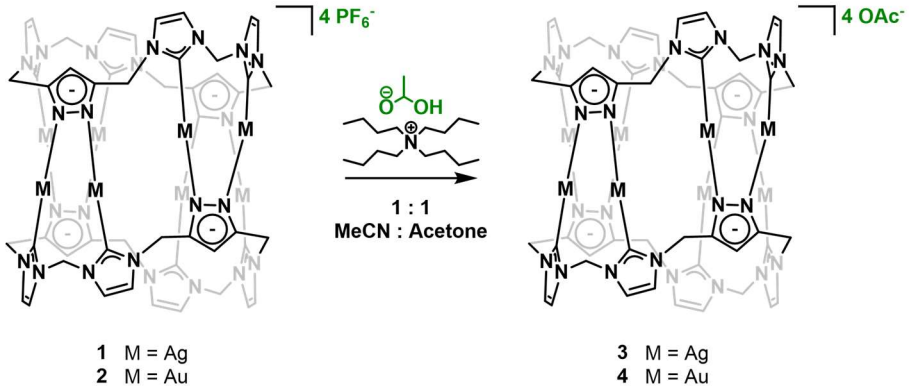

*Figure 14: Molecular structure of the pillarplex salts **1** $[Ag_8L^{Me}_2](PF_6)_4$, **2** $[Au_8L^{Me}_2](PF_6)_4$ and the anion exchange reaction towards pillarplex salts **3** $[Ag_8L^{Me}_2](OAc)_4$ and **4** $[Au_8L^{Me}_2](OAc)_4$.*

Single crystals suitable for SC-XRD measurements of **1** and **2** were obtained by slow diffusion of diethyl ether into a saturated solution of the respective pillarplex salt in acetonitrile. A combination of the solvents, water and acetone, was used to obtain suitable single crystals of the respective acetate pillarplex salts **3** $[Ag_8L^{Me}_2](OAc)_4$ and **4** $[Au_8L^{Me}_2](OAc)_4$. For each salt, single crystalline structures with large unit cells were observed, for which the location of the $[M_8L^{Me}_2]^{4+}$ cations was always possible to be determined by assignment of the heavy metal atoms. Due to varying quality of the obtained data, the location of the anions in some cases could only be determined partially. Nevertheless, the obtained crystal data was investigated towards the location of the counter anions, solvent molecules, the crystal arrangement and the observed (non-)covalent interactions. However, the solid-state structure analysis was quite complex, the best feasible models were discussed and the limitations due to data quality will be described in Chapter 3.1.5.

Beforehand, the diameters of the counter anions PF_6^- and acetate were analysed based on X-Ray diffraction data, where a medium diameter of 6.092 Å for PF_6^- and a medium diameter of 5.248 Å for the oxygen atoms of the acetate were calculated (Figure 15). The calculations based on XRD data indicate, that both anions exhibit a steric demand, which exceeds the pore opening of the pillarplex (4.3 Å[29]), which inhibits the anion to enter the cavity.

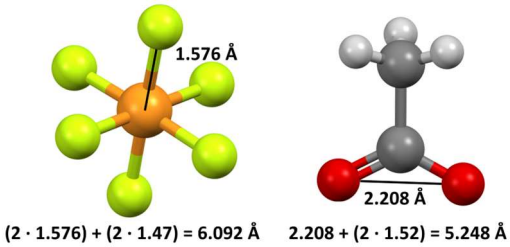

Figure 15: XRD data based calculations of the approximate diameter for PF_6^- with an average P-F distance of 1.576 Å[33] and the approximate diameter for acetate anion with an average O-O distance of 2.208 Å[33] with van-der-Waals radii for F 1.47 Å and O 1.52 Å.[34]

DFT Calculations

DFT (density functional theory) calculations were performed to investigate the location of the counter anions and possible interactions. The geometry optimisation performed with *ORCA* and an exchange-correlation GGA functional by Perdew-Burke-Ernzerhof (PBE). Def2 Aldrich basis sets were applied for the final geometry optimisations with the convergence criteria "TightOPT" and "TightSCF" (for details see Chapter 5.7). The positions of the counter anions were varied based on initial geometries obtained from single crystal X-Ray diffraction experiments. The DFT calculations were performed in the gas phase and with implicit implementation (CPCM) of solvent effects, namely MeCN for $[M_8L^{Me}_2](PF_6)_4$ and water for $[M_8L^{Me}_2](OAc)_4$. To confirm that the obtained geometries correspond to energetic minima, numeric frequency analysis with the same level of theory was performed and inspected for negative eigenfrequencies.

For optimised $[Ag_8L^{Me}_2](PF_6)_4$ in solution (MeCN), numeric frequency analysis showed negative eigenfrequencies even after several separate geometry optimisations and frequency analyses. However, only four negative eigenfrequencies with values < 10 cm^{-1} were obtained indicating that no saddle point was optimised. Due to the complexity of the pillarplex system, where the cation itself contains 124 atoms including eight metal atoms and the additional presence of the four anions (each containing seven atoms), the numeric frequency analysis was highly time-consuming and hence no further calculations were performed for the other materials.

The geometry optimisation of $[Ag_8L^{Me}_2](PF_6)_4$ in the gas phase revealed the encapsulation of one PF_6^- anion into the cavity (Figure 16A). This encapsulation was driven by the formation of metal coordination between F_{PF6} and the Ag(I) ions in the region of 2.927 – 2.989 Å, which exhibits slightly longer bond distances compared to bond distances obtained from crystal structures with an average distance of 2.499 Å[35]. This resulted in a structural deformation of the pillarplex cation on one side towards an oval shape. The other PF_6^- anions were calculated at the outside of the cation forming non-classical hydrogen bonds[36] between F_{PF6} and the hydrogen atoms of the organic rim. Notable, repeating the calculations with an implicit solvent model, no encapsulation of a counter anion PF_6^- into the cavity and no deformation of the pillarplex cation was observed (Figure 16B). This finding is in accordance with experimental NMR data, as no shifting or splitting of the signals in the ^{19}F and ^{31}P NMR spectra (F1S) was detected, which would indicate the encapsulation of the counter anion. These data suggest that the anions are located on the outside of the pore opening and form non-classical hydrogen bonds[36] with the hydrogen atoms of the organic rim.

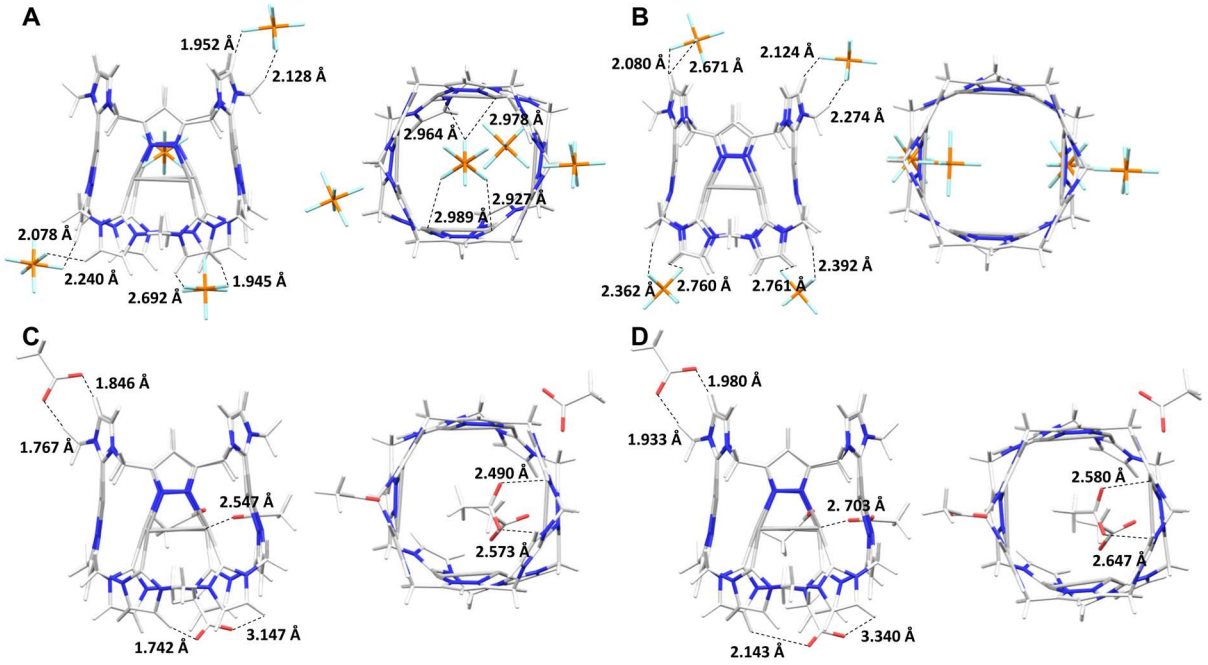

Figure 16: Optimised structures of (A) $[Ag_8L^{Me}_2](PF_6)_4$ in gas phase; (B) $[Ag_8L^{Me}_2](PF_6)_4$ in solution (MeCN); (C) $[Ag_8L^{Me}_2](OAc)_4$ in gas phase; (D) $[Ag_8L^{Me}_2](OAc)_4$ in solution (H_2O).

Geometry optimisation of $[Ag_8L^{Me}_2](OAc)_4$ was performed in the gas phase and in solution (Figure 16C+D). The starting geometry of the cation was taken from SC-XRD measurements, and two acetate anions were placed on the outside of the rim, while the two other anions were placed on the top of the pore opening. The calculations in gas phase and in solution revealed similar geometric arrangement of the pillarplex cation and anions with almost no change of the acetate anion locations relative to the pillarplex cation. Due to the small size of the acetate anions, encapsulation of these molecules into the pillarplex cavity was discovered, where one anion is completely located inside the cavity forming metal coordination of the oxygen atoms with the Ag(I) ions and one anion was located at the pore opening with the methyl group directed into the cavity. The OAc^- anions, which were located on the outside of the pillarplex cation showed the formation of hydrogen bonding of one anion in the small pocket of the organic rim and metal coordination of one OAc^- anion, which was located in close proximity to the Ag(I) ions. The metal-coordination between the acetate anions and Ag(I) revealed similar distances, when the OAc^- is located inside and outside of the cavity, in the range of 2.490 – 2.647 Å, and is in the similar range compared with coordinative bond distances obtained from crystal structures with average distances of 2.449 Å.[35]

As similar initial geometries for the DFT calculations for the respective $[Au_8L^{Me}_2](PF_6)_4$ and $[Au_8L^{Me}_2](OAc)_4$ were used, similar optimised geometries were obtained by DFT calculations (F97S).

Solid-state analysis

The cavities of the pillarplex salts **1**-**4** can host solvent molecules (e.g., Et_2O, MeCN, H_2O, acetone), which was analysed with ^{1}H NMR spectroscopy (F1S – F4S). An upfield shifting of the solvent signals indicate the encapsulation of such a solvent into the pillarplex cavity. In the case of **1** and **2** this behaviour was discovered for the Et_2O signals, while for **3** and **4** no shifts of the solvent signals were obtained. To further evaluate this, thermogravimetric measurements for pre-dried samples of **1** and **2** were performed. On one hand the thermostability of these salts was investigated, but the efficacy of the performed activation (100 °C *in vacuo*) was also evaluated. A minor loss of weight was followed by two major weight losses (F12S). The first one corresponds to 3.2% for **1** and 5.0% for **2** occurring between 30 °C and 350 °C. The shallow drop and minimal mass loss suggested the evaporation of diethyl ether that is encapsulated in the cavity, which is commonly observed during thermogravimetric analysis of MOFs.[37] The two major weight losses (350 – 400 °C; 400 – 800 °C) corresponds to 24.9% and approximately 15.5% for **1** and respectively 21.1% and 20.1% for **2**. Both pronounced losses of weight have been attributed to the decomposition of the organic parts of the samples. The calculated total mass percentage also corresponds to these measured weight losses. At 800 °C, a residue of approximately 55% was obtained, which roughly corresponds to the mass percentage of metal in the sample.

However, to ensure accessibility to the pillarplex cavity for adsorption experiments with N_2, CO_2 and C_4 hydrocarbons, these solvent molecules need to be removed. Hence, the samples were activated either by drying the white solids *in vacuo* at 100 °C for 72 h or by supercritical CO_2 activation, while their stability was monitored by ^{1}H NMR spectroscopy in solution and in solid-state, IR spectroscopy as well as powder X-Ray diffraction. The ^{1}H NMR spectra conducted before activation (labelled with as = as synthesised), contained the residual solvent signals of diethyl ether in **1** and **2** and acetone in **3** and **4** (for diethyl ether slight downfield shifted signals indicate the encapsulation inside the cavity). In contrast, in the ^{1}H NMR spectra conducted after activation (labelled with act = activated) no such signals were observed (F1S – F4S). Additionally, ^{1}H NMR spectroscopy was applied to verify that the chemical structure of the pillarplex salts was maintained by dissolving the samples after activation and checking for the integrity of the cation signals. IR spectra revealed similar signals before and after activation for the compound itself, while the intensity of the solvent signals decreased (F10S). The crystallinity of the pillarplex salts was monitored by powder X-Ray diffraction (Figure 17), for which the obtained pattern of the as synthesised samples displayed significantly higher crystallinity of the Ag(I)-pillarplex salts than for the Au(I) congeners. Following activation, **1** and **3** maintain the high crystallinity, displaying an identical set of reflections. This may indicate that the unit cell parameters and consequently the crystal arrangement remain unchanged. In contrast, the powder patterns of **2** and **4** already display minor crystallinity for the as synthesised samples, which is indicated by the presence of broad shoulders in the wider angular range. Visual inspection of samples **2** and **4** before and after activation revealed a strong discolouration of the white powders to a pink colour for **2** and a dark red colour for **4**. It is known, that colloidal gold solutions exhibit an intensive red colour due to the plasmon oscillation and show different colours dependent on the size and shape of the nanoparticles.[38-42] Based on this knowledge, it is proposed that during activation decomposition of the pillarplex salts could occur, which would lead to the formation of Au-nanoparticles. However, PXRD measurements (Cu K_α radiation, λ = 1.5406 Å) with typical broad reflections at 38.1° (111) and 44.3° (200) would reveal the formation of nanoparticles.[43-45] As the reflections for **2** and **4** are indeed broad signals and are detected at large angles of approximately 27°, 32°and 46°, a

comparison with the typical reflections of elemental Au-nanoparticles was conducted. The observed reflections are not detected at the identical angles, which is an indication that no nanoparticles were formed. The colour change might also be caused by the formation of large, nanocrystalline aggregates of pillarplex cations, where short Au(I)-Au(I) distances are present.[46-47] In summary, the Ag(I)-pillarplexes **1** and **3** exhibit high crystallinity before and after activation, while for the Au(I)-pillarplexes **2** and **4** only broad reflections in the wider angular range are detected.

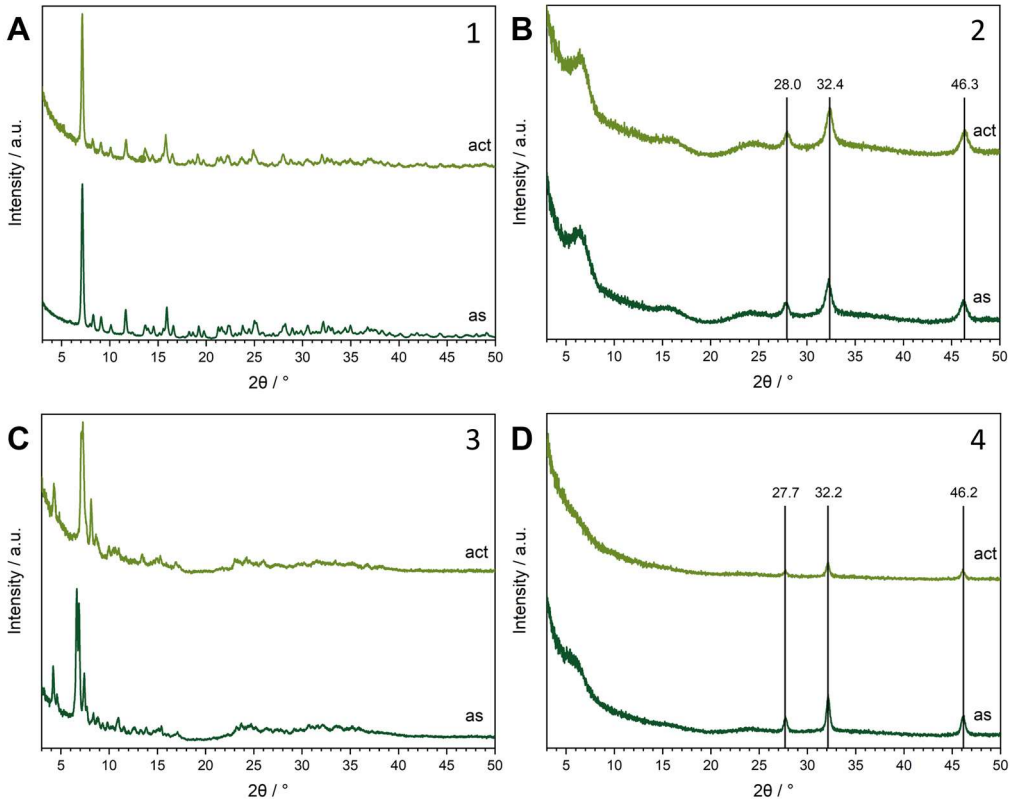

*Figure 17: PXRD patterns: (A) of **1** $[Ag_8L^{Me}{}_2](PF_6)_4$; (B) of **2** $[Au_8L^{Me}{}_2](PF_6)_4$; (C) of **3** $[Ag_8L^{Me}{}_2](OAc)_4$; (D) **4** $[Au_8L^{Me}{}_2](OAc)_4$ as synthesised (as) and activated (act).*

3.1.3 *Excursus* Theoretical Background for Gas Adsorption

In order to understand the results of the gas adsorption measurements in the following Chapter 3.1.4 (and 3.2.5) it is necessary to define the terms used according to the *IUPAC* definitions.[48]

Adsorption is defined as the accumulation of molecules, atoms or ions in the vicinity of a surface, whereas desorption is the reversed process to release the adsorbed material. To simplify the further explanation, a gas to solid adsorption is assumed. In such a gas / solid adsorption process (Figure 18A) the particle in the gas phase is called adsorptive. When this particle is adsorbed at the surface it is called adsorbate and the surface, where particles can adsorb, is called adsorbent. The most common type of adsorption is the physisorption, which described the interaction of a gas with a surface by attractive dispersion forces, repulsive forces and molecular interactions (e.g., polarisation, dipole). Besides the physisorption,

chemisorption can occur, where upon contact of adsorptive and adsorbent, the intermolecular forces create a chemical bond.

As porosity will be investigated in further studies, the term surface refers to the inner surface of a pore. However, a pore is classified according to its size.[49] Pores with a narrow width not exceeding 2 nm are considered micropores, pores with a width between 2 nm and 50 nm are called mesoporous and macropores exhibit a width greater than 50 nm. Based on this classification, the pillarplex with a pore opening of 4.3 Å (0.43 nm) is considered to be microporous.

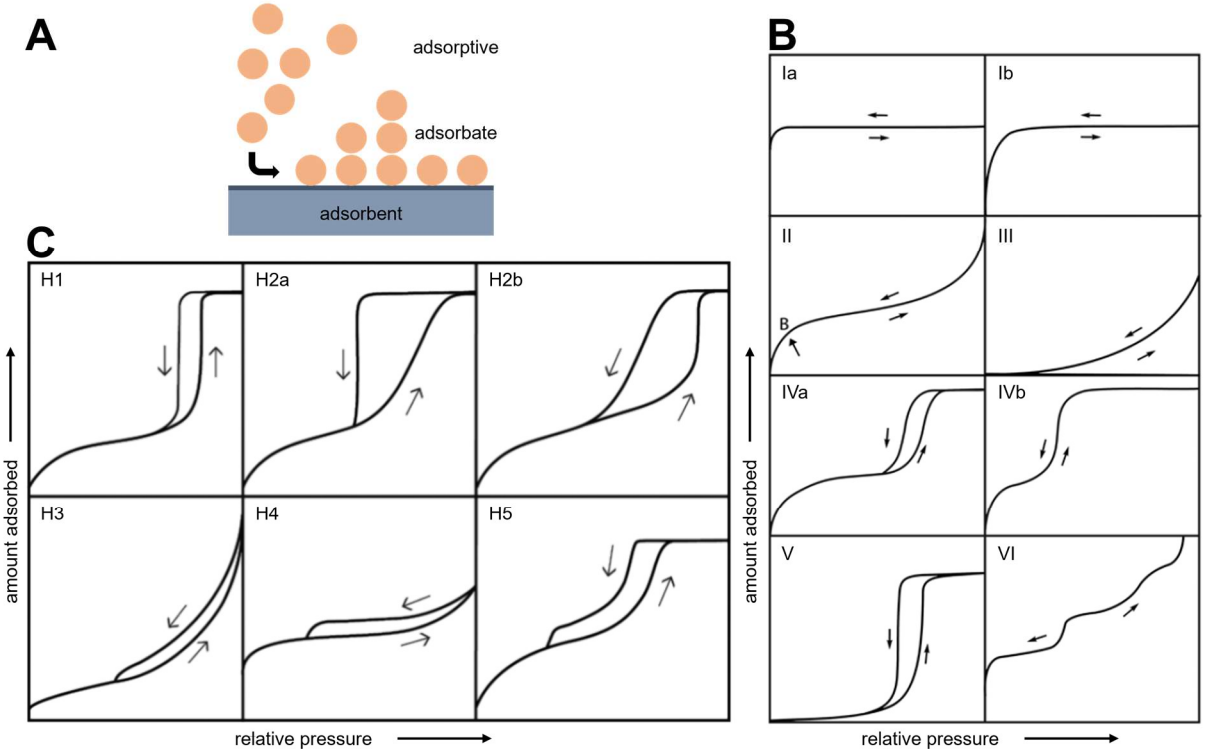

Figure 18: (A) Schematic representation of a gas-solid adsorption process with the adsorptive in gas phase, which is adsorbed at the surface of the adsorbent and then called adsorbate; (B) Isotherms classified by IUPAC into types I-VI; (C) Hystereses classified by IUPAC into types H1-H5. (B) and (C) are slightly varied and taken from [48].

After measuring the quantity of adsorbed gas, the data is represented as isotherms. The course of an isotherm is closely related to the pore structure of the adsorbent. *IUPAC* therefore identified eight types of physisorption isotherms (Figure 18B) with associated hysteresis curves (Figure 18C):[48]

Type I isotherms are common for microporous materials with a limited inner pore surface area. A steep uptake at low pressure is determined due to enhanced adsorbent-adsorptive interactions in narrow pore, which results in the filling of micropores. As the curve reaches a plateau of a limited value, the uptake is controlled by the accessible micropore volume rather than by the internal surface area. Normally, the desorption is fully reversible. Dependent on the narrowness of the micropores, it is decided whether isotherm type Ia or Ib is assigned. A less steep gas uptake is observed, the broader the pore size distribution is and potentially small mesopores can show isotherm type Ib.

Type II isotherms are determined for nonporous or macroporous adsorbents, where an unrestricted monolayer-multilayer adsorption up to high pressure is allowed. The completeness of the monolayer is indicated by point B and the more distinctive this point is,

the less of an overlap of monolayer coverage and multilayer adsorption is observed. Again, isotherm type II indicates reversible desorption.

Type III isotherms are similar to II, however no indication for the completeness of the monolayer is detected. This results by weak adsorbent-adsorbate interactions and hence adsorbed molecules are clustered at the favourable sites of the surface of a nonporous or microporous solid resulting in a theoretical “infinite” gas uptake.

Type IV isotherms are common for mesoporous adsorbents, where initial monolayer adsorption on the pore walls with following pore condensation occurs until a final saturation plateau is reached. This behaviour is determined by adsorbent-adsorptive interactions and interactions of molecules in the condensed state. When a pore width exceeds the critical width (large pores) a hysteresis is present (IVa), while for smaller pores, no hysteresis is accompanied (IVb).

Type V isotherms follow the curve of type III isotherms at low pressure dictated by the weak adsorbent-adsorbate interactions, while at higher pressure molecular clustering occurs with a following pore filling to reach a limited plateau.

Type VI isotherms a typical layer-by-layer adsorption curvatures, which are observed for nonporous surfaces. The step-height is the capacity of one layer and the sharpness dependents on the applied conditions (gas, temperature).

Hystereses appear when adsorption and desorption do not follow the same path. In general, this can be assigned to the metastability of adsorption due to capillary condensation and / or network effects (e.g., pore blocking, interpenetration, percolation).[50-52] Depending on the pore structure, different types of curves are observed, of which the most common ones are again classified according to *IUPAC*:

Type H1 hystereses are obtained for well-defined (mesoporous) pores of a cylindric shape with a narrow opening by delayed evaporation. The distribution of pore opening size corresponds to the magnitude of the hysteresis. In this type, network effects play a minimal role.

Type H2 hystereses are common for complex pore structures including disordered or connected pores, where network effects play a significant role. The variation in pore opening size distinguishes between a, characterised by a small pore opening and b featuring a wider pore opening size distribution.

Type H3 hystereses correspond to type II isotherms and are obtained for macroporous or nonporous absorbents. The steep step down in desorption can be caused by not completely filled macropores or delayed condensation at nonporous surfaces.

Type H4 hystereses are similar to H3, but a combination of types I and II isotherms, where the uptake at low pressure is explained by micropore filling. This behaviour is often observed for aggregated crystals or (micro-)mesoporous material.

Type H5 hystereses are obtained for pore structures, which contain open and partially blocked mesopores.

Based on the classifications presented in this chapter, the following gas adsorption experiments will be assessed.

3.1.4 Gas Adsorption and C_4 Hydrocarbon Uptake Experiments

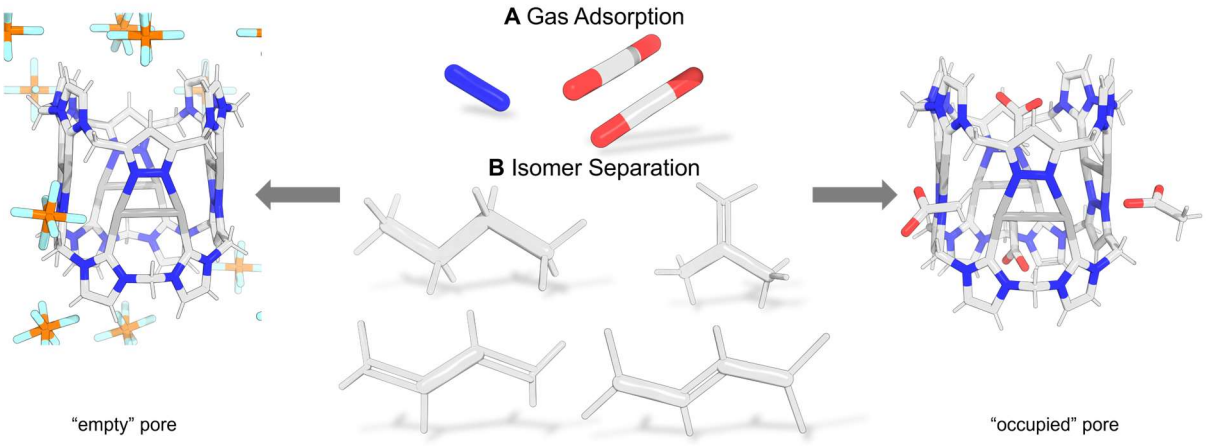

*Figure 19: Schematic overview of the (A) Gas adsorption experiments conducted with CO_2 and N_2; (B) Vapour adsorption experiments conducted with the C_4 hydrocarbons n-butane (C_4H_{10}), iso-butylene (i-C_4H_8), trans-2-butene (t2-C_4H_8) and 1,3-butadiene (1,3-C_4H_6), which were performed on the pillarplex salts **1**-**4**.*

As already mentioned in the introduction of this chapter, the pores of supramolecules can be utilised to encapsulate and probably store small molecules by the formation of host-guest complexes. Therefore, the synthesised pillarplex salts **1**-**4** will be tested towards their gas uptake of CO_2 and N_2 in BET measurements (Figure 19A). Additionally, their uptake of various C_4 hydrocarbon isomers is evaluated and compared (Figure 19B). The selective uptake or the selective separation of hydrocarbon isomers is highly interesting for industry since the hydrocarbons are obtained as mixtures with varying ratios by fluid catalytic cracking (FCC), steam cracking and methanol-to-olefins(MTO) processes.[53-54] The separation and especially the purification is crucial and accounts for high costs since it is nowadays achieved by distillation.[55-57] These processes require high energy and therefore the separation of C_4-hydrocarbons by adsorption would result in reduced cost and energy contributions.[58]

Before analysing the gas adsorption, the materials need to be activated to ensure solvent-free pores. The activation of the molecules can be achieved either at high temperatures *in vacuo* or by solvent exchange with following activation by supercritical CO_2 as discussed in Chapter 3.1.2. After activation, the gas adsorption experiments of the compounds **1**-**4** were conducted with N_2 at 77 K and with CO_2 at 195 K. The evaluation of the gas adsorption was performed based on the Brunauer-Emmett-Teller (BET) method, which aims to calculate the specific surface area of a material.[59-60]

The N_2 adsorption isotherm (Figure 20A) of $[Ag_8L^{Me}_2](PF_6)_4$ demonstrated the characteristics of a type II isotherm.[48] Initially, at low pressure (0 – 3 kPa) a steep uptake with a turning point at 33.2 $cm^3\ g^{-1}$ was observed. Subsequently, a plateau was reached spanning from 3.5 kPa up to 82.6 kPa with a gradual increase to an adsorbed volume of 47.1 $cm^3\ g^{-1}$. At higher pressure, starting at 82.6 kPa, another steep increase in gas adsorption was detected with an overall N_2 uptake of 68.9 $cm^3\ g^{-1}$ at 100 kPa. The desorption curve followed a similar pattern albeit a marginal hysteresis was present throughout the desorption process. The initial rapid uptake might be attributed to either the filling of micropores or the formation of a monolayer on a nonporous surface. Given that the pillarplex cation is considered a microporous material, the filling of the pillarplex pores was plausible. The slight increase in the plateau can be associated with mesopores. Due to the charged nature of the pillarplex cation and the presence of counter

anions, there may be mesoporous regions between the pillarplex cations in the solid-state, where nitrogen condensation could occur. This would be consistent with the observed minor hysteresis, which could be attributed to delayed evaporation of the adsorbate or network effects.

The CO_2 isotherm (Figure 20B) of **1** followed a type I isotherm[48], which featured a steep initial uptake at low pressure. The curve gradually approached a plateau, ultimately reaching a gas uptake of 60.2 $cm^3\ g^{-1}$ at 100 kPa. The desorption curve exhibits a minimal hysteresis, which cannot be aligned with a specific type. A type I isotherm is typically observed in microporous materials with limited inner pore surface. Therefore, it could be assumed that CO_2 can enter through the pillarplex pore openings and accumulate within the cavity until it is saturated. The hysteresis could be explained by adsorption metastability, originated from the delayed evaporation of the liquid-like adsorbate.

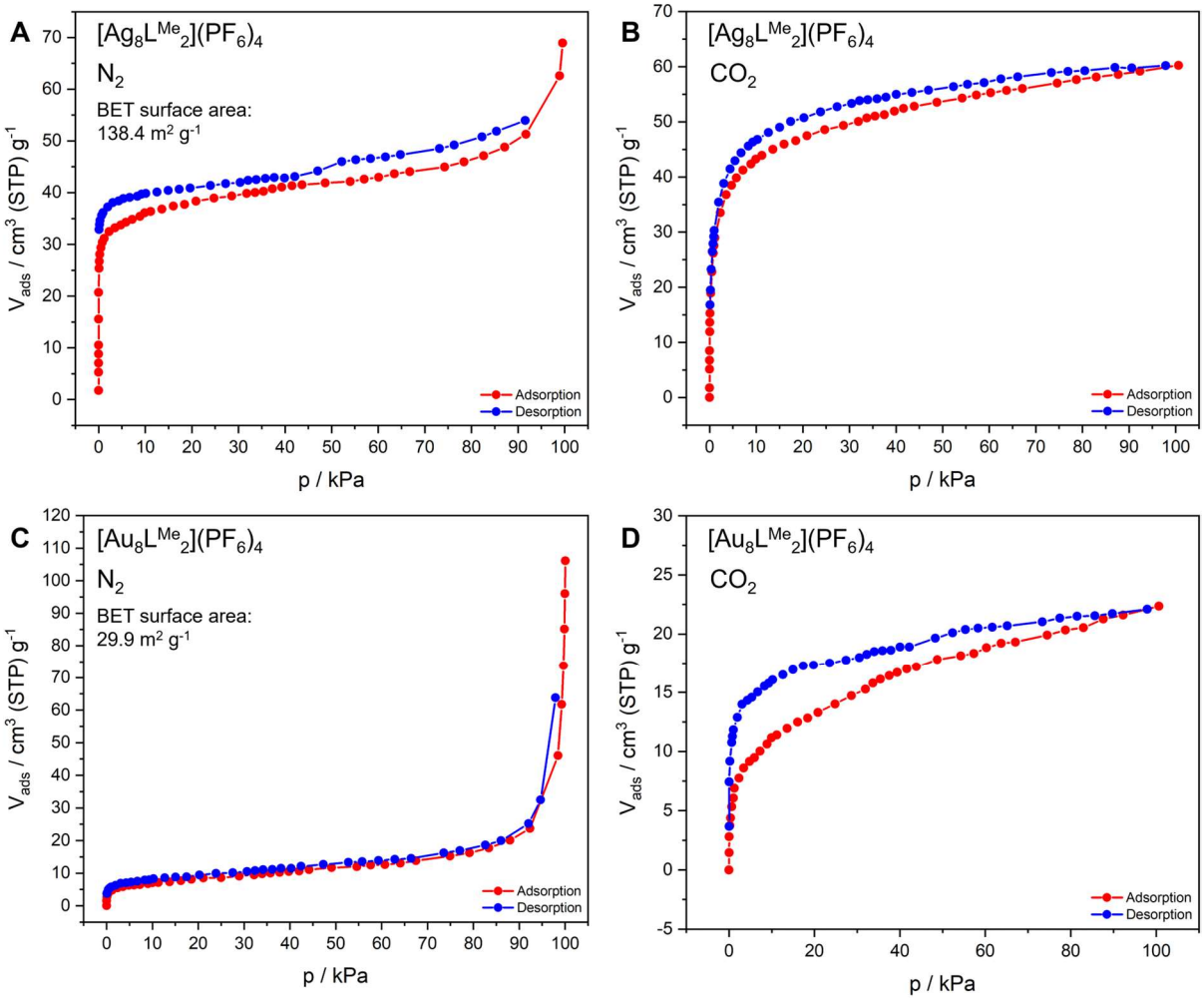

Figure 20: Physisorption Isotherms of (A) $[Ag_8L^{Me}_2](PF_6)_2$ for N_2 recorded at 77 K; (B) $[Ag_8L^{Me}_2](PF_6)_2$ for CO_2 recorded at 195 K; (C) $[Au_8L^{Me}_2](PF_6)_2$ for N_2 recorded at 77 K; (D) $[Au_8L^{Me}_2](PF_6)_2$ for CO_2 recorded at 195 K. Red circled lines represent the adsorption and blue circled lines represent the desorption.

The N_2 adsorption isotherm of **2** (Figure 20C) was assigned to follow a type II curvature.[48] A steep uptake at low pressure is extending to 4.9 kPa resulting in an adsorbed volume of 6.2 $cm^3\ g^{-1}$. Subsequently, a plateau was reached with a gas uptake of 16.2 $cm^3\ g^{-1}$ continuing up to 79.2 kPa. At higher pressure another steep increase in gas adsorption was detected leading to an overall adsorbed volume of 106.1 $cm^3\ g^{-1}$. The modest uptake at low pressure could originate from the uptake of gas into the microporous cavity of pillarplexes. However, it

is also plausible that this corresponded to a monolayer on macroporous or nonporous material. The shallow increase on the plateau could be elucidated by the addition of multiple layers on top of the monolayer on macroporous or nonporous materials. On the other hand, it could signify the uptake of gas within the mesoporous spaces between the pillarplex cations. At elevated pressure, the nitrogen condensation was enhanced by capillary condensation and therefore, the minimal hysteresis was observed during the desorption process could be caused by delayed evaporation or by network effects.

In the CO_2 isotherm of **2** (Figure 20D), which aligned with a type I isotherm[48], a similar behaviour to the CO_2 isotherm of **1** with a significant smaller gas uptake was noted. An initial steep uptake reached the limited value of approximately 22.4 $cm^3\ g^{-1}$ at 100 kPa. The isotherm was already categorised as type I, but due to a less pronounced steepness of the initial uptake, the assignment to a type Ib isotherm was more plausible.[48] This suggested the presence of a microporous material with a larger pore size distribution and a limited inner pore surface. The behaviour of a type Ib isotherm might indicate that CO_2 can enter the pillarplex cavity or might be caused by a combination of micropore filling and simultaneous filling of the mesoporous space exterior to the pillarplex cations. During the desorption process, a major hysteresis was observed, most likely classified as H2b. This could be resulted by network effects of complex pores with a wider pore size distribution, potentially attributed to the combination of microporous and mesoporous space within the material.

Comparison of the N_2 isotherms of **1** and **2** revealed a significant lower gas adsorption for **2**, which can be attributed to micropores. However, the overall gas uptake for **2** is higher reaching 106.2 $cm^3\ g^{-1}$. Upon examining the CO_2 isotherms, a significant higher gas uptake is reached for **1**. The isotherm type I suggested that CO_2 could enter the microporous cavity, which offered a limited pore surface for adsorption. The discrepancy of gas uptake (60.2 $cm^3\ g^{-1}$ for **1**, 22.4 $cm^3\ g^{-1}$ for **2**) could be attributed either to the metal ions (Ag *vs.* Au) or the arrangement in the solid-state. Although the exact influence of various metal remains unclear it has already been discovered that unsaturated metal sites enhance the interaction with the adsorbed species. This phenomenon, combined with the slight difference in the ionic radii[61] for Ag(I) and Au(I), may explain the higher microporosity for **1**.[62-65]

Given by previous suggestion of a partial occupation of the pillarplex cavity by the acetate anions for compounds **3** and **4**, it was anticipated that the gas uptake in the respective gas adsorption experiments would be lower than the measured one for **1** and **2**. However, the data obtained from the adsorption experiments with **3** and **4** yielded data of limited quality with a gas uptake < 10 $cm^3\ g^{-1}$. Therefore, no interpretation of the results is possible, which could be caused by the fact that these materials lack porous character.

However, comparing the obtained values (BET surface area 138.4 $m^2\ g^{-1}$ (**1**), 29.9 $m^2\ g^{-1}$ (**2**)) with literature-known organic and metal-organic polyhedral exhibiting BET surface areas > 1000 $m^2\ g^{-1}$,[66-73] the obtained gas uptake was in total comparatively modest. However, considering the narrow pore opening of the pillarplex (4.3 Å = 0.43 nm), the total pore volume of the pillarplex salts was also comparatively modest. This narrow but defined pore diameters of the related compounds **1**-**4** can be used for the separation of small molecules. Several organic molecules were already tested towards their separation by microporous materials[74-77] and recently, the separation of hydrocarbons was also investigated by supramolecular organic cavitands, where high selectivity's were achieved.[78-81] Until now, the pillarplex salts were tested towards only their encapsulation of linear alkanes (e.g. diamino dodecane,

dodecyl-diammonium)[29,31-32] in solution, and therefore, their applicability for vapour separation with the following C_4 hydrocarbons as proof-of-concept was explored: butane (C_4H_{10}), *iso*butylene (*i*-C_4H_8), *trans*-2-butene (*t*2-C_4H_8) and 1,3-butadiene (1,3-C_4H_6). The physisorption experiments were carried out using $[Ag_8L^{Me}{}_2](PF_6)_4$ (**1**), $[Au_8L^{Me}{}_2](PF_6)_4$ (**2**), $[Ag_8L^{Me}{}_2](OAc)_4$ (**3**) and $[Au_8L^{Me}{}_2](OAc)_4$ (**4**) at 298 K (Figure 21).

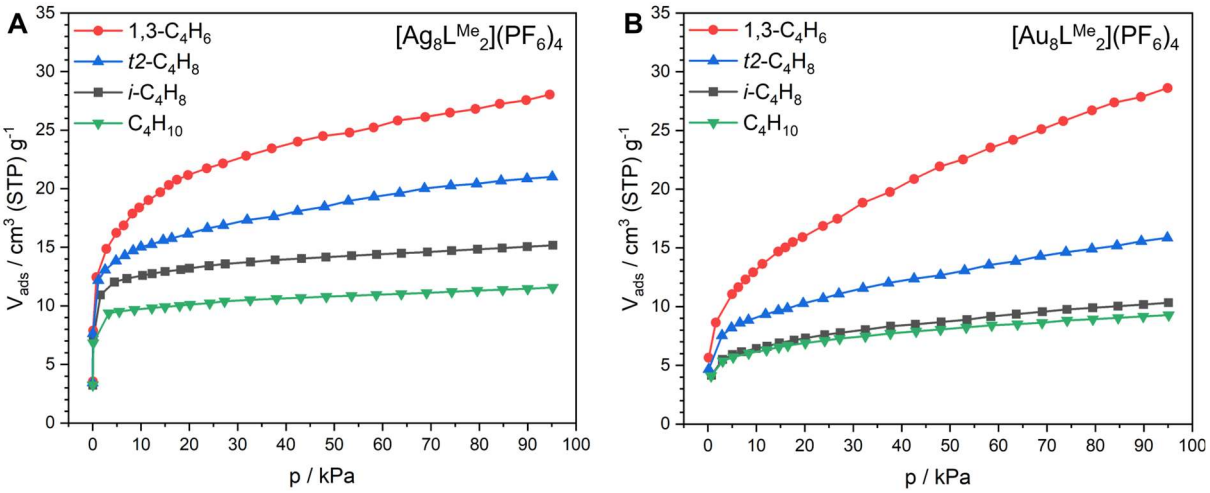

Figure 21: Adsorption isotherms for 1,3-C_4H_6 (red circles), t2-C_4H_8 (blue triangles), i-C_4H_8 (black squares) and C_4H_{10} (green triangles) on (A) $[Ag_8L^{Me}{}_2](PF_6)_4$; (B) $[Au_8L^{Me}{}_2](PF_6)_4$ measured at 298 K.

All experiments followed a type I isotherm suggesting that a microporous material is present, and the steepness of the initial uptake is dependent on the pore opening. The following trend of guest uptake was noted: 1,3-C_4H_6 (red) > *t*2-C_4H_8 (blue) > *i*-C_4H_8 (black) > C_4H_{10} (green).

As the determined isotherms of **1** are assigned to type I, an initial steep uptake at low pressure reached into a plateau. In general, **1** yielded the highest uptake of C_4 hydrocarbons with 28.1 $cm^3\ g^{-1}$ for 1,3-C_4H_6, 21.0 $cm^3\ g^{-1}$ for *t*2-C_4H_8, 15.2 $cm^3\ g^{-1}$ for *i*-C_4H_8 and 11.6 $cm^3\ g^{-1}$ for C_4H_{10} reached at 100 kPa (Table 1). However, the differences are not significant and hence the adsorption of C_4 molecules per pillarplex was calculated. This corresponds to 3.41 molecules of 1,3-C_4H_6, 2.5 molecules of *t*2-C_4H_8, 1.8 molecules of *i*-C_4H_8 and 1.4 molecules of C_4H_{10} per pillarplex. Similar isothermal behaviour was reported for **2**, where uptakes of 28.6 $cm^3\ g^{-1}$ for 1,3-C_4H_6, 15.9 $cm^3\ g^{-1}$ for *t*2-C_4H_8, 10.3 $cm^3\ g^{-1}$ for *i*-C_4H_8 and 9.3 $cm^3\ g^{-1}$ for C_4H_{10} were reached at 100 kPa (Table 1). Notably, a slightly higher uptake of 1,3-C_4H_6 was obtained for **2** and the disparity between the uptake of 1,3-C_4H_6 and the other C4 hydrocarbons became more pronounced. Again, the number of adsorbed molecules per pillarplex was determined revealing 4.4 molecules of 1,3-C_4H_6, 2.4 molecules of *t*2-C_4H_8, 1.6 molecules of *i*-C_4H_8 and 1.4 molecules of C_4H_{10} per pillarplex cation at 100 kPa.

The probability of adsorption of specific molecules is dependent on various factors, such as size of adsorbate, pore size, interactions. In order to elucidate the variations in the uptake of the four different C_4 hydrocarbons by compounds **1** and **2**, the kinetic diameter of the guest molecules and their polarisability was investigated (Table 1). 1,3-C_4H_6 and *t*2-C_4H_8 have a kinetic diameter of 4.31 Å[58], which is comparable in size to the pore opening of the pillarplex (4.3 Å).[29] Therefore, the encapsulation of 1,3-C_4H_6 and *t*2-C_4H_8 is in principle possible, although the differences in their uptake could not be explained by the kinetic diameters. Therefore, the polarisability is analysed and a higher polarisability was reported for 1,3-C_4H_6 compared to *t*2-C_4H_8 (86.4 *vs.* 81.8 · 10^{-25} cm^3).[58,82-84] The observed higher uptake of 1,3-C_4H_6 could be explained by this difference in polarisability. The hydrocarbons *i*-C_4H_8 and C_4H_{10}

exhibit a kinetic diameter, which exceeds the pore opening of the pillarplex (4.84 Å, 4.69 Å).[58,82-84] Investigations of the pillarplex rim have already shown that a certain flexibility of the cation is achievable[32,85], which would enable the encapsulation of the hydrocarbons *i*-C_4H_8 and C_4H_{10}. Considering only the kinetic diameter would result in a slightly higher probability for C_4H_{10} uptake, however the measured data yielded opposite results. Again, the differences in uptake could be explained due to the polarisability, which was slightly higher for C_4H_{10} ($82.0 \cdot 10^{25}$ cm^3, compared to $80.0 \cdot 10^{25}$ cm^3 for *i*-C_4H_8).[58] The differences in the uptake of **1** and **2** could be explained by the different ionic radii[61] for Ag(I) and Au(I), as the pore opening of the cavity was comparatively similar for **1** and **2** due to the hydrogen atoms of the rim determining the size of the entrance. No definite statement can be made, as other factors, such as coordinative interactions, dipole interactions, pore blocking, network effects, could influence the adsorption.

The uptake of C_4 hydrocarbons by **3** and **4** was also studied. However, an overall lower uptake was anticipated due to the results obtained from the N_2 gas adsorption measurements. Indeed, an overall lower uptake, following a similar trend (1,3-C_4H_6 > *t*2-C_4H_8 > *i*-C_4H_8 >= C_4H_{10}) as detected for **1** and **2**, was observed. The only notable difference was that *i*-C_4H_8 and C_4H_{10} exhibited almost no distinction in their adsorption behaviour. For **3** uptakes of 21.2 cm^3 g^{-1} for 1,3-C_4H_6, 8.7 cm^3 g^{-1} for *t*2-C_4H_8, 1.1 cm^3 g^{-1} for *i*-C_4H_8 and 1.0 cm^3 g^{-1} for C_4H_{10} were reached at 100 kPa. For 4 uptakes of 12.9 cm^3 g^{-1} for 1,3-C_4H_6, 6.0 cm^3 g^{-1} for *t*2-C_4H_8, 3.5 cm^3 g^{-1} for *i*-C_4H_8 and 3.4 cm^3 g^{-1} for C_4H_{10} were reached at 100 kPa (F14S).

*Table 1: Data obtained from the vapour adsorption measurements and the calculated IAST (ideal adsorbed solution theory) selectivity's for compounds **1** and **2**.*

		1 $[Ag_8L^{Me}_2](PF_6)_4$	**2** $[Au_8L^{Me}_2](PF_6)_4$
1,3-C_4H_6	V_{ads} [cm^3 g^{-1}]	28.1	28.6
kinetic diameter [Å]	4.31		
polarisability [cm^3]	$86.4 \cdot 10^{-25}$		
***t*2-C_4H_8**	V_{ads} [cm^3 g^{-1}]	21.0	15.9
kinetic diameter [Å]	4.31		
polarisability [cm^3]	$81.8 \cdot 10^{-25}$		
***i*-C_4H_8**	V_{ads} [cm^3 g^{-1}]	15.2	10.3
kinetic diameter [Å]	4.84		
polarisability [cm^3]	$80.0 \cdot 10^{-25}$		
C_4H_{10}	V_{ads} [cm^3 g^{-1}]	11.6	9.3
kinetic diameter [Å]	4.69		
polarisability [cm^3]	$82.0 \cdot 10^{-25}$		
IAST selectivity	1,3-C_4H_6 / C_4H_{10}	16.9	70.2
	1,3-C_4H_6 / *i*-C_4H_8	5.3	36.1
	1,3-C_4H_6 / *t*2-C_4H_8	1.2	4.1

Additionally, the ideal adsorbed solution theory (IAST) selectivity's were calculated from the single component adsorption isotherms, to evaluate adsorption selectivity of equimolar mixtures.[86-88] For the equimolar mixtures of 1,3-C_4H_6/C_4H_{10}, 1,3-C_4H_6/*i*-C_4H_8 and 1,3-C_4H_6/*t*2-C_4H_8 the calculated selectivity's amount to 16.9, 5.3 and 1.2 for **1** and 70.2, 36.1 and 4.1 for **2** at 100 kPa (Table 1). The highest IAST selectivity values were obtained for equimolar mixture 1,3-C_4H_8 / C_4H_{10}, which is in accordance with the obtained isotherms. However, **2** seems to exhibit a higher selectivity for gas separation than **1**, as generally higher values were determined.

3.1.5 Crystallographic Investigation

In order to examine the arrangement of pillarplex salts **1**-**4** in the solid-state and potentially discern any correlation between the determined gas uptake and the crystal arrangement, SC-XRD measurements were conducted with suitable single crystals. As mentioned above, the analysis of the solid-state structures was quite complex due to the observation of large unit cell parameters, varying quality of measurements and difficulties in assigning counter anions. Nevertheless, the best feasible models are described below.

1 $[Ag_8L^{Me}_2](PF_6)_4$, was solved and refined in the orthorhombic space group *P b c n* (No. 60) with the asymmetric unit containing one $[Ag_8L^{Me}_2]^{4+}$ cation, four PF_6^- counter anions and eight acetonitrile molecules. During refinement, a co-crystallised molecule of diethyl ether was identified inside the cavity, which, however, was treated with the SQUEEZE procedure[89] due to the strong disorder. By comparing the number of removed electrons with the number of electrons present in one molecule of diethyl ether (64 e^-), it was determined that exactly one molecule was encapsulated inside the cavity. In accordance with the DFT calculations, the counter anions are arranged close to the rim of the pillarplex cation, but outside of the cavity exhibiting non-classical hydrogen bonding[36] between H_{rim} and F_{PF6}. The crystal packing shows layers (along the b-axis) of chain-aligned pillarplex cations (along the a-axis, Figure 22A) with the PF_6^- counter anions staged in between. Considering the chain-aligned arrangement a repetition of two cationic units with a rotation angle of 44.95° and an argentophilic Ag(I)-Ag(I) distance of 3.791(1) Å is observed (Figure 22B). Additionally, every second cationic unit is pore-to-pore connected along the c-axis to the next layer of metallophilic chain-aligned pillarplex cations by numerous non-classical[36] H_{rim} to F_{PF6} interactions (Figure 22C+D).

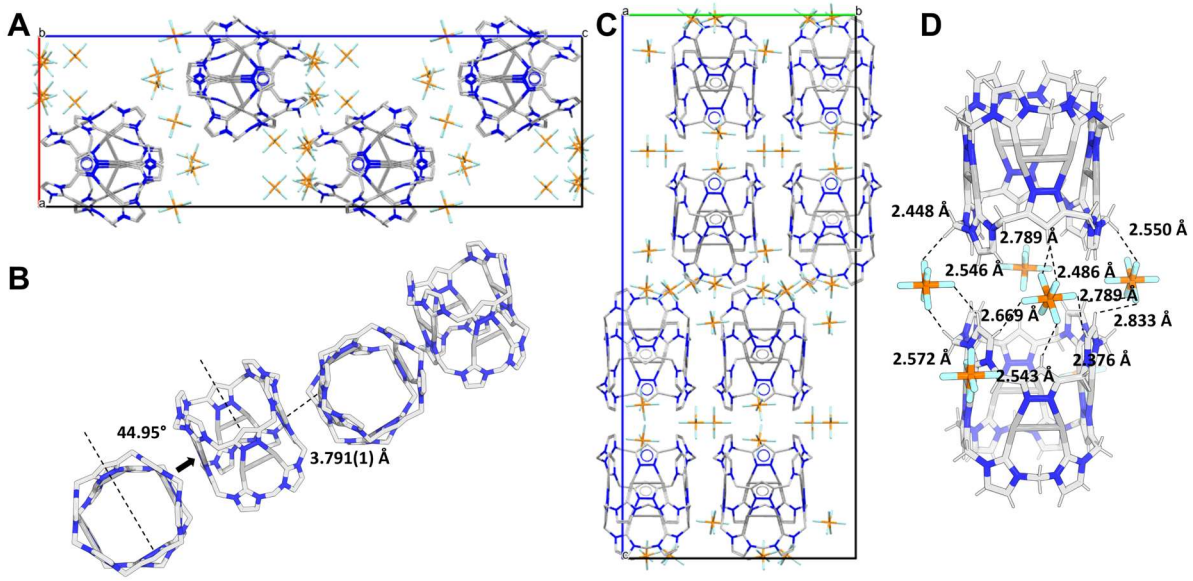

*Figure 22: Representation of the solid-state structure of **1** $[Ag_8L^{Me}_2](PF_6)_4$: (A) Crystal packing along a-axis, (B) Tilted chain alignment of $[Ag_8L^{Me}_2]^{4+}$ along the a-axis, (C) Crystal packing along the c-axis; (D) Non-covalent interactions between the $[Ag_8L^{Me}_2]^{4+}$ cations and the PF_6^- anions.*

In contrast, **2** $[Au_8L^{Me}_2](PF_6)_4$ crystalises in different polymorphs and two of the polymorphous structures could be determined by SC-XRD measurements. As both space groups led to valuable results, the structure of **2** was solved in the triclinic space group *P* 1 (No. 1) with parameters a = 15.0306(12) Å, b = 15.0397(12) Å, c = 16.2780(13) Å, α = 117.469(2)°, β = 117.486(2)°, γ = 90.070(3)° (Figure 23A-C) and in the triclinic space group *P* -1 (No. 2) with parameters a = 27.529(3) Å, b = 27.529(3) Å, c = 27.529(3) Å, α = 107.61°, β = 108.89°, γ = 111.94° (Figure 23D-F).

Polymorph **2a** was solved and refined in the space group *P* 1 with the asymmetric unit containing only one $[Au_8L^{Me}_2]^{4+}$ cation and six of the respective PF_6^- anions, of which four are partially occupied summing up to the residual two PF_6^- anions. The analysis of the occurring non-covalent interactions (Figure 23C) yields mainly non-classical hydrogen bonding. In particular between the counter anions and the pillarplex rim, non-classical hydrogen bonding[36] is observed (2.25 Å – 2.94 Å), while no aurophilic interactions are detected between neighbouring $[Au_8L^{Me}_2]^{4+}$ cations with Au(I)-Au(I) distances of 7.502(4) Å – 7.504(4) Å (Figure 23B). The crystal packing of **2a** along the b-axis is examined and a chain alignment of the $[Au_8L^{Me}_2]^{4+}$ cations is determined. The cations are not tilted towards each other and the chain-aligned layer of pillarplex cations form a zigzag arrangement with the next layer by the shift of the cations of the next layer into the space between the pillarplex cations of one layer. This shift might be influenced by the hydrogen bonding interactions with the counter anions, which are connecting the pillarplex cations from one layer to the next layer. Consequently, every second layer of $[Au_8L^{Me}_2]^{4+}$ shows a pore-alignment (along the c*-axis, Figure 23A) of those pillarplex cations $[Au_8L^{Me}_2]^{4+}$. Upon refinement of **2a**, a disorder of the $[Au_8L^{Me}_2]^{4+}$ cations is observed, where the second allocation of cation is rotated by 180°, resulting in the partial occupancy of the PF_6^- counter anions.

The second polymorph **2b** was solved in *P* -1 with the asymmetric unit containing four $[Au_8L^{Me}_2]^{4+}$ and sixteen PF_6^- units (Figure 23D-F). Four symmetrical independent $[Au_8L^{Me}_2]^{4+}$ cations (displayed in red, yellow, blue and green in Figure 23D) are present and are connected by aurophilic interactions with Au(I)-Au(I) distances of 3.57 Å – 4.43 Å (Figure 23D). The crystal packing along the a-axis (Figure 23E) displays the pore alignment of the yellow $[Au_8L^{Me}_2]^{4+}$ cations, where two PF_6^- anions are located in between two pore-aligned cations. The three other symmetrical independent cations surround the inner cation (yellow). These outer cations are tilted to the inner cation by 93.54° – 106.55° and to each other by 45.65° – 58.14°. The three outer cations form a helical-like structure laying around the inner cation, where every layer is rotated by 180°. The crystal packing along the b-axis shows a similar pore alignment of the cations (blue), where the PF_6^- molecules are located on the external sites of the rim forming non-classical hydrogen bonding[36] with the neighbouring pillarplex cations. Similar behaviour is observed for the cation, depicted in red colour, along the c-axis. The fourth symmetrical independent cation (green) also exhibits identical crystal arrangement but is not arranged along a specific crystallographic axis. Interestingly, analysis of the non-covalent interactions indicates an anomalous position of the two PF_6^- anions, as these anions are located in the pore opening of the pillarplex rim with a short distance to the Au(I) ions of 3.78 Å (Figure 23F).

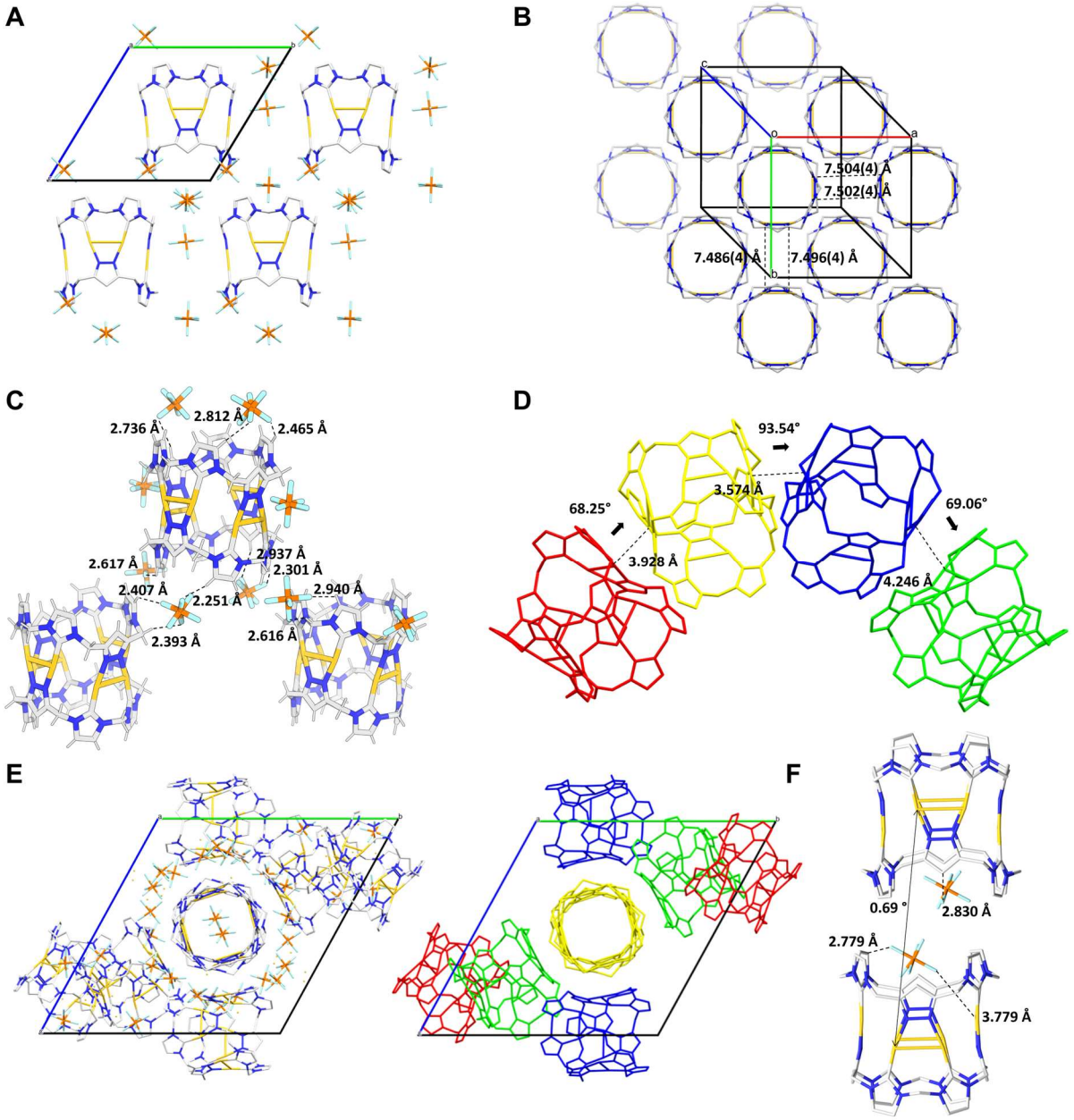

Figure 23: Representation of the solid-state structure of ***2a*** *$[Au_8L^{Me}_2](PF_6)_4$ in space group P 1: (A) Crystal packing along the c*-axis; (B) Crystal packing in top view of cationic $[Au_8L^{Me}_2]^4$ with Au(I)-Au(I) distances; (C) Non-covalent interactions of $[Au_8L^{Me}_2]^{4+}$ with counter anions PF_6^- with the main contribution of non-classical hydrogen bonding[36] of F_{PF6-} and H_{rim}; Representation of the solid-state structure of* ***2b*** *$[Au_8L^{Me}_2](PF_6)_4$ in space group P -1: (D) Four symmetrical-independent $[Au_8L^{Me}_2]^{4+}$ cations (displayed in red, yellow, blue and green) contained in the asymmetric unit with aurophilic Au(I)-Au(I) distances; (E) Crystal packing along the a-axis with a pore alignment of the central pillarplex cations (displayed in yellow); (F) Non-covalent interactions of $[Au_8L^{Me}_2]^{4+}$ with the PF_6^- anion.*

Although the diameter of acetate appears to be too sterically demanding to enter the pillarplex pore, the crystal structure of **3** and **4** results in partially occupied cavities, with each pore containing two acetate anions. Thereby, the methyl groups of the acetate ions point towards the middle of the cavity.

Although, the obtained crystal data for **3** $[Ag_8L^{Me}_2](OAc)_4$ was of limited quality, the $[Ag_8L^{Me}_2]^{4+}$ cation could be refined isotropically, while the acetate anions were refined

anisotropically. **3** crystallised in the monoclinic space group $P\,2_1/c$ (No. 14; a = 29.41(3) Å, b = 32.88(3) Å, c = 31.13(3) Å, α = γ = 90°, β = 115.620(19)°) with the asymmetric unit containing three $[Ag_8L^{Me}_2]^{4+}$ cations and twelve acetate anions respectively. Each pillarplex pore is occupied by two acetate molecules with the methyl group directed to the centre of the cavity and the oxygen atoms pointed towards the rim indicating hydrogen bonding with H_{rim}. The remaining two acetate molecules are located outside of the $[Ag_8L^{Me}_2]^{4+}$ cations suggesting metal coordination between the oxygen atoms. Additionally, they exhibit a short distance of 2.68 Å to the Ag(I) metal ion (Figure 24A). As depicted in Figure 24D, the rim of one cation is deformed to an oval pore opening with a diameter of 8.926 Å, while the diameter of the round rim is measured to be 9.014 Å. The structural analysis reveals co-crystallised water molecules, which form hydrogen bonding with the pillarplex rim, but were removed by SQUEEZE procedure.[89] Regarding the crystal packing of the pillarplex, the three symmetrical independent $[Ag_8L^{Me}_2]^{4+}$ cations form a metallophilic chain alignments in the c*-direction with short Ag(I)-Ag(I) distances of 3.22 Å to 3.45 Å with the cations being tilted by 33.30° - 135.40° (Figure 24B+C).

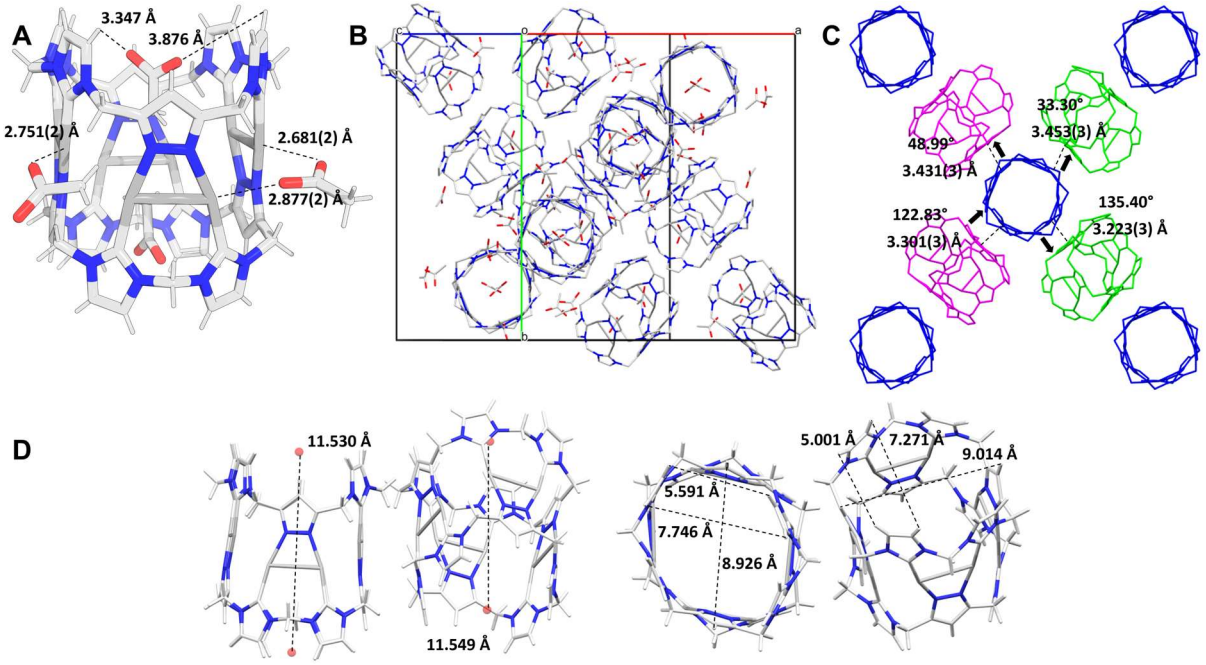

*Figure 24: Representation of the solid-state structure of **3** $[Ag_8L^{Me}_2](OAc)_4$: (A) Non-covalent interactions between the $[Ag_8L^{Me}_2]^{4+}$ cation and the OAc^- anions with contributions of hydrogen bonding and metal-coordination; (B) Crystal packing along the a-axis, (C) Tilted chain alignment of the three symmetrical independent cations (displayed in blue, green and pink); (D) Calculated differences of height and pore opening of the "normal" cation and the oval cation.*

A more detailed analysis of the crystal structure of **4** revealed two different polymorphs. **4a** was solved and refined in trigonal space group $R\bar{3}c$ (No. 167) with parameters a = 77.212(9) Å, b = 77.212(9) Å, c = 24.674(4) Å, α = β = 90°, γ = 120° and with an asymmetric unit containing 1 1/2 $[Au_8L^{Me}_2]^{4+}$ cations and respectively six counter anions. While three acetate anions are encapsulated in the cavity (*viz*. each cavity is occupied by two acetate ions with the methyl group pointing to the inside of the cavity), the residual acetate anions are located on the side-top of the pore opening. The distances for the hydrogen bonding of the $O_{acetate}$ and the H_{rim} are determined to reach from 2.252 Å to 2.586 Å (Figure 25A). Visualising the $[Au_8L^{Me}_2]^{4+}$ cations in colours by symmetry equivalent for clarity, the crystal packing of **4a**

shows large aggregate (displayed along the c-axis, Figure 25B), which can be divided into inner groups of three cations (depicted in green) and an outer ring of cations (depicted in blue). The cations of the internal group of three $[Au_8L^{Me}_2]^{4+}$ cations (green) are tilted by an angle of 34.04° towards each other in one direction (Au(I)-Au(I) distances of 3.527(4) Å) and are forming layers (perpendicular to the a-axis), where every second group of three pillarplex cations is tilted in the same direction (Figure 25C). The outer ring (depicted in blue, Figure 25D) can be divided into pairs of two cations, which are connected by Au(I)-Au(I) coordination (3.407(1) Å) and tilted towards each other with an angle of 35.79°. Those pairs of two $[Au_8L^{Me}_2]^{4+}$ cations construct the outer ring in a zigzag configuration tilted to each other by 111.50°. The large aggregates are itself interconnected by Au(I)-Au(I) metal coordination of two pillarplex cations (blue) with distances of 3.366(2) Å (Figure 25E).

On the other hand, **4b** was solved and refined in the orthorhombic space group *C c c a* (No. 68) with parameters a = 33.3585(34) Å, b = 59.7626(81) Å, c = 31.3472(31) Å, α = β = γ = 90°. Due to the limited quality of the crystal data, only partial occupation of the cavities by acetate ions could be refined. The asymmetric unit contains 4 1/2 independent $[Au_8L^{Me}_2]^{4+}$ cations (Figure 25F). Thereby, the methyl group point to the middle of the cavity. Three of the symmetrical independent $[Au_8L^{Me}_2]^{4+}$ are chain-aligned with short Au(I)-Au(I) distances of 3.389 Å – 3.463 Å, where the cations are tilted towards each other by 35.68 – 55.29°. A pore alignment along the c-axis of the $[Au_8L^{Me}_2]^{4+}$ cations (depicted in green and red, Figure 25G) is observed, which are alternating arranged along the a-axis.

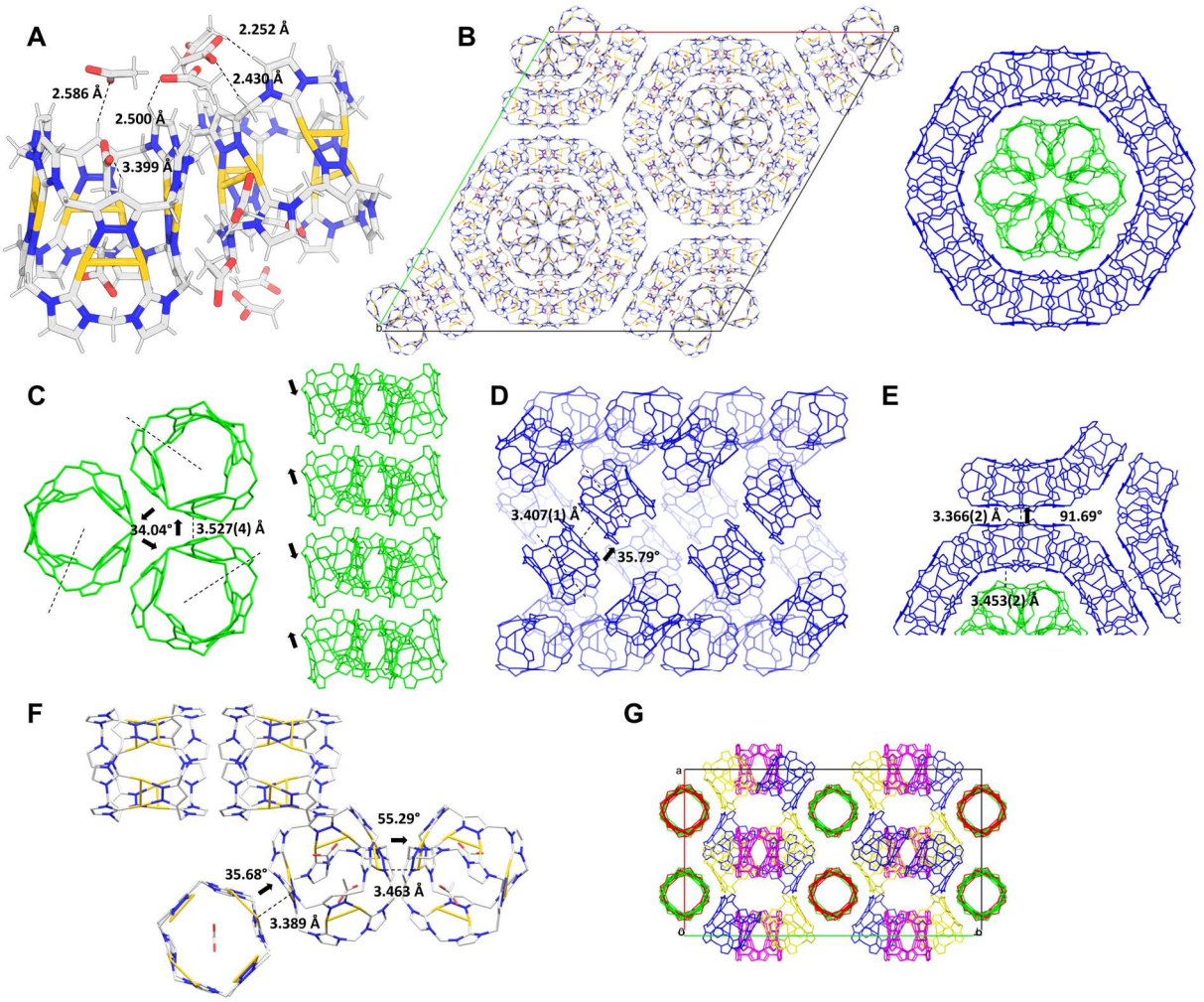

*Figure 25: Representation of the solid-state structure of **4a** $[Au_8L^{Me}{}_2](OAc)_4$ in space group $R\bar{3}c$: (A) Non-covalent interactions between the $[Au_8L^{Me}{}_2]^{4+}$ cations and the OAc^- anions, (B) Crystal packing along the c-axis exhibiting large aggregates, which are depicted as the symmetrical independent $[Au_8L^{Me}{}_2]^{4+}$ cations in blue and green for simplification, (D-F) arrangement of the symmetrical independent cations; Representation of the solid-state structure of **4b** $[Au_8L^{Me}{}_2](OAc)_4$ in space group C c c a: (F) Asymmetric unit containing 5 1/2 $[Au_8L^{Me}{}_2]^{4+}$ cations and encapsulated acetate anions; (G) Crystal packing of $[Au_8L^{Me}{}_2]^{4+}$ cations along the c-axis of the five symmetrical independent cations depicted in green, red, blue, yellow and pink.*

In summary, the arrangement of the pillarplex salts **1**-**4** in the solid-state can be influenced by various factors including the type of anions, hydrogen bonds, solvent interactions and metallophilic interactions. In the case of $[Ag_8L^{Me}{}_2](PF_6)_4$ (**1**) and $[Au_8L^{Me}{}_2](PF_6)_4$ (**2**) the counter anion PF_6^- was not encapsulated within the cavity, while for $[Ag_8L^{Me}{}_2](OAc)_4$ (**3**) and $[Au_8L^{Me}{}_2](OAc)_4$ (**4**) partial encapsulation by the counter anion acetate was observed. DFT calculations to optimise the geometry suggested the encapsulation of one PF_6^- anion into the pillarplex in the gas phase. However, when applying an implicit solvent model with MeCN, this encapsulation was no longer determined. This finding was further supported by NMR studies, which revealed no shift of the respective signals in the ^{19}F and ^{31}P NMR spectra.

Polymorphs were identified for both compounds **2** and **4**. The formation of polymorphs is influenced by various factors, such as the used solvent, solvent ratio, temperature, pressure and the presence of additives. Despite similar procedure for crystallisation attempts, variations in the factors solvent ratio, pressure conditions, glass equipment and environmental factors

like temperature fluctuations or vibrations from equipment in the fume hood could lead to the formation of polymorphs for compounds **1** and **3**. To assess the consistency between the bulk material and the single crystals, PXRD patterns were compared (F9S). While the measured PXRD patterns of **1** and **3** exhibited sharp reflections, those of **2** and **4** displayed only broad signals at large angles. Although the calculated patterns based on the SC-XRD measurements revealed similarities to the measured ones for **1** and **3**, a complete match was not obtained. This indicates that the bulk material may not be arranged in the same manner as in the single crystals. The calculated pattern for **2a**, **2b**, **4a** and **4b** revealed sharp reflections but could not be directly compared to those measured from the bulk material, as these diffractograms displayed only broad signals in the larger angular region.

3.1.6 Summary and Outlook

The literature-known pillarplex salts $[Ag_8L^{Me}_2](PF_6)_4$, $[Au_8L^{Me}_2](PF_6)_4$, $[Ag_8L^{Me}_2](OAc)_4$ and $[Au_8L^{Me}_2](OAc)_4$ were investigated towards their behaviour in gas adsorption experiments (N_2, CO_2), vapour adsorption experiments (1,3-C_4H_6, *t*2-C_4H_8, *i*-C_4H_8, C_4H_{10}) and their arrangement in the solid-state *via* SC-XRD measurements. The hypothesis that there might be a correlation between adsorption properties and solid-state arrangement, especially concerning the locations of counter anions (PF_6^- *vs.* OAc^-), the metal ion (Ag *vs.* Au) and the occurring interactions, was issued.

Suitable single crystals for compounds **1**-**4** were successfully obtained and analysed. **1** crystallised in a chain-aligned arrangement of $[Ag_8L^{Me}_2]^{4+}$ cations, tilted towards each other, with Ag(I)-Ag(I) distances of 3.79 Å. The layers of these chains were interconnected by non-classical hydrogen bonding[36] between the pillarplex rim and the counter anions PF_6^- (H_{rim} – F_{PF6}). **2** crystallised in two different polymorphs. **2a** exhibited a highly ordered structure with chain-aligned cations, indicating the absence of aurophilic interactions due to Au(I)-Au(I) distances of 7.50 Å. The cations formed a zigzag arrangement from layer to layer through non-classical hydrogen bonds[36] between H_{rim} and F_{PF6}. On the other hand, **2b** revealed four symmetrical independent cations, which are tilted and chain-aligned by Au(I)-Au(I) distances of 3.10 – 3.60 Å. A helical-like arrangement along the a-axis with three cations surrounding a pore alignment of $[Au_8L^{Me}_2]^{4+}$ cation with two PF_6^- located between them was discovered. Notable, the counter anions PF_6^- in all cases were located outside of the cavity, leaving the micropore accessible. This solid-state arrangement could allow additional (mesoporous) void volume between the cations, anions and co-crystallised solvent molecules. Although the unit cells obtained from SC-XRD and PXRD measurements were not identical, the crystal structures revealed that the PF_6^- anion is not encapsulated inside the cavity. This finding could explain the measured gas uptake behaviour for N_2 and CO_2. For **1** and **2** type II isotherms were observed for the uptake of N_2.[48] The initial steep uptake at low pressure might be attributed to either the presence of micropores followed by mesopore uptake or the formation of a monolayer on a nonporous material with subsequent multilayer formation.[48] Interestingly, **1** exhibited a higher gas uptake at low pressure, while **2** showed an overall higher gas uptake (68.9 $cm^3\ g^{-1}$ for **1** *vs.* 106.1 $cm^3\ g^{-1}$ for **2**). This behaviour was supported by the determined BET surface of 138.4 $m^2\ g^{-1}$ for **1** and of 29.9 $m^2\ g^{-1}$ for **2**, which could in both cases be assigned to the micropore surface. The CO_2 isotherms followed type I curvature, indicating gas

uptake in microporous material with a limited inner pore surface with an overall CO_2 uptake of 60.2 $cm^3\ g^{-1}$ for **1** and 22.4 $cm^3\ g^{-1}$ for **2**.[48] This finding would be in accordance with the observed microporous behaviour of **1** and **2** in the case of N_2 gas uptake.

Structure analysis of **3** revealed the encapsulation of two acetate anions per pillarplex cavity. Three symmetrical independent cations, tilted towards each other and chain-aligned with Ag(I)-Ag(I) distances ranging from 3.22 – 3.45 Å were observed. Besides the hydrogen bonds between counter anion and rim hydrogen atoms, metal coordination of O_{OAc} to Ag(I) with distances of 2.68-2.88 Å was identified. The crystallisation attempts for **4** resulted in two different polymorphs and in both cases partial occupation of the cavity by acetate anions was present. For **4a** the formation of large aggregates was observed, with an inner part containing three $[Au_8L^{Me}_2]^{4+}$ cations and an outer part containing pairs of cations arranged in a zigzag manner. Aurophilic interactions were determined between the three cations, the pairs of cations and between the inner and outer part. **4b** exhibited a mixture of chain-aligned and pore-aligned $[Au_8L^{Me}_2]^{4+}$ cations. However, not all acetate positions could be assigned due to limited data. In summary, for **3** and **4** the cavity of the pillarplex was partially occupied by acetate anions, thereby reducing the accessible void space inside the micropore. However, the crystal arrangement still allowed the presence of mesopores between the cations and anions. Unfortunately, the adsorption data for N_2 and CO_2 in the case of **3** and **4** displayed limited quality, potentially originated by the nature of the sample as it could lack porosity. Alternatively, the sample could have been compromised during the activation process, demonstrated by a colour change to pink or dark red. This could suggest the formation of nanoparticles in conjugation with the decomposition of the pillarplex.

The analysis of the arrangement of the pillarplex salts in the solid-state posed challenges given by the two polymorphous structures for **2** and **4**, which is also likely to occur for the Ag(I)-pillarplexes. Polymorphism and the inconsistency between the unit cells determined from single crystals and bulk powder material makes the evaluation of correlations between the crystal arrangement and the adsorption properties difficult. In order to examine the influences of the crystal arrangement on the adsorption properties, further extensive study must be carried out. One approach could be collecting single crystalline material, which will determined by SC-XRD and PXRD measurement for the consistency in the unit cell and perform gas adsorption measurements on this bulk material.

Moreover, vapour adsorption of C_4 hydrocarbons (1,3-C_4H_6, *t*2-C_4H_8, *i*-C_4H_8, C_4H_{10}) by pillarplex salts **1**-**4** was tested, where in all cases a consistence preference for the uptake of 1,3-C_4H_6 over *t*2-C_4H_8, *i*-C_4H_8 and C_4H_{10} was obtained. This observed trend could likely be explained by the differences in the kinetic diameters of the C_4 hydrocarbons or their polarisability.[58,82-84] The IAST selectivity calculations demonstrated the highest selectivity for the mixture 1,3-C_4H_8 / C_4H_{10} by $[Au_8L^{Me}_2](PF_6)_4$. To verify these theoretical findings, further adsorption studies involving equimolar gas mixtures would be the logical next step to explore the potential of pillarplex salts for gas separation. Additionally, the obtained crystal structures can be applied to molecular simulations[90-93] to identify specific adsorption sites and thereby analyse the preference for adsorbed gases for these sites. In particular, the micropores inside the pillarplex cavity can be thoroughly examined based on these calculations.

3.2 Expanding the Anionic Diversity of Pillarplex Salts

This chapter is based on work of this author, Jan Berger, Lena Schröck, Christian Jandl and the research internship of Hikmet Yanar, which was supervised by this author.

3.2.1 Introduction

In the context of crystal engineering, an investigation of various pillarplex salts will be conducted to understand the self-assembly of pillarplex components. As the pillarplexes exhibit salt character, variation of anions and modification of cations might influence the self-assembly of these supramolecular structures. Hence, investigation of the crystal arrangement, especially concerning the packing of the pillarplex cations towards each other and the location of the respective counter anions is performed (Figure 26). For the $[M_8L^{Me}_2]^{4+}$ cations, either pore alignment, chain alignment or a random mixture can be present. Pore alignment would enable access to the channels, if not tilted, whereas chain alignment would only provide access to isolated cavities.

Here, varying the metal would lead to an understanding of the effects of different metal radii (Ag(I) *vs.* Au(I)). The exchange of the anions already showed a strong influence on the solubility of pillarplex salts (e.g. $[M_8L^{Me}_2](PF_6)_4$ soluble in organic solvents, $[M_8L^{Me}_2](OAc)_4$ soluble in water) and therefore, various anions with different size, charge and shape are tested towards anion exchange reactions. The last point to be mentioned is the influence of the appropriate solvent on the self-assembly of supramolecules. In summary, variation of cation (Ag(I) *vs.* Au(I)), anion, solvent can influence the occurring (non-)covalent interactions, e.g., hydrogen bonding, π-interactions or metallophilic interactions. These interactions need to be identified and a potential structure-determining character on the crystal arrangement investigated.

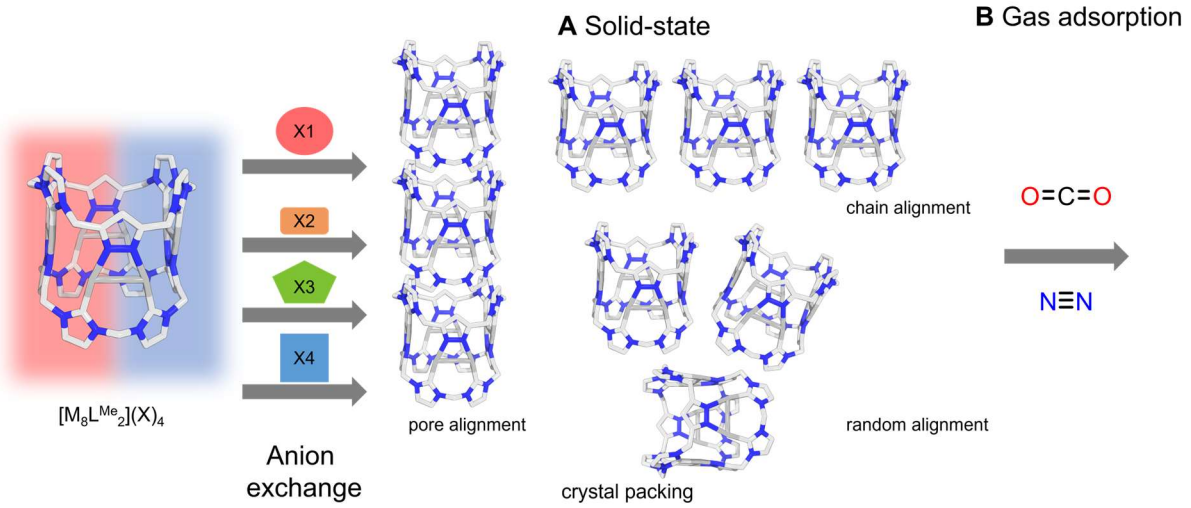

Figure 26: Overview of the anion exchange reactions of $[M_8L^{Me}_2](X)_4$ (with X = PF_6^-, OTf) with various anions differing in size, shape and charge and the (A) influences on the crystal packing in the solid-state; (B) Furthermore, the new pillarplex salts can be tested towards their gas uptake of small molecules, such as CO_2 and N_2.

As depicted in Figure 27 the anions are categorised into the following four classes: **X1** anions exhibit one negative charge and a round shape including halides and sulfide (S^{2-}) anion. Group **X2** includes the anions thiocyanate (SCN^-) and triiodide (I_3^-) demonstrating a longer, bar-like shape. The **X3** anions are still of inorganic nature but exhibit a slightly larger or more voluminous shape including the nitrate (NO_3^-), perchlorate (ClO_4^-), tetrafluoroborate (BF_4^-) and sulphate (SO_4^{2-}) with a tetrahedral shape. The organic anions (**X4**) have a charge of 2- and are sterically more demanding.

3.2.2 Theoretical Consideration towards the Size of Anions

Determination of the size of the anions

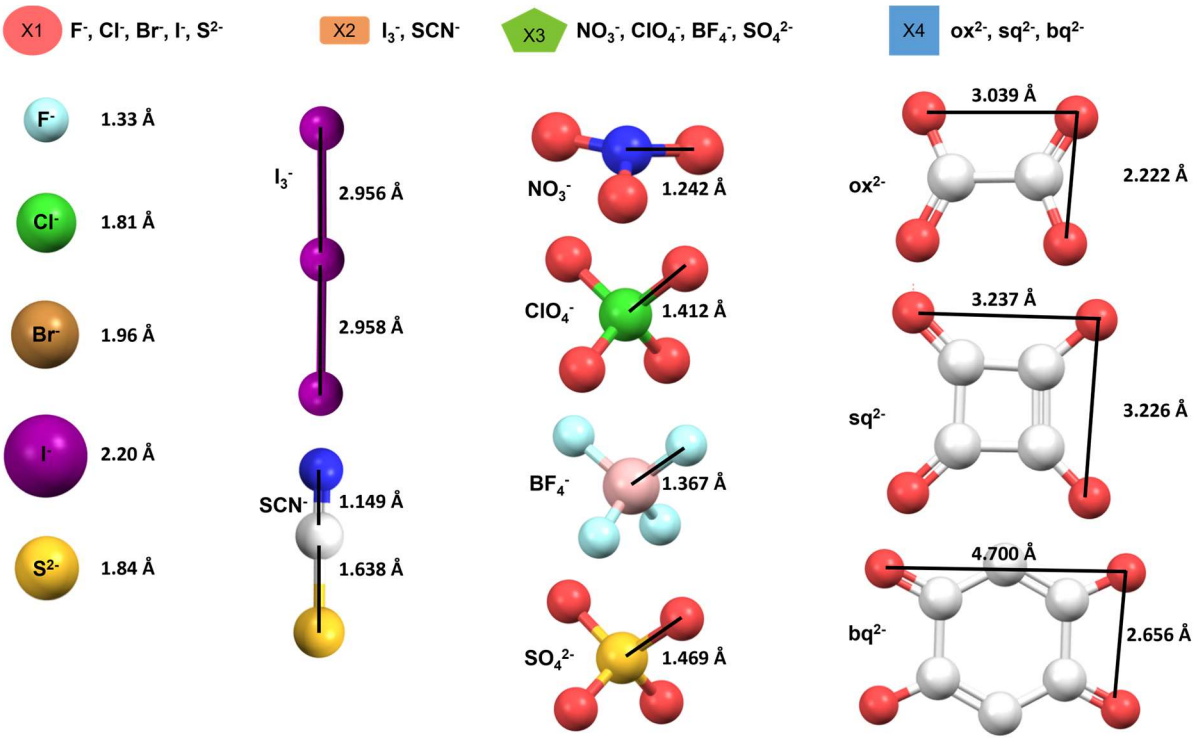

*Figure 27: The anions were divided into four groups: **X1** "spherical" shape with the respective ionic radii[94], **X2** "stick" shape, **X3** inorganic larger shape and **X4** organic sterically more demanding shape with a charge of 2-. The approximate "radius" for NO_3^-, ClO_4^-, BF_4^- and SO_4^{2-} were calculated based on the average distances.[33] The approximate "height" and "width" for I_3^-, SCN^-, ox^{2-}, sq^{2-} and bq^{2-} were calculated based on the average distances.[33] The following van-der-Waals radii were used for calculations: C 1.70 Å, N 1.55 Å, O 1.52 Å, F 1.47 Å, S 1.80 Å and I 1.98 Å.[34] Colour code: grey C, white H, red O, blue N, yellow S, pink B, turquoise F, green Cl.*

By analysing the size and shape of the anions, it may be possible to theoretically predict the probability of anions entering the pillarplex cavity (Figure 27, Table 2). Comparing the ionic radii of **X1** with the static pillarplex pore opening of 4.3 Å, all anions should be able to enter the cavity. Hence, similar to the crystal structure of $[M_8L^{Me}_2](OAc)_4$ partial occupation of the cavity by anions can be anticipated. The anions of group **X2** show a bar-like shape with a width between 3.60 Å and 3.96 Å, which theoretically could also enter the cavity. As the height of I_3^- nearly equals the height of the pillarplex cation the encapsulation of one anion per pillarplex unit may be feasible. For SCN^- either the encapsulation of one anion per pillarplex unit or the

partial encapsulation of two anions was assumed. For the group **X3**, the anions were simplified to a spherical shape. The diameter of these spheres was calculated by a combination of bond lengths based on XRD data and the van-der-Waals radii of the outer atoms. All calculated radii exceeded the size of the pillarplex pore opening. Hence, no partial occupation of the cavity was proposed. For the **X4** anions a comparable behaviour was assumed. However, those anions differ also by their charge of 2-, which exhibits possibilities for hydrogen bonding of one anion and a number of sites of the pillarplex cation (e.g., rim hydrogen atoms, metal ions). The anion could be located at the side of the pillarplex cation, where hydrogen bonding to both ligands and metal coordination of the conjugated π-system with the M(I) ions is possible. Otherwise, the coordination of one anion directly above the pore opening allows hydrogen bonding between the anion oxygen atoms and the rim hydrogen atoms. Furthermore, π-interactions of the aromatic areas of the ligands with the conjugated π-system of the anion is possible.

Table 2: Overview of the steric demand of the applied counter anions determined based on ionic radii and crystallographic data.[33,94]

X	F^-	Cl^-	Br^-	I^-	I_3^-	S^{2-}	SCN^-	NO_3^-	ClO_4^-	BF_4^-	SO_4^{2-}	ox^{2-}	sq^{2-}	bq^{2-}
Radius [Å]	1.33	1.81	1.96	2.20	-	1.84	-	5.52	5.86	5.67	5.98	-	-	-
Height [Å]	-	-	-	-	9.87	-	6.14	-	-	-	-	5.26	6.26	7.74
Width [Å]	-	-	-	-	3.96	-	3.60	-	-	-	-	6.08	6.28	5.70

3.2.3 Synthesis and Characterisation

Synthesis by anion exchange reactions

In addition to the theoretical investigation, such compounds can be synthesised by anion exchange reaction starting from $[M_8L^{Me}_2](PF_6)_4$ or $[M_8L^{Me}_2](OTf)_4$. These anion exchange reactions were performed by two different approaches using the tuneable solubility of the pillarplex salts (Figure 28, Table 3). While $[M_8L^{Me}_2](PF_6)_4$ is soluble in organic solvents, such as MeCN, DMF and DMSO, $[M_8L^{Me}_2](OTf)_4$ is soluble in both, organic solvents and aqueous solution. $[M_8L^{Me}_2](OAc)_4$ instead is only soluble in aqueous solutions.

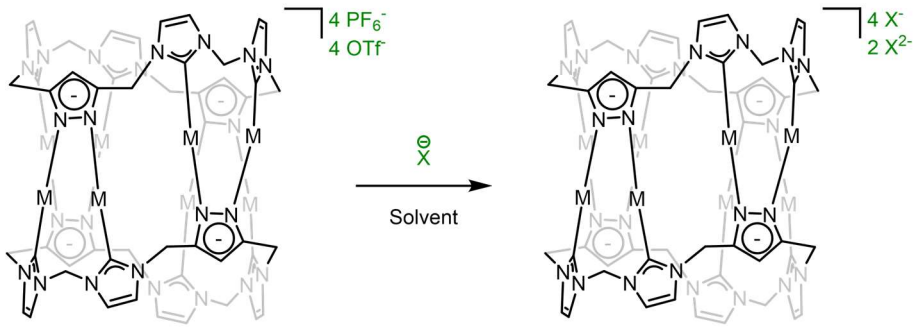

Figure 28: Synthetic route for the anion exchange reactions starting with $[M_8L^{Me}_2](PF_6)_4$ or $[M_8L^{Me}_2](OTf)_4$ with anion X^- to achieve $[M_8L^{Me}_2](X)_4$ or $[M_8L^{Me}_2](X)_2$.

One synthetic approach was already reported for the formation of $[M_8L^{Me}_2](OAc)_4$.[29] This approach was used for rather small inorganic anions (**X1**, **X2**, **X3**), as it was assumed that these would be soluble in aqueous environment, but not in an organic solvent. This literature-known procedure was then applied for the anions F^-, Cl^-, Br^-, I^-, I_3^-, SCN^-, NO_3^-, ClO_4^-, BF_4^- and SO_4- resulting in a fast – almost immediate formation of a precipitate. For the anions F^-, Cl^-, Br^-, I^-, SCN^-, NO_3^- and ClO_4^- a desired white precipitate was obtained. In contrast, for anion I_3^-, degradation of the pillarplex was observed during the synthesis, as determined by a colour change of the clear solution to a dark brown suspension. After purifying the dark precipitate, ^{1}H NMR spectroscopy suggested the decomposition of the pillarplex as neither ligand nor pillarplex signals could be assigned in the complex mixture of signals. The synthesis to obtain $[Ag_8L^{Me}_2](S_2)_2$ pillarplex was modified due to the unavailability of $(TBA)_2$-S as a sulfur source. Therefore, the solvent mixture of acetone:MeCN (1:1) was infused by H_2S gas and subsequently a solution of $[Ag_8L^{Me}_2](PF_6)_4$ in an acetone:MeCN mixture was slowly added. Upon addition of minimal amounts of $[Ag_8L^{Me}_2](PF_6)_4$ a colour change of the reaction mixture from clear to brown was noticed. This indicated the decomposition of the pillarplex salt, which was confirmed by ^{1}H NMR spectroscopy, where the proton signals of the macrocyclic ligand could be assigned. When using TBA_2-SO_4 as exchange reactant, a white precipitate was formed during the reaction, which could be isolated by centrifugation. After purification by washing the precipitate with acetone, the white solid was dried *in vacuo*. No solubility of this powder in the following organic solvents (MeCN, DMSO, DMF) or water was obtained and hence the measurement of an ^{1}H NMR spectrum was not possible. Although, a powder X-Ray diffractogram could be conducted, the reflections could not provide a clear indication for the formation of the respective $[Ag_8L^{Me}_2](SO_4)_2$ pillarplex salt and therefore no further evaluation was conducted.

In contrast to the previously described anion exchange reactions, the anion exchange reactions towards BF_4^- took a longer time and only after stirring the reaction mixture for 1 h, a white precipitate was formed, which could be isolated by centrifugation. ^{1}H, ^{11}B and ^{19}F NMR spectra confirmed the formation of the respective $[Ag_8L^{Me}_2](BF_4)_4$ pillarplex salt but with low yields of only 30%. This behaviour was considered due to relatively similar chemical environment of the BF_4^- and the PF_6^- anions and hence similar solubility was anticipated. However, simply changing the washing solvent from acetone to water, led to significant higher yields up to 91%.

Table 3: Overview of anion exchange reactions with the applied method and the used reactants.

	Method	$[M_8L^{Me}_2](X)_4$	Anion	Successful
F^-	precipitation	$[Ag_8L^{Me}_2](PF_6)_4$	TBA-F	x
Cl^-	precipitation	$[M_8L^{Me}_2](PF_6)_4$	TBA-Cl	x
Br^-	precipitation	$[M_8L^{Me}_2](PF_6)_4$	TBA-Br	x
I^-	precipitation	$[M_8L^{Me}_2](PF_6)_4$	TBA-I	(x)
I_3^-	precipitation	$[M_8L^{Me}_2](PF_6)_4$	TBA-I_3	-
S^{2-}	precipitation	$[Ag_8L^{Me}_2](PF_6)_4$	H_2S	-
SCN^-	precipitation	$[Ag_8L^{Me}_2](PF_6)_4$	TBA-SCN	x
NO^{3-}	precipitation	$[Ag_8L^{Me}_2](PF_6)_4$	TBA-NO_3	x
ClO_4^-	precipitation	$[Ag_8L^{Me}_2](PF_6)_4$	TBA-ClO_4	x
BF_4^-	precipitation	$[Ag_8L^{Me}_2](PF_6)_4$	TBA-BF_4	x
SO_4^{2-}	precipitation	$[Ag_8L^{Me}_2](PF_6)_4$	aqueous $(TBA)_2$-SO_4	?
ox^{2-}	column	$[Ag_8L^{Me}_2](OTf)_4$	oxalic acid	-
sq^{2-}	column	$[Ag_8L^{Me}_2](OTf)_4$	squaric acid	-
bq^{2-}	column	$[Ag_8L^{Me}_2](OTf)_4$	2,5-dihydroxy-1,4-benzoquinone	-

Another method for anion exchange reactions, was using a procedure based on anion exchange resins Amberlite^{TM} IRA-400 Chloride, which was placed in a small column. The resin was activated by 1 M NaOH-solution and rinsed with water until reaching a pH-value of nearly 7. Then, $[Ag_8L^{Me}_2](OTf)_4$ was dissolved in a small amount of water and transferred onto the column. While the pillarplex salt slowly passed through the resin, an exchange of the OTf^- anions by hydroxide anions occurred. Further addition of the *in-situ* synthesised $[Ag_8L^{Me}_2](OH)_4$ pillarplex to the corresponding acid as a diluted solution should result in the novel pillarplex salt. In the cases of **X4** anions, no conversion but a colour change towards dark suspensions was observed, indicating the decomposition of the pillarplex salt. This was evaluated by ^{1}H NMR spectroscopy and mass spectrometry, where only the typical signals of the macrocyclic ligand were detected. Here, various parameters can be changed to reach anion exchange reactions. One example would be changing the dilution of the respective acids in water towards higher pH-values. Otherwise, the acids can be deprotonated beforehand by weakly coordinating anions also resulting in a higher pH-value and probably better conversion towards the anion exchange.

After synthesis, the obtained powders were analysed by ^{1}H NMR spectroscopy. In general, the ^{1}H NMR spectra showed slight shifts of the pillarplex signals compared to the signals of $[Ag_8L^{Me}_2](PF_6)_4$ in DMSO-d_3, already indicating a change in the chemical environment of the pillarplex rim based on various (non-)covalent interactions for different anions. If the desired ligand signals were observed and the compound was analytically pure, full characterisation of the obtained compound was carried out. The powders were additionally analysed by solid-state NMR, IR and UV-vis spectroscopy, elemental analysis and ESI mass spectrometry. Their crystallinity has been examined by means of powder X-Ray diffraction experiments. To investigate the thermal stability of the salts for activation procedures, thermogravimetric analysis was performed.

Characterisation of Salts with X1 Anions (F^-, Cl^-, Br^-, I^-)

After synthesis and purification, the pillarplex salts were analysed by ^{1}H NMR spectroscopy in DMSO-d_6 to evaluated and assigned the signals of the rim hydrogen atoms. Although only diluted solutions of approximately c = 2 mg mL^{-1} are needed for determination of a ^{1}H NMR spectrum, problems with the solubility of the obtained compounds occurred during the preparation of the solutions. With the help of sonification and heating, solutions of $[Ag_8L^{Me}_2](F)_4$, $[Ag_8L^{Me}_2](Cl)_4$, $[Ag_8L^{Me}_2](Br)_4$, $[Ag_8L^{Me}_2](I)_4$, $[Au_8L^{Me}_2](Cl)_4$ and $[Au_8L^{Me}_2](Br)_4$ were homogenised and subjected to NMR spectroscopy. In the ^{1}H NMR spectra the desired signals were obtained but they were already slightly shifted (Figure 29). For $[Ag_8L^{Me}_2](I)_4$, an additional splitting of several signals was observed, which indicated that the pillarplex cation must still be partially intact. The obtained signals could also be a mixture of pillarplex cation and free macrocyclic ligand. Here, additional analysis methods (e.g., VT NMR experiments) must be applied to verify the successful synthesis of $[Ag_8L^{Me}_2](I)_4$. However, elemental analysis and ESI MS indicated the presence of the desired pillarplex salt. ^{31}P NMR spectra of all substances were additionally measured to ensure the full exchange of the PF_6^- anions. The complete disappearance of the signals at approximately -144 ppm verified the full conversion to the novel pillarplex salt. ^{1}H / ^{1}H COSY spectra were conducted to verify the coupling between the hydrogen atoms of the ligand, which indeed was identified for all compounds. Due to the limited solubility, the measured ^{13}C NMR spectra showed no or only a few signals. For $[Ag_8L^{Me}_2](F)_4$ additional ^{19}F NMR spectroscopy was performed, where one signal at -142.40 ppm indicated the

presence of the fluoride anion. For $[Au_8L^{Me}_2](F)_4$ and $[Au_8L^{Me}_2](I)_4$ the NMR solutions were also prepared, but no signals were obtained. Due to the low solubility of the pillarplex salts, solid-state ^1H and ^{13}C NMR spectroscopy was performed. The ^1H NMR spectra showed only one broad signal in the regions between 10 ppm and -5 ppm with two sharper shoulders, so no conclusion could be drawn based on these ^1H NMR spectra. The solid-state ^{13}C NMR spectra revealed sharp signals, similarly to the solid-state ^{13}C NMR spectrum of $[Ag_8L^{Me}_2](PF_6)_4$, which could be assigned to the carbon atoms in the pillarplex rim (F25S – F28S). In combination with elemental analysis and ESI mass spectrometry, the formation of the desired pillarplex salts was validated.

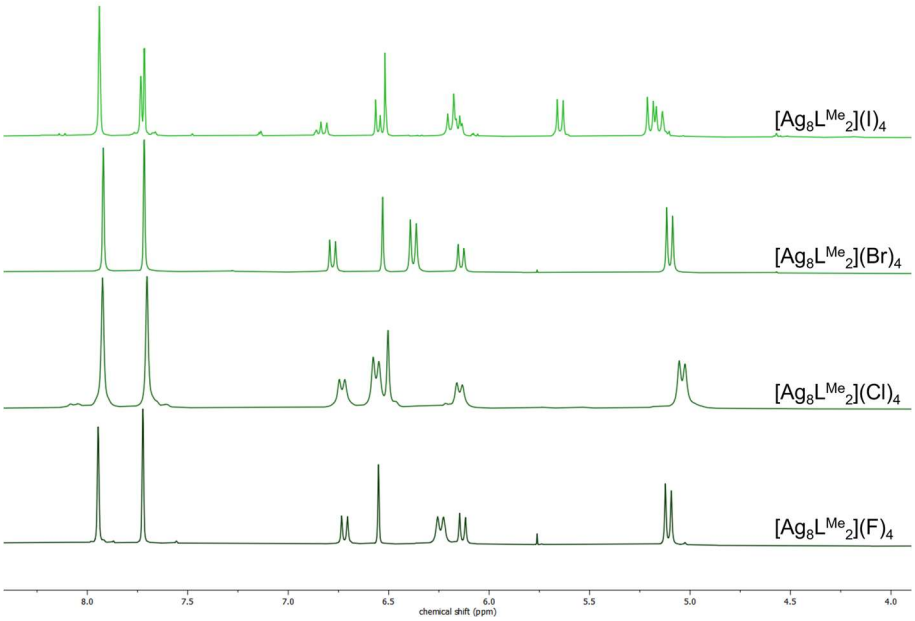

Figure 29: Stacked ^1H NMR spectra of $[Ag_8L^{Me}_2](F)_4$, $[Ag_8L^{Me}_2](Cl)_4$, $[Ag_8L^{Me}_2](Br)_4$ and $[Ag_8L^{Me}_2](I)_4$ in DMSO-d_6 (2.50 ppm) at 298 K.

The IR spectra revealed the typical bands for the $[Ag_8L^{Me}_2]^{4+}$ cation with additional halide bands at approximately 1200 cm^{-1} (Figure 30B). After testing the solubility of the obtained salts in water, similar solubility in DMSO and water was determined. UV-vis measurements were conducted in water, where absorption maxima at 224 – 237 nm for the Ag(I)-pillarplex salts were detected. For the Au(I)-pillarplex salts absorption maxima at 241 – 243 nm with an additional broad shoulder at 258 nm were observed. This could indicated the presence of aggregates or nanoparticle, as a bathochromic shift for shorter Au-Au distances is known.[95] After determining the absorption maxima for the Au(I) congeners, the next step would be to investigate their emission and luminescence properties and compare the obtained data to the literature-known properties of $[Ag_8L^{Me}_2](PF_6)_4$ (solid-state, λ_{max} = 430 nm, λ_{ex} = 335 nm with quantum yield of 40%)[29].

To investigate the powders in the solid-sate, powder X-Ray diffraction was performed (Figure 30A), where in general higher crystallinity of the Ag(I)-pillarplex salts than the Au(I)-pillarplex salts was discovered. A high amount of amorphous material for $[Ag_8L^{Me}_2](F)_4$ and $[Ag_8L^{Me}_2](I)_4$ was observed, while highly crystalline patterns were obtained for $[Ag_8L^{Me}_2](Cl)_4$ and $[Ag_8L^{Me}_2](Br)_4$. However, no pattern for the $[Au_8L^{Me}_2](X)_4$ salts was obtained, and only amorphous substances were achieved. To determine the thermal stability, TGA analysis was applied to the pre-dried pillarplex salts (100 °C *in vacuo*). At the beginning of every measurement a defect in the scaling led to small mass loss (max 1.7%). Although, the samples

were dried, a removal of solvent up to an amount of 8.3% was determined, which indicated that the solvent molecules were strongly bound in the solid-state. For example, encapsulation of such solvent molecules can require significant higher temperatures for complete removal. The Ag(I)-pillarplex salt showed a thermostability up to 290 °C with the decomposition starting at 250 °C for $[Ag_8L^{Me}_2](F)_4$, 290 °C for $[Ag_8L^{Me}_2](Cl)_4$ and $[Ag_8L^{Me}_2](Br)_4$ and 240 °C for $[Ag_8L^{Me}_2](I)_4$. The Au(I) congeners showed higher thermostability up to 330 °C with the start of the decomposition at 330 °C for $[Au_8L^{Me}_2](Cl)_4$ and 300 °C for $[Au_8L^{Me}_2](Br)_4$.

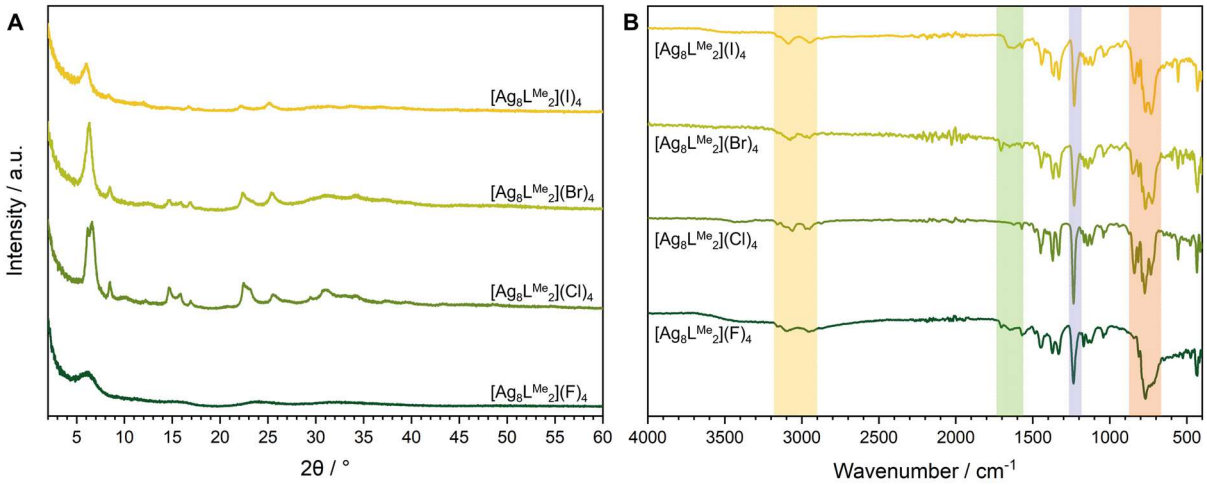

Figure 30: (A) PXRD patterns of $[Ag_8L^{Me}_2](F)_4$, $[Ag_8L^{Me}_2](Cl)_4$, $[Ag_8L^{Me}_2](Br)_4$ and $[Ag_8L^{Me}_2](I)_4$; (B) IR spectra of $[Ag_8L^{Me}_2](F)_4$, $[Ag_8L^{Me}_2](Cl)_4$, $[Ag_8L^{Me}_2](Br)_4$ and $[Ag_8L^{Me}_2](I)_4$.

The anion exchange reaction with **X1** anions was partially successful. While all Ag(I)-pillarplex salts could be synthesised, purified, and analysed, the anion exchange starting with $[Au_8L^{Me}_2](PF_6)_4$ worked only for Cl^- and Br^-, while for the other two anions (F^-, I^-), no evidence for the formation of the respective pillarplex salt was gathered. Before repeating the anion exchange reactions for these anions, the purity of the starting materials must be verified, as the Au(I)-pillarplex salts tent to form nanocrystalline arrangement in the solid-state. It is therefore necessary to examine the crystallinity and the colour of the reactant $[Au_8L^{Me}_2](PF_6)_4$ pillarplex.

However, the pillarplex salts containing the small halide anions seem to form relatively stable compounds, their solubility was limited and already solutions of 2 mg mL^{-1} were only obtained after treatment with ultra sonification and / or heat depending on the counter anion.

Characterisation of Salts with X2 Anions (SCN^-) and X3 Anions (NO_3^-, ClO_4^-, BF_4^-)

During the anion exchange reaction with anions of group **X2** and **X3**, white precipitates of the desired salts $[Ag_8L^{Me}_2](SCN)_4$, $[Ag_8L^{Me}_2](NO_3)_4$, $[Ag_8L^{Me}_2](ClO_4)_4$, $[Ag_8L^{Me}_2](BF_4)_4$ and $[Ag_8L^{Me}_2](SO_4)_2$ were obtained. For ^1H NMR spectroscopic analysis, diluted solutions of these purified solids in DMSO-d_6 were prepared. Compound $[Ag_8L^{Me}_2](SO_4)_2$ was not soluble in DMSO-d_6 and hence no signals in the ^1H NMR spectra were detected. For the other salts, the signal set of the rim protons indicated that at least the $[Ag_8L^{Me}_2]^{4+}$ cation stayed intact (Figure 31). No signals for the starting material were obtained in the ^{31}P NMR spectra, indicating that a complete anion exchange reaction must have proceeded. Additional ^{13}C and 2D NMR spectroscopy were performed to underpin the successful synthesis of the novel

pillarplex salts. For $[Ag_8L^{Me}_2](BF_4)_4$ the formation was also confirmed by ^{11}B and ^{19}F NMR spectroscopy, where one boron signal and a duplet signal for the fluorine atoms were confirmed (F24S). The chemical conformation of all salts was examined by elemental analysis and ESI mass spectrometry. Besides the predominant $[Ag_8L^{Me}_2]^{4+}$ signal in the mass spectra, signals for $[Ag_8L^{Me}_2]+(X)^{3+}$ and partially also signals for $[Ag_8L^{Me}_2]+(X)_2^{2+}$ were assigned which indicates the presence of the desired pillarplex salts (F30S – F31S).

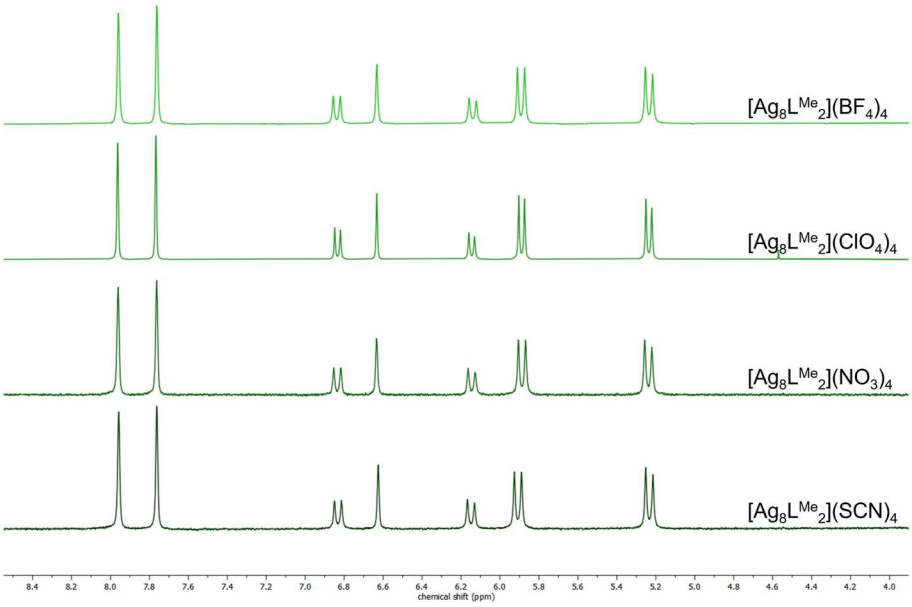

Figure 31: Stacked ^1H NMR spectra of $[Ag_8L^{Me}_2](SCN)_4$, $[Ag_8L^{Me}_2](NO_3)_4$, $[Ag_8L^{Me}_2](ClO_4)_4$ and $[Ag_8L^{Me}_2](BF_4)_4$ in DMSO-d_6 (2.50 ppm) at 298 K.

The IR spectra showed the typical bands for the $[Ag_8L^{Me}_2]^{4+}$ cation. Additionally, for each anion, specific bands were observed, as for SCN^- an additional S-C≡N band at approximately 2050 cm^{-1}, for ClO_4^- an additional Cl-O band at approximately 600 cm^{-1} and for NO_3^- an additional N-O band at approximately 1400 cm^{-1} were assigned and marked in Figure 32B. The absorption properties were investigated by UV-vis spectroscopy, where absorption maxima between 224 and 232 nm were detected for all synthesised compounds. Interestingly, the $[Ag_8L^{Me}_2](BF_4)_4$ pillarplex showed similar absorption properties as the $[Ag_8L^{Me}_2](PF_6)_4$ pillarplex with both absorption maxima at 227 nm. As the absorption maxima are all in a similar range, also compared to literature-known data of $[Ag_8L^{Me}_2](PF_6)_4$[29], the exchange of the counter anions only slightly affects the absorption behaviour.

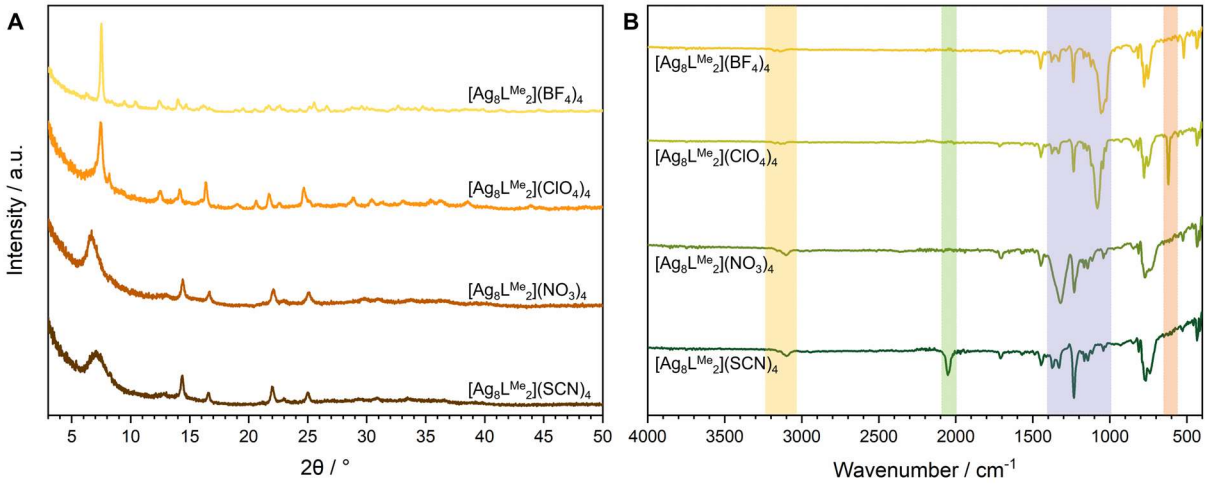

Figure 32: (A) PXRD patterns of $[Ag_8L^{Me}_2](SCN)_4$, $[Ag_8L^{Me}_2](NO_3)_4$, $[Ag_8L^{Me}_2](ClO_4)_4$ and $[Ag_8L^{Me}_2](BF_4)_4$; (B) IR spectra of $[Ag_8L^{Me}_2](SCN)_4$, $[Ag_8L^{Me}_2](NO_3)_4$, $[Ag_8L^{Me}_2](ClO_4)_4$ and $[Ag_8L^{Me}_2](BF_4)_4$.

The powder X-Ray diffraction experiments revealed partially high crystalline materials for $[[Ag_8L^{Me}_2](ClO_4)_4$ and $[Ag_8L^{Me}_2](BF_4)_4$, while the $[Ag_8L^{Me}_2](SCN)_4$ and $[Ag_8L^{Me}_2](NO_3)_4$ salts exhibited a combination of amorphous and crystalline character (Figure 32A). In the solid-state, the thermostability was tested by TGA measurements, which resulted in a behaviour for the thermal stability similar to other pillarplex salts. The temperatures for the start of decomposition were determined to be at 240 °C for $[Ag_8L^{Me}_2](SCN)_4$, 310 °C for $[Ag_8L^{Me}_2](NO_3)_4$ and 360 °C for $[Ag_8L^{Me}_2](BF_4)_4$. At the beginning of the measurement removal of solvent molecules was observed again up to 5% in all three mentioned compounds. The $[Ag_8L^{Me}_2](ClO_4)_4$ underwent abrupt decomposition at 370 °C due to the presence of perchlorate anions in the compound.

In summary, the anion exchange reaction with **X2** anions was successful for SCN^- and for **X3** anions successful for SCN^-, NO_3^-, ClO_4^- and BF_4^-. For SO_4^{2-} a white solid was indeed formed but due to solubility problems no conclusion on the obtained powder could be made. The $[Ag_8L^{Me}_2](BF_4)_4$ pillarplex was investigated towards the solubility and showed similar behaviour as the respective $[Ag_8L^{Me}_2](PF_6)_4$ salt, a good solubility in organic solvents such as MeCN, DMSO and DMF.

Characterisation of Salts with X4 Anions

As already described, the synthesis route with anion exchange resin did not yield the desired pillarplex salts and decomposition upon introduction of $[Ag_8L^{Me}_2]^{4+}$ into aqueous solutions of the acids.

During the characterisation a change in solubility for the pillarplex salts was detected. For the **X1** salts a limited solubility in organic solvents and in water was obtained. While the pillarplex salts containing **X2** anions showed good solubility in DMSO, which was also witnessed for most of the **X3** anions. The only exception in this regard was the product originated from anion exchange reaction with SO_4^{2-} anion, where no solubility in any solvent was observed. The synthesis of the **X4** pillarplex salts was not successful until now and the obtained powders exhibited limited solubility in all solvents. Thus, ^1H NMR spectroscopic data, conducted in DMSO-d_6, showed no signals of the ligand protons.

Crystallisation Attempts

Especially in the case of $[Ag_8L^{Me}_2](Cl)_4$, $[Ag_8L^{Me}_2](Br)_4$, $[Ag_8L^{Me}_2](SCN)_4$, $[Ag_8L^{Me}_2](NO_3)_4$, $[Ag_8L^{Me}_2](ClO_4)_4$ and $[Ag_8L^{Me}_2](BF_4)_4$ the obtained powders depicted high crystallinity in powder X-Ray diffraction measurements. As the main interest was put on the crystal arrangement – location of the anions, assembly of the $[M_8L^{Me}_2]^{4+}$ cations and intermolecular (non-)covalent interactions – of the various pillarplex salts, crystallisation attempts were performed for all obtained powders, where different approaches were applied:

1. Diffusion: After synthesis and purification, a saturated solution of the pillarplex salt (*ca.* 10 mg) in a solvent with relatively low vapour pressure (e.g., water, MeCN, DMF) was provided. This solution was filtered and transferred into an NMR tube, which was placed in a Schlenk flask. This Schlenk flask was filled with a solvent bearing a high(er) vapour pressure (e.g., acetone, diethyl ether, THF). Due to slow diffusion, slow precipitation of the pillarplex salt can lead to single crystals.
2. Layering: After synthesis and purification, a saturated solution of the pillarplex salt in a solvent with a lower vapour pressure (e.g., water, MeCN, DMF) was provided in a small vial. Another solvent (e.g., acetone, diethyl ether, THF) was then slowly layered on top of the saturated solution and crystallisation can occur at the boundary surface at room temperature.
3. Reaction in U-tube: The tube was partially filled with the solvent mixture acetone:MeCN (1:1). On one side of the U-tube a solution of $[M_8L^{Me}_2](PF_6)_4$ (1 eq.) and on the other side a solution of excess TBA-X (10 eq.) was slowly layered on top of the pure solvent mixture. Due to the gradual dilution of both reactants, a slow anion exchange reaction should result in the formation of single crystals.
4. “Solvothermal” crystallisation: The reactants were dissolved in a certain solvent and provided in a vial, which was sealed airtight. The vial was then placed in an oven, heated to 40 °C / 60 °C / 80 °C, kept at that temperature for 1-3 days and then slowly cooled to room temperature.
5. Low temperature / Solvent evaporation: The purified pillarplex salt was dissolved in a certain solvent. Either the sealed vial was placed in the fridge (4 °C) or in the freezer (-30 °C) to aim for slow crystallisation due to lower solubility of substrates at low temperatures or the vial was kept at ambient temperature with a small opening to the atmosphere to achieve crystallisation through slow evaporation of the solvent.

For the pillarplex salts obtained through anion exchange reaction with **X1** anions, the methods 1, 2, 3 and 5 were applied. For methods 1 and 5 the limited solubility caused problems as a highly saturated solution could not be obtained and immediate precipitation was observed, e.g., at low temperatures. Applying methods 2 and 3 was again problematic due to a rapid and immediate precipitation. Although the precipitates resulted in crystalline materials, no formation of single crystals suitable for X-Ray diffraction measurements was identified. The pillarplex salts containing **X2** and **X3** anions were subjected to crystallisation methods 1, 2 and 3. In the cases of $[Ag_8L^{Me}_2](SCN)_4$, $[Ag_8L^{Me}_2](NO_3)_4$ and $[Ag_8L^{Me}_2](ClO_4)_4$ applying methods 1 and 2 was accompanied by a fast precipitation resulting in crystalline material. A highly crystalline material was also collected after applying method 3. However, no single crystals could be identified. Although a slower precipitation of $[Ag_8L^{Me}_2](BF_4)_4$ could be achieved, no crystals suitable for single crystal X-Ray diffraction were obtained. As the synthesis route by anion exchange resin did not work for **X4** anions, crystallisation methods 2 and 4 were performed. Applying method

2 yielded off-white precipitates, which were analysed by powder X-Ray diffraction revealing amorphous materials. Crystallisation method 4 resulted in coloured suspensions, where the vials partially showed a metal mirror at the side.

In summary, single crystals were not successfully obtained. Nevertheless, crystalline powders were acquired for several components and were assessed towards their suitability for structure determination *via* micro-electron diffraction (ED) measurements.

3.2.4 Structural Investigation of $[Ag_8L^{Me}_2](BF_4)_4$ by Micro-ED

As no suitable crystals for SC-XRD measurements were obtained for $[Ag_8L^{Me}_2](BF_4)_4$, the highly crystalline materials were exposed to electron diffraction measurements. This method can evaluate the structure of microcrystalline powders.[96]

A microcrystalline powder of $[Ag_8L^{Me}_2](BF_4)_4$ suitable for electron diffraction measurements with a LaB_6 source (λ = 0.02851 Å) has been solved and refined in the monoclinic space group *P* 2/*n* (No. 13) with cell parameters a = 12.4(4) Å, b = 14.1(4) Å, c = 21.2(6) Å, α = γ = 90° and β = 93.18(6)°. A highly ordered structure with 1/2 $[Ag_8L^{Me}_2]^{4+}$ and the two respective BF_4^- anions contained in the asymmetric unit is discovered. Interestingly, no co-crystallised solvent molecules are assigned in the outer region of the pillarplex cations or in the cavity. Closer inspection reveals that the pore opening of the $[Ag_8L^{Me}_2]^{4+}$ cation is deformed into an oval form (Figure 33A) indicating a structural flexibility based on the interactions with counter anions. The occurring intermolecular interactions (Figure 33B) are mainly based on non-classical hydrogen bonding[36] of H_{rim} and F_{BF4}. Additionally, a metal coordination between Ag(I) ion and F_{BF4} is detected.

The crystal arrangement of the $[Ag_8L^{Me}_2]^{4+}$ cations is shown to be highly ordered. While the crystal packing along the a- and c-axis exhibits a chain alignment of the cations with metallophilic interactions of Ag(I)-Ag(I) ion distances of 4.312 Å (F39S), the crystal packing along the b-axis reveals a particularly interesting pore alignment (Figure 33C). This alignment leads to an accessible channel or a continuous cavity in the crystal arrangement, which could feature interesting encapsulation properties. The location of the anions plays an important role when examining the pore accessibility. Based on crystallographic data, the determined radius or diameter of 5.86 Å for the BF_4^- anion does not allow for encapsulation of the anions into the cavity. In the case of $[Ag_8L^{Me}_2](BF_4)_4$ the tetrahedral counter anion BF_4^- seems to perfectly fit in the empty space between neighbouring pillarplex cations yielding the highly symmetric crystal packing in all directions. Thus, serendipitously the BF_4^- anion with its ideal size and shape, facilitates the formation of a remarkably well-ordered crystal arrangement and a continuous cavity running through the pore-aligned pillarplex cations.

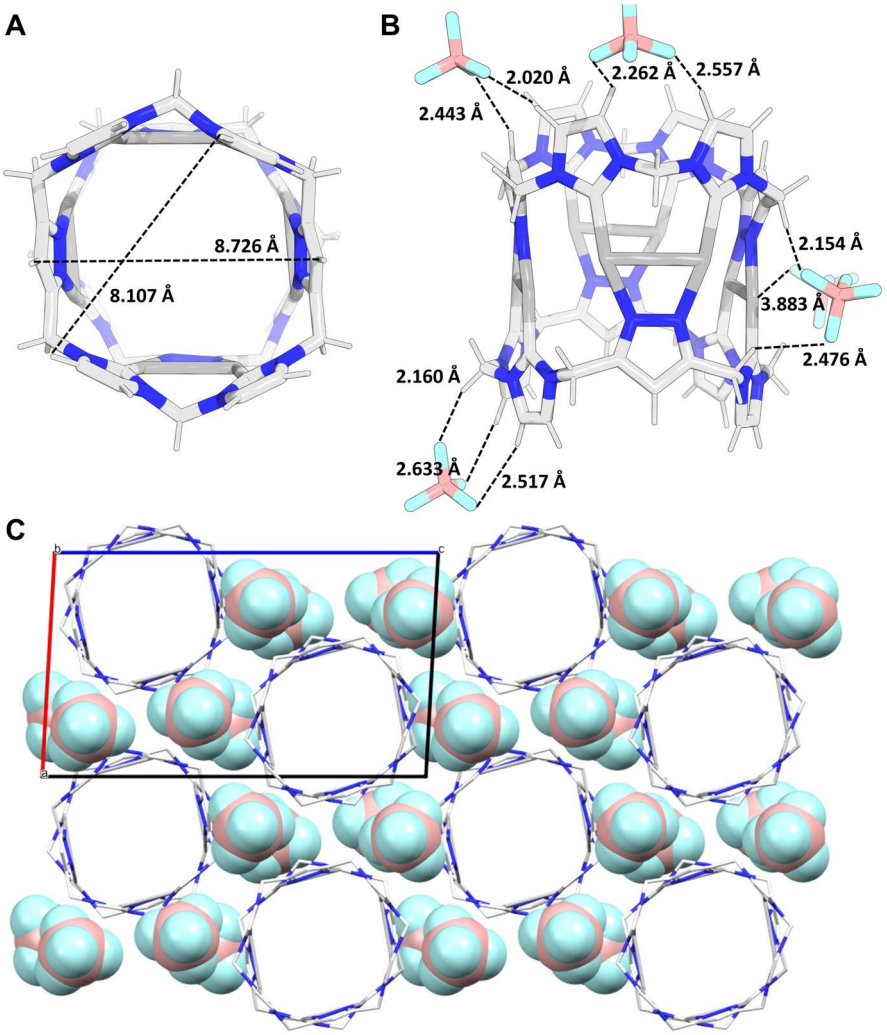

Figure 33: Representation of the molecular solid-state structure of $[Ag_8L^{Me}{}_2](BF_4)_4$: (A) Distorted pore opening of $[Ag_8L^{Me}{}_2]^{4+}$; (B) Non-classical hydrogen bonding[36] interactions between the hydrogen atom of the rim and the fluorine atoms of the counter anions; (C) Crystal packing along the b-axis exhibiting a highly ordered arrangement with $[Ag_8L^{Me}{}_2]^{4+}$ cations displayed in cabbed sticks and the BF_4^- counter anions displayed in space fill.

3.2.5 DFT Calculations Towards the Location of the Anions

Geometry optimisation calculations of $[Ag_8L^{Me}_2]^{4+}$ cation with different anions **X1**-**X4** were performed by DFT (for details see Chapter 5.7). For all calculations, the geometry of cation $[Ag_8L^{Me}_2]^{4+}$ determined by SC-XRD measurements of $[Ag_8L^{Me}_2](PF_6)_4$ (Chapter 3.1.5) was used. First, three of the PF_{6-} counter anions were removed and the fourth one was replaced with the targeted anions. Simultaneously, another calculation was conducted, positioning the targeted anion directly on top of the pore opening. In the case of halides and NO_3^-, it appeared that the hydrogen bonding with the rim was more favourable than encapsulation into the cavity. In particular, the position of the anion was calculated to be in the large pocket of the pillarplex rim with hydrogen bonds to the pyrazole hydrogen and the imidazolylidene hydrogen atoms. One of the remaining targeted counter anions was placed in the large pocket of the same ligand, while the two other anions were then positioned close to the small pocket of the other ligand. However, for the SCN^- anion, encapsulation within the cavity was observed for the calculation, where the anion was placed directly on top of the pore opening. In this case, the three other SCN- anions were placed above or besides the large pocket of the pillarplex leading to significant changes in the calculated positions during geometry optimisation. The geometry optimisation calculation of $[Ag_8L^{Me}_2](BF_4)_4$ utilised the crystal structure determined *via* micro-ED measurements as starting point. The DFT calculations were performed in the gas phase. For compound $[Ag_8L^{Me}_2](BF_4)_4$ the calculations were repeated using an implicit solvent model (MeCN).

As previously mentioned, no encapsulation of the **X1** anions (F^-, Cl^-, Br^-, I^-) into the pillarplex cavity was observed, although one anion was placed directly on top of the pore opening. In all these cases, the interactions with the organic rim by non-classical hydrogen bonding[36] seemed to determine the structure. On one ligand, the anions were moved towards the small pocket and one the other ligand towards the larger pocket during the steps of geometry optimisation calculations. In the small pocket hydrogen bonding with the two imidazolylidene units and the methylene bridge was discovered, while in the larger pocket hydrogen bonding of the X^- (X = F^-, Cl^-, Br^-, I^-) anions with two imidazolylidene units and the pyrazole hydrogen atom in the middle was detected. The organic rim on the side of the large pocket interactions showed a deformation of the pore opening. Here, the organic rim was bent towards the middle of the cavity and this deformation decreased with the size of the ionic radius of the anions exhibiting the strongest deformation for the F^- anion and no structural deformation of the rim with the I^- anion (Figure 34A+B, F98S). Such a structural flexibility of the pillarplex rim was already discovered for the $[Au_8L^t_2](PF_6)_4$, where non-classical hydrogen bonds[36] between H_{rim} and F_{PF6} yielded this mentioned deformation of the cation.[32] For the geometry optimised structures of $[Ag_8L^{Me}_2](F)_4$, $[Ag_8L^{Me}_2](Cl)_4$, $[Ag_8L^{Me}_2](Br)_4$ and $[Ag_8L^{Me}_2](I)_4$ strong non-classical hydrogen bonding[36] with distances of 1.623 – 3.202 Å between X^- and H_{rim} were obtained. A similar location of the counter anions for all anions of group **X1** was determined, however with an increased size of the anions (F^- < Cl^- < Br^- < I^-) less structural deformation of the pillarplex cation was monitored.

In contrast to the **X1** anions, the geometry optimisation of **X2** anions, precisely $[Ag_8L^{Me}_2](SCN)_4$ resulted in the encapsulation of one SCN^- anion inside the cavity, where metal coordination of N_{SCN} and weak metal coordination of S_{SCN} with the Ag(I) ions was discovered. The anions, which were located outside of the cavity, showed additional metal coordination with the Ag(I) ions similar to that revealed inside the cavity. One SCN^- anion formed hydrogen bonding with the H_{rim} in the small pocket of the pillarplex cation. Here, N_{SCN} to the methylene bridged proton

and S_{SCN} to the hydrogen atoms of the imidazolylidene units were assigned to the strongest interactions with distances of 2.30 Å (Figure 34C). Similar to the finding of encapsulation of SCN^- during geometry optimisation of $[Ag_8L^{Me}_2](SCN)_4$, the geometry optimised structure of $[Ag_8L^{Me}_2](PF_6)_4$ showed the encapsulation of one counter anion in the gas phase (see Chapter 3.1.2), although this behaviour was not verified by common analytical methods in the liquid phase (e.g., ^1H, ^{19}F, ^{31}P NMR spectroscopy). Hence, the encapsulation of SCN^- could also be the result of the gas phase calculation. However, the shape of the thiocyanate anion is relatively similar to the alkyl chains, which have already been investigated towards their encapsulation into the pillarplex pore in solution.[29,32,85,97] Therefore, it is anticipated that one SCN^- anions indeed could enter the cavity, which can be strengthened by a repeated geometry optimisation in an explicit solvent model (e.g., DMSO, H_2O).

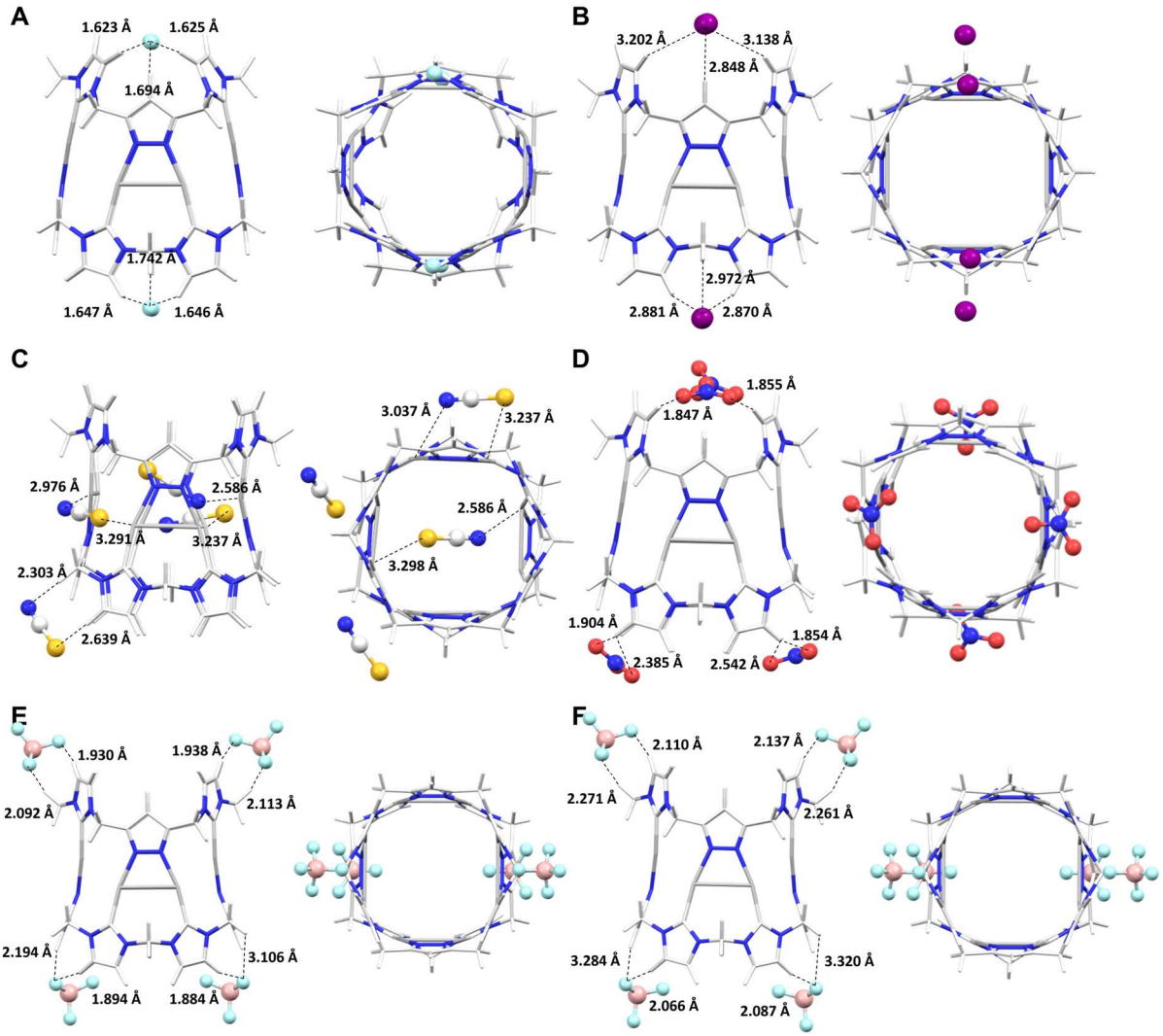

Figure 34: Optimised structures of (A) $[Ag_8L^{Me}_2](F)_4$ in gas phase; (B) $[Ag_8L^{Me}_2](I)_4$ in gas phase; (C) $[Ag_8L^{Me}_2](SCN)_4$ in gas phase; (D) $[Ag_8L^{Me}_2](NO_3)_4$ in gas phase; (E) $[Ag_8L^{Me}_2](BF_4)_4$ in gas phase; (F) $[Ag_8L^{Me}_2](BF_4)_4$ in solution (MeCN).

The pillarplex salts baring **X3** anions were analysing towards their optimised structure. For $[Ag_8L^{Me}_2](NO_3)_4$, the anions were calculated in the large pockets of the pillarplex rim, although two were placed in closer proximity to the small pockets. Strong hydrogen bonding between O_{NO3} and H_{rim} was depicted with distances of 1.84 – 2.54 Å. Whereas the NO_3^- anions on one

side of the cation were determined closer to the outer surrounding of the pillarplex, the two NO_3^- anions one the other side of the pillarplex cation were located more towards the top of the pore opening. This resulted in a deformation of the organic rim, where the hydrogen atoms of the rim were bent towards the anions in the inner of the pore opening (Figure 34D). Unfortunately, the geometry optimisation of $[Ag_8L^{Me}_2](ClO_4)_4$ (**X3**) reached no convergency and the counter anions ClO_4^- were dislocated during the optimisation steps. This effect occurred only for the perchlorate anion and no explanation for the dislocation could be provided. As the starting geometry for the geometry optimisation of $[Ag_8L^{Me}_2](BF_4)_4$ was obtained from the micro-ED measurements, similar symmetric positions of the counter anions around the pillarplex were observed. While on one side of the pillarplex cation the two BF_4^- anions were located in the small pocket, on the other side of the pillarplex the anions were situated in the larger pocket and non-classical hydrogen bonding[36] of the F_{BF4} with H_{rim} were detected in all cases. The organic rim on the side of the counter anions interacting with the larger pocket, showed a small structural deformation, with the hydrogen bent towards the centre of the cavity. The geometry optimisation of $[Ag_8L^{Me}_2](BF_4)_4$ in MeCN resulted in similar locations of the BF_4^- anions, however no deformation of the pillarplex cation was determined (Figure 34E+F). The geometry optimisations for anion group **X3** yielded a highly ordered arrangement of the anions towards the pillarplex cation, where a minimal structural deformation of the rim towards an oval shape was obtained. Through the optimisation of $[Ag_8L^{Me}_2](BF_4)_4$ in solution, this structural deformation was no longer observed, indicating that it may have been a result of the gas phase calculation.

Until now, the successful synthesis of pillarplexes bearing anion of group **X4** could not be achieved and therefore, no geometry optimisation calculations were performed.

In summary, no clear correlation between the size or shape of the counter anion and the partial encapsulation into the cavity could be determined. Nonetheless, for all anions (non-)covalent interactions, especially hydrogen bonding, with the organic rim of $[Ag_8L^{Me}_2]^{4+}$ were identified. Further investigations are required to distinguish whether the effects of structural deformation and encapsulation are due to gas phase calculations. Additionally, hydrophobic effects could influence the positioning of the counter anions making it crucial to explore the geometry optimisation in implicit solvent models (e.g., DMSO, H_2O).

3.2.6 N_2 Uptake by BET Experiments

The gas adsorption properties of the obtained salts were investigated by measurement of the N_2 isotherms at 77 K. Theoretical calculations indicated that one SCN^- anion (**X2**) could be encapsulated in the cavity. Therefore, the microporosity of $[Ag_8L^{Me}_2](SCN)_4$ was anticipated to be lower due to a partial occupied cavity. Halides (**X1**) and NO_3^- anions (**X3**) were positioned partially on top of the cavity, which could hinder the adsorption. Additionally, the structural deformation of the rim of $[Ag_8L^{Me}_2](F)_4$, $[Ag_8L^{Me}_2](Cl)_4$, $[Ag_8L^{Me}_2](Br)_4$, $[Ag_8L^{Me}_2](I)_4$ and $[Ag_8L^{Me}_2](NO_3)_4$ could also decrease the accessible pore volume. Before analysing the adsorption properties, the samples were activated to ensure solvent free micro- and / or mesopores. This was achieved by keeping the pre-dried powders for 3 days at 100 °C *in vacuo*.

The N_2 isotherm of $[Ag_8L^{Me}_2](F)_4$ (Figure 35A) exhibited a type II[48] curvature with a H3[48] hysteresis during the desorption process. It displayed a marginal gas uptake of 6.1 $cm^3\ g^{-1}$ at low pressure, which resulted in a plateau reaching from 4 kPa to 76 kPa with a minimal increase to 8.6 $cm^3\ g^{-1}$. At high pressure a steep uptake occurred with a maximum of 62.1 $cm^3\ g^{-1}$ at 93 kPa. The marginal uptake at low pressure could correspond to the filling of microporous pillarplex cavities or the formation of a monolayer on a nonporous material. The sharp increase at high pressure indicated the condensation of nitrogen, either within the mesoporous space between the pillarplex particles or due to the formation of multilayers. Notably, the isotherm showed minimal gas uptake into micropores, suggesting that a (partial) encapsulation of fluoride anions could be feasible. Considering the findings from DFT calculations, the micropores of the pillarplex could also be blocked by the positions of the anions and the structural deformation.

Exhibiting a similar curvature for the N_2 adsorption, the isotherm of $[Ag_8L^{Me}_2](Cl)_4$ (Figure 35B) was assigned to type II.[48] An initial steep uptake with 38.3 $cm^3\ g^{-1}$ at 3.6 kPa was followed by a gradual linear increase spanning from 3.6 – 81 kPa, where a gas uptake of up to 65.9 $cm^3\ g^{-1}$ was detected. Subsequently, a steep gas uptake exhibited a maximum at 93 kPa with 90.4 $cm^3\ g^{-1}$. The steep uptake at low pressure could be attributed to the filling of micropores or monolayer formation on nonporous material. Given the absence of a discreet turning point of the curve, it seemed to be more likely that the adsorption occurred on a nonporous material with no notable distinction between the monolayer and multilayer formation. During the desorption the distinct shape of a H4[48] hysteresis was determined. This could be the result of delayed evaporation of nitrogen or due to network effects[51] of the supramolecular assembly.

The N_2 isotherm of $[Ag_8L^{Me}_2](Br)_4$ (Figure 35C) can be described as a mixture of type II and type IVa.[48] At the beginning of the measurement, a steep uptake up to 29.5 $cm^3\ g^{-1}$ at 5 kPa was detected followed by a continuous increase, which end in a plateau at 72.0 $cm^3\ g^{-1}$ at 92 kPa. The initial uptake could be assigned to the filling of micropores with a following nitrogen condensation on mesoporous material due to the continuous increase. During the course of desorption, a large hysteresis from 94 kPa to 46 kPa was observed following the curvature of a H5[48] hysteresis. This distinct shape could indicate the presence of pore structures, which simultaneous contain open and partially blocked mesopores[48]. The structural deformation of the rim of $[Ag_8L^{Me}_2](Br)_4$ determined by DFT calculations could explain these pore structures.

Although the N_2 adsorption data for $[Ag_8L^{Me}_2](I)_4$ (Figure 35D) exhibited limited quality, the isotherm displayed a curvature following type Ib[48] isotherm with a H4[48] hysteresis during the desorption process. A steady increase in gas uptake reached a maximum of 5.5 $cm^3\ g^{-1}$ at 94 kPa. This behaviour could suggest the presence of a material with a pore size distribution ranging from micropore to small mesopores. However, no definitive conclusions could be drawn from this N_2 isotherm, which could be caused by factors such as application of a small sample quantity, a measurement error or by the nature of the sample itself. As the measurement was already repeated with similar outcomes, the compound $[Ag_8L^{Me}_2](I)_4$ seems to not possess porosity.

The N_2 isotherm for $[Au_8L^{Me}_2](Cl)_4$ (F41S) followed type II.[48] An initial small uptake of 11.4 $cm^3\ g^{-1}$ at 3 kPa was followed by a plateau reaching from 3 kPa to 60 kPa with a shallow increase up to 21.8 $cm^3\ g^{-1}$. At high pressure a steep gas uptake with a maximal adsorbed volume of 122.1 $cm^3\ g^{-1}$ at 92 kPa was observed. The curvature indicated a micropore filling at low pressure with following N_2 condensation in mesopores or the adsorption on nonporous material starting with a monolayer at low pressure and further formation of multilayers at higher

pressure. A small H3[48] hysteresis was obtained for $[Au_8L^{Me}_2](Cl)_4$ suggesting that either delayed evaporation in the mesopores or network effects[51] in the supramolecular arrangement could occur.

The N_2 gas uptake for $[Au_8L^{Me}_2](Br)_4$ (F41S) exhibited characteristics of a type IV[48] isotherm, where a modest gas uptake of 4.5 $cm^3\ g^{-1}$ at 6 kPa was obtained. Then, a plateau ranging from 6 – 53 kPa was formed. However, the N_2 isotherm of $[Au_8L^{Me}_2](Br)_4$ showed a dent in this plateau with an adsorbed volume of 3.1 $cm^3\ g^{-1}$. Applying a higher pressure than 53 kPa resulted in a steep gas uptake to a maximum of 12.6 $cm^3\ g^{-1}$ at 93 kPa. A significant hysteresis was observed, which can be described as a mixture of H1a and H2.[48] Due to the dent in the plateau (F41S, marked with an orange box) and the overall small gas uptake, the adsorption behaviour of $[Au_8L^{Me}_2](Br)_4$ was repeatedly tested yielding similar results. Consequently, no conclusion could be drawn. Several factors may have contributed to this outcome (e.g., quantity of sample, error during measurements). However, the most probable explanation was the absence of porosity in the pillarplex salt.

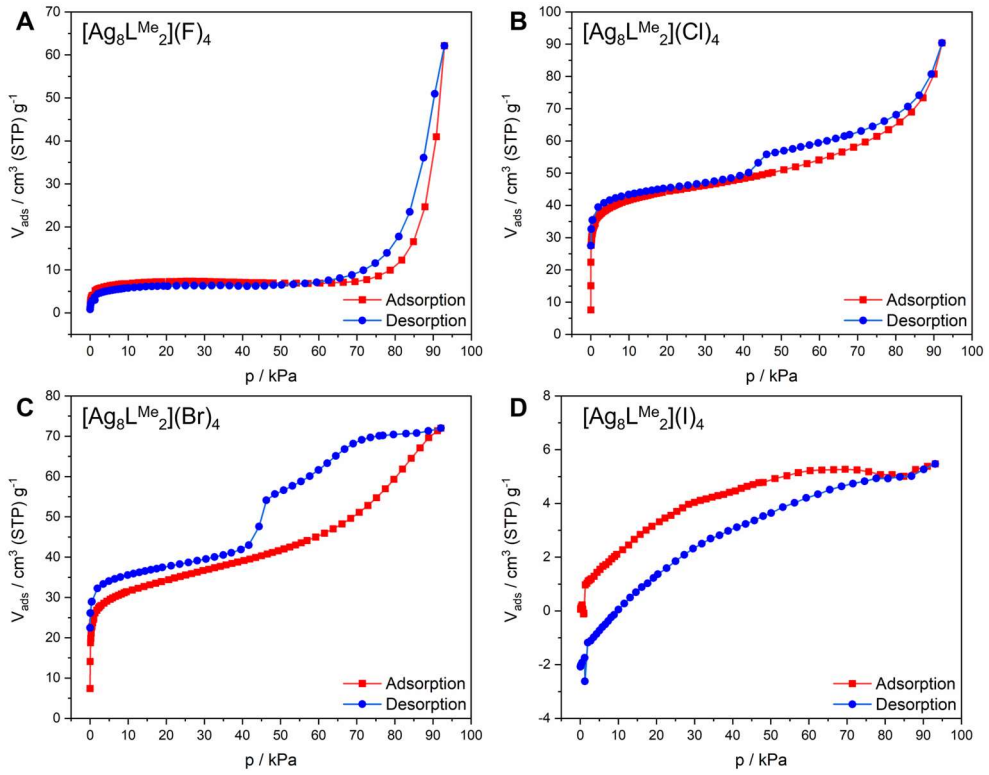

Figure 35: Physisorption Isotherms of (A) $[Ag_8L^{Me}_2](F)_4$; (B) $[Ag_8L^{Me}_2](Cl)_4$; (C) $[Ag_8L^{Me}_2](Br)_4$; (D) $[Ag_8L^{Me}_2](I)_4$ for N_2 recorded at 77 K. Lines are marked in red and blue represent the ad- and desorption branch.

Considering the N_2 gas adsorption for $[Ag_8L^{Me}_2](SCN)_4$ (Figure 36A) a type IV[48] isotherm was observed with a marginal uptake of 7.7 $cm^3\ g^{-1}$ at low pressure up to 4 kPa. The gas uptake ceased into a plateau at 9.3 $cm^3\ g^{-1}$ from 4 kPa to 82 kPa and afterwards, a steep uptake with a maximum of 35.2 $cm^3\ g^{-1}$ at 94 kPa was identified. The marginal uptake at low pressure could correspond to the filling of micropores. In DFT calculations the pillarplex cavity was partially occupied by one SCN^- anion, which could explain the small accessible microporous space. The following uptake at higher pressure could be attributed to the mesoporous space between pillarplex particles or the formation of layers on the nonporous material. During the desorption course, a H1[48] was determined, which could indicate the delayed evaporation of nitrogen from

in between pillarplex particles. As the hysteresis was obtained in the mesoporous range, the discrepancy between adsorbed and desorbed volume could also be explained by network effects (e.g., pore blocking, network defects).[51]

In contrast, $[Ag_8L^{Me}_2](NO_3)_4$ (Figure 36B) exhibited a completely different behaviour during the gas adsorption experiments and followed a type Ia[48] isotherm. Initially, a high and steep gas uptake of 37.2 $cm^3\ g^{-1}$ at 5 kPa concluded into a plateau, which continuously increase to an overall uptake of 44.6 $cm^3\ g^{-1}$ at 94 kPa. This type of isotherms is expected for microporous materials, where an initial filling of a pore is limited by the inner pore surface. The pillarplex cavity indeed exhibits microporous character, which could explain the observed behaviour for N_2 uptake of $[Ag_8L^{Me}_2](NO_3)_4$. Although DFT calculation suggested no encapsulation, the anions were positioned partially blocking the pore opening. This pore blocking could cause the marginal hysteresis, which was assigned to type H1.[48]

The N_2 isotherm of $[Ag_8L^{Me}_2](ClO_4)_4$ (Figure 36C) could be best characterised as a combination of type Ia[48] at low pressure and type II[48] at higher pressure. With a significant initial gas uptake of 73.7 $cm^3\ g^{-1}$ at 10 kPa, a plateau was reached at the adsorbed volume of 76.6 $cm^3\ g^{-1}$. Another small quantity of gas was adsorbed at high pressure (> 79 kPa) resulting in a maximum volume of 93.0 $cm^3\ g^{-1}$ at 94 kPa. It should be noted that a reversible desorption was determined showing no hysteresis. The shape of the isotherm suggested the presence of micropores, which were filled at low pressure. Furthermore, mesoporous space between the pillarplex cations could be present, where nitrogen condensation could occur.

A type II[48] isotherm was depicted for the N_2 adsorption of $[Ag_8L^{Me}_2](BF_4)_4$ (Figure 36D). Initially, a steep uptake to a volume of 32.7 $cm^3\ g^{-1}$ adsorbed gas at 5 kPa levelled into a plateau at 38.2 $cm^3\ g^{-1}$ reaching from 5 kPa to 80 kPa. The subsequent steep gas uptake led to a gas adsorption maximum of 90.8 $cm^3\ g^{-1}$ at 93 kPa. This type of isotherm suggested the presence of a nonporous or macroporous material. Thus, the initial gas uptake could be attributed to the formation of a monolayer, although the filling of micropores could also be feasible. The further increase in the adsorbed gas volume might be due to either the formation of multilayer or the uptake of nitrogen in mesoporous space. During the reversible desorption process a H3[48] hysteresis was detected. This could be the result of the presence of non-rigid aggregates or a macroporous network where no complete nitrogen condensation occurred. A crystal structure analysis of $[Ag_8L^{Me}_2](BF_4)_4$ revealed a highly ordered pore alignment of the pillarplex cations. Due to the positioning of the counter anions outside of the rim, a quasi-continuous channel was formed. Taking these findings into account, microporous space in the chain-aligned pillarplex cavity and mesoporous space in between the pillarplex cations and anions would be accessible. Therefore, a high N_2 gas uptake in the microporous range at low pressure was anticipated. Additionally, shallow increase at higher pressure could be explained by nitrogen condensation between the pillarplex particles. To assess the consistency of lattice parameters the calculated PXRD pattern from SC-XRD measurements was compared to the measured pattern of the bulk material of $[Ag_8L^{Me}_2](BF_4)_4$. Notably, similar patterns were observed suggesting that similarities in the solid-state arrangement for both samples were present. Nevertheless, no correlation could be established between the results of the single crystal analysis and the gas adsorption experiment, due to a relatively low overall volume of adsorbed gas compared to other pillarplex salts.

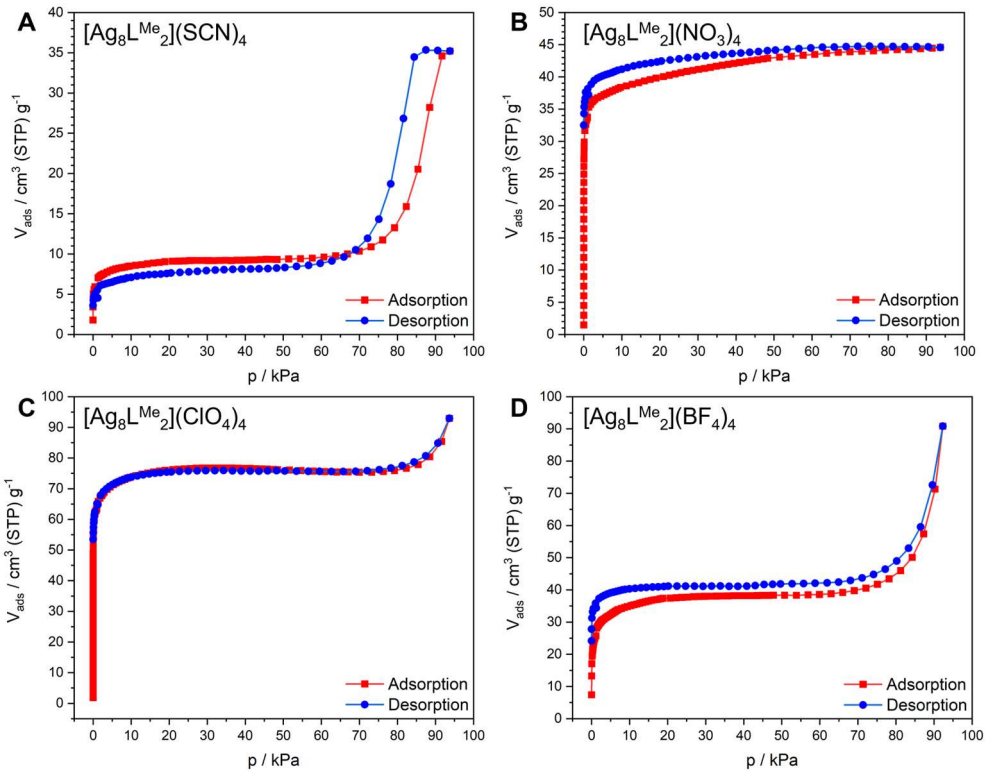

Figure 36: Physisorption Isotherms: (A) $[Ag_8L^{Me}{}_2](SCN)_4$; (B) $[Ag_8L^{Me}{}_2](NO_3)_4$; (C) $[Ag_8L^{Me}{}_2](ClO_4)_4$; (D) $[Ag_8L^{Me}{}_2](BF_4)_4$ for N_2 recorded at 77 K. Lines are marked in red and blue represent the ad- and desorption branch.

3.2.7 Summary and Outlook

In summary, the library of pillarplex salts could be extended by the successful synthesis of $[Ag_8L^{Me}{}_2](F)_4$, $[Ag_8L^{Me}{}_2](Cl)_4$, $[Ag_8L^{Me}{}_2](Br)_4$, $[Ag_8L^{Me}{}_2](I)_4$, $[Au_8L^{Me}{}_2](Cl)_4$, $[Au_8L^{Me}{}_2](Br)_4$, $[Ag_8L^{Me}{}_2](SCN)_4$, $[Ag_8L^{Me}{}_2](NO_3)_4$, $[Ag_8L^{Me}{}_2](ClO_4)_4$ and $[Ag_8L^{Me}{}_2](BF_4)_4$. However, some of the compounds still require further characterisation, particularly considering the structural analysis in order to assess the positions of the $[M_8L^{Me}{}_2]^{4+}$ cation, the counter anions and solvent molecules. Moreover, examination of the occurring (non-)covalent interactions between cation, anion and solvent molecules as well as the influence on the crystal arrangement must be concluded. Despite various crystallisation attempts, no suitable single crystals were obtained. Nonetheless, gradual precipitation might create microcrystalline powders, which could subsequently be analysed by electron diffraction analysis.

While the targeted pillarplex salts $[Ag_8L^{Me}{}_2](I_3)_4$ and $[Au_8L^{Me}{}_2](S)_2$ could not be synthesised as decomposition occurred during the anion exchange reactions, $[Au_8L^{Me}{}_2](I)_4$ and $[Ag_8L^{Me}{}_2](SO_4)_4$ yielded white precipitates. However, the analysis of these precipitates involved several problems. For $[Au_8L^{Me}{}_2](I)_4$ the ^1H NMR spectrum showed additionally signals and for $[Ag_8L^{Me}{}_2](SO_4)_4$ limited solubility hindered the measurement of NMR spectroscopy or mass spectrometry. Further purification steps could be implemented for $[Au_8L^{Me}{}_2](I)_4$ to verify the successful formation of the pillarplex salt. In the case of $[Ag_8L^{Me}{}_2](SO_4)_4$, further common

analysis methods (e.g., solid-state NMR spectroscopy, EA, IR, UV-vis) could be applied to determine whether the desired pillarplex salt was indeed obtained.

Microcrystalline powder of $[Ag_8L^{Me}_2](BF_4)_4$ could be analysed by electron diffraction and revealed a highly ordered crystal arrangement with pore-aligned $[Ag_8L^{Me}_2]^{4+}$ cations. Due the positioning of the counter anions BF_4^- on the exterior space of the pillarplex cations, an unoccupied quasi-continuous pore channel was identified. This finding renders the pillarplex salt exceptionally interesting for further studies towards its host-guest chemistry. After the synthesis of $[Ag_8L^{Me}_2](BF_4)_4$ a similar solubility to $[Ag_8L^{Me}_2](PF_6)_4$ was observed, which resulted in poor yields for the anion exchange from PF_6^- to BF_4^-. To shorten and optimise the synthetic route, this BF_4^- pillarplex salt could be directly obtained from $L^{Me}(BF_4)_4$. During the synthesis route to achieve $[M_8L^{Me}_2](PF_6)_4$, the ligand $L^{Me}_2(OTf)_4$ is synthesised and subjected to an anion exchange reaction with ammonium hexafluorophosphate to form $L^{Me}(PF_6)_4$. Through switching to ammonium tetrafluoroborate, the ligand $L^{Me}(BF_4)_4$ could directly be synthesised and further implemented into the $[Ag_8L^{Me}_2](BF_4)_4$ pillarplex.

To assess potential correlations, the geometry optimised structures obtained through DFT calculations were compared with the gas adsorption data. In principle, microporous space inside the pillarplex cavity and mesoporous space in between the pillarplex particles exists, where adsorption could occur. $[Ag_8L^{Me}_2](F)_4$ and $[Au_8L^{Me}_2](Cl)_4$ followed a type II[48] isotherm and $[Ag_8L^{Me}_2](SCN)_4$ followed a type IV[48] isotherm, where in all cases a marginal amount of gas is adsorbed in micropores and a high proportion is adsorbed in mesopores. Another explanation for this behaviour would be the formation of a monolayer on nonporous material with the following formation of multilayers. For $[Ag_8L^{Me}_2](F)_4$ and $[Au_8L^{Me}_2](Cl)_4$ DFT calculations revealed a pore blocking and structural deformation caused by the anions, while for $[Ag_8L^{Me}_2](BF_4)_4$ a partial occupation of the cavity by one SCN^- anion was observed. These findings could explain the marginal uptake in the microporous area. $[Ag_8L^{Me}_2](Cl)_4$, $[Ag_8L^{Me}_2](Br)_4$ and $[Ag_8L^{Me}_2](BF_4)_4$ followed type II[48] isotherms, where gas uptake was monitored in the range of micropores and mesopores. While the geometry optimised structures of $[Ag_8L^{Me}_2](Cl)_4$ and $[Ag_8L^{Me}_2](Br)_4$ revealed no anion encapsulation, the pore opening was blocked by the positions of counter anions accompanied by a structural deformation of the rim. For $[Ag_8L^{Me}_2](BF_4)_4$ a slight deformation of the pore opening to an oval shape was obtained *via* SC-XRD measurements. Nevertheless, microporous space was accessible in the pillarplex cavity. The adsorption behaviour could therefore indicate that initial nitrogen filling of the pillarplex cavity is followed by nitrogen condensation in the accessible space between pillarplex particles. With a significant gas uptake into micropores and following minor uptake in mesopores, $[Ag_8L^{Me}_2](NO_3)_4$ and $[Ag_8L^{Me}_2](ClO_4)_4$ featured characteristics of type Ia[48] isotherms. This suggested nitrogen uptake primarily into micropores with a confined inner pore surface. The DFT calculations indicated partial pore blocking by the counter anions rather than encapsulation. Consequently, the pillarplex cavity seems to be accessible for N_2, while nitrogen condensation in the mesoporous void between pillarplex particles is at a low level. The compounds $[Ag_8L^{Me}_2](I)_4$ and $[Au_8L^{Me}_2](Br)_4$ demonstrated an overall low gas uptake, suggesting nonporous characteristics of these materials. This hypothesis was supported by the determined PXRD pattern of the activated samples, which showed an amorphous phase.

No clear conclusions regarding correlations could be drawn due to diverse gas adsorption results and the lack of structural analysis data. However, the presented results suggest that there is indeed a potential connection between the counter anions, the pore accessibility and gas adsorption properties.

3.3 Pillarplex Salts with Mixed Anions

3.3.1 Introduction

The pillarplex consists of the cation $[M_8L_2]^{4+}$ and respective counter anions. To date, only a limited number of counter anions has been examined and exclusively pillarplex salts bearing a single type of counter anions were synthesised and analysed. However, the pillarplex cation is offering a charge of 4+, which in theory enables the introduction of up to four different counter anions (Figure 37). Moreover, the range of counter anions can be expanded to metal-containing anions, where supplementary interaction sites are introduced into the system. Furthermore, (non-)covalent interactions play a significant role in the crystal arrangement and by introducing divers counter anions, the range of occurring (non-)covalent interactions (e.g., hydrogen bonding, coordinative bond) can be enhanced.

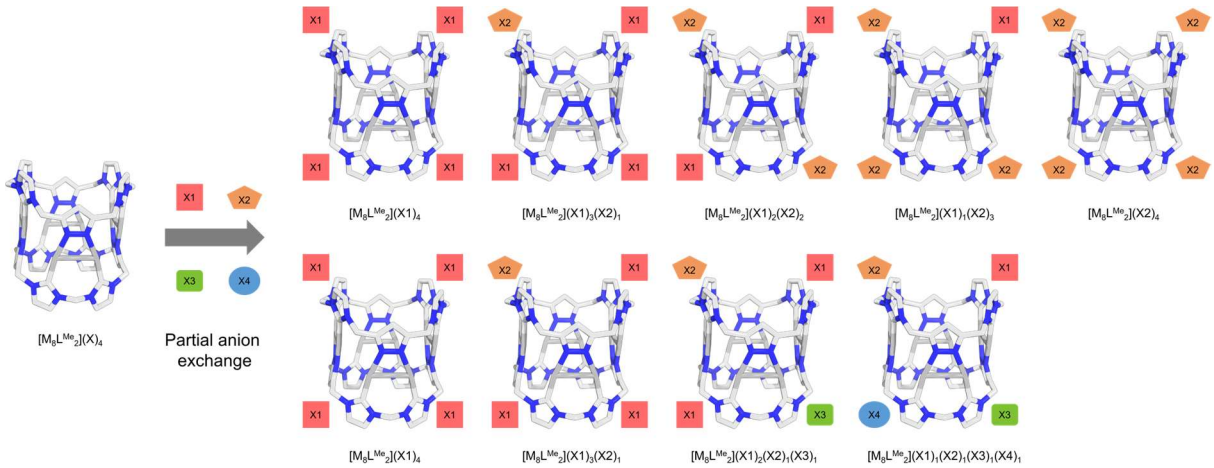

*Figure 37: Overview of the possibilities for partial anion exchange reactions of $[M_8L_2](X)_4$ (M = Ag(I), Au(I); L = L^{Me}, L^t; X = PF_6^-, OTf) with anions **X1**-**X4** varying in size and shape to achieve.*

3.3.2 $[Au_8L^{Me}_2](PF_6)_{2.5}(AuCl_2)_{1.5}$

The incorporation of metal-containing anions was accomplished through crystallisation attempts after the transmetalation reaction from $[Ag_8L^{Me}_2](PF_6)_4$ to the respective Au(I)-pillarplex salt. During the transmetalation reaction to form $[Au_8L^{Me}_2](PF_6)_4$ an excess of Au(I)-precursor was provided to ensure that a full conversion was reached. To a solution of 8.5 eq. Au(THT)Cl (THT = tetrahydrofuran) in MeCN, a solution of $[Ag_8L^{Me}_2](PF_6)_4$ (1 eq.) was slowly added and the reaction mixture was stirred overnight at 40 °C under exclusion of light. The purification was performed following the literature-known procedure[29] and the obtained white powder was analysed *via* ^{1}H NMR spectroscopy towards its purity. The desired signal set for the pillarplex cation was assigned in the ^{1}H NMR spectrum, and the presence of the PF_6^- anion was reviewed and confirmed by ^{31}P NMR spectroscopy, where one signal at approximately -144 ppm was detected. In order to perform crystallisation attempts, the white

powder was re-dissolved in MeCN in a small NMR tube. This tube was placed in a Schlenk-flask, which was partially filled with Et_2O and sealed to obtain single-crystals by slow vapour diffusion of Et_2O into the saturated solution.

Colourless block-shaped crystals suitable for single-crystal X-Ray diffraction were obtained crystalising in the triclinic space group *P*-1 (No. 2). The asymmetric unit contains one $[Au_8L^{Me}_2]^{4+}$ cation, 2 1/2 PF_6^- anions, one 1/2 $AuCl_2^-$ anions and additionally, one 1/2 co-crystallised acetonitrile molecules. During the transmetalation reaction of $[Ag_8L^{Me}_2](PF_6)_4$ with Au(THT)Cl to form the corresponding $[Au_8L^{Me}_2](PF_6)_4$ pillarplex salt, the side product $[Au_8L^{Me}_2](PF_6)_{2.5}(AuCl_2)_{1.5}$ emerged, where a partial exchange of the PF_6^- counter anions by $AuCl_2^-$ counter anions was discovered.

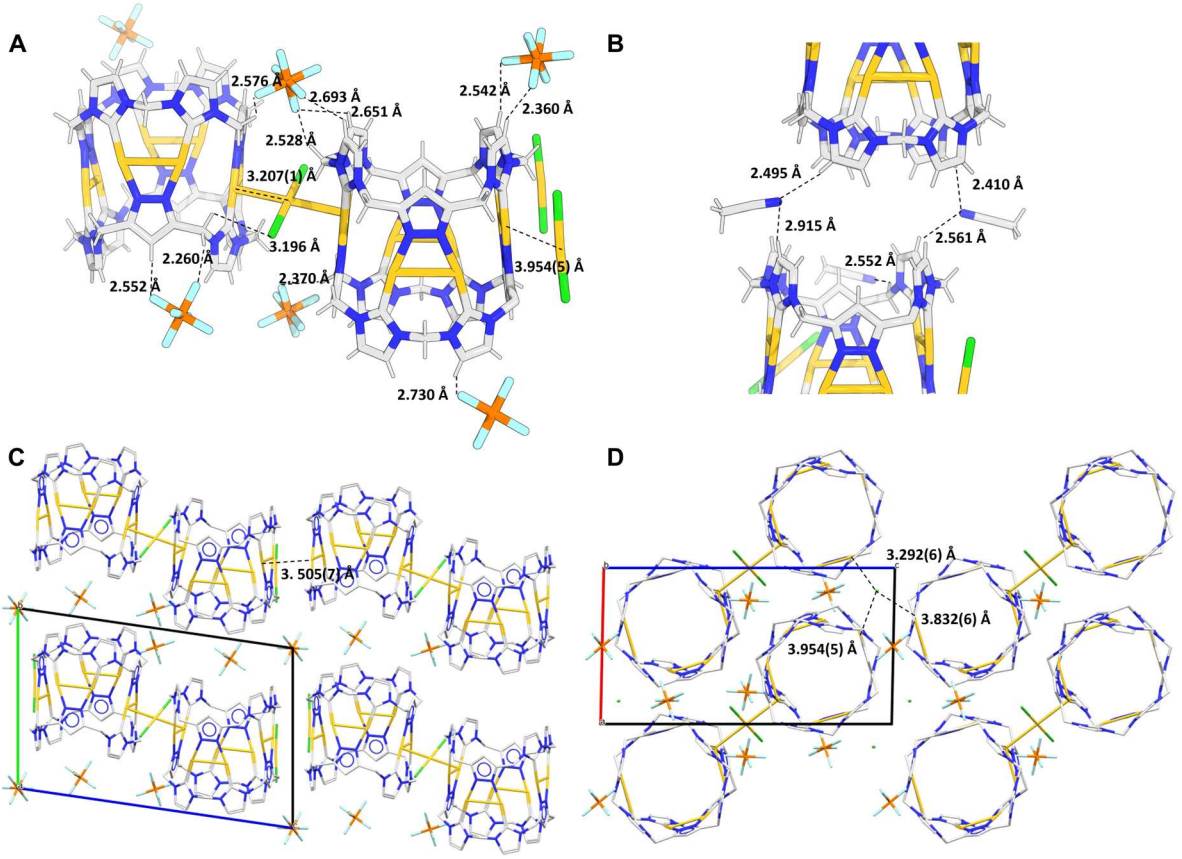

Figure 38: Representation of the solid-state structure of $[Au_8L^{Me}_2](PF_6)_{2.5}(AuCl_2)_{1.5}$: (A) Non-covalent interactions of $[Au_8L^{Me}_2]^{4+}$ with metallophilic Au-Au interactions and non-classical hydrogen bonding[36] of H_{rim} with halides of the counter anion (F_{PF6-} and Cl_{AuCl2}); (B) Hydrogen bonding interactions of H_{rim} with N_{MeCN}; (C) Crystal packing along the a-axis (zigzag chain alignment); (C) Crystal packing along the b-axis (pore alignment).

Two independent $AuCl_2^-$ anions are present (see Figure 38A) with one being located at an inversion centre and bridged in between two $[Au_8L^{Me}_2]^{4+}$ cations connecting these towards a metallophilic chain alignment by relatively short distances of 3.207(1) Å (Au(I)-Au_{AuCl2}(I)). The other isolated $AuCl_2^-$ anion is located in the void between three $[Au_8L^{Me}_2]^{4+}$ cations forming also metallophilic interactions with distances of 3.954(5) Å. Besides the obvious metallophilic interactions, non-classical hydrogen bonding[36] is observed between the counter anions and the hydrogen atoms of the rim. The chloride of the $AuCl_2^-$ anion forms hydrogen bonding with the methyl group of one acetonitrile molecule as well as hydrogen bonding with the H_{rim} of the neighbouring pillarplex cation. The acetonitrile molecules additionally form hydrogen bonding with N-H_{rim} (Figure 38B). Above and below the $AuCl_2^-$ anion connecting two pillarplex cations,

one PF_6^- anion is located forming non-classical hydrogen bonding[36] with the methylene bridged hydrogen atoms and hydrogen atoms of the imidazolylidene units. As already mentioned, the $AuCl_2^-$ anions connect the cations in a chain alignment, which is additionally retrieved by examining the crystal packing along the a-axis (Figure 38C), where the pairs of two $[Au_8L^{Me}_2]^{4+}$ cations connected by one $AuCl_2^-$ anion are forming zigzag chains. Here, Au(I)-Au(I) distances between the neighbouring $[Au_8L^{Me}_2]^{4+}$ cations of 4.505(7) Å are observed and with the second $AuCl_2^-$ anion a triangle of Au(I)-Au_{AuCl2}(I)-Au(I) bonds is formed (3.292(6) Å, 3.832(6) Å, 3.954(5) Å). The crystal packing along the b-axis showed a pore alignment of the $[Au_8L^{Me}_2]^{4+}$ cations (Figure 38D).

In summary, the mixed anion salt $[Au_8L^{Me}_2](PF_6)_{2.5}(AuCl_2)_{1.5}$ was obtained with metal-containing $AuCl_2^-$ counter anion. Moreover, the crystal packing shows a high ordered system, where the counter anions seem to strongly influence the arrangement. The obtained pore alignment of pillarplex cations $[Au_8L^{Me}_2]^{4+}$ in the solid-state align the isolated cavities of each pillarplex cation into a channel-shaped cavity. Another highly interesting feature of the $[Au_8L^{Me}_2](PF_6)_{2.5}(AuCl_2)_{1.5}$ salt are the short Au(I)-Au(I) distances (3.954(5) Å).

3.3.3 $[Ag_8L^t_2]_2(PF_6)_5(OTf)_3$

This chapter is based on the master thesis of Tom Calmus, which was supervised by this author.

Furthermore, a $[Ag_8L^t_2]^{4+}$ pillarplex salt featuring a combination of PF_6^- and OTf^- counter anions was discovered. The synthesis route for the triazole pillarplex is altered to the one for the pyrazole based pillarplex. Initially, the ligand $L^t(OTf)_4$ is coordinated with Ag(I) ions to yield the corresponding $[Ag_8L^t_2](OTf)_4$ pillarplex, followed by an anion exchange reaction to synthesise $[Ag_8L^t_2](PF_6)_4$. After this anion exchange, the white precipitate was purified and isolated. Subsequently, a saturated solution of the solid was prepared in an NMR tube and sealed within a Schlenk-flask partially filled with Et_2O. By slow diffusion of Et_2O into the NMR tube, colourless fragment-shaped single crystals were obtained and analysed *via* single crystal X-Ray diffraction measurements. The crystal structure was solved and refined in the triclinic space group *P* -1 and were determined to be a double salt including OTf^- and PF_6^- anions. With unit cell parameters a = 21.296(8) Å, b = 23.072(9) Å, c = 23.305(9) Å, α = 118.657(10)°, β = 90.594(12)°, γ = 98.005(12)°, the asymmetric unit contains two $[Ag_8L^t_2]^{4+}$ cations, three OTf^- anions, five PF_6^- anions and three co-crystallised MeCN solvent molecules.

The occuring interactions were analysed (Figure 39A) exhibiting mainly intermolecular non-classical hydrogen bondings[36] between the organic rim and the fluorine atoms of the counter anions. Additionally, classical hydrogen bonding of the H_{rim} with N_{MeCN} of the solvent molecules and with O_{OTf} of the triflate anions was observed. The oxygen atoms of the triflate and the fluorine atoms of the PF_6^- anion revealed metal coordination with the Ag(I) ion and the hydrogen atoms of MeCN showed H-π-interactions with the aromatic imidazolylidene unit. In Figure 39B the arrangement of the $[Ag_8L^t_2]^{4+}$ cations is depicted, where two cations form a slightly twisted chain alignment with a torsion angle of 25.48°. This pair of two pillarplex cations exhibit argentophilic interactions of Ag(I)-Ag(I) with a distance of 3.567 Å. Additionally, the neighbouring pairs of two pillarplex cations are chain-aligned with Ag(I)-Ag(I) distances of

4.894 Å and 5.748 Å. Figure 39C+D display the following described features for the crystal arrangement of the $[Ag_8L^t_2]^{4+}$ cations alongside the c- and b-crystallographic axes. In c-direction a pore alignment of every second layer of cations is established (Figure 39C). However interpenetrated layers of the chain alignment were detected, where the interpenetration results from π-interactions of the organic rim of neighbouring cations – especially the imidazolylidene units on both sides of one cation. In the next layer the pairs of two cations always lay in the "empty" void between two of the cation pairs of the previous layer. Along the crystallographic b-axis a block arrangement of two layers of cations is depicted, where in between the blocks the majority of the counter anions is located (Figure 39D).

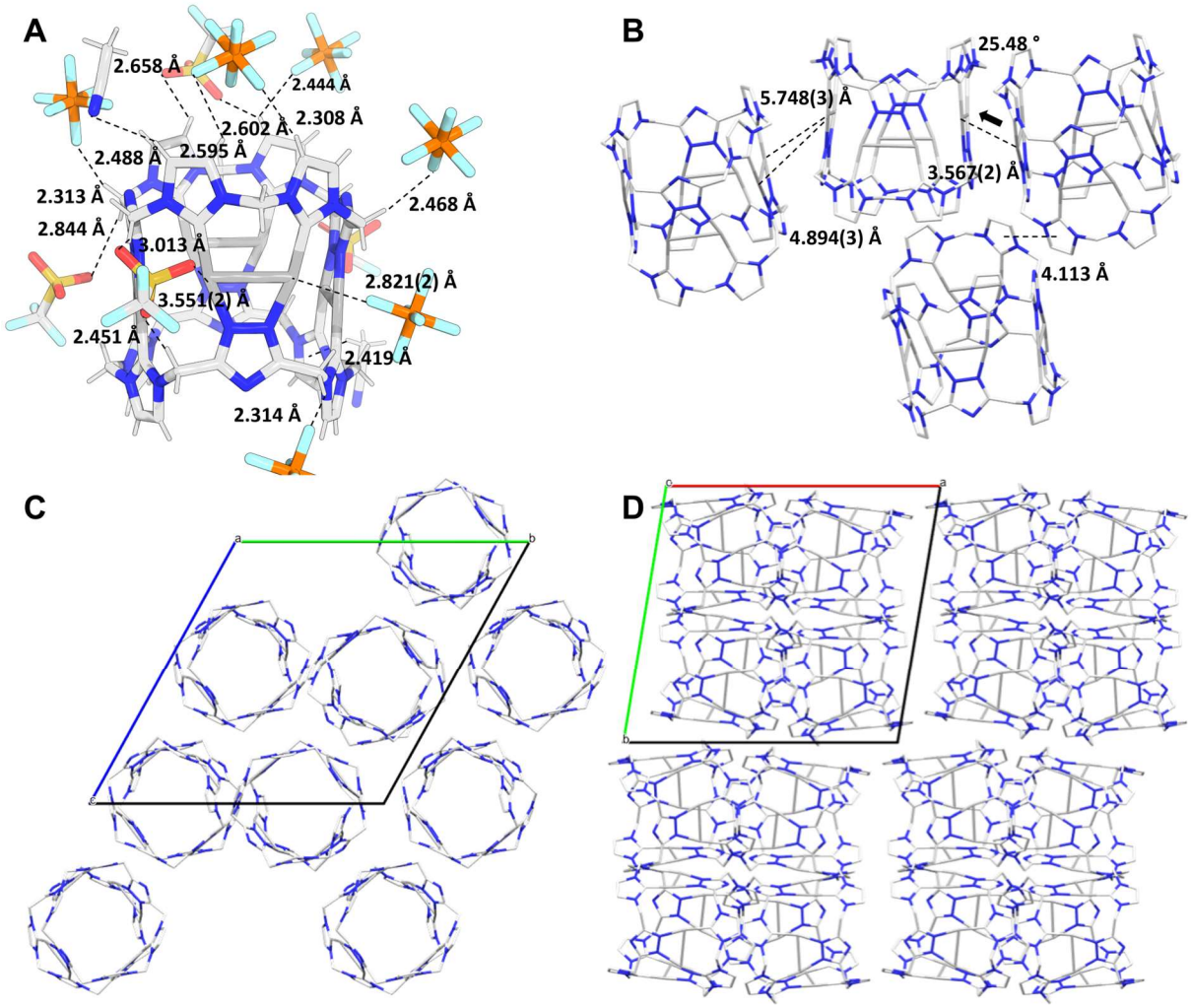

Figure 39: Representation of the solid-state structure of $[Ag_8L^t_2]_2(PF_6)_5(OTf)_3$: (A) Non-covalent interactions of $[Ag_8L^t_2]^{4+}$ with classical hydrogen bonding of H_{rim} with O_{OTf} and N_{MeCN} non-classical hydrogen[36] of H_{rim} with counter anion F_{PF6-} and F_{OTf}, and metal coordination O_{OTf} and F_{PF6}; (B) Argentophilic interactions in chain alignment of $[Ag_8L^t_2]^{4+}$ with the cations being tilted towards each other by 25.48°; (C) Crystal packing along the c-axis exhibiting a pore alignment of $[Ag_8L^t_2]^{4+}$; (D) Crystal packing along the b-axis exhibiting a chain alignment of $[Ag_8L^t_2]^{4+}$ (in blocks).

To conclude, a mixed triazole based pillarplex salt $[Ag_8L^{Me}_2]_2(PF_6)_5(OTf)_3$ has been studied in terms of cation arrangement and occurring interactions. Comparison with the crystal structures of $[Ag_8L^t_2](OTf)_4$ and $[Ag_8L^t_2](PF_6)_4$ revealed similarities (F42S).[32] In the mixed triazole based pillarplex structure the formation of neighbouring cation pairs, tilted towards each other by 25.48°, was observed, which was also discovered for $[Ag_8L^t_2](OTf)_4$, where the neighbouring

$[Ag_8L^t_2]^{4+}$ cations are tilted by 61.61°. While for $[Ag_8L^t_2](OTf)_4$ hydrogen bonds between O_{OTf} or S_{OTf} with H_{rim} were obtained, besides the hydrogen bonds of F_{PF6} or O_{OTf} with H_{rim} the formation of Ag(I)-Ag(I) interaction was noted for $[Ag_8L^t_2]_2(PF_6)_5(OTf)_3$. In particular, these metallophilic interactions between two neighbouring $[Ag_8L^t_2]^{4+}$ cations with short distances (3.567 Å) stand out. This was also reported for $[Au_8L^t_2](PF_6)_4$, where an Au(I)-Au(I) chain alignment with distances of 4.517 Å was identified. In this case, the shape of the $[Au_8L^t_2]^{4+}$ cation differs, as the imidazolylidene units are bent towards each other resulting in a compressed pore opening of 2.93 Å. The distortion originates from interactions of H_{rim} with one PF_6^- anion, which is located on top of the pore opening.[32] In contrast, no variation of cation shape was discovered for $[Ag_8L^t_2]_2(PF_6)_5(OTf)_3$.

3.3.4 Summary and Outlook

After analysing the crystal arrangement of various pillarplex salt containing one anion in Chapter 3.2., several crystal structure analyses showed that pillarplex salts containing two different anions can be obtained and were analysed *via* SC-XRD measurements. Although the introduction of another anion leads to additional complexity of the structure solution, the achieved mixed anion salts could feature interesting properties (e.g., solubility, host-guest chemistry, porosity, photo chemistry).

The salt $[Au_8L^{Me}_2](PF_6)_{2.5}(AuCl_2)_{1.5}$ was obtained as a side product of the transmetalation in a crystallisation attempt, and therefore the formation must be investigated starting with the full characterisation of the metal precursor Au(THT)Cl. This metal precursor was only analysed by ^{1}H NMR spectroscopy, where the metal species, such as $AuCl_2^-$ are silent. Performing an additional elemental analysis should help to verify the purity of the metal precursor especially regarding the metal content. However, if no $AuCl_2^-$ is detected in the metal precursor the mechanism on how the $AuCl_2^-$ anion is implemented as counter anion has to be investigated. The prospect of further anion exchange reactions with the metal-containing anion can then be explored by a titration of an Au(I) source into a solution of pure $[Au_8L^{Me}_2](PF_6)_4$. An intriguing possibility is the investigation of the photophysical properties of $[Au_8L^{Me}_2](PF_6)_{2.5}(AuCl_2)_{1.5}$ or other pillarplex salts containing Au(I) counter anions, since it is known that the lengths of the Au(I)-Au(I) distances influence the absorption, luminescence and lifetime properties.

An incomplete anion exchange yielded the pillarplex salt $[Ag_8L^t_2]_2(PF_6)_5(OTf)_3$, which exhibited metallophilic chain-aligned pairs of neighbouring cations tilted towards each other, similarly to the literature-known structures of $[Ag_8L^t_2](OTf)_4$ and $[Ag_8L^t_2](PF_6)_4$. Achieving a selective synthesis of $[M_8L^t_2](PF_6)_X(OTf)_{4-X}$ while controlling the ratio of PF_6^- to OTf^- would be of high interest, as the influence on the crystal arrangement could be evaluated. This could be accomplished by either adjusting the stoichiometry during the anion exchange reaction or post-synthetic modification (e.g., titration) of a single anionic salt.

3.4 Crystal Structure of a Hexacationic Ag(I)-Pillarplex-Dodecyl-Diammonium Pseudorotaxane as Terephthalate Salt

This chapter is based on the publication: "Crystal structure of a hexacationic Ag(I)-pillarplex-dodecyl-diammonium pseudo-rotaxane as terephthalate salt" Alexandra A. Heidecker*, Moritz Bohn and Alexander Pöthig*; *Zeitschrift für Kristallographie – Crystalline Materials*, **2022**, *237* (4-5), 167-177. https://doi.org/10.1515/zkri-2021-2076.

3.4.1 Introduction

In order to make predictions for the formation of an assembly based on supramolecules in the solid-state, a profound understanding of the parameters influencing this arrangement is required. In particular, in the solid-state the sensitivity to interactions on the surface or the building units of the supramolecule can be exploited for applications, such as separation, catalysis or molecular recognition.[98-108]

To achieve the formation of a controlled supramolecular arrangement, various tools can be employed to analyse the (non-)covalent interactions that occur between individual supramolecules. This information can be used to gain further insights into how to achieve the controlled formation of a supramolecular assembly. As the pillarplex system is a combination of organic macrocyclic ligands linked by metal coordination to form a supramolecular organometallic host, the applicability of tools needs to be investigated (Figure 40).

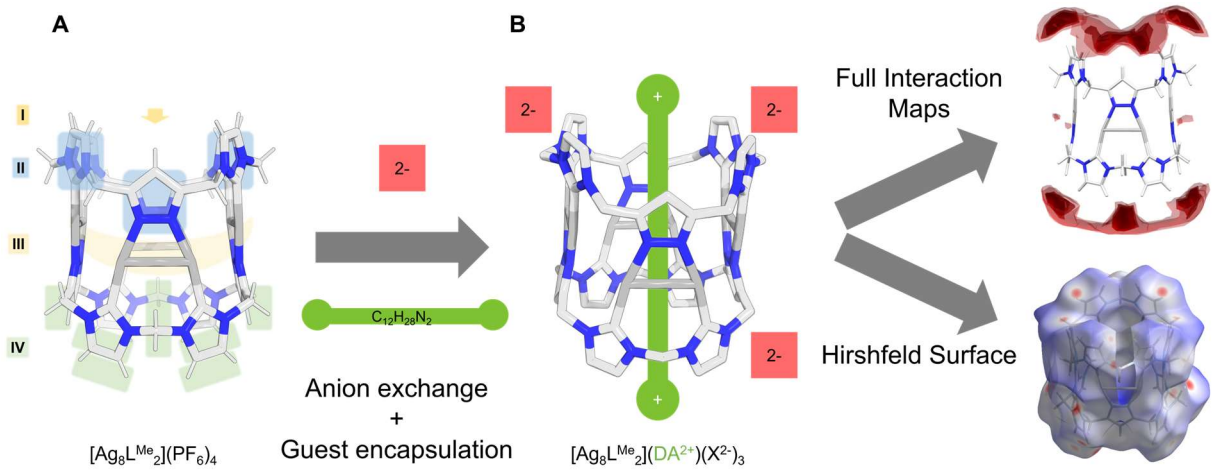

Figure 40: Overview of (A) Cation $[Ag_8L^{Me}_2]^{4+}$ marked with the four regions for the specific (non-)covalent interactions: (I) Cavity, (II) Aromatic ligands, (III) Metal ions and (IV) Rim; (B) Synthesis of the pseudorotaxane $[Ag_8L^{Me}_2](DA)(X^{2-})3$ and the applied analytical methods Full Interaction Maps (FIMs) and Hirshfeld surface analysis to investigate the obtained (non-)covalent interactions.

The first step is to understand the target molecule $[M_8L^{Me}_2](X)_4$ and the interactions that may occur. Therefore, the pillarplex cation $[M_8L^{Me}_2]^{4+}$ is divided into the four regions where specific non-covalent interactions are anticipated:

(I) Hydrophobic cavity: Mainly dispersion or electrostatic interactions can occur here. As the tubular cavity is partially formed by the M(I) ions a minor contribution of metal coordination to the sum of interactions may occur. The nature of the interactions involved in guest

encapsulation in the pillarplex cavity has already been studied by quantum chemical calculations, which indicate that van der Waals forces are the main driving force for encapsulation with a contribution of approximately 50%, followed by orbital polarisation and electrostatic forces (20%) and only a marginal contribution from the metal coordination.[109]

(II) Aromatic ligands: These are constructed by pyrazole and imidazolylidene units, where π-interactions are predicted. The influence of the aromatic ligands has already been observed in ^{1}H NMR spectroscopy, where shielding of the guest protons by ring current effects led to a shift of the proton signals for the encapsulated guest.

(III) Metal ions: The pillarplexes contain either Ag(I) or Au(I) with the potential for metal coordination. Due to steric reasons, the metal coordination is mainly anticipated to occur on the outside of the pillarplex cation, but in principle these interactions are feasible in the inside of the cavity. However, smart design of the guest must be performed to achieve the physical proximity for metal coordination inside the cavity. SAXS measurements already showed, that M^{+} ions can be accommodated despite strong repulsion forces. Although Au(I) complexes are coordinatively saturated, Ag(I) complexes can offer additional coordination sites.[110-112]

(IV) Rim: The organic ligand is built up by pyrazole, imidazolylidene and methylene units, which offer a range of possibilities for interactions, mainly attributed to hydrogen bonding. In general, the small and large pockets of the pillarplex rim contain aromatic C-H hydrogen atoms. Additionally, the methylene bridges offer aliphatic hydrogen atoms partially directing towards the metal ions of the pillarplex cation. The strong influence of hydrogen bonds in regard to the rim hydrogen atoms was already reported for $[M_8L^t_2](X)_4$ (with X = PF_6^-, OTf^-), where the pyrazole unit is exchanged by a triazole unit.[32] In the case of $[Au_8L^t_2](PF_6)_4$ non-classical hydrogen bonding[36] between the counter anion and the organic rim led to a deformation of the pore opening, due to the coordination of one PF_6^- anion to all hydrogen atoms of the four imidazolylidene units located directly on top of the cavity (see Chapter 1.3).

3.4.2 FIMs analysis of $[Ag_8L^{Me}_2]^{4+}$

To determine the aforementioned regions of potential interaction sites, the tool Full Interaction Maps (FIMs) was used to review the applicability towards the organometallic pillarplex system.

Implemented in the program Mercury, the tool FIMs is able to visualise regions, where specific interactions are anticipated based on experimentally determined data (CSD database).[113] Beforehand, the targeted molecule is divided into smaller groups by the program IsoStar[114] and arranged into so-called central groups, which contain the data of specific properties. The program SuperStar[115] combines those smaller groups into the large targeted molecule and calculates the scattering plots for the whole molecule. The program Mercury[116] has various probes (Figure 41) implemented for which the maps of potential interactions sites can be determined. For each probe a specific colour visualises the interaction sites, whereby the shading indicates the probability of specific interactions. Dark regions exhibit strong and brighter regions indicate less probability for the specific interaction. Besides the implemented probes, individual probes can be added. However enough information on the specific properties must be embedded in the CSD database for appropriate visualisation of the interaction regions.

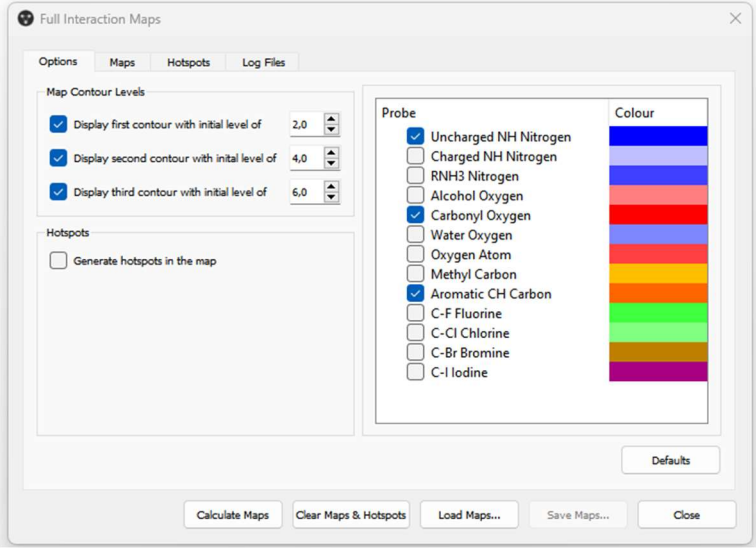

Figure 41: Overview of the probes implemented into Mercury.[116]

As the main interest lies in the arrangement of the $[M_8L^{Me}_2]^{4+}$ cations, this fragment was exposed to the FIMs analysis. The calculated maps of this fragment can be used to predict interaction sites and thereby assign potential locations of the counter anions and solvent molecules in the solid-state. The program IsoStar[114] divided the pillarplex cation into the following seven central groups: aromatic CH, aromatic C(sp^3), aromatic N, aromatic dimethyl amino, ethylene, aliphatic methylene and substituted carbon groups (F43S). Notably, only the organic parts of $[Ag_8L^{Me}_2]^{4+}$ were detected and the presence of metal ions was neglected.

For the investigation of $[Ag_8L^{Me}_2]^{4+}$ by FIMs analysis oxygen (probe: carbonyl oxygen) and nitrogen (probe: uncharged NH) were chosen, as they have the potential to perform hydrogen bonding, π-interactions and metal coordination. The obtained interaction maps can be seen in Figure 42. The visualised interaction regions for probe carbonyl oxygen exhibited large areas close to the rim, located on top of the pore opening (seen in the top view). The strong influence of hydrogen bonding in this specific area was in accordance with the already observed deformation of $[M_8L^t_2](X)_4$.[32] Additionally, small regions were identified close to the aliphatic hydrogen atoms of the CH_2 groups. However, the regions for interaction sites were only determined outside of the cavity and no probability for hydrogen bonding inside the cavity was calculated and displayed. Detailed investigation of the regions for interaction sites with probe uncharged NH nitrogen exhibited small areas at the outside of the rim, where π-interactions with the aromatic units were anticipated. Additionally, above and below the pore opening and in close proximity on the inside of the pore opening small interaction sites were defined. Furthermore, the calculated interaction sites were located exclusively close to the pyrazole unit, although the imidazolylidene units exhibit aromatic character too. Hence, the formation of π-interactions with uncharged N is feasible. As mentioned before, no central groups were assigned to the metal ions and therefore no interaction sites were calculated close to the Ag(I) ions. The analysis tool FIMs was developed for the use in biochemistry for drug design[113] and therefore, a limited amount of metal-containing structures was implemented. Nevertheless, individual metal probes can be designed, but it must be considered that the database might not contain enough data to calculated sufficient interaction regions.

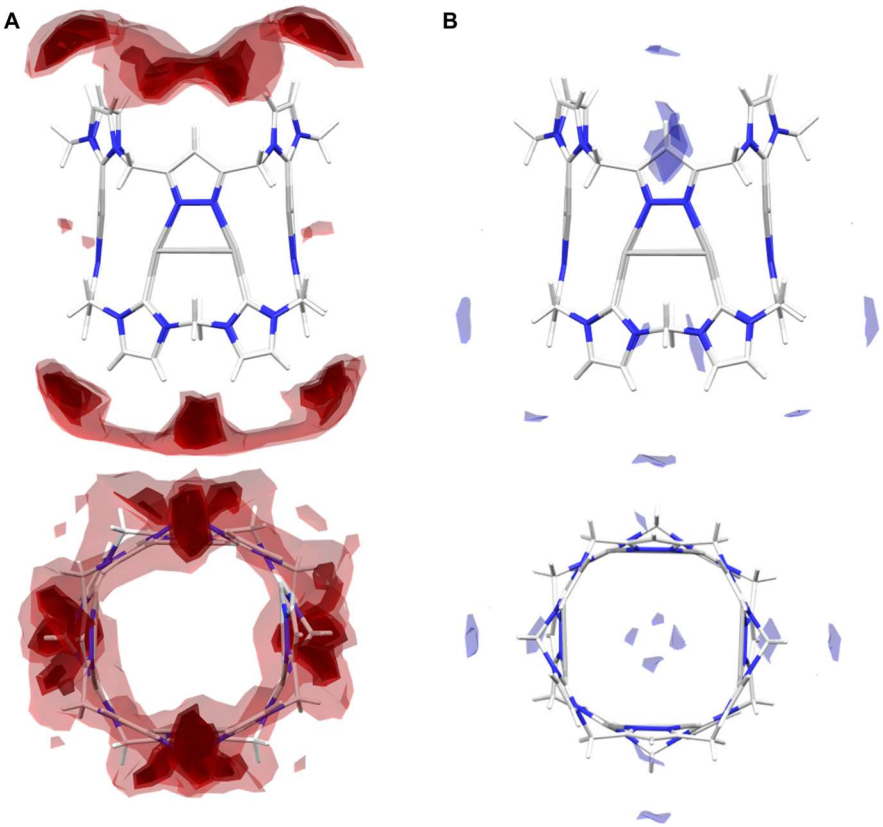

Figure 42: FIMs analysis of cation $[M_8L^{Me}{}_2]^{4+}$ towards (A) Acceptor probe carbonyl oxygen; (B) Donor probe uncharged NH nitrogen with the side view displayed at the top and the top view displayed at the bottom.

In summary, the FIMs tool provides suitable maps for interaction sites in the case of organic molecules or organic components of molecules. However, its applicability is limited for metal coordination and, in particular, for interaction regions inside a cavity.

3.4.3 Synthesis of $[Ag_8L^{Me}{}_2](DA)(BDC)_x$ and Crystal Structure Investigation

Synthesis of $[Ag_8L^{Me}{}_2](DA)(BDC)_x$

A pseudorotaxane was experimentally designed, which contained all four mentioned possibilities for (non-)covalent interactions (I, II, III, IV, Figure 40A) and was used to validate the use and applicability of FIMs analysis on the pillarplex system. Therefore, a pseudorotaxane containing $[Ag_8L^{Me}{}_2]^{4+}$ as ring component and initially 1,12 dodecane diamine as a guest was synthesised. As the literature-known anions PF_6^- and OTf^- only exhibit the potential for non-classical hydrogen bonding[36], the pseudorotaxane was further subjected to an anion exchange reaction with terephthalic acid and base DIPEA yielding the hexacationic $[Ag_8L^{Me}{}_2](DA)(BDC)_x$ (with DA = dodecyl diammonium, BDC benzene-1,4-dicarboxylic acid) salt (Figure 43).

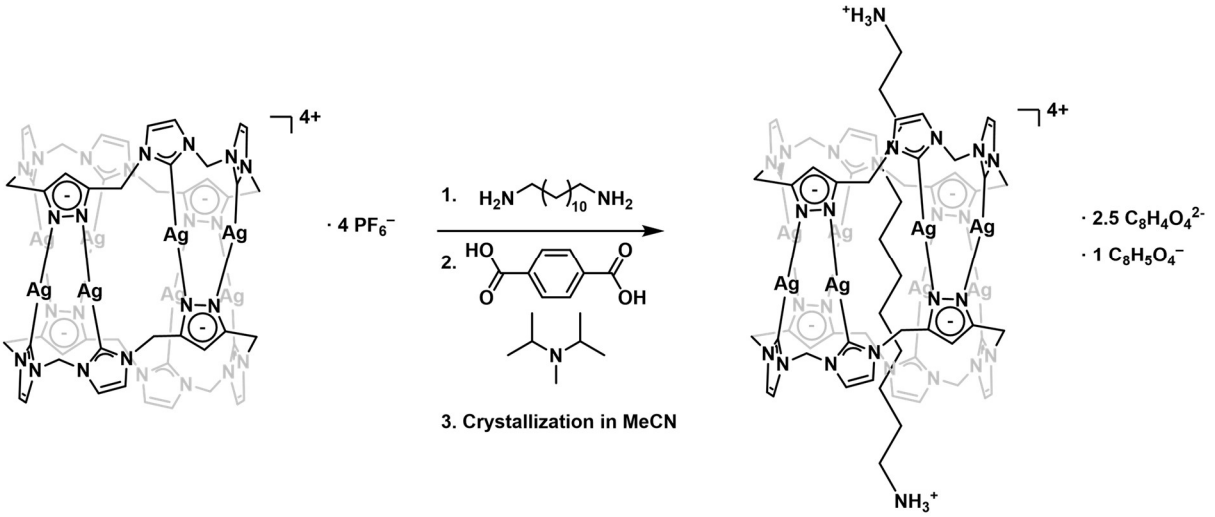

Figure 43: Synthetic reaction for $[Ag_8L^{Me}{}_2](DA)(BDC)_x$ salt. Slightly varied and taken from [31].

After combining all compounds, the reaction mixture was stirred at room temperature overnight and the solvent was removed by evaporation. The obtained off-white solid was washed with Et_2O and dried *in vacuo*. The successful formation of pseudorotaxane $[Ag_8L^{Me}{}_2](DA)(BDC)_x$ was validated by NMR spectroscopy and ESI mass spectrometry (see Chapter 5.8.1).

Crystal Structure Analysis

Colourless, octahedral-shaped crystals were suitable for SC-XRD measurement after being obtained by slow diffusion of the solvent MeCN. The crystals were solved and refined in the monoclinic space group *P* $2_1/c$ (No. 14) and the asymmetric unit cell contains one $[Ag_8L^{Me}{}_2]^{4+}$ cation, one guest (dodecyl-diammonium), 3 1/2 terephthalate anions and twenty-two co-crystallised water molecules. The pillarplex cation $[Ag_8L^{Me}{}_2]^{4+}$ (Figure 44A) exhibits a similar molecular structure to literature-known structures[29,97] with geometric parameters in the range of 3.1028 to 3.4541 Å for Ag(I)-Ag(I) distances, 2.070 Å for Ag(I)-C distances and 2.094 Å for Ag(I)-N distances. A chain alignment of $[Ag_8L^{Me}{}_2]^{4+}$ cations is revealed in the direction of the crystallographic b- and c-axes, where two neighbouring cations are tilted towards each other with an angle of 72.61° (Figure 44B). Thus, a chain of two alternating cations is observed. Along the a-axis, these chain-aligned pillarplex cations form layers, where from one layer to the next layer the pairs of alternating cations are shifted by one cation. As the asymmetric unit contains only 3 1/2 terephthalate units, the location of these molecules and their protonation state has been determined. The three terephthalates (1, 2, 3) are located at general positions and the fourth on is located at the specific Wyckoff position 2*a*, where a twofold axis is ranging through the middle of the molecule (Figure 44C). During refinement, residual electron density close to the nitrogen atom of the guest molecule was observed. The assignment of hydrogen atoms at these positions suggested that the initial guest 1,12-diamino dodecane was protonated due to slightly acidic conditions, probably caused by the presence of terephthalic acid. Thus, dodecyl diammonium was *in-situ* formed and encapsulated to form the respective pseudorotaxane $[Ag_8L^{Me}{}_2]^{4+}$(DA). The four-times positively charged cation combined with the two-times positively charged guest, led to the assumption, that counter anions with a total charge of 6- are present. The state of protonation of the terephthalate units is differentiated by

comparison of the C-O bond lengths and the residual electron density in proximity of the oxygen atoms. In summary, three terephthalate unit show relatively similar C-O bond lengths of 1.25 Å, indicating that a delocalised negative charge is distributed over the two oxygen atoms and hence both carboxylic acid groups are deprotonated. Meanwhile, one terephthalate unit exhibits one longer and one shorter C-O bond (1.223 Å *vs.* 1.313 Å), which indicates that this unit is partially deprotonated, and thus, the hydroxy hydrogen atom is calculated and refined at the ideal position (Figure 44C). As already mentioned, twenty-two water molecules are co-crystallised in the asymmetric unit. This network of water molecules seems to have a crucial impact on the stability of the crystal structure and strongly influences the crystal packing.

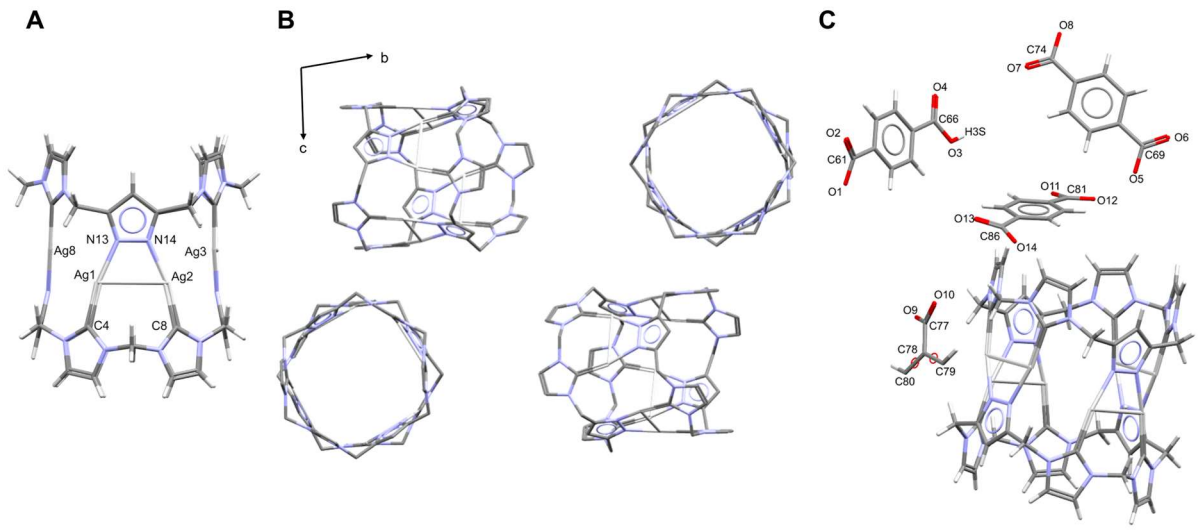

Figure 44: Detailed representation of the solid-state structure of $[Ag_8L^{Me}{}_2](DA)(BDC)_x$: (A) Molecular structure of the cation $[Ag_8L^{Me}{}_2]^{4+}$ with selected marked atoms; (B) Crystal packing along the a-axis of cations showing chain alignment with a tilted angle of 72.61°; (C) Location and protonation state of the terephthalate units. Slightly varied and taken from [31].

(Non-)Covalent Interactions

After thoroughly examination of the molecular structure accurately assigning the hydrogen atoms, the (non-)covalent interactions were analysed based on the four defined regions (Figure 45):

(I) Cavity: This region allowed the encapsulation of a guest molecule. The selected guest extends the cavity on the top and the bottom. One side of the dodecyl diammonium crystallised in an anti-periplanar conformation, while the atoms sticking out of the bottom of the cavity adopted a bent configuration, favouring a gauche formation. This bent fashion led to a lower energetic profile primarily due to intermolecular hydrogen bonding of the alkyl chain with the rim. Notably, protonated amine groups were identified providing an additional hydrogen donating group, which was stabilised by hydrogen bonding with two terephthalate units and one water molecule.

(II) Aromatic ligands: In this region, π-interactions were determined between imidazolylidene units and terephthalate units. These interactions occurred either directly between two neighbouring pillarplex cations through π-stacking of the respective imidazolylidene units or between two neighbouring pillarplex cations, which were connected by one terephthalate unit exhibiting π-stacking with both respective imidazolylidene units. In both cases, the neighbouring pillarplex cations were distorted of approximately 65°.

(III) Metal ions: Within this region coordinative interactions between Ag(I) and the oxygen atom of water molecules (O_{H2O}) were detected, as well as coordinative interactions between Ag(I) and the oxygen atoms of terephthalate units (O_{te}).

(IV) Rim: In particular intermolecular hydrogen bonding was anticipated and indeed verified by hydrogen bonding between the organic rim and the oxygen atoms of solvent and anion molecules (O_{H2O}, O_{te}).

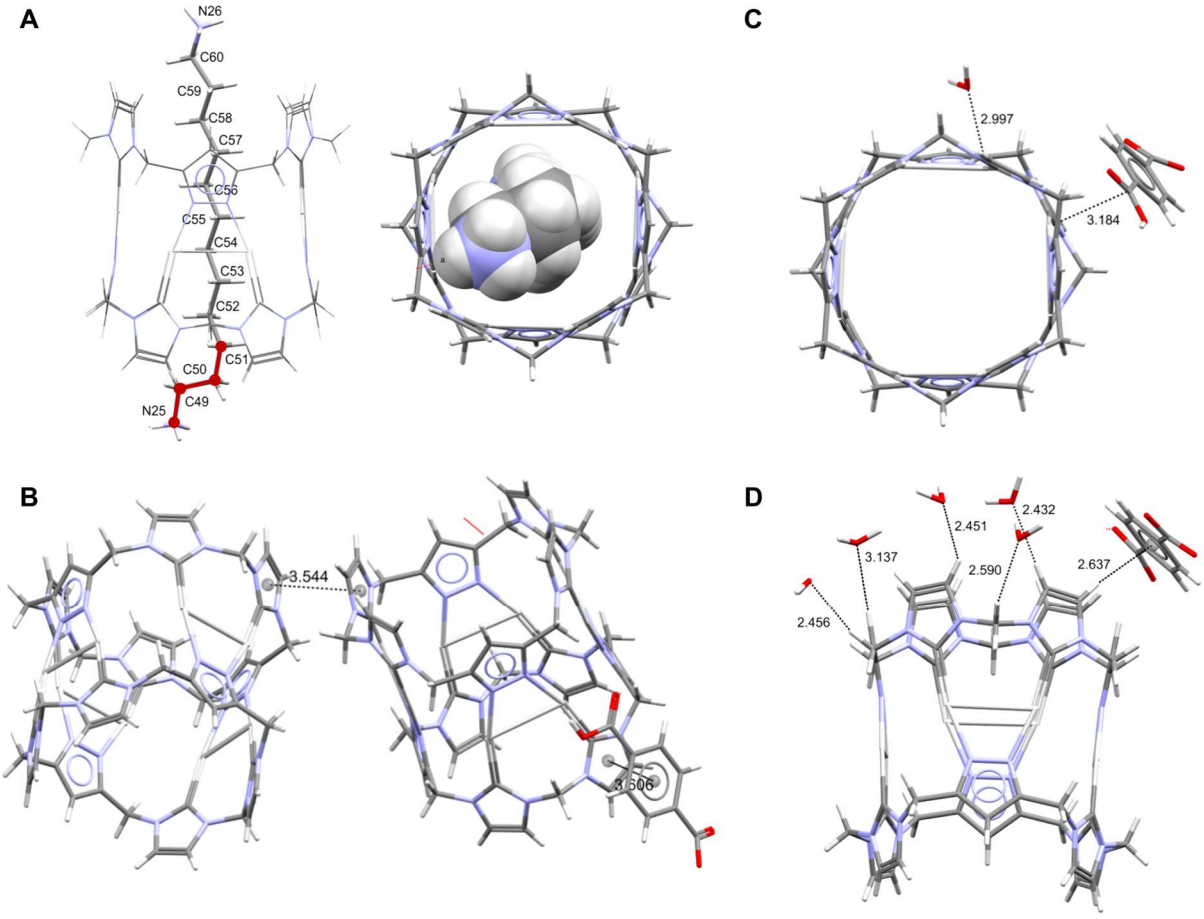

Figure 45: Representation of the occurring (non-)covalent interactions of the solid-state structure of $[Ag_8L^{Me}_2](DA)(BDC)_x$: (A) Cavity with encapsulated guest dodecyl diammonium; (B) Aromatic ligands, where either direct π-interactions of neighbouring imidazolylidene units or indirect π-interactions through one terephthalate unit were observed; (C) Metal coordinative interactions of Ag(I) with the oxygen atoms of terephthalate and water molecules; (D) Hydrogen bonding at the organic rim with the oxygen atoms of water and terephthalate units. Slightly varied and taken from [31].

The synthesised pseudorotaxane showed interactions in all four regions. However, the (non-)covalent interactions are strongly influenced by the choice of solvent and especially in this case by the presence of water, which formed a hydrate shell around the pillarplex system.

3.4.4 Hirshfeld Surface Analysis of Dodecyl Diammonium and $[Ag_8L^{Me}_2]^{4+}$

Calculation and visualisation of isosurfaces and a quantification of the occurring interactions can be achieved by the program CrystalExplorer.[117-119] Within the calculated surface of a specific molecule, interactions are identified and colour-coded based on the distance from the surface to the exterior and the interior atoms. Blue regions represent contacts with longer distances, white regions indicate contacts at an average distance and red regions signify contacts shorter than the van der Waals radii of the atoms.

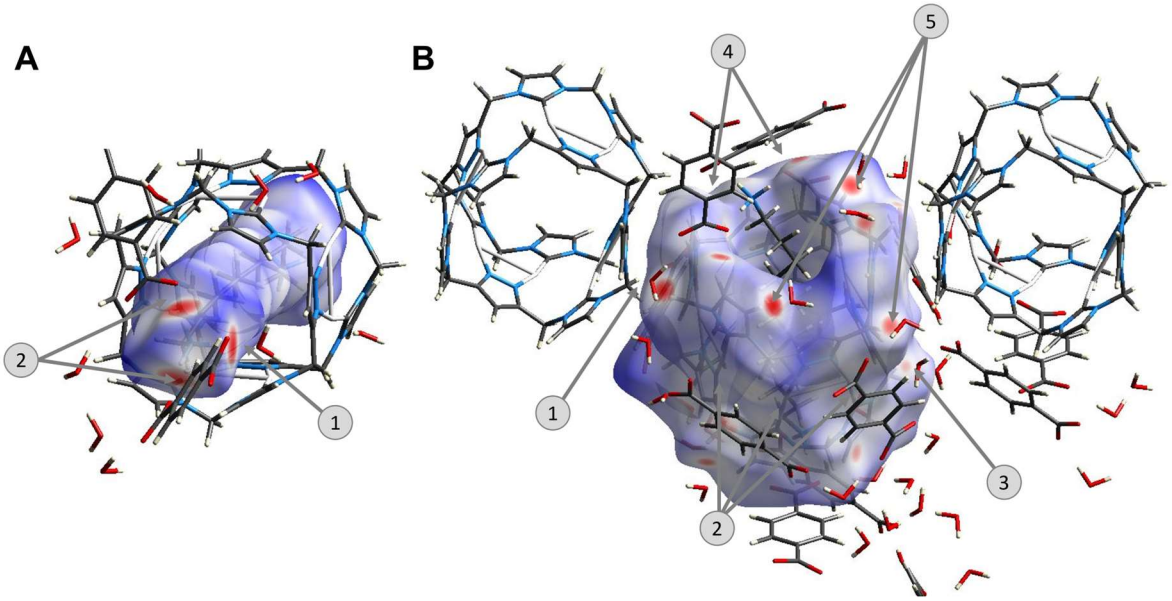

Figure 46: Hirshfeld surface analysis of (A) Guest molecule in the solid-state showing intermolecular interactions of the -NH_3^+ groups with terephthalate and water units; (B) $[Ag_8L^{Me}_2]_{4+}$ in the solid-state showing intermolecular contacts. Slightly varied and taken from [31].

With this method, a theoretical validation of the identified interactions in the crystal structure can be gained. Hence, the Hirshfeld surfaces of the guest dodecyl diammonium and the pillarplex cation $[Ag_8L^{Me}_2]^{4+}$ were calculated (Figure 46) and analysed towards the defined interaction regions of the pillarplex.

(I) Cavity: To analyse the interactions inside the cavity, the Hirshfeld surface of the guest molecule was illustrated, and a highly symmetrical surface was visualised. The surface of the alky chain showed blue and white regions indicating the absence of strong interactions in the hydrophobic cavity. At the functional groups (ammonium) three strong interactions on both sides of the surface were displayed, where hydrogen bonding with one water oxygen atom (1) and with two carboxylate groups (2) of respective terephthalate units were observed similarly to the crystal structure analysis.

(II) Aromatic ligands: The interactions of the organic aromatic ligands were analysed based on the calculated Hirshfeld surface of cation $[Ag_8L^{Me}_2]^{4+}$, where π-stacking of the imidazolylidene units of two neighbouring pillarplex cations (1) was identified.

(III) Metal ions: The Ag(I) ions of the cation exhibited coordinative bonding either with the aromatic ring or the carboxylate group of the terephthalate unit (2), as well as metal coordination of oxygen atoms of the water molecules (3).

(IV) Rim: The predicted hydrogen bonds at the organic rim of $[Ag_8L^{Me}{}_2]^{4+}$ were discovered between the aromatic ring and the carboxylate group of terephthalate unit and the hydrogen atoms at the rim (4). Additionally, strong interactions were observed between the hydrogen atoms of the rim and several oxygen atoms of water (5).

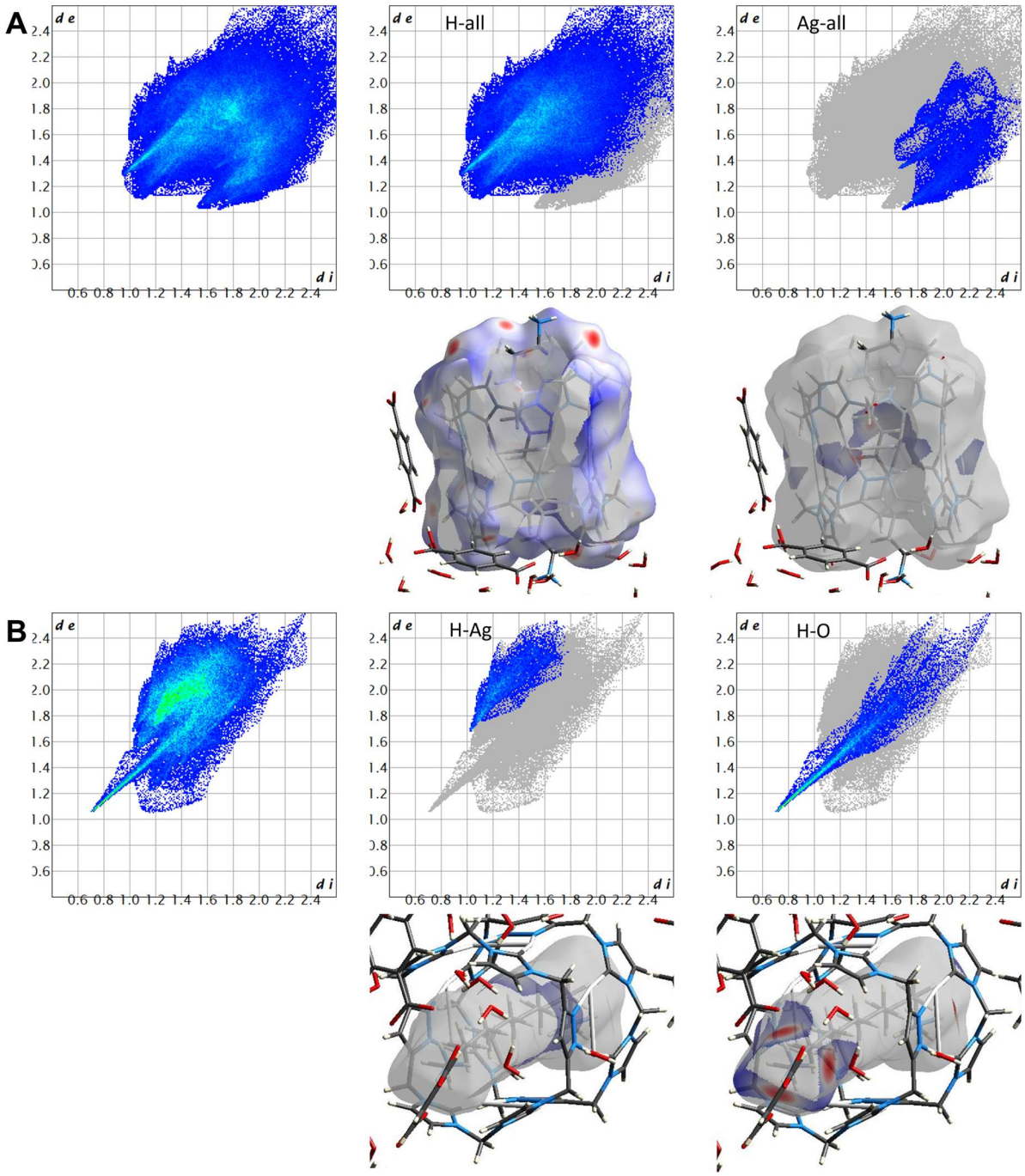

Figure 47: Fingerprint plot diagram for (A) $[Ag_8L^{Me}{}_2]^{4+}$ highlighting all interactions, all hydrogen bonding interactions (H-all) and all metal coordinative interactions (Ag-all); (B) Guest dodecyl diammonium highlighting all interactions, all hydrogen to metal interactions (H-Ag) interactions and all hydrogen to oxygen interactions (H-O). Slightly varied and taken from [31].

For further evaluation of the calculated Hirshfeld surface, the fingerprint plots (Figure 47) were analysed towards the contribution of specific interactions in comparison to the sum of all interactions of the isosurface. In particular, the contribution of hydrogen bonding (H•••X) and metal coordination (Ag•••X) was investigated (Table 4). Due to applying the SQUEEZE[89] procedure, implemented in Platon, to remove disordered solvent molecules a hole was created in proximity to $[Ag_8L^{Me}_2]^{4+}$. This affected the fingerprint plots as the area, where electron density was removed no longer carries information. Hence, the surface and the fingerprint plots were calculated based on interactions with atoms that are further apart from $[Ag_8L^{Me}_2]^{4+}$. This could contribute to the overall interactions and was noted especially in the fingerprint plots. However, only the interactions with distances higher than 2.5 Å were affected and their influence is chemically not reasonable. Therefore, the interest focused on the short-range interactions, which were discussed and thus, the obtained information reflected reasonable results.

Table 4: Contribution [%] of interactions based on the fingerprint plots of the Hirshfeld surface analysis. Taken from [31].

Dodecyl diammonium	**Contribution [%]**	**$[Ag_8L^{Me}_2]^{4+}$ Hydrogen**	**Contribution [%]**	**$[Ag_8L^{Me}_2]^{4+}$ Metal**	**Contribution [%]**
H•••all	100.0	H•••all	65.2	Ag•••all	7.7
H•••Ag	10.2	H•••Ag	0.3	Ag•••Ag	0.0
H•••N	16.3	H•••N	0.4	Ag•••N	0.0
H•••C	25.3	H•••C	8.3	Ag•••C	1.2
H•••H	31.4	H•••H	40.8	Ag•••H	5.2
H•••O	16.8	H•••O	15.4	Ag•••O	1.2

The interactions within the cavity were solely based on hydrogen bonding, where 10.2% originated from Ag•••H agnostic interactions[120] and 16.8% were assigned to hydrogen bonding of the functional ammonium groups with oxygen atoms of terephthalate units and one water molecule. In the interactions of cation $[Ag_8L^{Me}_2]^{4+}$, the highest contribution was attributed to hydrogen bonding (65.2%), and only a marginal contribution of 7.7% was considered as metal coordination interactions. Overall, the dominant interactions in this system were identified as hydrogen bonding, thus strengthening the suggestion that the formed network of water molecules contributed a lot to the stability of the arrangement in the solid-state.

3.4.5 Conclusion and Outlook

The tool FIMs was applied to the cationic $[Ag_8L^{Me}_2]^{4+}$ and proved to be suitable for organic molecules or the organic parts of an organometallic system. However, limitations were detected in this case for the use towards identifying interaction sites for metal coordination and interaction regions inside a cavity, which were not displayed probably due to the relatively close distances to other atoms. Nevertheless, FIMs analysis can be applied as a tool to predict hydrogen bonding interactions of the pillarplex rim.

The pseudorotaxane $[Ag_8L^{Me}_2](DA)(BDC)_x$ was successfully synthesised containing all four potential interaction regions: (I) Cavity, (II) Aromatic ligands, (III) Metal ions and (IV) Rim. Suitable crystals were collected and subjected to SC-XRD measurements, in particular to

analyse the crystal structure towards occurring (non-)covalent interaction. Indeed, all anticipated interactions were identified in the classified regions with the main contribution of hydrogen bonding between the organic rim and anions as well as solvent molecules.

By CrystalExplorer, the isosurfaces of guest molecule dodecyl diammonium and the pillarplex cation $[Ag_8L^{Me}_2]^{4+}$ were visualised. Besides the apparent hydrogen bond interactions, π-stacking and metal coordination were determined. Additionally, the Hirshfeld surface of dodecyl diammonium revealed interactions inside the pillarplex cavity. Thus, the Hirshfeld surface analysis proved to be a powerful tool for the investigation of organometallic supramolecules. Additionally, the fingerprint plots provided the possibility to quantify occurring interactions, whereas in this case mainly hydrogen bonding with 100% for the guest interactions and 65% for the cation interactions were attributed. A minor contribution of 7.7% of the overall interactions determined by the isosurface of $[Ag_8L^{Me}_2]^{4+}$ were assigned to metal coordination.

3.5 Rim-Functionalisation of Pillarplex

This chapter is partially based on the master thesis of Julian Zuber, which was supervised by this author.

3.5.1 Introduction

Functional groups that can act as linking units are required to incorporate the pillarplex cation into extended structures. Therefore, functionalisation is a necessity, which can be achieved by various approaches, such as functionalising the rim. This has already been investigated by our group by exchanging the pyrazole unit for a triazole unit, which, due to the added lone pair of electrons, led to a potential *N*-donor group (Figure 48A).[32] As previously mentioned (Chapter 1.3), the triazole-based pillarplex displayed a shape-adaptivity dependent on the counter anion. Non-classical hydrogen bonds[36] were observed between the fluorine atoms of the PF_6^- anion and the hydrogen atoms of the imidazolylidene units. This led to a bending of the methylene bridge between the two imidazolylidene units thus providing a shape-adaptive rim flexibility. However, the functionalisation is located directly at the rim rendering the steric accessibility of the additional lone pair of electrons challenging.

Therefore, either the introduction of a good leaving group for further functionalisation or the direct introduction of functionality at the rim by C-C bond formation would allow the pillarplexes to be used as building blocks for network materials (Figure 48B). In order to ensure unhindered pillarplex formation, late-stage modification of the rim was targeted. By performing the late-stage modification directly on the pillarplex, there is no need to adapt the synthesis procedures. However, if a functional group is introduced at an earlier stage of the ligand synthesis, changes in solubility of intermediates or side reactions may occur or the route, described in literature, may no longer be applicable resulting in significant amount of work to adjust the overall synthesis. The strategy would therefore be to systematically investigate the functionalisation starting directly at the pillarplex and working backwards step by step along the synthesis route. Three regions can be identified in the study of the possibilities for the introduction of functionalities (Figure 48): Pyrazole unit (marked in blue), imidazolylidene unit (marked in green) and methylene bridges (marked in orange).

The pyrazole unit was selected as the target for the rim-functionalisation since the acidic hydrogen atom can easily be substituted. In theory, the other regions – imidazolylidene hydrogen atoms or methylene hydrogen atoms – could also be viable options for introducing a functionality. Preliminary results have demonstrated, that the introduction of substituents on the backbone of the imidazolylidene unit can lead to the assembly of novel organometallic complexes.[121] As the methylene bridges are bent towards the outside of the pillarplex cation and carry two hydrogen atoms, the selective introduction of functional groups at these positions is rather challenging. In addition, there are already preliminary findings regarding the bromination of the pyrazole unit, which has prompted further investigation into the introduction of a bromine group at this position. Furthermore, the introduction of potential linker motifs will be examined by Suzuki-Miyaura cross-coupling reactions to substitute the bromine atom with different substrates and under varying reaction conditions.

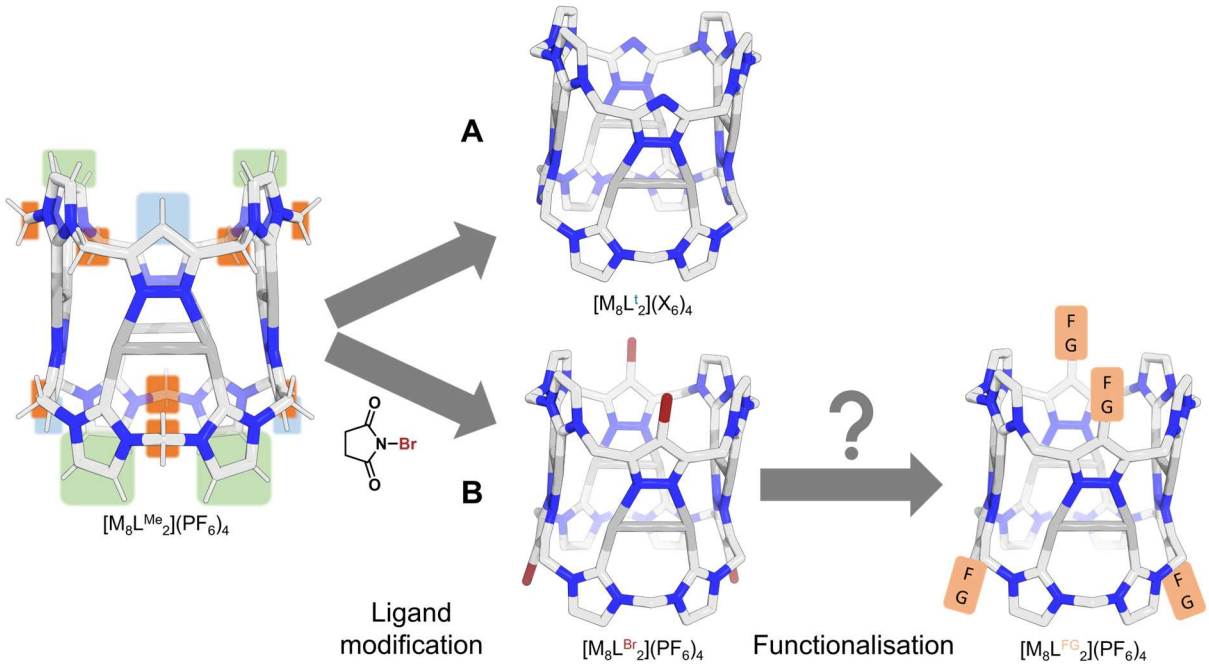

Figure 48: Overview of the proposed rim-functionalisation reactions of $[M_8L^{Me}_2](PF_6)_4$ with the two marked regions (imidazolylidene units marked with green and pyrazole units marked with blue), where introduction of a functionality could be achieved. (A) Literature-known exchange of the pyrazole unit with a triazole unit; (B) Bromination of the pyrazole unit with suggested further conversion to large functional groups (FG, displayed in orange).

3.5.2 Synthesis and Characterisation of $L^{Br}(PF_6)_4$ and $[M_8L^{Br}_2](PF_6)_4$

The late-stage modification to substitute the pyrazole hydrogen atom with a bromine atom was examined starting with $[M_8L^{Me}_2](PF_6)_4$ (Figure 49B). However, stirring the reaction mixture at room temperature for several hours led to no conversion and simply the proton signal set of $[M_8L^{Me}_2](PF_6)_4$ in ^{1}H NMR spectroscopy was obtained. To activate the *N*-bromo succinimide (NBS), the reaction was exposed either to heat or UV radiation or both. For all reactions, $[Ag_8L^{Me}_2](PF_6)_4$ as well as $[Au_8L^{Me}_2](PF_6)_4$, a direct colour change from a clear whitish solution to a dark brown or a dark purple was observed accompanied by the formation of a suspension due to formed precipitate. The colour change and precipitate indicated the decomposition of the pillarplex salts, nevertheless, the solvent of the reaction mixture was reduced *in vacuo* and the obtained precipitate was washed with water to remove excess of *N*-hydroxy succinimide (NHS). ^{1}H NMR spectroscopy supported the decomposition of the pillarplexes as only proton signals of the macrocyclic ligand were obtained.

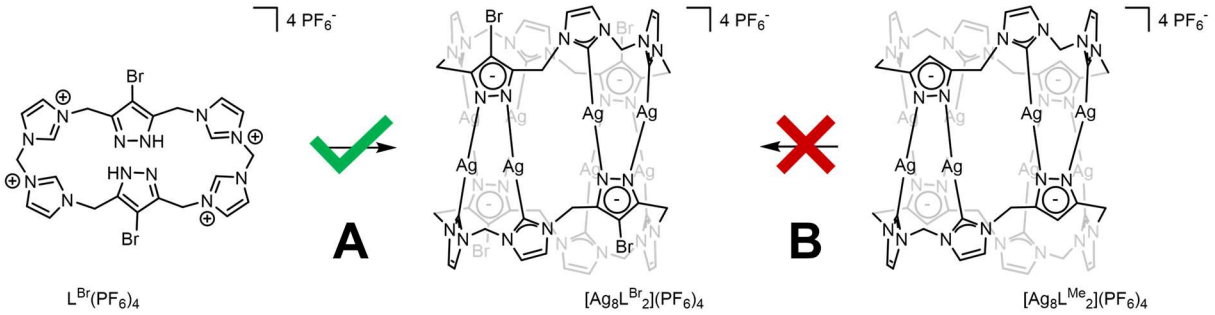

Figure 49: Attempted synthesis routes to achieve the brominated pillarplex $[Ag_8L^{Br}_2](PF_6)_4$: (A) Starting with the brominated macrocyclic ligand $L^{Br}(PF_6)_4$ following the literature-known synthesis route for pillarplex formation; (B) Starting with the direct bromination of $[Ag_8L^{Me}_2](PF_6)_4$ with reagent NBS.

Since the direct bromination of the previously formed pillarplex was not successful, bromination of the macrocyclic ligand $L^{Me}(PF_6)_4$ was examined next. Therefore, the ligand was provided in MeCN and NBS was added (Figure 49A). After stirring the reaction at room temperature for 1 h, the solvent was removed *in vacuo* and the precipitate was washed with H_2O. Drying *in vacuo* yielded a white solid, which was analysed by ^{1}H NMR spectroscopy. The ^{1}H NMR spectrum (Figure 50) revealed a similar signal set as it was observed for the ligand $L^{Me}(PF_6)_4$. However, the signal of the hydrogen atom at the pyrazole unit (6.48 ppm, marked with a green box) was missing indicating the successful deprotonation with following bromination of these positions. Interestingly, a signal for the hydrogen atoms at the pyrazole moiety was detected (11.85 ppm, marked with a dark blue circle), which was not observable in the ^{1}H NMR spectrum of $L^{Me}(PF_6)_4$. Such acidic hydrogen atoms can be rapidly exchanged with the protons of the deuterated solvent and thus often no signal is detected. Since for $L^{Br}(PF_6)_4$ a signal for the H_{NH} is noted, the introduction of the bromine atom may have changed the acidity to subsequently hinder the proton exchange.

The desired brominated ligand was then fully characterised starting with ^{13}C, ^{19}F, ^{31}P and 2D NMR spectroscopy (F45S). The ^{13}C NMR spectra revealed the seven signals, which are slightly shift compared to the once identified for $L^{Me}(PF_6)_4$. To ensure, that no additional anion exchange had occurred, the ^{19}F and ^{31}P NMR spectra were evaluated for the presence of the counter anion and indeed the anticipated signals were detected (^{19}F NMR spectrum: -71.77, -78.65 ppm, ^{31}P NMR spectrum: -144.79 ppm). Additionally, the elemental analysis and ESI mass spectrometry (m / Z = 466.0009 for $L^{Br}(PF_6)_2^{2+}$; 1076.9653 for $L^{Br}(PF_6)_3^{+}$) confirmed the successful bromination. IR spectroscopic measurements (F48S) were performed to verify the presence of the desired C-Br band and indeed an additional band 610 cm^{-1} was observed, which can be assigned to the stretching vibration of the C-Br bond.[122]

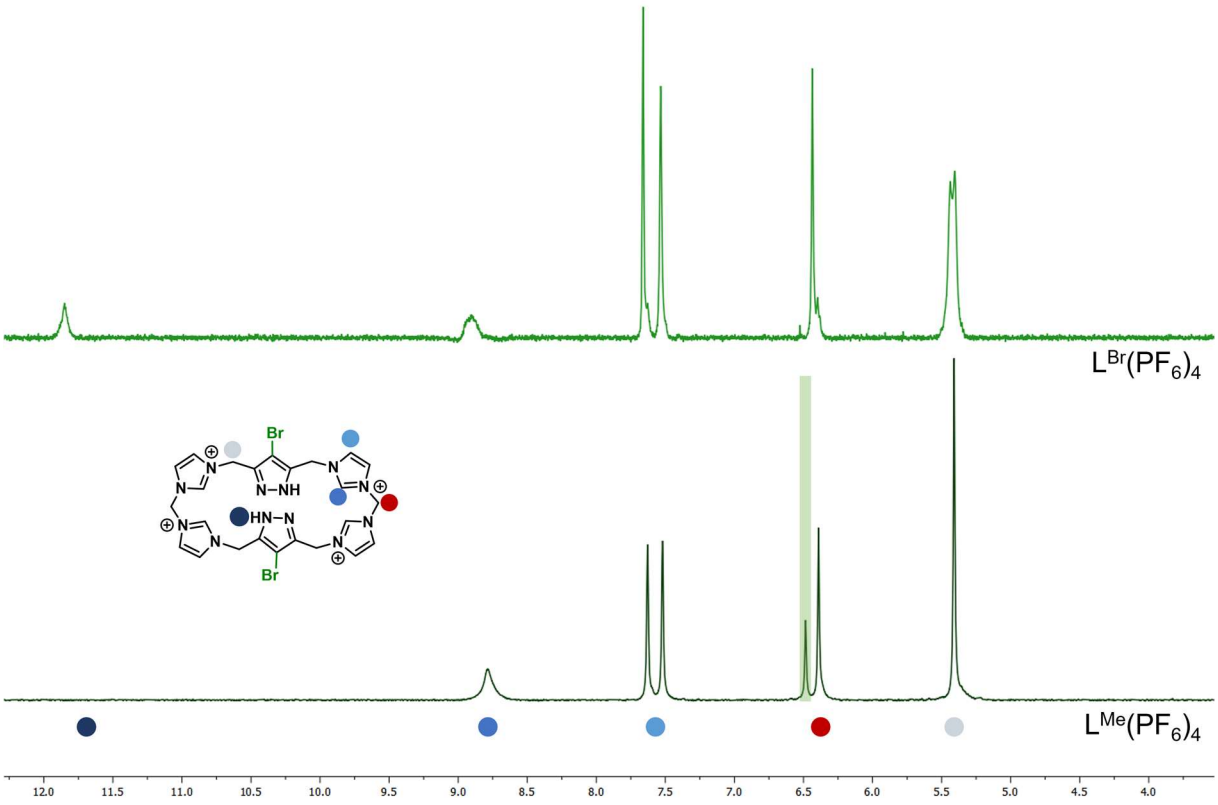

Figure 50: Comparison of the ^{1}H NMR spectra of $L^{Br}(PF_6)_4$ and $L^{Me}(PF_6)_4$ measured in MeCN-d_3 (1.94 ppm) at 298 K. The hydrogen atoms of the ligand were assigned to the signals and respectively marked with coloured circles. The signal at 6.48 ppm of $L^{Me}(PF_6)_4$ was assigned to the pyrazole hydrogen atom and was marked with a green box.

The brominated ligand $L^{Br}(PF_6)_4$ was further examined towards the formation of the respective $[Ag_8L^{Br}_2](PF_6)_4$ pillarplex. Following the literature-known synthesis[29], Ag_2O as Ag(I) ion source and the brominated ligand were provided in MeCN and stirred at room temperature overnight. After purification by filtration, a white solid was obtained which was dried *in vacuo* and analysed by ^{1}H NMR spectroscopy (Figure 51). A signal set similar to that recorded for $[Ag_8L^{Me}_2](PF_6)_4$ verified the successful formation of the brominated Ag(I)-pillarplex. Obviously, the signal at the pyrazole position (6.68 ppm, marked with a green box) was missing. Additionally, a shift of the duplet signals of the hydrogen atoms of the imidazolylidene unit was detected from 7.54 ppm for $[Ag_8L^{Me}_2](PF_6)_4$ to 7.62 ppm for $[Ag_8L^{Br}_2](PF_6)_4$ exhibiting a significant lower coupling constant of ^2J = 2.0 Hz. Through the introduction of the electron withdrawing bromine atom at the pyrazole unit, the chemical surrounding of these imidazolylidene units were adapted, which led to the observed downfield shift. Additionally, the imidazolylidene hydrogen atoms appear to be more chemical similar as they exhibit an almost identical shift in the ^{1}H NMR spectrum with a low coupling constant. The slightly shifted signals of the solvent Et_2O (literature values: 1.11, 3.41 ppm[123]) indicate the presence of partial encapsulated diethyl ether in the cavity. The obtained compound was further characterised with ^{13}C, ^{19}F, ^{31}P and 2D NMR spectroscopy (F46S), which strengthened the successful formation of the desired $[Ag_8L^{Br}_2](PF_6)_4$ pillarplex by exhibiting the two signals at -71.75 ppm and -73.63 ppm in the ^{19}F NMR spectrum as well as the signal at -144.59 ppm in the ^{31}P NMR spectrum. ESI mass spectrometry (m / Z = 533.8227 for $[Ag_8L^{Br}_2]^{4+}$; 760.0837 for $[Ag_8L^{Br}_2](PF_6)^{3+}$; 1212.6084 for $[Ag_8L^{Br}_2](PF_6)_2^{2+}$) and elemental analyses confirmed the chemical composition. The IR spectrum was analysed

and indeed the additional band for the C-Br stretching vibration was detected at approximately 800 cm^{-1}, while the C-H band at 780 cm^{-1} was missing (F49S).

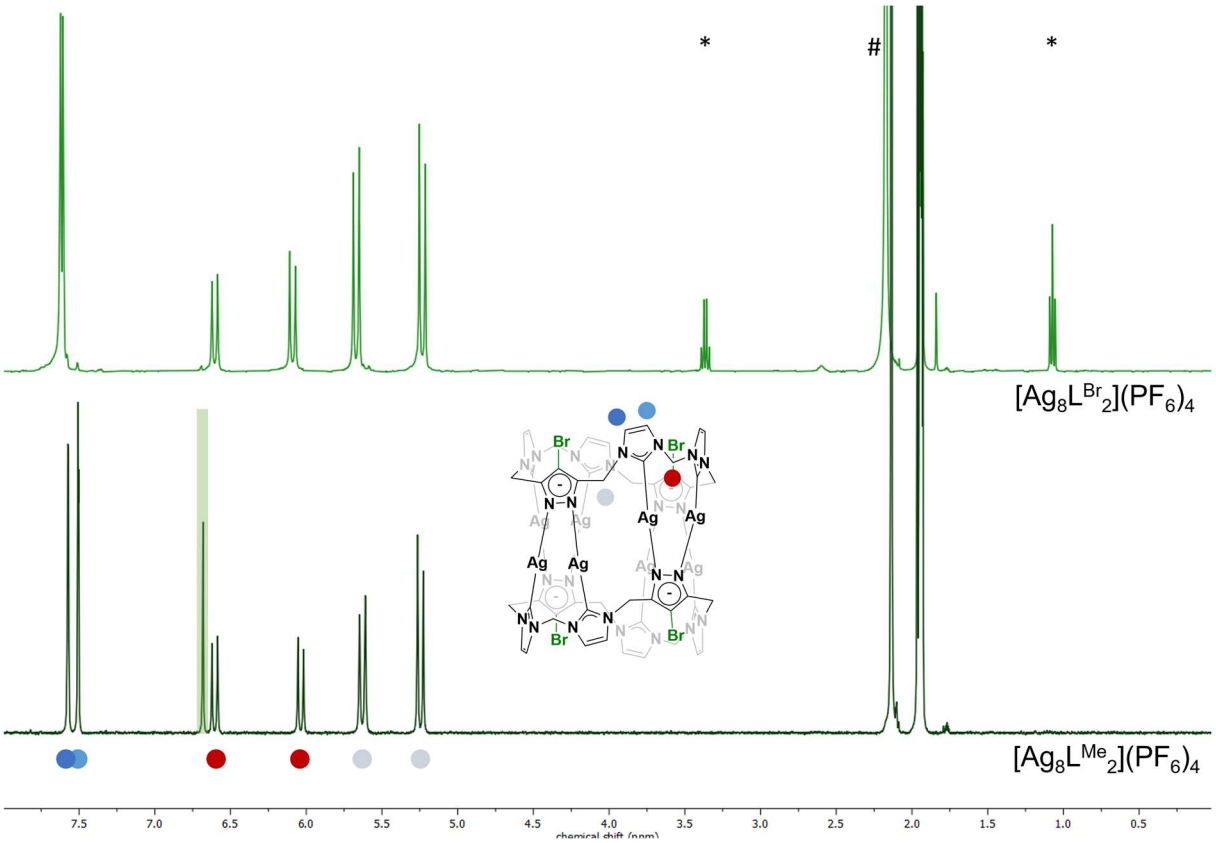

*Figure 51: ^{1}H NMR spectra of $[Ag_8L^{Br}_2](PF_6)_4$ and $[Ag_8L^{Me}_2](PF_6)_4$ in MeCN-d_3 (1.94 ppm) at 298 K. Solvent impurities were marked with # for water (2.13 ppm) and * for Et_2O (1.07 and 3.37 ppm). The hydrogen atoms of the pillarplex were assigned to the signals and respectively marked with coloured circles. The signal at 6.68 ppm of $[Ag_8L^{Me}_2](PF_6)_4$ was assigned to the pyrazole hydrogen atom and was marked with a green box.*

By slow diffusion of Et_2O into a saturated solution of $[Ag_8L^{Br}_2](PF_6)_4$ in MeCN, suitable crystals for SC-XRD measurement were obtained. The colourless fragments of $[Ag_8L^{Br}_2](PF_6)_4$ were solved and refined in the orthorhombic space group *P n m a* (No. 62) with the asymmetric unit containing 1/2 $[Ag_8L^{Br}_2]^{4+}$ cation and two 1/2 PF_6^- anions (with a total occupation corresponding to two PF_6^-). No co-crystallised solvent molecules could be assigned, however residual electron density was removed by the SQUEEZE[89] procedure inside the cavity indicating that there might be a solvent molecule – most probably Et_2O – partially encapsulated. This is in accordance with the amount of residual solvent, which was already observed in the ^{1}H NMR spectrum (Figure 51, Et_2O marked with *). The molecular structure of $[Ag_8L^{Br}_2](PF_6)_4$ is analysed for occurring non-covalent interactions, and mainly non-classical hydrogen bonds[36] between the organic rim and the counter anions are assumed (Figure 52A). Indeed, interactions between F_{PF6} with the H_{rim} atoms are associated to non-classical hydrogen bonding[36]. The evaluation of one $[Ag_8L^{Br}_2]^{4+}$ cation and the position of the respective PF_6^- anions reveals that these counter anions are located close to the organic rim of the cation. Besides the hydrogen bond, the fluorine atoms of the anions coordinate to Ag(I) ions with small distances of 2.982 Å. The crystal packing along the b-axis exhibits a chain alignment of $[Ag_8L^{Br}_2]^{4+}$ cations (Figure 52C), which are always 180° tilted towards the neighbouring cation. Additionally, the cations are shifted towards the middle of the next one, which is explained by Ag(I)-Br coordination with distances of 3.613 to 4.131 Å. In the direction of the crystallographic c-axis a pore alignment of $[Ag_8L^{Br}_2]^{4+}$ is discovered (Figure 52B), where the counter anions are

in all cases located on the outside of the organic rim and hence an accessible pore opening is assumed.

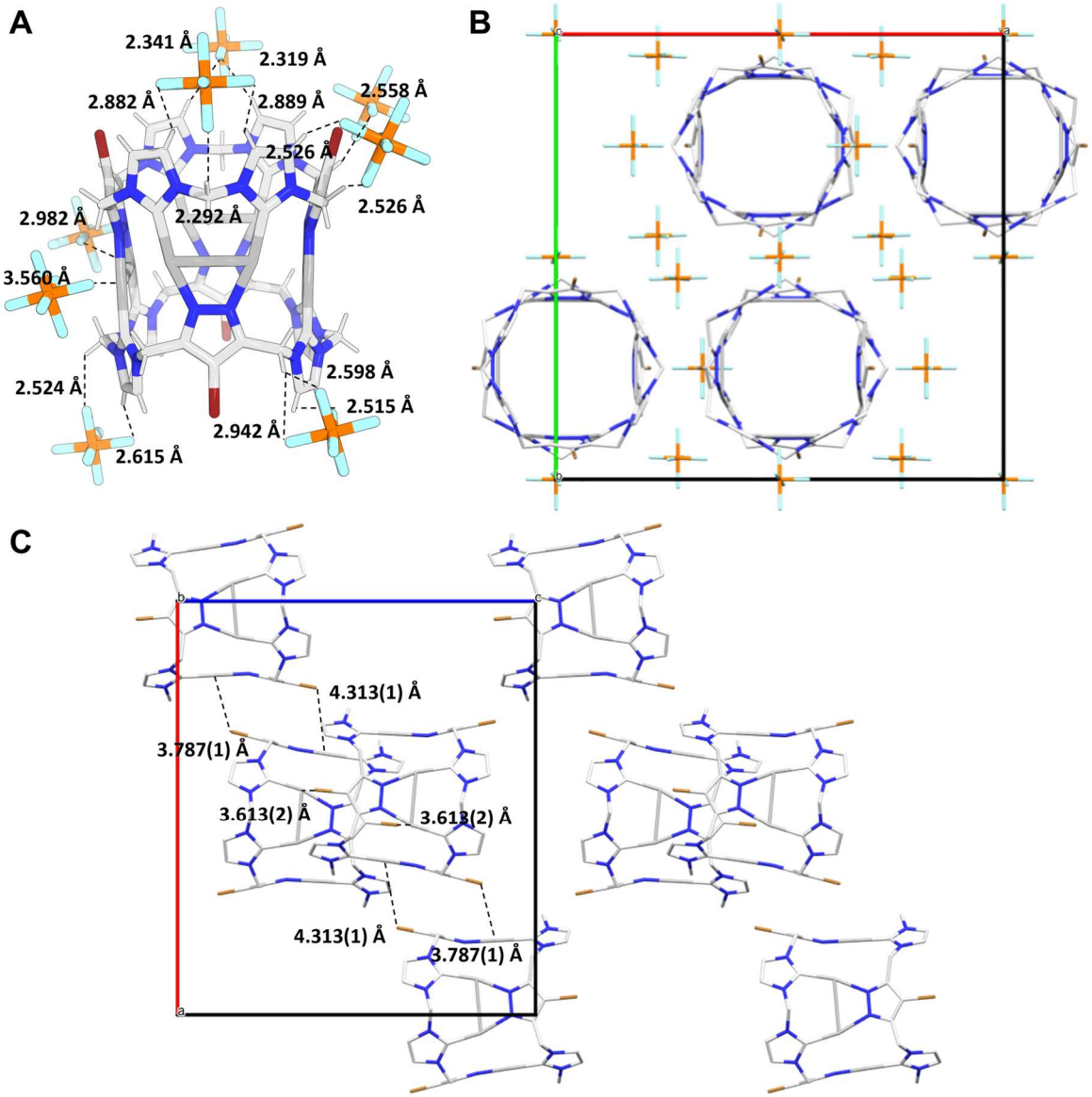

Figure 52: Representation of the solid-state structure of $[Ag_8L^{Br}{}_2](PF_6)_4$: (A) Non-covalent interactions of $[Ag_8L^{Me}{}_2]^{4+}$ cation with counter anions, non-classical hydrogen bonding[36] of H_{rim} with the fluorine atoms of the PF_6^- anion; (B) Crystal packing along the c-axis exhibiting a pore alignment of $[Ag_8L^{Br}{}_2]^4$; (C) Crystal packing along the b-axis exhibiting a chain alignment of $[Ag_8L^{Br}{}_2]^{4+}$ with Ag(I)-Br coordination.

To achieve the brominated Au(I) congener, a transmetalation reaction of $[Ag_8L^{Br}{}_2](PF_6)_4$ with Au(THT)Cl was performed. In this case, the complete exclusion of light sources was crucial for the successful synthesis, as otherwise a dark purple solution was obtained, which can be caused by the formation of Au-nanoparticles. The purification led to a white powder, which was analysed with ^{1}H NMR spectroscopy to confirm the presence of the typical signal set of the pillarplex rim (Figure 53). Again, the pillarplex signal set showed profound shifts, particularly the signal of the methylene bridge between the imidazolylidene units and the signal of the imidazolylidene hydrogen atoms. Both signals exhibit a downfield shift, which is resulted by the introduction of the electron withdrawing bromine atom. Interestingly, the duplet of the

imidazolylidene unit merged to one singlet signal indicating that these hydrogen atoms are chemical similar. The successful formation of $[Au_8L^{Br}_2](PF_6)_4$ was complimented by ^{13}C, ^{19}F and ^{31}P NMR spectroscopy (F47S). Mass spectrometry (m / Z = 711.9454 for $[Au_8L^{Br}_2]^{4+}$; 997.5817 for $[Au_8L^{Br}_2](PF_6)^{3+}$; 1568.8562 for $[Au_8L^{Br}_2](PF_6)_2^{2+}$) and elemental analysis confirmed the successful synthesis. Comparison of the IR spectrum of the brominated Au(I)-pillarplex with the spectrum of $[Au_8L^{Me}_2](PF_6)_4$ revealed the additional band for the C-Br stretching vibration at 790 cm^{-1}, while the band of the C-H stretching vibration at 780 cm^{-1} is not detectable (F50S).

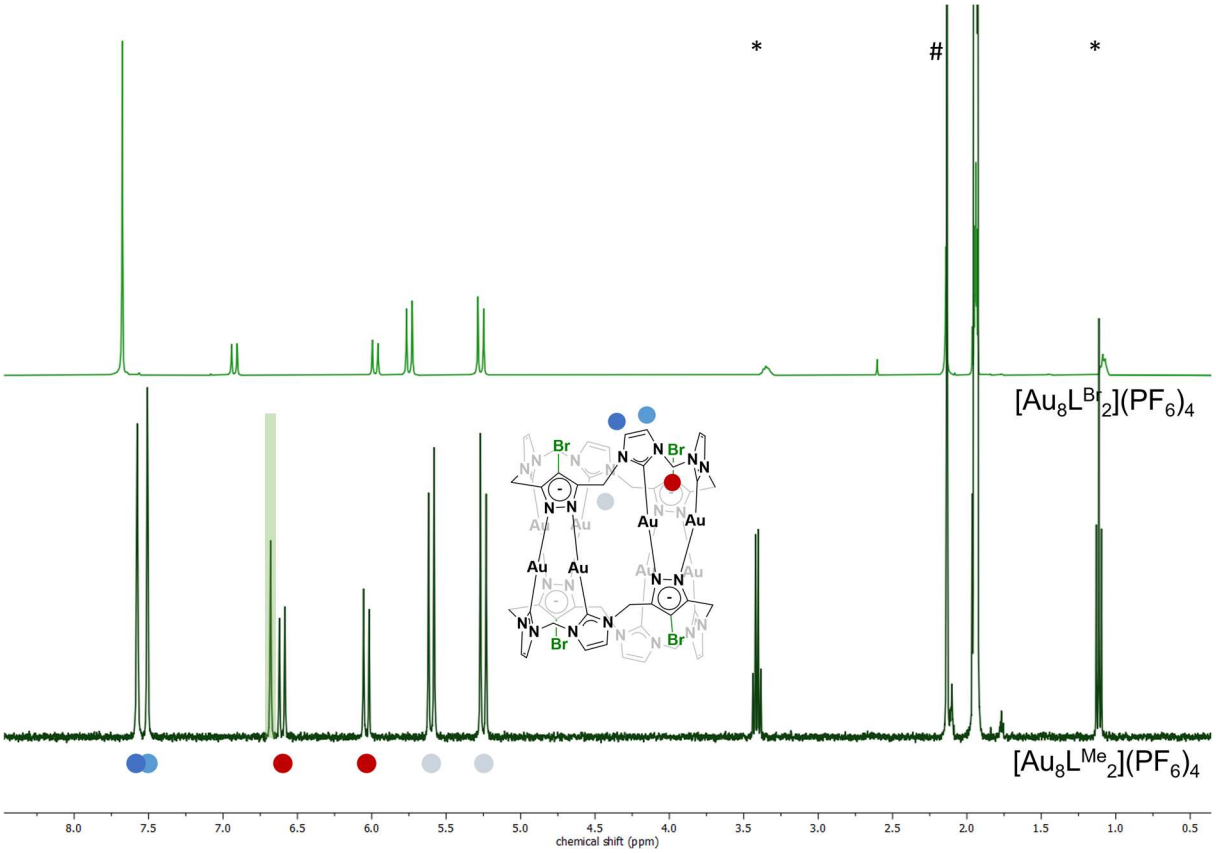

*Figure 53: ^1H NMR spectra of $[Au_8L^{Br}_2](PF_6)_4$ and $[Au_8L^{Me}_2](PF_6)_4$ in MeCN-d_3 (1.94 ppm) at 298 K. Solvent impurities were marked with # for water (2.13 ppm) and * for Et_2O (1.11 and 3.41 ppm). The hydrogen atoms of the pillarplex were assigned to the signals and respectively marked with coloured circles. The signal at 6.68 ppm of $[Au_8L^{Me}_2](PF_6)_4$ was assigned to the pyrazole hydrogen atom and was marked with a green box.*

Exposing colourless crystals to single crystal X-Ray diffraction yielded the molecular structure of $[Au_8L^{Br}_2](PF_6)_4$, which was solved and refined in the tetragonal space group $P\,4_1\,2_1\,2$ (No. 92). The asymmetric unit contains 1/2 $[Au_8L^{Me}_2]^{4+}$ cation, two PF_6^- anions and one acetonitrile molecule. Analysing the crystal structure of $[Au_8L^{Br}_2](PF_6)_4$ in terms of non-covalent interactions (Figure 54A), similar interactions as discovered for $[Ag_8L^{Br}_2](PF_6)_4$ with mainly non-classical hydrogen bonding[36] are predicted. And indeed, non-classical hydrogen bonds[36] between F_{PF6} and H_{rim} are reported. Due to the presence of one MeCN molecule per asymmetric unit, additional hydrogen bonds between N_{MeCN} of the co-crystallised solvent molecule and H_{rim} are observed. Interestingly, non-classical hydrogen bonding[36] of the H_{rim} atoms with the bromine atom of a neighbouring pillarplex cation is detected with distances of 2.976 and 3.111 Å. Investigating the arrangement of $[Au_8L^{Br}_2]^{4+}$ (Figure 54C), results in a chain alignment with Au(I)-Au(I) distances of 7.112 to 7.127 Å along the a-axis, where all cations exhibit the same spatial orientation. With the H_{rim} to bromine interactions mentioned above, a

zigzag arrangement of two layers of pillarplex cations is encountered, where each cation of one layer is tilted by 78.83° with respect to the cation of the next layer. Along the crystallographic c-axis (Figure 54B), an interpenetrated pore alignment of $[Au_8L^{Br}{}_2]^{4+}$ is observed. Combined with the crystal packing of $[Au_8L^{Br}{}_2]^{4+}$ cations along the b-axis, it can be concluded that in every fourth layer the cations have a similar orientation and are therefore pore-aligned. Similar to $[Ag_8L^{Br}{}_2](PF_6)_4$, the counter anions are located around the rim of the pillarplex cation. However, for the tilted $[Au_8L^{Br}{}_2]^{4+}$ cations by 78.83°, the positions of the counter anions are assigned directly above the pore opening of the cation in the next layer. Thus, the pore openings of the pillarplex cation are partially blocked in the solid-state arrangement.

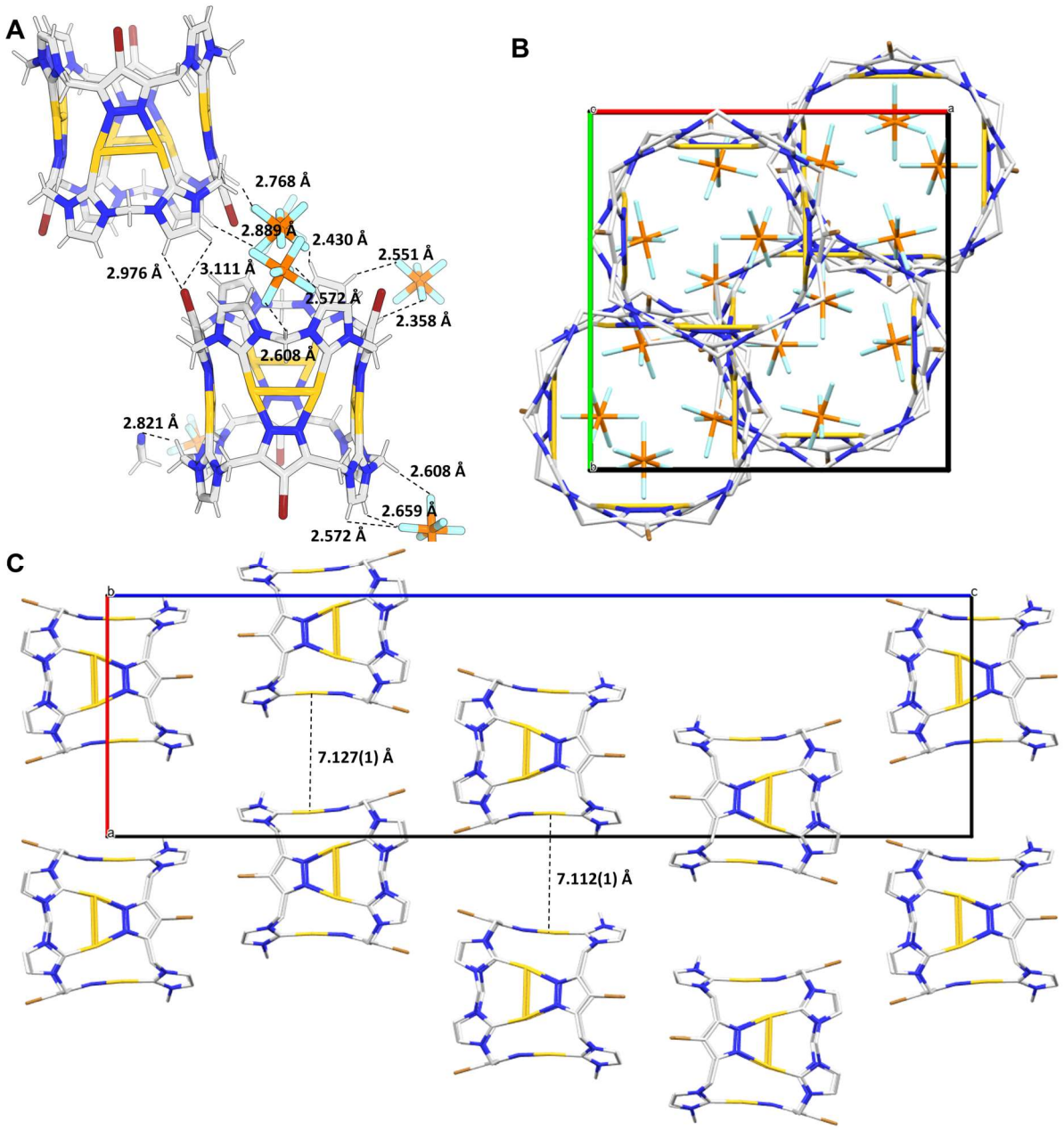

Figure 54: Representation of the solid-state structure of $[Au_8L^{Br}{}_2](PF_6)_4$: (A) Non-covalent interactions of $[Au_8L^{Me}{}_2]^{4+}$ cation with counter anions, non-classical hydrogen bonding[36] of H_{rim} with the fluorine atoms of the PF_6^- anion and H_{rim} with the bromine atom of the neighbouring cation; (B) Crystal packing along the c-axis exhibiting interpenetrated

pores; (C) Crystal packing along b-axis exhibiting chain alignment with Au(I)-Au(I) distances of 7.112(1) Å and 7.127(1) Å.

3.5.3 Functionalisation Attempts with $L^{Br}(PF_6)_4$

After successful bromide functionalisation, further cross coupling reactions were evaluated to introduce units, which can act as connecting linker motifs for the formation of extended structures. The Suzuki-Miyaura cross coupling reaction was targeted since it showed sufficient reactivity to substitute the desired position at the pyrazole unit.[124-126] Following literature-known synthetic routes, a Pd(II) catalyst in combination with phosphine ligand (e.g., SPhos, Xphos) and a weak base (e.g., Cs_2CO_3) were utilised, to facilitate the coupling with the boronic acid bearing a desired functionality (Figure 55). The addition of bulky phosphine ligands leads to enhanced activation of the Pd(II) catalyst.[127-128] Additionally, the addition of a base can promote the coordination of the Pd(II) catalyst and the substrate as well as accelerate the reductive elimination of the Suzuki-Miyaura coupling.[129] The big advantage of the applied synthesis route is the air-stability of all compounds.

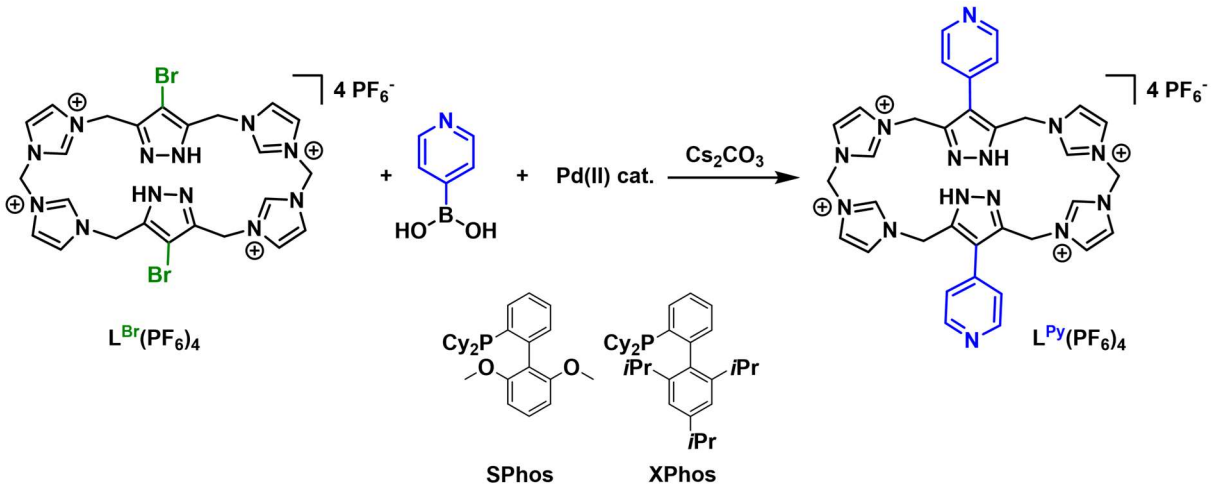

Figure 55: Reaction scheme for the functionalisation attempts of $L^{Br}(PF_6)_4$ by a Suzuki-Miyaura cross coupling reaction with the substrate 4-pyridylboronic acid. The Pd(II) catalyst was in situ formed by combination of $Pd(OAc)_2$ and bulky phosphine ligands (SPhos, Xphos).

The functionalisation attempts (for details Chapter 5.8.2) were started with $L^{Br}(PF_6)_4$ and as reactant the 4-pyridylboronic acid was chosen. $L^{Br}(PF_6)_4$ 4-pyridylboronic acid and base Cs_2CO_3 were provided in a vial and non-dried solvent was added. Before adding the catalyst to the reaction mixture, the "activated" Pd(II) catalyst was synthesised by providing $Pd(OAc)_2$ (10 mol%) with either SPhos or XPhos (20 mol%) in a minimum of water and stirring the mixture at room temperature for 5 min. The combined reaction mixture was either heated under stirring or subjected to a microwave at specific temperatures. During the microwave reaction, all volatiles were evaporated, leaving a black solid. Nevertheless, a ^{1}H NMR spectrum was measured, where no signals were obtained besides the residual solvent signal of DMSO-d_6. The other batches were kept at a specific temperature for 24 h and filtered. The filtrate was concentrated to dryness and both solids were subjected to ^{1}H NMR spectroscopy. In the ^{1}H NMR spectra, no evidence could be collected for the formation of the desired product, although in the complex mixture of signals, the assignment of the ligand was partially possible.

3.5.4 Summary and Outlook

The approach of a late-stage introduction of a bromide group at the pyrazole unit of the macrocyclic ligand $L^{Me}(PF_6)_4$ was achieved and further conversion to the Ag(I)- and Au(I)-pillarplex was enabled. The brominated compounds $L^{Br}(PF_6)_4$, $[Ag_8L^{Br}_2](PF_6)_4$ and $[Au_8L^{Br}_2](PF_6)_4$ were synthesised, purified and characterised by common analytical methods. No suitable single crystals for $L^{Br}(PF_6)_4$ were obtained, however the structural evaluation of this compound would be particularly interesting as the sterically demanding bromide group might influence the conformation of the macrocyclic ligand. For instance, $L^{Me}(PF_6)_4$ crystallises in a bowl-shape with one acetonitrile coordinated to the four imidazolium protons.[130] For $[Ag_8L^{Br}_2](PF_6)_4$ and $[Au_8L^{Br}_2](PF_6)_4$ suitable crystals were collected and measured *via* SC-XRD measurements. Both structures exhibited pore and chain alignment of the pillarplex cations. While for $[Ag_8L^{Br}_2](PF_6)_4$ an Ag(I)-Br coordination with distances of 3.613 – 4.313 Å were observed, for $[Au_8L^{Br}_2](PF_6)_4$ mainly hydrogen bonds between the bromine atom and H_{rim} with distances of 2.976 – 3.111 Å were discovered. The introduction of a bromine atom with an increased steric demand and a lone pair of electrons into the pillarplex system adds an intriguing aspect to the study of guest encapsulation especially regarding the alky chains known from literature (e.g., α,ω-diamino alkanes, α,ω-dicarboxylic acids).[29,31-32,85,97]

The brominated ligand was examined towards a further functionalisation of the pyrazole moiety *via* Suzuki-Miyaura cross coupling reactions with 4-pyridylboronic acid as reactant. However, no attempts were successful necessitating further investigations into the functionalisation of the brominated ligand.

One obstacle, which could occur in further modifying the brominated ligand is the formation of a dinuclear complex with $L^{Me}(PF_6)_4$, where the analogues for Ni(II), Pt(II) and Pd(II) were already investigated.[131-132] For the literature-known synthesis of these complexes and the Suzuki-Miyaura reaction, comparable reaction conditions were applied, involving the exposure of the macrocyclic ligand to a metal(II) source under basic conditions. Therefore, further functionalisation attempts have to be conducted directly with the brominated pillarplex salts to hinder the previously mentioned side reaction. The Ag(I)-pillarplexes are prone towards transmetalation[132], thus the most promising approaches for the introduction of further substituents would be the direct functionalisation of $[Au_8L^{Br}_2](PF_6)_4$. Additionally, the use of Pd(II) precursors requires the presence of counter anions, which in the applied synthetic route was acetate. With the charged nature of the ligand and the pillarplex salt, anion exchange reactions might occur as side reactions. By selecting viable starting compounds, this side reaction should be eliminated, choosing similar counter anions for $[L^{Br}]^{4+}$ or $[M_8L^{Br}_2]^{4+}$ and the palladium catalyst.

3.6 Pillarplex Pseudorotaxanes with α,ω-Dicarboxylic Acids

This chapter is based on the publication: "Silver and Gold Pillarplex Pseudorotaxanes with α,ω-Dicarboxylic Acids" Alexandra A. Heidecker, Michele Stasi, Alexander Spears, Job Boekhoven and Alexander Pöthig*; *ChemPlusChem*, **2023**, e202300234. https://doi.org/10.1002/cplu.202300234.

3.6.1 Introduction

Introducing a functionality to the pillarplex system can also be achieved by an encapsulation of a guest molecule bearing one or more functional groups. The steric demand of the functional groups must be considered, as shape-selective encapsulation of linear over aromatic, branched guests[29,31-32,97] into the pillarplex cavity was identified. However, starting with functionalised groups bearing a relatively small steric demand, led to the idea of encapsulating a guest carrying dicarboxylic acid groups on both ends of the linear alkyl chain (Figure 56). The central alkyl chain matches with the hydrophobic cavity and in addition, these functional groups could lead to a subsequential build-up towards further coordination polymers.

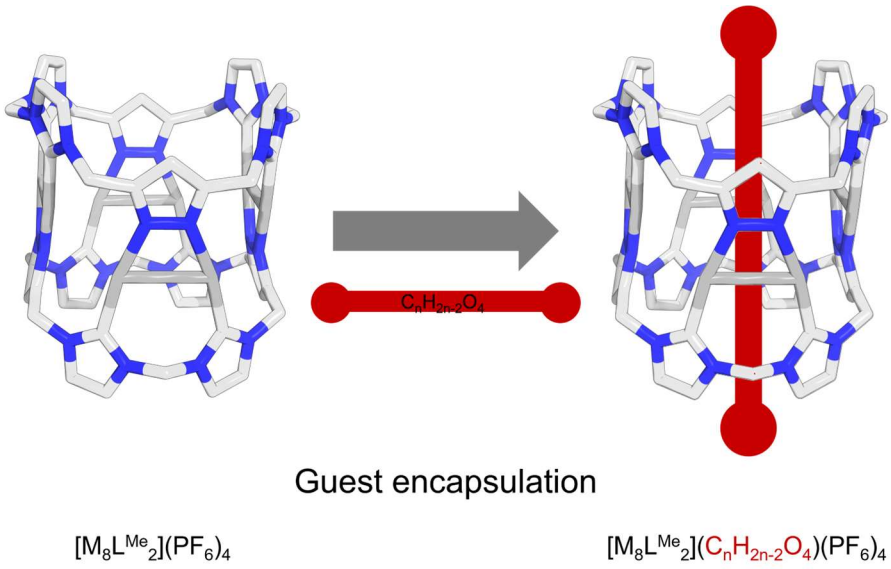

Figure 56: Overview of the guest encapsulation of α,ω-dicarboxylic acids into cationic $[M_8L^{Me}_2]^{4+}$ as ring component to yield pseudorotaxanes $[M_8L^{Me}_2](C_nH_{2n-2}O_4)(PF_6)_4$.

Based on crystallographic data, the diameter of a -COOH group was calculated to be 5.34 Å.[33] In contrast, the pore opening of the pillarplex exhibits a diameter of 4.3 Å. Assuming a static behaviour of the host system, it becomes evident that the carboxylic acid group is sterically already too demanding to enter the cavity. Hence, successful guest encapsulation would require a conformational change of the pillarplex (e.g., ligand dissociation or breathing effects). SOCs typically exhibit static behaviour due to strong organometallic bonds. Nevertheless, a dynamic behaviour was already observed for the $[M_8L^t_2](X)_4$ pillarplex, where the pore opening was pressed form a circular towards an oval shape by non-classical hydrogen bonding[36] of the H_{rim} and fluorine atoms of the counter anions.[32]

3.6.2 Investigation of Pillarplex Pseudorotaxanes

Synthesis

The pseudorotaxanes were synthesised by combining 1.1 eq. of the guest ($C_8H_{14}O_4$, $C_{10}H_{18}O_4$, $C_{12}H_{22}O_4$, $C_{14}H_{26}O_4$) and 1 eq. of $[M_8L^{Me}{}_2](PF_6)_4$ in MeCN, stirring at room temperature for 10 min and removing the solvent *in vacuo*. Beforehand the dicarboxylic acids were tested towards their solubility in organic solvents (DMSO *vs.* MeCN), where limited solubility (*ca.* 1 g L^{-1}) of all acids in MeCN and a significant higher solubility in DMSO (*ca.* 1000 g L^{-1}) was determined. Due to the main driving force for guest encapsulation being the strong hydrophobic cavity the host-guest complexes were formed indicated by the almost immediate solvation of the respective dicarboxylic acid. The chemical composition of the isolated white powders was analysed by NMR spectroscopy (^1H, ^{13}C, ^{31}P and COSY), in the solvents DMSO-d_6 and MeCN-d_3. For all host-guest complexes, one set of pillarplex signals was assigned and additionally, the guest signals were broadened and upfield shifted due to shielding effects of the aromatic ligands (Figure 57).

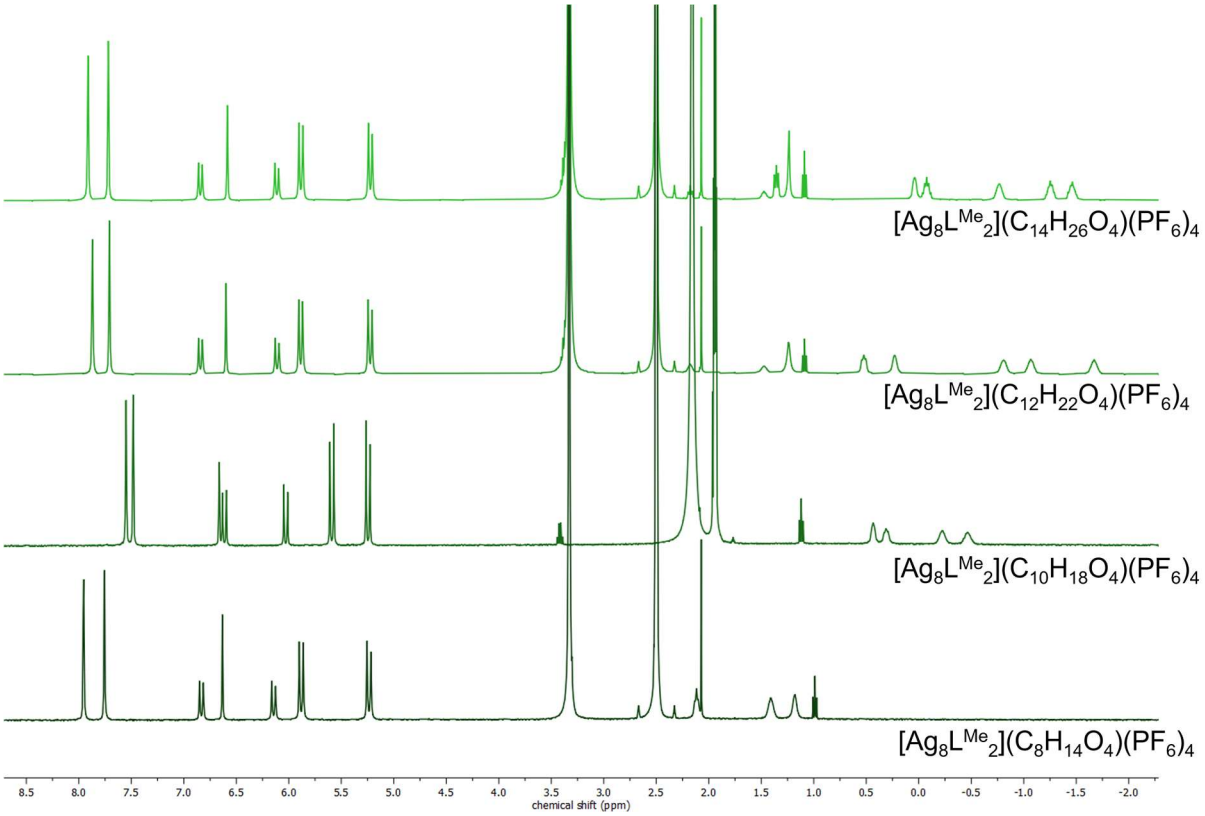

Figure 57: ^1H NMR spectra of $[Ag_8L^{Me}{}_2](C_8H_{14}O_4)(PF_6)_4$ in DMSO-d_6 (2.50 ppm) at 298 K, $[Ag_8L^{Me}{}_2](C_{10}H_{18}O_4)(PF_6)_4$ in MeCN-d_3 (1.94 ppm) at 298 K, $[Ag_8L^{Me}{}_2](C_{12}H_{22}O_4)(PF_6)_4$ in DMSO-d_6 (2.50 ppm) at 298 K and $[Ag_8L^{Me}{}_2](C_{14}H_{26}O_4)(PF_6)_4$ in DMSO-d_6 (2.50 ppm) at 298 K.

While using MeCN-d_3 as solvent, signals of acidic hydrogen atoms were often not detectable. In order to verify the protonation state of the encapsulated acids, the ^1H NMR spectra were measured in DMSO-d_6, where the signals of the acidic hydrogen atoms were assigned (11.34 ppm – 11.92 ppm). The chemical composition of the pseudorotaxanes was additionally determined by elemental analysis and ESI mass spectrometry. As only signals for the pillarplex cations including partial anions ($[M_8L^{Me}{}_2]^{4+}$, $[M_8L^{Me}{}_2](PF_6)^{3+}$) were observed in the mass spectrum, measurements were repeated at low voltage to avoid guest removal. However, no

additional signals were obtained at lower voltage. By contrast, the IR spectra displayed additional bands for the dicarboxylic acids, from which the protonation state could supplementary be verified.

To further investigate the guest binding, 2D NMR spectroscopy was performed. DOSY NMR in MeCN-d_3 and DMSO-d_6 spectra supported the formation of one species and thus, one specific interaction for all pseudorotaxanes was obtained and diffusion coefficients of $8.81 \cdot 10^{-11}$ $m^2\,sec^{-1}$ and $9.14 \cdot 10^{-11}$ $m^2\,sec^{-1}$ for complexes $[Ag_8L^{Me}{}_2](C_8H_{14}O_4)(PF_6)_4$ and $[Au_8L^{Me}{}_2](C_8H_{14}O_4)(PF_6)_4$ in DMSO-d_6 were calculated. The residual DOSY NMR spectra were measured in MeCN-d_3 and diffusion coefficient between $6.20 \cdot 10^{-10}$ $m^2\,sec^{-1}$ and $7.98 \cdot 10^{-10}$ $m^2\,sec^{-1}$ were determined. NOESY NMR spectra were conducted to investigate potential coupling of guest molecules with the organic rim of the pillarplex cation. However, only for complexes $[Ag_8L^{Me}{}_2](C_{12}H_{22}O_4)(PF_6)_4$ and $[Ag_8L^{Me}{}_2](C_{14}H_{26}O_4)(PF_6)_4$ cross coupling signals in DMSO-d_6 were resolved, while cross coupling signals for complexes $[Ag_8L^{Me}{}_2](C_8H_{14}O_4)(PF_6)_4$ and $[Au_8L^{Me}{}_2](C_8H_{14}O_4)(PF_6)_4$ in MeCN-d_3 were detected.

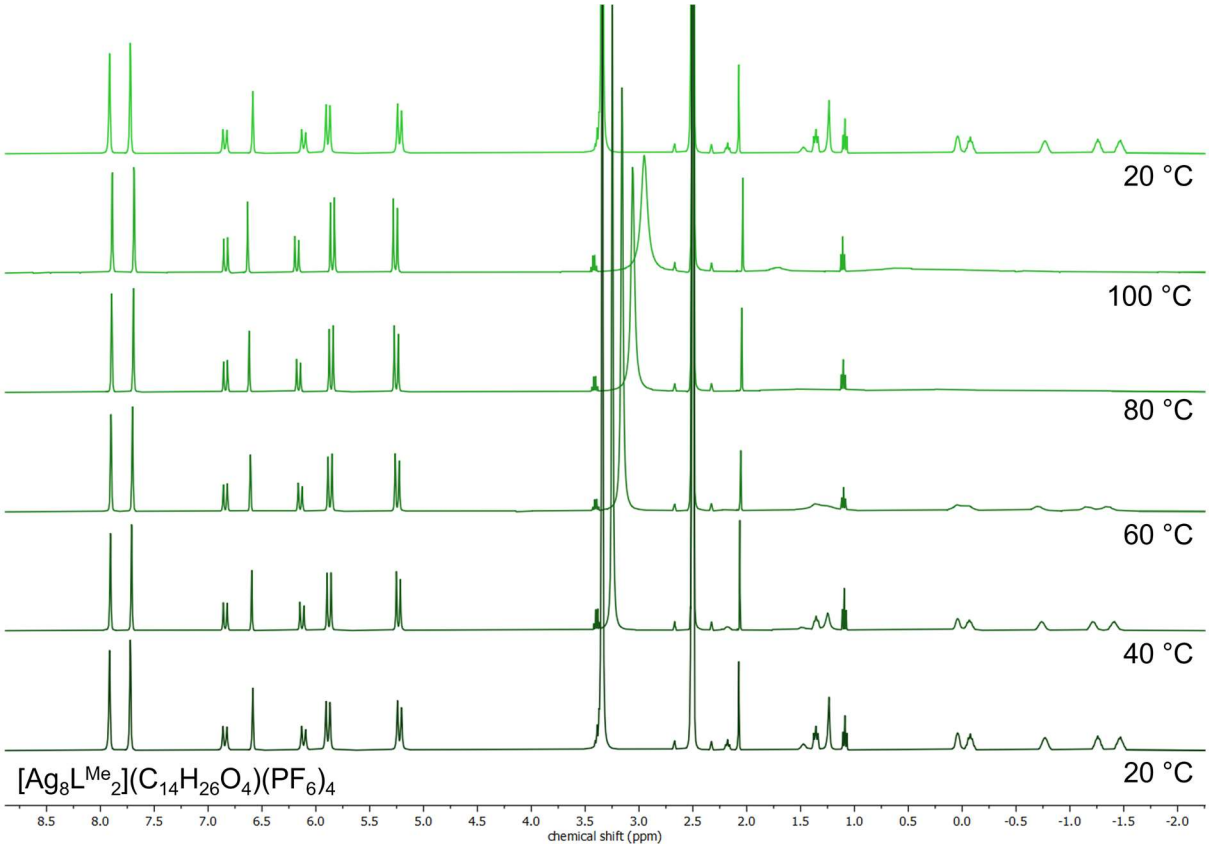

Figure 58: VT NMR spectra of $[Ag_8L^{Me}{}_2](C_{14}H_{26}O_4)(PF_6)_4$ in DMSO-d_6 (2.50 ppm) yielding a dissociation temperature between 60 °C and 80 °C.

The thermal stability and dissociation temperature of the host-guest complexes was assessed by variable temperature NMR experiments, where ^{1}H NMR spectra were recorded with intervals of 20 °C in solvent DMSO-d_6 (see exemplary in Figure 58). Due to the boiling point of the solvent these measurements were only conducted in DMSO-d_6. The guest signals were monitored during the heating process and broadened signals at elevated temperatures indicated the fast exchange of free and bound guest molecules. Hence, the stronger the broadening of the signals, the more guest was located outside of the cavity. Pseudorotaxanes

containing shorter dicarboxylic acids as guest molecules exhibited lower dissociation temperatures between 40 – 60 °C. In contrast, complexes with longer dicarboxylic acids as guests showed higher dissociation temperatures, reaching up to 80 – 100 °C for $[Au_8L^{Me}_2](C_{14}H_{26}O_4)(PF_6)_4$. Overall, the host system itself demonstrated a high thermal stability since no change in the proton signal set of the organic rim was observed.

To determine the absorption properties of all pseudorotaxanes, UV-vis spectroscopy was conducted in solution (MeCN, $c = 1 \cdot 10^{-5}$ mol L^{-1}) and in the solid-state. Absorption maxima were allocated in the range of 240-270 nm for the Ag(I) congeners and 230-340 nm for the Au(I) congeners. Additionally, the pseudorotaxanes containing Au(I) ions were tested towards their emissive and luminescence properties. No emission in solution was detected due to the presence of a guest molecule, which quenched the emission of $[Au_8L^{Me}_2]^{4+}$. This destabilisation of the excited state upon guest encapsulation was already theoretically investigated.[109] However, in solid-sate, hypsochromic shifted absorption maxima with λ_{max} = 315-325 nm were determined. Since the wavelength of the absorption maxima were utilised as excitation radiation, the respective excitation maxima were shifted to 394-402 nm in comparison to the unoccupied pillarplex, which exhibits an absorption maximum at λ_{max} = 430 nm after being excitement by a radiation of λ_{ex} = 335 nm. The crystallinity of the pseudorotaxanes was ananylsed *via* powder X-Ray diffraction, where significantly higher crystallinity for the Ag(I) congeners was detected. The Au(I) complexes showed one strong reflection at approximately $2\theta = 3°$, a large amount of amorphous substance and broad reflections at high angles indicating the formation of large nanocrystalline aggregates.

Single Crystal Analysis

Crystallisation attempts were performed by dissolving each pseudorotaxane in MeCN. The solution was filtered and transferred into an NMR tube. These tubes were placed in a Schlenk-flask filled with THF and airtightly sealed. By slow diffusion of THF into the saturated solution of pseudorotaxane in MeCN, suitable single crystals for $[Ag_8L^{Me}_2](C_{10}H_{18}O_4)(PF_6)_4$, $[Ag_8L^{Me}_2](C_{12}H_{22}O_4)(PF_6)_4$ and $[Ag_8L^{Me}_2](C_{14}H_{26}O_4)(PF_6)_4$ were obtained. Colourless crystals of $[Ag_8L^{Me}_2](C_{10}H_{18}O_4)(PF_6)_4$ were refined and solved in the monoclinic space group *C* 2 (No. 5) with the asymmetric unit containing 1/2 $[Ag_8L^{Me}_2]^{4+}$, two disordered PF_6^- anions and two THF molecules. For pseudorotaxane $[Ag_8L^{Me}_2](C_{10}H_{18}O_4)(PF_6)_4$ small plate-shaped crystals crystallised in the monoclinic space group *I* 2 (No. 5) with the asymmetric unit containing 2 1/2 $[Ag_8L^{Me}_2]^{4+}$ cations, nine PF_6^- anions and 13 THF molecules. $[Ag_8L^{Me}_2](C_{10}H_{18}O_4)(PF_6)_4$ yielded plate-shaped crystals, which were resolved in the triclinic space group No. 2 (*P* -1). The asymmetric unit in this case contains two $[Ag_8L^{Me}_2]^{4+}$ cations, 12 co-crystallised THF molecules and nine PF_6^- anions with a total occupancy of the respective eight PF_6^- anions. No explicit guest refinement inside the cavity was possible due to highly disordered electron density, which showed the rough shape of an alky chain. The residual electron density was removed by the SQUEEZE[89] procedure. To examine the encapsulation of the dicarboxylic acids, theoretical investigation was performed based on the electrons, which were removed from the cavity in one unit cell. By comparison of the calculated electrons for each guest molecule and the electrons theoretically squeezed per guest molecule, the presence of guest molecule in the cavity could be verified (Table 5).

Table 5: Comparison of the theoretical calculated number of electrons for guest molecules $C_{10}H_{18}O_4$, $C_{12}H_{22}O_4$ and $C_{14}H_{26}O_4$ with the number of electrons removed during SQUEEZE[89] procedure to determine the amount of guest molecules in the unit cell.

	Calc. e-	Sum of squeezed e-	Guest in unit cell
$C_{10}H_{18}O_4$	110	250	2
$C_{12}H_{22}O_4$	126	876	10
$C_{14}H_{26}O_4$	142	597	4

As the encapsulated dicarboxylic acids exhibit strong potential for non-covalent interactions in particular, hydrogen bonding of the functional groups, the solvent accessible void (1.2 Å) inside the cavity was visualised in Mercury.[116] The crystal packing of the pseudorotaxanes was evaluated towards the intermolecular interactions of cation, anion and solvent molecule. Additionally, detailed investigation of the location and characteristics of the guest void was conducted.

For $[Ag_8L^{Me}_2](C_{10}H_{18}O_4)(PF_6)_4$, isolated $[Ag_8L^{Me}_2]^{4+}$ cations were observed with the void of potential guest molecule mainly visualised inside the cavity (Figure 59C, depicted in yellow). Theoretical investigation of $C_{10}H_{18}O_4$ yielded an average length of 15.17 Å (F55S). Compared to the height of the pillarplex cations with 11.7 Å[29], this calculated length indicates that the guest molecule sticks out of the cavity by a small proportion. Hence, no strong influence of the interactions of the carboxylic acid groups with either the H_{rim} or neighbouring $[Ag_8L^{Me}_2]^{4+}$ cations was anticipated. However, hydrogen bonding with PF_6- anions or THF molecules was feasible as those were located close to the rim. Through the analysis of non-covalent interactions of $[Ag_8L^{Me}_2]^{4+}$, especially non-classical hydrogen bonding[36] with the PF_6^- anions and classical hydrogen bonding with the oxygen atoms of the THF was assigned (Figure 59A). These interactions strongly determined the crystal packing for the pseudorotaxane. Two THF molecules were directly located on top of the rim and therefore could influence the accessibility of the pillarplex cavity. The crystal packing showed highly symmetric chain alignment of the $[Ag_8L^{Me}_2]^{4+}$ cations in a- and b-direction (Figure 59B, F56S), where the counter anions were located close to the rim. These one-dimensional chains of pseudorotaxanes were arranged in layers, where a zigzag formation of one layer to the next layer was obtained. Hence, every second layer was located in the middle of the two chains on top and bottom forming the mentioned zigzag formation (F56S).

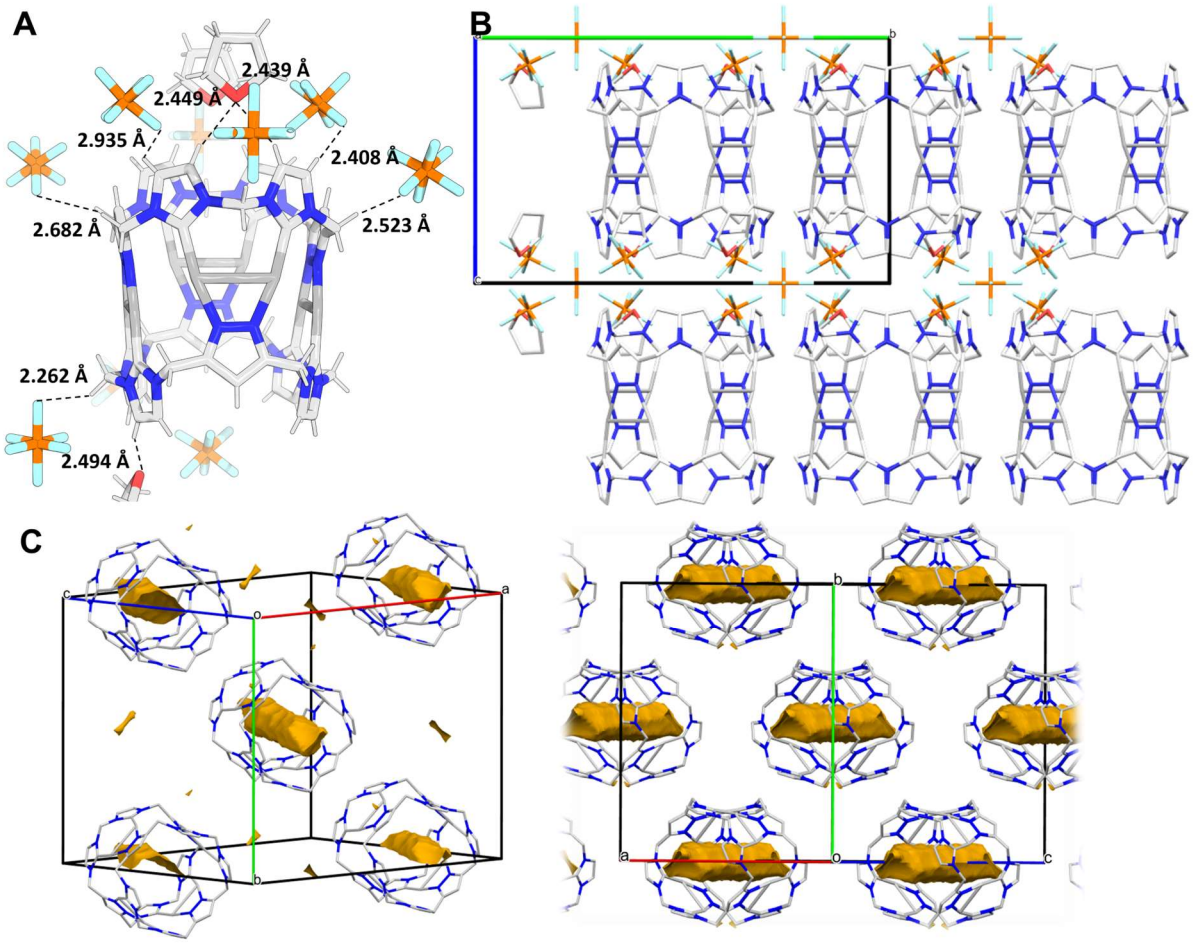

Figure 59: Representation of the solid-state structures of $[Ag_8L^{Br}_2](C_{10}H_{18}O_4)(PF_6)_4$: (A) Non-covalent interactions of $[Ag_8L^{Me}_2]^{4+}$ cation with counter anions, non-classical hydrogen bonding[36] of H_{rim} with the fluoride atoms of the PF_6^- anion and H_{rim} with the oxygen atom of the THF; (B) Crystal packing along the a-axis with chain alignment, location of the counter anions close to the rim; (C) Crystal packing of $[Ag_8L^{Me}_2]^{4+}$ with intra-pore solvent accessible surface (yellow, radius 1.2 Å) showing separated, non-connected voids.

The molecular structure of $[Ag_8L^{Me}_2](C_{12}H_{22}O_4)(PF_6)_4$ was analysed towards non-covalent interaction of the pillarplex cation (Figure 60A), where mainly non-classical hydrogen bonding[36] between the fluorine atoms of the counter anions and the hydrogen atoms of the rim were identified. Additionally, the oxygen atoms of the THF molecules formed classical hydrogen bonding with the methylene bridged hydrogen atoms.

When examining the length of a $C_{12}H_{22}O_4$ chain, an average length of 17.59 Å (F55S) was calculated, which is comparably longer than the height of the pillarplex cation measuring 11.7 Å. Consequently, this suggested, that the guest sticked out of the cavity, which was already observed for 1,12-diamino dodecane.[97] The protrusion of the carboxylic acid groups significantly influences the crystal packing through the contribution of hydrogen bonding interactions. Since the guest could not be explicitly refined, the crystal arrangement of $[Ag_8L^{Me}_2]^{4+}$ was analysed (Figure 60B). Here, an interpenetrated chain alignment of three symmetrical independent cations (depicted in blue, red, green) was observed. The Ag(I)-Ag(I) distances forming the chains were relatively long reaching distances of 10.263 Å and 10.330 Å. Distances of approximately 5 Å were determined between two cations in the pore alignment, which could allow hydrogen bonding of the respective encapsulated carboxylic acids either

with neighbouring carboxylic acids or with the rim of neighbouring $[Ag_8L^{Me}{}_2]^{4+}$ cations. The visualised voids for the solvent accessible surface strengthened this prediction, as the $[Ag_8L^{Me}{}_2]^{4+}$ cations were arranged in the already explained pore alignment with quasi-continuous channels of voids (Figure 60C, depicted in yellow).

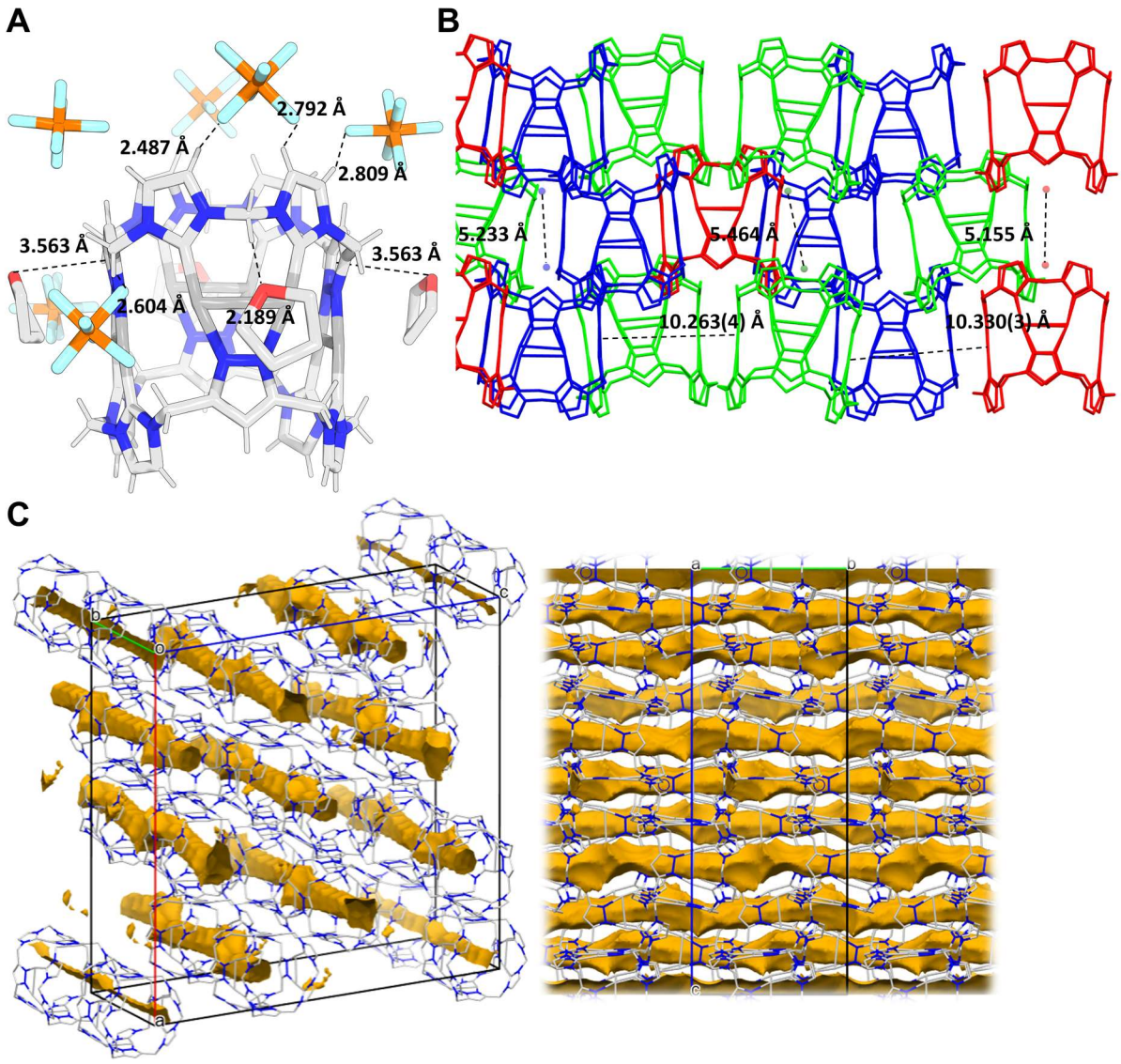

Figure 60: Representation of the solid-state structures of $[Ag_8L^{Br}{}_2](C_{12}H_{22}O_4)(PF_6)_4$: (A) Non-covalent interactions of $[Ag_8L^{Me}{}_2]^{4+}$ cation with counter anions, non-classical hydrogen bonding[36] of H_{rim} with the F_{PF6} and H_{rim} with the O_{THF}; (B) Interpenetrated chain alignment (distances 10.330 Å, 10.263 Å) of three symmetrical independent cations with pore-to-pore distances of 5.233 Å, 5.464 Å, 5.155 Å; (C) Crystal packing of $[Ag_8L^{Me}{}_2]^{4+}$ with intra-pore solvent accessible surface (yellow, radius 1.2 Å) showing connected voids along the c-axis.

A similar arrangement was examined for the crystal structure analysis of $[Ag_8L^{Me}{}_2](C_{14}H_{26}O_4)(PF_6)_4$. In this case, interpenetrated layers were obtained along the a-axis with distances of 5.354 Å and 5.443 Å between the pore-aligned $[Ag_8L^{Me}{}_2]^{4+}$ cations. Additionally, chain alignment with Ag(I)-Ag(I) distances of 8.410 Å (Figure 61B) was observed. The analysis of non-covalent interactions (Figure 61A) revealed non-classical hydrogen bonding[36] of H_{rim} and F_{PF6}, classical hydrogen bonding of O_{THF} to H_{rim} and metal coordination

of the oxygen atom of THF molecules with Ag(I) ions. Once again, the solvent accessible void surface was examined (Figure 61C, depicted in yellow), where quasi-continuous channels were visualised. The longer guest molecules were accommodated in these channels, which suggested that the carboxylic acids potentially form hydrogen bonding interactions either between neighbouring carboxylic acid groups or with neighbouring pillarplex cations. This suggestion was further supported by theoretical calculations based on crystallographic data, where an average length of 20.59 Å for $C_{14}H_{26}O_4$ molecules was determined (F55S), compared to the height of $[Ag_8L^{Me}{}_2]^{4+}$ with 11.7 Å. Therefore, it is likely that the guest protrudes from the cavity and plays a significant role in the formation of structure-decisive interactions.

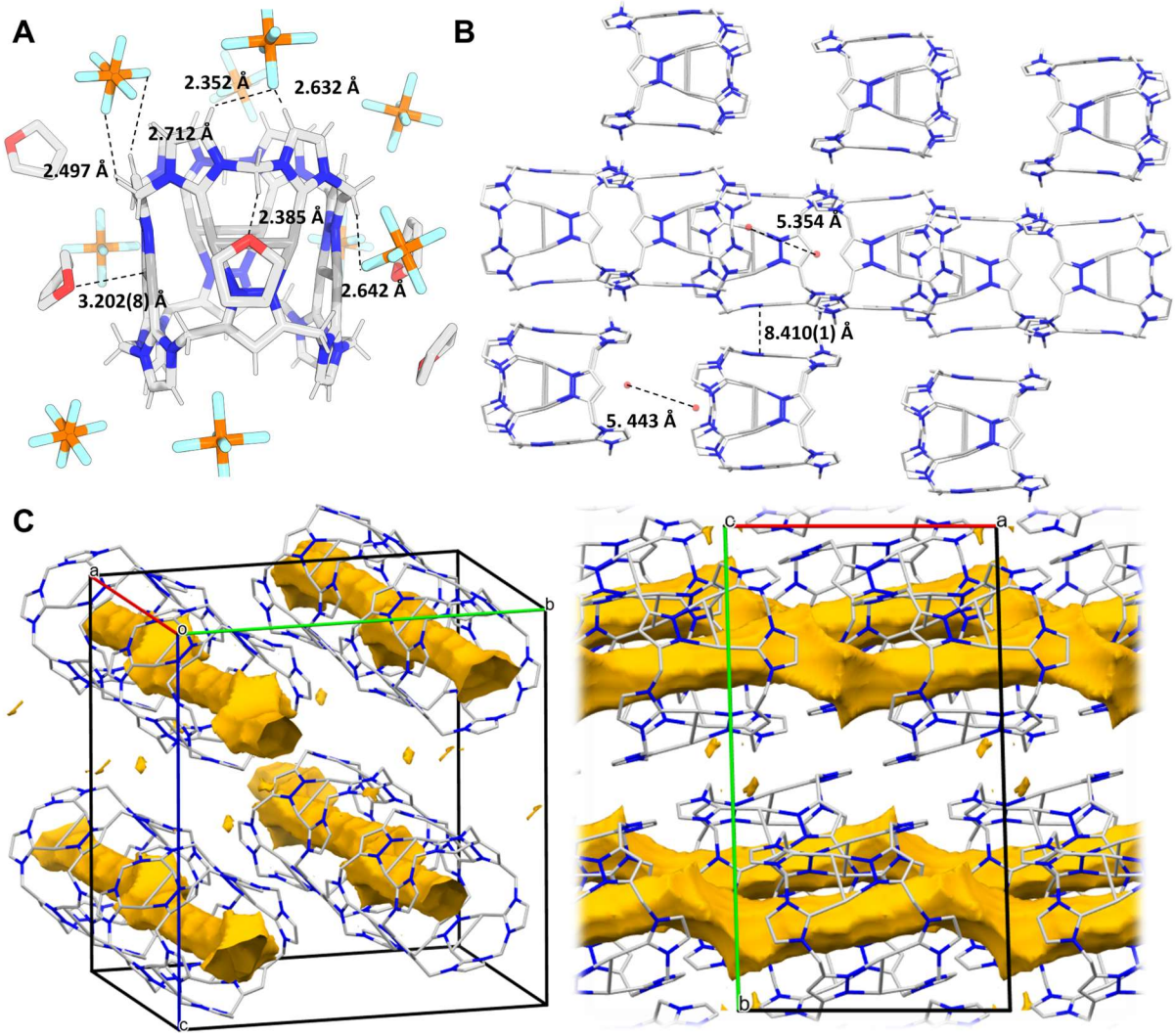

Figure 61: Representation of the solid-state structures of $[Ag_8L^{Br}{}_2](C_{14}H_{26}O_4)(PF_6)_4$: (A) Non-covalent interactions of $[Ag_8L^{Me}{}_2]^{4+}$ cation with counter anions, non-classical hydrogen bonding[36] of H_{rim} with the F_{PF6}, H_{rim} with the O_{THF} and Ag(I) to O_{THF} metal coordination; (B) Interpenetrated chain alignment (distance 8.410 Å) with pore-to-pore distances of 5.354 Å, 5.443 Å; (C) Crystal packing of $[Ag_8L^{Me}{}_2]^{4+}$ with intra-pore solvent accessible surface (yellow, radius 1.2 Å) showing connected voids along the a-axis.

Hirshfeld surface analysis

With the program CrystalExplorer[117-119], non-covalent interactions were visualised and quantified. As the location of the guest molecules could not be assigned, the interactions of $[Ag_8L^{Me}_2]^{4+}$ with the counter anions and solvent molecules were analysed. However, strong (probably structure-determining) hydrogen bonding interaction were anticipated for the carboxylic acid groups.

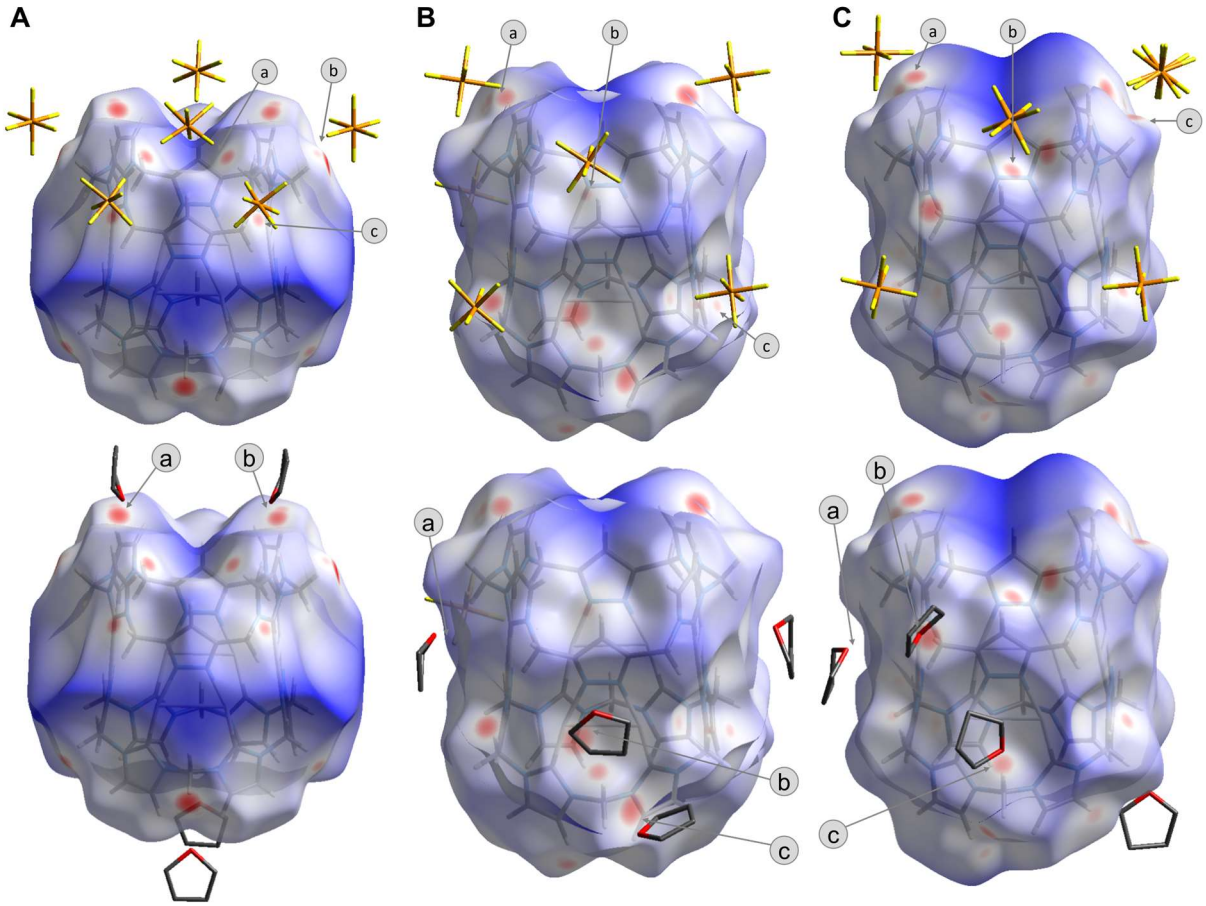

Figure 62: Hirshfeld surface analysis of $[Ag_8L^{Me}_2]^{4+}$ showed non-classical hydrogen bonding[36] of H_{rim} with F_{PF6}, classical hydrogen bonding H_{rim} with O_{THF} and metal coordination of Ag(I) with O_{THF}: (A) For complex $[Ag_8L^{Me}_2](C_{10}H_{18}O_4)(PF_6)_4$; (B) For complex $[Ag_8L^{Me}_2](C_{12}H_{22}O_4)(PF_6)_4$; (C) For complex $[Ag_8L^{Me}_2](C_{14}H_{26}O_4)(PF_6)_4$. Partially taken from [31].

For the surface analysis of $[Ag_8L^{Me}_2](C_{10}H_{18}O_4)(PF_6)_4$ two major interactions of the hydrogen atoms of the pillarplex cation with O_{THF} and F_{PF6} were observed (Figure 62A). Here, the THF molecules were located on top of the rim, blocking the pore opening. Quantification of the obtained interactions showed a small contribution of metal coordination (Ag•••all) of 2.8% and major contribution of hydrogen bonding with 83.5%, of which 54.6% are contributed towards a fluorine atom (all•••F). The Hirshfeld surface analysis of $[Ag_8L^{Me}_2](C_{12}H_{22}O_4)(PF_6)_4$ and $[Ag_8L^{Me}_2](C_{10}H_{18}O_4)(PF_6)_4$ showed similar behaviour with mainly non-classical hydrogen bonding[36] of the fluorine atom of anion PF_6^- with the hydrogen atoms of the rim. The THF molecules were located in a lateral style towards the $[Ag_8L^{Me}_2]^{4+}$ cation and formed classical hydrogen bonding interactions with the hydrogen atoms of the methylene bridges or metal coordination with the Ag(I) ions. When quantifying the interactions of $[Ag_8L^{Me}_2](C_{12}H_{22}O_4)(PF_6)_4$ (Figure 62B) the contribution of metal coordination (Ag•••all) was elevated to 5.9% by the additional presence of THF molecules. Still hydrogen bonding provided the major contribution

with H•••all of 79.2% of which 43.8% belonged to non-classical hydrogen bonding[36] with fluorine atoms (all•••F) and 8.4% belonged to classical hydrogen bonding with oxygen atoms (all•••O). For $[Ag_8L^{Me}{}_2](C_{12}H_{22}O_4)(PF_6)_4$ (Figure 62C) a contribution of metal coordination (Ag•••all) of 6.0%, and 78.3% of hydrogen bonding (H•••all) were quantified and the hydrogen bonding was divided into 43.6% non-classical hydrogen bonding[36] with fluorine atoms (all•••F) and 9.3% classical hydrogen bonding with oxygen atoms (all•••O).

3.6.3 Host-Guest Equilibria by ^{1}H NMR and ITC Titration Experiments

NMR titration

To determine the binding constants of the host-guest complexes, titration experiments were conducted. In ^{1}H NMR spectroscopy, a behaviour of upfield shifting of the guest proton signals upon encapsulation was utilised for further evaluation. To examine the dependency of binding constants on the used solvent, the ^{1}H NMR titrations were carried out in the solvents MeCN-d_3 and DMSO-d_6. 1.425 M solutions of the respective guest molecule and 2.850 M solutions of the pillarplexes $[Ag_8L^{Me}{}_2](PF_6)_4$ and $[Au_8L^{Me}{}_2](PF_6)_4$ were provided in MeCN-d_3 and DMSO-d_6. 0.4 mL of the guest solution was placed in an NMR tube and the ^{1}H NMR spectrum was recorded. Then 0.2 equivalents of the host solution were added and subsequently, the ^{1}H NMR spectrum was measured. This process was repeated until a 1:1 ratio of host:guest was reached. Then 1 equivalent of the host was added and the respective ^{1}H NMR spectrum was acquired. ^{1}H NMR spectroscopy was also conducted on a ratio of 3:1 (host:guest). For comparison of the free host signals, a sample of pure pillarplex was measured. During the titration process using this method, the overall concentration changed due to inevitable dilution, which was considered during the evaluation and determination of the binding constant.

The ^{1}H NMR spectra of the titrations of $C_8H_{14}O_4$ and $C_{10}H_{18}O_4$ into $[M_8L^{Me}{}_2]^{4+}$ in MeCN-d_3 revealed a continuous upfield shift of the guest signals. For the titrations of $C_{12}H_{22}O_4$ and $C_{14}H_{26}O_4$ into $[M_8L^{Me}{}_2]^{4+}$ in MeCN-d_3, the guest signals exhibited strong broadening. Nevertheless, a continuous upfield shifting was detected and the assignment was possible. For ^{1}H NMR titration spectra in DMSO-d_6 minimal shifting of the guest signals of the shorter acids $C_8H_{14}O_4$ into $[M_8L^{Me}{}_2]^{4+}$ and $C_{10}H_{18}O_4$ into $[Ag_8L^{Me}{}_2]^{4+}$ was noted. In contrast, the titration of longer acids $C_{10}H_{18}O_4$ into $[Au_8L^{Me}{}_2]^{4+}$ and $C_{12}H_{22}O_4$ or $C_{14}H_{26}O_4$ into $[M_8L^{Me}{}_2]^{4+}$ exhibited two signal sets for the guest protons. Furthermore, after the addition of more than 1 equivalent of host, a second signal set of host signals was observed.

The result indicated a solvent dependency. All guest signals displayed a slow but steady upfield shift during the addition of pillarplex in MeCN-d_3 (Figure 63A), while in DMSO-d_6 the longer acids showed the appearance of two signal sets upon addition of more than 1 equivalent host. This suggested, that on signal set was assigned to the free guest and the other one to the encapsulated guest (Figure 63B). Hence, a dynamic equilibrium in MeCN-d_3 and a more static equilibrium in DMSO-d_6 for the host-guest complex formation was identified.

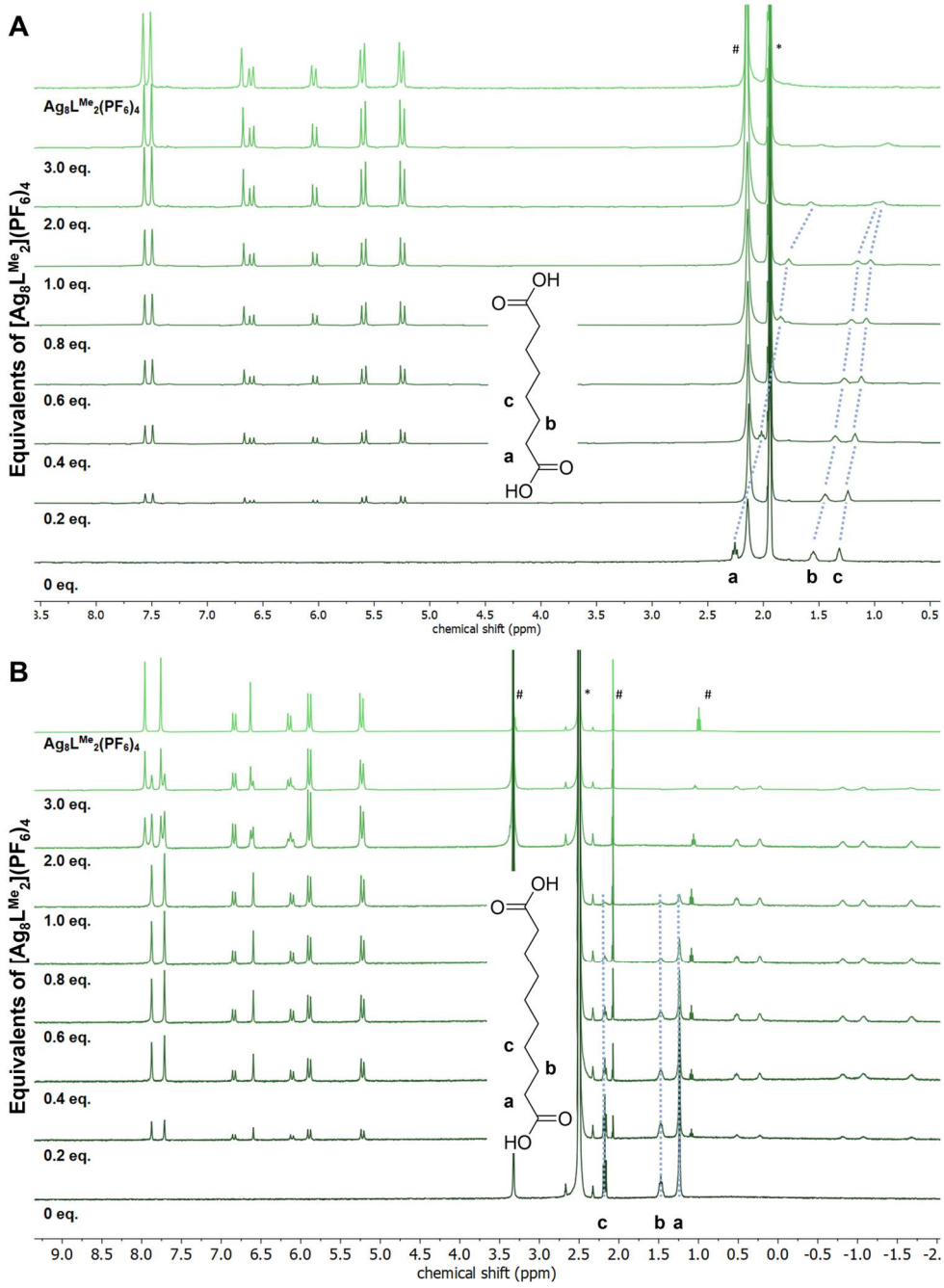

*Figure 63: ^{1}H NMR titration (400 MHz, 298 K) of a 2.85 mM solution of $[Ag_8L^{Me}{}_2](PF_6)_4$ into a 1.43 mM solution of $C_nH_{2n-2}O_4$: (A) $C_8H_{14}O_4$ in MeCN-d_3 (1.94 ppm, marked with *); (B) $C_{10}H_{18}O_4$ in DMSO-d_6 (2.50 ppm, marked with *). Solvent impurities were marked with # (water in MeCN-d_3 at 2.13 ppm, water in DMSO-d_6 at 3.33 ppm, Et_2O in DMSO-d_6 at 3.38, 1.09 ppm). The signals between 5 and 8 ppm were assigned to $[Ag_8L^{Me}{}_2]^{4+}$, the proton signals of the guest were upfield shifted and detected in the range of 2.5 ppm to -2 ppm.*

The evaluation of the obtained data was performed by the following programs:

1. Analysis by DynaFit[133] and Job Plot

Line fitting and determination of the binding constants K_d (k_{dissoc}) was calculated using nonlinear least-square regression analysis with a mechanism of H + G <==> HG. The dilution of the overall concentration was described by the keywords plot titration and by defining the concentrations as variables [H] and [G]. The signal shifts of H_a (CH_2 group attached next to the carboxylate group) were used as data for the calculation. For the titration of $[Au_8L^{Me}_2](PF_6)_4$ against $C_{12}H_{22}O_4$ and $C_{14}H_{26}O_4$, these signals could not be assigned properly, and no binding constant could be determined. By utilising this method binding constants in the region of 0.0019-1.99 · 10^{-3} M were obtained (Table 6). Job Plot analysis was used to verify the stoichiometry of the obtained host-guest complexes, which in all cases resulted in a ratio of 1:1.

2. Analysis by BindFit[134]

For this method, all guest signals were considered during the calculation of the binding constant and a 1:1 ratio of the host-guest complex formation was assumed. Again, no conclusive results were obtained for the titrations of $[Au_8L^{Me}_2]^{4+}$ against $C_{12}H_{22}O_4$ and $C_{14}H_{26}O_4$ as the guest signals could not be assigned. The signals of the host systems showed slight shifts and hence these values were tested towards suitability of this method. However, no conclusive results were obtained. The molefractions and host-guest complex ratio were calculated. Fhe titration of $C_8H_{14}O_4$ into $[Ag_8L^{Me}_2]^{4+}$ no encapsulation was observed and a relatively slow encapsulation of $C_8H_{14}O_4$ into $[Au_8L^{Me}_2]^{4+}$ was determined. The dissociation constants calculated by this method were determined in the range of 3.99 · 10^{-3} – 2.15 · 10^{-5} M (Table 6).

3. Analysis of Static Equilibria by Integral Ratio

As already mentioned, while using DMSO-d_6 a slower or more static equilibrium of the host-guest complex was detected by for the formation of two species of guest signals in the ^{1}H NMR spectra. This phenomenon occurred for the titrations of $C_{12}H_{22}O_4$ and $C_{14}H_{26}O_4$ into $[Ag_8L^{Me}_2]^{4+}$ and of $C_{10}H_{18}O_4$, $C_{12}H_{22}O_4$ and $C_{14}H_{26}O_4$ into $[Au_8L^{Me}_2]^{4+}$. Already after the addition of 0.2 eq. of host, the guest signals were split into one signal set strongly shifted to the upper field and one signal set at the initial positions. Upon addition of further equivalents of host, no change was observed and after the addition of more than 1 equivalent of pillarplex, a second set of proton signals for the pillarplex hydrogen atoms could be assigned. This indicated the simultaneous presence of occupied and empty host. No suitable program could be used to determine the binding constant with this titration data, but a comparison of the integrals of free and encapsulated guest proton signal could be performed. Assuming a 1:1 ratio of host:guest in the complex, following equation was employed:

$$H + G \overset{K_a}{\rightarrow} or \overset{K_d}{\leftarrow} HG \quad with\ K_a = \frac{1}{K_d} = \frac{[HG]}{[H][G]}$$

$$[H] = K_d \cdot \frac{[HG]}{[G]} \quad with\ [G] = [G]_0 - [HG]$$

After re-arranging the equation and filling in the initial concentrations $[H]_0$ and $[G]_0$, a linear fitting of the obtained data was performed. Thus, the binding constant for the host-guest complexes $[Ag_8L^{Me}_2](C_{12}H_{22}O_4)(PF_6)_4$, $[Ag_8L^{Me}_2](C_{14}H_{26}O_4)(PF_6)_4$ and the Au(I) congeners

$[Au_8L^{Me}_2](C_{10}H_{18}O_4)(PF_6)_4$, $[Au_8L^{Me}_2](C_{12}H_{22}O_4)(PF_6)_4$, $[Au_8L^{Me}_2](C_{14}H_{26}O_4)(PF_6)_4$ were calculated in the range of 2.63-8.97 · 10^{-5} M (Table 6).

Table 6: Data of binding constants K_d [M] obtained from ^{1}H NMR and ITC titration experiments. The results obtained from ^{1}H NMR titration were evaluated with DynaFit[133], BindFit[134] and for static equilibria the binding constants were determined from the integral ratio of free and encapsulated guest molecules.

	DynaFit		**BindFit**		**Integral**		**ITC**	
	K_d [M]	Stoic.	K_d [M]	Stoic.	K_d [M]	Stoic.	K_d [M]	Stoic.
$[Ag_8L^{Me}_2](C_8H_{14}O_4)(PF_6)_4$	$1.99 \cdot 10^{-3}$	1	$3.99 \cdot 10^{-3}$	-	-	-	$4.80 \cdot 10^{-7}$	1
$[Ag_8L^{Me}_2](C_{10}H_{18}O_4)(PF_6)_4$	$0.11 \cdot 10^{-3}$	1	$1.54 \cdot 10^{-4}$	1	-	-	$5.75 \cdot 10^{-7}$	0.6
$[Ag_8L^{Me}_2](C_{12}H_{22}O_4)(PF_6)_4$	$0.19 \cdot 10^{-5}$	1	$4.17 \cdot 10^{-6}$	1	$6.49 \cdot 10^{-5}$	1	$6.12 \cdot 10^{-7}$	0.35
$[Ag_8L^{Me}_2](C_{14}H_{26}O_4)(PF_6)_4$	$0.10 \cdot 10^{-5}$	1	$2.15 \cdot 10^{-6}$	1	$2.63 \cdot 10^{-5}$	1	$2.01 \cdot 10^{-7}$	0.35
$[Au_8L^{Me}_2](C_8H_{14}O_4)(PF_6)_4$	$0.66 \cdot 10^{-3}$	1	$6.30 \cdot 10^{-4}$	1	-	-	$7.77 \cdot 10^{-6}$	1
$[Au_8L^{Me}_2](C_{10}H_{18}O_4)(PF_6)_4$	$0.13 \cdot 10^{-3}$	1	$3.50 \cdot 10^{-4}$	1	$5.63 \cdot 10^{-5}$	1	$1.63 \cdot 10^{-6}$	1
$[Au_8L^{Me}_2](C_{12}H_{22}O_4)(PF_6)_4$	-	1	-	-	$8.97 \cdot 10^{-5}$	1	$2.29 \cdot 10^{-7}$	0.40
$[Au_8L^{Me}_2](C_{14}H_{26}O_4)(PF_6)_4$	-	1	-	-	$4.14 \cdot 10^{-5}$	1	$8.50 \cdot 10^{-8}$	0.31

ITC titration

ITC titration was performed in pure and degassed MeCN at 25 °C. Beforehand control titrations of dicarboxylic acids into pure solvent were conducted to correct the heat of dilution. Solutions with a concentration of 30 µM for host and 200 µM for guest were produced. The host solution was provided, and the guest solution was gradually added with one initial injection of 0.4 µL, followed by subsequent injections of 0.2 µL. Each injection lasted for 4 s and a spacing between injections a of 150 s was adhered to. To ensure homogeneous mixing,the solutions were stirred at a rate of 750 rpm. Data analysis of ITC only relies on heat changes without a dependency of the chosen signal, as seen in ^{1}NMR titration experiments. The data was then fitted using a non-linear least square regression algorithm implemented within the ITC analysis software employing the binding isotherm model of “one-set of site”.

All titrations resulted in a strong enthalpy-driven encapsulation of guest due to non-covalent interactions of the alky chain with the hydrophobic cavity. A small entropic penalty was observed with an increase from shorter to longer acids, which was based on the co-localisation and decreased conformational freedom of the alkyl chain. Dissociation constants K_d were determined in the range of 2.01 · 10^{-7} to 8.50 · 10^{-8} M (Table 6), which were consistent with the similar structure of the substrates and the interactions. While ITC titration uses quadratic equation to fit the binding isotherm, the obtained constants are independent from the concentration of free guest. However, the operation of the titration was in the similar concentration range as the determined binding constants, which avoided “titration regime” and an overestimation of the K_d values.[135] As a results, the ITC method seemed to be more suitable to determine the binding constants compared to the ^{1}H NMR titration approach. The stoichiometries derived from ITC titration differed from those obtained by ^{1}H NMR titration. In the case of host-guest complexes with longer acids $C_{12}H_{22}O_4$ and $C_{14}H_{26}O_4$, a ratio of 3:1 (pillarplex:guest) was observed. This observation indicated that one guest could bind to more than one pillarplex, which was in accordance with the higher enthalpy and the decrease in entropy. The longer lengths of $C_{12}H_{22}O_4$ and $C_{14}H_{26}O_4$ enabled the possibility of non-covalent interactions, particularly hydrogen bonding between the carboxylic acid groups and the rim of

neighbouring pillarplex cations. This allowed the interaction of three pillarplex cations with one guest molecules.

3.6.4 Conclusion and Outlook

A successful guest encapsulation of α,ω-dicarboxylic acids ($C_8H_{14}O_4$, $C_{10}H_{18}O_4$, $C_{12}H_{22}O_4$, $C_{14}H_{26}O_4$) into the cavity of $[M_8L^{Me}_2](PF_6)_4$ (M = Ag(I), Au(I)) was achieved, although the α,ω-dicarboxylic acids exhibited a diameter of 5.4 Å, which exceeded the pore opening of the pillarplex with 4.3 Å. By a combination of the already known shape-selective guest encapsulation of linear molecules and the hydrophobic effects between the cavity and the alky chain, the formation of pseudorotaxanes $[M_8L^{Me}_2](C_nH_{2n-2}O_4)(PF_6)_4$ indicated a certain flexibility of the pillarplex cation. This was supported by ^{1}H NMR and ITC titration experiments, where an enthalpy driven guest uptake was determined. To determine the binding constants, different methods (e.g., ITC and ^{1}H NMR) were conducted, which exhibited a strong dependency of the used solvent for the calculation of the respective binding constants. This behaviour must be further evaluated towards different solvents (e.g., MeCN, DMSO, H_2O), as those exhibit different hydrophobic effects and can influence the formation of host-guest complexes. Additionally, the possibility of solvent encapsulation in the cavity could influence the formation of the host-guest pseudorotaxanes and thus, the determination of the dissociation constant.

For $[Ag_8L^{Me}_2](C_{10}H_{18}O_4)(PF_6)_4$, $[Ag_8L^{Me}_2](C_{12}H_{22}O_4)(PF_6)_4$ and $[Ag_8L^{Me}_2](C_{14}H_{26}O_4)(PF_6)_4$ suitable single crystals were resolved *via* SC-XRD measurements. While the $[Ag_8L^{Me}_2]^{4+}$ cations and the respective counter anions were assigned, residual electron density was identified inside the cavity. This indicated the presence of the guest molecules, however due to a strong disorder, the electrons were treated and remove. Although no explicit refinement of the guest molecules was possible, the obtained accessible voids was visualised to analyse the location of the guest molecules. The crystal arrangement was investigated with focus on the visualised void. For $[Ag_8L^{Me}_2](C_{10}H_{18}O_4)(PF_6)_4$ isolated voids were identified, indicating that the guest molecules is primarily situated inside the pillarplex cavity. The potential interactions were therefore limited to the proximity of the pore opening. In the cases of longer guest molecules, $[Ag_8L^{Me}_2](C_{12}H_{22}O_4)(PF_6)_4$ and $[Ag_8L^{Me}_2](C_{14}H_{26}O_4)(PF_6)_4$, the void exhibited quasi-continuous channels in a tilted pore alignment of $[Ag_8L^{Me}_2]^{4+}$. The functional groups of the longer guest molecules sticked out of the cavity and thus formed hydrogen bonding with either the rim of neighbouring pillarplex cations or with neighbouring dicarboxylic acid groups. These interactions strongly influenced the arrangement towards the observed pore-aligned network. However, the defined location of the α,ω-dicarboxylic acid guest molecules and especially the location of the functional groups must be investigated for further implementation of the pseudorotaxanes in network materials. As the carboxylic acid groups can strongly influence hydrogen bonding interactions towards a specific crystal arrangement, one approach to achieve a network would be the formation of hydrogen bonded organometallic frameworks (HOFs).[4,76,99,136]

3.7 Utilising $[M_8L^{Me}_2]$(α,ω-Dicarboxylic Acid)$(X)_4$ as Building Blocks

3.7.1 Introduction

After introducing the dicarboxylic acid groups to the pillarplex system, attempts to implement the resulting pseudorotaxane into network materials were evaluated. In general, two ways to achieve this are possible (Figure 64):

1. Coordination Polymer (CP) or Metal Organic Framework (MOF):

By reacting the pseudorotaxane with suitable metal precursors coordinative bonds between the central metal ions and the carboxylate functional groups can be formed, which result in the formation of periodic networks. Such multi-dimensional materials bear $[M_8L^{Me}_2]^{4+}$ as ring component and hence the resulting material additionally carry the in-built properties of the pillarplex.

2. Covalent Organic Polymer (COP) or Covalent Organic Framework (COF):

By implementing a covalent bond between the -COOH group and another organic functional group (e.g., diamino group) more dimensional materials can be synthesised. Here, a precise composition can be obtained including light-weighted organic molecules linked by a strong covalent bond.

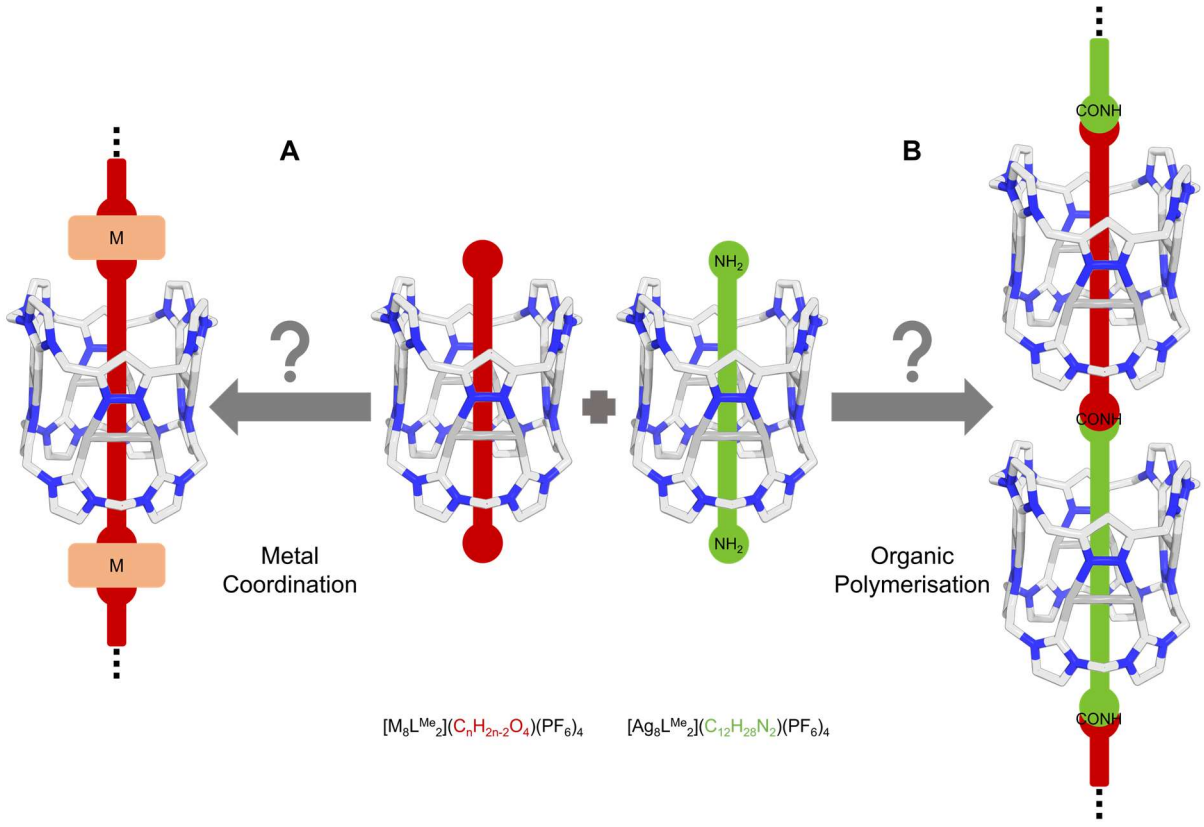

Figure 64: Overview of the suggested approaches to use pseudorotaxanes $[M_8L^{Me}_2](C_nH_{2n-2}O_4)(PF_6)_4$ and $[M_8L^{Me}_2](C_{12}H_{28}N_2)(PF_6)_4$ for the formation of extended structures: (A) Formation of a CP by coordinative bonding of the carboxylate unit with a suitable metal precursor; (B) Formation of an organic polymer by a covalent amide bond between the carboxylate and the amine units.

To increase the activity of the pseudorotaxanes, the respective deprotonated pseudorotaxanes were investigated as building blocks. The synthesis can either be performed by the encapsulation of deprotonated dicarboxylic acids (Synthesis route A) or by deprotonation of the already synthesised pseudorotaxane (Synthesis route B, for details see Chapter 5.8.3). Test reactions were performed using $C_{12}H_{22}O_4$ and the $[Ag_8L^{Me}_2](PF_6)_4$ pillarplex. For synthesis route A, the acid (1 eq.) was subjected to KOH (2 eq.) in water and stirred at room temperature overnight. Removal of the solvent *in vacuo* yielded a white solid, which was washed with Et_2O and analysed by ^{1}H NMR spectroscopy. In the ^{1}H NMR spectrum no signal for the acidic proton was detected, which can also occur due to the rapid exchange of these acidic protons. However, a change in solubility of the obtained solid was additionally detected. While $C_{12}H_{22}O_4$ displayed poor solubility in water, the synthesised $C_{12}H_{20}O_4K_2$ was very well soluble in water and hence the deprotonation was successful. $C_{12}H_{20}O_4K_2$ was provided in water and $[Ag_8L^{Me}_2](PF_6)_4$ in MeCN was added. The successful encapsulation was analysed by ^{1}H NMR spectroscopy, where the typical shift of the guest signals was observed. For synthesis route B the dicarboxylic acid (1.1 eq.) was encapsulated into $[Ag_8L^{Me}_2](PF_6)_4$ in MeCN, KOH (2.2 eq., 1 mg mL^{-1} in water) was added and the reaction mixture was stirred at room temperature overnight. Again, the solvent was removed *in vacuo* and washing with Et_2O yielded a white solid. The ^{1}H NMR spectrum of the potential deprotonated pseudorotaxane revealed the successful encapsulation by shifting of the guest proton signals. However, residual signals for free dicarboxylic acid were observed (1.7-2.5 ppm) and additionally the acidic proton signal at 8.44 ppm (F60S, marked in yellow box) indicated, that only partial deprotonation took place. These results clearly indicate that the synthesis route A is more suitable to achieve a deprotonated pseudorotaxane.

3.7.2 Synthesis Attempts towards Coordination Polymers

After successful introduction of carboxylic acid groups into a host-guest complex containing pillarplex as ring component, the further implementation of these compounds into coordination polymers was evaluated. The thermal stability of the pseudorotaxanes was taken into account and hence a peak temperature of 60 °C was applied for all coordination attempts. In the following section, the synthesis routes (1-11) and the outcome will be described. Details of the attempts are outlined in Chapter 5.8.3.

The first attempt to obtain a carboxylate metal coordination was tested by the formation of rotaxanes containing metalorganic complexes as stopper units (Figure 65). Here, the complexes $[Cu(Xantphos)(MeCN)_2][PF_6]$ (Xantphos = (9,9-dimethyl-9*H*-xanthene-4,5-diyl)bis (diphenylphosphane)) and $[Mo_2(DAniF)_3(OAc)]$ (DAniF = *N*,*N*`-di-p-anisylformamidine) were used as metal precursors since those are available and known to conduct metal coordination with carboxylate groups.[137-138] The metal complexes are sensitive towards oxygen and moisture and therefore the following reactions were performed under inert gas conditions. A variation of the metal ion from Mo to Cu was attempted, however the synthesis of $[Cu_2(DAniF)_3(OAc)]$ was not successful.

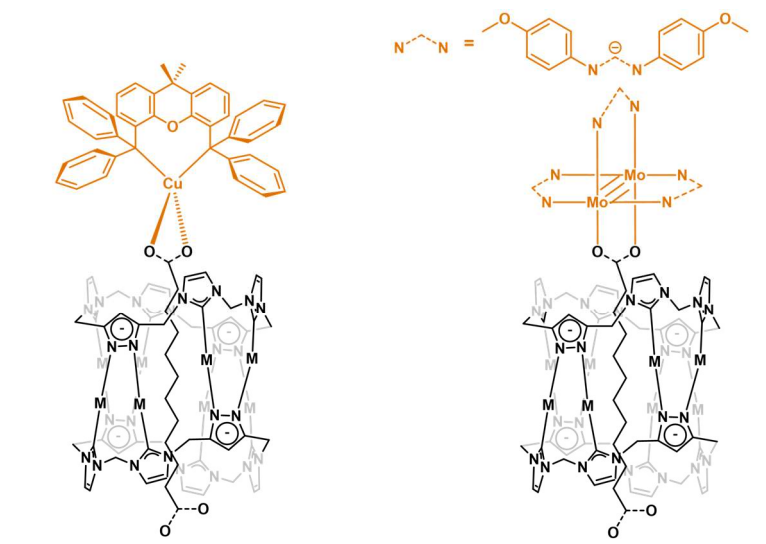

Figure 65: Schematic representation of the pillarplex rotaxanes containing dicarboxylic acids as axle compounds and metalorganic stopper units. (A) Pillarplex-Cu(Xantphos)-Rot; (B) Pillarplex-Mo(DAniF)-Rot.

Synthesis route 1: The metal precursor (2 eq.) was dissolved in dry MeCN, where $[Mo_2(DAniF)_3(OAc)]$ yielded a yellow solution and $[Cu(Xantphos)(MeCN)_2][PF_6]$ yielded a colourless solution. A solution of the pseudorotaxane (1 eq.) either containing $C_{12}H_{22}O_4$ or $C_{12}H_{20}O_4K_2$ as guest molecules in MeCN was slowly added. Due to low solubility of pseudorotaxane $[Ag_8L^{Me}_2](C_{12}H_{20}O_4K_2)(PF_6)_4$ in MeCN a solvent mixture of MeCN:MeOH of 1:1 was used for this reaction. The reaction mixtures were stirred at room temperature and visual inspection showed colour changes of all reaction mixtures. While the reactions containing $[Mo_2(DAniF)_3(OAc)]$ and $[Ag_8L^{Me}_2](C_{12}H_{22}O_4)(PF_6)_4$ showed a colour change to orange as well as precipitation of an orange solid, in the reaction mixtures with the deprotonated pseudorotaxane the precipitation of a dark red solid was observed. To support the deprotonation of the carboxylic acid groups, additive Cs_2CO_3 (6 eq.) was added to one reaction batch, which in this case revealed a colour change to brown. In the reaction mixtures containing $[Cu(Xantphos)(MeCN)_2][PF_6]$ as metal precursor, no colour change but the formation of an off-white precipitate was identified. Altogether, the precipitates obtained in all reactions were isolated by Whatman® filtration and the solids were washed with Et_2O and dried *in vacuo*. ^{1}H NMR spectroscopy was conducted and analysed towards the signals of the desired rotaxane. Unfortunately, ^{1}H NMR spectra revealed complex mixtures of signals, in which not even the assignment of the pillarplex and the metal precursor signals was possible. Only for the reaction of $[Mo_2(DAniF)_3(OAc)]$ with $[Ag_8L^{Me}_2](C_{12}H_{22}O_4)(PF_6)_4$ the assignment of signals to both substances was feasible. However, impurities were still identified that could not be removed even by repeated purification and hence the obtained orange solid could not be isolated and further analysed. Therefore, no conclusion could be drawn as the proton signals could also be the result of the simultaneous presence of separated pseudorotaxane and metal complex (F61S).

To achieve more dimensional materials, solvothermal synthesis conditions were applied. Pseudorotaxane, metal precursor and additives, such as acetic acid (AcOH) or α,ω-dicarboxylic acids ($C_{12}H_{22}O_4$, $C_{14}H_{26}O_4$), were provided in a screw cap vial (for details see Chapter 5.8.3). After adding a solvent, the vials were sealed airtight and placed in an oven.

The reaction mixtures were heated to 60°C for a specific time and slowly cooled to room temperature by leaving the samples in the oven. Afterwards, the reaction mixtures were inspected for colour changes of the solution, for precipitation and in case of a precipitate for the crystallinity of the obtained solid. Metal precursors, such as $Zn(NO_3)_2$, $Co(NO_3)_2$, $Zn(OAc)_2$, $Cu(OAc)_2$ were chosen, since various synthesis routes for the formation of extended structures with these metal ions are described in literature.[139-142] The additives α,ω-dicarboxylic acids were chosen as components for pillars, which are second linker units for higher tailoring of the structure.[143] In the case of bulky pillarplex linker motifs, the pillar molecules can facilitate the linkage of the building units to create a more-dimensional expanded network.

Synthesis route 2: $[Ag_8L^{Me}_2](C_{12}H_{22}O_4)(PF_6)_4$ (1 eq.) and $Zn(NO_3)_2$ (2 eq.) were provided, and similar conditions were applied with the four different solvents MeCN, MeCN:H_2O, DMF and DMSO. In all cases, colourless solutions were obtained, and the formation of a white precipitate was monitored. The precipitates were isolated *via* filtration and analysed by powder X-Ray diffraction, which yielded amorphous material for all attempts.

Synthesis route 3: $[Ag_8L^{Me}_2](C_{12}H_{22}O_4)(PF_6)_4$ and $[Ag_8L^{Me}_2](C_{14}H_{26}O_4)(PF_6)_4$ (1 eq.) were combined with 2 equivalents of the metal precursors $Zn(NO_3)_2$, $Zn(OAc)_2$ and $Co(NO_3)_2$. As solvents DMF and MeCN were investigated and the additive AcOH for activation of the metal precursor was added. Due to the steric demand of the pillarplex pseudorotaxanes, one equivalent of the respective free acids ($C_{12}H_{22}O_4$ or $C_{14}H_{26}O_4$) was added to achieve the formation of pillar-layered network materials. After applying solvothermal conditions, the vials were inspected for colour change and the presence of precipitate. For reaction condition 3.14 (Chapter 5.8.3, T11S) single crystals were observed, which were measured in SC-XRD measurement and will be discussed in Chapter 3.7.4. The reaction mixtures containing metal precursor $Zn(NO_3)_2$ yielded white precipitates, while for the attempts containing $Co(NO_3)_2$ and $Zn(OAc)_2$ brown precipitates were obtained. All precipitates were isolated by filtration and analysed by powder X-Ray diffraction measurements, in which no pattern was detected, and hence amorphous material was formed. The solubility was tested with common solvents to potentially perform NMR spectroscopy, however in all cases the solids proofed to be insoluble. The addition of AcOH seemed to destroy the pillarplex, as for these reactions colourless solutions with black precipitate were observed, which indicates decomposition of the pillarplex. This assumption was strengthened by the observation of purely ligand signals in the ^{1}H NMR spectrum.

Synthesis route 4: $[Ag_8L^{Me}_2](C_{12}H_{22}O_4)(PF_6)_4$ and metal precursor $Zn(OAc)_2(H_2O)_2$ were provided in DMF. One batch was subjected to solvothermal conditions, while the other batch was kept at room temperature. After solvothermal treatment a viscous, colourless material was obtained, which was analysed by ^{1}H NMR spectroscopy, DLS and ESI mass spectrometry. The NMR and mass spectra showed only the pillarplex signals and the DLS measurements yielded aggregates in the same size than the pseudorotaxane. These findings lead to the conclusion that no reaction took place. However, the reaction has to be repeated, and the obtained viscous material needs to be further investigated to reveal its chemical composition. The change in viscosity could also be driven by strong non-covalent interactions of the pillarplex with the solvent DMF.

Synthesis route 5: Pseudorotaxane $[Ag_8L^{Me}_2](C_{12}H_{22}O_4)(PF_4)_4$ was combined with Cu(I)- and Cu(II)-based metal precursors, where a direct colour change was observed upon addition of the metal salts. The reaction mixtures containing Cu(I) salts immediately changed towards a dark colour with a dark solid precipitating. The Cu(II) salts yielded blue solutions with a dark

solid precipitating. All isolated solids were analysed by PXRD measurements and were identified as amorphous material.

During the coordination attempts following synthesis route 5 one common problem was observed, which was the transmetalation reaction or the decomposition of the pillarplex. To avoid this problem, further crystallisation attempts were also performed using Ag(I) metal precursors. The pseudorotaxane $[Ag_8L^{Me}_2](C_{12}H_{22}O_4)(PF_4)_4$ was combined with Ag-PF_6, Ag-OAc and Ag-OTf salts in DMF and solvothermal conditions were applied. Afterwards, optical investigation towards precipitation and colour change was performed and the obtained solids were analysed towards their crystallinity. Again, only amorphous materials were obtained, and no crystals observed, which could be subjected to SC-XRD measurement for structural investigation. However, the colour of the precipitated and isolated solids was white and hence no decomposition of the pillarplex was assumed. As the solvothermal conditions only yielded amorphous material, further coordination attempts were subjected to layering of the reactants following the procedure displayed in Figure 66 and the possibility to form single crystals or crystalline materials at the boundary surface.

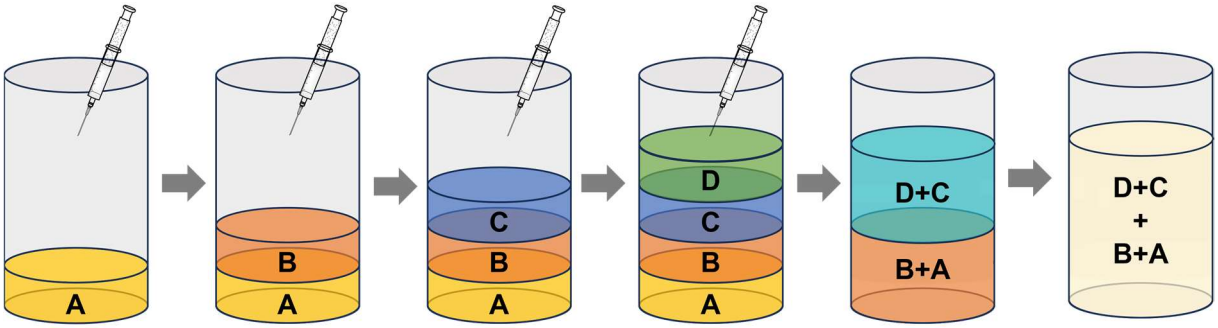

Figure 66: Schematic representation of the layering process, which was applied for crystallisation attempts: Layer A contains the pillarplex pseudorotaxane (+ additive) in solvent mixture 1; Layer B contains the solvent mixture 1; Layer C contains the solvent mixture 2; Layer D contains the metal precursor (+ additive) in solvent mixture 2. Layering steps B and C are optional.

Synthesis route 6[144-145]: $[Ag_8L^{Me}_2](C_{12}H_{22}O_4)(PF_4)_4$ and either base 2,6-DMP (2,6-dimethyl pyridine) or DPEA (dipropyl ethylamine) were dissolved in DMF:H_2O and provided as solution A. The layer B containing the solvent mixture DMF:H_2O was added on top, as well as layer C, which contained the solvent mixture MeOH:MeCN. Finally, layer D with the metal precursor $Ag(NO_3)$ in the solvent mixture MeOH:MeCN was added on top. Simultaneously to the crystallisation attempts, where the vials were kept at room temperature, the batches were also subjected to solvothermal conditions. In all cases, white precipitates were formed, which were isolated by filtration and the crystallinity was analysed by powder X-Ray diffraction experiments. In several samples following this synthesis route, colourless crystals were discovered, which could be measured in single crystal X-Ray diffraction experiments. Unfortunately, the data showed limited quality, where only the isotropic refinement of the $[Ag_8L^{Me}_2]^{4+}$ cation and nitrate anions was possible. Inside the pillarplex cavity electron density was visible indicating the presence of a guest molecule. However, no explicit refinement of this guest molecule was possible due to shielding effect and strong disorder. Interestingly, the crystal structure analysis showed, that only an anion exchange reaction occurred and several mixed anion pillarplex salts were achieved (T10S, F64 – F65S).

Here, the second common problem during coordination attempts – anion exchange – was observed. The utilised metal precursors were carrying a counter anion (e.g., NO_3^-, OAc^-) and as the pillarplex system itself is a charged system, the side reaction towards anion exchange occurred. Therefore, the next step would be to use a metal precursor containing the identical metal and counter anion as the provided pillarplex pseudorotaxane.

Synthesis route 7:[145] Following the layering process, solution A containing $[Ag_8L^{Me}_2](C_{12}H_{22}O_4)(PF_6)_4$ (1 eq.) and 2,6-DMP (1 eq.) in DMF:H_2O was provided. The two solvent layers were added and then solution D containing the metal precursor Ag-PF_6 in MeOH:MeCN was slowly added. After keeping the vial at room temperature for reactions by slow mixing of the reactants at the boundary surface, optical inspection showed no precipitation or colour change. Hence, the solvents were removed *in vacuo* and ^{1}H NMR spectroscopy was performed, where no evidence for coordination was identified as unchanged proton signals were detected.

Synthesis route 8:[144] The conditions were slightly altered and hence the two solvent mixture layers (B, C) were added on top of layer A containing $[Ag_8L^{Me}_2](C_{12}H_{22}O_4)(PF_6)_4$ (1 eq.) and pyridine (1 eq.). Finally, the metal precursor Ag-PF_6 in H_2O was added, and the crystallisation attempts were kept at room temperature. Again, no precipitation or colour change was obtained after several days and ^{1}H NMR spectroscopy yielded no conclusive results since unchanged pillarplex proton signals were detected. Similar equivalents and compounds were directly mixed and solvothermal conditions were applied. Again, a dark precipitate and a metal mirror on the side of the vials was observed indicating the decomposition of the pillarplex.

Synthesis route 9: Simultaneously, two batches containing pseudorotaxane (1 eq.), DIPEA (2.2 eq.) and an excess of Ag-PF_6 with 4 equivalents were dissolved in DMF. One batch was stirred at room temperature for 3 h and then kept at that temperature for slow crystallisation, where amorphous white powder precipitated. The other batch was heated to 60 °C, stirred at that temperature for 3 h and then slowly cooled to room temperature. This method yielded a dark precipitate, which was analysed by powder X-Ray diffraction as amorphous powder.

One attempt towards the implementation of a pseudorotaxane not bearing PF_6^- but acetate as counter anion was planned. Although acetate anions can partially occupy the cavity, successful formation of the pseudorotaxane $[Ag_8L^{Me}_2](C_{12}H_{22}O_4)(OAc)_4$ was verified by ^{1}H NMR spectroscopy (F63S). This compound was then used in a literature-known[146] route to potentially synthesise a pillarplex containing MOF with a topology reminiscent of HKUST-1 (HKUST = Hong Kong University of Science and Technology). Here, Cu_2-paddlewheel metal units are connected by four benzene-1,3,5-tricarboxylate linker giving a 3D structure.[147]

Synthesis route 10:[146] $[Ag_8L^{Me}_2](C_{12}H_{22}O_4)(OAc)_4$ was dissolved in a solvent mixture of DMF:H_2O (1:5) and $Cu(OAc)_2(H_2O)_7$ (1 eq.) was added as metal source. During stirring the reaction mixture at room temperature for 3 h, no precipitation occurred. Therefore, the reaction mixture was kept at room temperature and after several days the solvent of the blue solution was reduced *in vacuo*. ^{1}H NMR spectroscopy was conducted, where no evidence for the formation of a coordinative bond between the pseudorotaxane and Cu(II) metal atoms appeared.

Especially, while applying solvothermal conditions, decomposition of the pillarplex was observed indicated by the formation of amorphous dark precipitates. When handling $[Ag_8L^{Me}_2]^{4+}$ the possibility of transmetalation has to be considered. To eliminate this side reaction, coordination attempts were also performed with the respective Au(I) congeners, as these exhibited higher stability due to stronger Au(I)-ligand bonds.

Synthesis route 11: Crystallisation attempts were performed with the pseudorotaxane $[Au_8L^{Me}_2](C_{12}H_{22}O_4)(PF_6)_4$ and the metal precursors Ag-PF_6, $[Mo_2(DaniF)_3(OAc)]$ and $[Cu(XanthPhos)(MeCN)_2(PF_6)_2]$. For the attempt containing Mo(II) and Cu(II), Cs_2CO_3 as additive was provided to activate the carboxylic acid groups. Again, the layering process was applied but this time only one solvent (MeCN) was used. Layer A contained the pseudorotaxane (+ additive), layer B/C contained the pure solvent MeCN, and layer D contained the metal precursor. The vials were either kept at room temperature or placed in the freezer (-30 °C) for crystallisation at the boundary surface. A colour change of the vials containing $[Mo_2(DaniF)_3(OAc)]$ to orange was visible but no further colour change or the precipitation of a solid was observed.

Summary

In summary, several attempts to implement the pillarplex pseudorotaxane by a coordinative bond into extended structures were performed:

1. The formation of a rotaxane with metal-containing stopper motifs was tackled, since the obtained molecules still exhibit molecular structures, which should allow for straightforward analysis. Although preliminary NMR analysis suggested the formation of the targeted species (Pillarplex-Mo(DAniF)-rotaxane), further purification and hence isolation and complete characterisation was not possible.

2. The formation of extended materials with metal precursors, such as $Zn(NO_3)_2$, $Co(NO_3)_2$ or $Zn(OAc)_2$ was tackled. All attempts proved to be unsuccessful due to varying reasons, which could be attributed to either decomposition, transmetalation or anion exchange. To prevent the transmetalation and / or the anion exchange reactions in further attempts, Ag(I)-pillarplex pseudorotaxanes were combined with metal precursors bearing either identical metal ions (e.g., $AgPF_6$, Ag(OAc), Ag(OTf), $Ag(NO_3)$) and / or identical counter anions (e.g., $AgPF_6$, $Cu(PF_6)(MeCN)_4$). Nevertheless, no evidence for successful implementation of the Ag(I)-pillarplex into extended structures could yet be discovered.

3. Since the Au(I) based pillarplex is less prone towards transmetalation[148-149], first attempts to form a rotaxane with metal-containing stopper motifs (e.g., Pillarplex-Mo(DAniF)-rotaxane) and to form extended structures with metal precursors (e.g., $AgPF_6$) were conducted. Due to time constraints, no results can be presented. However, these approaches are the most promising ones, with particular emphasis on the use of $[Cu(Xantphos)(MeCN)_2][PF_6]$ as metal precursor in combination with pillarplex $[Au_8L^{Me}_2](PF_6)_4$ or $[Mo_2(DaniF)_3(OAc)]$ in combination with pillarplex $[Au_8L^{Me}_2](OAc)_4$, since they carry the same cation.

3.7.3 Synthesis Attempts towards Covalent Organic Polymers

First, the encapsulation of the more reactive acid chloride $C_{12}H_{20}O_4Cl_2$ into $[Ag_8L^{Me}_2](PF_6)_4$ was investigated but led to a brown precipitate upon addition of the acid chloride, which indicated the formation of Ag-nanoparticles. This finding was corroborated with ^{1}H NMR spectroscopy, where only residual signals for the macrocyclic ligand were identified. As the $[Au_8L^{Me}_2](PF_6)_4$ pillarplex exhibits higher stability, further encapsulation studies could be performed to evaluate the stability of the Au(I) based pillarplex towards the acid chlorides. Another way to activate the dicarboxylic acid was tested by the addition of DCC (*N*,*N*`-dicyclohexyl carbodiimide), which is known for catalysing the amine formation.[150]

The two pseudorotaxanes $[Ag_8L^{Me}_2](C_{12}H_{28}N_2)(PF_6)_4$ and $[Ag_8L^{Me}_2](C_{12}H_{22}O_4)(PF_6)_4$ were prepared and their purity was confirmed by ^{1}H and DOSY NMR spectroscopy, in which the presence of only one species was recognised. After obtaining the pseudorotaxanes$[Ag_8L^{Me}_2](C_{12}H_{22}O_4)(PF_6)_4$, two batches were provided for further reactions. To one of these batches (synthesis route A), three equivalents of DCC were added and the reaction mixture stirred for another 15 min at room temperature, while the second batch remained untreated. Afterwards, both batches were slowly added to a solution of $[Ag_8L^{Me}_2](C_{12}H_{26}N_2)(PF_6)_4$, which in both cases led to the formation of a white precipitate. Nevertheless, the reaction mixtures were stirred for 1 h to ensure full conversion and then the white solids were isolated by centrifugation. After washing with Et_2O and drying *in vacuo*, ^{1}H and DOSY NMR spectroscopy were performed. The obtained spectra (F68S – F69S) were analysed towards the possible formation of a polymer containing $[Ag_8L^{Me}_2](PF_6)_4$ as ring component. However, NMR spectroscopy yielded unconclusive results with diffusion coefficients in the same range ($d = 5.56 / 5.98 \cdot 10^{-10}$ m^2 sec^{-1}) as the ones obtained for the pseudorotaxanes ($d = 5.76 \cdot 10^{-10}$ m^2 sec^{-1}). The ^{1}H NMR spectra showed indications for the combination of both pseudorotaxanes by the simultaneously presence of two signals sets of pillarplex hydrogen atoms and coupling of those signal sets. Additionally, DLS measurements were performed in solvent DMF to investigate the sizes of the isolated aggregates (Figure 67). Size distribution analysis revealed aggregates with the average size of 255 nm following synthesis route A and 122 nm following synthesis route B, which is significantly larger compared to the average size of 28.2 nm determined for aggregates of $[Ag_8L^{Me}_2](PF_6)_4$ (F70S). The obtained data indicated that indeed larger aggregates were formed, however the presence of DCC led to aggregates with a larger size and an overall smaller size distribution.

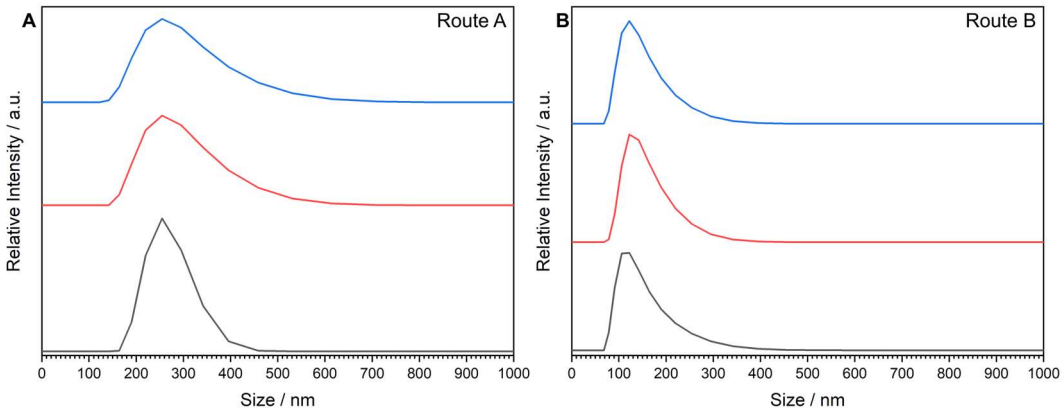

Figure 67: Size distribution measured by DLS measurements in DMF (1 mg mL^{-1}) of (A) white solid obtained following synthesis route A; (B) white solid obtained following synthesis route B. The average size of (A) 255 nm and (B) 122 nm are calculated based on n = 3 measurements (black, red, blue).

Summary

First attempts to combine the pseudorotaxanes $[Ag_8L^{Me}{}_2](C_{12}H_{22}O_4)(PF_6)_4$ and $[Ag_8L^{Me}{}_2](C_{12}H_{28}N_2)(PF_6)_4$ to form a covalently bound organic polymer were performed and yielded inconclusive results. To draw a conclusion on the polymer synthesis, further studies need to be performed. The ^{1}H NMR spectra showed impurities and therefore another way of purification has to be established and further analysation methods (e.g., GPC) should be applied to corroborate the formation of a polymer containing $[Ag_8L^{Me}{}_2]^{4+}$ as ring component.

3.7.4 *Excursus* Proligand Coordination Polymer

This chapter is partially based on the research internship of Alexander Spears, which was supervised by this author. In this chapter only preliminary results are displayed.

Introduction

In Chapter 3.7.2 various metal coordination attempts were presented to implement the pseudorotaxane $[Ag_8L^{Me}{}_2](C_{12}H_{22}O_4)(PF_6)_4$ into network materials. The problems of anion exchange reactions and transmetalation were already described. However, another problem could be the instability of the pillarplexes – especially the Ag(I) congener – towards acidic conditions. By introducing dicarboxylic acid as guest molecules and using MeCN as solvent, the reaction mixtures were acidic enough to yield decomposition of the Ag(I)-coordination bonds of the pillarplex. As the macrocyclic ligand itself is a supramolecule and exhibits cationic character, the formation of coordination polymers incorporating the ligand as organic ligand unit would be possible (Figure 68).

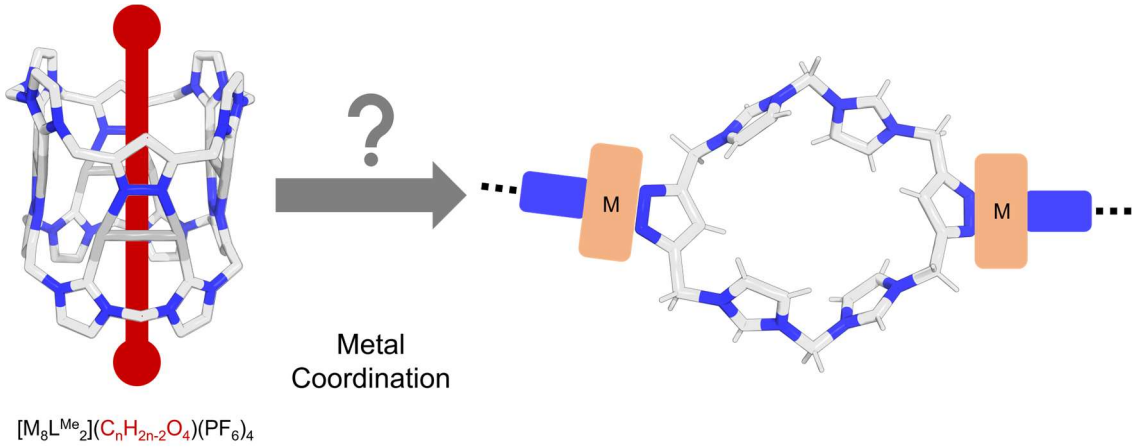

Figure 68: Schematic overview of the decomposition of pseudorotaxane $[Ag_8L^{Me}_2](C_{12}H_{22}O_4)(PF_6)_4$ with simultaneous anion exchange reaction and metal coordination of the macrocyclic proligand with provided metal precursor.

Synthesis and Crystallographic Investigation

Pseudorotaxanes $[Ag_8L^{Me}_2](C_{12}H_{22}O_4)(PF_6)_4$ (1 eq.), $Zn(NO_3)_2$ (2 eq.) as metal precursor were provided in a vial and solvent MeCN was added. Solvothermal conditions at 60 °C for 3 days were applied (for details see Synthesis route 8, Chapter 5.8.3). During this time, no colour change of the colourless reaction mixture was observed, but a white precipitate was formed. Optical analysis with a microscope indicated tiny colourless crystals, which were suitable for single crystal X-Ray diffraction. Due to their small size and poor scattering, only data with moderate quality was obtained. Nevertheless, the data was sufficient to yield structural evidence for the formed coordination polymer. During the solvothermal synthesis a decomposition of not only the pillarplex pseudorotaxane but also the pillarplex cation itself was observed and the free macrocyclic ligand L^{Me} formed a coordination polymer with the provided Zn(II) precursors. Simultaneously, as the metal precursor contained NO_3^- anions, anion exchange reaction from PF_6^- to NO_3^- was observed yielding the chemical formula $[Zn_2L^{Me}(NO_3)_6(OH)_2]$ for the coordination polymer.

The NHC carbene atoms of the macrocyclic ligand are protonated, and the nitrogen atoms of the pyrazole unit are coordinated with the *N*-donating group to one Zn(II) ion (Figure 69A). The coordination sphere of the Zn(II) exhibits tetrahedral character, where one nitrate anion, one oxygen (or hydroxy, as determined by charge compensation) and two nitrogen atoms of the pyrazole unit of ligand L^{Me} are coordinated. Two ligands L^{Me} are therefore coordinated through their pyrazole units by two Zn(II) ions forming a 1D chain alignment. The nitrate and hydroxy groups coordinated to Zn(II) are alternating pointing up and down relative to the ligand chains. By this alternating arrangement of nitrate, a stacking of the 1D chains by hydrogen bonding between the oxygen atoms of the nitrate or the hydroxy with the hydrogen atoms of neighbouring ligands is established. Hence, the stacked chains are always shifted to the site of approximately half a ligand (Figure 69B).

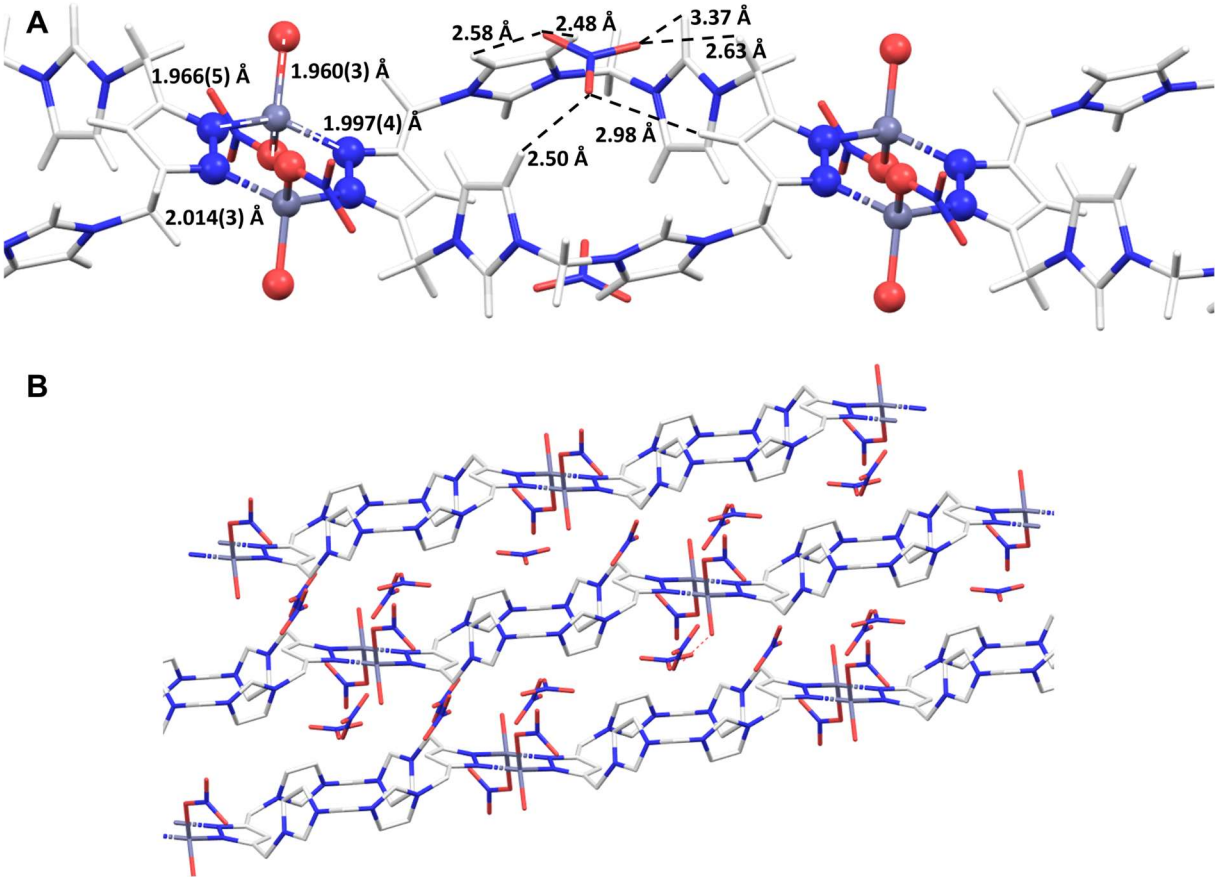

Figure 69: Representation of the solid-state structures of $[Zn_2L^{Me}_2(NO_3)_3(OH)_2]$: (A) Chain alignment of $[Zn_2L^{Me}(NO_3)_3(OH)_2]$ with tetrahedral geometry of Zn(II) and non-covalent interactions of cation L^{Me} with counter anions NO_3^-; (B) Crystal packing of stacked 1D chains.

Summary

The formation of a 1D chained extended material was achieved by the coordination of macrocyclic ligand L^{Me} with a Zn(II) metal precursor. These 1D chains are interconnected by non-covalent interactions forming layers, where every second layer is identical.

3.7.5 Outlook

In conclusion, the introduction of pillarplex pseudorotaxanes into materials is challenging.

1. Coordination polymers: Many insights were gained from the performed coordination experiments, as side reactions such as transmetalation and anion exchange reactions were identified. First experiments to implement the Au(I)-pillarplex, which typically does not undergo transmetalation reactions due to more stable Au-NHC bonds, were conducted. The crystallisation attempts to form rotaxanes with metal-containing stopper motifs (Pillarplex-Cu(Xantphos)-rotaxane, Pillarplex-Mo(DAniF)-rotaxane) and the crystallisation attempts to form extended structures with metal precursor $AgPF_6$ could not be completely analysed. Further steps should focus on the implementation of Au(I)-pillarplex salts in extended structures. This should be done *via* a combination with metal precursors (e.g., Ag(I), Au(I), Cu(II), Zn(II)) and counter anions (e.g., PF_6^-, OAc^-, OTf^-), which are identical to the ones of the pillarplex.

However, to avoid the mentioned problems of anion exchange and transmetalation, further implementation of the pillarplex pseudorotaxane into more dimensional materials with purely organic precursors could be studied.

2. Organic coordination polymer: Initial attempts to form an organic polymer containing $[Ag_8L^{Me}_2]^{4+}$ as ring component were made by the combination of pseudorotaxanes with axle components α,ω-dicarboxylic acid and α,ω-diamine. So far, this has only led to inconclusive results. Therefore, in future studies the activation of the axle component prior or during the synthesis could lead to the formation of the desired pillarplex-containing organic polymers. Activation of the functional group dicarboxylic acid could be achieved *via* transformation of the acid group to either an acid chloride or anhydride.

3. Ligand coordination polymer: The observation of $[Zn_2L^{Me}(NO_3)_6(OH)_2]$ offers the possibility to form coordination polymers containing the macrocyclic ligand as linker motif. Therefore, an understanding of the reaction conditions, reaction mechanism and then the replication of $[Zn_2L^{Me}(NO_3)_6(OH)_2]$ has to be achieved. Additionally, further coordination polymers could be synthesised with variations of the ligand (e.g., L^{Me}, L^{Br}, L^t), metal precursor (e.g., Zn(II), Co(II), Cu(II)) and counter anion (e.g., PF_6^-, OAc^-, OTf^-). As the macrocyclic ligand itself is a supramolecular entity, the resulting more dimensional materials can be evaluated towards their host-guest chemistry.

3.8 Pillarplex Rotaxane with Pyridine as Functionality

3.8.1 Introduction

Another method to introduce a functionality into the pillarplex system is the formation of rotaxanes with the stopper molecules bearing the desired functionality. The synthesis of mechanically interlocked rotaxanes lead to increased thermal stability, where no temperature-induced de-threatening of the host and guest can occur. The functionality at the stopper units can further be utilised to implement these rotaxanes into expanded materials, where the in-built properties of the pillarplexes are simultaneously implemented into the synthesised more dimensional materials. The literature-known $[M_8L^{Me}_2][2]Rot(OTf)_4$[97] showed a reversible release and re-encapsulation of the Ag(I) metal ions upon a change in the pH value, where a strong decrease of rigidity along with the release of the metal ions was obtained. When implementing a pillarplex rotaxane into an extended structure, the pH dependent switching between a purely organic rotaxane with low rigidity and a metalorganic rotaxane with a rigid $[M_8L^{Me}_2]^{4+}$ ring component would be incorporated. However, the stability of the network towards various pH values needs to be analysed beforehand or the external stimulus has to be changed if limited stability of the network towards high pH values was observed.

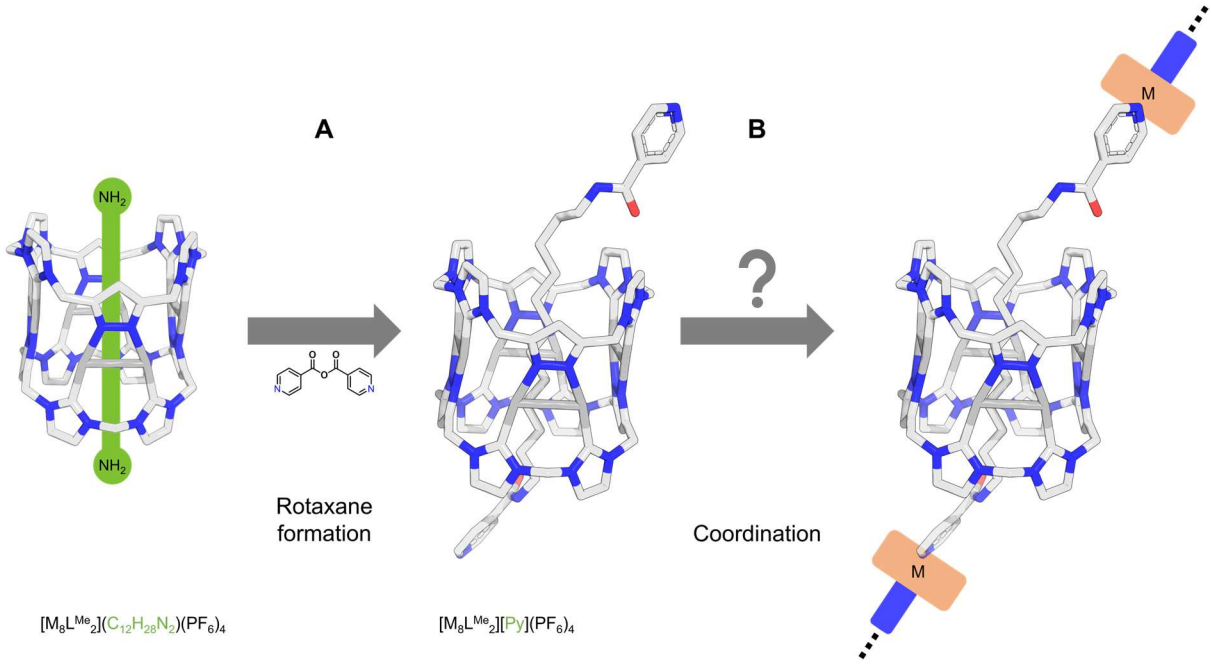

Figure 70: Overview of the formation of (A) Pillarplex rotaxanes $[M_8L^{Me}_2][Py](PF_6)_4$ following literature-known synthetic procedure with pseudorotaxane $[M_8L^{Me}_2](C_{12}H_{28}N_2)(PF_6)_4$ and isonicotinic anhydride; (B) Potential further implementation into extended materials by coordinative bonding with suitable metal precursor.

As functional groups, carboxylic acid and pyridine were targeted (exemplary shown for pyridine in Figure 70). Until now, the formation of pillarplex rotaxanes was performed by the encapsulation of 1,12-diaminododecane into $[M_8L^{Me}_2](OTf)_4$, which was further reacted with an anhydride (e.g., 3,5-di-*tert*-butylbenzoic anhydride) in combination with a base.

3.8.2 *Excursus* Anhydride Syntheses

For the introduction of a pyridine unit, the isonicotinic anhydride was available and was further used for the synthesis of the respective $[M_8L^{Me}{}_2][Py](PF_6)_4$ rotaxane. However, the introduction of a carboxylic acid group turned out to be more difficult. The anhydride of terephthalic acid was not commercially available and therefore reactions based on literature[97,151] were performed (Figure 71). The reactions A and B yielded brown suspension, which were analysed by ^{1}H NMR spectroscopy and combinations of terephthalic acid, anhydride and polymeric material could be assigned. Further attempts to isolate the desired anhydride were performed by column chromatography and crystallisation, where mixtures of various compounds were still detected. Reaction C yielded the acid chloride, however no further conversion to the anhydride was observed.

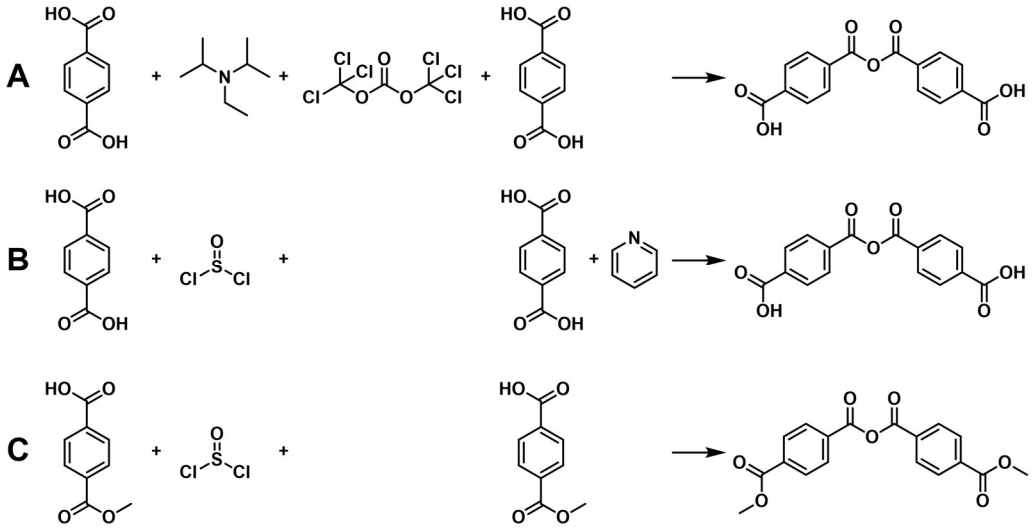

Figure 71: Reaction equations for the formation of anhydrides based on benzoic acid derivatives: (A) Conversion of terephthalic acid with triphosgene and DIPEA as base; (B) Conversion of terephthalic acid with thionyl chloride and pyridine as base; (C) Conversion of 4-(methoxycarbonyl)benzoic acid with thionyl chloride.

Until now, the rotaxane was formed by $[M_8L^{Me}{}_2](C_{12}H_{26}N_2)(X)_4$ bearing the amino group. However, the guest could be changed, and a linear anhydride could be encapsulated into the pillarplex and further converted to a rotaxane by the addition a stopper containing an amino group. To achieve this, the synthesis of a linear anhydride moiety is necessary and possible encapsulation into the pillarplex has to be investigated.

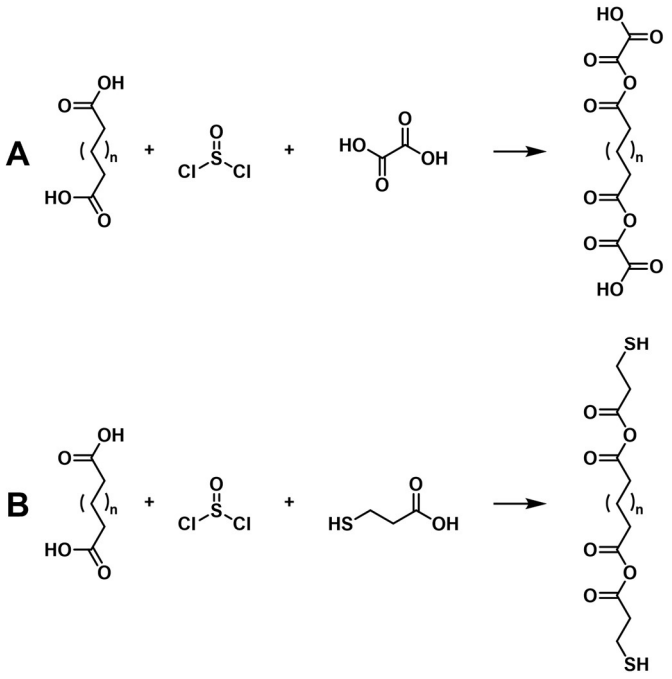

Figure 72: Reaction equations for the formation of anhydrides based on long α,ω-dicarboxylic acids: (A) Conversion of dicarboxylic acid with thionyl chloride and oxalic acid; (B) Conversion of dicarboxylic acid with thionyl chloride and 3-mercaptopropanoic acid.

The two different approaches in Figure 72 were tested with dicarboxylic acid $C_{12}H_{22}O_4$, where small molecule on both sides of the dicarboxylic acid were introduced. Unfortunately, reactions A and B were not successful.

3.8.3 Investigation of Pyridine Pillarplex Rotaxanes

The literature-known[97] route for the rotaxane formation was followed using isonicotinic anhydride. After the encapsulation of the 1,12-diamine dodecane into the cavity, no cooling of the reaction mixture was performed as no beneficial impact was identified for this step. After the isolation and purification of $[Ag_8L^{Me}_2][Py](PF_6)_4$ characterisation with NMR spectroscopy, elemental analysis and ESI mass spectrometry was performed (F72S, F74S). In the ^{1}H NMR spectrum (Figure 73) the encapsulated guest showed the typical upfield shifted broad signals in the region of 3 to -2 ppm. The pyridine signals were slightly shifted in comparison to the reactant and the ratio of integrals fitted the suggested formation of the rotaxane. One singlet signal for the formed imide bond was observed at 7.03 ppm. The solubility of the pyridine-based rotaxane was limited to organic solvents, such as MeCN and DMF. Additionally, the values determined by elemental analysis and the m / Z signals at 557.4807 for $[Ag_8L^{Me}_2][Py]^{4+}$ and 791.6250 for $[Ag_8L^{Me}_2][Py](PF_6)^{3+}$ confirmed the successful synthesis of rotaxane $[Ag_8L^{Me}_2][Py](PF_6)_4$ (F74S). Nevertheless, transmetalation towards the Au(I) congener was performed and the obtained white powder showed even worse solubility. Hence, only ^{1}H NMR spectrum could be measured, where the encapsulated alky chain signals were observed and additionally the shifted pyridine signals (F73S). Again, m / Z signals at 735.6042 for $[Au_8L^{Me}_2][Py]^{4+}$ and 1029.1317 for $[Au_8L^{Me}_2][Py](PF_6)^{3+}$ verified the findings of the ^{1}H NMR spectrum (F74S).

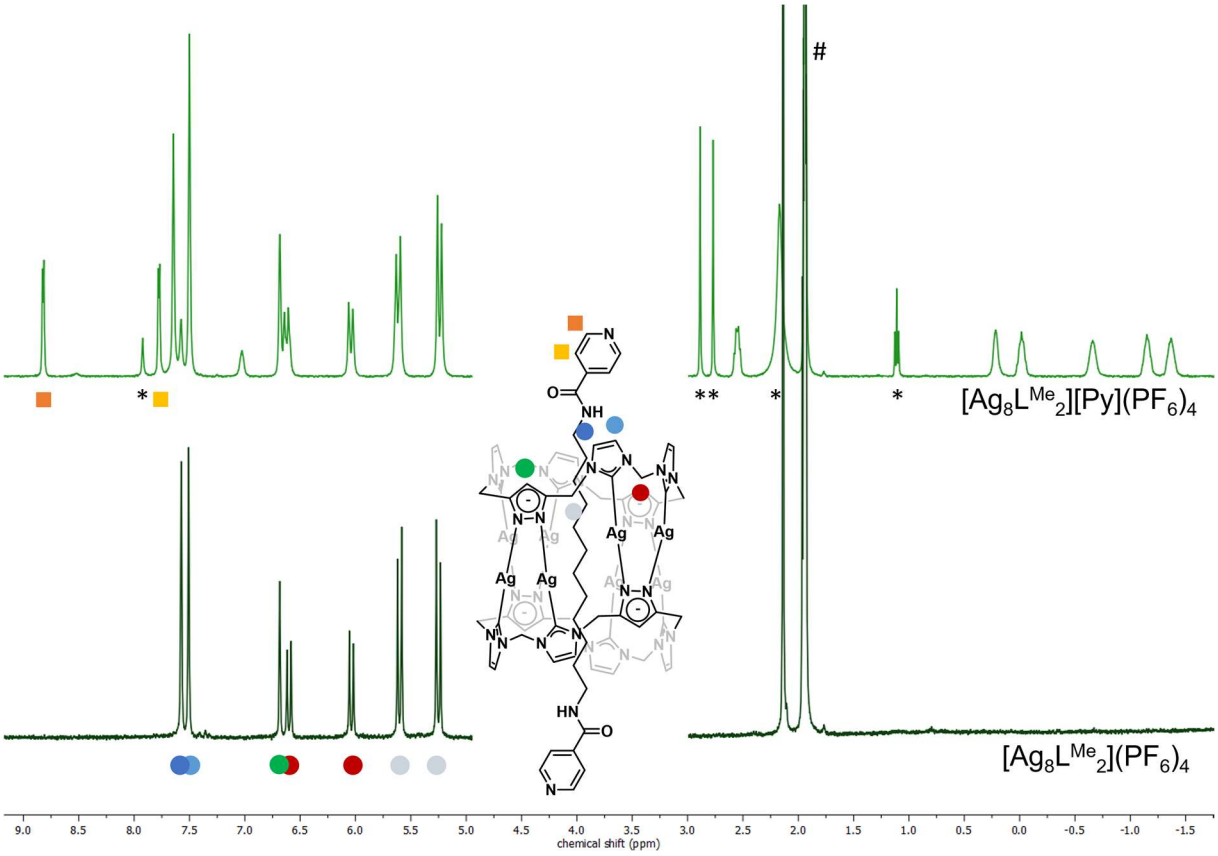

*Figure 73: ^{1}H NMR spectra of $[Ag_8L^{Me}{}_2](PF_6)_4$ and $[Ag_8L^{Me}{}_2][Py](PF_6)_4$ in MeCN-d_3 (1.94 ppm, marked with #) at 298 K. Solvent impurities were marked with * for Et_2O (3.14, 1.11 ppm), H_2O (2.16 ppm) and DMF (7.92, 2.89, 2.77 ppm).*

To determine the crystallinity of the obtained solids, powder X-Ray diffraction measurements were performed, where only small contribution of crystalline material and high contribution of amorphous material was observed. Especially for the $[Au_8L^{Me}{}_2][Py](PF_6)_4$ rotaxane no reflections at low θ angles were detected and again broad reflections at higher angles could indicate the formation of nanocrystalline aggregates (F50S).

Several crystallisation attempts to obtain the structural confirmation of the formed rotaxanes were performed. One approach was the slow diffusion of various ethers (Et_2O, THF) into a saturated solution of the respective pyridine-based rotaxanes in either MeCN or DMF. Another approach was the slow evaporation of the solvent MeCN of a saturated solution of $[Ag_8L^{Me}{}_2][Py](PF_6)_4$, which was provided in a vial and kept at room temperature for several days with an opening. Due to the limited solubility, crystallisation under solvothermal conditions in DMF were attempted. The rotaxanes were provided in three vials, which was airtightly sealed and separately heated to 60 °C, 80 °C or 100 °C for 3 hours. Afterwards, the oven was slowly cooled to room temperature and the vials were inspected. In all attempts no suitable crystals had formed.

Geometry Optimisation by DFT Calculations

As no suitable crystals for the determination of the chemical structure were obtained, geometry optimisation calculations by DFT towards the energetic minimum were performed (Figure 74, for details see Chapter 5.7). As template, the crystal structure of the literature-known rotaxane was used and the stopper units were exchanged to the desired pyridine motifs. Due to the

complexity of the pillarplexes, the estimated geometry optimisation was performed in the gas phase without the presence of counter anions.

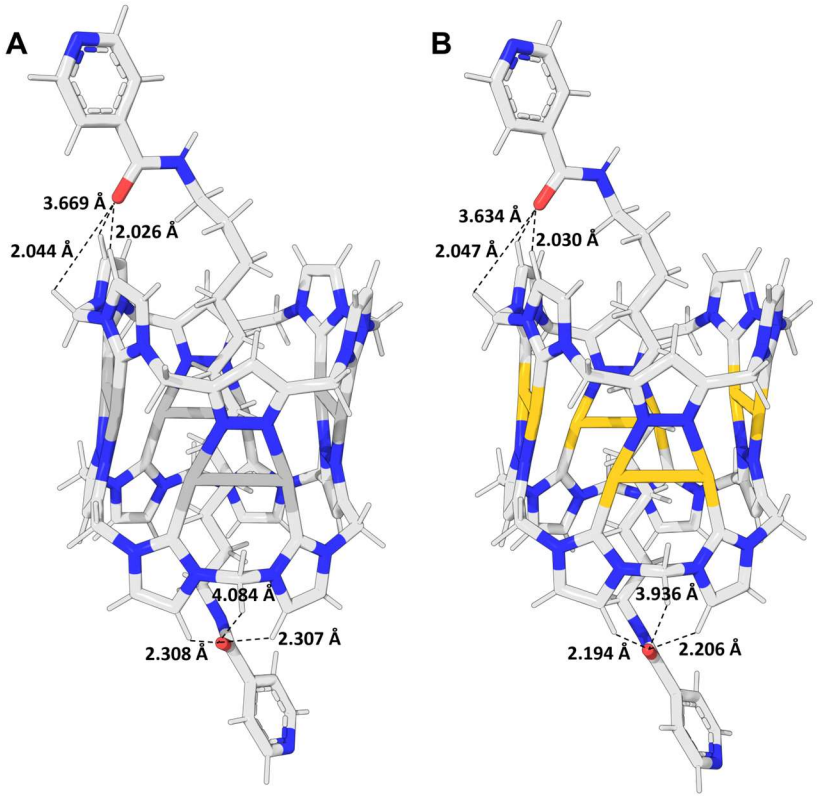

Figure 74: Optimised structures of (A) $[Ag_8L^{Me}{}_2]^{4+}$[Py]; (B) $[Au_8L^{Me}{}_2]^{4+}$[Py] in gas phase displayed with the observed non-covalent interactions between the carbonyl groups and H_{rim}.

As already observed in the crystal structure analysis of the literature-known rotaxane $[M_8L^{Me}{}_2][2]Rot(OTf)_4$[97], the carbonyl oxygen of the imide bond showed classical hydrogen bonding with the hydrogen atoms of the organic rim. It was determined that the carbonyl was pointing towards the small interaction pocket of the pillarplex rim, where two imidazolylidene units are connected by a methylene bridge.

3.8.4 Coordination Attempts with Pyridine Pillarplex Rotaxane

The major challenge for the implementation of $[M_8L^{Me}{}_2][Py](PF_6)_4$ into network is the possibility of transmetalation while using the Ag(I)-based pillarplex and the presence of various counter anions. To circumvent these problems, the further attempts for coordination were performed with the metal precursor Ag-PF_6, where a similar metal ion and similar counter anions were present (for details see Chapter 5.8.4). This strategy was recently used by Sue et al[152], where a pyridine-based compound was subjected to Ag-PF_6 to form larger aggregates. Following this synthesis route, the pyridine-based rotaxane and Ag-PF_6 (2, 3, 4 eq.) were provided in a solvent and the reaction mixture was stirred at room temperature for various hours. Each reaction was divided into two batches, where one batch was kept at room temperature for crystallisation attempts by slow evaporation of the solvent and the other batch was reduced to a solid by solvent removal *in vacuo*. The obtained solids were analysed by ^{1}H NMR

spectroscopy. No conclusive results could be drawn from the collected data and further synthetic approaches and analysis of the formed solids must be performed.

Coordination attempts following the layering method described in Chapter 3.7.2 were performed, where layer A containing the pyridine-based rotaxane in DMF was provided and layer B containing only DMF as well as layer C containing only MeCN as solvent was slowly added on top. As the top layer D, a solution of Ag-PF_6 in MeCN was slowly added and the vials were kept at room temperature for slow mixing and hence crystallisation at the boundary surface.

Additionally, several coordination attempts were performed following a solvothermal synthesis (for details see Chapter 5.8.4) with metal ions (e.g., $Zn(NO_3)_2$) known for their coordination of pyridine units.[153] Due to the steric demand of the $[M_8L^{Me}_2]^{4+}$ cation as ring component, terephthalic acid was added to the reaction mixture acting as pillar molecule (F76S). For these reactions, $[M_8L^{Me}_2][Py](PF_6)_4$ was dissolved in a solvent mixture of DMF:H_2O (4:1) and provided in a vial. As metal precursor $Zn(NO_3)_2$ and $Cd(NO_3)_2$ (2 eq.) were used and either 0.5 or 1 equivalents of terephthalic acid was added. The obtained white suspensions were shaken and placed in an oven. As a higher thermal stability of the rotaxanes was predicted, the temperature maximum for solvothermal conditions was set to 100 °C. After slowly cooling to room temperature, the vials were investigated towards formed precipitate or single crystalline material. Interestingly, a metal mirror was discovered on the side walls of the vials as well as the formation of a black precipitate and a colourless solution. As the formation of the metal mirror indicated that a reduction of at least one metal species has taken place, this solid was not further analysed. Most probably the presence of terephthalic acid led to the decomposition of the Ag(I)-pillarplex forming unstable Ag(I)-species in solution, which are resulted in the metal mirror. The black precipitate was filtered, carefully washed with minimal amounts of Et_2O and subjected to powder X-Ray diffraction measurements, which yielded amorphous material. Most likely, only organic components or pillarplex derivatives were proposed to remain in the colourless solution and hence, the filtrate was concentrated *in vacuo* and analysed by ^{1}H NMR spectroscopy. A complex mixture of signals was observed, where assignment of the macrocyclic ligand signals was possible.

3.8.5 Summary and Outlook

The synthesis of pillarplex rotaxanes $[M_8L^{Me}{}_2][Py](PF_6)_4$ with a pyridine motif incorporated in the stopper unit was aimed and the successful synthesis was indicated by NMR spectroscopy, ESI mass spectrometry and elemental analysis. The synthesised $[M_8L^{Me}{}_2][Py](PF_6)_4$ rotaxanes must be further analysed, especially towards their structural composition by either SC-XRD or micro-ED measurements.

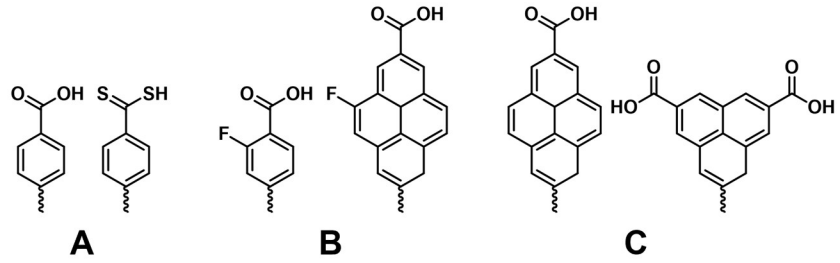

Figure 75: Molecular structures of potential stopper units, which can be evaluated towards the implementation into pillarplex rotaxanes: (A) Benzoic acid / benzothioic acid; (B) Fluorinated benzoic acid / fluorinated pyrene-2-carboxylic acid; (C) Pyrene-2-carboxylic acid / phenalene-2,5-dicarboxylic acid.

The scope of introduced functionalities can be broadened, starting with the investigation towards carboxylate or thiocarboxylate units (Figure 75A). As the solubility of the synthesised pyridine-based rotaxanes was limited, the introduction of substituents (e.g., fluorinated substituents, Figure 75B) at the rotaxane stopper units could be beneficial to increase the solubility of the formed rotaxanes. However, expanding the size of the stopper molecules by the introduction of a larger aromatic system could be beneficial due to steric reasons. Especially, when further implementation of the rotaxane into network materials is planned, the enhanced distance of the ligand unit embedded in the stopper unit to the pillarplex cation could be beneficial. Additionally, the geometric parameters for further coordination attempts could be changed and stopper molecules containing two or more functional groups (e.g., bis- or tris-carboxylates, Figure 75C) could be introduced into the pillarplex rotaxane system.

Further investigation of the coordination attempts has to be performed, especially the combination of $[Au_8L^{Me}{}_2][Py](PF_6)_4$ rotaxane with Ag-PF_6 as metal precursor seemed to be promising. Until now, these reactants were only combined at room temperature, where no reaction was observed. However, with the predicted higher thermal stability of rotaxanes the coordination attempts can be repeated at higher temperatures to possibly form 1D chains containing $[Au_8L^{Me}{}_2]^{4+}$ as ring component. When implementing the pillarplex into extended structures, the steric demand of $[M_8L^{Me}{}_2]^{4+}$ cations and the four counter anions for each pillarplex cation must be considered. The introduction of pillar molecules, which exhibit less steric demand than the pillarplexes, could ensure enough space to arrange pillarplex cations in network materials. Hence, while working towards more dimensional networks with $[M_8L^{Me}{}_2]^{4+}$ as ring component, the addition of pillar molecules must be investigated and evaluated towards the influence of length and rigidity of the aromatic system of these pillar molecules.

3.9 Photochemistry of Au(I)-Pillarplexes and Pillarplex Rotaxanes Containing *N*-naphthalimide as (Photo-)Active Unit

This chapter is partially based on the bachelor thesis of Felix Suttor and the research internship of Markus Plagmann and Elisabeth Springl, which were supervised by this author.

3.9.1 Introduction

The $[Au_8L^{Me}_2](X)_4$ pillarplex was already analysed towards its luminescence in solution and in solid-state, reporting an emission maximum located at 430 nm (λ_{max} = 335 nm) for $[Au_8L^{Me}_2](PF_6)_4$ in the solid-state and a quantum yield of 40%. Interestingly, the influence of guest encapsulation on the emission was theoretically rationalised.[109] Upon guest encapsulation a quenching of the emission was detected. This was explained as for a free $[Au_8L^{Me}_2]^{4+}$ cation the calculated T_1 state geometry exhibits a variation parameter for the Au(I)-Au(I) distances. Compared to the ground state, the excited state shows small contraction, which are hindered due to the formation of a host-guest complex. For the excited state T_1 of the host-guest complex no contractions of the Au(I)-Au(I) distances were calculated indicating a limited structural flexibility since the guest hinders the contractions. Hence, it is postulated that the structural flexibility is necessary for exhibiting emission as the excited state T_1 decays into ground state S_o by Au(I)-Au(I) distance shortening upon excitation. Therefore, guest quenching by steric hinderance was identified. Additionally, the emission process was dependent on the solvent, as in MeCN a quenching of emission was identified, which is explained by the capability of MeCN as solvent to enter the pillarplex cavity. In water emission was detected as the hydrophobic nature of the pillarplex cavity hinders the encapsulation of water.

Au(I) complexes show photoluminescence due to strong aurophilic interactions between Au(I)-Au(I) interactions and Au(I)-π interactions.[154-158] However, comparing the photoluminescence in solution and in the solid-state, the emission is strongly influenced by the concentration. Aggregates of complexes exhibit stronger emission efficiency at the same wavelength than the respective single molecule, which is described as AiE – aggregation induced emission[159-161].

To further understand the photophysical properties, the solvent dependency and the possibility of aggregation induced emission of $[Au_8L^{Me}_2](X)_4$ must be investigated (Figure 76). With various counter anions the solubility of pillarplex salts can be varied with $[Au_8L^{Me}_2](PF_6)_4$ being soluble in MeCN, $[Au_8L^{Me}_2](OTf)_4$ being soluble in MeCN and water and $[Au_8L^{Me}_2](OAc)_4$ being soluble in H_2O. Through addition of a less polar solvent (e.g., Et_2O or acetone) the respective pillarplex salt can be precipitated. The pillarplex salts were provided in different ratios of solvent mixtures to possibly achieve aggregation.

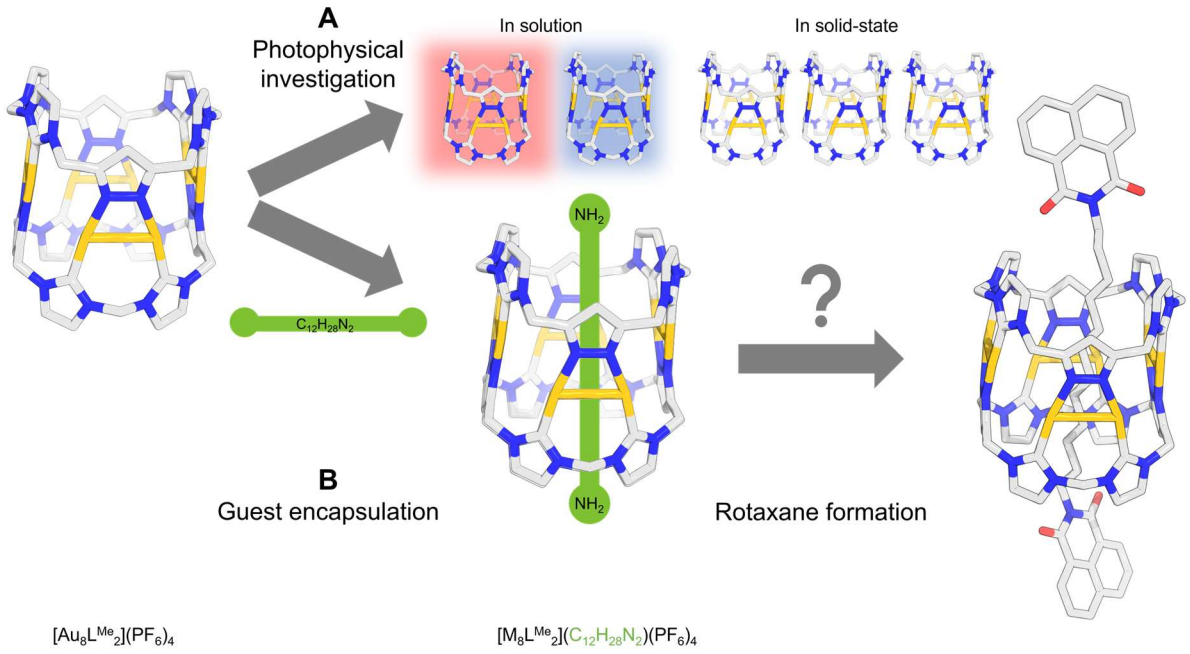

Figure 76: Overview of the (A) Photophysical investigation of $[Au_8L^{Me}{}_2](X)_4$ pillarplex salts in solution and in the solid-state; (B) Targeted guest encapsulation of 1,12-diamino dodecane with further conversion to form a pillarplex rotaxane. By choosing naphthalic anhydride derivatives as stopper motifs, chromophores are introduced into the pillarplex system.

The pillarplex $[Au_8L^{Me}{}_2](X)_4$ shows intrinsic luminescence and can act as host component for the formation of mechanically interlocked molecules. By organisation of the compounds in a MIM the relative position of the donor and acceptor groups for a photoinduced charge transfer within a MIM in principle can be achieved, as shown in perylenediimide-pillar[5]arene rotaxanes.[162] A naphthalene based moiety is targeted to be introduced as stopper moiety into the pillarplex system and tested towards the possibility of photoinduced charge transfer inside the synthesised MIM and hence the applicability of this system (Figure 76).[163-166]

3.9.2 Photophysical Investigation of $[M_8L^{Me}_2](PF_6)_4$

The literature-known pillarplex salts $[Ag_8L^{Me}_2](PF_6)_4$ and $[Au_8L^{Me}_2](PF_6)_4$ were analysed towards their photophysical properties, starting with the determination of the molar absorption coefficient ε *via* UV-vis spectroscopy. Therefore, four stock solutions with specific concentrations were prepared and investigated *via* UV-vis spectroscopy in order to determine their absorption maxima (Figure 77A+C). By linear regression of the absorption maxima at different concentrations, the coefficients $\varepsilon = 0.966 \cdot 10^{-2}$ mol cm^{-2} for $[Ag_8L^{Me}_2](PF_6)_4$ and $\varepsilon = 1.065 \cdot 10^{-2}$ mol cm^{-2} for $[Au_8L^{Me}_2](PF_6)_4$ were calculated (Figure 77B+D).

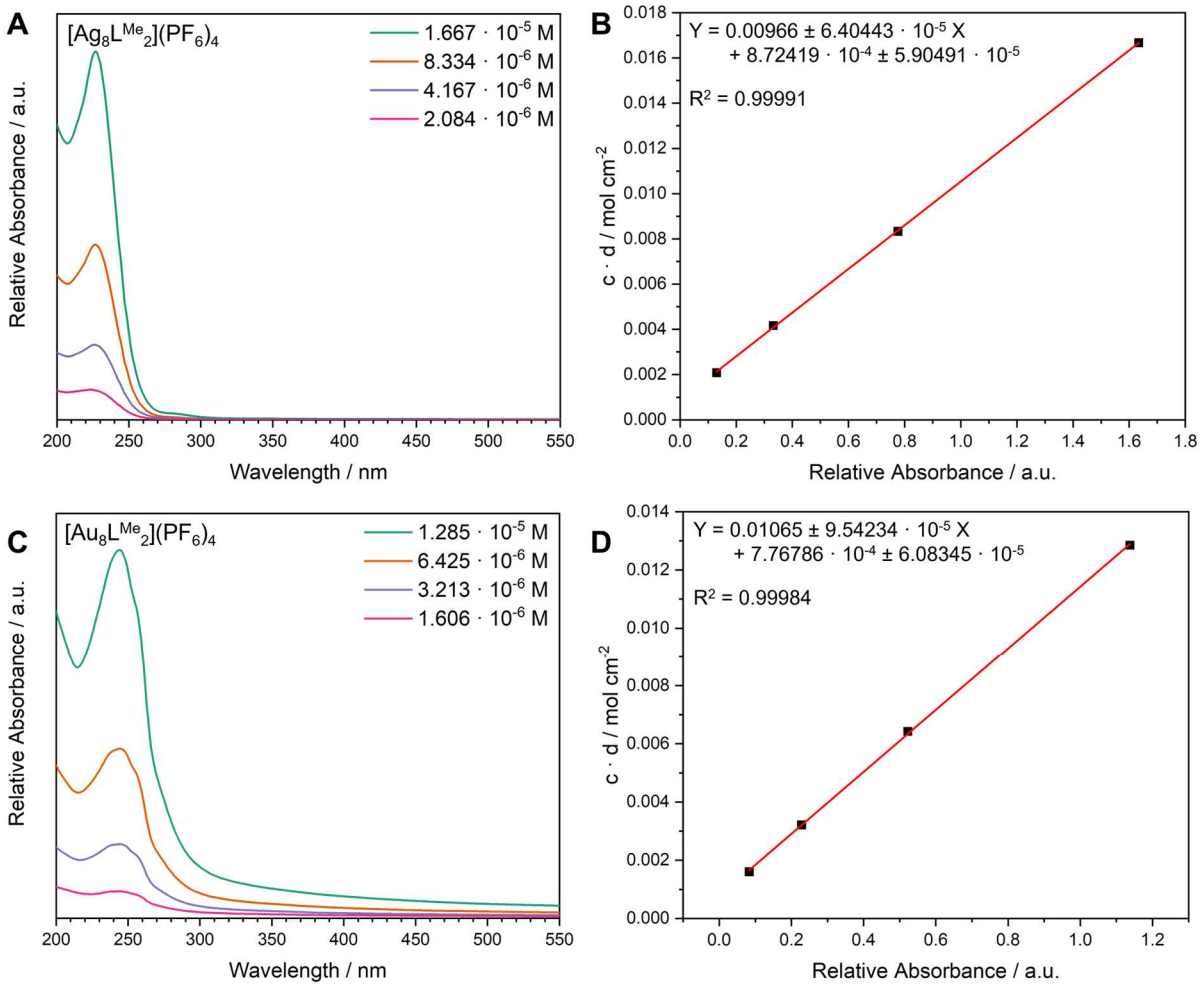

Figure 77: (A) UV-vis spectra of $[Ag_8L^{Me}_2](PF_6)_4$ (MeCN, 298 K) with specified concentrations; (B) Calculation of the extinction coefficient $\varepsilon = 0.966 \cdot 10^{-2}$ mol cm^{-2} by linear regression at absorption $\lambda = 243.98804$ nm of $[Ag_8L^{Me}_2](PF_6)_4$; (C) UV-vis spectra of $[Au_8L^{Me}_2](PF_6)_4$ (MeCN, 298 K) with specified concentrations; (D) Calculation of the extinction coefficient $\varepsilon = 1.065 \cdot 10^{-2}$ mol cm^{-2} by linear regression at absorption $\lambda = 243.98804$ nm of $[Au_8L^{Me}_2](PF_6)_4$.

Moreover, the dependency of solvent induced aggregation of the $[Au_8L^{Me}_2](PF_6)_4$ pillarplex and the possible influence of the induced aggregation towards the photophysical properties was investigated. Hence, stem solutions of $[Au_8L^{Me}_2](PF_6)_4$ in various MeCN:Et_2O ratios were prepared. With an elevated ratio of Et_2O in the solvent mixture, the solubility of the pillarplex salt decreased and the formation of aggregates increased as the overall concentration was kept constant. UV-vis and emission spectroscopy were measured and examined for their

maxima. The obtained data were then analysed towards a possible correlation between the solvent ratios and their photophysical properties (Table 7).

Table 7: Data obtained from UV-vis, emission spectroscopy and DLS measurements of $[Au_8L^{Me}_2](PF_6)_4$ for the specific solvent mixtures (c = 6.425 · 10^{-6} M): Absorption maxima λ_{max} [nm], average size of aggregates [nm].

MeCN:Et_2O	Absorption λ_{max} [nm]	Emission λ_{max} [nm]	Size [nm]
10:0	235	391	61.9
9:1	239	391	63.5
8:2	239	392	43.8
7:3	239	385	45.1
6:4	240	401	46.4
5:5	241	407	43.8
4:6	241	407	43.8
3:7	244	412	46.1
2:8	249	414	19.6
1:9	252	414	48.4
0:10	261, 286	398	255-531

To evaluate a potential dependency of the formation of larger aggregates on the added amount of Et_2O in the respective solutions, dynamic light scattering experiments were performed. However, no clear correlation between the size of the aggregates and the solvent mixtures could be determined in DLS measurement. For the solvent ratio 0:10 (MeCN:Et_2O) a suspension of $[Au_8L^{Me}_2](PF_6)_4$ was provided, which identified the formation of large aggregates with sizes of 255 nm – 531 nm. This outcome was anticipated given that the pillarplexes containing PF_6^- as counter anions is insoluble in Et_2O.

The UV-vis absorption spectra were analysed with the focus on their maxima at λ_{max}. In pure MeCN, a broad signal with the highest peak at 235 nm was observed. The solvent ratios of 9:1, 8:1 and 7:3 exhibited a similar pattern, with the absorption maxima recorded at 239 nm. Subsequent solvent ratios displayed slight bathochromic shifts of the maxima, with a more pronounced shift detected for the solvent ratio 2:8. Since no solubility of $[Au_8L^{Me}_2](PF_6)_4$ in Et_2O could be achieved, this absorption spectrum was measured in the solid-state, revealing two maximal signals at 261 nm and 286 nm. Overall, a bathochromic shift of the absorption maximum with increasing amount of Et_2O in the solvent mixtures a was detected (Figure 78A).

As known from photophysics, there is a strong correlation between the absorption and the excitation spectra. Therefore, the wavelength of the absorption maxima were utilised as excitation radiation for the luminescence experiments. Again, the excitation spectra were examined with respect to their maxima at λ_{max}. In the cases of solvent ratios 10:0 and 9:1, comparable maxima were identified at 391 nm. However, a marginal shift to 392 nm was observed for the 8:2 solvent ratio. With an excitation maximum at 385 nm, the excitation spectrum of $[Au_8L^{Me}_2](PF_6)_4$ in solvent ratio 7:3 can be considered an outlier. The maximum at 401 nm for the solvent ratio 6:4 falls within the anticipated range. With increasing amount of Et_2O in the solvent mixture, the maxima shift towards longer wavelengths. However, the excitation spectrum labelled with the solvent ratio 0:10 was measured in the solid-state, where a hypsochromic shift towards the shorter wavelengths of 398 nm was observed. Similar to the absorption experiments, an overall bathochromic shift of the excitation maxima with increasing amount of Et_2O in the solvent mixtures was concluded (Figure 78B). These findings align with the principles of photophysics as the absorption maxima were utilised as excitation wavelengths, leading to a corresponding shift in the excitation maxima.

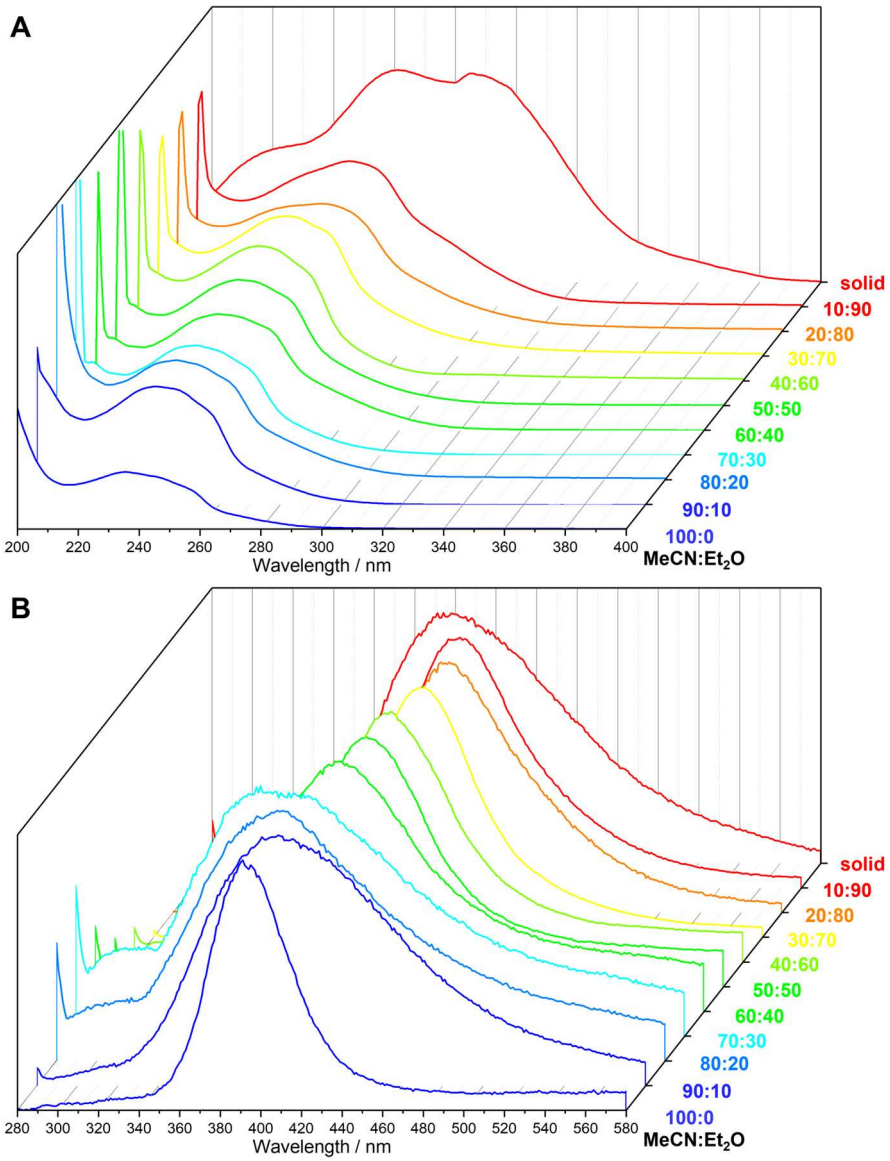

Figure 78: (A) Stacked UV-vis absorption spectra of $[Au_8L^{Me}_2](PF_6)_4$; (B) Stacked excitation spectra of $[Au_8L^{Me}_2](PF_6)_4$ with specified solvent ratios (c = 6.425 · 10^{-6} M).

The slight bathochromic shift observed in both absorption and excitation maxima concerning the solvent ratios can be attributed to either intramolecular motion or intermolecular interactions. The formation of pillarplex aggregates is anticipated with an increased amount of Et_2O. Additionally, intramolecular motions become more progressively constrained within these aggregates, even in the solid-state.[160] However, intermolecular interactions are normally stronger when molecules are embedded into an aggregate or solid arrangement.[161,167-168] For $[Au_8L^{Me}_2]^{4+}$ intermolecular interactions were already analysed in crystal arrangements (see Chapter 3.1.4) and besides hydrogen bonding, in particular Au(I)-Au(I) coordination was discovered. The observed bathochromic shift of the absorption and excitation maxima might therefore be explained by the enhanced intermolecular interaction (e.g., Au(I)-Au(I), π-π stacking) of $[Au_8L^{Me}_2](PF_6)_4$ upon formation of aggregates.[168]

3.9.3 *Excursus* Problems of Nanoparticle Presence in $[Au_8L^{Me}_2](X)_4$

During the synthesis of $[Au_8L^{Me}_2](PF_6)_4$ an exclusion of light is necessary due to the presence of Au(I) ions. Although light was excluded, during the transmetalation of $[Ag_8L^{Me}_2](PF_6)_4$ to $[Au_8L^{Me}_2](PF_6)_4$ a colour change from white to purple was monitored, which can indicate the formation of gold nanoparticles or aggregates of pillarplex cations. Nevertheless, the pillarplex was isolated and purified to yield a purple solid. To differentiate between nanoparticles and aggregates, the amount of gold was determined by elemental analysis. For aggregates of pillarplexes a mass fraction of 50.62% is calculated, while a higher value is predicted for nanoparticles. Indeed, an elevated mass fraction (64%) was detected most likely resulted by the presence of nanoparticles. Two different approaches for the removal of the formed nanoparticles were applied.

The first approach was the removal of nanoparticles by filtration. Therefore, $[Au_8L^{Me}_2](PF_6)_4$ was dissolved in MeCN and either filtered through a syringe filter or over Celite®. The obtained filtrate still showed a purple colouration indicating that the removal was not effective. The second approach was dissolving the pillarplex $[Au_8L^{Me}_2](PF_6)_4$ in MeCN followed by a centrifugation. Also, this approach did not lead to a complete purification of the raw product, as the solid was still purple after reprecipitation in Et_2O. Additionally, the same method was used for $[Au_8L^{Me}_2](OAc)_4$, which was synthesised through an anion exchange reaction from $[Au_8L^{Me}_2](PF_6)_4$. Unfortunately, even after precipitating white $[Au_8L^{Me}_2](PF_6)_4$ species, the subsequent anion exchange reaction led to the formation of a purple solid. As $[Au_8L^{Me}_2](OAc)_4$ was obtained as purple solid, investigations on the formation of the purple colour must be performed, as the colouration again could either originate in the presence of nanoparticles, which were stabilised by acetate anions, or due to crystal arrangement towards larger aggregates in the solid-state. By UV-vis spectroscopy the differences between the white solids and the purple solids have to be elucidated.

Since the $[Au_8L^{Me}_2](PF_6)_4$ pillarplex could be achieved as a white solid, the formation of nanoparticles can likely be hindered by storage of respective Au(I) compounds at low temperatures (-30 °C) and under the strict exclusion of light.

3.9.4 Synthesis of (Photo-)Active Pillarplex Rotaxanes

In the following chapter, the synthesis of rotaxane containing chromophores in the stopper unit and the investigation of their photophysical properties was aimed. As targeted chromophore moiety 1,8-naphthalic anhydride and 1,4,5,8-naphthalenetetracarboxylic dianhydride were chosen and their further implementation into the pillarplex system was performed following literature-known synthetic routes (Figure 80).[97,169-171]

The first approach started with the encapsulation of 1,12-diamino dodecane offering reactive functional groups on both sides of the pillarplex as ring component, where imide formation with the 1,8-naphthalic anhydride was achieved (Figure 80A).[172] The pillarplex salts $[Ag_8L^{Me}{}_2](PF_6)_4$ in MeCN and $[Ag_8L^{Me}{}_2](OTf)_4$ in EtOH were tested for the rotaxane formation. After the addition of 1,12-diamino dodecane, the reaction mixture was stirred at room temperature for several minutes to ensure full encapsulation of the guest molecules. Then, 1,8-naphthalic anhydride was added and the reaction mixture was stirred at 50 °C overnight and afterwards cooled to room temperature. All volatiles were removed *in vacuo* and a white solid was obtained. This white solid was redissolved in EtOH or MeCN and precipitated in Et_2O, dried *in vacuo* and analysed *via* ^{1}H NMR spectroscopy. The respective rotaxane $[Ag_8L^{Me}{}_2][NMI\text{-}C_{12}](PF_6)_4$ (NMI = *N*-naphthalene monoimide, C_{12} = dodecane alky chain) showed slight shifts of the proton signals in the ^{1}H NMR spectrum (Figure 79) and coupling between the NMI moiety and the pillarplex proton signals in 2D NMR spectroscopy.

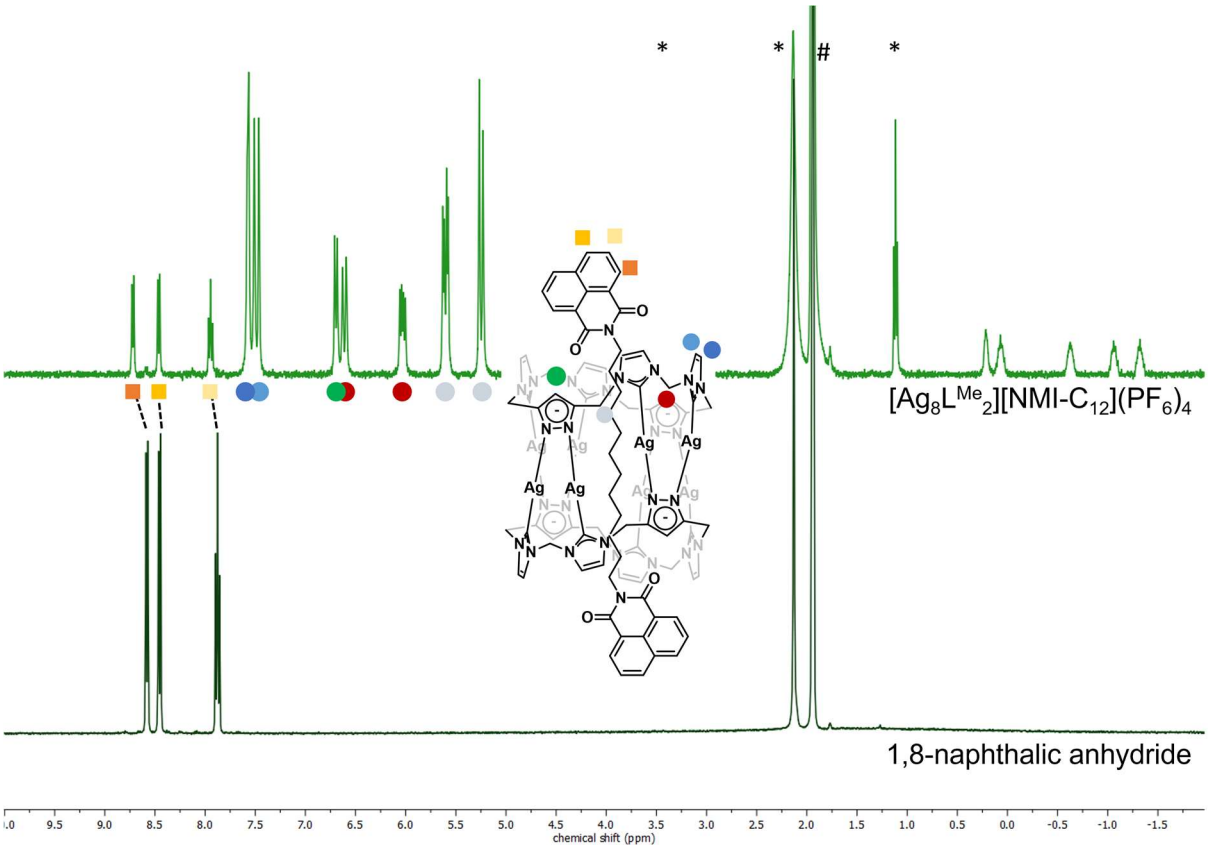

*Figure 79: ^{1}H NMR spectra of 1,8-naphthalic anhydride and $[Ag_8L^{Me}{}_2][NMI\text{-}C_{12}](PF_6)_4$ in MeCN-d_3 (1.94 ppm, marked with #) at 298 K. Solvent impurities were marked with * for Et_2O (3.14, 1.11 ppm) and H_2O (2.16 ppm).*

For the reaction of $[Ag_8L^{Me}{}_2](OTf)_4$ with 1,12-diamino dodecane and 1,8-naphthalic anhydride the proton signals shifted and the 2D NMR spectroscopy showed a coupling between the

stopper moieties and the pillarplex cation. Crystallisation attempts were performed by providing saturated solutions of the desired rotaxanes $[Ag_8L^{Me}{}_2][NMI\text{-}C_{12}](PF_6)_4$ in MeCN and $[Ag_8L^{Me}{}_2][NMI\text{-}C_{12}](OTf)_4$ in EtOH in NMR tubes. These NMR tubes were placed in a Schlenk flask filled with THF and slow diffusion of THF into the saturated solution of rotaxane was performed to achieve suitable crystals for SC-XRD measurements. Until now, suitable crystals could not be obtained and hence the structural analysis cannot validate the formation of the respective rotaxanes.

When introducing the stopper moiety 1,4,5,8-naphthalenetetracarboxylic dianhydride reactivity on both sides was available and by introduction of dodecane-1-amine or 1,12-diamino dodecane on these positions the molecules *N,N'*-(1-dodecyl)-1,4,5,8-naphthalene tetracarboxydiamide or *N,N'*-(12-aminododecyl)-1,4,5,8-naphthalenetetracarboxydiamide[169] could be synthesised (Figure 80B). Here, the naphthalene unit was located between two alky chains, which offer the possibility to act as a guest molecule to form (pseudo-)rotaxanes containing two $[M_8L^{Me}{}_2]^{4+}$ cations as ring components[169-170]. However, the synthesised molecules showed limited solubility in H_2O and organic solvents (DMF, DMSO, MeCN). Still *N,N'*-(12-aminododecyl)-1,4,5,8-naphthalenetetracarboxydiamide was combined with the PF_6^- and the OTf^- pillarplex salt in order to investigate if the formation of the respective pseudorotaxanes was successful. ^{1}H NMR spectroscopy suggested the formation of the pseudorotaxanes by upfield shifting of the proton signals of the alkyl chains. The encapsulation of *N,N'*-(1-dodecyl)-1,4,5,8-naphthalenetetracarboxydiamide as guest molecule was investigated with the $[Ag_8L^{Me}{}_2](OTf)_4$ pillarplex, where again the proton signals again suggested the successful formation of the respective pseudorotaxane $[Ag_8L^{Me}{}_2]_2(NDI\text{-}C_{12})(OTf)_4$ (C_{12} = dodecane alky chain). For both compounds purification must be performed, the solubility tested, and further characterisation methods must be applied to strengthen the suggestion that the pseudorotaxanes were formed. Especially, for structural evaluation suitable crystalline material must be obtained either to perform SC-XRD or micro-ED measurements.

The pseudorotaxane $[Ag_8L^{Me}{}_2]_2(NDI\text{-}C_{12}NH_2)(OTf)_4$ ($C_{12}NH_2$ = 12-aminododecane alky chain) containing *N,N'*-(12-aminododecyl)-1,4,5,8-naphthalene tetracarboxydiamide as guest molecule offered the terminal $-NH_2$ groups for further formation of a rotaxane. Following the literature-known synthesis route[97] for the formation of a pillarplex rotaxanes, the pseudorotaxane was provided in EtOH and 3,5-di*tert*-butyl benzoic anhydride (3 eq.) and DIPEA (6 eq.) were added. After stirring the reaction mixture at room temperature overnight, filtration over Celite® was performed and an oily substance was precipitated by the addition of an excess of Et_2O. The oily substance was washed with Et_2O and subsequently dried *in vacuo.* ^{1}H NMR spectroscopy was performed to confirm the formation of the respective rotaxane. No conclusive results could be drawn from the obtained silent ^{1}H NMR spectra and hence further investigation on the rotaxane formation must be performed. The formed rotaxane (Figure 80B) as well as the reactants *N,N'*-(1-dodecyl)-1,4,5,8-naphthalene tetracarboxydiamide and *N,N'*-(12-aminododecyl)-1,4,5,8-naphthalenetetracarboxydiamide showed limited solubility. To overcome this problem, the introduction of functional groups (e.g., fluorinated substitutes) might lead to an increase of the solubility.

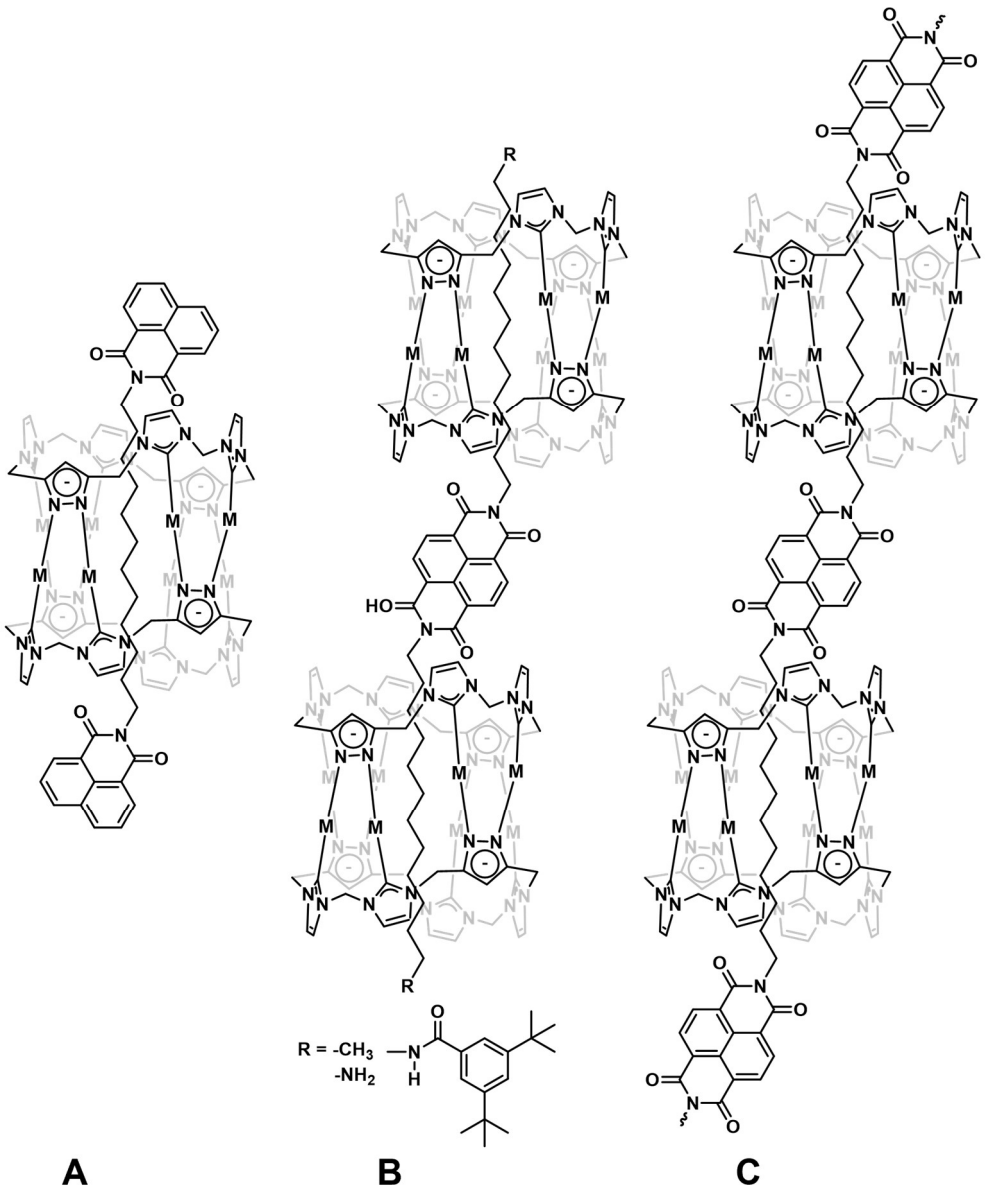

Figure 80: Chemical structures of the targeted rotaxanes (A) $[Ag_8L^{Me}{}_2][NMI](X)_4$ formed with 1,8-naphthalic anhydride, (B) $[Ag_8L^{Me}{}_2]_2[NDI\text{-}R_2](X)_4$ with NDI = naphthalene diimide and R = C_{12} or $C_{12}NH_2$; (C) Polymeric 1D chains of $[Au_8L^{Me}{}_2]^{4+}$ formed with 1,12-diamino dodecane and 1,4,5,8-naphthalenetetracarboxylic dianhydride.

Additionally, 1,4,5,8-naphthalenetetracarboxylic dianhydride could be used to potentially form polymeric 1D chains as seen in Figure 80C.[171] This implementation of the pillarplex as ring component in an organic network material was tested by dissolving $[Ag_8L^{Me}{}_2](OTF)_4$ and 1,12-diamino dodecane in a solvent mixture of EtOH:toluene. The dianhydride (2 eq.) was added and the reaction mixture heated to 80 °C for several hours. After removal of the solvent a dark red solid was obtained, which showed no solubility in all tested solvents for evaluation by ^{1}H NMR spectroscopy.

3.9.5 Summary and Outlook

The $[Au_8L^{Me}_2](PF_6)_4$ pillarplex was examined towards a possible solvent induced aggregation and the influence of aggregation towards the photophysical properties. Therefore, UV-vis and emission spectroscopy was measured in varying solvent ratios (MeCN:Et_2O), where a bathochromic shift of absorption and excitation maxima was identified. These observations could be elucidated by the argument of intermolecular interactions, in particular Au(I)-Au(I) coordination, which is contingent upon the formation of pillarplex aggregates in the presence of higher quantities of Et_2O.

Additionally, the pillarplex $[Au_8L^{Me}_2](OAc)_4$ has to be analysed towards its photophysical properties. First, purification must be achieved either by direct formation of pure, white $[Au_8L^{Me}_2](OAc)_4$ pillarplex or by the removal of the nanoparticles, which are formed during synthesis. Afterwards, the UV-vis spectroscopy, fluorescence spectroscopy and DLS measurements must be performed for $[Au_8L^{Me}_2](OAc)_4$ in the solvent mixture H_2O:acetone in the ratios 10:0 to 0:10. The solvent mixture was chosen based on the high solubility of the acetate pillarplex in water and the precipitation behaviour by the addition of acetone. Additionally, SAXS measurements can be performed for these samples as the use of the machine was limited to aqueous solutions containing only a minimal amount of organic solvent. Therefore, the SAXS measurements of $[Au_8L^{Me}_2](OAc)_4$ in pure H_2O and in the solvent ratios 9:1 and 8:2 (H_2O:acetone) can be conducted. The pillarplex $[Au_8L^{Me}_2](OTf)_4$ can also be characterised towards its photophysical properties. Due to the solubility of $[Au_8L^{Me}_2](OTF)_4$ in water and in MeCN, this pillarplex can be examined in both solvent mixtures (MeCN:Et_2O and H_2O:acetone) and a potential solvent-dependency can be investigated.

The investigation of (photo-)active pillarplex (pseudo)rotaxanes is still in the early stages. Although the successful formation of $[Ag_8L^{Me}_2][NMI\text{-}C_{12}](PF_6)_4$ and $[Ag_8L^{Me}_2][NMI\text{-}C_{12}](OTf)_4$ was indicated by NMR spectroscopy and mass spectrometry, crystallisation attempts must be performed to obtain single crystals for SC-XRD measurements. The pseudorotaxanes $[Ag_8L^{Me}_2][NMI\text{-}C_{12}](PF_6)_4$ (R = CH_3, NH_2) and rotaxane $[Ag_8L^{Me}_2]_2[NDI\text{-}NHCO\text{-}t\text{BuPh}](OTf)_4$ were only subjected to ^{1}H NMR spectroscopy. Due to their restricted solubility, a poor signal-to-noise ratio was obtained, and no conclusions could be derived from the acquired data. Nevertheless, all synthetic attempts must be repeated to gain a deeper understanding regarding the formation and purification of the desired (pseudo)rotaxanes. Afterwards, evaluation of the chemical composition and structural investigation by SC-XRD or micro-ED must be carried out. To overcome the observed limited solubility, substituents could be introduced at the NMI or NDI moiety (e.g., fluoride, chloride). Full characterisation of the respective Ag(I)-based compound has to be performed and furthermore, the transmetalation reaction to form the Au(I) congeners must be examined. As the introduced NMI or NDI unit can act as chromophores, the photophysical characterisation of the (pseudo)rotaxanes has to be analysed towards a potential influence by the introduced stopper motifs.

3.10 Supramolecular Re-Arrangements

This chapter is partially based on the master thesis of Tom Calmus and the research internship of Lukas Sippach, which were supervised by this author.

3.10.1 Introduction

Group 11 metal(I) complexes have attracted attention due to their structural diversity and their possibility to self-assemble into supramolecular structures.[173] With template-directed synthesis new porous materials with novel topologies can be built, where the pore size, volume and shape can be controlled through the selection of a suitable template.[174] After the successful assembly of a supramolecular architecture the template can either be removed or left within the pores.[175]

Several MIMs are synthesised by a passive templating effect of metal cations, where the coordination of the metal ion to the reactants leads to the folding and threading due to the presence of several interaction sites.[176-178] The active templating effect promotes the arrangement of the building unit and the formation of a covalent bond in order to introduce the mechanic bond into the system.[179] Besides metallic templates, a broad diversity of organic templates can be chosen bearing different functional groups, which form non-covalent interactions for the pre-arrangement of building units and further conversion to the desired supramolecule.[180] Additionally, when a template is acting as a guest molecule, the in-built properties and functionalities can strongly influence the properties of the desired supramolecule. This would influence the applicability towards host-guest interactions, catalytic activity and photoactivity of the MIMs.[174] Suitable templates can be solvent molecules (organic, ionic liquids), organic compounds bearing functional groups, metalorganic compounds (e.g., metalloporphyrine), inorganic compounds (small gases, halogens) or surfactants.[174]

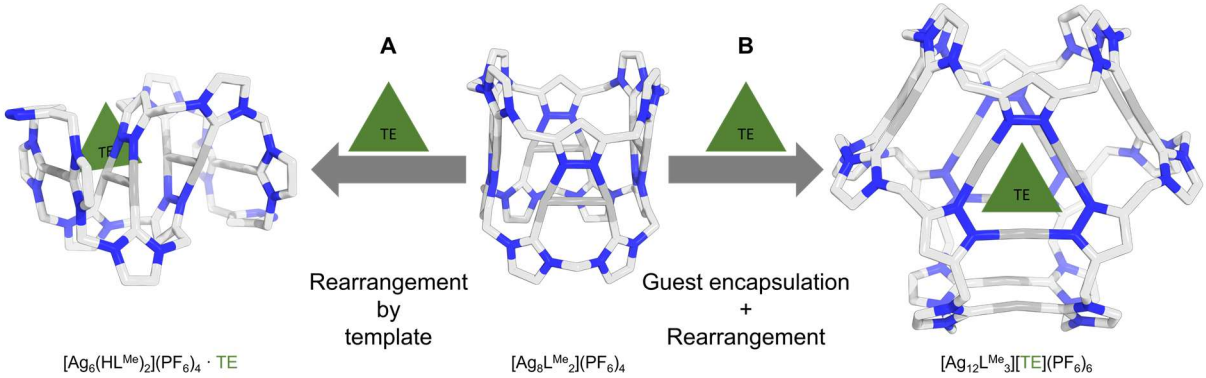

Figure 81: Overview of the re-arrangements of $[Ag_8L^{Me}_2](PF_6)_4$ with template (TE): (A) S-shaped complex $[Ag_6(HL^{Me})_2](PF_6)_4 \cdot TE$; (B) Trillarplex $[Ag_{12}L^{Me}_3][TE](PF_6)_6$.

By using appropriate templates, novel supramolecular assemblies can be built with the macrocyclic ligand $L^{Me}(PF_6)_4$ or the pillarplex $[Ag_8L^{Me}_2](PF_6)_4$ that could not be synthesised directly (Figure 81). Adjustments on the bulkiness of the rim opens up square-planar, tetrahedral or octahedral coordination geometries deviating from the already known linear coordination observed in the pillarplexes.[173]

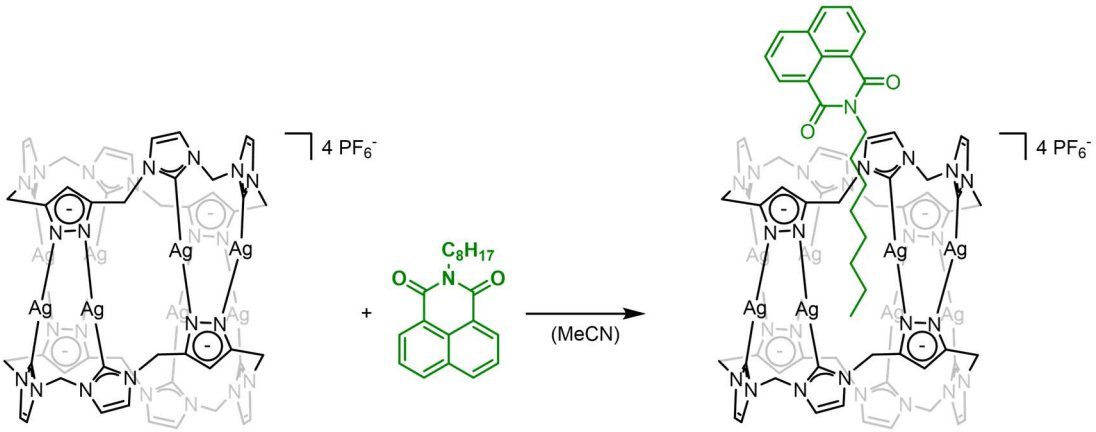

Figure 82: Synthesis route for the formation of a semi-rotaxane $[Ag_8L^{Me}{}_2][NONI](PF_6)_4$ with pillarplex $[Ag_8L^{Me}{}_2](PF_6)_4$ and N-octyl naphthalimide (NONI).

An interaction of a guest molecule with the metal ions inside the cavity was triggered by introducing a guest molecule, which was bearing a stopper unit on one side and an alky chain at the other side with a potential functionality (e.g., ketone, aldehyde, acid). The length of the alkyl chain must be varied to determine whether there is a forced interaction with the functional group in the inner vicinity of the metal ions (e.g., Ag(I) and Au(I)). To make sure, that the alkyl chain comes into proximity to the metal ions, first synthesis attempts were performed with *N*-octyl naphthalimide (*N*ONI) (Figure 82).

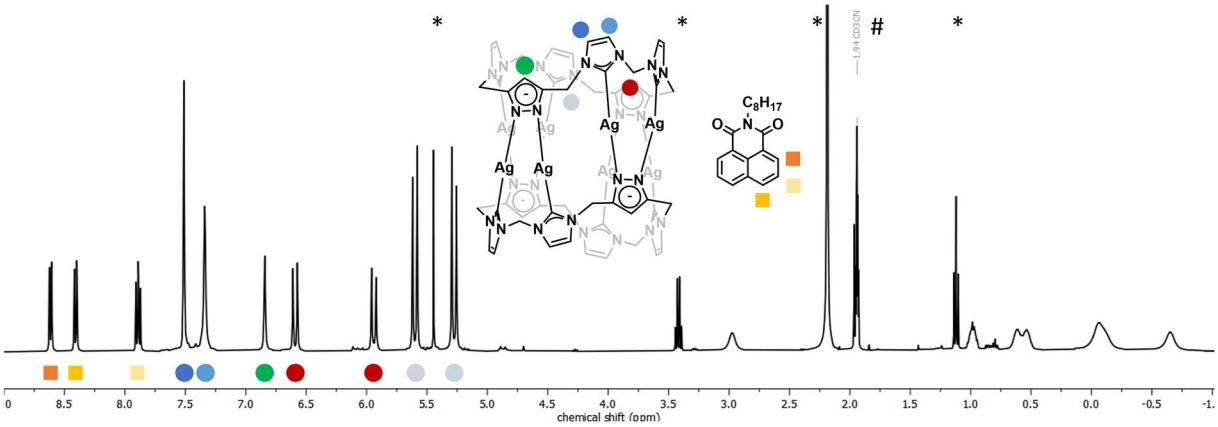

*Figure 83: ^{1}H NMR spectra of semi-rotaxane $[Ag_8L^{Me}{}_2][NONI](PF_6)_4$ in MeCN-d_3 (1.94 ppm, marked with #) at 298 K. Solvent impurities were marked with * for Et_2O (3.14, 1.11 ppm), H_2O (2.16 ppm) and DCM (5.45 ppm).*

^{1}H NMR spectroscopy suggested the successful synthesis of the desired semi-rotaxane by upfield shifting of the alkyl proton signals (Figure 83). Crystal attempts were set up to obtain single crystalline material to evaluate the structural conformation. Therefore, a saturated solution of $[Ag_8L^{Me}{}_2][NONI](PF_6)_4$ in MeCN was prepared and suitable single crystals were obtained by the slow diffusion of diethyl ether.

3.10.2 Investigation of $[Ag_{12}L^{Me}_3](PF_6)_6$

Crystallographic Investigation

Yellow, cube-shaped crystals were obtained, which were suitable for SC-XRD measurement. The yellow crystals showed good stability, meaning that no degradation of single crystals was observed upon exposure to air. This contrary behaviour was discovered for $[M_8L^{Me}_2](PF_6)_4$. Instead of achieving the desired semi-rotaxane, a symmetric complex containing twelve Ag(I) ions and three macrocyclic ligands was assigned. The instability of the Ag(I)-pillarplex in the presence of a template led to the dissociation and further re-coordination of the macrocyclic ligands and the Ag(I) ions.

The diffraction data was refined and solved in the monoclinic space group *P* 2_1 / *m* (No. 11) with the parameters a = 20.710(2) Å, b = 14.3430(16) Å, c = 22.738(2) Å, α = 90°, β = 96.735(3)° and γ = 90°. The asymmetric unit contains 1/2 $[Ag_{12}L^{Me}_3]^{6+}$ cation, three PF_6^- anions and three MeCN molecules. The Ag(I) ions show two different coordination spheres (Figure 84A). Three Ag(I) ions are arranged in a triangular fashion with short distances of 3.403 Å – 3.454 Å for the Ag(I)-Ag(I) bond. These ions are bound to the nitrogen atoms of the pyrazole units. The other Ag(I) ions are linearly coordinated to two NHC units and exhibit distances to the triangular arranged Ag(I) ions of 3.771 Å – 3.921 Å. This type of coordination of the Ag(I) ions leads to the formation of a triangular complex with three oval shaped pore openings. With the oval shape a distance of 10.353 Å for the broad pore opening and a distance of 9.740 Å for the narrow pore opening is determined (Figure 84B).

Due to the overall triangular shape of the obtained complex, the included three macrocyclic ligands and the pillarplex salt $[Ag_8L^{Me}_2](PF_6)_4$ used as precursor the complex was named trillarplex. During the crystal structure refinement, residual electron density was located inside the cavity with the approximate shape of the *N*ONI template. Due to the strong disorder of the electron density no explicit position of the template was possible. The alkyl chain of the guest molecule showed the potential of sticking out of one pore opening of the macrocyclic ligands. With DFT calculation the location of the counter anion inside the cavity could be determined. The conjugated π-system of the guest molecules was layered in a parallel manner towards the triangle of Ag(I) ions, which was in accordance with the crystal structure determined by SC-XRD measurements, where a bending of the Ag(I) triangle towards the inner of the cavity was observed.[181]

A detailed inspection of the shape of the trillarplex from the side shows a bending of the triangular arranged Ag(I) ions towards the inner of the cavity (6.069 Å – 6.278 Å), indicating that metal-to-π interactions between the Ag(I) ions and the aromatic π-system of the template are occurring (Figure 84B). Additional non-covalent interaction of the trillarplex cation $[Ag_{12}L^{Me}_3]^{6+}$ can be assigned to non-classical hydrogen bonding[36] between fluorine atoms of the counter anion PF_6^-, classical hydrogen bonding between the nitrogen atom of the MeCN molecules and hydrogen atoms of the rim, π-interactions of the pyrazole moieties with the hydrogen atoms of the MeCN molecules and metal coordination between the Ag(I) ions and N_{MeCN} or F_{PF6} (Figure 84C). The crystal arrangement (Figure 84D) of the $[Ag_{12}L^{Me}_3]^{6+}$ cations shows a symmetric zigzag layering of chain aligned trillarplex cations. The cations in the chain alignment showed Ag(I)-Ag(I) distances of 8.064 Å – 8.274 Å. The zigzag arrangement of $[Ag_{12}L^{Me}_3]^{6+}$ cations can determine the overall structure by metallophilic interactions of Ag(I) to Ag(I) ions with distances of 5.487 Å. Additionally, the PF_6^- counter anions are located between

two neighbouring cations covered by the zigzag crystal arrangement of the trillarplex cations (Figure 84E).

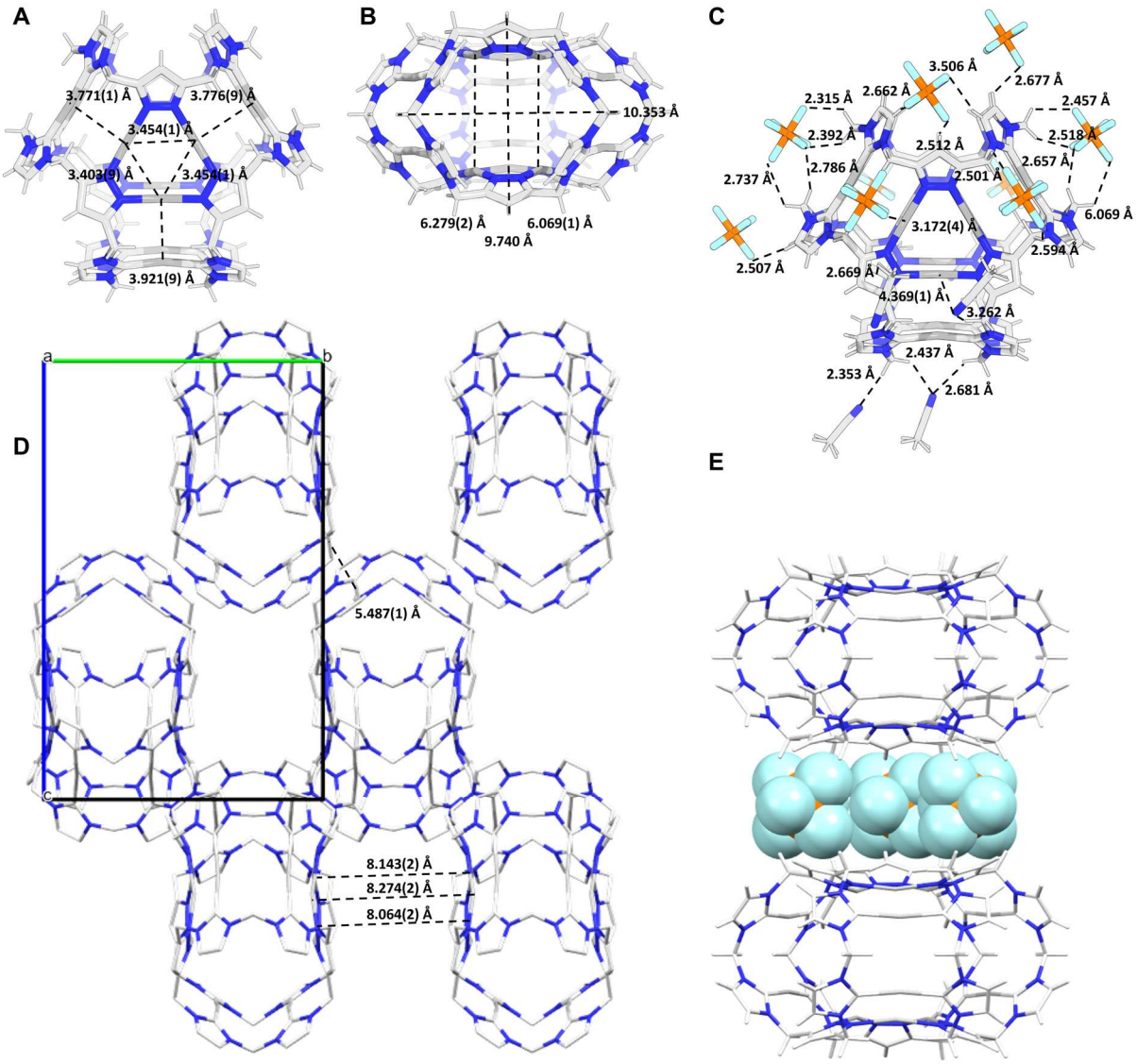

Figure 84: Representation of the solid-state structures of $[Ag_{12}L^{Me}{}_3][TE](PF_6)_6$: (A) Side view of $[Ag_{12}L^{Me}{}_3]^{6+}$, (B) Top view of pore opening of $[Ag_{12}L^{Me}{}_3]^{6+}$; (C) Non-covalent interactions of $[Ag_{12}L^{Me}{}_3]^{6+}$ with non-classical hydrogen bonding[36] of F_{PF6} and H_{rim}, classical hydrogen bonding of N_{MeCN} with H_{rim}, metal coordination of Ag(I) with N_{MeCN}, Ag(I) with F_{PF6} and π-interactions of H_{MeCN} with the pyrazole unit; (D) Crystal packing of $[Ag_{12}L^{Me}{}_3]^{6+}$ along the a-axis; (E) Stacking of two $[Ag_{12}L^{Me}{}_3]^{6+}$ cations with three PF_6^- anions in between (displayed in space fill).

Hypothesis

The trillarplex $[Ag_{12}L^{Me}{}_3](PF_6)_6$ was probably synthesised by the re-arrangement of pillarplex $[Ag_8L^{Me}{}_2](PF_6)_4$ with the template *N*ONI in solution as Ag(I)-NHC self-assemblies are dependent on temperature and concentration.[182] In order to design the selective formation of trillarplex $[M_{12}L^{Me}{}_3](PF_6)_6$ (M = Ag(I), Au(I)), a hypothetic synthetic route was defined in Figure 85 either starting with the respective $[M_8L^{Me}{}_2](PF_6)_4$ pillarplex or the macrocyclic ligand $L^{Me}(PF_6)_4$.

It has already been observed that the pillarplex $[Ag_8L^{Me}_2](PF_6)_4$ could be converted into the respective trillarplex $[Ag_{12}L^{Me}_3](PF_6)_6$. Thus, this step was confirmed to be successful and can be used as a starting point to further explore the selective synthesis based on re-arrangement. Another possibility to directly achieve $[M_{12}L^{Me}_3](PF_6)_4$ would be the template-directed synthesis starting with the macrocyclic ligand $L^{Me}(PF_6)4$, a suitable template TE and an Ag(I) source similar to the pillarplex synthesis in a weak base approach.[174,183-184]

The prospect of creating the $[Au_{12}L^{Me}_3](PF_6)_6$ trillarplex is highly intriguing. Previous pillarplex syntheses have demonstrated that $[Ag_8L^{Me}_2](PF_6)_4$ can undergo transmetalation to yield the corresponding $[Au_8L^{Me}_2](PF_6)_4$. However, the stability of the Au(I)-pillarplex should be enhanced owing to the stronger Au(I)-NHC bonds.[148-149] Therefore, a re-arrangement of $[Au_8L^{Me}_2](PF_6)_4$ pillarplex into $[Au_{12}L^{Me}_3](PF_6)_4$ trillarplex is not anticipated to be effective, as no dissociation of $[Au_8L^{Me}_2](PF_6)_4$ should take place. Consequently, the object is to achieve the transmetalation of the selectively synthesised $[Ag_{12}L^{Me}_3](PF_6)_4$ trillarplex to form the respective Au(I) based trillarplex.

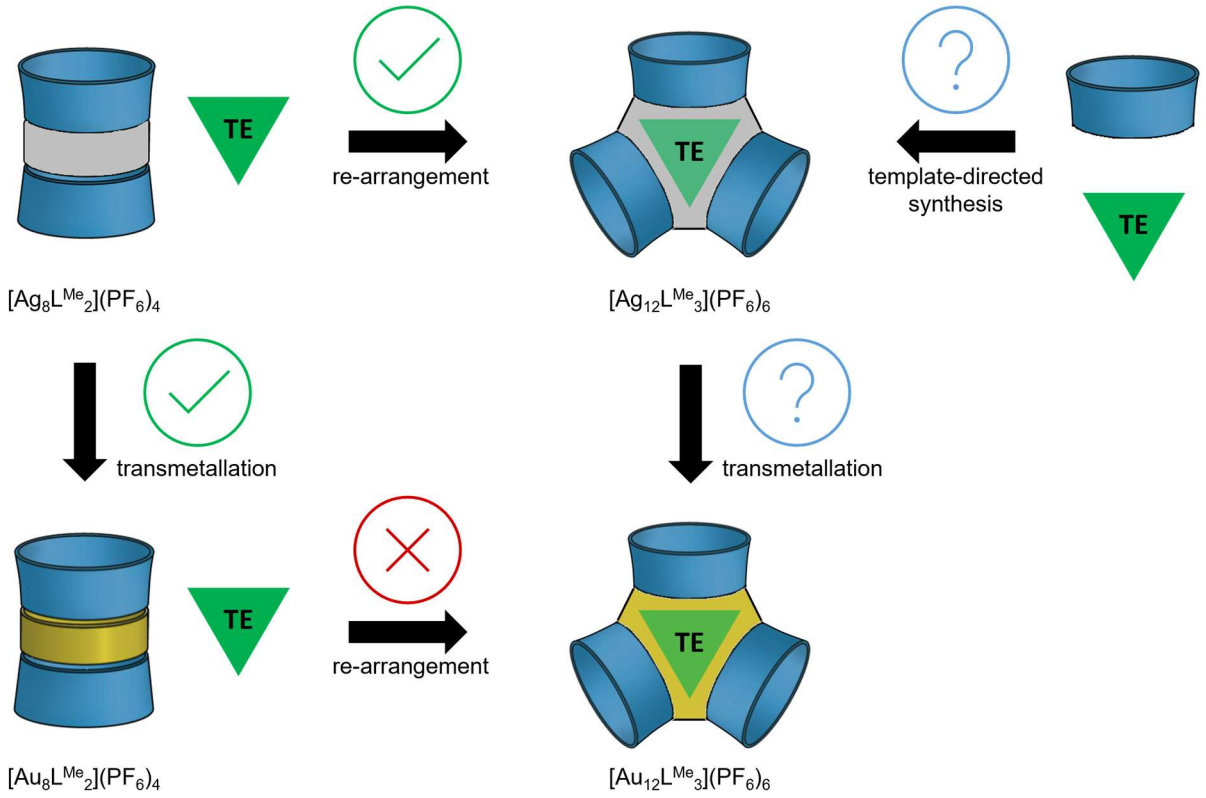

Figure 85: Schematic representation of the hypothetical synthetic procedure for the formation of trillarplex $[M_{12}L^{Me}_3](PF_6)_4$ either by re-arrangement of $[M_8L^{Me}_2](PF_6)_4$ with template TE or by the template-directed synthesis starting with macrocyclic ligand $L^{Me}(PF_6)_4$, metal source and base Ag_2O and template TE.

Attempts for Selective (Template-Directed) Synthesis

Until now, the trillarplex $[Ag_{12}L^{Me}_3](PF_6)_6$ was obtained as a side product by the slow diffusion of Et_2O into saturated solutions of $[Ag_8L^{Me}_2](PF_6)_4$. The previously described crystallisation attempts were repeated with template TE1 (*N*-methyl naphthalimide *N*NI) and similar crystals data was obtained. Additionally, enough material was collected by crystal picking to measure a ^{1}H NMR spectrum of $[Ag_{12}L^{Me}_3][NONI](PF_6)_6$ (Figure 86). An upfield shift of the alkyl hydrogen

atoms of TE2 and a slight shift of the rim hydrogen atoms of the trillarplex compared to the typical proton signals of the pillarplex (displayed in purple) was observed. The imidazolylidene hydrogen atoms (signals at 7.55 and 7.52 ppm) exhibited a pronounced roof effect, which might be explained by the tilt of the ligand towards the centre of the pore opening. This might lead to the closer proximity of the imidazolylidene hydrogen atoms towards each other.

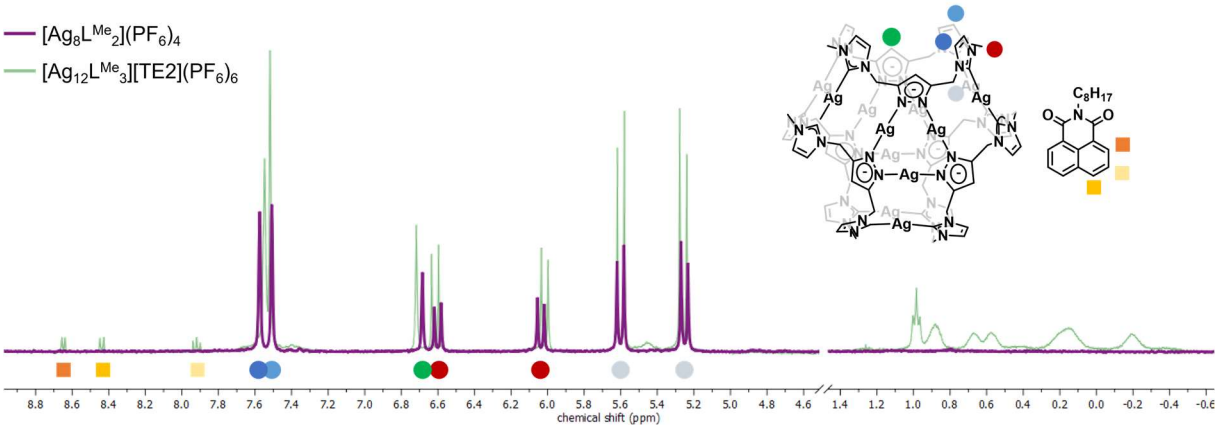

Figure 86: Section of ^{1}H NMR spectra of $[Ag_8L^{Me}_2](PF_6)_4$ (displayed in purple) and $[Ag_{12}L^{Me}_3][TE2](PF_6)_6$ (displayed in green) in MeCN-d_3 (1.94 ppm) at 298 K.

Selective synthesis routes of the trillarplex were investigated based on the defined hypothetical routes described in Figure 85 starting either with the macrocyclic ligand $L^{Me}(PF_6)_4$ or the pillarplex $[Ag_8L^{Me}_2](PF_6)_4$. Furthermore, the influence of the used template (Figure 87), solvent, time, temperature and many more factors were tested. The details for all tested conditions are depicted in Chapter 5.8.6.

In order to directly assemble the trillarplex, different templates (compare Figure 87) were tested towards their suitability. Due to the triangular shape and the C_3 symmetry, TE3, TE4 and TE5 were additionally chosen as potential suitable templates. These templates additionally bear the possibility of further pre- or post-synthetic modification of the guest molecule through reactivity at the three functional groups -NH_2, -COOH and -Cl.

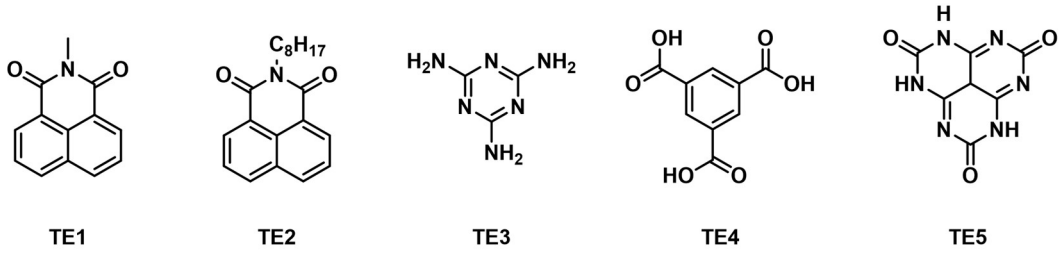

Figure 87: Chemical structures of the templates used for the selective synthesis of $[Ag_{12}L^{Me}_3](PF_6)_6$: TE1 N-methyl naphthalene monoimide (NMMI), TE2 N-octyl naphthalimide (NONI), TE3 1,3,5-triazine-2,4,6-triamine, TE4 trimesic acid and TE5 1H-1,3,4,6,7,9-hexaazaphenalene-2,5,8(3H,3a1H,6H)-trione.

First approaches for the selective synthesis of $[Ag_{12}L^{Me}_3](PF_6)_6$ were started by the template-directed synthesis using ligand $L^{Me}(PF_6)_4$ (3 eq.) and the metal precursor Ag_2O, which was employed as metal source and weak base. The synthetic route for the formation of the pillarplex was followed, in which the reactants were provided in MeCN and stirred overnight at room temperature under exclusion of light. In different batches of these syntheses, the following parameters were varied: equivalents of the metal precursor, templates (TE1, TE2, TE3, TE4), equivalents of template, solvent ratio (MeCN *vs.* MeCN:Et_2O), temperature (rt *vs.*

80 °C) and reaction time (16 h, 24 h, 3 days). Each batch has undergone the same work-up procedure. The brown suspensions were filtered over Celite® to remove excess of Ag_2O. Further Ag-based components were precipitated from the brown filtrate by addition of Et_2O. Afterwards, an excess of Et_2O was added to yield off-white precipitates, which were isolated by centrifugation and dried. The solids were analysed by ^{1}H NMR spectroscopy and mass spectrometry. The shifts of the aromatic rim proton signals and the alkyl / aromatic proton signals of the guest or template (TE) were monitored and compared to the respective signals observed in the ^{1}H NMR spectra of $[Ag_8L^{Me}_2](PF_6)_4$ and $[Ag_{12}L^{Me}_3][TE2](PF_6)_6$. Across all batches, only the aromatic proton signals of $[Ag_8L^{Me}_2](PF_6)_4$ were reported and there was no indication of the successful formation of the trillarplex.

Subsequently, the formation of the trillarplex was aimed by a combination of $L^{Me}(PF_6)_4$, $[Ag_8L^{Me}_2](PF_6)_4$ an excess of template TE1 (10 eq.). The reactants were provided in a solvent mixture of 1:1 (MeCN:Et_2O). While one batch was stirred at room temperature, the other ones were exposed to external stimuli (e.g., UV-light irradiation or additives) to accelerate the *in-situ* decomposition of the pillarplex. Due to the presence of one additional equivalent of $L^{Me}(PF_6)_4$ and TE, the following self-assembly to the trillarplex was proposed. The reaction mixtures were concentrated to dryness and ^{1}H NMR spectra were measured. However, for the batch stirred at room temperature, separate signal sets for pillarplex and free ligand were obtained and for the batches exposed to external stimuli the signal set for free ligand was assigned.

Final approaches for the synthesis of $[Ag_{12}L^{Me}_3][TE](PF_6)_6$ were performed based on the re-arrangement of $[Ag_8L^{Me}_2](PF_6)_4$ in the presence of a template (as described in Figure 85). $[Ag_8L^{Me}_2](PF_6)_4$ (1, 3 eq.) was provided in different solvent mixtures (MeCN, MeCN:Et_2O) and the templates TE1, TE2, TE3, TE4, TE5 were added in different equivalents (0.55 eq., 0.7 eq., 1.0 eq., 1.6 eq., 10 eq.). Due to the low solubility of TE5 in MeCN, this reaction was performed in DMF. After stirring the reaction mixtures at specific temperatures (rt, 40 °C, 80 °C) each batch was subsequently divided into two portions. While one portion was set up as crystallisation attempt, where slow diffusion of a solvent with lower polarity was allowed, the other portion was analysed by ^{1}H NMR spectroscopy. Again, the shifts of the aromatic rim proton signals and the alkyl / aromatic proton signals of the guest or template (TE) were monitored. Comparison with the ^{1}H NMR spectrum of $[Ag_{12}L^{Me}_3](PF_6)_6$ yielded no favourable outcomes. The efforts to crystallise the desired compound were repeatedly inspected and when suitable single crystals for SC-XRD measurements were acquired, these crystals underwent SC-XRD analysis to assess their structure.

3.10.4 Investigation of $[Ag_6(HL^{Me})_2](PF_6)_4$

Crystallographic Investigation

Colourless cube-shaped crystals were obtained in the crystallisation attempt, where $[Ag_8L^{Me}_2](PF_6)_4$ and template TE1 (10 eq.) were provided in MeCN and an excess of Et_2O was added by slow diffusion (Chapter 5.8.6, No. 3.12). The reaction solution was kept at room temperature for 5 days until the formation of single crystals was observed. The obtained data was solved and refined in the orthorhombic space group *C m m a* (No. 67) with the following parameters a = 23.9846(19) Å, b = 29.650(2) Å, c = 14.7846(12) Å, α = β = γ = 90°.

Interestingly, when using template TE1 another complex could be re-arranged by a self-assembly of the macrocyclic ligand $L^{Me}(PF_6)_4$ with Ag(I) ions, which exhibits a S shape. The asymmetric unit contains 1/2 of the $[Ag_6(HL^{Me})_2]^{4+}$ cation, 2/3 PF_6^- and 1/4 TE1. The C21-C21´ bond of the template is modelled at the special Wyckoff position *8m*, where a point symmetry leads to the display of the mirrored molecule of TE1 (Figure 88A).

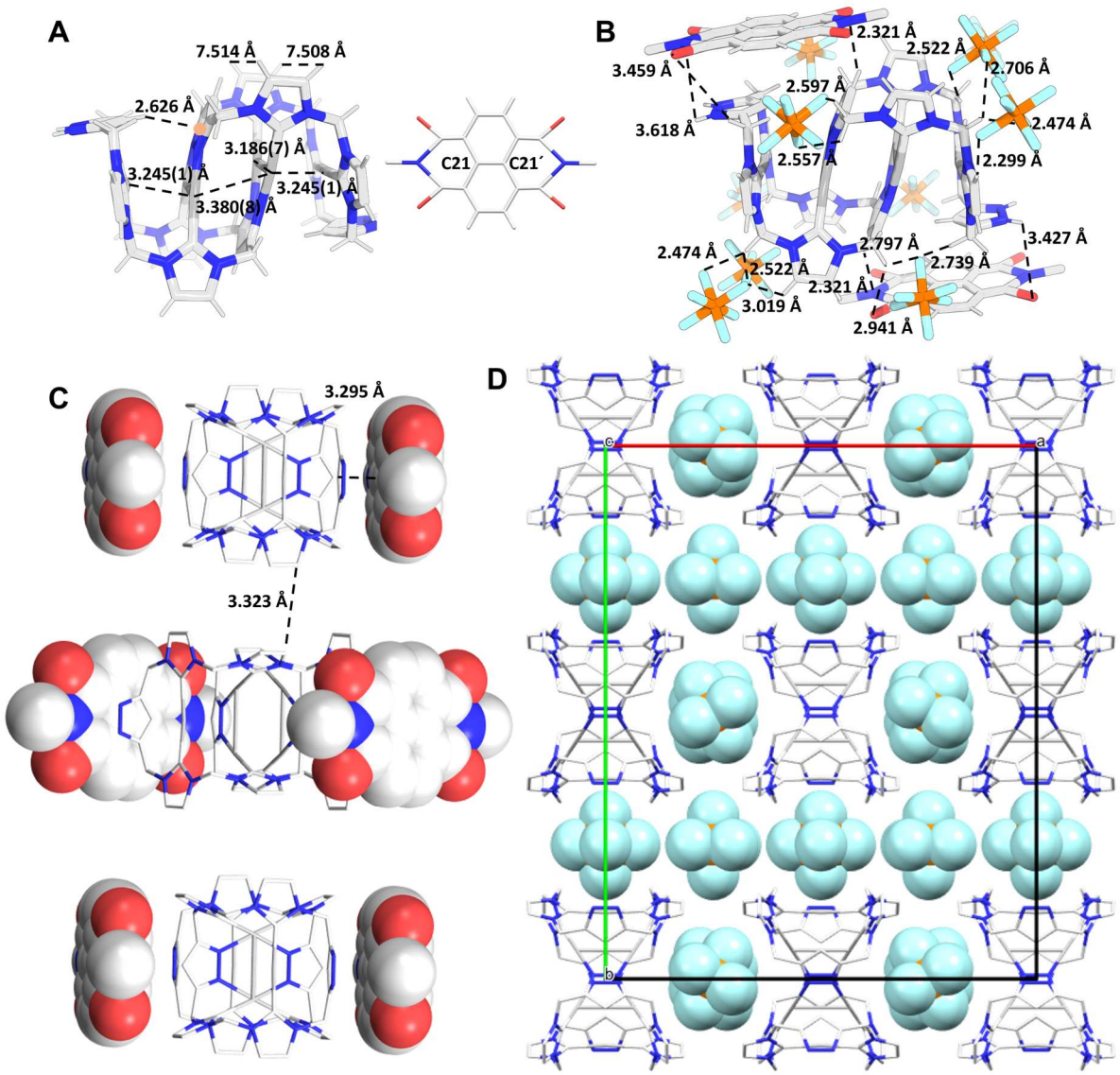

Figure 88: Representation of the solid-state structures of $[Ag_6(HL^{Me})_2](PF_6)_4$: (A) Side view of $[Ag_6L^{Me}_2]^{4+}$ and side view of template with C21-C21' bond (Wyckoff position 8m); (B) Non-covalent interactions of $[Ag_6L^{Me}_2]^{4+}$ with non-classical hydrogen bonding[36] of F_{PF6} and H_{rim}, classical hydrogen bonding of N_{NNI} and O_{NNI} with H_{rim}; (C) π-stacking of TE1 and $[Ag_6L^{Me}_2]^{4+}$ along the chain alignment; (D) crystal packing of $[Ag_6L^{Me}_2]^{4+}$ cations with PF_6^- anions in between.

The six Ag(I) ions are arranged in a 1:2:2:1 sequence, with two Ag(I) ions on either side linearly coordinated between two NHC units, and the inner Ag(I) pairs coordinated by two NHC units on one side and a pyrazole unit on the other side. The outer pyrazole unit of the macrocyclic ligand is protonated, and the ligand is strongly bent towards a concave bowl shape (Figure 88A). The protonation state of the pyrazole unit was determined based on the number of PF_6^- anions present in the asymmetric unit and resulted in the chemical composition of the S-shaped complex of $[Ag_6(HL^{Me})_2](PF_6)_4$. The non-covalent interactions are monitored between the counter anions and the S-shaped cation (Figure 88B) with the main distribution attributed

to non-classical hydrogen bonding[36] of F_{PF6} and hydrogen atoms of the rim. Additional hydrogen bonds are identified between the carbonyl oxygen atoms and the nitrogen atoms of TE1 with the methylene bridged hydrogen atoms or the protonated pyrazole units. The mirrored template is placed on top of two protonated pyrazole units of one $[Ag_6L^{Me}_2]^{3+}$ cation by π-stacking interactions between the conjugated aromatic systems and the cations form chain aligned 1D structures, where every second cation is tilted by 180° (Figure 88C). The counter anions PF_6^- are intercalated between the chain aligned $[Ag_6L^{Me}_2]^{4+}$ cations (depicted in Figure 88D), where the crystal packing along the c-axis shows the implementation of the PF_6^- anions in between the S-shaped complexes.

Attempts for Selective (Template-Directed) Synthesis

The crystallisation attempts for the direct synthesis of the S-shaped complex $[Ag_6(HL^{Me})_2](PF_6)_4$ were repeated under the same conditions where previously successful crystal growth was observed (for details see Chapter 5.8.6). However, a protonation of the macrocyclic ligand occurred during the re-arrangement a slightly acidic environment, presumably from MeCN, seemed to be present. As a result, either this acidic characteristic could lead to a protonation, or the addition of weak acids could increase the formation of the S-shaped complex. Nonetheless, until now, the re-arrangement of the pillarplex $[Ag_8L^{Me}_2](PF_6)_4$ into the S-shaped complex $[Ag_6(HL^{Me})_2](PF_6)_4$ could not be repeated.

3.10.4 Summary and Outlook

During crystallisation attempts to form a respective semi-rotaxane, the re-arrangement of $[Ag_8L^{Me}_2](PF_6)_4$ into the two other complexes trillarplex $[Ag_{12}L^{Me}_3](PF_6)_6$ and S-shaped $[Ag_6L^{Me}_2](PF_6)_4$ was observed. As the formation of the trillarplex $[Ag_{12}L^{Me}_3](PF_6)_6$ was discovered to be successful and could be reproduced, several crystallisation and synthesis attempts have already been made to investigate the re-arrangement towards this complex. However, no conclusion could be drawn from the performed reactions.

One influence on the re-arrangement of pillarplex into trillarplex is the availability of a suitable template, which in this case was identified as *N*-methyl naphthalimide or *N*-octylnaphthalimide. This templating effect was strengthened due to the structural deformation of the Ag(I) triangle towards the inner of the cavity by π-interactions in the determined crystal structures. Further investigations on the influence of solvent mixture or solvent ratio, temperature, reaction time or pH value have to be performed to achieve a selective synthesis of the desired trillarplex. If a selective route for the synthesis of the $[Ag_{12}L^{Me}_3](PF_6)_6$ trillarplex can be developed, the driving forces for the formation of the host-guest complex, the properties of the trillarplex in solution and in the solid-state and the further transmetalation to a $[Au_{12}L^{Me}_3](PF_6)_6$ trillarplex need to be investigated (see hypothetical synthesis route in Figure 85).

Although the residual electron density inside the trillarplex cavity could not be explicitly modelled into the guest molecules (*N*MMI or *N*ONI, the shape of the combined electron density indicated the location of these guest molecules. As the trillarplex exhibited a pore opening of approximately 10.35 Å, the question arises if the guest molecule could be post-synthetically

removed from the trillarplex cavity. The possibility of guest removal would make the trillarplex cavity accessible for further encapsulation studies. Using crystallographic data as input, the width of 8.85 Å for the *N*NI unit was calculated. Based on the theoretical calculations the pore opening exhibits a broad enough opening for the removal of the guest molecule. However, the guest was strongly bound inside the cavity by metal-π interactions.

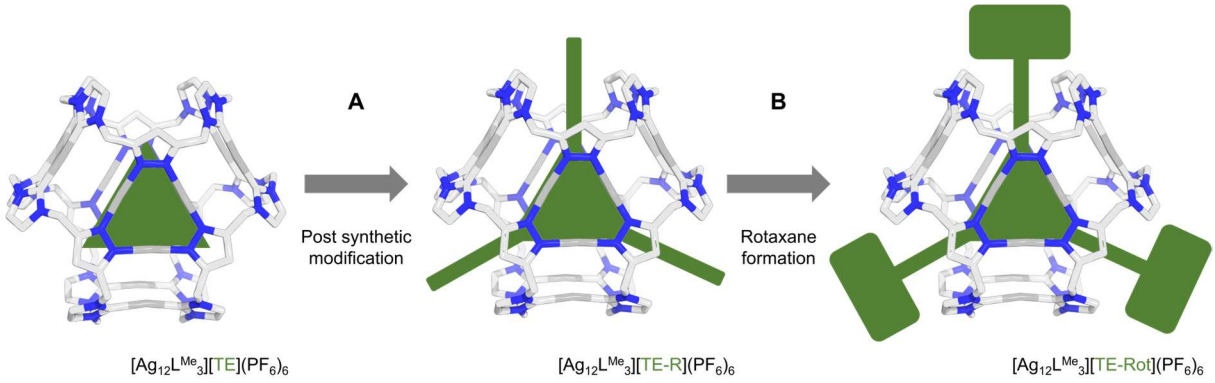

Figure 89: Overview on the potential host-guest complexes with $[Ag_{12}L^{Me}{}_3]^{6+}$ cation acting as supramolecular host system: (A) Post-synthetic modification of the template TE by introduction of long alky chains; (B) Formation of a MIM by the introduction of stopper motifs to the previously introduced long alky chains.

Besides the post-synthetic removal of the guest molecule an exchange of guest molecule before the assembly of the trillarplex should in theory be possible and would lead to interesting host-guest complexes. For the templating effect during the synthesis of the trillarplex a broad range of templates could be tested, and especially templates with a C_3 symmetry seemed to be suitable due to the possibility of interactions. The *N*NI templates could be exchanged by reasonable templates, which were already described in Figure 87. As the templates TE3, TE4 and TE5 bearing functional groups at the three edges, possible post-synthetic modification of the trillarplex host-guest complex could be achieved (Figure 89). Long alkyl chains could be added to the three functionalised sides of the C_3 symmetrical guest molecules, which would stick out of the cavity at the three pore openings. Host-guest complexes with a similar structural arrangement could already be synthesised and were named suit[n]ane[185], where the guest molecules with limbs was encapsulated into one supramolecular component acting as suite for the guest molecule. When introducing alkyl chains bearing functional groups at the end position, the formation of a rotaxane with the trillarplex $[Ag_{12}L^{Me}{}_3]^{6+}$ cation as ring component could be achieve, where a triangular guest molecule is embedded into the trillarplex and stoppered by the introduction of three motifs at each edge of the guest molecule (see Figure 89).

3.11 Encapsulation Studies of Perfluorinated Guest Molecules

This chapter is based on work by this author and Soumya Mukherjee.

3.11.1 Introduction

Accompanied by intrinsic porosity, the solubility of the pillarplex salts can be varied by anion exchange reactions.[29] Hence, this material is highly interesting regarding the use as filtering agent in aqueous systems. Perfluorinated substances are polar, linear molecules, which are water soluble, have a low vapour pressure, low volatility and cannot be easily removed from water. The contamination of perfluorinated alkyl substances is detectable in almost all environmental and biological systems and affects millions of people worldwide. Hence, the need for the development of effective remediation techniques gains more attention.[186-188] The selective encapsulation of guest molecules into supramolecules with specific non-covalent interactions is a promising approach.

Strategy

A non-water-soluble material is provided as a “sponge” and placed into water, which is contaminated with perfluorinated substances. By shape selective encapsulation of the perfluorinated substances into the cavity of the sponge material, PFCs are selectively removed from the contaminated water. No dissolution of the material and in the best-case scenario the “sponge” material is recyclable. Meaning, that the encapsulated perfluorinated substances can be easily removed and collected by washing the “sponge” material with a solvent. As the pillarplex is a charged molecule and the solubility of it can be changed by simple anion exchange reactions, the idea was to provide $[M_8L^{Me}{}_2](PF_6)_4$ pillarplex, which is not soluble in water and exhibits a free cavity. Later, this material is tested towards possible encapsulation of perfluorinated substances (Figure 90).

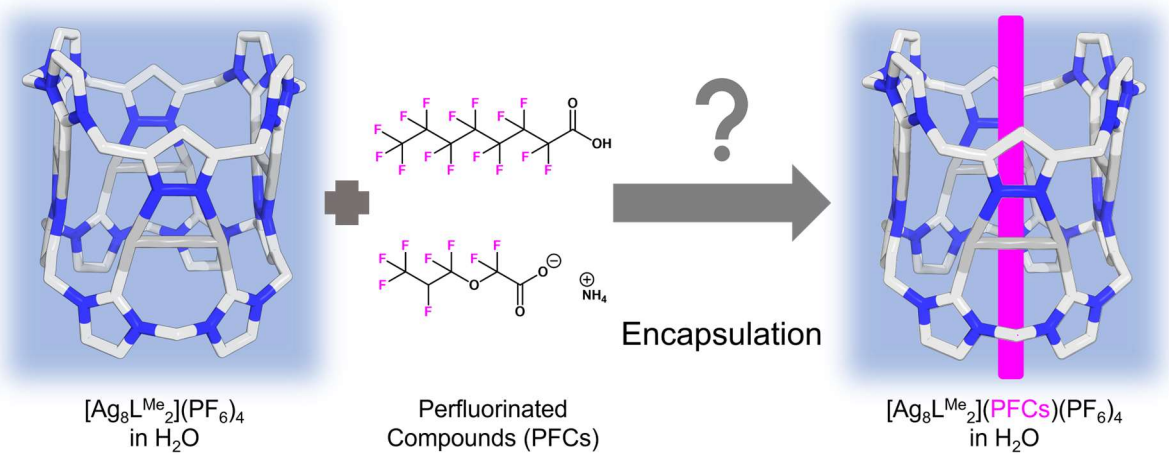

Figure 90: Overview of the possibility to encapsulate perfluorinated compounds (PFCs) into the $[Ag_8L^{Me}{}_2](PF_6)_4$ pillarplex in solid-state suspended in H_2O to yield pseudorotaxane $[Ag_8L^{Me}{}_2](PFCs)(PF_6)_4$.

3.11.2 Encapsulation Studies of *n*-Butanol, PFOA and GenX

First encapsulation studies were performed on an NMR scale in deuterated MeCN as solvent, where the substances $[Ag_8L^{Me}{}_2](PF_6)_4$ and PFCs were dissolved. As the solvent *n*-butanol was planned to be used for further encapsulation studies of PFCs into solid $[Ag_8L^{Me}{}_2](PF_6)_4$, initial encapsulation studies of this solvent into the pillarplex cavity were performed. To test the capability of the empty pillarplex pore to encapsulate solvent or PFCs, ^1H and ^{19}F NMR studies were performed, where a high field shift of the guest signals normally indicates successful encapsulation into the cavity. As depicted in Figure 91, the proton signals of the butanol were shifted to the upfield that indicates an encapsulation of the solvent. Although the solvent can be encapsulated into the cavity, a stronger affinity of the perfluorinated substances could shift the host-guest complex formation towards the favoured side, meaning that the perfluorinated compounds replace the solvent molecules inside the cavity.

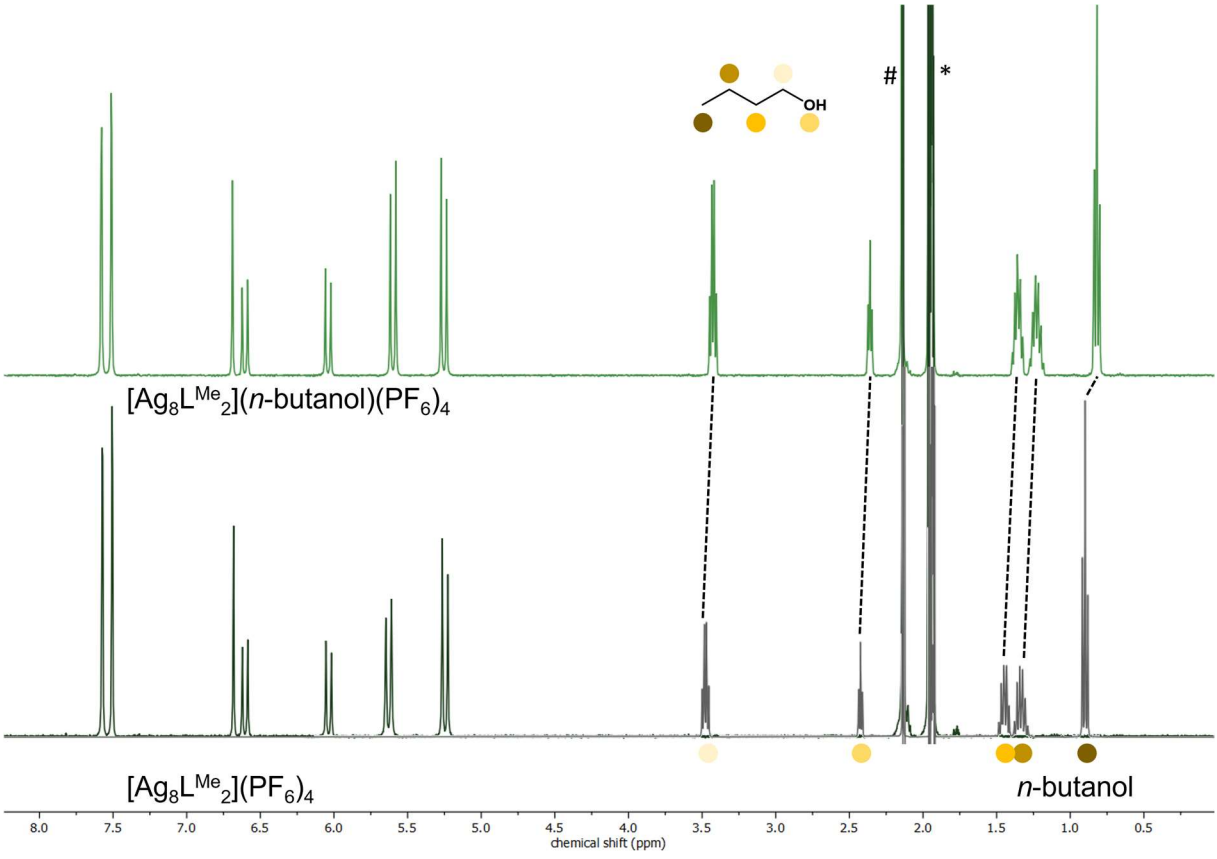

*Figure 91: ^1H NMR spectra of empty $[Ag_8L^{Me}{}_2](PF_6)_4$ pillarplex (dark green) and free n-butanol (grey) displayed at the bottom in comparison with a solution containing 1 eq. $[Ag_8L^{Me}{}_2](PF_6)_4$ and 1 eq. n-butanol after stirring at room temperature for 15 min, where upfield shifting of the n-butanol proton signals indicate encapsulation. Spectra were measured in MeCN-d_3 (1.94 ppm, marked with *) at 298 K. Solvent impurities were marked with # for water (2.13 ppm).*

As main focus of this study, the two perfluorinated substances perfluorooctanoic acid (PFOA) and ammonium perfluoro(2-methyl-3-oxahexanoate) (GenX) were chosen and encapsulation studies were performed as proof-of-principle.

Theoretical Consideration

Beforehand, the crystal structure of PFOA was analysed towards the diameter of the -CF_2 groups (Figure 92). By assuming repulsion forces of the fluorine atoms anti-periplanar conformation of the neighbouring -CF_2 groups was defined and hence a diameter of 5.622 Å was determined. This diameter exceeded the static pore opening of the pillarplex cation with 4.3 Å. Based on the theoretic calculations only partial encapsulation of PFCs into the pillarplex cavity should be possible.

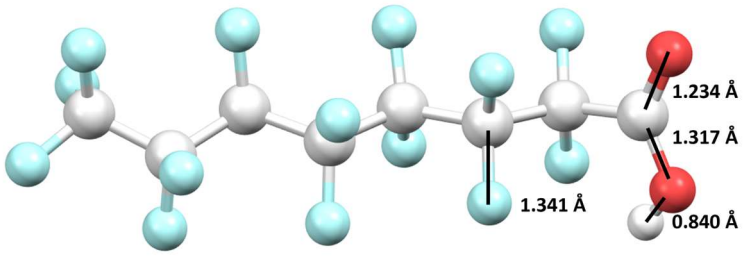

Figure 92: Calculation of the diameter 5.622 Å of PFOA based on average distances[33] obtained from crystallographic data (KEQREG, No. 1530103)[35] and the van-der-Waals radius for F of 1.47 Å[34].

Encapsulation Studies

As already mentioned, the proof-of-principle for PFC encapsulation in solution was tested. Therefore, $[Ag_8L^{Me}_2](PF_6)_4$ (1 eq.) and the PFC (1 eq.) were dissolved in MeCN-d_3 and stirred at room temperature towards potential encapsulation. The solutions were then monitored by ^{1}H and ^{19}F NMR spectroscopy to observe shifts of the guest molecule signals. The first encapsulation study was performed using PFOA (Figure 93, F94S) and for comparison ^{1}H and ^{19}F NMR spectra of the reactants were measured and the signals assigned based on literature.[189] In the ^{1}H NMR spectrum only a slight shift of the acidic proton was observed and in the ^{19}F NMR spectrum the signal of the -CF_2 group directly attached to the acid were undergo an upfield shift. This behaviour indicated the partial encapsulation of the PFOA with the acid group pointing towards the inner of the pillarplex cavity, which was in accordance with the theoretical investigations.

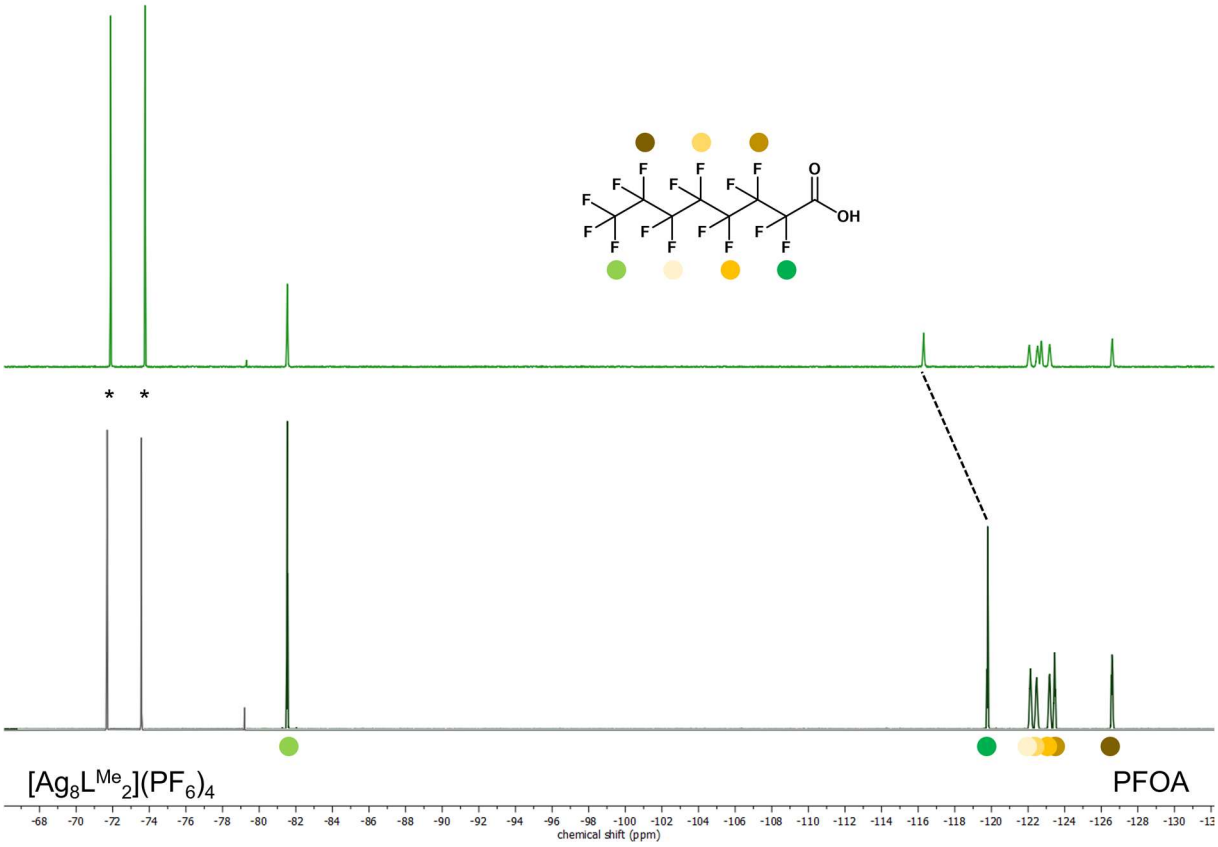

Figure 93: ^{19}F NMR spectra of PFOA and pillarplex $[Ag_8L^{Me}{}_2](PF_6)_4$ (grey) and PFOA (dark green) displayed at the bottom in comparison with a solution containing 1 eq. $[Ag_8L^{Me}{}_2](PF_6)_4$ and 1 eq. PFOA after stirring at room temperature for 15 min (light green). Spectra were measured in MeCN-d_3 at 298 K.

For the targeted guest GenX similar encapsulation studies were performed and again, the ^{19}F NMR spectrum was analysed towards the shifting of the potential guest signals (Figure 94). Interestingly, an upfield shift of the signal for the -CF group directly attached to the carboxylate, but no further changes were observed. This study revealed the same results as for the encapsulation of PFOA, i.e., the partial encapsulation of GenX with the carboxylate moiety pointing into the cavity of the pillarplex.

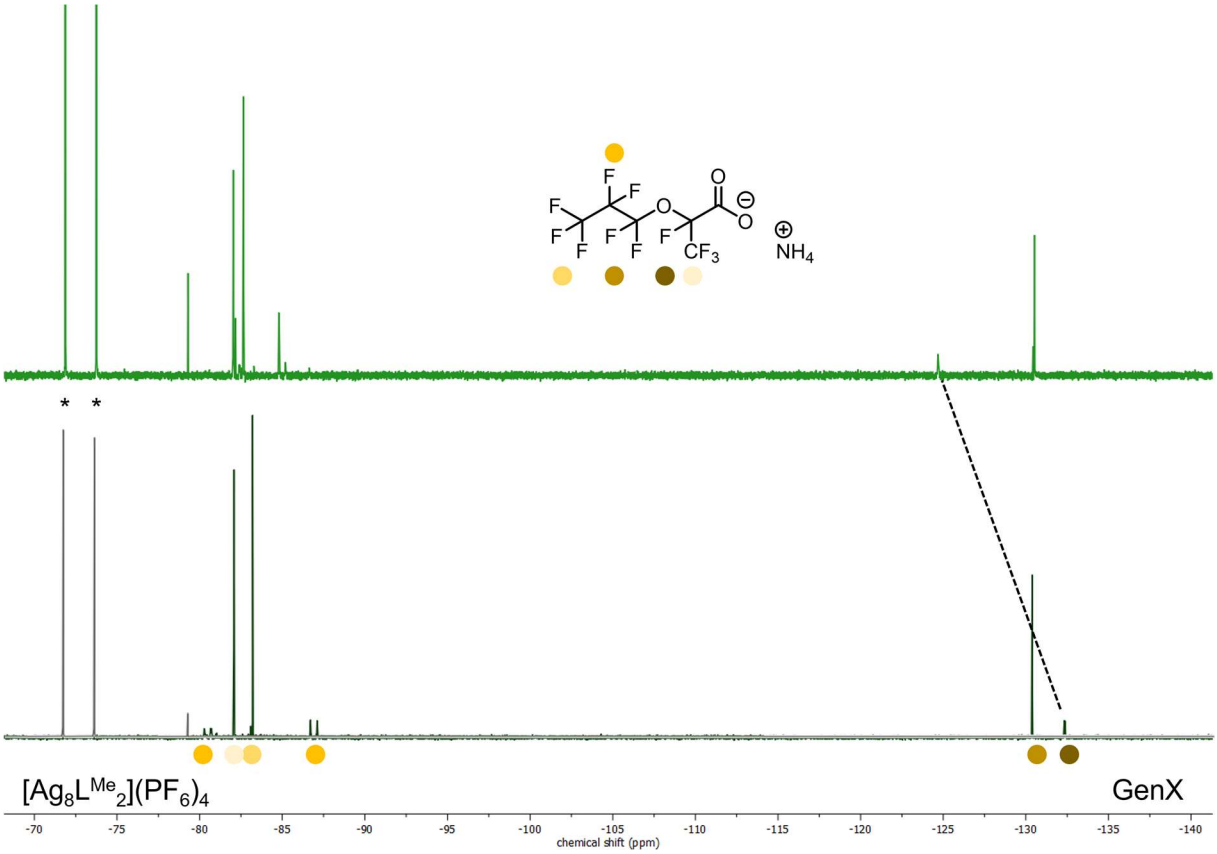

Figure 94: ^{19}F NMR spectra of pillarplex $[Ag_8L^{Me}_2](PF_6)_4$ (grey) and GenX (dark green) displayed at the bottom in comparison with a solution containing 1 eq. $[Ag_8L^{Me}_2](PF_6)_4$ and 1 eq. GenX after stirring at room temperature for 15 min (light green). Spectra were measured in MeCN-d_3 at 298 K.

3.11.3 Summary and Outlook

Unfortunately, the pillarplex cavity with a pore opening of 4.3 Å appeared to be too small to completely encapsulate fluorinated substances. The NMR studies in solution indicated that only the neighbouring -CF_2 groups of the carboxylic acid or carboxylate moiety can be encapsulated into the cavity. However, the encapsulation of fluorinated substances in aqueous solutions can be tested as the hydrophobic cavity and the presence of PFCs would benefit the guest encapsulation. Additionally, the potential encapsulation of partially fluorinated substances into the pillarplex cavity can be tested accompanied by theoretical investigation of the diameter of -CHF groups, which would probably fit better into the pore opening.

3.12 Encapsulation of Heterocyclic Guest Molecules

So far, predominantly linear alkyl chains have been studied towards their host-guest chemistry with pillarplexes $[M_8L^{Me}{}_2](X)_4$. For some solvent molecules, the potential of encapsulation has already been discovered (e.g., Et_2O, see Chapter 3.1), with heteroatom to metal coordination occurring inside the cavity. To broaden the spatial extend of the guest molecules, five-membered heterocycles can be studied. THF was chosen as target molecule since it carries an oxygen atom (similar to Et_2O) that can theoretically interact with the metal ions inside the pillarplex cavity (Figure 95).

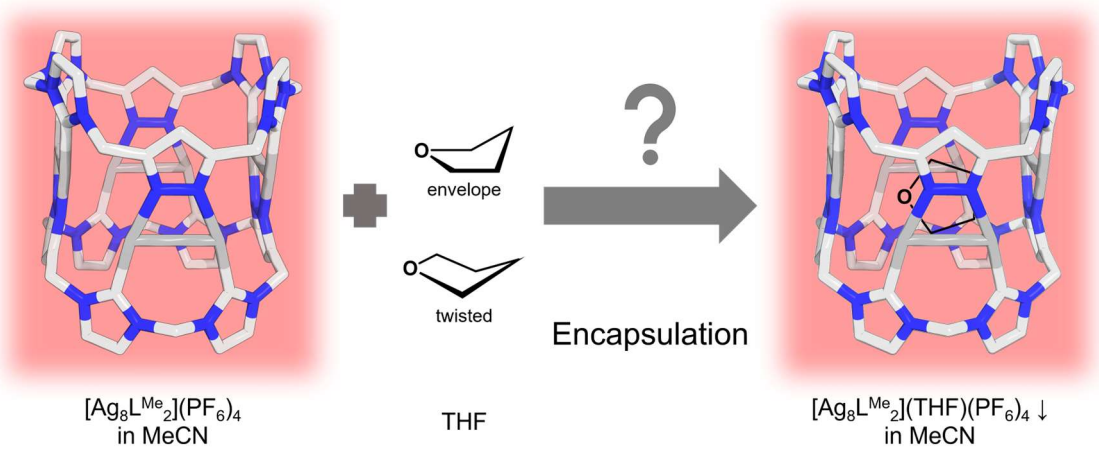

Figure 95: Overview of the possibility to encapsulate THF (envelope or twisted conformation) into the $[Ag_8L^{Me}{}_2](PF_6)_4$ pillarplex in solution with subsequent precipitation of $[Ag_8L^{Me}{}_2](THF)_x(PF_6)_4$ due to the addition of less polar solvent THF.

Although, a shape-selective encapsulation of linear alky chains[29,31-32,97] was described, very recently the encapsulation of tetrahydrofuran (THF) molecules bearing a five-membered aliphatic system, was achieved (Figure 96).

By crystallisation attempts of $[Ag_8L^{Me}{}_2](PF_6)_4$ in MeCN and slow diffusion of THF into the saturated solution, suitable single crystals were obtained, which were refined and solved in the triclinic space group *P*-1 (No. 2) with the following parameters a = 14.7482(8) Å, b = 16.0408(12) Å, c = 22.9771(16) Å, α = 79.231(3)°, β = 76.639(2)° and γ = 78.791(2)°. The asymmetric unit contains one $[Ag_8L^{Me}{}_2]^{4+}$ cation, four PF_6^-, one DMF and four THF molecules, of which three are located either inside the pillarplex cavity or the pore opening of the rim. Depicted in Figure 96A, the cation $[Ag_8L^{Me}{}_2]^{4+}$ exhibits non-classical hydrogen bonding[36] between F_{PF6} and H_{rim}. One DMF and one THF molecule are located on the outside of the pillarplex cation, and both exhibit a metal coordination of the oxygen atoms with the Ag(I) ions with distances of 3.157 Å for O_{DMF} and 3.180 Å for O_{THF}. Additionally, the oxygen atom of DMF interacts with the methylene hydrogen atoms of the rim (2.173 Å) and non-classical hydrogen bonding of the hydrogen atoms of THF (H_{THF}) with F_{PF6} (2.435 – 2.486 Å) are detected. In the middle of the cavity, electron density was detected, which could be assigned to one disordered THF molecule. While one position of the THF molecule was modelled in an enveloped conformation, the other respective position was represented in a twisted conformation each exhibiting a probability of approximately 50%. This THF molecule is completely encapsulated in the cavity exhibiting metal coordination between O_{THF} and Ag(I) ions. Additionally, two THF molecules are positioned in the pore opening of the $[Ag_8L^{Me}{}_2]^{4+}$ cation, where one displays a twisted and the other one an envelope conformation (Figure 96C). Two $[Ag_8L^{Me}{}_2]^{4+}$ cations are

chain-aligned by metallophilic Ag(I)-Ag(I) interactions with distances of 4.250 Å and are tilted by 180° to each other. However, these two cations are arranged in a zigzag manner driven by π-interactions with the imidazolylidene units of the neighbouring cations (Figure 96B+D).

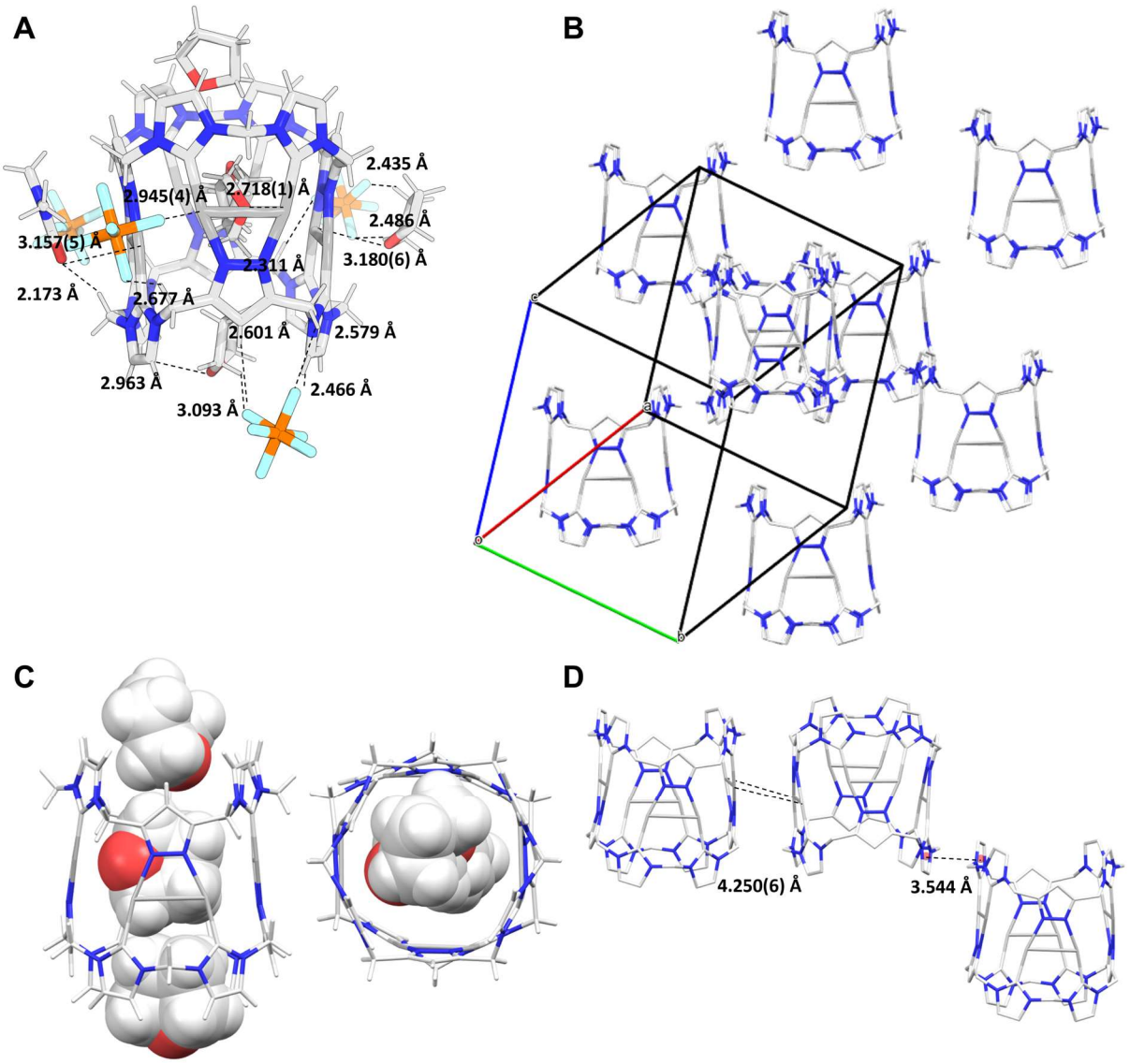

Figure 96: Representation of the solid-state structures of $[Ag_8L^{Me}{}_2](THF)_3(PF_6)_4$: (A) Non-covalent interactions of $[Ag_8L^{Me}{}_2]^{4+}$ bearing non-classical hydrogen bonding[36] between F_{PF6} and H_{rim} and classical hydrogen bonding of O_{THF} to H_{rim}; (B) Zigzag arrangement of $[Ag_8L^{Me}{}_2]^{4+}$; (C) Side and top view of THF molecules (displayed in a space fill) encapsulated into $[Ag_8L^{Me}{}_2]^{4+}$ (displayed as capped sticks); (D) Crystal arrangement of $[Ag_8L^{Me}{}_2]^{4+}$ dictated by Ag(I)-Ag(I) and π-π interactions of neighbouring imidazolylidene units.

The implementation of five-membered heterocyclic compounds opens up a broad variety of guest molecules, which have to be further investigated towards their behaviour in host-guest complexes.

3.13 References for Chapter 3

1 C. E. Wilmer, O. K. Farha, Y.-S. Bae, J. T. Hupp, R. Q. Snurr, *Energy Environ. Sci.,* **2012**, *5*, 9849.
2 C. Perego, R. Millini, *Chem. Soc. Rev.,* **2013**, *42*, 3956.
3 S. Mukherjee, D. Sensharma, K.-J. Chen, M. J. Zaworotko, *Chem. Commun.,* **2020**, *56*, 10419.
4 J. Yang, J. Wang, B. Hou, X. Huang, T. Wang, Y. Bao, H. Hao, *Chem. Eng. J.,* **2020**, *399*, 125873.
5 J. Yu, A. Corma, Y. Li, *Adv. Mater.,* **2020**, *32*, 2006277.
6 D. Taylor, S. J. Dalgarno, Z. Xu, F. Vilela, *Chem. Soc. Rev.,* **2020**, *49*, 3981.
7 P. Peng, X.-H. Gao, Z.-F. Yan, S. Mintova, *Natl. Sci. Rev.,* **2020**, *7*, 1726.
8 Y. Wu, B. M. Weckhuysen, *Angew. Chem. Int. Ed.,* **2021**, *60*, 18930.
9 R. L. Siegelman, E. J. Kim, J. R. Long, *Nat. Mater.,* **2021**, *20*, 1060.
10 A. Khobotov-Bakishev, L. Hernández-López, C. von Baeckmann, J. Albalad, A. Carné-Sánchez, D. Maspoch, *Adv. Sci.,* **2022**, *9*, 2104753.
11 J. Albalad, L. Hernández-López, A. Carné-Sánchez, D. Maspoch, *Chem. Commun.,* **2022**, *58*, 2443.
12 B. D. Egleston, A. Mroz, K. E. Jelfs, R. L. Greenaway, *Chem. Sci.,* **2022**, *13*, 5042.
13 S. Yu, G.-L. Xing, L.-H. Chen, T. Ben, B.-L. Su, *Adv. Mater.,* **2020**, *32*, 2003270.
14 A. G. Slater, A. I. Cooper, *Science,* **2015**, *348*, 1.
15 H. Wang, Y. Jin, N. Sun, W. Zhang, J. Jiang, *Chem. Soc. Rev.,* **2021**, *50*, 8874.
16 T. Stolar, K. Užarević, *Cryst. Eng. Comm.,* **2020**, *22*, 4511.
17 C. M. Reddy, G. Rama Krishna, S. Ghosh, *Cryst. Eng. Comm.,* **2010**, *12*, 2296.
18 A. K. Nangia, G. R. Desiraju, *Angew. Chem. Int. Ed.,* **2019**, *58*, 4100.
19 G. R. Desiraju, *Angew. Chem. Int. Ed.,* **2007**, *46*, 8342.
20 R. Custelcean, *Chem. Soc. Rev.,* **2010**, *39*, 3675.
21 S. Kitagawa, S.-i. Noro, T. Nakamura, *Chem. Commun.,* **2006**, 701.
22 T. D. Bennett, F.-X. Coudert, S. L. James, A. I. Cooper, *Nat. Mater.,* **2021**, *20*, 1179.
23 A. I. Cooper, *ACS Cent. Sci.,* **2017**, *3*, 544.
24 A. J. Gosselin, A. M. Antonio, K. J. Korman, M. M. Deegan, G. P. A. Yap, E. D. Bloch, *J. Am. Chem. Soc.,* **2021**, *143*, 14956.
25 W. Zhu, J. Guo, Y. Ju, R. E. Serda, J. G. Croissant, J. Shang, E. Coker, J. O. Agola, Q.-Z. Zhong, Y. Ping, F. Caruso, C. J. Brinker, *Adv. Mater.,* **2019**, *31*, 1806774.
26 S. Mollick, S. Mukherjee, D. Kim, Z. Qiao, A. V. Desai, R. Saha, Y. D. More, J. Jiang, M. S. Lah, S. K. Ghosh, *Angew. Chem. Int. Ed.,* **2019**, *58*, 1041.
27 A. J. Gosselin, G. E. Decker, A. M. Antonio, G. R. Lorzing, G. P. A. Yap, E. D. Bloch, *J. Am. Chem. Soc.,* **2020**, *142*, 9594.
28 J. Qin, Q. Chen, C. Yang, Y. Huang, *J. Alloys Compd.,* **2016**, *654*, 39.
29 P. J. Altmann, A. Pöthig, *J. Am. Chem. Soc.,* **2016**, *138*, 13171.
30 A. Pöthig, A. Casini, *Theranostics,* **2019**, *9*, 3150.
31 A. A. Heidecker, M. Bohn, A. Pöthig, *Z. Krist. - Cryst. Mater.,* **2022**, *237*, 167.
32 S. Guan, T. Pickl, C. Jandl, L. Schuchmann, X. Zhou, P. J. Altmann, A. Pöthig, *Org. Chem. Front.,* **2021**, *8*, 4061.
33 **ConQuest2022.3.0**, CCDC, **2023**. PF_6^- 4047 hits, Dist1 = 1.576(2) Å; OAc^- 704 hits, Dist1 = 2.208(3) Å; I_3^- 1470 hits, Dist1 = 2.956(37) and Dist2 = 2.958(19) Å; SCN^- 896 hits, Dist1 = 1.638(3) Å and Dist2 = 1.149(3) Å; NO_3^- 1788 hits, Dist1 = 1.242(3) Å; ClO_4^- 5076 hits, Dist1 = 1.412(3) Å; BF_4^- 2824 hits, Dist1 = 1.367(2) Å; SO_4^{2-} 1843 hits, Dist1 = 1.469(1) Å; ox^{2-} 502 hits, Dist1 = 3.039(148) Å and Dist2 = 2.222(3) Å; sq^{2-} 159 hits, Dist1 = 3.237(2) Å and Dist2 = 3.226(3) Å; bq^{2-} 194 hits, Dist1 = 4.700(1) Å and Dist2 = 2.656(1) Å; -COOH 3340 hits, Dist1 = 2.222(1) Å; PFOA 1 hit, Dist1 = 1.234(0) Å, Dist2 = 1.317(0) Å, Dist3 = 0.840(0) Å and Dist4 = 1.341(1) Å; 24.09.2023.
34 A. Bondi, *J. Phys. Chem.,* **1964**, *68*, 441.

35 I. J. Bruno, J. C. Cole, P. R. Edgington, M. Kessler, C. F. Macrae, P. McCabe, J. Pearson, R. Taylor, *Acta Cryst. B,* **2002**, *58*, 389.
36 M. J. Ajitha, K.-W. Huang, *Synth.,* **2016**, *48*, 3449.
37 C. Healy, K. M. Patil, B. H. Wilson, L. Hermanspahn, N. C. Harvey-Reid, B. I. Howard, C. Kleinjan, J. Kolien, F. Payet, S. G. Telfer, P. E. Kruger, T. D. Bennett, *Coord. Chem. Rev.,* **2020**, *419*, 213388.
38 Y. Sun, Y. Xia, *Science,* **2002**, *298*, 2176.
39 V. R. Reddy, *Synlett,* **2006**, *2006*, 1791.
40 J. Zheng, C. Zhou, M. Yu, J. Liu, *Nanoscale,* **2012**, *4*, 4073.
41 X.-X. Gou, T. Liu, Y.-Y. Wang, Y.-F. Han, *Angew. Chem. Int. Ed.,* **2020**, *59*, 16683.
42 P. K. Jain, X. Huang, I. H. El-Sayed, M. A. El-Sayed, *Acc. Chem. Res.,* **2008**, *41*, 1578.
43 X. Ren, Y. Song, A. Liu, J. Zhang, P. Yang, J. Zhang, M. An, *RSC Adv.,* **2015**, *5*, 64997.
44 K. Sneha, M. Sathishkumar, S. Kim, Y.-S. Yun, *Process Biochem.,* **2010**, *45*, 1450.
45 S. Krishnamurthy, A. Esterle, N. C. Sharma, S. V. Sahi, *Nanoscale Research Letters,* **2014**, *9*, 627.
46 J. L. Montaño-Priede, M. Sanromán-Iglesias, N. Zabala, M. Grzelczak, J. Aizpurua, *ACS Sens.,* **2023**, *8*, 1827.
47 C. Xie, W. Niu, P. Li, Y. Ge, J. Liu, Z. Fan, X. Liu, Y. Chen, M. Zhou, Z. Li, M. Ma, Y. Yue, J. Wang, L. Zhu, K. Luo, Y. Zhang, Y. Wu, L. Wang, B. Xu, H. Zhang, Z. Zhao, Y. Tian, *Nano Res.,* **2022**, *15*, 6678.
48 M. Thommes, K. Kaneko, A. V. Neimark, J. P. Olivier, F. Rodriguez-Reinoso, J. Rouquerol, K. S. W. Sing, *Pure Appl. Chem.,* **2015**, *87*, 1051.
49 K. S. W. Sing, *Pure Appl. Chem.,* **1985**, *57*, 603.
50 P. Rajniak, R. T. Yang, *AIChE J.,* **1993**, *39*, 774.
51 B. D. Adkins, B. H. Davis, *Langmuir,* **1987**, *3*, 722.
52 G. Mason, D. H. Everett, *Proc. R. Soc. A: Math. Phys. Eng. Sci.,* **1983**, *390*, 47.
53 M. Bender, *ChemBioEng Rev.,* **2014**, *1*, 136.
54 B. S. Greensfelder, H. H. Voge, *Ind. Eng. Chem.,* **1945**, *37*, 514.
55 Patent: I. TAMOTSU, **2000**, US9062262B2: 1,3-Butadiene separation from a crude C4 stream using catalytic extractive distillation, USA.
56 J. H. Schulze, Malte *C4-Hydrocarbons and Derivatives: Resources, Production, Marketing*, Springer Berlin, Heidelberg, GER, **1989**.
57 J. A. Kent: *Kent and Riegel's Handbook of Industrial Chemistry and Biotechnology,* 11, Springer, New York, New York, USA, **2007**.
58 M. Gehre, Z. Guo, G. Rothenberg, S. Tanase, *ChemSusChem,* **2017**, *10*, 3947.
59 J. Rouquerol, F. Rouquerol, P. Llewellyn, G. Maurin, K. Sing: *Adsorption by Powders and Porous Solids: Principles, Methodology and Applications*, Academic Press, Elsevier, **2013**.
60 S. Lowell, J. E. Shields, M. A. Thomas, M. Thommes: *Characterization of Porous Solids and Powders: Surface Area, Pore Size and Density*, Kluwer Academic Publishers, **2004**.
61 M. S. Liao, W. H. E. Schwarz, *Acta Cryst. B,* **1994**, *50*, 9.
62 D. Britt, H. Furukawa, B. Wang, T. G. Glover, O. M. Yaghi, *Proc. Natl. Acad. Sci. U.S.A,* **2009**, *106*, 20637.
63 A. C. McKinlay, B. Xiao, D. S. Wragg, P. S. Wheatley, I. L. Megson, R. E. Morris, *J. Am. Chem. Soc.,* **2008**, *130*, 10440.
64 H. Wu, W. Zhou, T. Yildirim, *J. Am. Chem. Soc.,* **2009**, *131*, 4995.
65 P. D. C. Dietzel, B. Panella, M. Hirscher, R. Blom, H. Fjellvåg, *Chem. Commun.,* **2006**, 959.
66 G. R. Lorzing, B. A. Trump, C. M. Brown, E. D. Bloch, *Chem. Mater.,* **2017**, *29*, 8583.
67 D. Nam, J. Huh, J. Lee, J. H. Kwak, H. Y. Jeong, K. Choi, W. Choe, *Chem. Sci.,* **2017**, *8*, 7765.
68 A. Carné-Sánchez, G. A. Craig, P. Larpent, V. Guillerm, K. Urayama, D. Maspoch, S. Furukawa, *Angew. Chem. Int. Ed.,* **2019**, *58*, 6347.

69 S. Ivanova, E. Köster, J. J. Holstein, N. Keller, G. H. Clever, T. Bein, F. Beuerle, *Angew. Chem. Int. Ed.,* **2021**, *60*, 17455.
70 T. Tozawa, J. T. A. Jones, S. I. Swamy, S. Jiang, D. J. Adams, S. Shakespeare, R. Clowes, D. Bradshaw, T. Hasell, S. Y. Chong, C. Tang, S. Thompson, J. Parker, A. Trewin, J. Bacsa, A. M. Z. Slawin, A. Steiner, A. I. Cooper, *Nat. Mater.,* **2009**, *8*, 973.
71 J. T. A. Jones, T. Hasell, X. Wu, J. Bacsa, K. E. Jelfs, M. Schmidtmann, S. Y. Chong, D. J. Adams, A. Trewin, F. Schiffman, F. Cora, B. Slater, A. Steiner, G. M. Day, A. I. Cooper, *Nature,* **2011**, *474*, 367.
72 G. Zhang, O. Presly, F. White, I. M. Oppel, M. Mastalerz, *Angew. Chem. Int. Ed.,* **2014**, *53*, 1516.
73 A. J. Gosselin, C. A. Rowland, E. D. Bloch, *Chem. Rev.,* **2020**, *120*, 8987.
74 Z. Bao, G. Chang, H. Xing, R. Krishna, Q. Ren, B. Chen, *Energy Environ. Sci.,* **2016**, *9*, 3612.
75 R.-B. Lin, H. Wu, L. Li, X.-L. Tang, Z. Li, J. Gao, H. Cui, W. Zhou, B. Chen, *J. Am. Chem. Soc.,* **2018**, *140*, 12940.
76 J. Gao, Y. Cai, X. Qian, P. Liu, H. Wu, W. Zhou, D.-X. Liu, L. Li, R.-B. Lin, B. Chen, *Angew. Chem. Int. Ed.,* **2021**, *60*, 20400.
77 B. Liang, X. Zhang, Y. Xie, R.-B. Lin, R. Krishna, H. Cui, Z. Li, Y. Shi, H. Wu, W. Zhou, B. Chen, *J. Am. Chem. Soc.,* **2020**, *142*, 17795.
78 G. Zhang, W. Lin, F. Huang, J. Sessler, N. M. Khashab, *J. Am. Chem. Soc.,* **2023**.
79 Y. Ding, L. O. Alimi, J. Du, B. Hua, A. Dey, P. Yu, N. M. Khashab, *Chem. Sci.,* **2022**, *13*, 3244.
80 H. Yao, Y.-M. Wang, M. Quan, M. U. Farooq, L.-P. Yang, W. Jiang, *Angew. Chem. Int. Ed.,* **2020**, *59*, 19945.
81 M. Maes, L. Alaerts, F. Vermoortele, R. Ameloot, S. Couck, V. Finsy, J. F. M. Denayer, D. E. De Vos, *J. Am. Chem. Soc.,* **2010**, *132*, 2284.
82 H. Kim, Y. Jung, *J. Phys. Chem. Lett.,* **2014**, *5*, 440.
83 C. Gücüyener, J. van den Bergh, A. M. Joaristi, P. C. M. M. Magusin, E. J. M. Hensen, J. Gascon, F. Kapteijn, *J. Mater. Chem.,* **2011**, *21*, 18386.
84 X. Tian, X. Zhang, L. Wei, S. Zeng, L. Huang, S. Zhang, *Green Chem.,* **2010**, *12*, 1263.
85 A. A. Heidecker, M. Stasi, A. Spears, J. Boekhoven, A. Pöthig, *ChemPlusChem,* **2023**, *n/a*, e202300234.
86 N. F. Cessford, N. A. Seaton, T. Düren, *Ind. Eng. Chem. Res.,* **2012**, *51*, 4911.
87 S. Furmaniak, S. Koter, A. P. Terzyk, P. A. Gauden, P. Kowalczyk, G. Rychlicki, *Phys. Chem. Chem. Phys.,* **2015**, *17*, 7232.
88 K. S. Walton, D. S. Sholl, *AIChE J.,* **2015**, *61*, 2757.
89 A. Spek, *Acta Cryst. C,* **2015**, *71*, 9.
90 L. Sarkisov, P. A. Monson, *Langmuir,* **2001**, *17*, 7600.
91 A. Groß, *ChemPhysChem,* **2010**, *11*, 1374.
92 C. Verma, H. Lgaz, D. K. Verma, E. E. Ebenso, I. Bahadur, M. A. Quraishi, *J. Mol. Liq.,* **2018**, *260*, 99.
93 R. Pelalak, R. Soltani, Z. Heidari, R. E. Malekshah, M. Aallaei, A. Marjani, M. Rezakazemi, S. Shirazian, *Sci. Rep.,* **2021**, *11*, 1967.
94 R. Shannon, *Acta Cryst. A,* **1976**, *32*, 751.
95 V. Amendola, M. Meneghetti, *J. Phys. Chem. C,* **2009**, *113*, 4277.
96 M. Gemmi, E. Mugnaioli, T. E. Gorelik, U. Kolb, L. Palatinus, P. Boullay, S. Hovmöller, J. P. Abrahams, *ACS Cent. Sci.,* **2019**, *5*, 1315.
97 P. J. Altmann, A. Pöthig, *Angew. Chem. Int. Ed.,* **2017**, *56*, 15733.
98 R. A. Smaldone, R. S. Forgan, H. Furukawa, J. J. Gassensmith, A. M. Z. Slawin, O. M. Yaghi, J. F. Stoddart, *Angew. Chem. Int. Ed.,* **2010**, *49*, 8630.
99 J. Liang, S. Xing, P. Brandt, A. Nuhnen, C. Schlüsener, Y. Sun, C. Janiak, *J. Mater. Chem. A,* **2020**, *8*, 19799.
100 H. Guo, J. Ye, Z. Zhang, Y. Wang, X. Yuan, C. Ou, Y. Ding, C. Yan, J. Wang, Y. Yao, *Inorg. Chem.,* **2020**, *59*, 11915.
101 N. Song, T. Kakuta, T.-a. Yamagishi, Y.-W. Yang, T. Ogoshi, *Chem,* **2018**, *4*, 2029.

102 K. Jie, Y. Zhou, E. Li, F. Huang, *Acc. Chem. Res.,* **2018**, *51*, 2064.
103 Y. Huang, R.-H. Gao, M. Liu, L.-X. Chen, X.-L. Ni, X. Xiao, H. Cong, Q.-J. Zhu, K. Chen, Z. Tao, *Angew. Chem. Int. Ed.,* **2021**, *60*, 15166.
104 R. X. Cheng, F. Y. Tian, Y. Q. Zhang, K. Chen, Q. J. Zhu, Z. Tao, *J. Mater. Sci.,* **2020**, *55*, 16497.
105 R.-H. Gao, Y. Huang, K. Chen, Z. Tao, *Coord. Chem. Rev.,* **2021**, *437*, 213741.
106 T. Ogoshi, S. Takashima, T.-a. Yamagishi, *J. Am. Chem. Soc.,* **2015**, *137*, 10962.
107 K. Jie, Y. Zhou, E. Li, R. Zhao, F. Huang, *Angew. Chem. Int. Ed.,* **2018**, *57*, 12845.
108 J.-R. Wu, Y.-W. Yang, *Angew. Chem. Int. Ed.,* **2021**, *60*, 1690.
109 M. Rojas-Poblete, P. L. Rodríguez-Kessler, R. Guajardo Maturana, A. Muñoz-Castro, *Phys. Chem. Chem. Phys.,* **2021**, *23*, 15917.
110 A. Cebollada, A. Vellé, M. Iglesias, L. B. Fullmer, S. Goberna-Ferrón, M. Nyman, P. J. Sanz Miguel, *Angew. Chem. Int. Ed.,* **2015**, *54*, 12762.
111 A. Vellé, L. Rodríguez-Santiago, M. Sodupe, P. J. Sanz Miguel, *Chem. Eur. J.,* **2020**, *26*, 997.
112 T. Wagner, A. Pöthig, H. M. S. Augenstein, T. D. Schmidt, M. Kaposi, E. Herdtweck, W. Brütting, W. A. Herrmann, F. E. Kühn, *Organometallics,* **2015**, *34*, 1522.
113 P. A. Wood, T. S. G. Olsson, J. C. Cole, S. J. Cottrell, N. Feeder, P. T. A. Galek, C. R. Groom, E. Pidcock, *Cryst. Eng. Comm.,* **2013**, *15*, 65.
114 A. S. Novikov, *Cryst.,* **2021**, *11*, 162.
115 M. L. Verdonk, J. C. Cole, R. Taylor, *J. Mol. Biol.,* **1999**, *289*, 1093.
116 C. F. Macrae, I. Sovago, S. J. Cottrell, P. T. A. Galek, P. McCabe, E. Pidcock, M. Platings, G. P. Shields, J. S. Stevens, M. Towler, P. A. Wood, *J. Appl. Crystallogr.,* **2020**, *53*, 226.
117 D. Jayatilaka, S. K. Wolff, D. J. Grimwood, J. J. McKinnon, M. A. Spackman, *Acta Cryst. A,* **2006**, *62*, s90.
118 P. R. Spackman, M. J. Turner, J. J. McKinnon, S. K. Wolff, D. J. Grimwood, D. Jayatilaka, M. A. Spackman, *J. Appl. Crystallogr.,* **2021**, *54*, 1006.
119 C. F. Mackenzie, P. R. Spackman, D. Jayatilaka, M. A. Spackman, *IUCrJ,* **2017**, *4*, 575.
120 G. R. Desiraju, *J. Chem. Soc., Dalton Trans.,* **2000**, 3745.
121 S. Guan, **2021**, Dissertation: *Investigation and Application of Multinuclear Coinage Metal Organometallic Complexes*, Technical University of Munich (Munich).
122 S. M. Soliman, A. M. A. Badr, *Polyhedron,* **2019**, *171*, 323.
123 G. R. Fulmer, A. J. M. Miller, N. H. Sherden, H. E. Gottlieb, A. Nudelman, B. M. Stoltz, J. E. Bercaw, K. I. Goldberg, *Organometallics,* **2010**, *29*, 2176.
124 L. Jedinák, R. Zátopková, H. Zemánková, A. Šustková, P. Cankař, *J. Org. Chem.,* **2017**, *82*, 157.
125 D. Thierry, E.-S. Mazen, V. Jean-Pierre, M. Nuno, B. Geneviève, *Chem. Lett.,* **2011**, *40*, 1434.
126 L. Jedinák, P. Cankař, *Eur. J. Org. Chem.,* **2016**, *2016*, 2013.
127 S. D. Walker, T. E. Barder, J. R. Martinelli, S. L. Buchwald, *Angew. Chem. Int. Ed.,* **2004**, *43*, 1871.
128 T. E. Barder, S. D. Walker, J. R. Martinelli, S. L. Buchwald, *J. Am. Chem. Soc.,* **2005**, *127*, 4685.
129 C. Amatore, A. Jutand, G. Le Duc, *Chem. Eur. J.,* **2011**, *17*, 2492.
130 P. J. Altmann, C. Jandl, A. Pöthig, *Dalton Trans.,* **2015**, *44*, 11278.
131 P. J. Altmann, A. Pöthig, *Chem. Commun.,* **2016**, *52*, 9089.
132 T. Pickl, A. Pöthig, *Organometallics,* **2021**, *40*, 3056.
133 P. Kuzmič, *Anal. Biochem.,* **1996**, *237*, 260.
134 **http://supramolecular.org/**, 07.06.2023.
135 I. Jarmoskaite, I. AlSadhan, P. P. Vaidyanathan, D. Herschlag, *eLife,* **2020**, *9*, e57264.
136 R.-B. Lin, Y. He, P. Li, H. Wang, W. Zhou, B. Chen, *Chem. Soc. Rev.,* **2019**, *48*, 1362.
137 M. Aust, A. J. Herold, L. Niederegger, C. Schneider, D. C. Mayer, M. Drees, J. Warnan, A. Pöthig, R. A. Fischer, *Inorg. Chem.,* **2021**, *60*, 19242.

138 F. A. Cotton, C. Y. Liu, C. A. Murillo, D. Villagrán, X. Wang, *J. Am. Chem. Soc.,* **2003**, *125*, 13564.
139 H. Li, M. Eddaoudi, M. O'Keeffe, O. M. Yaghi, *Nature,* **1999**, *402*, 276.
140 V. A. Dubskikh, A. A. Lysova, D. G. Samsonenko, A. N. Lavrov, K. A. Kovalenko, D. N. Dybtsev, V. P. Fedin, *Mol.,* **2021**, *26*, 1269.
141 Y.-R. Lee, J. Kim, W.-S. Ahn, *Korean J. Chem. Eng.,* **2013**, *30*, 1667.
142 N. Stock, S. Biswas, *Chem. Rev.,* **2012**, *112*, 933.
143 F. ZareKarizi, M. Joharian, A. Morsali, *J. Mater. Chem. A,* **2018**, *6*, 19288.
144 H.-Y. Gong, B. M. Rambo, E. Karnas, V. M. Lynch, K. M. Keller, J. L. Sessler, *J. Am. Chem. Soc.,* **2011**, *133*, 1526.
145 C.-P. Li, J. Chen, M. Du, *Cryst. Eng. Comm.,* **2010**, *12*, 4392.
146 J. Huo, M. Brightwell, S. El Hankari, A. Garai, D. Bradshaw, *J. Mater. Chem. A,* **2013**, *1*, 15220.
147 S. S.-Y. Chui, S. M.-F. Lo, J. P. H. Charmant, A. G. Orpen, I. D. Williams, *Science,* **1999**, *283*, 1148.
148 C. Boehme, G. Frenking, *Organometallics,* **1998**, *17*, 5801.
149 S. Budagumpi, R. S. Keri, G. Achar, K. N. Brinda, *Adv. Synth. Catal.,* **2020**, *362*, 970.
150 G. T. Hermanson: *Bioconjugate Techniques,* 3, Academic Press, Elsevier, London, UK, **2013**.
151 W. J. L. Wood, A. W. Patterson, H. Tsuruoka, R. K. Jain, J. A. Ellman, *J. Am. Chem. Soc.,* **2005**, *127*, 15521.
152 X. Wan, S. Li, Y. Tian, J. Xu, L.-C. Shen, H. Zuilhof, M. Zhang, A. C.-H. Sue, *Chem,* **2022**, *8*, 2136.
153 J. G. M. de Carvalho, R. A. Fischer, A. Pöthig, *Inorg. Chem.,* **2021**, *60*, 4676.
154 O. Tsutsumi, M. Tamaru, H. Nakasato, S. Shimai, S. Panthai, Y. Kuroda, K. Yamaguchi, K. Fujisawa, K. Hisano, *Mol.,* **2019**, *24*, 4606.
155 J. Ruiz, D. Sol, M. A. Mateo, M. Vivanco, R. Badía-Laiño, *Dalton Trans.,* **2020**, *49*, 6561.
156 R. Zhong, A. Pöthig, D. C. Mayer, C. Jandl, P. J. Altmann, W. A. Herrmann, F. E. Kühn, *Organometallics,* **2015**, *34*, 2573.
157 B.-H. Xia, H.-X. Zhang, C.-M. Che, K.-H. Leung, D. L. Phillips, N. Zhu, Z.-Y. Zhou, *J. Am. Chem. Soc.,* **2003**, *125*, 10362.
158 H. V. Huynh, S. Guo, W. Wu, *Organometallics,* **2013**, *32*, 4591.
159 Y. Hong, J. W. Y. Lam, B. Z. Tang, *Chem. Soc. Rev.,* **2011**, *40*, 5361.
160 Y. Chen, J. W. Y. Lam, R. T. K. Kwok, B. Liu, B. Z. Tang, *Mater. Horiz.,* **2019**, *6*, 428.
161 Z. Zhao, H. Zhang, J. W. Y. Lam, B. Z. Tang, *Angew. Chem. Int. Ed.,* **2020**, *59*, 9888.
162 N. Pearce, K. E. A. Reynolds, S. Kayal, X. Z. Sun, E. S. Davies, F. Malagreca, C. J. Schürmann, S. Ito, A. Yamano, S. P. Argent, M. W. George, N. R. Champness, *Nat. Commun.,* **2022**, *13*, 415.
163 S. N. Deger, S. J. Weishäupl, A. Pöthig, R. A. Fischer, *Energies,* **2022**, *15*, 2437.
164 J. Baggerman, D. C. Jagesar, R. A. L. Vallée, J. Hofkens, F. C. De Schryver, F. Schelhase, F. Vögtle, A. M. Brouwer, *Chem. Eur. J.,* **2007**, *13*, 1291.
165 B. J. Slater, E. S. Davies, S. P. Argent, H. Nowell, W. Lewis, A. J. Blake, N. R. Champness, *Chem. Eur. J.,* **2011**, *17*, 14746.
166 Z.-Q. Cao, H. Li, J. Yao, L. Zou, D.-H. Qu, H. Tian, *Asian J. Org. Chem.,* **2015**, *4*, 212.
167 C. Cunha, A. Pinto, A. Galvão, L. Rodríguez, J. S. Seixas de Melo, *Inorg. Chem.,* **2022**, *61*, 6964.
168 F. Würthner, T. E. Kaiser, C. R. Saha-Möller, *Angew. Chem. Int. Ed.,* **2011**, *50*, 3376.
169 V. Tumiatti, A. Milelli, A. Minarini, M. Micco, A. Gasperi Campani, L. Roncuzzi, D. Baiocchi, J. Marinello, G. Capranico, M. Zini, C. Stefanelli, C. Melchiorre, *J. Med. Chem.,* **2009**, *52*, 7873.
170 D. G. Hamilton, L. Prodi, N. Feeder, J. K. M. Sanders, *J. Chem. Soc., Perkins Trans.,* **1999**, 1057.
171 Z. Zhang, X. Chen, H. Zhang, W. Liu, W. Zhu, Y. Zhu, *Adv. Mater.,* **2020**, *32*, 1907746.

172 X.-Q. Liu, K. Zhang, J.-F. Gao, Y.-Z. Chen, C.-H. Tung, L.-Z. Wu, *Angewandte Chemie,* **2020**, *132*, 23662.
173 K. Fujisawa, Y. Ishikawa, Y. Miyashita, K.-i. Okamoto, *Inorg. Chim. Acta,* **2010**, *363*, 2977.
174 Z. Zhang, M. J. Zaworotko, *Chem. Soc. Rev.,* **2014**, *43*, 5444.
175 P. S. Bols, H. L. Anderson, *Acc. Chem. Res.,* **2018**, *51*, 2083.
176 P. L. Anelli, N. Spencer, J. F. Stoddart, *J. Am. Chem. Soc.,* **1991**, *113*, 5131.
177 Y. Sato, R. Yamasaki, S. Saito, *Angew. Chem. Int. Ed.,* **2009**, *48*, 504.
178 J. Guo, P. C. Mayers, G. A. Breault, C. A. Hunter, *Nat. Chem.,* **2010**, *2*, 218.
179 S. M. Goldup, D. A. Leigh, T. Long, P. R. McGonigal, M. D. Symes, J. Wu, *J. Am. Chem. Soc.,* **2009**, *131*, 15924.
180 X.-Y. Chen, D. Shen, K. Cai, Y. Jiao, H. Wu, B. Song, L. Zhang, Y. Tan, Y. Wang, Y. Feng, C. L. Stern, J. F. Stoddart, *J. Am. Chem. Soc.,* **2020**, *142*, 20152.
181 T. Calmus, **2021**, Masterthesis: *Experimental and Theoretical Evaluation of host-guest interactions of pillarplex cavitands*, Technical University of Munich (Munich).
182 R. C. Nishad, S. Kumar, A. Rit, *Angew. Chem. Int. Ed.,* **2022**, *61*, e202206788.
183 J. A. Bravo, F. M. Raymo, J. F. Stoddart, A. J. P. White, D. J. Williams, *Eur. J. Org. Chem.,* **1998**, *1998*, 2565.
184 E. A. Martynova, N. V. Tzouras, G. Pisanò, C. S. J. Cazin, S. P. Nolan, *Chem. Commun.,* **2021**, *57*, 3836.
185 W. Liu, C. L. Stern, J. F. Stoddart, *J. Am. Chem. Soc.,* **2020**, *142*, 10273.
186 O. S. Arvaniti, A. S. Stasinakis, *Sci. Total Environ.,* **2015**, *524-525*, 81.
187 W. Ji, L. Xiao, Y. Ling, C. Ching, M. Matsumoto, R. P. Bisbey, D. E. Helbling, W. R. Dichtel, *J. Am. Chem. Soc.,* **2018**, *140*, 12677.
188 P. Li, D. Zhi, X. Zhang, H. Zhu, Z. Li, Y. Peng, Y. He, L. Luo, X. Rong, Y. Zhou, *J. Environ. Manage.,* **2019**, *250*, 109488.
189 H. Omorodion, M. Palenzuela, M. Ruether, B. Twamley, J. A. Platts, R. J. Baker, *New J. Chem.,* **2018**, *42*, 7956.

4. Conclusion and Outlook

The work of this thesis focused on the investigation of $[M_8L^{Me}_2]^{4+}$ cation as potential building block in the solid-state. The conducted research can be divided into the following areas:

I Self-assembly of $[M_8L_2](X)_4$ in solid-state: An enhanced understanding of the literature-known pillarplex salts $[M_8L^{Me}_2](PF_6)_4$ and $[M_8L^{Me}_2](OAc)_4$ was achieved *via* crystallographic investigations. The aim was to analyse the cation arrangement, the position of counter anions and the underlaying non-covalent interactions. Prominent (non-)classical hydrogen bonding interactions between the pillarplex rim and counter anions as well as metal coordination between M(I) ions and counter anions or solvent molecules were identified. For the Au(I) congeners polymorphous structures were uncovered. During crystal structure analysis it was revealed that PF_6^- did not encapsulate leaving the micropore inside the pillarplex cavity empty. However, by positioning PF_6^- anions above the pore opening, the pore entrance could partially be blocked. In the case of the acetate pillarplex salts, partial occupation of the cavity by encapsulated counter anions was determined *via* SC-XRD measurements. Furthermore, the gas adsorption experiments revealed a gas uptake of N_2 and CO_2 by all compounds. The most promising outcomes were obtained with $[Ag_8L^{Me}_2](PF_6)_4$ and $[Au_8L^{Me}_2](PF_6)_4$ exhibiting BET surface areas of 138.4 $m^2\ g^{-1}$ and 29.9 $m^2\ g^{-1}$. This observation indicated that the Ag-pillarplex possess a higher microporous and the Au(I) congener a higher mesoporous volume. To evaluate the potential for gas separation, vapour adsorption experiments with individual C_4 hydrocarbons were conducted. In general, the following trend was monitored: 1,3-butadiene > *trans*-2-butene > *iso*-butylene > *n*-butane. Again, $[Ag_8L^{Me}_2](PF_6)_4$ and $[Au_8L^{Me}_2](PF_6)_4$ exhibited the best results. Notably, the best selectivity according to IAST was determined for an equimolar mixture of 1,3-butadiene and *n*-butane using $[Au_8L^{Me}_2](PF_6)_4$.

The diversification of pillarplex salts can be accomplished by alternating various parameters, such as a variation of the metal ion (Ag(I) *vs.* Au(I)), variation of the counter anion (PF_6^- *vs.* OAc^-) or a modification of the organic rim (L^{Me} *vs.* L^t *vs.* L^{Br}). We extended the library by successful synthesis of $[Ag_8L^{Me}_2](X)_4$ (X = F, Cl, Br, I, SCN, NO_3, ClO_4, BF_4) and $[Au_8L^{Me}_2](X)_4$ (X = Cl, Br). However, further analysis for several compound is still required including structural analysis *via* SC-XRD or micro-ED measurements. For $[Ag_8L^{Me}_2](BF_4)_4$, electron diffraction yielded a highly ordered arrangement of $[Ag_8L^{Me}_2]^{4+}$ with quasi-continuous pores formed due to pore alignment. This arrangement makes the salt a compelling candidate for further guest encapsulation studies, such as encapsulation of long alkyl chains extending through multiple cations. Attempts to synthesis $[Ag_8L^{Me}_2](I_3)_4$, $[Ag_8L^{Me}_2](SO_4)_4$ or introduce organic counter anions (propionic acid, squaric acid, 2,5-dihydroxy-1,4-benzoquinone) were not successful. Variation in the synthetic approach or changes in the pH-values must be addressed to include organic anions with a potential conjugated π-system. Gas adsorption experiments with N_2 were conducted to assess potential correlations between crystal arrangement, presence of accessible porosity (micro- *vs.* meso- *vs.* nonporous) and gas uptake. No conclusions could be drawn, but preliminary results suggested that there may be potential connections between the positions of the counter anions, pore accessibility and gas adsorption behaviour.

Another parameter space to explore is the simultaneous incorporation of multiple types of counter anions to synthesise mixed pillarplex salts. Through crystallisation processes, $[Au_8L^{Me}_2](PF_6)_{2.5}(AuCl_2)_{1.5}$ and $[Ag_8L^t_2]_2(PF_6)_5(OTf)_3$ were discovered, which exhibited particular crystal structures with strong metallophilic interactions (3.954 Å for Au(I)-Au(I) and 3.567 Å for

Ag(I)-Ag(I)). Additionally, (non-)classical hydrogen bonding interactions between the counter anions and the hydrogen atoms of the rim were identified. The implementation of the counter anion $AuCl_2^-$ further expands the parameter space, as it allows the inclusion of metal-containing anions, which could lead to interesting behaviour due to potential metal-to-metal coordination. Additionally, a pillarplex salt containing terephthalate units as counter anions was achieved by crystallisation attempts and subjected to crystal structure analysis. The tools Full Interaction Maps (FIMs) and Hirshfeld surface analysis were applied and tested for their applicability to organometallic supramolecules. While FIMs provided interaction regions for the organic components, Hirshfeld surface analysis revealed contributions of metal coordination.

II Rim functionalisation: To achieve implementation of pillarplex cations in network materials, the functionalisation of the rim was attempted by the introduction of potential linking. The pyrazole C-H position was selected as target, where a bromine group was successfully introduced yielding $L^{Br}(PF_6)_4$. Following the literature-known synthesis for the formation of pillarplexes provided $[Ag_8L^{Br}_2](PF_6)_4$, which could be further transmetalated to $[Au_8L^{Br}_2](PF_6)_4$. The introduced bromine functionality exhibited structure-decisive characteristics through formation of non-classical hydrogen bonds and metal coordination with neighbouring $[M_8L^{Br}_2]^{4+}$ cations. To further introduce functional groups (e.g., pyridine), Suzuki-Miyaura cross-coupling reaction conditions were applied to the brominated species. However, no successful results were obtained utilising the brominated ligand $L^{Br}(PF_6)_4$. For the Ag(I)-pillarplex system, transmetalation could occur and due to the charged nature of all pillarplex systems the possibility of anion exchange reactions must be considered. To overcome these challenges, further synthetic modification approaches should examine the metal ions of the pillarplex, metal ions of catalysts and the counter anions of both systems. The most promising approach should either utilise $[Au_8L^{Br}_2](PF_6)_4$ to avoid transmetalation, catalytic systems with identical counter anion PF_6^- or exploring strategies to eliminate a metal-containing catalytic system.

III Mechanically interlocked pillarplex systems: Another method to introduce a functional group into the pillarplex system involves the formation of (pseudo-)rotaxanes. The initial target group consisted of α,ω-dicarboxylic acids with varying alky chain lengths ($C_8H_{14}O_4$, $C_{10}H_{18}O_4$, $C_{12}H_{22}O_4$, $C_{14}H_{26}O_4$). Although the calculated diameter of -COOH with 5.34 Å based on SC-XRD data exceeds the pillarplex pore opening (4.3 Å), successful synthesis of the respective eight pseudorotaxanes $[M_8L^{Me}_2](C_2H_{2n-2}O_4)(PF_6)_4$ (M = Ag(I), Au(I); n = 8, 10, 12, 14) was achieved indicating a certain flexibility of the rim. Their host-guest behaviour was investigated by NMR and ITC titration experiments revealing a dependency between the binding affinity, the alky chain length and the solvent (MeCN *vs.* DMSO). The most reasonable results were obtained by ITC titration exhibiting binding constant in the range of $1.63 \cdot 10^{-6}$ – $8.50 \cdot 10^{-8}$ M. Through crystal structure analysis, the arrangement of $[Ag_8L^{Me}_2]^{4+}$ and anions was identified. However, no discrete modelling of the guest molecules was possible due to strong disorder. The residual electron density attributed to the guest molecules was treated and removed, revealing isolated voids for short guest molecule ($C_{10}H_{18}O_4$) and tilted quasi-continuous voids for longer dicarboxylic acids ($C_{12}H_{22}O_4$, $C_{14}H_{26}O_4$). The implementation of the pseudorotaxanes $[M_8L^{Me}_2](C_nH_{2n-2}O_4)(PF_6)_4$ into network materials was attempted by metal coordination. Unfortunately, no successful results were achieved, however significant challenges due to decomposition of the pillarplex, transmetalation or anion exchange reactions were identified. To circumvent these problems, alternative approaches must be evaluated, which could be the utilisation of Au(I)-based pseudorotaxanes to eliminate transmetalation, the employment of identical counter anions or the formation of covalently bound organic polymers.

During coordination attempts, the coordination polymer $[Zn_2(L^{Me})(NO_3)_6(OH)_2]$ was discovered forming 1D chains of macrocyclic ligand coordinated by Zn(II) nodes.

The next objective was the inclusion of pyridine as stopper motifs to form rotaxanes. Although the chemical composition was verified by standard analytical methods (NMR, IR, UV-vis spectroscopy, mass spectrometry, elemental analysis), the desired rotaxane could not be structurally validated *via* SC-XRD measurements. Based on the aforementioned knowledge, coordination attempts were focused on the addition of $Ag(I)PF_6$ to form 1D chains or applying solvothermal conditions to construct more dimensional materials. Until now no successful outcomes were documented. Further investigation towards pillar-layered materials must be evaluated along with the utilisation of $[Au_8L^{Me}_2][Py](PF_6)_4$ and metal precursors bearing identical counter anions.

IV Besides the investigation of pillarplexes as building blocks for solid-state materials, further research was conducted on the photophysics, rearrangement and guest encapsulation of the pillarplex system: Extinction coefficients for $[M_8L^{Me}_2](PF_6)_4$ in MeCN were determined ($\varepsilon = 0.966 \cdot 10^{-2}$ mol cm^{-2} for M = Ag, $\varepsilon = 1.065 \cdot 10^{-2}$mol cm^{-2} for M = Au) and $[Au_8L^{Me}_2](PF_6)_4$ was further investigated to explore emission quenching through guest encapsulation or the occurrence of aggregation induced emission. Indeed, a bathochromic shift in the absorption and excitation spectra was observed, which could be explained by enhanced intermolecular interactions upon the formation of $[Au_8L^{Me}_2](PF_6)_4$ aggregates. Preliminary results were obtained towards the formation of (pseudo-)rotaxane with incorporated chromophores in the stopper unit, such as *N*-naphthalene monoimide or *N*-naphthalene diimide, to assess their potential influence on the photophysics of the pillarplex system.

The lability of the $[Ag_8L^{Me}_2](PF_6)_4$ pillarplex was identified and utilised to discover novel supramolecular architectures – namely trillarplex $[Ag_{12}L^{Me}_3][TE](PF_6)_6$ and S-shaped complex $[Ag_6(HL^{Me})_2](PF_6)_4 \cdot TE$ – by the introduction of a suitable template (TE = template) motifs. Since these architectures were only observed during crystallisation procedures, a selective (template-directed) synthesis was already explored and will require further evaluation. After the successful formation of the trillarplex, an extensive investigation of its host-guest chemistry is necessary, especially regarding the potential removal of the template from the cavity or the formation of a rotaxane through post-synthetic modification of the encapsulated guest molecule at the three pore opening sites.

To evaluate the potential to apply $[Ag_8L^{Me}_2](PF_6)_4$ for the removal of perfluorinated compounds, this pillarplex salt was tested towards the encapsulation of PFOA and GenX in solution. Only partial encapsulation was observed by ^{19}F NMR spectroscopy but further investigation regarding partial fluorinated compounds in water could benefit the strength of host-guest interactions.

Additionally, the encapsulation of five-membered heterocycles was observed by the encapsulation of THF into $[Ag_8L^{Me}_2]^{4+}$, where metal coordination of Ag(I) and O_{THF} (2.72 Å) was detected. The overall crystal packing of $[Ag_8L^{Me}_2](PF_6)_4$ cations was determined by metallophilic Ag(I)-Ag(I) interactions (4.250 Å) and non-classical hydrogen bonds between pillarplex rim and counter anions PF_6^-. This opens a broad variety of potential guest molecules for the pillarplex system.

5. Experimental Section

5.1 General Materials and Methods

Unless otherwise stated, all chemicals and solvents were purchased by commercial suppliers. The reactions including air and moisture-sensitive compounds were carried out under Schlenk technique using Argon 4.6 from *Westfalen* or in the glovebox UNIlab from *MBraun*. The dry solvents were purchased from the SPS-800 from *MBraun* without further purification. Technical solvents were distilled prior to use. Deuterated solvents were purchased by *Euroisotop* and used without further purification.

Nuclear magnetic resonance spectroscopy (NMR)

The measurements of NMR spectra were performed with a *Bruker* DRX400 or a *Bruker* AV400 spectrometer with the frequency of 400 MHz for ^{1}H, 101 MHz for ^{13}C and 162 MHz for ^{31}P. Unless otherwise stated the samples were measured at 298 K. The chemical shifts are given in parts per million (ppm) and referenced to the solvent signal. The signal multiplicity is given in the following abbreviations: s (singlet), d (duplet), t (triplet), quartet (c), quintet (q), m (multiplet). The spectra were analysed with the software *MestreNova* (Version 12.0.2.20910). ^{1}H DOSY spectra were processed by the *Bayesian* method implemented in *MestReNova* software.

Electron Spray Ionisation Mass Spectrometry (ESI MS)

The ESI mass distributions were taken using a Exactive Plus Orbitrap system by *Thermo Fisher Scientific*. The samples were dissolved and filtered over a syringe filter. Polystyrene was used as an external standard for the calibration of the LCT Q-TOF mass spectrometer.

Fourier Transformation Infrared Spectroscopy (FT IR)

Infrared spectra were measured with the Alpha FT IR from *Bruker* containing a platinum diamond ATR device. The measurement ranges from 450 to 4000 cm^{-1}. The compounds were measured as solids under inert conditions in the glovebox. Signal intensities were described with the abbreviations s for strong, m for medium and w for weak. The spectra were analysed with the software *OPUS* (Version 7.5).

Liquid UV-vis spectroscopy was measured on a double-beam Lambda 365 UV-Vis spectrophotometer from *PerkinElmer*.

Solid UV-vis spectroscopy was measured on a UV-VIS-NIR spectrophotometer *Shimadzu* UV-3600 Plus.

Emission spectroscopy in the solid state was measured on a FS5 spectrofluorometer from *Edinburgh Instruments*.

Dynamic Light scattering (DLS) measurements were performed on a *Malvern* Zetasizer Nano instrument. The samples were filtered through a 200 nm PTFE syringe filter into a 10 mm quartz cuvette and the cuvette was placed in the instrument. After equilibrating at the desired temperature for 10 minutes prior to the measurement, twelve measurement runs were averaged for one experiment to avoid statistical errors. The general-purpose method of the *Malvern* Zetasizer software is used for data analysis.

Elemental analysis (EA) of C, H, N and S were performed with Euro Elemental Analyszer from *Euro Vector*.

Powder X-Ray diffraction measurements were either performed on STOE STADI P Powder X-ray Diffractometer with Mo Kα1 radiation (0.7093 nm) at 298 K. The samples were provided in capillaries and measured in a Debye-Sherrer geometry. The range of measurement was 1-40 ° with a step size of 0.015 °. Or measurements were performed on *Rigaku* MiniFlex 600-C Powder X-ray Diffractometer with Cu K_α radiation (λ_1=1.5406 Å, λ_2=1.5444 Å, I_2/I_1=0.5) at 298 K. The samples were provided on silicon single-crystal wafers using *Bragg-Brentano* geometry. The range of measurement was 3-50 ° (2θ) with a step size of 0.01 ° and a scan rate of 5 or 10 degrees per minute.

Thermalgravimetric Analysis (TGA) was performed at a TGA/STA 409 PC apparatus from *Mettler-Toledo Intl. Inc.* under synthetic air with a continuous ramp of 10 K min^{-1}. The sample was provided in aluminium oxide crucibles and data was evaluated by the software *STARe 14.00*.

Scanning Electron Microscopy (SEM) was performed with a *Jeol* JSM-7500F field emission scanning electron microscope with the Gentle Beam mode. The obtained pictures were analysed with the supplier software.

Solubility was tested by providing 1 mL of the solvent and slow addition of substance as solid.

5.2 Nuclear Magnetic Resonance Spectroscopy Titration Experiments

To a 1.425 mM solution of guest ($C_8H_{14}O_4$, $C_{10}H_{16}O_4$, $C_{12}H_{22}O_4$, $C_{14}H_{26}O_4$) in DMSO-d_6 or MeCN-d_3 a 2.850 mM solution of $[M_8L^{Me}_2](PF_6)_4$ in DMSO-d_6 or MeCN-d_3 was added and ^{1}H NMR spectroscopy was performed.

Data for the NMR titration of $[M_8L^{Me}_2](PF_6)_4$ and guests in MeCN-d_3 or DMSO-d_6:

eq.guest	eq.host	c_{host} [mM]	c_{guest} [mM]	V_{host} [mL]	V_{guest} [mL]	V_{tot} [mL]	[guest]/ ([host]+[guest])	[hoest]/ ([host]+[guest])
1	0	0	1.425	0	0.4	0.4	1.0	0.0
1	0.2	0.259	1.295	0.04	0.4	0.44	0.833	0.167
1	0.4	0.475	1.1875	0.08	0.4	0.48	0.714	0.286
1	0.6	0.657	1.096	0.12	0.4	0.52	0.625	0.375
1	0.8	0.814	1.017	0.16	0.4	0.56	0.556	0.444
1	1.0	0.950	0.950	0.20	0.4	0.6	0.500	0.500
1	2.0	1.425	0.712	0.40	0.4	0.8	0.333	0.667
1	3.0	1.710	0.570	0.60	0.4	1.0	0.250	0.750
0	1	2.850	0.0	0.4	0.0	0.4	0.0	1.0

DynaFit[1] and Job Plot:

Line fitting [*task = fit*] and the determination of the binding constant K_d [*data = equilibria*] of the NMR titration [*mechanism: H + G <==> HG : K dissoc*] was performed using DynaFit[1] (nonlinear least-square regression analysis). In the equilibrium binding experiment, the total concentration of titrant changes due to inevitable dilution. To take this into account, keywords [*plot titration*] and [*variable H, H*] were added in the [*data*] block. The shift of H_A (CH_2 group attached right beside the carboxylic acid group) was used for response [*intensive*] for the titrations. In the exceptional cases $[Au_8L^{Me}_2](PF_6)_4$ against $C_{12}H_{22}O_4$ and $C_{14}H_{26}O_4$ the protons H_{CCHC} (CH at pyrazole unit) were used for response for the calculation of the Job-Plots. For the complexes $[Ag_8L^{Me}_2](C_8H_{14}O_4)(PF_6)_4$, $[Ag_8L^{Me}_2](C_{10}H_{18}O_4)(PF_6)_4$, $[Ag_8L^{Me}_2](C_{12}H_{22}O_4)(PF_6)_4$, $[Ag_8L^{Me}_2](C_{14}H_{26}O_4)(PF_6)_4$, $[Au_8L^{Me}_2](C_8H_{14}O_4)(PF_6)_4$ and $[Au_8L^{Me}_2](C_{10}H_{18}O_4)(PF_6)_4$ line fitting and the determination of the binding constant led to reasonable results with good fitting and good regression. Line fitting was also performed for the other complexes ($[Au_8L^{Me}_2](C_{12}H_{22}O_4)(PF_6)_4$, $[Au_8L^{Me}_2](C_{14}H_{26}O_4)(PF_6)_4$) but did not yield good fitting and regressions. A similar analysis using the same model is not applicable for the longer dicarboxylic acids due to the broadened proton signals H_A.

BindFit:[2-3]

The input files, calculated fits and further information is accessible via the database http://supramolecular.org.[2] All assigned guest signals were included into the input file. For the titrations of $[M_8L^{Me}_2](PF_6)_4$ into $C_8H_{14}O_4$ the determination of a binding constant was possible, but the calculation of the mole fractions yielded no conclusive results as no encapsulation of $C_8H_{14}O_4$ into $[Ag_8L^{Me}_2](PF_6)_4$ and relatively slow encapsulation of $C_8H_{14}O_4$ into $[Au_8L^{Me}_2](PF_6)_4$ were observed. For the cases of $[Au_8L^{Me}_2](PF_6)_4$ against $C_{12}H_{22}O_4$ and $C_{14}H_{26}O_4$ the protons H_{CCHC} (CH at pyrazole unit) were used, which did not yield suitable results.

Calculated binding constant from the NMR titrations of $[M_8L^{Me}_2](PF_6)_4$ and guests in MeCN-d_3:

host	guest	ratio	K_d [M]	Error [%]
$[Ag_8L^{Me}_2](PF_6)_4$	$C_8H_{14}O_4$	1:1	$3.985 \cdot 10^{-3}$	3.318
$[Ag_8L^{Me}_2](PF_6)_4$	$C_{10}H_{18}O_4$	1:1	$1.542 \cdot 10^{-4}$	25.469
$[Ag_8L^{Me}_2](PF_6)_4$	$C_{12}H_{22}O_4$	1:1	$4.172 \cdot 10^{-6}$	416.635
$[Ag_8L^{Me}_2](PF_6)_4$	$C_{14}H_{26}O_4$	1:1	$2.147 \cdot 10^{-6}$	8.237
$[Au_8L^{Me}_2](PF_6)_4$	$C_8H_{14}O_4$	1:1	$6.299 \cdot 10^{-4}$	5.361
$[Au_8L^{Me}_2](PF_6)_4$	$C_{10}H_{18}O_4$	1:1	$3.502 \cdot 10^{-4}$	11.860

Integral ratios for slow host-guest exchange:

The titrations of $C_{12}H_{22}O_4$, $C_{14}H_{26}O_4$ into $[Ag_8L^{Me}_2](PF_6)_4$ and $C_{10}H_{18}O_4$, $C_{12}H_{22}O_4$, $C_{14}H_{26}O_4$ into $[Au_8L^{Me}_2](PF_6)_4$ a slow equilibrium was observed. Comparison of the integral ratios of the free (H_X) and encapsulated (H_A) guest ratio was performed and with the known concentrations $[H]_0$ and $[G]_0$ the following equation could be used for calculating the binding constant K_d.

$$[H] = \frac{1}{K_\alpha} \cdot \frac{[HG]}{[G]} = K_d \cdot \frac{[HG]}{[G]} \qquad with\ H + G \overset{K_\alpha}{\rightarrow} HG$$

Data from the NMR titrations with slow equilibrium of $[M_8L^{Me}_2](PF_6)_4$ and guests in DMSO-d_6:

	K_d [M]	R [M]
$C_{12}H_{22}O_4$ into $[Ag_8L^{Me}_2](PF_6)_4$	$6.49 \cdot 10^{-5}$	$9.53 \cdot 10^{-1}$
$C_{12}H_{22}O_4$ into $[Ag_8L^{Me}_2](PF_6)_4$	$2.63 \cdot 10^{-5}$	$9.24 \cdot 10^{-1}$
$C_{12}H_{22}O_4$ into $[Ag_8L^{Me}_2](PF_6)_4$	$5.63 \cdot 10^{-5}$	$9.75 \cdot 10^{-1}$
$C_{12}H_{22}O_4$ into $[Ag_8L^{Me}_2](PF_6)_4$	$8.97 \cdot 10^{-5}$	$9.58 \cdot 10^{-1}$
$C_{12}H_{22}O_4$ into $[Au_8L^{Me}_2](PF_6)_4$	$4.14 \cdot 10^{-5}$	$9.57 \cdot 10^{-1}$

5.3 Isothermal Calorimetry Titration Experiments (ITC)

Isothermal titration experiments were performed on a MicroCal PEAQ-ITC from Malvern Pananalytical. All experiments were performed at 25°C in pure acetonitrile. The reference cell was filled with acetonitrile.
For all the titrations the following conditions were used: sample cell was filled with either $[Au_8L^{Me}{}_2](PF_6)_4$ or $[Ag_8L^{Me}{}_2](PF_6)_4$ to a final concentration of 30 µM. The dicarboxylic acid was loaded in the titration syringe to a concentration of 200 µM. Titration was performed with 1 injection of 0.4 µL followed by 18 injections of 2 µL. Injection duration was set to 4 s, spacing between injections 150 s and stirring speed to 750 rpm to ensure homogeneous mixing of the solution.
For each dicarboxylic acid, a control titration versus acetonitrile was performed and used to correct the heat of dilution.
Data were fitted using a non-linear least squares regression algorithm provided by the Malvern PEAQ-ITC Analysis Software. For all titration, a “one-set of site” binding isotherm was used. Errors correspond to errors of the fit.

5.4 Brunauer-Emmett-Teller (BET)

Adsorption measurements were carried out on a *MICORMETRICS 3Flex* Physisorption from Micromeritics Instrument Corp., which uses a manometric method to determine the amount adsorbed under an equilibrated gas pressure. Nitrogen isotherms were measured at 77 K. Adsorption data was processed using the 3Flex Software Version 5.01 by Micromeritics Instrument Corp. and plotted in OriginPro 2020. To create open data access, prevent issues with data mining and facilitate machine learning all isotherms are given as adsorption information files in the appendix.[4] Conversion of measurement files was done using an open access web application.[5] Activated samples were transferred into pre-weighed sample tubes and capped with Micromeritics CheckSeals. Samples were subsequently heated at 80 °C, 72 h under dynamic vacuum of ~ 10^{-3} mbar using a SmartVac Prep by Micromeritics Instrument Corp. to ensure absence of unwanted adsorbates and identical pre-measurement states of all samples. The mass of the adsorbent was then recorded, generally in the range of 20-50 mg.

Free space of the sample tube is determined prior to measuring each adsorption isotherm using helium (99.999 vol%). A liquid nitrogen bath is used for measurements at 77 K and a dry ice cooling bath is used for measurements at 195 K.

The apparent surface area of the materials was derived using the Brunauer- Emmett-Teller (BET) model, is hence given as apparent BET surface area and based on N_2 isotherms measured at 77 K. To determine the BET area for microporous materials care was taken to adhere to the Rouquerol criteria.[6-7] The BET surface area was calculated between values of 0.01 and 0.1 p/p_0 of the relative pressure range.

5.5 Single Crystal X-Ray Diffraction (SC-XRD)

X-ray intensity data were collected on a Bruker D8 Venture single crystal X-Ray diffractometer equipped with a CMOS detector (Bruker Photon-100), a TXS rotating anode with MoKα (λ=0.71073 Å) and a Helios mirror optic using the software package APEX3 and APEX4.[8] Measurements were performed on a single crystal coated with perfluorinated ether and the crystal was fixed on top of a Kapton micro sampler, transferred to the diffractometer and frozen under a stream of cold nitrogen. A matrix scan was used to determine the initial lattice parameters. Reflections were merged and corrected for Lorenz and polarisation effects, scan speed and background using SAINT.[9] Absorption corrections, including odd and even ordered spherical harmonics were performed using SADABS.[9] Based on systematic absences, E-statistics, and successful refinement of the structures, the space group was assigned. The structure was solved by direct methods[10] with aid of successive difference fourier maps, refined using APEXIII and APEX4 software, in conjugation with SHELXL-2018/3, SHELXL-2019/1 and SHELXLE.[10-12] Hydrogen atoms were calculated in ideal positions with $U_{iso}(H) = 1.2\ U_{eq}(C)$. Non-hydrogen atoms were refined using anisotropic displacement parameters. Full-matrix least-squares refinements were carried out by minimising $\Sigma w(F_o^2 - F_c^2)^2$ with the SHELXL weighting scheme.[9] Neutral atom scattering factors for all atoms and anomalous dispersion corrections for the non-hydrogen atoms were taken from *International Tables for Crystallography*.[13]

The disordered molecule was treated as a diffused contribution to the overall scattering without specific atom positions using the PLATON/SQUEEZE procedure.[14] Images of the crystal structure were generated with MERCURY and PLATON.21.[15-16] Published structures with are marked with CCDC numbers containing the supplementary crystallographic data. This data is provided free of charge by The Cambridge Crystallographic Data Centre. Data of the unpublished structures is provided in the Appendix.

5.6 Micro Electron Diffraction (micro ED)

Samples were finely dispersed on standard TEM grids (amorphous carbon on Cu) and measured on an ELDICO *ED-1* electron diffractometer at room temperature using the software ELDIX. The device is equipped with a LaB_6 source operating at an acceleration voltage of 160 kV (λ = 0.02851 Å) and a hybrid-pixel detector (Dectris QUADRO). Suitable crystals were identified in STEM imaging mode and diffraction was recorded in continuous rotation mode with a beam diameter of ca. 750 nm. The later parts of measurements showing significant beam damage were omitted.

Data for kinematical refinement were processed and evaluated using the APEX4 software package. After unit cell determination the frames were integrated and corrected for Lorentz effects, scan speed, background, and absorption using SAINT and SADABS. Space group determination was based on systematic absences, E statistics, and successful refinement of the structure. The structure was solved using ShelXT and refined with ShelXL in conjunction with ShelXle. Least squares refinements were carried out within the kinematic approximation by minimising $\Sigma w(F_{obs}^2 - F_{calc}^2)^2$ with the ShelXL weighting scheme and using neutral electron

scattering factors. H atoms were placed in calculated positions based on typical distances for neutron diffraction and refined with a riding model and $U_{iso}(H) = 1.2 \cdot U_{eq}(C)$. Restraints on geometries and anisotropic displacement parameters were used to ensure convergence within physically meaningful limits, if necessary.

5.7 Computational Methods

Quantum chemical calculations were performed with the *ORCA 4.2.1* or the *ORCA 5.0* software packages.[17-19] An exchange-correlation function by Perdew-Burke-Ernzerhof (PBE) was used for geometry optimisations and the electronic energy of an optimised geometry was determined with a single point calculation using the range-separated-hybrid GGA functional ωB97X.[20-21] To account for weak dispersion interactions, Grimme´s atom-pairwise dispersion correction (D3) with a Becke-Johnson damping (BJ) was applied to obtain more accurate energies.[22-23]

For the convergence criteria of the final geometry optimisation, the keywords “TigthOPT” and “TightSCF” were chosen. Def2 basis sets by Alrich with implemented single-ζ valence split (def2-SVP) or triple-ζ valence split (def2-TZVPP), which was added due to the presence of metal ions to improve the quality of the obtained results, were used.[24-25] The “resolution-of-identity” (RI-J) approximation for the evaluation of the Coulomb matrices and the “chain-of-spheres” (COSX) algorithm for exchange treatment were employed for acceleration purposes. Partially, numeric frequency analyses at the same level of theory as the geometry optimisations were performed to confirm that the calculations had converged to an energetic minimum, where almost no negative eigenfrequencies were obtained.

Avogadro 1.2.0 was used to edit the starting geometries of the calculations and *Chemcraft 1.8* was used to visualise the spectra.[26]

5.8 Experimental Details

Au(THT)Cl[27], $L^{Me}(OTf)_4$, $L^{Me}(PF_6)_4$, $[M_8L^{Me}_2](OTf)_4$, $[M_8L^{Me}_2](PF_6)_4$, $[Au_8L^{Me}_2](OAc)_4$, $[M_8L^{Me}_2]$[1,12.diaminododecane]$(PF_6)_4$, $[M_8L^{Me}_2]$[Rotaxane]$(OTf)_4$ were synthesised according to literature.[28-29] The templates TE1 (*N*-methylnaphthalimide) and TE2 (*N*-heptyl-1,8-naphthalimide) were synthesis according to adapted synthetic routes.[30]

5.8.1 Anion Exchange Reactions

Synthesis of $[Ag_8L^{Me}_2](OAc)_4$

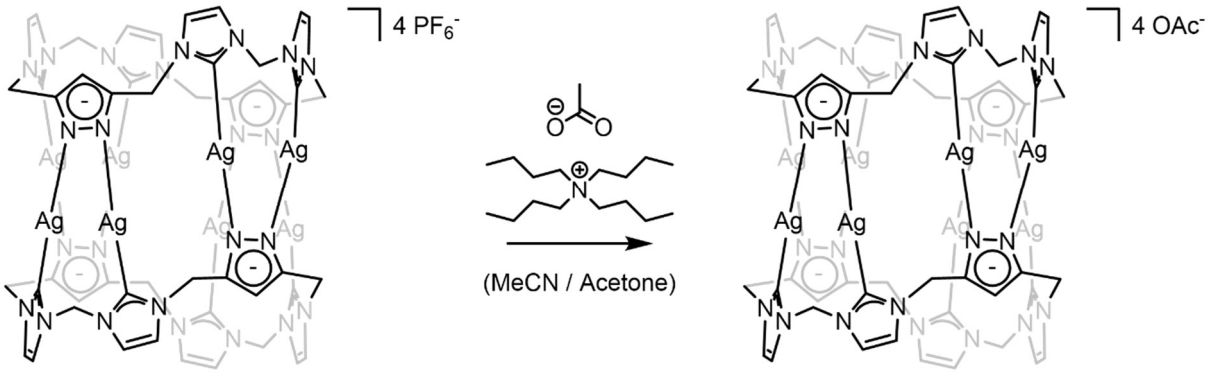

A solution of $[Ag_8L^{Me}_2](PF_6)_4$ (100.00 mg, 41.67 µmol, 1 eq.) was dissolved in a 1:1 solvent mixture of acetone and acetonitrile (20 mL) and dropwise added to a solution of tetrabutyl ammonium acetate (87.95 mg, 291.68 µmol, 7 eq.) in 20 mL of a 1:1 mixture of acetone and acetonitrile under vigorous stirring. After stirring the suspension at rt for 30 min, the white precipitate was isolation by centrifugation and washed with acetone 3 x 5 mL. For further purification, the white residue was redissolved in a minimum amount of water and precipitated by an excess of acetone. Again, the solid was isolated by centrifugation and washed with acetone (3 x 5 mL). $[Ag_8L^{Me}_2](OAc)_4$ was dried *in vacuo* and obtained as a white powder.

Yield: white powder, 77.97 mg, 37.92 µmol, 91%.

^{1}H NMR (400.13 MHz, D_2O): δ (ppm) = 7.65 (d, ^3J = 1.96 Hz, 8H, H_{NCHC}), 7.56 (d, ^3J = 1.92 Hz, 8H, H_{NCHC}), 6.77 (s, 4H, H_{CCHC}), 6.75 (d, ^2J = 15.73 Hz, 4H, H_{CH2}), 6.17 (d, ^2J = 14.82 Hz, 4H, H_{CH2}), 5.58 (d, ^2J = 15.11 Hz, 8H, H_{CH2}), 5.30 (d, ^2J = 15.16 Hz, 8H, H_{CH2}), 1.88 (s, 12H, H_{OAc}).

^{13}C{^{1}H} NMR (100.62 MHz, D_2O+MeCN-d_3): δ (ppm) = 180.86, 149.08, 122.67, 121.66, 102.03, 64.53, 63.75, 48.01, 22.64, 12.66.

EA (%): calc. C 29.84, H 3.49, N 14.91; measured C 29.91, H 3.37, N 14.30 for $[Ag_8L^{Me}_2](OAc)_4] \cdot 11\ H_2O$.

ESI-MS (H_2O): *m/z* = 454.9125, calc. 454.91 for $[Ag_8L^{Me}_2]^{4+}$, 626.2233, calc. 626.22 for $[Ag_8L^{Me}_2](OAc)^{3+}$, 968.8419, calc. 968.84 for $[Ag_8L^{Me}_2](OAc)_2^{2+}$.

SC-XRD (MoK_α, λ = 0.71073 Å): colourless fragment, monoclinic *P* $2_1/c$, a = 29.41(3) Å, b = 32.88(3) Å, c = 31.13(3) Å, α = 90°, β = 115.620(19)°, γ = 90°, R = 9.90% (HeiAl18).

General Synthesis Route of $[M_8L^{Me}_2](X)_4$ by Precipitation

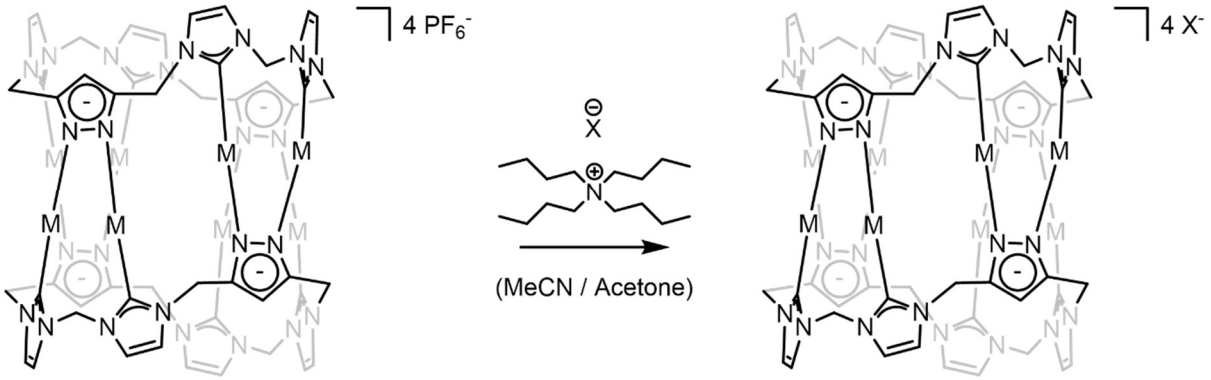

A solution of $[M_8L^{Me}_2](PF_6)_4$ (1 eq.) was dissolved in a 1:1 solvent mixture of acetone and acetonitrile and dropwise added to a solution of TBA-X (5 eq.) in a 1:1 mixture of acetone and acetonitrile under vigorous stirring. After stirring the suspension at rt for 30 min, the white precipitate was isolation by centrifugation and washed with acetone. For further purification, the white residue was redissolved in a minimum amount of water and precipitated by an excess of acetone. Again, the solid was isolated by centrifugation and washed with acetone. $[M_8L^{Me}_2](X)_4$ was dried *in vacuo* and obtained as a powder.

Crystallisation attempts A:

In the bottom of a U-tube a solvent mixture of MeCN:acetone was provided. On one side a solution of $[M_8L^{Me}_2](PF_6)_4$ (1 eq. in MeCN:acetone) was slowly poured on top and on the other side a solution of TBA-X (5 eq., MeCN:acetone) was slowly added. The U-tubes were kept at rt.

Crystallisation attempts B:

In an NMR tube a solution of $[M_8L^{Me}_2](X)_4$ was provided and placed in a Schlenk-tube filled with acetone. The Schlenk-tube was sealed and kept at rt, where slow diffusion of acetone into the NMR tube was expected.

$[Ag_8L^{Me}_2](F)_4$

Reagents: $[Ag_8L^{Me}_2](PF_6)_4$ (100.00 mg, 41.67 µmol, 1 eq.); TBA fluoride (54.06 mg, 208.35 µmol, 5 eq.).

Yield: bright yellow powder, 69 mg, 36.25 µmol, 87%.

^{1}H NMR (400.13 MHz, DMSO-d_6): δ (ppm) = 7.94 (s, 8H, H_{NCHC}), 7.72 (s, 8H, H_{NCHC}), 6.73 (d, ^2J = 14.5 Hz, 4H, H_{CH2}), 6.55 (s, 4H, H_{CCHC}), 6.23 (d, ^2J = 14.5 Hz, 4H, H_{CH2}), 6.13 (d, ^2J = 14.6 Hz, 8H, H_{CH2}), 5.11 (d, ^2J = 14.5 Hz, 8H, H_{CH2}).

^{1}H NMR (300 MHz): δ (ppm) = 5.31, 1.11, 0.09.

^{19}F NMR (376.46 MHz, DMSO-d_6): δ (ppm) = -142.40.

^{13}C NMR (75 MHz): δ (ppm) = 206.42, 177.72, 150.83, 125.26, 105.53, 65.64, 49.74, 28.67, 19.38, 13.63, -1.28.

EA (%): calc. C 30.41, H 2.34, N 17.73; measured C 29.29, H 3.48, N 13.94 for $[Ag_8L^{Me}{}_2](F)_4]$.

UV-vis (H_2O, c = 1 · 10^{-5} mol/L): I_{max} (nm) = 227.

$[Ag_8L^{Me}{}_2](Cl)_4$

Reagents: $[Ag_8L^{Me}{}_2](PF_6)_4$ (80.00 mg, 33.34 µmol, 1 eq.); TBA chloride (45.99 mg, 166.68 µmol, 5 eq.).

Yield: white powder, 57 mg, 29.01 µmol, 87%.

^{1}H NMR (400.13 MHz, DMSO-d_6): δ (ppm) = 7.92 (s, 8H, H_{NCHC}), 7.70 (s, 8H, H_{NCHC}), 6.73 (d, ^2J = 14.2 Hz, 4H, H_{CH2}), 6.56 (d, ^2J = 14.7 Hz, 4H, H_{CH2}), 6.50 (s, 4H, H_{CCHC}), 6.15 (d, ^2J = 14.3 Hz, 8H, H_{CH2}), 5.04 (d, ^2J = 14.7 Hz, 8H, H_{CH2}).

^{1}H NMR (300 MHz): δ (ppm) = 7.26, 4.51, 0.45, -0.41.

^{13}C NMR (125.83 MHz, DMSO-d_6): δ (ppm) = 149.46, 124.41, 122.36, 103.80, 94.72, 81.72, 81.60, 64.70, 47.56, 31.19, 1.65.

^{13}C NMR (75 MHz): δ (ppm) = 204.49, 180.90, 152.10, 148.17, 125.64, 123.82, 122.45, 104.21, 63.66, 53.46, 48.32, 28.61, 27.22, -3.12.

DOSY NMR (400.13 MHz, DMSO-d_6): δ (m^2 sec^{-1}) = 8.50 · 10^{-11}.

EA (%): calc. C 29.95, H 2.07, N 17.14; measured C 28.08, H 2.37, N 15.12 for $[Ag_8L^{Me}{}_2](Cl)_4]$.

ESI-MS (H_2O): m/z = 454.9124 $[Ag_8L^{Me}{}_2]^{4+}$, calc. 454.91 for $[Ag_8L^{Me}{}_2]^{4+}$; 618.2071 $[Ag_8L^{Me}{}_2](Cl)^{3+}$, calc. 618.21 for $[Ag_8L^{Me}{}_2](Cl)^{3+}$; 945.7932 $[Ag_8L^{Me}{}_2](Cl)_2{}^{2+}$, calc. 945.79 for $[Ag_8L^{Me}{}_2](Cl)_2{}^{2+}$.

UV-vis (H_2O, c = 1 · 10^{-5} mol/L): I_{max} (nm) = 226.

$[Ag_8L^{Me}{}_2](Br)_4$

Reagents: $[Ag_8L^{Me}{}_2](PF_6)_4$ (100.00 mg, 41.67 µmol, 1 eq.); TBA bromide (66.75 mg, 208.35 µmol, 5 eq.).

Yield: white powder, 67 mg, 36.42 µmol, 85%.

^{1}H NMR (400.13 MHz, DMSO-d_6): δ (ppm) = 7.92 (d, ^2J = 1.9 Hz, 8H, H_{NCHC}), 7.72 (d, ^2J = 1.9 Hz, 8H, H_{NCHC}), 6.78 (d, ^2J = 14.4 Hz, 4H, H_{CH2}), 6.53 (s, 4H, H_{CCHC}), 6.38 (d, ^2J = 14.7 Hz, 4H, H_{CH2}), 6.14 (d, ^2J = 14.5 Hz, 8H, H_{CH2}), 5.10 (d, ^2J = 14.8 Hz, 8H, H_{CH2}).

^{1}H NMR (300 MHz): δ (ppm) = 7.36, 4.09, 0.19.

^{13}C NMR (75 MHz): δ (ppm) = 204.60, 182.83, 180.48, 150.14, 148.10, 126.23, 122.09, 105.02, 63.42, 50.45, 48.27, 33.22, 28.45, -1.64.

EA (%): calc. C 26.95, H 2.07, N 15.71; measured C 27.76, H 2.53, N 14.16 for $[Ag_8L^{Me}_2](Br)_4]$.

ESI-MS (H_2O): m/z = 454.9130 $[Ag_8L^{Me}_2]^{4+}$, calc. 454.91 for $[Ag_8L^{Me}_2]^{4+}$; 632.8573 $[Ag_8L^{Me}_2](Br)^{3+}$, calc. 632.86 for $[Ag_8L^{Me}_2](Br)^{3+}$; 989.7439 $[Ag_8L^{Me}_2](Br)_2^{2+}$, calc. 989.74 for $[Ag_8L^{Me}_2](Br)_2^{2+}$.

UV-vis (H_2O, c = 1 · 10^{-5} mol/L): I_{max} (nm) = 224.

$[Ag_8L^{Me}_2](I)_4$

Reagents: $[Ag_8L^{Me}_2](PF_6)_4$ (100.00 mg, 41.67 µmol, 1 eq.); TBA iodide (76.54 mg, 208.35 µmol, 5 eq.).

Yield: white powder, 75 mg, 32.22 µmol, 78%.

^{1}H NMR (400.13 MHz, DMSO-d_6): δ (ppm) = 7.92 (d, ^2J = 1.8 Hz, 8H, H_{NCHC}), 7.71 (dd, ^2J = 1.8 Hz, 8H, H_{NCHC}), 6.82 (d, ^2J = 14.3 Hz, 2H, H_{CH2}), 6.53 (s+d, ^2J = 18.5 Hz, 6H, H_{CCHC} + H_{CH2}), 6.25 (d, ^2J = 14.7 Hz, 4H, H_{CH2}), 6.16 (dd, ^2J = 14.5, 4.2 Hz, 4H, H_{CH2}), 5.69 (d, ^2J = 14.4 Hz, 4H, H_{CH2}), 5.16 (dd, ^2J = 19.1, 14.6 Hz, 8H, H_{CH2}).

^{1}H NMR (300 MHz): δ (ppm) = 7.31, 0.94.

^{13}C NMR (75 MHz): δ (ppm) = 206.69, 181.09, 150.45, 148.08, 124.39, 122.29, 106.18, 63.55, 51.53, 48.25, 32.69, 29.80, 14.91, 1.68.

EA (%): calc. C 24.77, H 1.91, N 14.44; measured C 25.83, H 2.23, N 12.90 for $[Ag_8L^{Me}_2](I)_4]$.

UV-vis (H_2O, c = 1 · 10^{-5} mol/L): I_{max} (nm) = 237.

$[Au_8L^{Me}_2](F)_4$

Reagents: $[Au_8L^{Me}_2](PF_6)_4$ (100.00 mg, 32.13 µmol, 1 eq.); TBA fluoride (41.68 mg, 160.64 µmol, 5 eq.).

Yield: brown powder, no signals for the desired pillarplex salt were obtained in ^{1}H NMR spectroscopy.

$[Au_8L^{Me}_2](Cl)_4$

Reagents: $[Au_8L^{Me}_2](PF_6)_4$ (80.00 mg, 25.70 µmol, 1 eq.); TBA chloride (35.46 mg, 1628.51 µmol, 5 eq.).

Yield: off-white powder, 51 mg, 19.02 µmol, 74 %.

^{1}H NMR (400.13 MHz, DMSO-d_6): δ (ppm) = 8.05 (s, 8H, H_{NCHC}), 7.88 (s, 8H, H_{NCHC}), 7.07 (s, 4H, H_{CCHC}), 6.97 (d, ^2J = 14.6 Hz, 4H, H_{CH2}), 6.14 (d, ^2J = 14.8 Hz, 4H, H_{CH2}), 5.84 (d, ^2J = 14.7 Hz, 8H, H_{CH2}), 5.41 (d, ^2J = 14.9 Hz, 8H, H_{CH2}).

^{1}H NMR (300 MHz): δ (ppm) = 7.49, 1.39, 0.14.

^{13}C NMR (75 MHz): δ (ppm) = 204.47, 183.72, 180.54, 152.12, 148.21, 124.09, 106.52, 104.17, 63.83, 53.31, 49.48, 48.34, 28.62, 27.03, -3.35.

EA (%): calc. C 21.56, H 1.66, N 12.57; measured C 20.24, H 1.82, N 10.42 for $[Au_8L^{Me}_2](Cl)_4$.

ESI-MS (H_2O): m/z = 633.0356 $[Au_8L^{Me}_2]^{4+}$, calc. 633.03 for $[Au_8L^{Me}_2]^{4+}$; 855.7022 $[Au_8L^{Me}_2](Cl)^{3+}$, calc. 855.71 for $[Au_8L^{Me}_2](Cl)^{3+}$; 1301.0408 $[Au_8L^{Me}_2](Cl)_2^{2+}$, calc. 1301.04 for $[Au_8L^{Me}_2](Cl)_2^{2+}$.

UV-vis (H_2O, c = 1 · 10^{-5} mol/L): I_{max} (nm) = 243, 258.

$[Au_8L^{Me}_2](Br)_4$

Reagents: $[Au_8L^{Me}_2](PF_6)_4$ (100.00 mg, 32.13 µmol, 1 eq.); TBA bromide (51.46 mg, 160.64 µmol, 5 eq.).

Yield: off-white powder, 62 mg, 23.77 µmol, 74 %.

^{1}H NMR (400.13 MHz, DMSO-d_6): δ (ppm) = 8.02 (s, 8H, H_{NCHC}), 7.87 (s, 8H, H_{NCHC}), 7.06 (s, 4H, H_{CCHC}), 7.00 (d, ^2J = 14.7 Hz, 4H, H_{CH2}), 6.12 (d, ^2J = 14.7 Hz, 4H, H_{CH2}), 5.87 (d, ^2J = 14.7 Hz, 8H, H_{CH2}), 5.39 (d, ^2J = 14.8 Hz, 8H, H_{CH2}).

^{1}H NMR (300 MHz): δ (ppm) = 7.23, 1.34, 0.03.

^{13}C NMR (75 MHz): δ (ppm) = 204.22, 168.82, 166.95, 148.93, 124.65, 124.04, 108.40, 106.71, 64.27, 50.15, 49.34, 29.78, 0.87.

EA (%): calc. C 20.21, H 1.55, N 11.79; measured C 20.94, H 1.94, N 10.26 for $[Au_8L^{Me}_2](Br)_4$.

ESI-MS (H_2O): m/z = 633.0351 $[Au_8L^{Me}_2]^{4+}$, calc. 633.04 for $[Au_8L^{Me}_2]^{4+}$; 871.0152 $[Ag_8L^{Me}_2](Br)^{3+}$, calc. 871.02 for $[Ag_8L^{Me}_2](Br)^{3+}$.

UV-vis (H_2O, c = 1 · 10^{-5} mol/L): I_{max} (nm) = 241, 258.

$[Au_8L^{Me}_2](I)_4$

Reagents: $[Au_8L^{Me}_2](PF_6)_4$ (100.00 mg, 32.13 µmol, 1 eq.); TBA iodide (59.01 mg, 160.64 µmol, 5 eq.).

^{1}H NMR (300 MHz): δ (ppm) = 7.67, 4.03, 1.28, 0.14.

^{13}C NMR (75 MHz): δ (ppm) = 181.31, 168.92, 167.25, 149.17, 147.78, 124.10, 107.45, 105.97, 64.08, 50.15, 48.66, 29.43, 2.17.

Yield: off-white powder, 94 mg, 22.21 µmol, 96%.

EA (%): calc. C 18.96, H 1.46, N 12.06; measured C 17.52, H 1.54, N 8.78 for $[Au_8L^{Me}{}_2](I)_4]$.

UV-vis (H_2O, c = 1 · 10^{-5} mol/L): I_{max} (nm) = 242, 258

$[Ag_8L^{Me}{}_2](I_3)_4$

Reagents: $[Ag_8L^{Me}{}_2](PF_6)_4$ (10.00 mg, 0.032 µmol, 1 eq.); TBA triiodide (9.98 mg, 0.016 µmol, 5 eq.).

Yield: orange solid, no signals for the desired pillarplex salt were obtained in ^{1}H NMR spectroscopy.

$[Ag_8L^{Me}{}_2](SCN)_4$

Reagents: $[Ag_8L^{Me}{}_2](PF_6)_4$ (50.00 mg, 20.83 µmol, 1 eq.); TBA thiocyanate (31.20 mg, 104.17 µmol, 5 eq.).

Yield: white powder, 38 mg, 18.54 µmol, 89%.

^{1}H NMR (400.13 MHz, DMSO-*d_6*): δ (ppm) = 7.96 (s, 8H, H_{NCHC}), 7.76 (s, 8H, H_{NCHC}), 6.83 (d, ^2J = 14.3 Hz, 4H, H_{CH2}), 6.63 (s, 4H, H_{CCHC}), 6.15 (d, ^2J = 14.6 Hz, 4H, H_{CH2}), 5.91 (d, ^2J = 14.7 Hz, 8H, H_{CH2}), 5.23 (d, ^2J = 14.7 Hz, 8H, H_{CH2}).

^{13}C NMR (125.83 MHz, DMSO-*d_6*): δ (ppm) = 129.50, 47.63, 30.75.

DOSY NMR (400.13 MHz, DMSO-*d_6*): d (m^2 sec^{-1}) = 9.14 · 10^{-11}.

EA (%): calc. C 30.43, H 2.16, N 19.11, S 6.25; measured C 31.70, H 2.61, N 17.27, S 5.92 for $[Ag_8L^{Me}{}_2](SCN)_4]$.

ESI-MS (H_2O): m/z = 454.9126 $[Ag_8L^{Me}{}_2]^{4+}$, calc. 454.91 for $[Ag_8L^{Me}{}_2]^{4+}$; 625.8760 $[Ag_8L^{Me}{}_2](SCN)^{3+}$, calc. 625.87 for $[Ag_8L^{Me}{}_2](SCN)^{3+}$; 967.7977 $[Ag_8L^{Me}{}_2](SCN)_2{}^{2+}$, calc. 967.79 for $[Ag_8L^{Me}{}_2](SCN)_2{}^{2+}$.

UV-vis (H_2O, c = 1 · 10^{-5} mol/L): I_{max} (nm) = 224.

$[Ag_8L^{Me}{}_2](NO_3)_4$

Reagents: $[Ag_8L^{Me}{}_2](PF_6)_4$ (50.00 mg, 20.83 µmol, 1 eq.); TBA nitrate (31.61 mg, 104.17 µmol, 5 eq.).

Yield: white powder, 40 mg, 19.37 µmol, 93%.

^{1}H NMR (400.13 MHz, DMSO-*d_6*): δ (ppm) = 7.96 (d, ^2J = 2.0 Hz, 8H, H_{NCHC}), 7.77 (d, ^2J = 1.9 Hz, 8H, H_{NCHC}), 6.83 (d, ^2J = 14.6 Hz, 4H, H_{CH2}), 6.63 (s, 4H, H_{CCHC}), 6.15 (d, ^2J = 14.6 Hz, 4H, H_{CH2}), 5.89 (d, ^2J = 14.7 Hz, 8H, H_{CH2}), 5.24 (d, ^2J = 14.9 Hz, 8H, H_{CH2}).

DOSY NMR (400.13 MHz, DMSO-d_6): d (m^2 sec^{-1}) = $9.14 \cdot 10^{-11}$.

EA (%): calc. C 27.88, H 2.14, N 18.96; measured C 28.86, H 2.60, N 16.93 for $[Ag_8L^{Me}{}_2](NO_3)_4]$.

ESI-MS (H_2O): m/z = 454.9124 $[Ag_8L^{Me}{}_2]^{4+}$, calc. 454.91 for $[Ag_8L^{Me}{}_2]^{4+}$; 627.2127 $[Ag_8L^{Me}{}_2](NO_3)^{3+}$, calc. 627.22 for $[Ag_8L^{Me}{}_2](NO_3)^{3+}$; 971.8149 $[Ag_8L^{Me}{}_2](NO_3)_2{}^{2+}$, calc. 971.81 for $[Ag_8L^{Me}{}_2](NO_3)_2{}^{2+}$.

UV-vis (H_2O, c = $1 \cdot 10^{-5}$ mol/L): I_{max} (nm) = 225.

$[Ag_8L^{Me}{}_2](ClO_4)_4$

Reagents: $[Ag_8L^{Me}{}_2](PF_6)_4$ (50.00 mg, 20.83 µmol, 1 eq.); TBA perchlorate (30.51 mg, 104.17 µmol, 5 eq.).

Yield: white powder, 42 mg, 18.96 µmol, 91%.

^{1}H NMR (400.13 MHz, DMSO-d_6): δ (ppm) = 7.96 (s, 8H, H_{NCHC}), 7.76 (s, 8H, H_{NCHC}), 6.84 (d, ^2J = 14.4 Hz, 4H, H_{CH2}), 6.63 (s, 4H, H_{CCHC}), 6.15 (d, ^2J = 14.6 Hz, 4H, H_{CH2}), 5.89 (d, ^2J = 14.7 Hz, 8H, H_{CH2}), 5.24 (d, ^2J = 14.8 Hz, 8H, H_{CH2}).

^{13}C NMR (125.83 MHz, DMSO-d_6): δ (ppm) = 202.42, 159.02, 148.86, 123.79, 103.74, 57.58, 47.62, 30.75.

DOSY NMR (400.13 MHz, DMSO-d_6): d (m^2 sec^{-1}) = $8.81 \cdot 10^{-11}$.

EA (%): calc. C 26.00, H 2.00, N 15.16; measured C 27.65, H 2.30, N 13.90 for $[Ag_8L^{Me}{}_2](ClO_4)_4]$.

ESI-MS (H_2O): m/z = 454.9129 $[Ag_8L^{Me}{}_2]^{4+}$, calc. 454.91 for $[Ag_8L^{Me}{}_2]^{4+}$; 639.5331 $[Ag_8L^{Me}{}_2](ClO_4)^{3+}$, calc. 639.34 for $[Ag_8L^{Me}{}_2](ClO_4)^{3+}$; 1008.7719 $[Ag_8L^{Me}{}_2](ClO_4)_2{}^{2+}$, calc. 1008.77 for $[Ag_8L^{Me}{}_2](ClO_4)_2{}^{2+}$.

UV-vis (H_2O, c = $1 \cdot 10^{-5}$ mol/L): I_{max} (nm) = 232.

$[Ag_8L^{Me}{}_2](SO_4)_2$

Reagents: $[Ag_8L^{Me}{}_2](PF_6)_4$ (10.00 mg, 4.17 µmol, 1 eq.); TBA_2 sulfate 50% solution in water (24.21 mg, 20.83 µmol, 5 eq.).

Yield: white powder, due to low solubility of substance in MeCN-d_3 and DMSO-d_6 no signals for the desired pillarplex salt were obtained in ^{1}H NMR spectroscopy.

$[Ag_8L^{Me}_2](BF_4)_4$

Reagents: $[Ag_8L^{Me}_2](PF_6)_4$ (50.00 mg, 20.83 µmol, 1 eq.); TBA tetrafluoro borate (34.20 mg, 104.17 µmol, 5 eq.).

Yield: white powder, 39 mg, 18.96 µmol, 91%.

^{1}H NMR (400.13 MHz, DMSO-d_6) δ (ppm) = 7.96 (s, 8H, H_{NCHC}), 7.76 (s, 8H, H_{NCHC}), 6.84 (d, ^2J = 14.4 Hz, 4H, H_{CH2}), 6.63 (s, 4H, H_{CCHC}), 6.14 (d, ^2J = 14.5 Hz, 4H, H_{CH2}), 5.89 (d, ^2J = 14.7 Hz, 8H, H_{CH2}), 5.23 (d, ^2J = 14.86 Hz, 8H, H_{CH2}).

^{13}C NMR (125.83 MHz, DMSO-d_6) δ (ppm) = 206.71, 179.42, 179.28, 177.42, 177.28, 148.91, 123.82, 122.80, 103.20, 63.79, 47.63, 30.81.

^{11}B NMR (128.38 MHz, DMSO-d_6) δ (ppm) = -1.29.

^{19}F NMR (376.46 MHz, DMSO-d_6) δ (ppm) = -148.17, -148.23.

EA (%): calc. C 26.60, H 2.05, N 15.51; measured C 28.85, H 2.50, N 14.44 for $[Ag_8L^{Me}_2](BF_4)_4] \cdot 2.6$ acetone.

ESI-MS (H_2O): m/z = 454.9126 $[Ag_8L^{Me}_2]^{4+}$, calc. 454.91 for $[Ag_8L^{Me}_2]^{4+}$; 625.8760 $[Ag_8L^{Me}_2](BF_4)^{3+}$, calc. 625.88 for $[Ag_8L^{Me}_2](BF_4)^{3+}$; 967.7977 $[Ag_8L^{Me}_2](BF_4)_2^{2+}$, calc. 967.79 for $[Ag_8L^{Me}_2](BF_4)_2^{2+}$.

UV-vis (MeCN, c = 1 · 10^{-5} mol/L): I_{max} (nm) = 227.

micro-ED (LaB_6 electron, λ = 0.02851 Å): white powder, monoclinic *P* 1 2/*n* 1, a = 12.4(4) Å, b = 14.1(4) Å, c = 21.2(6) Å, α = 90 °, β = 93.18(6) °, γ = 90 °, R = 24.37% (AHE-157-4).

Synthesis of $[Ag_8L^{Me}_2](S)_2$

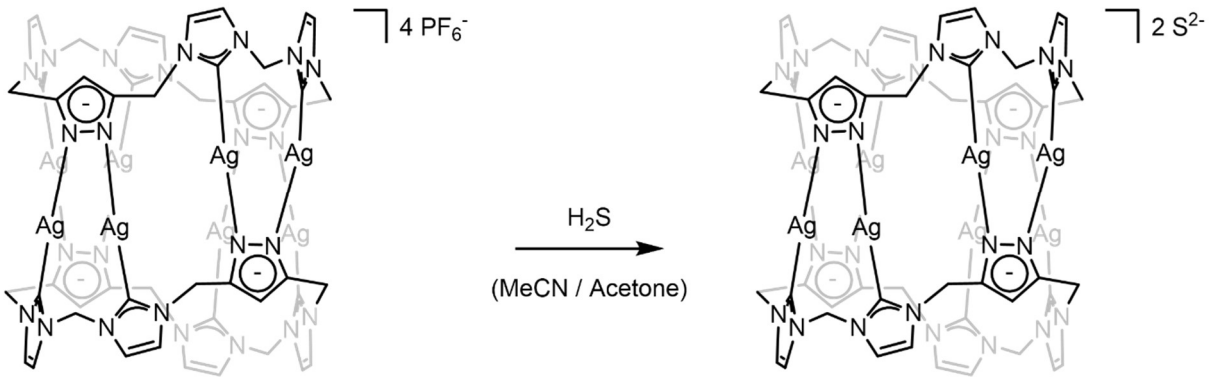

A solution of $[Ag_8L^{Me}_2](PF_6)_4$ (10 mg, 0.0042 µmol, 1 eq.) was dissolved in a 1:1 solvent mixture of acetone and acetonitrile and this solution was induced by gaseous H_2S (excess). The reaction mixture was afterwards stirred at rt for 30 min. A brownish precipitate was isolation by centrifugation and washed with acetone. The brown solid was dried *in vacuo* and analysed by NMR spectroscopy. No pillarplex signals were observed indicating the decomposition of $[Ag_8L^{Me}_2](PF_6)_4$ by the presence of H_2S.

^{1}H NMR (400.13 MHz, DMSO-d_6): δ (ppm) = 2.05 (acetonitrile),1.82 (s).

General Synthesis Route of $[Ag_8L^{Me}{}_2](X)_2$ by Ion Exchange Resin

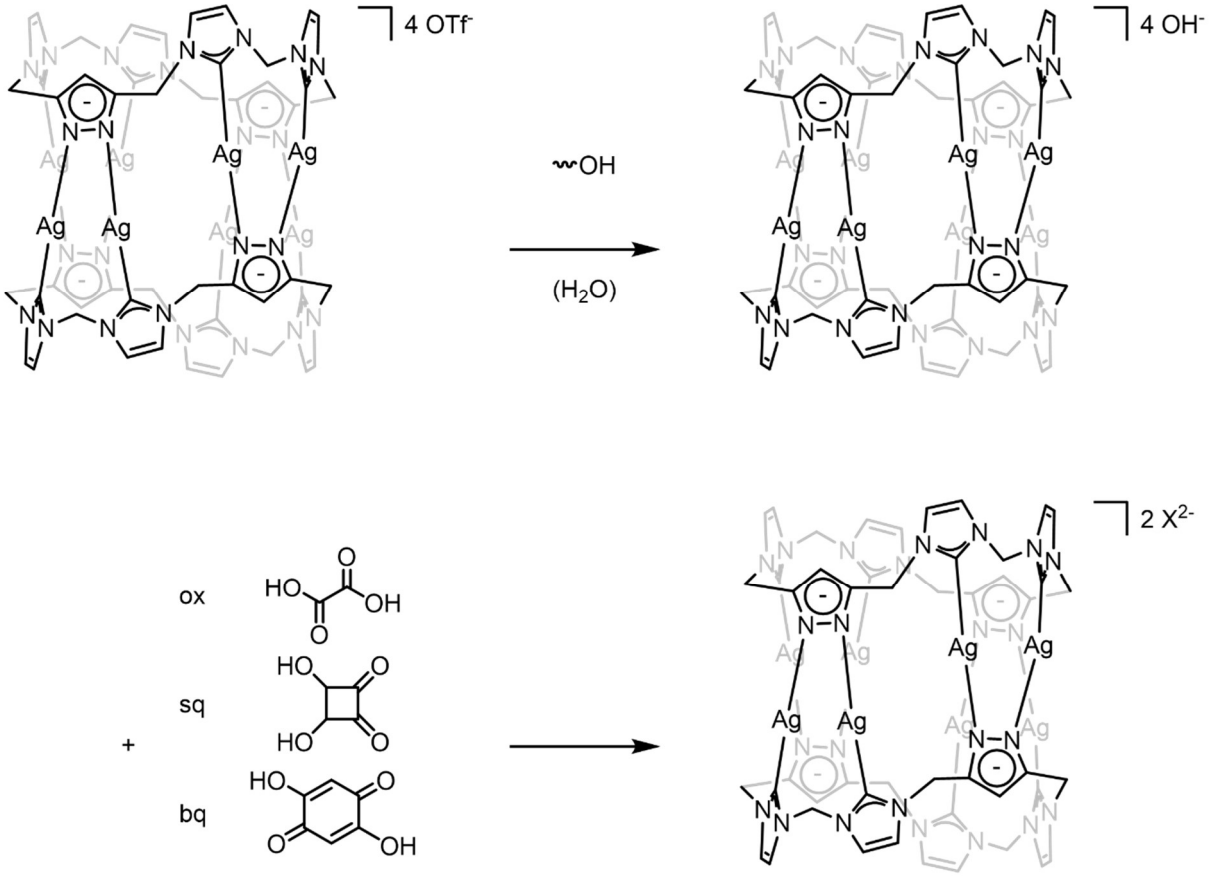

$[Ag_8L^{Me}{}_2](OTf)_4$ (1 eq.) was dissolved in water (if not completely soluble, a few drops of MeCN were added) and transferred to the column. Here, the activated column material induced an exchange of OTf^- anions to HO^-. $[Ag_8L^{Me}{}_2](OH)_4$ was *in situ* dropwise added to a diluted solution of respective acid (6 eq.) to yield the desired pillarplex salt. The obtained suspension was concentrated to dryness and analysed with ^{1}H NMR spectroscopy.

Column preparation:

Amberlite IRA-400 was suspended in water and transferred into a column (d = 1 cm, h = 2 cm). The column material was activated by passing through a NaOH-solution (5%, 4 mL). Afterwards, the column was washed with water until pH 7 was reached.

Crystallisation attempts:

$[Ag_8L^{Me}{}_2](OTf)_4$ were dissolved in H_2O and provided in a vial. A diluted solution of respective acids (6 eq., 0.1 M) was provided and slowly layered on top of the pillarplex solution. One

batch was kept at rt. Other batches were placed in an oven, heated to 60 °C or 80 °C and kept at that temperature overnight and afterwards slowly cooled down to rt.

Solubility:

	H_2O	MeCN	THF	acetone	Et_2O
Oxalic acid (ox)	x	x	x	x	x
Squaric acid (sq)	x				
2,5-dihydroxy-1,4-benzoquinone (bq)	x			(x)	

$[Ag_8L^{Me}_2](ox)_2$

Reagents: $[Ag_8L^{Me}_2](OTf)_4$ (5.00 mg, 2.07 µmol, 1 eq.); oxalic acid (1.12 mg, 12.42 µmol, 6 eq.).

Yield: dark purple powder / beige powder, ^{1}H NMR analysis indicates decomposition and partially showed the signals of free L^{Me}.

^{1}H NMR (400.13 MHz, MeCN-d_3) δ (ppm) = 7.77 (s, 4H, H_{NCHC}), 7.55 (s, 4H, H_{NCHC}), 6.59 (s, 6H, H_{CH2} + H_{CCHC}), 5.43 (s, 8H, H_{CH2}).

$[Ag_8L^{Me}_2](sq)_2$

Reagents: $[Ag_8L^{Me}_2](OTf)_4$ (5.00 mg, 2.07 µmol, 1 eq.); squaric acid (1.42 mg, 12.42 µmol, 6 eq.).

Yield: slightly brown powder, ^{1}H NMR analysis indicates decomposition and showed the signals of free L^{Me}.

^{1}H NMR (400.13 MHz, MeCN-d_3) δ (ppm) = 9.20 (s, H_{NCHN}), 7.76 (s, 4H, H_{NCHC}), 7.52 (s, 4H, H_{NCHC}), 6.57 (s, 4H, H_{CH2}), 6.42 (s, 2H, H_{CCHC}), 5.39 (s, 8H, H_{CH2}).

$[Ag_8L^{Me}_2](bq)_2$

Reagents: $[Ag_8L^{Me}_2](OTf)_4$ (5.00 mg, 2.07 µmol, 1 eq.); 2,5-dihydroxy-1,4-benzoquinone (1.74 mg, 12.42 µmol, 6 eq.).

Yield: brown powder, no signals for the desired pillarplex salt were obtained in ^{1}H NMR spectroscopy and the colour change to brown suggests the decomposition of the pillarplex.

Synthesis of $[Au_8L^{Me}_2](PF_6)_2(AuCl_2)_2$

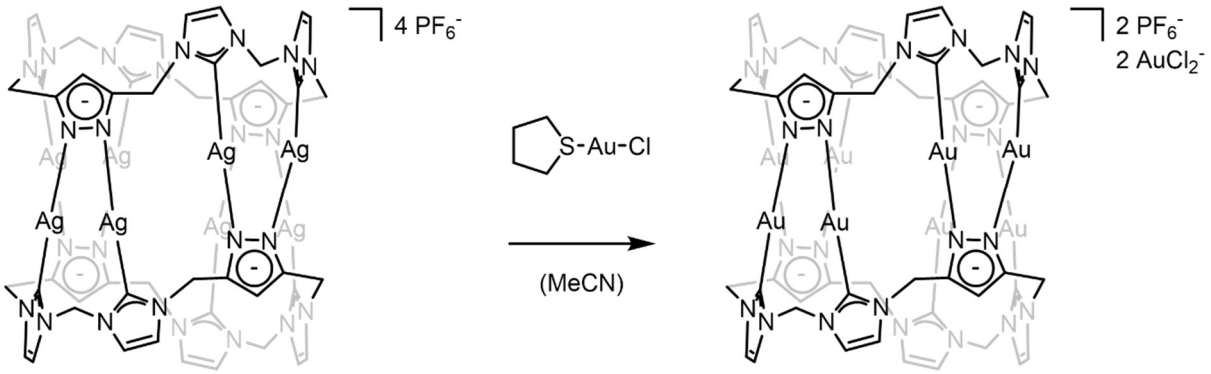

Au(THT)Cl (113.55 mg, 354.19 µmol, 8.5 eq.) in acetonitrile was provided and a solution of $[Ag_8L^{Me}_2](PF_6)_4$ (100 mg, 41.67 µmol, 1 eq.) in acetonitrile was slowly added. The reaction mixture was stirred overnight at 40 °C under the exclusion of light. After addition of 1 eq. diethyl ether to precipitate the obtained side product AgCl, the suspension was filtered over Celite® and to the filtrate an excess of diethyl ether was added to precipitate the desired product. The white solid was isolated by centrifugation, washed with diethyl ether (2 x 5 mL) and dried *in vacuo*. A white solid was obtained, which was redissolved in a minimal amount of MeCN and transferred into NMR tubes. For crystallisation attempts, these tubes were placed in a Schlenk-flask filled with diethyl ether. Suitable single crystals were obtained.

Yield: white powder, 98 mg, 31.67 µmol, 76%.

^{1}H NMR (400.13 MHz, MeCN-d_3): δ (ppm) = 7.64 (d, ^2J = 2.1 Hz, 8H, H_{NCHC}), 7.56 (d, ^2J = 2.1 Hz,8H, H_{NCHC}), 7.07 (s, 4H, H_{CCHC}), 6.92 (d, ^2J = 14.9 Hz, 4H, H_{CH2}), 5.93 (d, ^2J = 15.0 Hz, 4H, H_{CH2}), 5.73 (d, ^2J = 15.1 Hz, 8H, H_{CH2}), 5.27 (d, ^2J = 15.1 Hz, 8H, H_{CH2}).

SC-XRD (MoK_α, λ = 0.71073 Å): colourless block, triclinic *P* -1, a = 12.2674(7) Å, b = 14.9679(9) Å, c = 23.1156(15) Å, α = 98.263(2) °, β = 91.045(2) °, γ = 90.821(2) °, R = 3.69% (HeiAl55).

Synthesis of Pseudorotaxane $[Ag_8L^{Me}{}_2](C_{12}H_{30}N_2{}^{2+})(C_8H_4O_4{}^{2-})_{2.5}(C_8H_5O_4{}^-)$

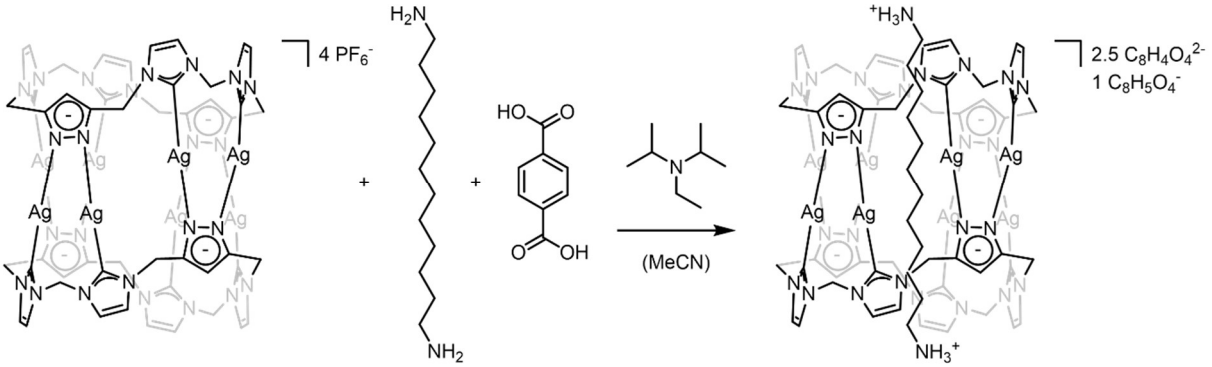

$[Ag_8L^{Me}{}_2](PF_6)_4$ (10 mg, 4.17 µmol, 1 eq.) was dissolved in dry DMF under inert conditions. Then 1,12-diaminododecane (0.918 mg, 4.58 µmol, 1.1 eq.) was added and the reaction mixture was stirred at rt for 10 min. The reaction mixture was cooled down to -50°C and terephthalic acid (1.52 mg, 9.17 µmol, 2.2 eq.) and DIPEA (4.2 µL, 25.02 µmol, 6 eq.) were added. After allowing the reaction mixture to warm up to rt overnight, the solvent was removed *in vacuo*. The obtained off-white solid was washed with diethyl ether (2 x 2 mL) and dried in vacuo to yield a white solid. Suitable crystals for single crystal X-Ray diffraction were obtained by slow evaporation of acetonitrile as solvent.

Additional Information on this compound can be obtained from the supporting information of ZKristallogr. – Crystalline Materials ***2022****, 237 (4-5), 167-177 (DOI: 10.1515/zkri-2021-2076).*

CCDC 2113226 contains the supplementary crystallographic data for this compound.

5.8.2 Functionalisation of Ligand and Pillarplex

Synthesis of Brominated Ligand $L^{Br}(PF_6)_4$

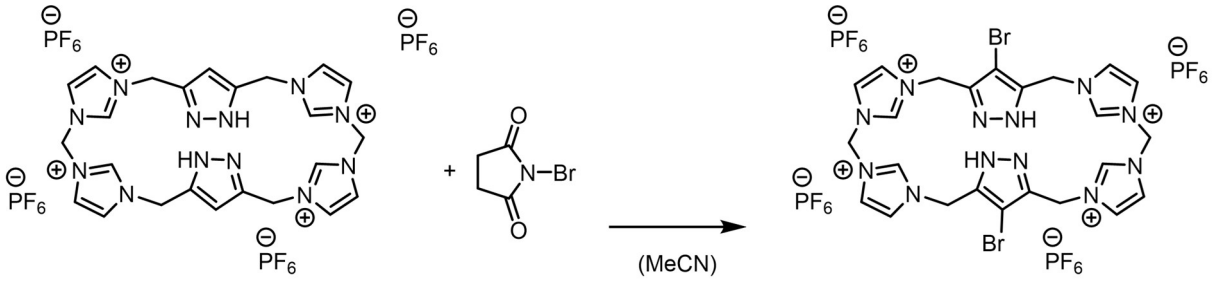

$L^{Me}(PF_6)_4$ (60.00 mg, 56.37 µmo, 1 eq.) was dissolved in 3 mL acetonitrile and separately NBS (22.07 mg, 124.01 µmol, 2.2 eq.) was dissolved in acetonitrile (3 mL). The NBS solution in acetonitrile was slowly added to the ligand solution in acetonitrile and the reaction mixture was stirred at rt for 10 min. From a clear solution, the functionalised ligand was precipitated by the addition of an excess of Et_2O. The obtained slightly off-white precipitate was isolated by centrifugation and washed with a large amount of water (2 x 10 mL) to remove the residual NHS. The wet solid was afterwards suspended in diethyl ether and isolated by centrifugation. Drying *in vacuo* yielded an off-white powder.

Yield: off-white powder, 52 mg, 42.55 µmol, 76%.

^{1}H NMR (400.13 MHz, MeCN-d_3): δ [ppm] = 11.85 (s, 2H, H_{NH}), 8.91 (s, 4H, H_{NCHN}), 7.66 (t, ^3J = 2.0 Hz, 4H, H_{NCHC}), 7.53 (s, 4H, H_{NCHC}), 6.42 (s, 4H, H_{CH2}), 5.42 (d, ^2J = 13.4 Hz, 8H, H_{CH2}).

^{13}C NMR (125.83 MHz, MeCN-d_3): δ [ppm] = 150.39, 124.37, 123.35, 103.92, 66.19, 65.22, 49.22.

^{19}F NMR (376.46 MHz, MeCN-d_3): δ [ppm] = -71.77, -78.65.

^{31}P NMR (161.99 MHz, MeCN-d_3): δ [ppm] = -144.79 (q).

EA (%): calc. C 23.59, H 2.14, N 13.75; measured C 24.25, H 2.07, N 13.14 for $L^{Me}(PF_6)_4$.

ESI-MS (CH_3CN): m/z = 466.0009 $L^{Br}(PF_6)_2^{2+}$, calc. 466.00 for $L^{Br}(PF_6)_2^{2+}$; 1076.9653 $L^{Br}(PF_6)_3^{+}$, calc. 1076.97 for $L^{Br}(PF_6)_3^{+}$, 144.9632 PF_6^-, calc. 144.96 for PF_6^-.

Synthesis of Brominated Silver-Pillarplex $[Ag_8L^{Br}_2](PF_6)_4$

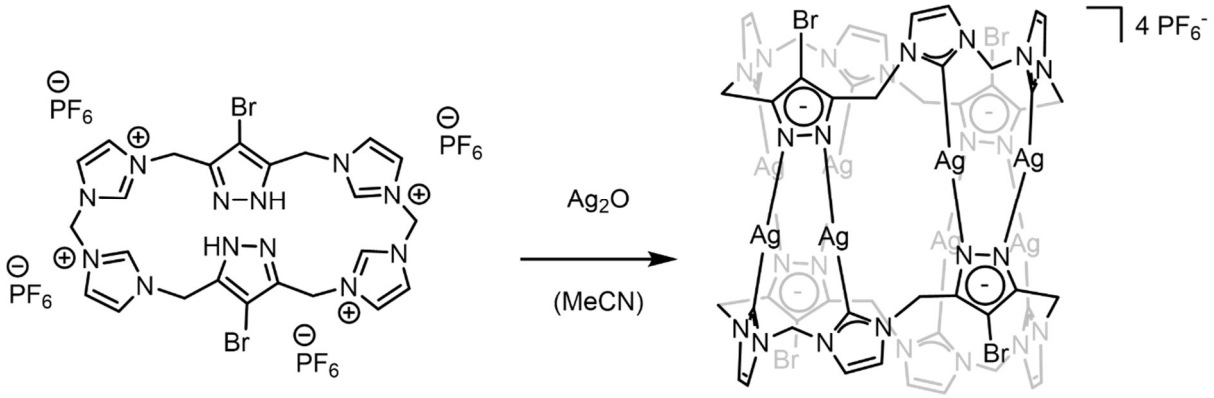

$L^{Br}(PF_6)_4$ (100.00 mg, 81.82 µmol, 1 eq.) and Ag_2O (94.80 mg, 409.09 µmol, 5 eq.) were provided in a flask and acetonitrile (25 mL) as solvent was added. Under the exclusion of light, the reaction mixture was stirred overnight at rt and then the residual Ag_2O was removed by filtration over Celite®. A light brown solution was obtained, where diethyl ether was added until a brown precipitate and a clear solution was obtained. The brown precipitate was removed by filtration over Celite® and to the filtrate an excess of diethyl ether was added to precipitate $[Ag_8L^{Br}_2](PF_6)_4$ as white solid. The solid was isolated by centrifugation and washed with diethyl ether (2 x 5 mL). After drying the solid *in vacuo,* a white powder was obtained.

Yield: white powder, 140 mg, 51.56 µmol, 63%.

^{1}H NMR (400.13 MHz, MeCN-d_3): δ [ppm] = 7.62 (d, ^2J = 2.0 Hz, 8H, H_{NCHC}), 7.60 (d, ^2J = 2.0 Hz,8H, H_{NCHC}), 6.60 (d, ^2J = 14.8 Hz, 4H, H_{CH2}), 6.09 (d, ^2J = 14.8 Hz, 4H, H_{CH2}), 5.67 (d, ^2J = 15.4 Hz, 8H, H_{CH2}), 5.23 (d, ^2J = 15.5 Hz, 8H, H_{CH2}).

^{13}C NMR (125.83 MHz, MeCN-d_3): δ [ppm] = 148.18, 125.55, 122.93, 94.68, 66.14, 65.43, 47.80, 15.48.

^{19}F NMR (376.46 MHz, MeCN-d_3): δ [ppm] = -71.75, -73.63.

^{31}P NMR (161.99 MHz, MeCN-d_3): δ [ppm] = -144.59 (q).

EA (%): calc. C 21.23, H 1.48, N 12.38; measured C 22.49, H 1.90, N 11.50 for $[Ag_8L^{Me}_2](PF_6)_4$.

ESI-MS (CH_3CN): m/z = 533.8227 $[Ag_8L^{Br}_2]^{4+}$, calc. 533.82 for $[Ag_8L^{Br}_2]^{4+}$, 760.0837 $[Ag_8L^{Br}_2](PF_6)^{3+}$, calc. 760.09 for $[Ag_8L^{Br}_2](PF_6)^{3+}$, 1212.6084 $[Ag_8L^{Br}_2](PF_6)_2^{2+}$, calc. 1212.61 for $[Ag_8L^{Br}_2](PF_6)_2^{2+}$, 144.9633 PF_6^-, calc. 144.96 for PF_6^-.

SC-XRD (MoK_α, λ = 0.71073 Å): colourless fragment, orthorhombic *P n m a*, a = 24.1845(15) Å, b = 24.0406(15) Å, c = 20.9494(13) Å, α = 90 °, β = 90 °, γ = 90 °, R = 9.61% (HeiAl12).

Synthesis of Brominated Gold-Pillarplex $[Au_8L^{Br}{}_2](PF_6)_4$

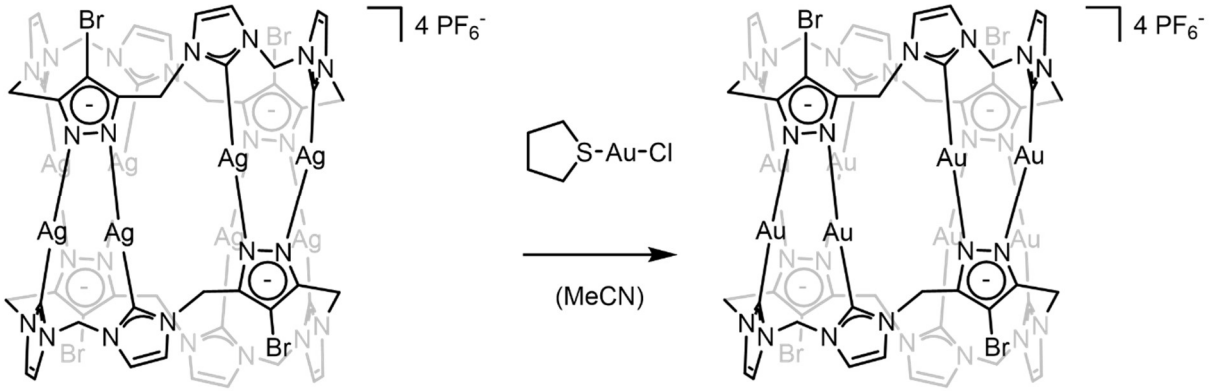

Au(THT)Cl (20.07 mg, 62.61 µmol, 8.5 eq.) was dissolved in 2 mL acetonitrile and a solution of $[Ag_8L^{Br}{}_2](PF_6)_4$ (20.00 mg, 7.37 µmol, 1 eq.) in 2 mL of acetonitrile was slowly added. The reaction mixture was stirred under the exclusion of light for 16 h at rt. Then 1 eq. of diethyl ether (3 mL) was added to precipitate the formed side product AgCl. The filtration over Celite® provided a clear solution to which an excess of diethyl ether was added to precipitate $[Au_8L^{Br}{}_2](PF_6)_4$ as a white solid.

Yield: white powder, 14 mg, 4.08 µmol, 56%.

^{1}H NMR (400.13 MHz, MeCN-d_3): δ [ppm] = 7.68 (s, 16H, H_{NCHC}), 6.92 (d, ^2J = 15.0 Hz, 4H, H_{CH2}), 5.98 (d, ^2J = 15.0 Hz, 4H, H_{CH2}), 5.75 (d, ^2J = 15.5 Hz, 8H, H_{CH2}), 5.27 (d, ^2J = 15.5 Hz, 8H, H_{CH2}).

^{13}C NMR (125.83 MHz, MeCN-d_3): δ [ppm] = 168.43, 147.20, 125.39, 123.76, 97.45, 66.14, 64.13, 47.13, 30.25, 15.54.

^{19}F NMR (376.46 MHz, MeCN-d_3): δ [ppm] = -71.69, -73.57.

^{31}P NMR (161.99 MHz, MeCN-d_3): δ [ppm] = -144.59 (q).

EA (%): calc. C 16.82, H 1.18, N 9.81; measured C 15.38, H 1.26, N 7.92 for $[Au_8L^{Me}{}_2](PF_6)_4$.

ESI-MS (CH_3CN): m/z = 711.9454 $[Au_8L^{Br}{}_2]^{4+}$, calc. 711.95 for $[Au_8L^{Br}{}_2]^{4+}$, 997.5817 $[Au_8L^{Br}{}_2](PF_6)^{3+}$, calc. 997.58 for $[Au_8L^{Br}{}_2](PF_6)^{3+}$, 1568.8562 $[Au_8L^{Br}{}_2](PF_6)_2{}^{2+}$, calc. 1568.86 for $[Au_8L^{Br}{}_2](PF_6)_2{}^{2+}$, 144.9634 PF_6^-, calc. 144.96 for PF_6^-.

SC-XRD (MoK_α, λ = 0.71073 Å): colourless fragment, tetragonal $P\,4_1\,2_1\,2$, a = 14.3499(8) Å, b = 14.3499(8) Å, c = 51.556(4) Å, α = 90 °, β = 90 °, γ = 90 °, R = 5.15% (HeiAl14).

Suzuki Coupling Reaction Attempts

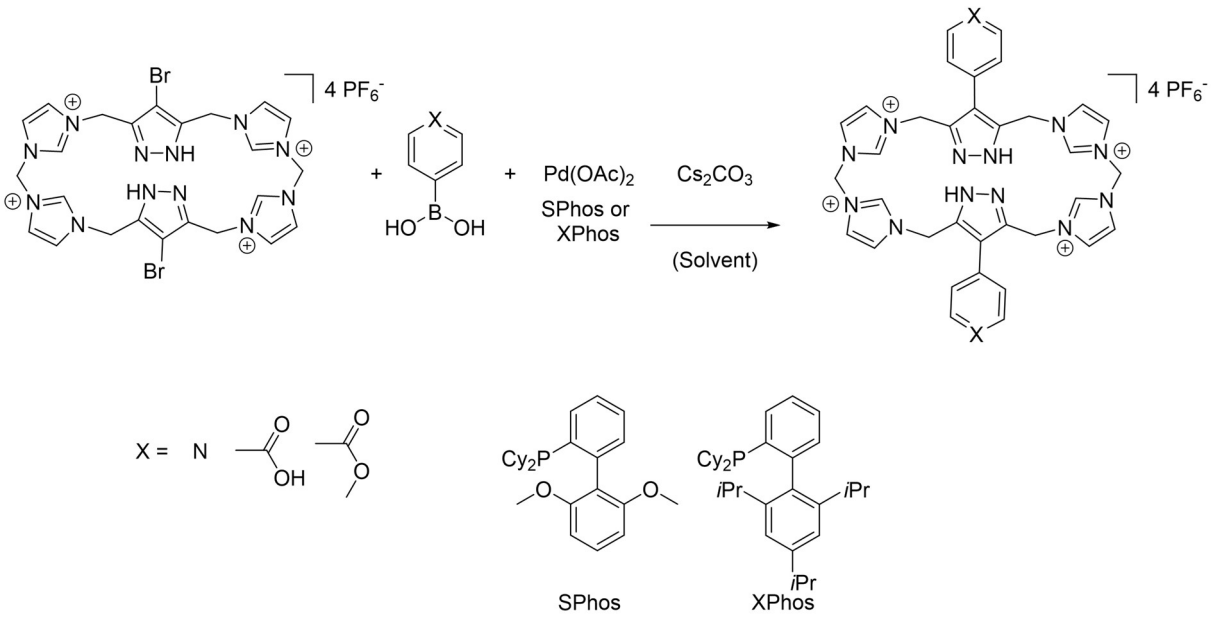

$L^{Br}(PF_6)_4$ (1 eq.) was provided in the solvent, boronic acid (3 eq.) and Cs_2CO_3 (10 eq.) were added. A solution of $Pd(OAc)_2$ (10 mol%) mixed with the ligand (20 mol%) in water was added. The reaction was monitored by ^1H NMR spectroscopy.

Suzuki coupling reactions starting with $L^{Br}(PF_6)_4$:

No.	X	Ligand	Solvent	T [°C]	t [d]
1	N	XPhos	Dioxane	95	2
2	N	SPhos	Dioxane	95	2
3	N	-	Dioxane	95	2
4	N	XPhos	DMF	95	2
5	N	SPhos	DMF	95	2
6	N	-	DMF	95	2
7	N	XPhos	MeCN	80	2
8	N	SPhos	MeCN	80	2
9	N	-	MeCN	80	2

5.8.3 Synthesis and Functionalisation of Pseudorotaxanes with α,ω-Dicarboxylic Acids

General Synthesis Route for Pseudorotaxanes $[M_8L^{Me}_2](Diacid)(PF_6)_4$

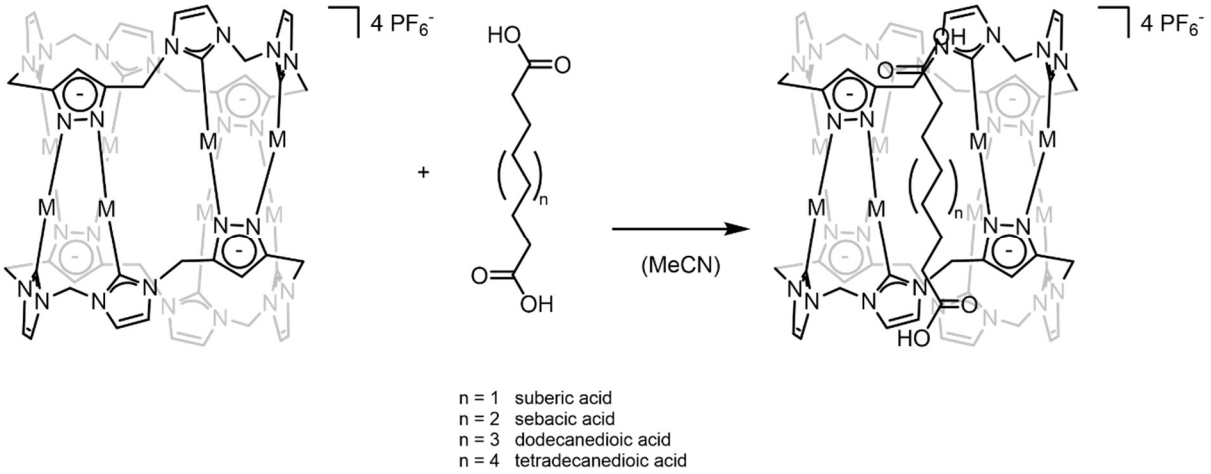

$[M_8L^{Me}_2](PF_6)_4$ (1 eq.) and $C_nH_{2n-2}O_4$ (1.1 eq.) were dissolved in acetonitrile and the mixture was stirred at room temperature for 10 min. The solvent was removed *in vacuo* at rt and the residue was redissolved in a minimal amount of acetonitrile and precipitated by an excess of diethyl ether. After drying *in vacuo*, a solid was obtained.

Additional Information on these compounds can be obtained at the supporting information of ChemPlusChem, ***2023****, e202300234. (DOI: 10.1002/cplu.202300234).*

CCDC 2196097-2196097 contain the supplementary crystallographic data for these compounds.

Synthesis of Pseudorotaxanes with deprotonated dicarboxylic acid

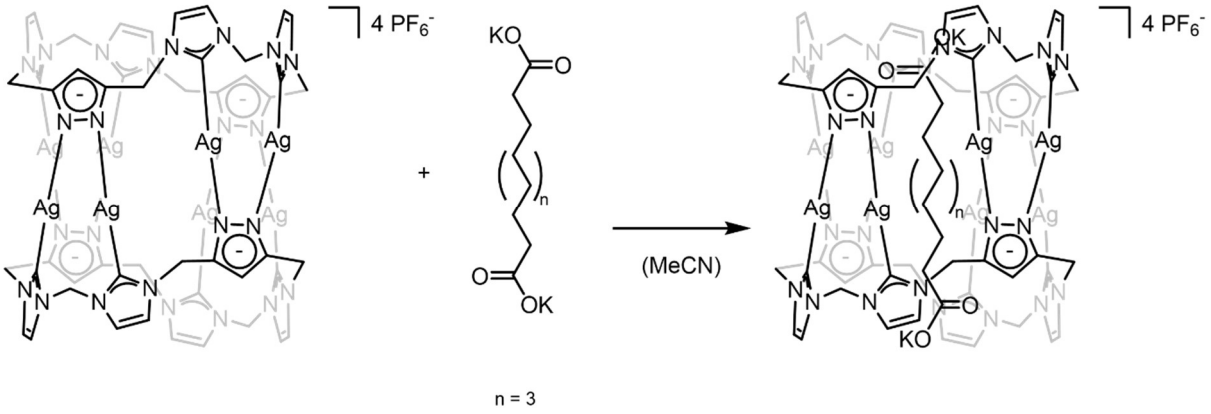

Analytic for $C_{12}H_{20}O_4K_2$:

^{1}H NMR (400.13 MHz, D_2O): δ [ppm] = 2.15 (t, ^3J = 7.5 Hz, 4H), 1.53 (t, ^3J = 7.5 Hz, 6H), 1.28 (s, 10H).

Synthesis route A:

KOH (301.20 mg, 5.37 mmol, 2 eq.) was dissolved in water and dodecanedioic acid (618.19 mg, 2.68 mmol, 1 eq.) was added. The reaction mixture was stirred for 30 min at rt and afterwards, the solvent was removed. 1.28 mg (4.17 µmol, 1 eq.) of the obtained white solid residue was dissolved in water and combined with a solution of $[Ag_8L^{Me}_2](PF_6)_4$ (11.28 mg, 4.17 µmol, 1 eq.) in acetonitrile. The reaction mixture was stirred overnight at rt and then the solvent was removed *in vacuo*. The obtained white solid was washed with diethyl ether (2 x 2 mL) and analysed by ^{1}H NMR spectroscopy.

^{1}H NMR (400.13 MHz, D_2O): δ [ppm] = 7.69 (s, 8H, H_{NCHC}), 7.64 (s, 8H, H_{NCHC}), 6.85 (s, 4H, H_{CCHC}), 6.75 (d, ^2J = 14.7 Hz, 4H, H_{CH2}), 6.18 (d, ^2J = 14.8 Hz, 4H, H_{CH2}), 5.55 (d, ^2J = 15.1 Hz, 8H, H_{CH2}), 5.32 (d, ^2J = 15.1 Hz, 8H, H_{CH2}), 1.52 (t, ^3J = 7.2 Hz, 4H), 0.73 (d, ^2J = 19.6 Hz, 4H), -0.69 (s, 4H), -1.09 (s, 4H), -1.81 (s, 4H).

Synthesis route B:

$[Ag_8L^{Me}_2](PF_6)_4$ (10.00 mg, 4.17 µmol, 1 eq.) was dissolved in 2 mL of acetonitrile and dodecanedioic acid (0.96 mg, 4.17 µmol, 1 eq.) were added. After stirring at rt for 30 min, 0.5 mL of a 1 mg mL^{-1} solution of KOH (0.47 mg, 8.36 µmol, 2 eq.) in water was slowly added and the reaction mixture continuously stirred at rt overnight. This yielded a white precipitate, which was isolated by centrifugation and washed with diethyl ether (2 x 2 mL). The obtained white solid was dried *in vacuo* and analysed by ^{1}H NMR spectroscopy.

^{1}H NMR (400.13 MHz, D_2O): δ [ppm] = 7.68 (s, 8H, H_{NCHC}), 7.62 (s, 8H, H_{NCHC}), 6.83 (s, 4H, H_{CCHC}), 6.75 (d, ^2J = 14.7 Hz, 4H, H_{CH2}), 6.16 (d, ^2J = 14.8 Hz, 4H, H_{CH2}), 5.54 (d, ^2J = 15.1 Hz, 8H, H_{CH2}), 5.30 (d, ^2J = 15.3 Hz, 8H, H_{CH2}), 1.50 (s, 4H), 0.70 (s, 4H), -0.70 (s, 4H), -1.11 (s, 4H), -1.82 (s, 4H).

CP Attempts for pseudorotaxanes

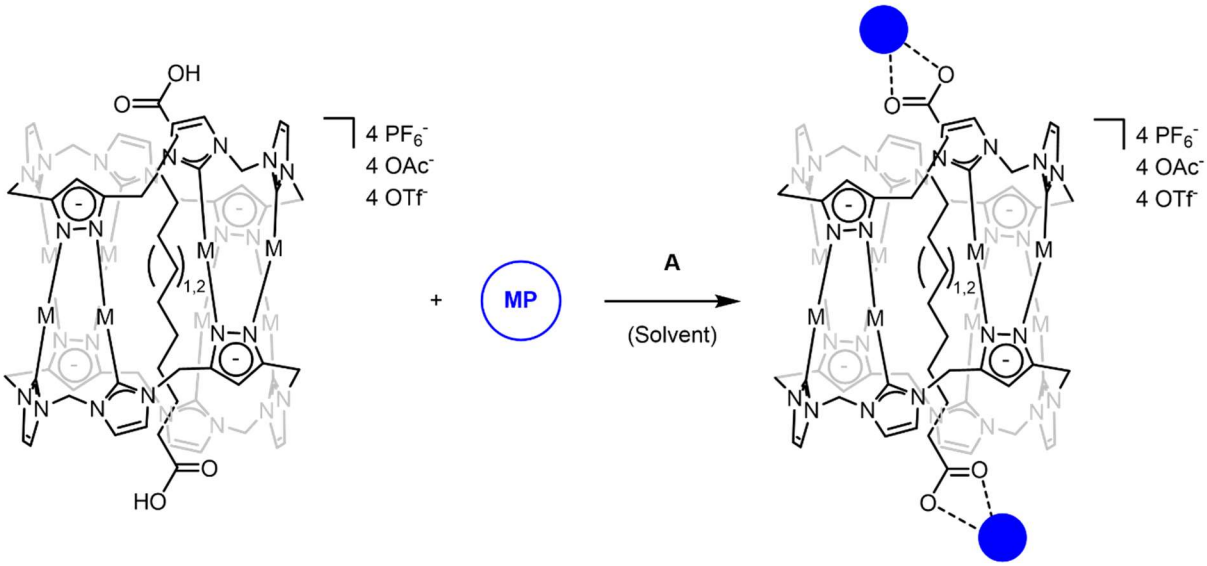

Synthesis route 1:[31] AHE-142, AHE-143, AHE-147, AH-AS11, AH-AS12

Synthesis was performed in the glovebox under inert conditions and dry solvents were used. MP (2 eq.) was dissolved in MeCN and PR (1 eq.) in MeCN was dropwise added. The reaction mixture was stirred at rt for various hours and afterwards Whatmann® filtration was performed. After washing the precipitate with Et_2O, the residual solvent of the filtrate was removed *in vacuo*.

Synthesis route 2: AHE-083

PR (1 eq.) was dissolved in solvent and $Zn(NO_3)_2$ (2 eq.) was added. The vials were sealed air-tight and placed in an oven. The oven was heated to 60 °C and kept at that temperature for 3 days. Afterwards the oven was slowly cooled down to rt.

Synthesis route 3: AH-AS-09

PR (1 eq.), MP (2 eq.) and additives were placed in a vial, 2 mL of solvent was added, and the vials were sealed airtight. After carefully shaking the vials were placed in an oven, heated to 60 °C and kept at that temperature for 3 days. Afterwards, the reaction mixtures were slowly cooled down to rt.

Synthesis route 4: AHE-170

PR (1 eq.) and MP (2 eq.) were dissolved in DMF. The vail was sealed air-tight and either kept at rt for several days or placed in an oven, heated to 60 °C and kept at that temperature for 1 day. Afterwards, the reaction mixture was cooled down to rt.

Synthesis route 5: AHE-141

Stem solutions of PR and MP were provided and combined in a 3mL vial and 1 mL of DMF were added. The vials were sealed air-tight and placed in an oven. The oven was heated to 60 °C and kept at that temperature for 3 days. Then the reaction mixtures were slowly cooled down to rt.

Synthesis route 6:[32-33] AHE-159, AHE-160

PR (1 eq.) and a base (2,6-DMP or DIPEA, 1 eq.) were dissolved in DMF:H_2O and provided in a vial. $AgNO_3$ (1 eq.) was dissolved in a solvent mixture of MeOH:MeCN. The solutions were stirred at rt for 10 min and afterwards combined. Either the solution of PR and base was provided in a vial and the solution of $AgNO_3$ was slowly layered on top, the vials were sealed air-tight and kept at rt or at 60 °C for 3 days and afterwards cooled down slowly. Or both solutions were combined, stirred and kept at rt of at 60 °C for 3 days and afterwards slowly cooled down to rt.

Synthesis route 7:[33] AHE-166

$AgPF_6$ (1 eq.) was dissolved in a 1:1 mixture of MeOH:MeCN (5 mM). PR (1 eq.) and 2,6-DMP (1 eq.) were dissolved in a 1:1 mixture of DMF:H_2O (5 mM). In a vial the solution of PR and 2,6-DMP was provided and a layer of solvent mixture DMF:H_2O was slowly layered on top. A second layer of solvent (MeOH:MeCN) was slowly poured on top and then the solution of $AgPF_6$ was slowly layered on top. The vials were sealed air-tight and kept on rt.

Synthesis route 8:[32] AHE-167

$AgPF_6$ (1 eq.) was dissolved in a H_2O (5 mM). PR (1 eq.) and pyridine (1 eq.) were dissolved in a 1:1 mixture of DMF:MeCN (5 mM). In a vial the solution of $AgPF_6$ was provided and a layer of solvent (H_2O) was slowly layered on top. A second layer of solvent (DMF:MeCN) was slowly poured on top and then the solution of PR and pyridine slowly layered on top. The vials were sealed air-tight and kept on rt.

Synthesis route 9: AHE-174

PR (10.00 mg, 3.80 µmol, 1 eq.) and $AgPF_6$ (3.85 mg, 15.21 µmol, 4 eq.) were dissolved in DMF (3 mL) and DIPEA (1.5 µL, 8.36 µmol, 2.2 eq.) was added. The reaction mixture was either stirred at rt for 3 h and then kept at rt. Or heated to 60 °C, stirred at that temperature for 3 h and slowly cooled down to rt.

Synthesis route 10:[34] AHE-149

PR (1 eq.) was dissolved in a solvent mixture of H_2O:DMF (5:1) and Cu(OAc)2 (1 eq.) was added. The reaction mixture was stirred at rt for 3 h and kept at rt afterwards.

Synthesis route 11: AHE-193, AHE-194, AHE-195

Synthesis was performed in the glovebox under inert conditions and dry solvents were used. PR (1 eq.) and additive (6 eq.) were dissolved in MeCN, MP (2 eq.) was dissolved in MeCN. The solution of PR in MeCN was provided in a vial and the solution of MP in MeCN was slowly layered on top. The vials were sealed air-tight and placed in the freezer (-30 °C).

Reaction conditions for coordination attempts starting with $[M_8L^{Me}_2](PF_6)_4$:

No.	M	Acid	eq. (PR)	MP	eq. (MP)	Additive	eq. (A)	Solvent	Volume [mL]	T [°C]	t [d]
1.1	Ag-PF_6	C12	1	$Mo_2(DAniF)_3(OAc)$	2	-	-	MeCN	10	rt	0.5
1.2	Ag-PF_6	C12	1	$Mo_2(DAniF)_3(OAc)$	2	Cs_2CO_3	6	MeCN	10	rt	1
1.3	Ag-PF_6	C12K2	1	$Mo_2(DAniF)_3(OAc)$	2	-	-	MeCN:MeOH	10	rt	2
1.4	Ag-PF_6	12	1	Cu(XanthPhos)$(MeCN)_2(PF_6)_2$	2	-	-	MeCN	10	rt	0.5
2.1	Ag-PF_6	C12	1	$Zn(NO_3)_2$	2	-	-	MeCN	2	60	3
2.2	Ag-PF_6	C12	1	$Zn(NO_3)_2$	2	-	-	MeCN:H_2O	2	60	3
2.3	Ag-PF_6	C12	1	$Zn(NO_3)_2$	2	-	-	DMF	2	60	3
2.4	Ag-PF_6	C12	1	$Zn(NO_3)_2$	2	-	-	DMSO	2	60	3
3.1	Ag-PF_6	C12	1	$Zn(NO_3)_2$	2	-	-	DMF	2	60	3
3.2	Ag-PF_6	C12	1	$Zn(NO_3)_2$	2	-	-	MeCN	2	60	3
3.3	Ag-PF_6	C14	1	$Zn(NO_3)_2$	2	-	-	DMF	2	60	3
3.4	Ag-PF_6	C14	1	$Zn(NO_3)_2$	2	-	-	MeCN	2	60	3
3.5	Ag-PF_6	C12	1	$Zn(NO_3)_2$	2	AcOH	0.2	DMF	2	60	3
3.6	Ag-PF_6	C14	1	$Zn(NO_3)_2$	2	AcOH	0.2	DMF	2	60	3
3.7	Ag-PF_6	C12	1	$Zn(OAc)_2$	2	-	-	DMF	2	60	3
3.8	Ag-PF_6	C14	1	$Zn(OAc)_2$	2	-	-	DMF	2	60	3
3.9	Ag-PF_6	C12	1	$Co(NO_3)_2$	2	-	-	DMF	2	60	3

3.10	Ag-PF_6	C14	1	$Co(NO_3)_2$	2	-	-	DMF	2	60	3
3.11	Ag-PF_6	C12	1	$Zn(NO_3)_2$	2	C12	1	DMF	2	60	3
3.12	Ag-PF_6	C12	1	$Zn(NO_3)_2$	2	C12	1	MeCN	2	60	3
3.13	Ag-PF_6	C14	1	$Zn(NO_3)_2$	2	C14	1	DMF	2	60	3
3.14	Ag-PF_6	C14	1	$Zn(NO_3)_2$	2	C14	1	MeCN	2	60	3
3.15	Ag-PF_6	C12	1	$Zn(NO_3)_2$	2	C12, AcOH	1, 0.2	DMF	2	60	3
3.16	Ag-PF_6	C14	1	$Zn(NO_3)_2$	2	C14, AcOH	1, 0.2	DMF	2	60	3
3.17	Ag-PF_6	C12	1	$Zn(OAc)_2$	2	C12	1	DMF	2	60	3
3.18	Ag-PF_6	C14	1	$Zn(OAc)_2$	2	C14	1	DMF	2	60	3
3.19	Ag-PF_6	C12	1	$Co(NO_3)_2$	2	C12	1	DMF	2	60	3
3.20	Ag-PF_6	C14	1	$Co(NO_3)_2$	2	C14	1	DMF	2	60	3
4.1	Ag-PF_6	C12	1	$Zn(OAc)_2(H_2O)_2$	2	-	-	DMF	2	rt	-
4.2	Ag-PF_6	C12	1	$Zn(OAc)_2(H_2O)_2$	2	-	-	DMF	2	60	1
5.1	Ag-PF_6	C12	1	$AgPF_6$	2	-	-	DMF	1.6	60	3
5.2	Ag-OAc	C12	1	Ag(OAc)	2	-	-	DMF	1.6	60	3
5.3	Ag-OTf	C12	1	Ag(OTf)	2	-	-	DMF	1.6	60	3
5.4	Ag-PF_6	C12	1	$Cu(PF_6)(MeCN)_4$	2	-	-	DMF	1.6	60	3
5.5	Ag-PF_6	C12	1	$Cu(OAc)_2$	1	-	-	DMF:H_2O	2.1	60	3
5.6	Ag-PF_6	C12	1	$Cu(OAc)_2$	2	-	-	DMF:H_2O	2.1	60	3
5.7	Ag-PF_6	C12	1	Cu(OTf)(benzene)	2	-	-	DMF	1.6	60	3
5.8	Ag-PF_6	C12	1	$Cu(OTf)_2$	1	-	-	DMF	1.6	60	3
5.9	Ag-PF_6	C12	1	$Cu(OTf)_2$	2	-	-	DMF	1.6	60	3
6.1	Ag-PF_6	C12	1	$AgNO_3$	1	2,6-DMP	1	DMF:H_2O, MeOH:MeCN	1.51	rt	-
6.2	Ag-PF_6	C12	1	$AgNO_3$	1	2,6-DMP	1	DMF:H_2O, MeOH:MeCN	1.51	60	3
6.3	Ag-PF_6	C12	1	$AgNO_3$	1	DPEA	1	DMF:MeCN, H_2O	1.5	rt	-
6.4	Ag-PF_6	C12	1	$AgNO_3$	1	DPEA	1	DMF:MeCN, H_2O	1.5	60	3

7.1	Ag-PF_6	C12	1	$AgPF_6$	1	2,6-DMP	1	DMF:H_2O, MeOH:MeCN	0.4	rt	-
7.2	Ag-PF_6	C12	1	$AgPF_6$	1	2,6-DMP	1	DMF:H_2O, MeOH:MeCN	0.4	60	-
7.3	Ag-PF_6	C12	1	$AgPF_6$	1	2,6-DMP	1	DMF:H_2O, MeOH:MeCN	0.8	rt	-
7.4	Ag-PF_6	C12	1	$AgPF_6$	1	2,6-DMP	1	DMF:H_2O, MeOH:MeCN	0.8	60	-
8.1	Ag-PF_6	C12	1	$AgPF_6$	1	pyridine	1	DMF:MeOH, H_2O	0.4	rt	-
8.2	Ag-PF_6	C12	1	$AgPF_6$	1	pyridine	1	DMF:MeOH, H_2O	0.4	60	-
8.3	Ag-PF_6	C12	1	$AgPF_6$	1	pyridine	1	DMF:MeOH, H_2O	0.8	rt	-
8.4	Ag-PF_6	C12	1	$AgPF_6$	1	pyridine	1	DMF:MeOH, H_2O	0.8	60	-
9.1	Ag-PF_6	C12	1	$AgPF_6$	4	DIPEA	2.2	DMF	3	rt	-
9.2	Ag-PF_6	C12	1	$AgPF_6$	4	DIPEA	2.2	DMF	3	60	1
10.1	Ag-OAc	C12	1	$Cu(OAc)_2$	1	-	-	DMF	2	rt	-
10.2	Ag-OAc	C12	1	$Cu(OAc)_2$	1	-	-	DMF:H_2O	2	rt	-
11.1	Au-PF_6	C12	1	$AgPF_6$	2	-	-	MeCN	2	rt, -30	-
11.2	Au-PF_6	C12	1	$Mo_2(DAniF)_3(OAc)$	2	-	-	MeCN	2	rt, -30	-
11.3	Au-PF_6	C12	1	$Mo_2(DAniF)_3(OAc)$	2	Cs_2CO_3	6	MeCN	2	rt, -30	-
11.4	Au-PF_6	C12	1	Cu(XanthPhos)$(MeCN)_2(PF_6)_2$	2	-	-	MeCN	2	rt, -30	-
11.5	Au-PF_6	C12	1	Cu(XanthPhos)$(MeCN)_2(PF_6)_2$	2	Cs_2CO_3	6	MeCN	2	rt, -30	-

Synthesis of $[Ag_8L^{Me}_2](C_{12}H_{20}O_4Cl_2)(PF_6)_4$

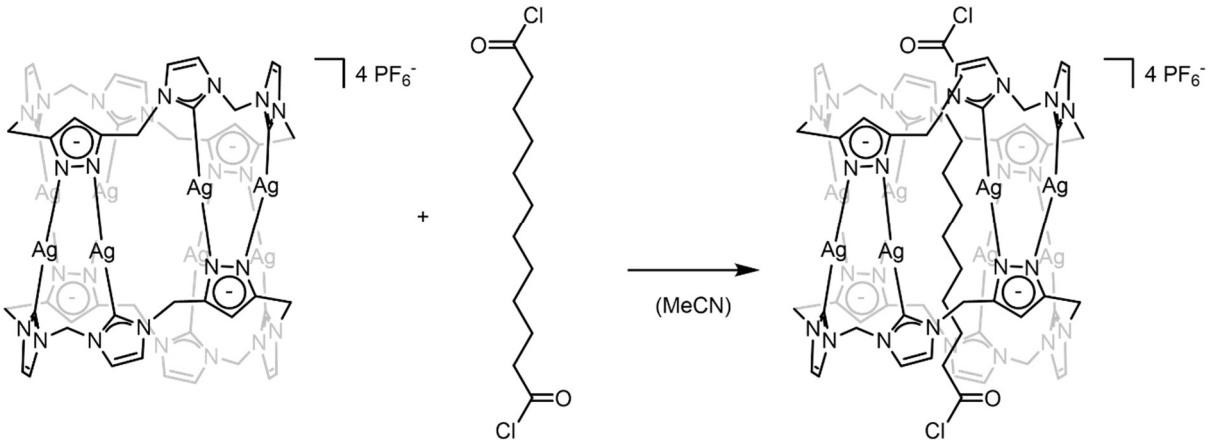

$[Ag_8L^{Me}_2](PF_6)_4$ (8.98 mg, 3.74 µmol, 1 eq.) and $C_{12}H_{20}O_4Cl_2$ (1.00 mg, 3.74 µmol, 1 eq.) were dissolved in acetonitrile and the mixture was stirred at room temperature for 10 min. While stirring, the reaction mixture slowly turned from a clear solution to a brownish suspension. The solvent was removed *in vacuo* at rt and the residue was redissolved in a minimal amount of acetonitrile and precipitated by an excess of diethyl ether. After drying *in vacuo*, a brown solid was obtained. Analysis with ^{1}H NMR spectroscopy showed no pillarplex signals and it was concluded that the dicarboxylic acid chloride leads to a decomposition of $[Ag_8L^{Me}_2](PF_6)_4$.

Synthesis of Covalent Organic Pillarplex Polymer

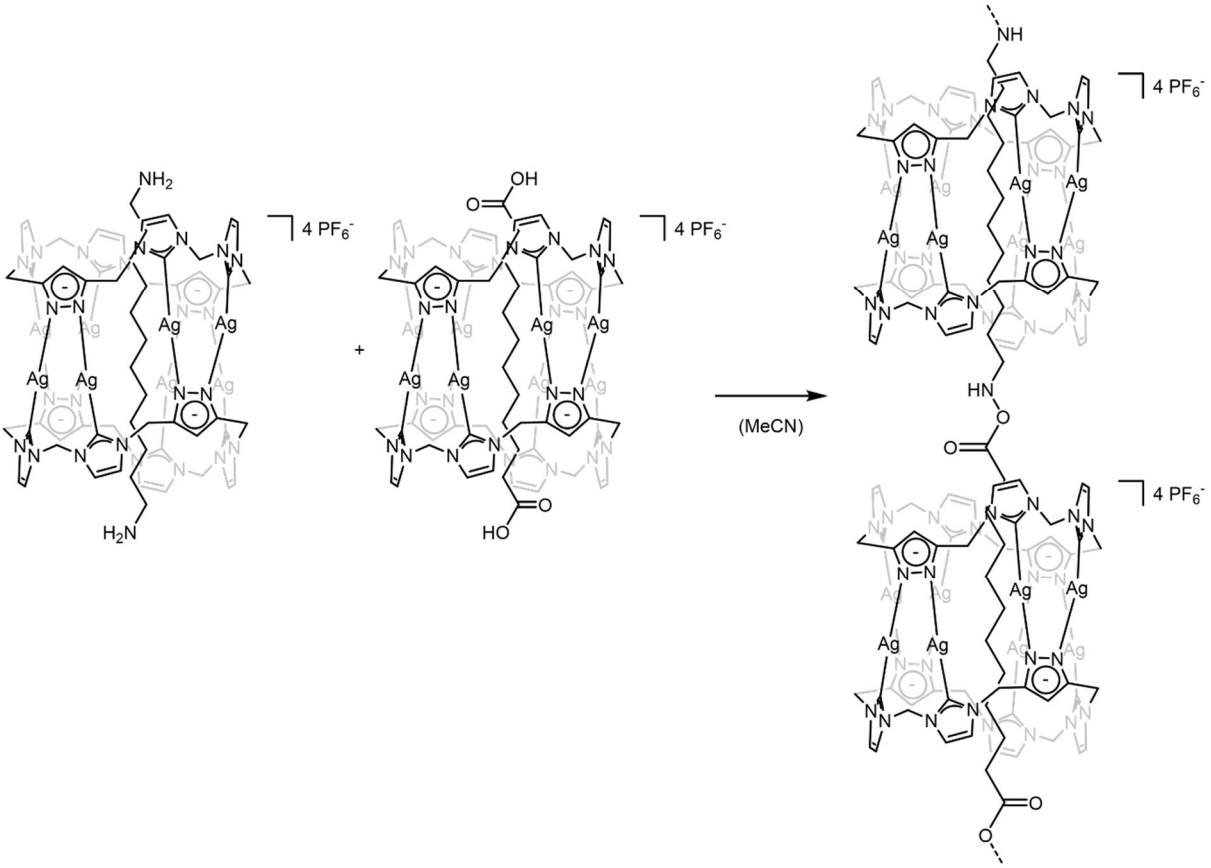

$[Ag_8L^{Me}{}_2](PF_6)_4$ (11.98 mg, 4.99 µmol, 1 eq.) and $C_{12}H_{26}N_2$ (1.00 mg, 4.99 µmol, 1 eq.) were dissolved in acetonitrile (2 mL) to form the pseudorotaxane $[Ag_8L^{Me}{}_2](C_{12}H_{26}N_2)(PF_6)_4$ (expected yield: 10.08 mg, 4.99 µmol). $[Ag_8L^{Me}{}_2](PF_6)_4$ (12.31 mg, 5.13 µmol, 1 eq.) and $C_{12}H_{22}O_4$ (1.30 mg, 5.64 µmol, 1 eq.) were dissolved in acetonitrile (2 mL) to form the pseudorotaxane $[Ag_8L^{Me}{}_2](C_{12}H_{22}O_4)(PF_6)_4$ (10.72 mg, 5.23 µmol).

Analytics for pseudorotaxane 1:

^{1}H NMR (400.13 MHz, MeCN-d_3): δ [ppm] = 7.61 (s, 8H, H_{NCHC}), 7.52 (s, 8H, H_{NCHC}), 6.66 (s, 4H, H_{CCHC}), 6.63 (d, d, ^2J = 14.9 Hz, 8H, H_{CH2}), 6.04 (d, ^2J = 14.8 Hz, 8H, H_{CH2}), 5.59 (d, ^2J = 15.2 Hz, 8H, H_{CH2}), 5.25 (d, ^2J = 15.2 Hz, 8H, H_{CH2}), 2.09 (s, 8H), 1.77 (m, 4H), 1.25 (m, 4H), 0.80 (m, 4H), 0.40 (m, 4H), 0.08 (m, 4H).

DOSY NMR (400.13 MHz, MeCN-d_3): d (m^2 sec^{-1}) = $5.76 \cdot 10^{-10}$.

Analytics for pseudorotaxane 2:

^{1}H NMR (400.13 MHz, MeCN-d_3): δ [ppm] = 7.58 (s, 8H, H_{NCHC}), 7.50 (s, 8H, H_{NCHC}), 6.67 (s, 4H, H_{CCHC}), 6.62 (d, d, ^2J = 14.8 Hz, 8H, H_{CH2}), 6.04 (d, ^2J = 14.8 Hz, 8H, H_{CH2}), 5.59 (d, ^2J = 15.1 Hz, 8H, H_{CH2}), 5.25 (d, ^2J = 15.1 Hz, 8H, H_{CH2}), 2.09 (s, 4H), 1.19 (m, 4H), 0.59 (m, 4H), -0.01 (m, 4H), -0.50 (m, 4H).

DOSY NMR (400.13 MHz, MeCN-d_3): d (m^2 sec^{-1}) = $5.76 \cdot 10^{-10}$.

Synthesis route A:

The two pseudorotaxane solutions (1:1) were combined and the mixture was stirred at room temperature for 10 min. While stirring, the reaction mixture slowly turned from a clear solution to a brownish suspension. The solvent was removed *in vacuo* at rt and the residue was redissolved in a minimal amount of acetonitrile and precipitated by an excess of diethyl ether. After drying *in vacuo*, a brown solid was obtained.

^{1}H NMR (400.13 MHz, MeCN-d_3): δ [ppm] = 7.58 (s, 8H), 7.51 (s, 8H), 7.41(d, 1H), 7.34 (d, 1H), 6.68 (s, 4H), 6.63 (s, 4H), 6.59 (s, 4H), 6.10 (s, 1H), 6.04 (d, 4H), 5.93 (m, 0.5H), 5.60 (d, 8H), 5.51 (d, 0.5H), 5.41 (m, 1H), 5.25 (d, 8H), 5.18 (d, 1H), 4.87 (d, 1H), 4.71 (s, 0.2H, H_{H2O}), 3.41 (c, 2.3H), 3.29 (c, 0.3H), 1.11 (t, 4H), 0.80 (t, 0.7H), 0.65 (t, 0.5H), 0.25 (s, 0.5H), -0.63 (s, 0.5H), -0.88 (s, 0.5H), -1.39 (s, 0.3H).

DOSY NMR (400.13 MHz, MeCN-d_3): d (m^2 sec^{-1}) = $5.98 \cdot 10^{-10}$.

Synthesis route B: Activation of the encapsulated dicarboxylic acid by DCC

To solution [A] DCC (3.18 mg, 15.39 µmol, 3 eq.) as activation agent was added and stirred at rt for 15 min. The two pseudorotaxane solutions were combined and the mixture was stirred at room temperature for 10 min. While stirring, the reaction mixture slowly turned from a clear solution to a brownish suspension. The solvent was removed *in vacuo* at rt and the residue was redissolved in a minimal amount of acetonitrile and precipitated by an excess of diethyl ether. After drying *in vacuo*, a brown solid was obtained.

^{1}H NMR (400.13 MHz, MeCN-d_3): δ [ppm] = 7.59 (s, 8H), 7.52 (s, 5.5H), 7.48 (d, 1H), 7.44 (t, 2H), 7.41 (d, 0.6 H), 7.36 (d, 1H), 7.33 (t, 0.3H), 6.69 (s, 4H), 6.63 (d, 4H), 6.59 (d, 4H), 6.11 (s, 1H), 6.06 (s, 4H), 6.03 (s, 4H), 5.93 (d, 1H), 5.60 (dd, 8H), 5.51 (d, 0.7H), 5.44 (m, 1H), 5.27 (dd, 8H), 5.18 (d, 0.5H), 4.88 (m, 1H), 4.71 (s, 0.5H, H_{H2O}), 3.98 (t, 1H), 3.74 (s, 1H), 3.40 (c, 1.7H), 3.29 (c, 0.7H), 2.00 (m, 1.6H), 1.89 (m, 2H), 1.73 (m, 2H), 1.59 (m, 3H), 1.43 (c, 3H), 1.22 (t, 1H), 1.09 (t, 2.5H), 0.82 (m, 2H), 0.58 (s, 1H), -0.07 (s, 0.7H), -0.15 (s, 0.7H), -0.58 (s, 1H), -0.69 (s, 1.5H), -0.97 (s, 2H), -1.23 (s, 1.5H), -1.93 (s, 1.3H).

DOSY NMR (400.13 MHz, MeCN-d_3): d (m^2 sec^{-1}) = $5.56 \cdot 10^{-10}$.

5.8.4 Synthesis of Pyridine-Rotaxanes and Synthesis Attempts for Coordination Polymers

Synthesis of $[Ag_8L^{Me}_2][Py](PF_6)_4$

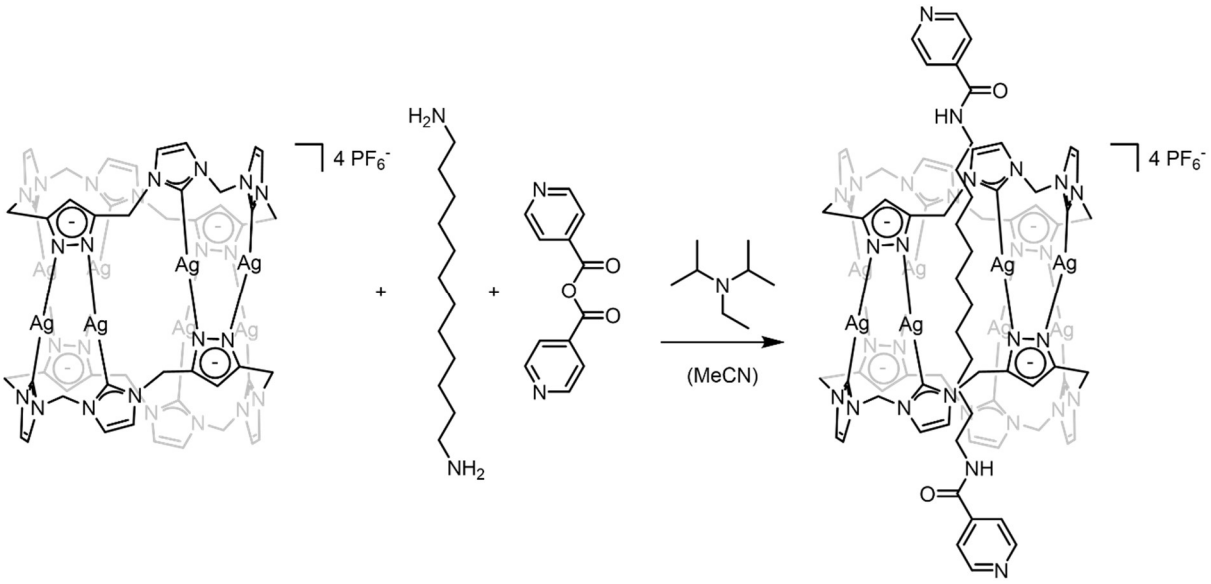

$[Ag_8L^{Me}_2](PF_6)_4$ (100.00 mg, 41.67µmol, 1 eq.) was dissolved in acetonitrile, 1,12-diamino dodecane (9.18 mg, 45.84 µmol, 1.1 eq.) was added and the reaction mixture was stirred at rt for 20 min. After cooling the reaction mixture to 0 °C, isonicotinic anhydride (28.53 mg, 125.01 µmol, 3 eq.) and DIPEA (43.55 µL, 250.02 µmol, 6 eq.) as base were added. After stirring overnight, while the reaction mixture was allowed to warm up to rt, a clear solution with a white precipitate was obtained. The white solid was isolated by using a Whatman® filtration, which yielded a clear solution. To the filtrate an excess of diethyl ether was added to yield the expected pillarplex rotaxane as white precipitate. Isolation of the white solid was performed by centrifugation and the obtained solid was washed with diethyl ether (3 x 5 mL). After drying *in vacuo*, $[Ag_8L^{Me}_2][Py](PF_6)_4$ was obtained as white powder.

Yield: white powder, 100 mg, 35.97 µmol, 86%.

^{1}H NMR (400.13 MHz, MeCN-d_3): δ [ppm] = 8.82 (d, 4H, H_{Py}), 7.92 (H_{DMF}), 7.78 (d, 4H, H_{Py}), 7.65 (s, 8H, H_{NCHC}), 7.50 (s, 8H, H_{NCHC}), 7.03 (s, 2H, H_{NHCO}), 6.68 (s, 4H, H_{CCHC}), 6.62 (d, ^2J = 14.9 Hz, 4H, H_{CH2}), 6.04 (d, ^2J = 14.9 Hz, 4H, H_{CH2}), 5.61 (d, ^2J = 15.5 Hz, 8H, H_{CH2}), 5.24 (d, ^2J = 15.1 Hz, 8H, H_{CH2}), 3.14 (H_{Et2O}), 2.89 (H_{DMF}), 2.77 (H_{DMF}), 2.55 (c, 4H), 2.16 (H_{H2O}), 1.11 (H_{Et2O}), 0.22 (s, 4H), -0.02 (s, 4H), -0.66 (s, 2H), -1.15 (s, 4H), -1.37 (s, 4H).

^{13}C NMR (100.62 MHz, MeCN-d_3): δ [ppm] = 151.59, 150.02, 142.92, 124.69, 123.60, 122.00, 104.08, 49.47, 34.56, 30.55, 27.50.

^{31}P NMR (161.99 MHz, MeCN-d_3): δ [ppm] = -144.57 (q).

DOSY NMR (400.13 MHz, MeCN-d_3): d (m^2 sec^{-1}) = $5.76 \cdot 10^{-10}$.

EA (%): calc. C 31.10, H 2.90, N 14.11; measured C 31.68, H 2.90, N 13.88 for $[Ag_8L^{Me}_2][Py](PF_6)_4$.

ESI-MS (CH_3CN): m/z = 454.9115 $[Ag_8L^{Me}{}_2]^{4+}$, calc. 454.91 for $[Ag_8L^{Me}{}_2]^{4+}$, 557.4807 $[Ag_8L^{Me}{}_2][Py]^{4+}$, calc. 557.48 for $[Ag_8L^{Me}{}_2][Py]^{4+}$, 791.6250 $[Ag_8L^{Me}{}_2][Py](PF_6)^{3+}$, calc. 791.63 for $[Ag_8L^{Me}{}_2][Py](PF_6)^{3+}$.

Synthesis of $[Au_8L^{Me}{}_2][Py](PF_6)_4$

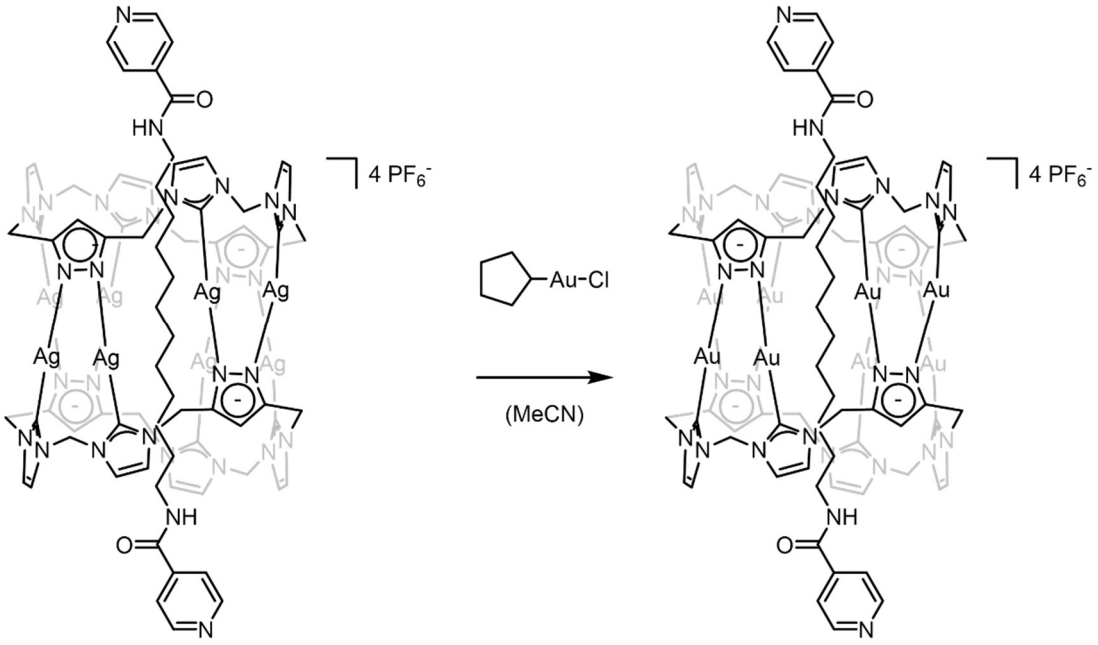

Au(THT)Cl (19.60 mg, 61.14 µmol, 8.5 eq.) was dissolved in 2 mL acetonitrile and a solution of $[Ag_8L^{Me}{}_2][Py](PF_6)_4$ (20 mg, 7.19 µmol, 1 eq.) in 3 mL of acetonitrile was slowly added. The reaction mixture was stirred under the exclusion of light for 16 h at rt. Then 1 eq. of diethyl ether (0.5 mL) was added to precipitate the formed side product AgCl. The filtration over Celite® provided a clear solution to which an excess of diethyl ether was added to precipitate $[Au_8L^{Me}{}_2][Py](PF_6)_4$ as an off-white solid.

Yield: white powder, 16 mg, 4.58 µmol, 64%.

^{1}H NMR (400.13 MHz, MeCN-d_3): δ [ppm] = 8.83 (d, ^2J = 2.0 Hz, 2H, H_{Py}), 7.77 (d, 2H, ^2J = 5.1 Hz, H_{Py}), 7.71 (d, ^2J = 2.1 Hz, 8H, H_{NCHC}), 7.65 (s, 2H, H_{NHCO}), 7.56 (d, ^2J = 2.4 Hz, 8H, H_{NCHC}), 7.06 (s, 4H, H_{CCHC}), 6.96 (d, ^2J = 14.8 Hz, 4H, H_{CH2}), 5.93 (d, ^2J = 14.8 Hz, 4H, H_{CH2}), 5.74 (d, ^2J = 15.1 Hz, 8H, H_{CH2}), 5.27 (d, ^2J = 15.1 Hz, 8H, H_{CH2}), 3.41 (H_{Et2O}), 2.89 (H_{DMF}), 2.14 (H_{H2O}), 1.11 (H_{Et2O}), 0.45 (s, 4H), 0.08 (s, 4H), -0.43 (s, 4H), -0.98 (s, 4H), -1.14 (s, 4H).

ESI-MS (CH_3CN): m/z = 633.0348 $[Au_8L^{Me}{}_2]^{4+}$, calc. 633.04 for $[Au_8L^{Me}{}_2]^{4+}$, 735.6042 $[Au_8L^{Me}{}_2][Py]^{4+}$, calc. 735.60 for $[Au_8L^{Me}{}_2][Py]^{4+}$, 1029.1317 $[Au_8L^{Me}{}_2][Py](PF_6)^{3+}$, calc. 1029.13 for $[Au_8L^{Me}{}_2][Py](PF_6)^{3+}$.

CP Attempts for Py-Rotaxanes

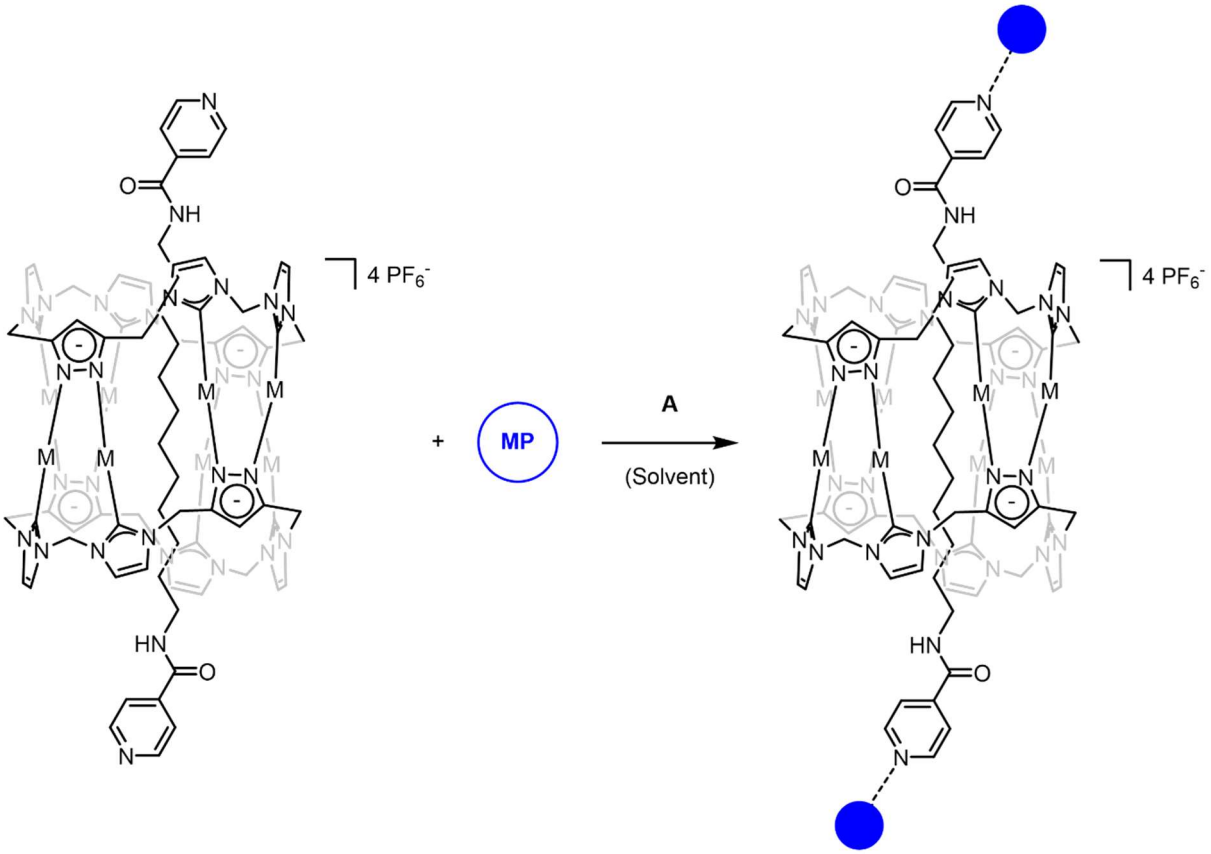

Synthesis route 1: AHE-151, AHE-168, AHE-175

$[Ag_8L^{Me}_2][Py](PF_6)_4$ (1 eq.) and $AgPF_6$ (2 / 3 eq.) were provided in solvent and stirred at rt for various hours. The solvent of the reaction mixture was either removed *in vacuo* or evaporated over time for possible crystallisation.

Synthesis route 2: AHE-182, AHE-183

$[M_8L^{Me}_2][Py](PF_6)_4$ (1 eq.) was dissolved in 0.8 mL of DMF and provided in a vial and 1 mL of DMF was slowly layered on top. $AgPF_6$ (2 / 4 eq.) was dissolved in MeCN and 0.8 mL of this solution was slowly layered on top. The vials were kept at rt.

Synthesis route 3:[35] AHE-155

$[Ag_8L^{Me}_2][Py](PF_6)_4$ (1 eq.), MP (2 eq.) and additive (0.5 / 1 eq.) were provided in a vial and a solvent mixture of DMF:H_2O (4:1) was added. The vials were carefully shaken and placed in an oven. After heating at 100 °C for 18 h, the oven was slowly cooled down to rt.

Reaction conditions for coordination attempts starting with $[M_8L^{Me}_2][Py](PF_6)_4$:

No.	M	eq. (R)	MP	eq. (MP)	Additive	eq. (A)	Solvent	Volume [mL]	T [°C]	t [h]
1.1	Ag-PF_6	1	$AgPF_6$	3	-	-	DMF	4	rt	2
1.2	Ag-PF_6	1	$AgPF_6$	2	-	-	DMSO	3	rt	72
1.3	Ag-PF_6	1	$AgPF_6$	2	-	-	DMF	3	rt	72
1.4	Ag-PF_6	1	$AgPF_6$	2	-	-	MeCN	3	rt	72
1.5	Ag-PF_6	1	$AgPF_6$	4	-	-	DMF	3	rt	-
2.1	Ag-PF_6	1	$AgPF_6$	2	-	-	DMF	2.6	rt	-
2.2	Ag-PF_6	1	$AgPF_6$	4	-	-	DMF	2.6	rt	-
2.3	Au-PF_6	1	$AgPF_6$	2	-	-	DMF	2.6	rt	-
2.4	Au-PF_6	1	$AgPF_6$	4	-	-	DMF	2.6	rt	-
3.1	Ag-PF_6	1	$Zn(NO_3)_2$	2	terephthalic acid	0.5	4 DMF: 1 H_2O	2	100	18
3.2	Ag-PF_6	1	$Zn(NO_3)_2$	2	terephthalic acid	1	4 DMF: 1 H_2O	2	100	18
3.3	Ag-PF_6	1	$Cd(NO_3)_2$	2	terephthalic acid	0.5	4 DMF: 1 H_2O	2	100	18
3.4	Ag-PF_6	1	$Cd(NO_3)_2$	2	terephthalic acid	1	4 DMF: 1 H_2O	2	100	18

5.8.5 Synthesis of Naphthalimide-Rotaxanes

Synthesis of $[Ag_8L^{Me}{}_2][NMI\text{-}C_{12}](PF_6)_4$

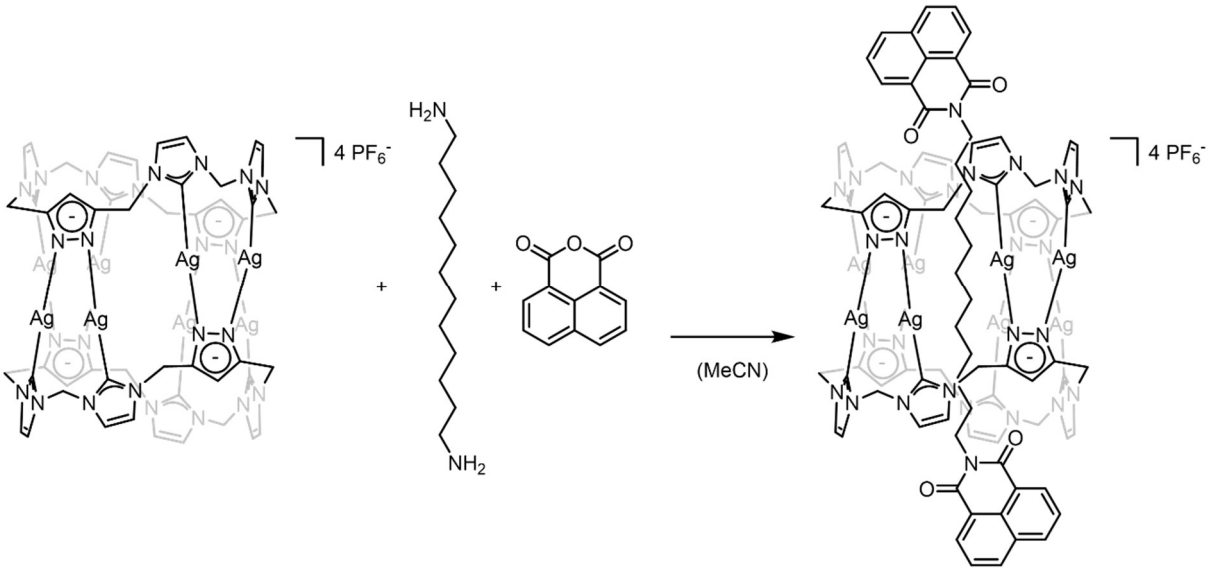

Synthesis taken from[36] and adapted. $[Ag_8L^{Me}{}_2](PF_6)_4$ (40.0 mg, 16.67 µmol, 1 eq.) was dissolved in MeCN (10 mL), 1,12-diamino dodecane (3.34 mg, 16.67 µmol, 1 eq.) was added and the reaction mixture was stirred at rt for 20 min. 1,8-naphthalic anhydride (6.61 mg, 33.34 µmol, 2 eq.) was added and the reaction mixture was heated to 50 °C. After stirring overnight at that temperature, a clear solution with a white precipitate was obtained. The white solid was isolated by using a Whatman® filtration, which yielded a clear solution. To the filtrate an excess of diethyl ether was added to yield the expected pillarplex rotaxane as white precipitate. Isolation of the white solid was performed by centrifugation and the obtained solid was washed with diethyl ether (3 x 5 mL). After drying *in vacuo*, $[Ag_8L^{Me}{}_2][NMI](PF_6)_4$ was obtained as white powder.

^{1}H NMR (400.13 MHz, MeCN-d_3): δ [ppm] = 8.72 (d, ^2J = 7.3 Hz, 4H, H_{NMI}), 8.46 (d, ^2J = 8.3 Hz, 4H, H_{NMI}), 7.95 (t, ^3J = 7.8 Hz, 4H, H_{NMI}), 7.64 – 7.40 (m, 16H, H_{NCHC}), 6.70 (d, ^2J = 9.9 Hz, 4H, H_{CCHC}), 6.61 (dd, ^2J = 14.6, 2.7 Hz, 4H, H_{CH2}), 6.03 (dd, ^2J = 14.9, 7.8 Hz, 4H, H_{CH2}), 5.60 (dd, ^2J = 15.1, 6.3 Hz, 8H, H_{CH2}), 5.29 – 5.20 (m, 8H, H_{CH2}), 0.21 (s, 4H), 0.07 (s, 4H), -0.63 (s, 4H), -1.06 (s, 4H), -1.32 (s, 4H).

^{31}P NMR (161.99 MHz, MeCzN-d_3): δ [ppm] = -144.54 (q).

DOSY NMR (400.13 MHz, MeCN-d_3): d (m^2 sec^{-1}) = $5.36 \cdot 10^{-10}$.

EA (%): calc. C 34.08, H 2.72, N 12.3011; measured C 29.93, H 2.73, N 12.45 for $[Ag_8L^{Me}{}_2][NMI](PF_6)_4$.

Synthesis of $[Ag_8L^{Me}_2][NMI\text{-}C_{12}](OTf)_4$

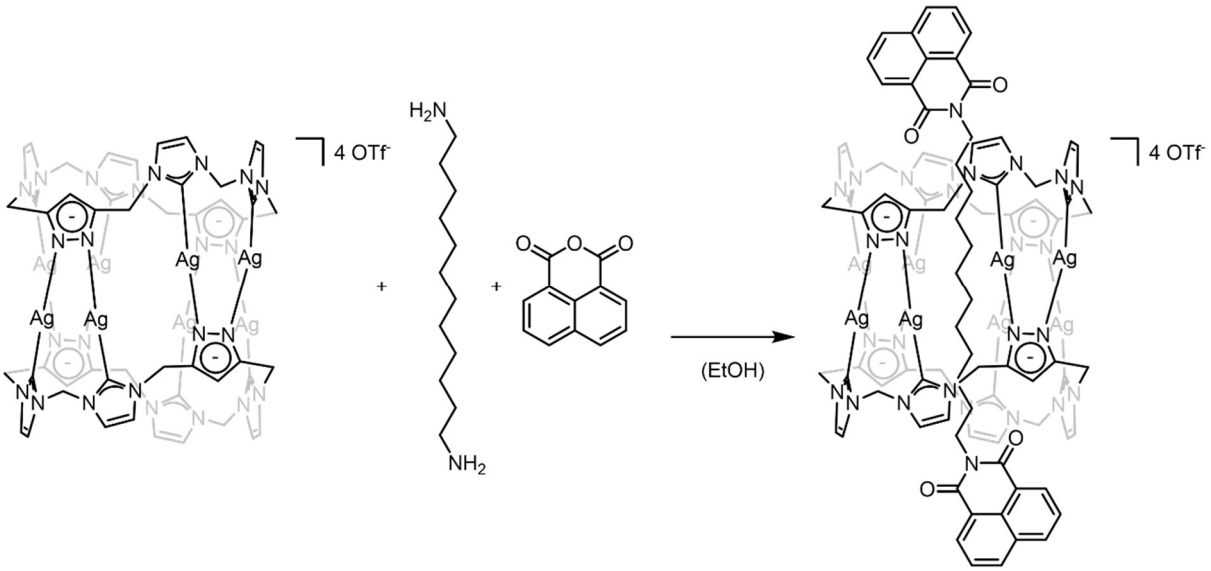

Synthesis taken from[36] and adapted. $[Ag_8L^{Me}_2](OTf)_4$ (46.20 mg, 19.12 µmol, 1 eq.) was dissolved in ethanol (10 mL), 1,12-diamino dodecane (4.21 mg, 21.03 µmol, 1.1 eq.) was added and the reaction mixture was stirred at rt for 20 min. 1,8-naphthalic anhydride (8.33 mg, 42.04 µmol, 2.2 eq.) was added and the reaction mixture was heated to 50 °C. After stirring overnight at that temperature, a clear solution with a white precipitate was obtained. The white solid was isolated by using a Whatman® filtration, which yielded a clear solution. To the filtrate an excess of diethyl ether was added to yield the expected pillarplex rotaxane as white precipitate. Isolation of the white solid was performed by centrifugation and the obtained solid was washed with diethyl ether (3 x 5 mL). After drying *in vacuo*, $[Ag_8L^{Me}_2][NMI](OTf)_4$ was obtained as white powder.

Yield: white powder, 40 mg, 13.38 µmol, 70%.

^{1}H NMR (400.13 MHz, MeCN-d_3): δ [ppm] = 8.72 (d, ^2J = 7.1 Hz, 4H, H_{NMI}), 8.46 (d, ^2J = 8.5 Hz, 4H, H_{NMI}), 7.94 (t, ^3J = 7.8 Hz, 4H, H_{NMI}), 7.74 – 7.39 (m, 16H, H_{NCHC}), 6.70 (d, ^2J = 5.6 Hz, 4H, H_{CCHC}), 6.62 (d, ^2J = 15.2 Hz, 4H, H_{CH2}), 6.09 – 5.99 (m, 4H, H_{CH2}), 5.60 (d, ^2J = 15.2 Hz, 8H, H_{CH2}), 5.24 (d, ^2J = 15.2 Hz, 8H, H_{CH2}), 0.21 (s, 4H), 0.07 (s, 4H), -0.62 (s, 4H), -1.07 (s, 4H), -1.33 (s, 4H).

^{19}F NMR (376.46 MHz, MeCN-d_3): δ [ppm] = -80.06.

EA (%): calc. C 35.51, H 2.71, N 12.23, S 4.31; measured C 31.29, H 2.93, N 11.86, S 4.31 for $[Ag_8L^{Me}_2][NMI](OTf)_4$.

ESI-MS (CH_3CN): m/z = 454.9113 $[Ag_8L^{Me}_2]^{4+}$, calc. 454.91 for $[Au_8L^{Me}_2]^{4+}$, 656.2049 $[Ag_8L^{Me}_2](OTf)^{3+}$, calc. 656.20 for $[Ag_8L^{Me}_2](OTf)_2^{2+}$, 1058.7799 $[Ag_8L^{Me}_2](OTf)_3^{+}$, calc. 1058.78 for $[Ag_8L^{Me}_2](OTf)_3^{+}$.

UV-vis (MeCN): I_{max} (nm) = 206, 232, 291.

Synthesis of $[Au_8L^{Me}_2][NMI\text{-}C_{12}](OTf)_4$

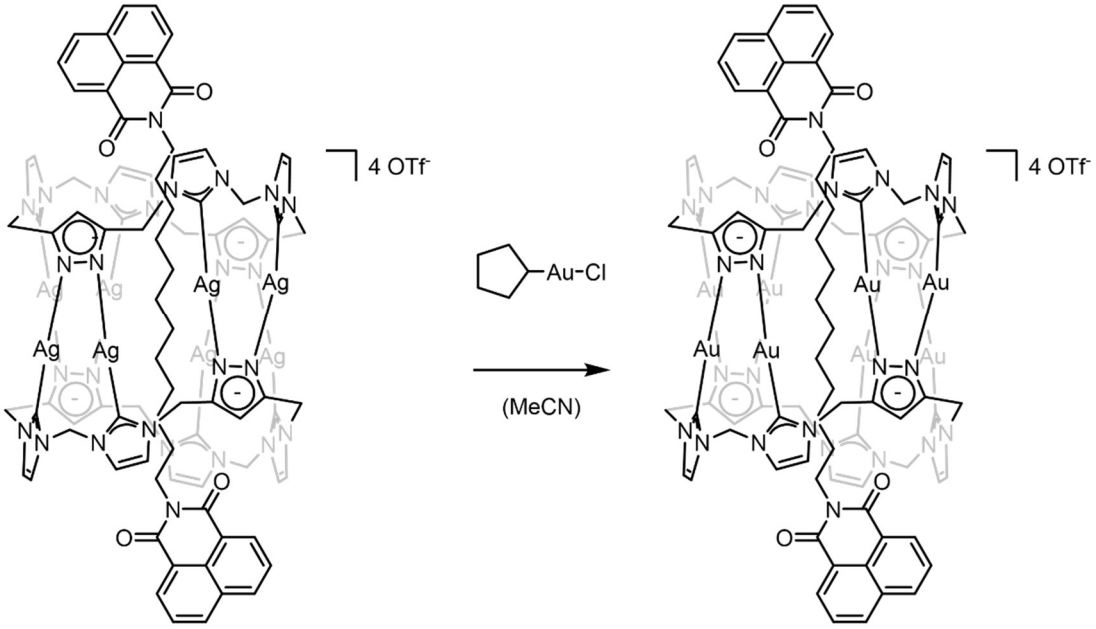

Au(THT)Cl (32.27 mg, 100.67 µmol, 8.1 eq.) was dissolved in 3 mL of acetonitrile and a solution of $[Ag_8L^{Me}_2][NMI\text{-}\mathbf{C_{12}}](OTf)_4$ (37.00 mg, 12.43 µmol,1 eq.) in 3 mL of acetonitrile was slowly added. The reaction mixture was stirred under the exclusion of light for 16 h at rt. Then 1 eq. of diethyl ether (0.5 mL) was added to precipitate the formed side product AgCl. The filtration over Celite® provided a clear solution to which an excess of diethyl ether was added to precipitate $[Au_8L^{Me}_2][NMI](OTf)_4$ as an off-white solid.

Yield: white powder, due to low solubility of substance in MeCN-d_3 and DMSO-d_6 no signals for the desired pillarplex rotaxane were obtained in ^{1}H NMR spectroscopy.

Synthesis of $[Ag_8L^{Me}_2]_2[NDI\text{-}C_{12}](OTf)_4$

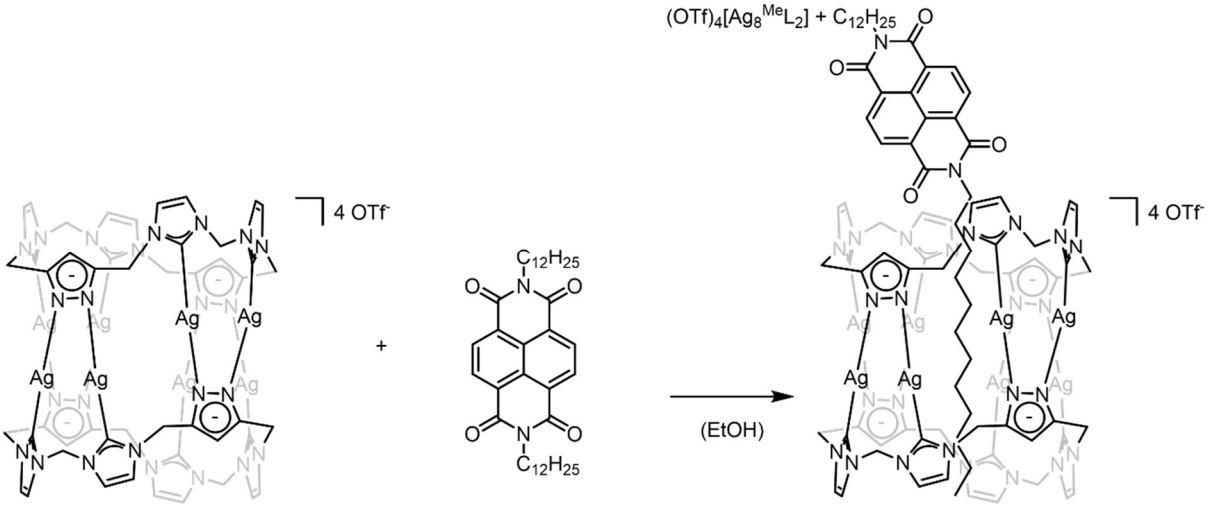

$[Ag_8L^{Me}_2](OTf)_4$ (15.0 mg, 6.21 µmol, 2 eq.) was dissolved in MeCN-d_3 and *N*,*N'*-(1-dodecyl)-1,4,5,8-naphthalenetetracarboxydiamide (1.87 mg, 3.10 µmol, 1 eq.) was dissolved in DCM-d_2. Both solutions were mixed, and the reaction mixture was stirred at rt for 20 min. ^{1}H NMR spectroscopy was performed.

^{1}H NMR (400.13 MHz, MeCN-d_3): δ [ppm] = 11.93, 8.96, 8.94, 7.74, 7.62, 7.61, 7.57, 7.56, 7.51, 7.51, 6.70, 6.63, 6.59, 6.46, 6.09, 6.05, 5.65, 5.62, 5.41, 5.41, 5.41, 5.26, 5.23, 0.86, 0.16, 0.07, -0.20, -0.57, -0.84.

Synthesis of $[Ag_8L^{Me}_2]_2[NDI\text{-}C_{12}NH_2](OTf)_4$

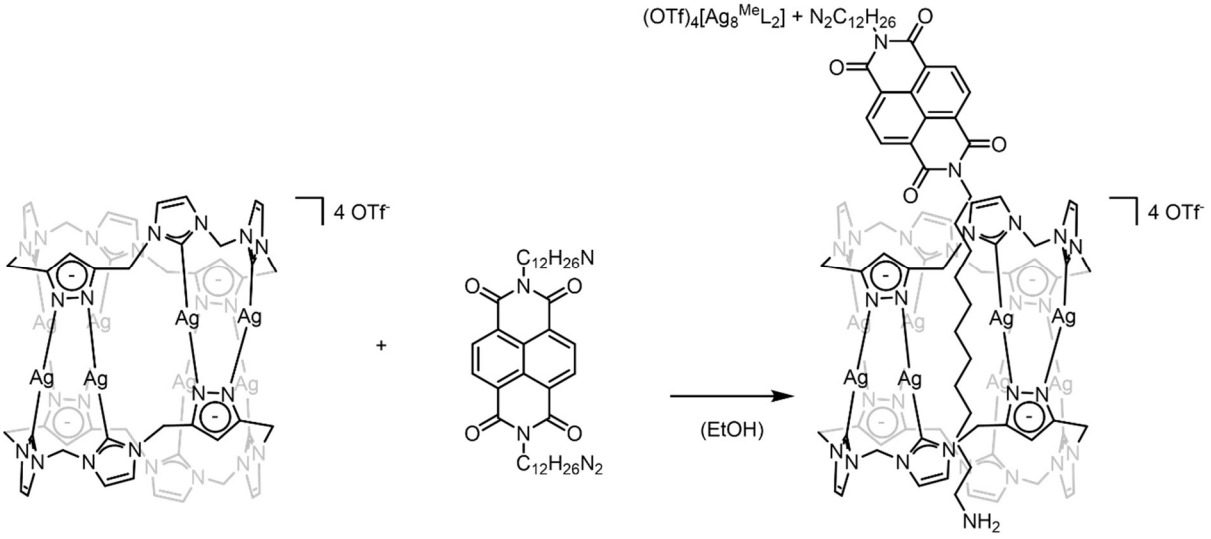

$[Ag_8L^{Me}_2](OTf)_4$ (15.0 mg, 6.21 µmol, 2 eq.) and *N*,*N'*-(12-aminododecyl)-1,4,5,8-naphthalenetetracarboxydiamide[37] (1.96 mg, 3.10 µmol, 1 eq.) were dissolved in MeOH-d_4. Both solutions were mixed, and the reaction mixture was stirred at rt for 20 min. ^{1}H NMR spectroscopy was performed.

^{1}H NMR (400.13 MHz, MeOH-d_4): δ [ppm] = 9.01, 7.94, 7.86, 7.79, 7.76, 7.73, 6.94, 6.85, 6.81, 6.76, 6.65, 6.60, 6.23, 6.19, 5.76, 5.72, 5.52, 5.33, 5.29, 1.85, 1.34, 0.19, 0.00, -0.42, -0.97.

Synthesis of $[Ag_8L^{Me}_2]_2$[NDI-NHCO-*t*BuPh](OTf)$_4$

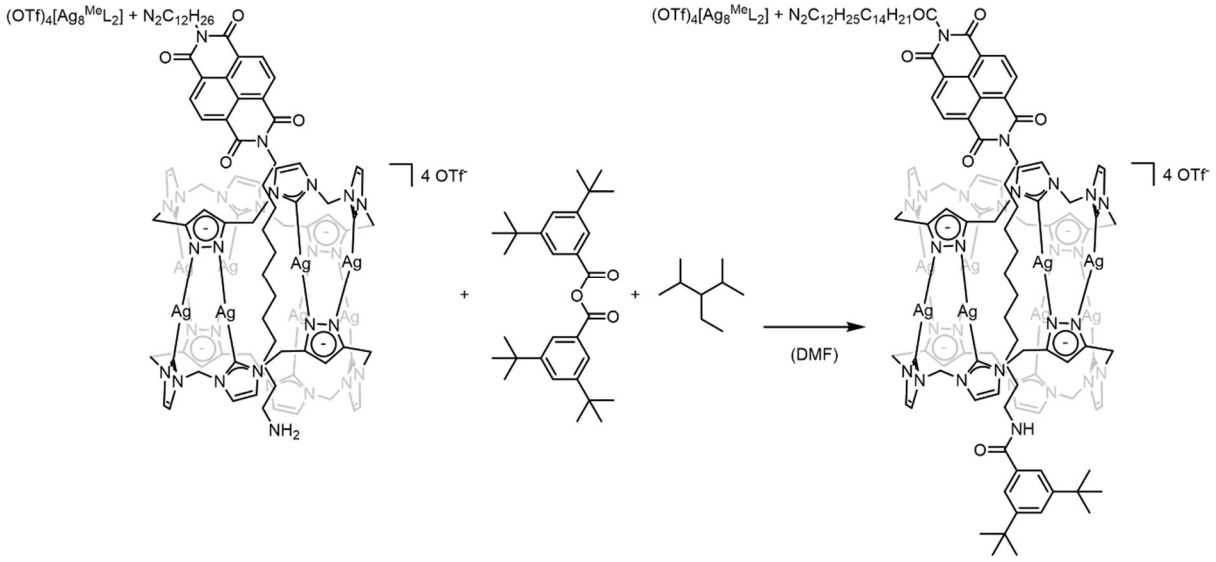

$[Ag_8L^{Me}_2]_2$[NDI-$C_{12}NH_2$](OTf)$_4$ (15.0 mg, 5.79 µmol, 1 eq.) was provided in degassed DMF. 3,5-di*t*-butyl benzoic anhydride (3.66 mg, 17.37 µmol, 3 eq.) and DIPEA (4.49 mg, 34.74 µmol, 6 eq) were added and the reaction mixture was stirred at rt overnight. Afterwards, filtration over Celite® was performed and the filtrate was subjected to an excess of Et_2O for precipitation. The white solid was dried *in vacuo* and ^{1}H NMR spectroscopy was performed.

^{1}H NMR (400.13 MHz, MeCN-d_3): δ [ppm] = 7.93, 7.73, 7.67, 7.60, 7.50, 7.47, 6.67, 6.03, 5.71, 5.67, 5.24, 5.20, 2.89, 2.77, 0.28, 0.02, -0.67.

Synthesis of 1D chains of $[Ag_8L^{Me}_2]_2[NDI\text{-}NHCO](OTf)_4$

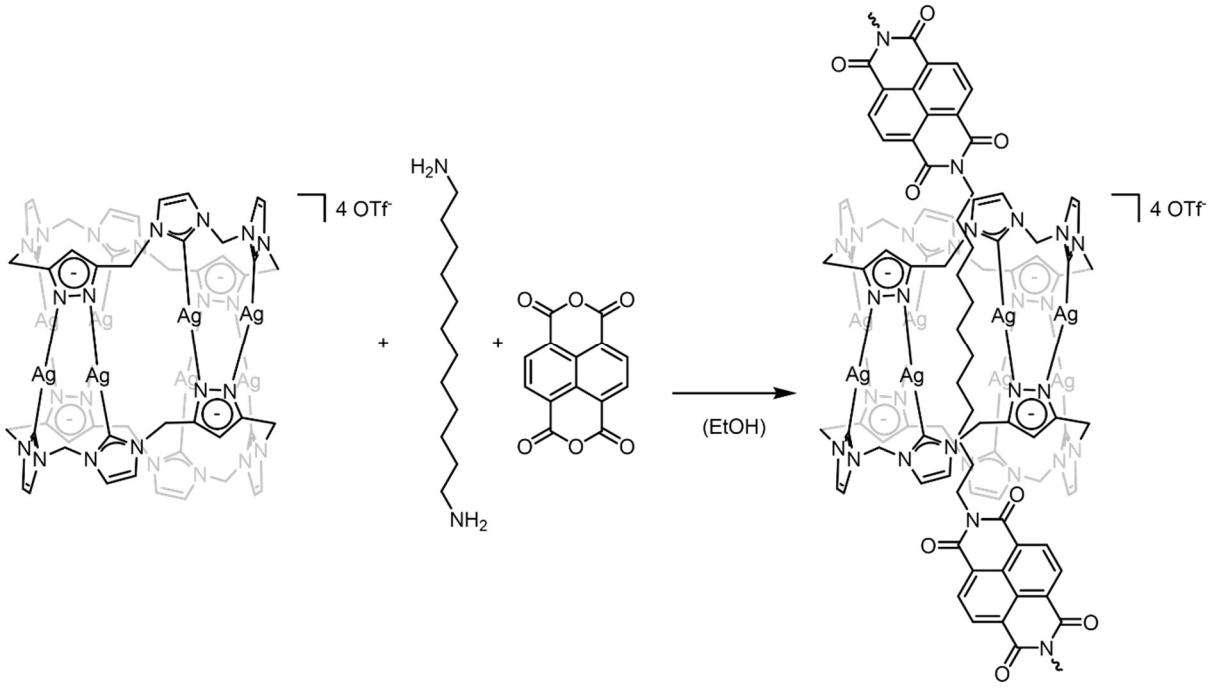

$[Ag_8L^{Me}_2](OTf)_4$ (1 eq.) and 1,12-diamino dodecane (1.1 eq.) were provided in a EtOH:toluene (1:1) mixture and stirred at rt for 20 min. 1,4,5,8-naphthalenetetracarboxylic dianhydride (2 eq.) was added and the reaction mixture was stirred at 80°C overnight. Afterwards, the solvent was removed *in vacuo* a dark red solid was obtained, of which a ^{1}H NMR spectrum was measured. A low solubility in organic solvents (DMF, MeCN, toluene) was observed and no proton signals were obtained in the ^{1}H NMR spectrum.

5.8.6 Synthesis of Supramolecular Arrangements

Synthesis of Trillarplex $[Ag_{12}L^{Me}{}_3][TE](PF_6)_6$

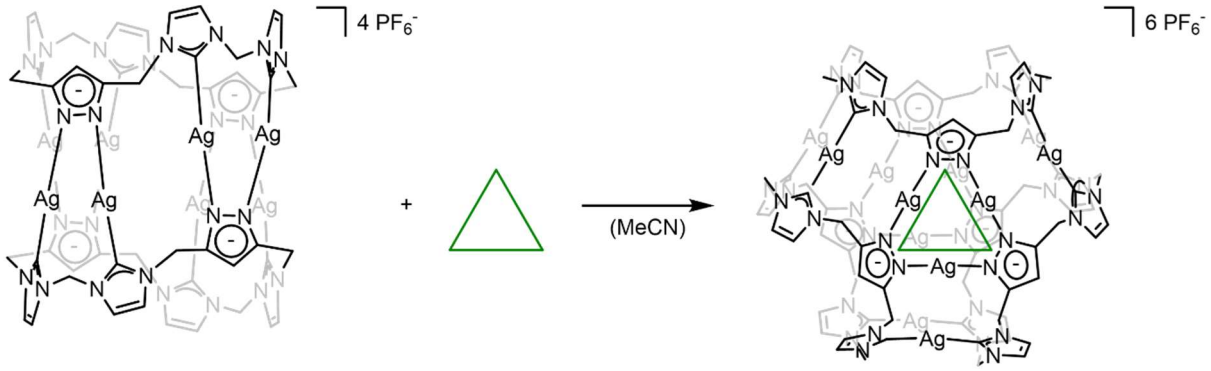

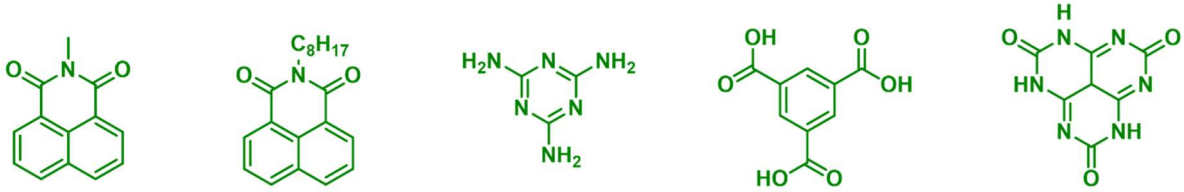

TE1 TE2 TE3 TE4 TE5

$[Ag_8L^{Me}{}_2](PF_6)_4$ (5.00 mg, 2.08 µmol, 1 eq.) and TE2 (644.64 µg, 2.08 µmol, 1 eq.) were dissolved in MeCN (1.5 mL) and transferred into an NMR tube. This NMR tube was placed in a Schlenk-flask filled with Et_2O. The Schlenk-flask was sealed and kept at rt for 7 days. Yellow precipitate including single crystals were collected from the bottom of the NMR tube. The yellow precipitate was dried *in vacuo* and the single crystals were measured using X-Ray diffraction. Using TE1 in a similar synthetic route yielded yellow single crystals with identical cell parameters.

Yield: yellow powder.

^{1}H NMR (400.13 MHz, MeCN-d_3): δ [ppm] = 8.65 (d, ^2J = 7.2 Hz, 0.66H, H_{NMI}), 8.44 (d, ^2J = 8.1 Hz, 0.66H, H_{NMI}), 7.92 (t, ^3J = 15.3, 7.9 Hz , 0.66H, H_{NMI}), 7.55 (s, 12H, H_{NCHC}), 7.52 (s, 12H, H_{NCHC}), 6.72 (s, 6H, H_{CCHC}), 6.62 (d, ^2J = 14.8 Hz, 6H, H_{CH2}), 6.02 (d, ^2J = 14.8 Hz, 6H, H_{CH2}), 5.60 (d, ^2J = 15.1 Hz, 12H, H_{CH2}), 5.26 (d, ^2J = 15.2 Hz, 12H, H_{CH2}), 1.84 (s, 3H), 1.80 – 1.74 (m, 3H), 0.98 (t, J = 7.6 Hz, 6H), 0.88 (s, 2H), 0.67 (s, 2H), 0.57 (s, 2H), 0.15 (s, 3H), -0.20 (s, 2H).

^{13}C NMR (125.83 MHz, MeCN-d_3): δ [ppm] = 267.07, 241.57, 240.37, 220.94, 182.31, 166.45, 147.17, 146.81, 140.32, 127.20.

^{31}P NMR (161.97 MHz, MeCN-d_3): δ [ppm] = -144.59 (q).

SC-XRD (MoK$_\alpha$, λ = 0.71073 Å): yellow cube, monoclinic P 2_1 / m, a = 20.710(2) Å, b = 14.3430(16) Å, c = 22.738(2) Å, α = 90 °, β = 96.735(3) °, γ = 90 °, R = 6.68% (CalTo7).

Reaction conditions for the selective synthesis of $[Ag_{12}L^{Me}_3](PF_6)_6$:

No.	SM	eq. (SM)	MP	eq. (MP)	TE	eq. (TE)	Solvent	Ratio	A	eq. (A)	T [°C]	t [h]
1.1	L-PF_6	3	Ag_2O	13	TE1	1	MeCN	-	-	-	rt	24
1.2	L-PF_6	3	Ag_2O	13	TE1	1	MeCN	-	-	-	80	24
1.3	L-PF_6	3	Ag_2O	13	TE2	1	MeCN	-	-	-	rt	24
1.4	L-PF_6	3	Ag_2O	13	TE2	1	MeCN	-	-	-	80	24
1.5	L-PF_6	3	Ag_2O	13	TE2	1	MeCN:Et_2O	1:100	-	-	rt	-
1.6	L-PF_6	3	Ag_2O	24	TE3	0.55	MeCN	-	-	-	rt	16
1.7	L-PF_6	3	Ag_2O	1	TE3	0.55	MeCN:Et_2O	1:100	-	-	rt	-
1.8	L-PF_6	3	Ag_2O	24	TE4	0.55	MeCN	-	-	-	rt	16
1.7	L-PF_6	3	Ag_2O	1	TE4	0.55	MeCN:Et_2O	1:100	-	-	rt	-
2.1	L-PF_6	1	Ag-PF_6	1	TE1	10	MeCN:Et_2O	1:1	-	-	rt	24
2.2	L-PF_6	1	Ag-PF_6	1	TE1	10	MeCN:Et_2O	1:1	UV-light	-	rt	24
2.3	L-PF_6	1	Ag-PF_6	1	TE1	10	MeCN:Et_2O	1:1	H_2O	0.1	rt	24
2.4	L-PF_6	1	Ag-PF_6	1	TE1	10	MeCN:Et_2O	1:1	TfOH	0.1	rt	24
3.1	Ag-PF_6	1	-	-	TE1	0.7	MeCN	-	-	-	rt	24
3.2	Ag-PF_6	1	-	-	TE1	0.7	MeCN	-	-	-	80	24
3.3	Ag-PF_6	1	-	-	TE1	0.7	MeCN:Et_2O	1:1000	-	-	rt	24
3.4	Ag-PF_6	1	-	-	TE1	0.7	MeCN:Et_2O	1:1000	-	-	80	24
3.5	Ag-PF_6	1	-	-	TE1	1	MeCN	-	-	-	rt	24
3.6	Ag-PF_6	1	-	-	TE1	1	MeCN:Et_2O	1:100	-	-	rt	-
3.7	Ag-PF_6	1	-	-	TE1	1.6	MeCN:Et_2O	1:100	-	-	rt	-
3.8	Ag-PF_6	1	-	-	TE1	1.6	MeCN:Et_2O	1:100	-	-	rt	-
3.9	Ag-PF_6	1	-	-	TE1	10	MeCN	-	-	-	rt	24
3.10	Ag-PF_6	1	-	-	TE1	10	MeCN	-	-	-	40	24
3.11	Ag-PF_6	1	-	-	TE1	10	MeCN	-	-	-	80	24
3.12	Ag-PF_6	1	-	-	TE1	10	MeCN:Et_2O	1:1000	-	-	rt	24
3.13	Ag-PF_6	1	-	-	TE1	10	MeCN:Et_2O	1:1000	-	-	80	24
3.14	Ag-PF_6	1	-	-	TE2	1	MeCN	-	-	-	rt	24
3.15	Ag-PF_6	1	-	-	TE2	1	MeCN	-	-	-	80	24
3.16	Ag-PF_6	1	-	-	TE2	1	MeCN:Et_2O	100:1	-	-	rt	24
3.17	Ag-PF_6	1	-	-	TE2	10	MeCN	-	-	-	rt	24
3.18	Ag-PF_6	1	-	-	TE2	10	MeCN	-	-	-	80	24
3.19	Ag-PF_6	1	-	-	TE2	10	MeCN:Et_2O	100:1	-	-	rt	24
3.20	Ag-PF_6	1	-	-	TE2	1	MeCN:Et_2O	1:100	-	-	rt	-
3.21	Ag-PF_6	3	-	-	TE3	0.55	MeCN	-	-	-	rt	16
3.22	Ag-PF_6	3	-	-	TE3	0.55	MeCN:Et_2O	1:100	-	-	rt	-
3.23	Ag-PF_6	3	-	-	TE4	0.55	MeCN	-	-	-	rt	16
3.24	Ag-PF_6	3	-	-	TE4	0.55	MeCN:Et_2O	1:100	-	-	rt	-
3.25	Ag-PF_6	1	-	-	TE5	0.7	MeCN	-	-	-	rt	72
3.26	Ag-PF_6	1	-	-	TE5	0.7	DMF	-	-	-	rt	72

Synthesis of S-shaped complex $[Ag_6(HL^{Me})_2](PF_6)_4 \cdot TE1$

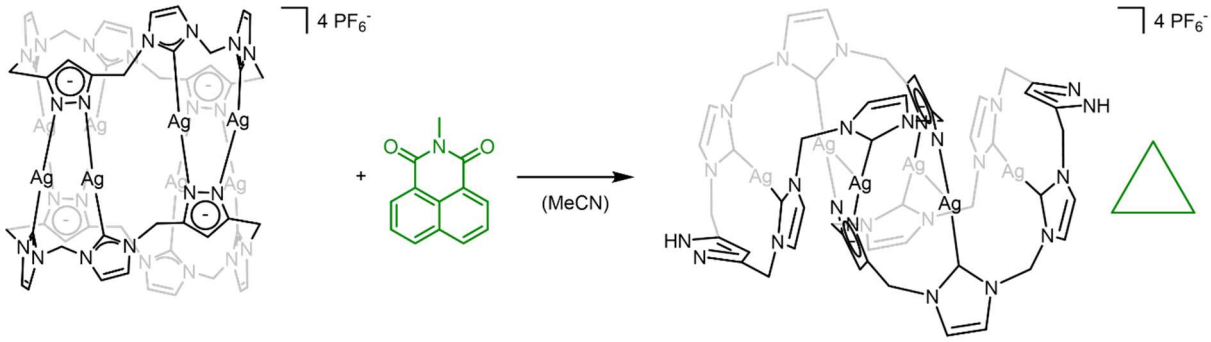

$[Ag_8L^{Me}_2](PF_6)_4$ (10.00 mg, 4.17 µmol, 1 eq.) and TE1 (880.14 µg, 4.17 µmol, 1 eq.) were dissolved in MeCN (1.5 mL) and transferred into an NMR tube. This NMR tube was placed in a Schlenk-flask filled with Et_2O. The Schlenk-flask was sealed and kept at rt for several days. White precipitate including single crystals was collected from the bottom of the NMR tube. The single crystals were measured using X-Ray diffraction.

SC-XRD (MoK_α, λ = 0.71073 Å): colourless rectangle, orthorhombic *C m a a*, a = 23.9846(19) Å, b = 29.650(2) Å, c = 14.7846(12) Å, α = 90 °, β = 90 °, γ = 90 °, R = 5.79% (HeiAl49).

Reaction conditions for the selective synthesis of $[Ag_6(HL^{Me})_2](PF_6)_4$:

No.	SM	eq. (SM)	TE	eq. (A)	Additive	Solvent	Ratio	Volume [mL]	T [°C]	t [h]
1.1	Ag-PF_6	1	TE1	10	-	MeCN	-	3	rt	72
1.2	Ag-PF_6	1	TE1	10	-	MeCN:Et_2O	1:1000	3	rt	72
1.3	Ag-PF_6	1	TE1	10	-	DMF	-	3	rt	72

5.8.7 Encapsulation Studies of Perfluorinated Guest Molecules

Encapsulation of PFOA

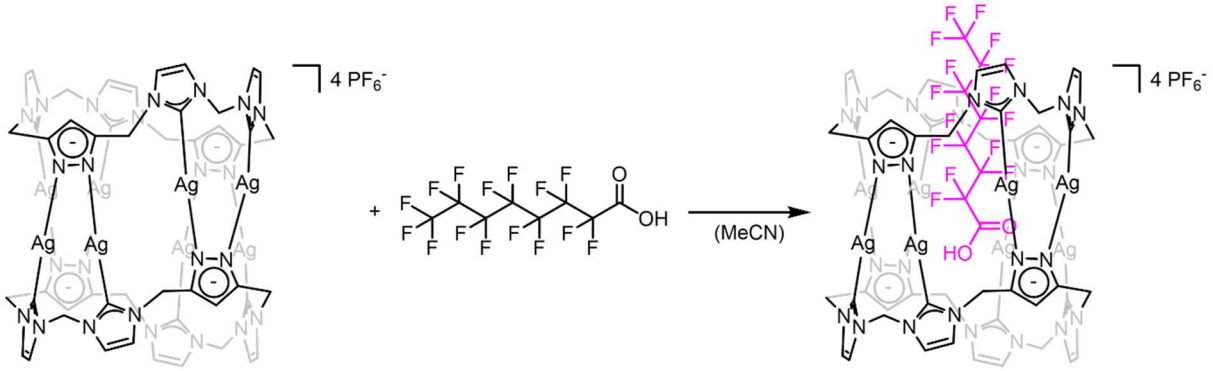

$[Ag_8L^{Me}_2](PF_6)_4$ (5.00 mg, 2.08 µmol, 1 eq.) was provided in MeCN-d_3 and PFOA (0.863 mg, 2.08 µmol, 1 eq.) was provided as stem solution (5 mg mL^{-1}). The reaction mixture was stirred at rt for 10 min and transferred into an NMR tube. The encapsulation of the PFOA guest was tracked by ^{1}H and ^{19}F NMR spectroscopy.

Analytics for PFOA:

^{1}H NMR (400.13 MHz, MeCN-d_3): δ [ppm] = 3.13 (s, 1H, H_{OH}).

^{19}F NMR (376.46 MHz, MeCN-d_3): δ [ppm] = -81.54, -119.79, -122.13, -122.48, -123.17, -123.45, -126.59.

Analytics after encapsulation studies:

^{1}H NMR (400.13 MHz, MeCN-d_3): δ [ppm] = 7.59 (d, ^{2}J = 1.9 Hz, 8H, H_{NCHC}), 7.50 (d, ^{2}J = 1.9 Hz, 8H, H_{NCHC}), 6.67 (s, 4H, H_{CCHC}), 6.62 (d, ^{2}J = 14.8 Hz, 4H, H_{CH2}), 6.04 (d, ^{2}J = 14.9 Hz, 4H, H_{CH2}), 5.68 (d, ^{2}J = 15.0 Hz, 8H, H_{CH2}), 5.22 (d, ^{2}J = 15.1 Hz, 8H, H_{CH2}).

^{19}F NMR (376.46 MHz, MeCN-d_3): δ [ppm] = -71.89 (F_{PF6}), -73.76 (F_{PF6}), -79.31, -81.54 (F_{COCF2}), -116.30, -122.06, -122.52, -122.73, -123.18, -126.60.

Encapsulation of GenX

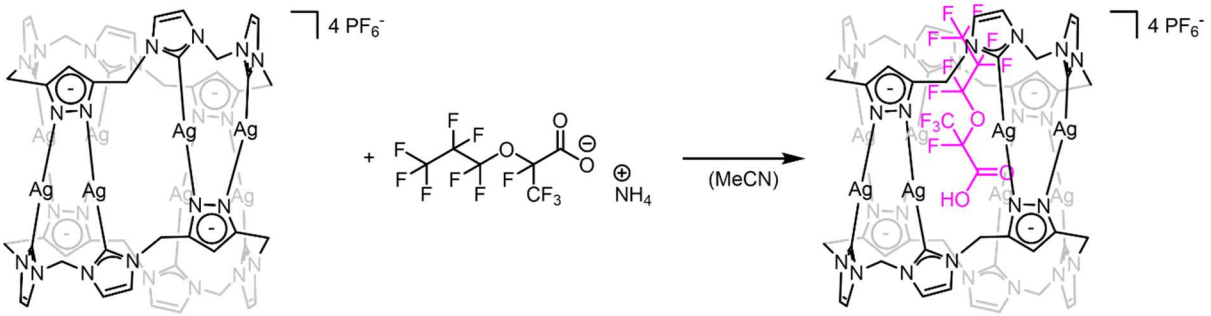

$[Ag_8L^{Me}_2](PF_6)_4$ (5.00 mg, 2.08 µmol, 1 eq.) was provided in MeCN-d_3 and PFOA (0.863 mg, 2.08 µmol, 1 eq.) was provided as stem solution (5 mg mL^{-1}). The reaction mixture was stirred at rt for 10 min and transferred into an NMR tube. The encapsulation of the PFOA guest was tracked by ^{1}H and ^{19}F NMR spectroscopy.

Analytics for GenX:

^{19}F NMR (376.46 MHz, MeCN-d_3): δ [ppm] = -80.29, -80.66 (d, ^{2}J = 8.3 Hz), -81.03, -82.08 (t, ^{2}J = 7.2 Hz), -83.09, -83.21 (d, ^{2}J = 2.8 Hz), -86.71 (t, ^{3}J = 7.3 Hz), -87.11 (t, ^{2}J = 7.0 Hz), -130.38 (d, ^{2}J = 3.1 Hz), -132.35 (d, ^{2}J = 19.8 Hz).

Analytics after encapsulation studies:

^{1}H NMR (400.13 MHz, MeCN-d_3): δ [ppm] = 7.58 (d, ^{2}J = 2.0 Hz, 8H, H_{NCHC}), 7.50 (d, ^{2}J = 1.9 Hz, 8H, H_{NCHC}), 6.67 (s, 4H, H_{CCHC}), 6.62 (d, ^{2}J = 14.7 Hz, 4H, H_{CH2}), 6.04 (d, ^{2}J = 14.9 Hz, 4H, H_{CH2}), 5.66 (d, ^{2}J = 15.1 Hz, 4H, H_{CH2}), 5.23 (d, ^{2}J = 15.1 Hz, 4H, H_{CH2}).

^{19}F NMR (376.46 MHz, MeCN-d_3): δ [ppm] = -71.87 (F_{PF6}), -73.75 (F_{PF6}), -79.29, -82.04 (t, ^{3}J = 6.7 Hz), -82.17 (t, ^{2}J = 7.4 Hz), -82.65 (d, ^{2}J = 2.8 Hz), -84.80 (d, ^{2}J = 5.5 Hz), -85.20, -124.69, -130.43, -130.52.

5.9 References for Chapter 5

1 P. Kuzmič, *Anal. Biochem.,* **1996**, *237*, 260.
2 **http://supramolecular.org/**, 07.06.2023.
3 P. Thordarson, *Chem. Soc. Rev.,* **2011**, *40*, 1305.
4 J. D. Evans, V. Bon, I. Senkovska, S. Kaskel, *Langmuir,* **2021**, *37*, 4222.
5 **https://clownfish-app-lzoex.ondigitalocean.app/**, 07.07.2023.
6 M. Thommes, K. Kaneko, A. V. Neimark, J. P. Olivier, F. Rodriguez-Reinoso, J. Rouquerol, K. S. W. Sing, *Pure Appl. Chem.,* **2015**, *87*, 1051.
7 J. Rouquerol, P. Llewellyn, F. Rouquerol, *Studies in Surface Science and Catalysis,* **2007**, *160*, 49.
8 *APEX suite of crystallographic software: APEX 3/4, Version 2015-5.2, Version 2021-10-0*, Bruker AXS Inc., Madison, Wisconsin, USA **2015, 2021**.
9 *SAINT: Version 8.40A and SADABS, Version 2016/2*, Bruker AXS Inc., Madison, Wisconsin, USA, **2016**.
10 G. Sheldrick, *Acta Cryst. A,* **2015**, *71*, 3.
11 C. B. Hubschle, G. M. Sheldrick, B. Dittrich, *J. Appl. Crystallogr.,* **2011**, *44*, 1281.
12 G. Sheldrick, *Acta Cryst. C,* **2015**, *71*, 3.
13 A. J. C. Wilson: *International Tables for Crystallography*, Vol. C (Ed.: A. J. Wilson), Kluwer Academic Publishers, Dordrecht, The Netherlands, 1992, Tables 6.1.1.4 (pp. 500–502), 4.2.6.8 (pp. 219–222), and 4.2.4.2 (pp. 193–199), **1993**.
14 A. Spek, *Acta Cryst. C,* **2015**, *71*, 9.
15 C. F. Macrae, I. J. Bruno, J. A. Chisholm, P. R. Edgington, P. McCabe, E. Pidcock, L. Rodriguez-Monge, R. Taylor, J. van de Streek, P. A. Wood, *J. Appl. Crystallogr.,* **2008**, *41*, 466.
16 A. Spek, *Acta Cryst. D,* **2009**, *65*, 148.
17 F. Neese, *Wiley Interdiscip. Rev. Comput. Mol.,* **2012**, *2*, 73.
18 F. Neese, *Wiley Interdiscip. Rev. Comput. Mol.,* **2022**, *12*, e1606.
19 F. Neese, *Wiley Interdiscip. Rev. Comput. Mol.,* **2018**, *8*, e1327.
20 N. Mardirossian, M. Head-Gordon, *Phys. Chem. Chem. Phys.,* **2014**, *16*, 9904.
21 J. P. Perdew, K. Burke, M. Ernzerhof, *Phys. Rev. Lett.,* **1996**, *77*, 3865.
22 S. Grimme, S. Ehrlich, L. Goerigk, *J. Comput. Chem.,* **2011**, *32*, 1456.
23 S. Grimme, *J. Comput. Chem.,* **2006**, *27*, 1787.
24 A. Schäfer, H. Horn, R. Ahlrichs, *J. Chem. Phys.,* **1992**, *97*, 2571.
25 A. Schäfer, C. Huber, R. Ahlrichs, *J. Chem. Phys.,* **1994**, *100*, 5829.
26 M. D. Hanwell, D. E. Curtis, D. C. Lonie, T. Vandermeersch, E. Zurek, G. R. Hutchison, *J. Cheminformatics,* **2012**, *4*, 17.
27 O. Tsutsumi, M. Tamaru, H. Nakasato, S. Shimai, S. Panthai, Y. Kuroda, K. Yamaguchi, K. Fujisawa, K. Hisano, *Mol.,* **2019**, *24*, 4606.
28 P. J. Altmann, C. Jandl, A. Pöthig, *Dalton Trans.,* **2015**, *44*, 11278.
29 P. J. Altmann, A. Pöthig, *J. Am. Chem. Soc.,* **2016**, *138*, 13171.
30 T. Calmus, **2021**, Masterthesis: *Experimental and Theoretical Evaluation of host-guest interactions of pillarplex cavitands*, Technical University of Munich (Munich).
31 M. Aust, A. J. Herold, L. Niederegger, C. Schneider, D. C. Mayer, M. Drees, J. Warnan, A. Pöthig, R. A. Fischer, *Inorg. Chem.,* **2021**, *60*, 19242.
32 H.-Y. Gong, B. M. Rambo, E. Karnas, V. M. Lynch, K. M. Keller, J. L. Sessler, *J. Am. Chem. Soc.,* **2011**, *133*, 1526.
33 C.-P. Li, J. Chen, M. Du, *Cryst. Eng. Comm.,* **2010**, *12*, 4392.
34 J. Huo, M. Brightwell, S. El Hankari, A. Garai, D. Bradshaw, *J. Mater. Chem. A,* **2013**, *1*, 15220.
35 J. G. M. de Carvalho, R. A. Fischer, A. Pöthig, *Inorg. Chem.,* **2021**, *60*, 4676.
36 X.-Q. Liu, K. Zhang, J.-F. Gao, Y.-Z. Chen, C.-H. Tung, L.-Z. Wu, *Angew. Chem. Int. Ed.,* **2020**, *59*, 23456.

37 V. Tumiatti, A. Milelli, A. Minarini, M. Micco, A. Gasperi Campani, L. Roncuzzi, D. Baiocchi, J. Marinello, G. Capranico, M. Zini, C. Stefanelli, C. Melchiorre, *J. Med. Chem.,* **2009**, *52*, 7873.
38 S. Guan, T. Pickl, C. Jandl, L. Schuchmann, X. Zhou, P. J. Altmann, A. Pöthig, *Org. Chem. Front.,* **2021**, *8*, 4061.
39 A. S. Novikov, *Cryst.,* **2021**, *11*, 162.
40 A. Bondi, *J. Phys. Chem.,* **1964**, *68*, 441.
41 **ConQuest2022.3.0**, CCDC, **2023**. PF_6^- 4047 hits, Dist1 = 1.576(2) Å; OAc^- 704 hits, Dist1 = 2.208(3) Å; I_3^- 1470 hits, Dist1 = 2.956(37) and Dist2 = 2.958(19) Å; SCN^- 896 hits, Dist1 = 1.638(3) Å and Dist2 = 1.149(3) Å; NO_3^- 1788 hits, Dist1 = 1.242(3) Å; ClO_4^- 5076 hits, Dist1 = 1.412(3) Å; BF_4^- 2824 hits, Dist1 = 1.367(2) Å; SO_4^{2-} 1843 hits, Dist1 = 1.469(1) Å; ox^{2-} 502 hits, Dist1 = 3.039(148) Å and Dist2 = 2.222(3) Å; sq^{2-} 159 hits, Dist1 = 3.237(2) Å and Dist2 = 3.226(3) Å; bq^{2-} 194 hits, Dist1 = 4.700(1) Å and Dist2 = 2.656(1) Å; -COOH 3340 hits, Dist1 = 2.222(1) Å; PFOA 1 hit, Dist1 = 1.234(0) Å, Dist2 = 1.317(0) Å, Dist3 = 0.840(0) Å and Dist4 = 1.341(1) Å; 24.09.2023.

6. Appendix

6.1 Supplementary Information of the Experimental Part

Adsorption Studies of $[M_8L^{Me}_2](PF_6)_4$ and $[M_8L^{Me}_2](OAc)_4$:

T1S: Table of crystal data, data collection and structure refinement of $[Ag_8L^{Me}_2](PF_6)_4$, $[Au_8L^{Me}_2](PF_6)_4$, $Ag_8L^{Me}_2](OAc)_4$, $[Au_8L^{Me}_2](OAc)_4$:

Identification code		HeiAl11-TXS	HeiAl28	HeiAl18	HeiAl05
Chemical formula		$C_{48}H_{44}N_{24}Ag_8P_4F_{24}$ + 6.126 C_2H_3N	$C_{24}H_{22}N_{12}Au_4P_2F_{12}$	$C_{152}H_{144}Ag_{24}N_{72}O_{8+8}C_2H_3O_2$	$C_{48}H_{44}Au_8N_{24}$ + 3.847 $C_2H_3O_2$
Formula weight	[g mol^{-1}]	1767.62	1556.33	6168.61	8279.26
Temperature	[K]	100(2)	100(2)	100(2)	100(2)
Wavelength	[Å]	0.71073	0.71073	0.71073	0.71073
Crystal system		orthorhombic	triclinic	monoclinic	trigonal
Space group		*P b c n*	*P* 1	*P* 1 2_1/*c* 1	*R* -3 *c*
Unit cell dimensions		a = 16.7300(9) Å, α = 90°	a = 15.0306(12) Å, α = 117.469(2)°	a = 29.41(3) Å, α = 90°	a = 77.212(9) Å, α = 90°
		b = 22.9008(12) Å, β = 90°	b = 15.0397(12) Å, β = 117.486(2)°	b = 32.88(3) Å, β = 115.620(19)°	b = 77.212(9) Å, β = 90°
		c = 53.335(3) Å, γ = 90°	c = 16.2780(13) Å, γ = 90.070(3)°	c = 31.13(3) Å, γ = 90°	c = 24.674(4) Å, γ = 120°
Volume	[Å^3]	20434.3(19)	2787.1(4)	27140.0(40)	127391(36)
Z		12	2	4	18
Calc. Density	[g cm^{-3}]	1.724	1.854	1.510	1.943
Absorption coefficient	[mm^{-1}]	1.655	10.617	1.746	12.437
F(000)		10294	1408	12000	67567
Diffractometer		TXS rotating anode	TXS rotating anode	TXS rotating anode	TXS rotating anode
Radiation source		Mo K_α	Mo K_α	Mo K_α	Mo K_α
Theta range for data collection	[°]	2.15 – 26.02	2.53 – 26.47	1.77 – 25.35	2.11 – 26.02
Index ranges		-20<=h<=20, -28<=k<=28, -65<=l<=65	-18<=h<=18, -18<=k<=18, -30<=l<=30	-35<=h<=35, -39<=k<=39, -36<=l<=36	-95<=h<=91, -95<=k<=94, -27<=l<=30
Reflections collected		434230	11444	431160	250032
Independent reflections		20123 [R_{int} = 0.0674]	6405 [R_{int} = 0.0796]	49345 [R_{int} = 0.0363]	27904 [R_{int} = 0.1107]
Coverage of independent reflections	[%]	99.9	99.9	99.4	99.9
Absorption correction		Multi-Scan	Multi-Scan	Multi-Scan	Multi-Scan
Max., min. transmission		0.5520, 0.7680	0.6073, 0.7454	0.6487, 0.7454	0.4559, 0.7454
Structure solution		direct methods	direct methods	direct methods	direct methods

Refinement method		Full-matrix least-squares on F^2	Full-matrix least-squares on F^2	Full-matrix least-squares on F^2	Full-matrix least-squares on F^2
Refinement program		SHELXL (Sheldrick 2018), ShelXle (Huebschle 2011)	SHELXL (Sheldrick 2018), ShelXle (Huebschle 2011)	SHELXL (Sheldrick 2018), ShelXle (Huebschle 2011)	SHELXL (Sheldrick 2018), ShelXle (Huebschle 2011)
Function minimised		$\sum w(F_o^2 - F_c^2)^2$	$\sum w(F_o^2 - F_c^2)^2$	$\sum w(F_o^2 - F_c^2)^2$	$\sum w(F_o^2 - F_c^2)^2$
Data / restraints / parameters		20123 / 666 / 1255	11444 / 5475 / 1427	49345 / 1614 / 1526	27904 / 633 / 1302
Goodness-of-Fit on F^2		1.175	1.366	1.074	1.013
Δ/σ_{max}		0.002	0.288	0.062	1.511
Final R indices	I > 2σ(I)	16448 data, R1 = 0.0940, wR2 = 0.2018	6405 data, R1 = 0.0883, wR2 = 0.2120	37031 data, R1 = 0.0990, wR2 = 0.2469	19133 data, R1 = 0.0510, wR2 = 0.1343
	All data	R1 = 0.1116, wR2 = 0.2113	R1 = 0.1575, wR2 = 0.2354	R1 = 0.1255, wR2 = 0.2777	R1 = 0.0883, wR2 = 0.1604
Weighting scheme		W = 1 / [$\sum^2(FO^2)$ + $(0.0364P)^2$ + 540.5414P] where P = (FO^2+2FC^2) / 3	W = 1 / [$\sum^2(FO^2)$ + $(0.1000P)^2$] where P = (FO^2+2FC^2) / 3	W = 1 / [$\sum^2(FO^2)$ + $(0.1151P)^2$ + 368.5500P] where P = (FO^2+2FC^2) / 3	W = 1 / [$\sum^2(FO^2)$ + $(0.1026P)^2$] where P = (FO^2+2FC^2) / 3
Largest diff. peak, hole	[eÅ^{-3}]	2.183, -3.272	1.965, -2.339	4.864, -3.372	3.329, -1.681
R.M.S. deviation from mean	[eÅ^{-3}]	0.197	0.287	0.190	0.235

F1S: ^{1}H NMR spectra of **1** $[Ag_8L^{Me}{}_2](PF_6)_4$ as synthesized (as) and activated (act) in MeCN-d_3 with the residual solvent signal at 1.94 ppm. Solvent impurities are marked with * for diethyl ether (1.18 ppm, 3.49 ppm) and # for water (2.13 ppm), ^{19}F and ^{31}P NMR spectra in MeCN-d_3:

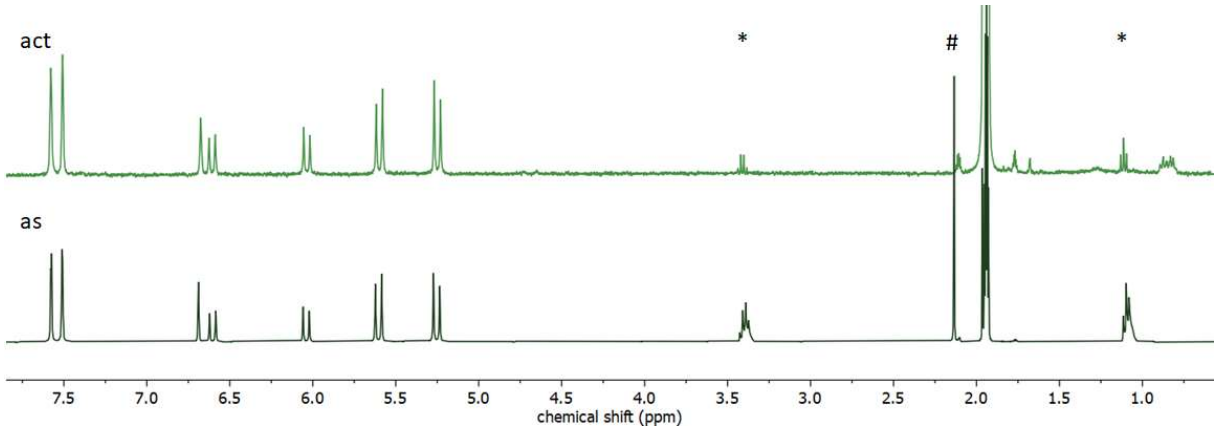

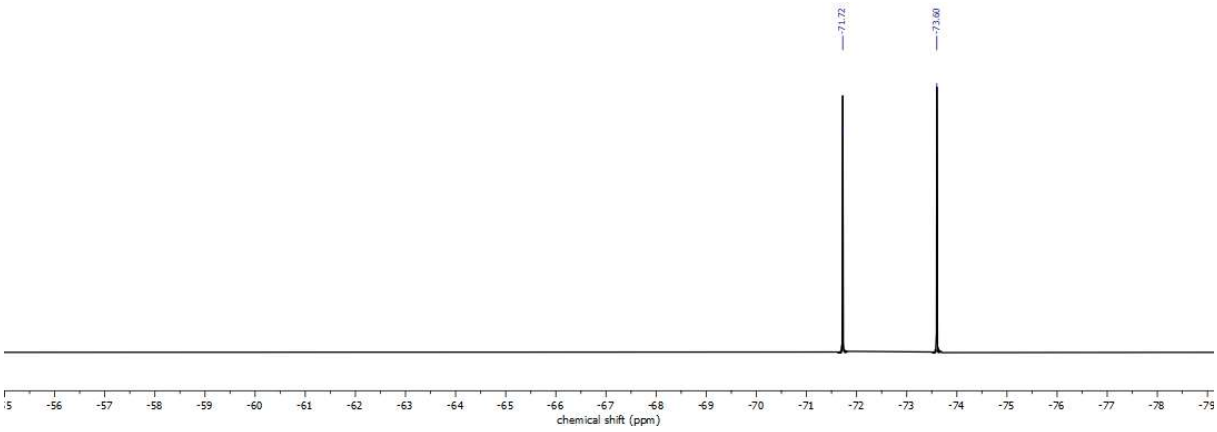

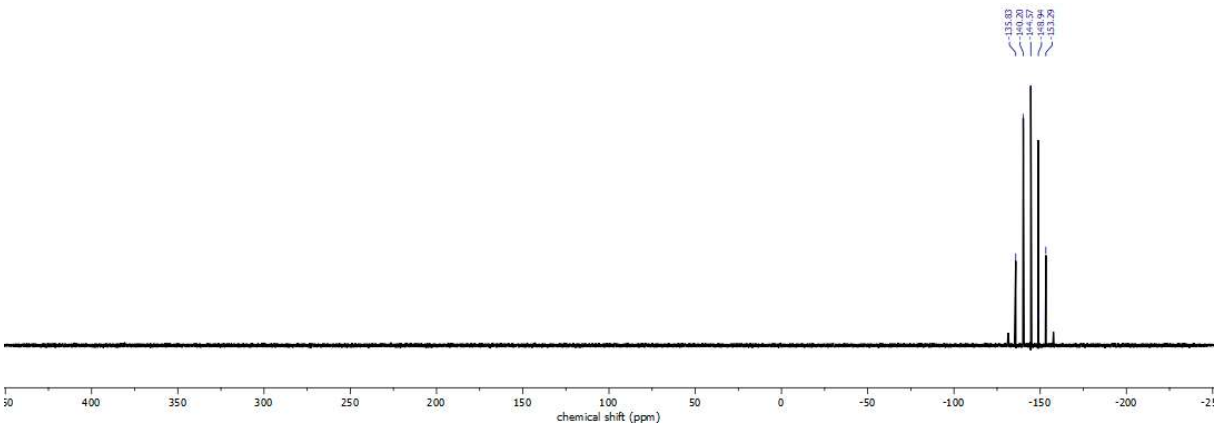

F2S: ^{1}H NMR spectra of **2** $[Au_8L^{Me}_2](PF_6)_4$ as synthesized (as) and activated (act) in MeCN-d_3 with the residual solvent signal at 1.94 ppm. Solvent impurities are marked with * for diethyl ether (1.18 ppm, 3.49 ppm) and # for water (2.13 ppm):

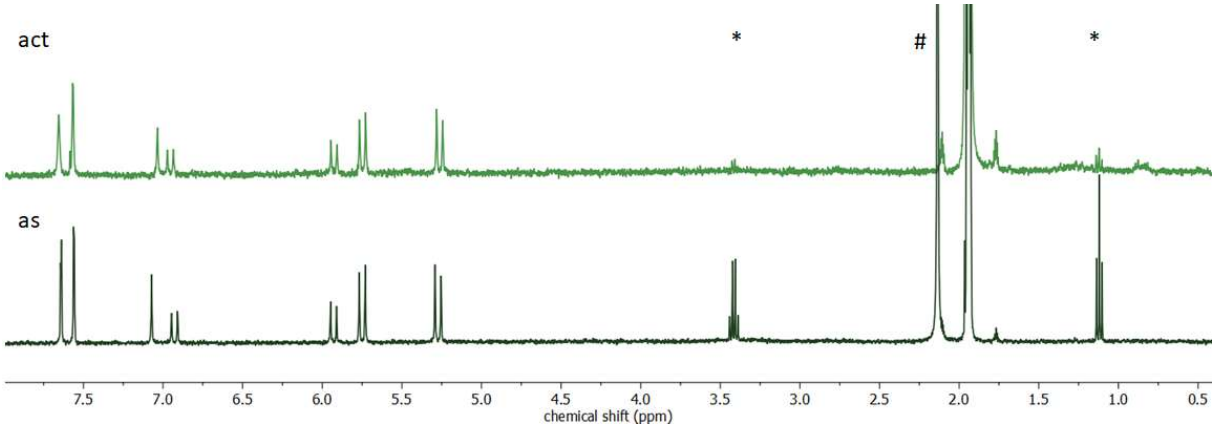

F3S: ^{1}H NMR spectra of **3** $[Ag_8L^{Me}_2](OAc)_4$ as synthesized (as) and activated (act) in D_2O with the residual solvent signal at 4.79 ppm. Solvent impurities are marked with * for acetone (2.22 ppm):

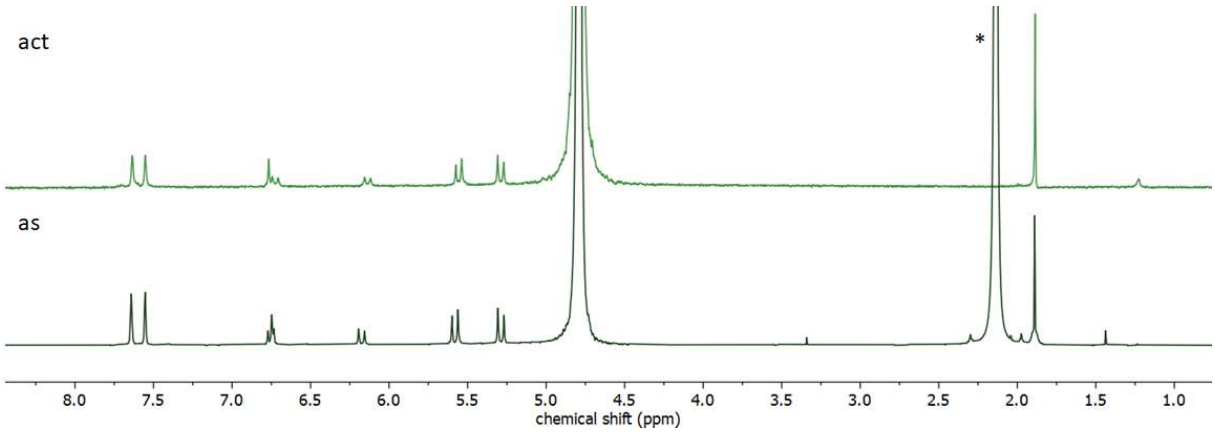

F4S: ^{1}H NMR spectra of **4** $[Au_8L^{Me}_2](OAc)_4$ as synthesized (as) and activated (act) in D_2O with the residual solvent signal at 4.79 ppm:

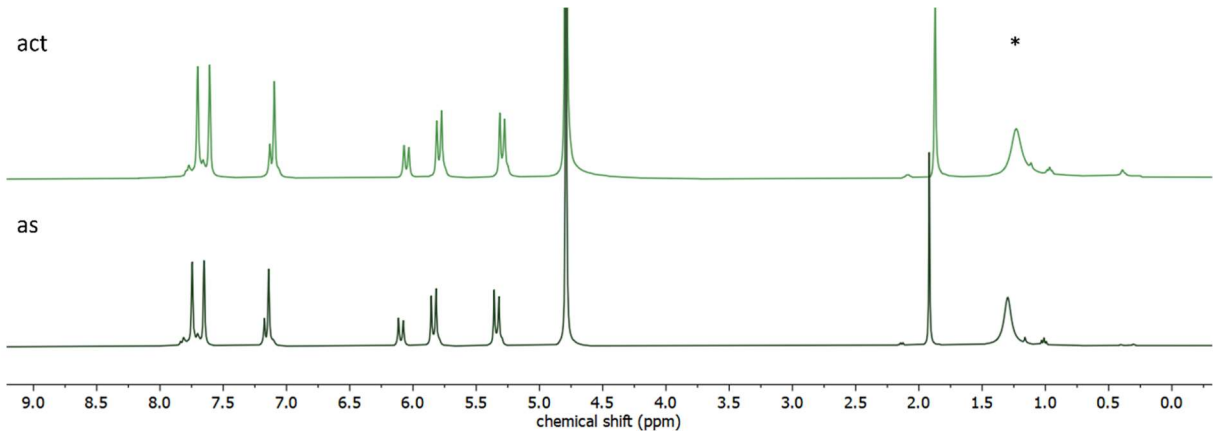

F5S: ^{1}H NMR spectrum of $[Ag_8L^{Me}_2](PF_6)_4$ in solid state:

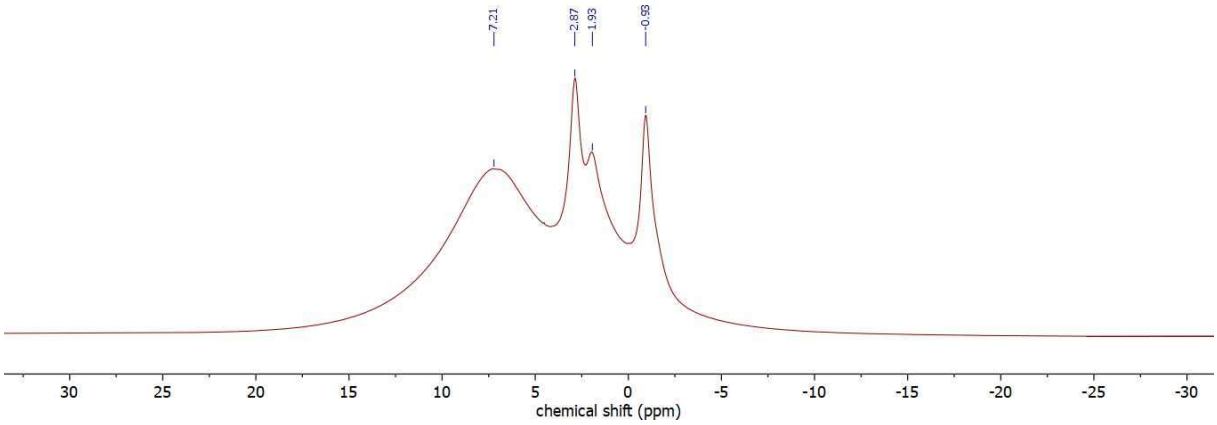

F6S: ^{13}C NMR spectrum of $[Ag_8L^{Me}_2](PF_6)_4$ in solid state:

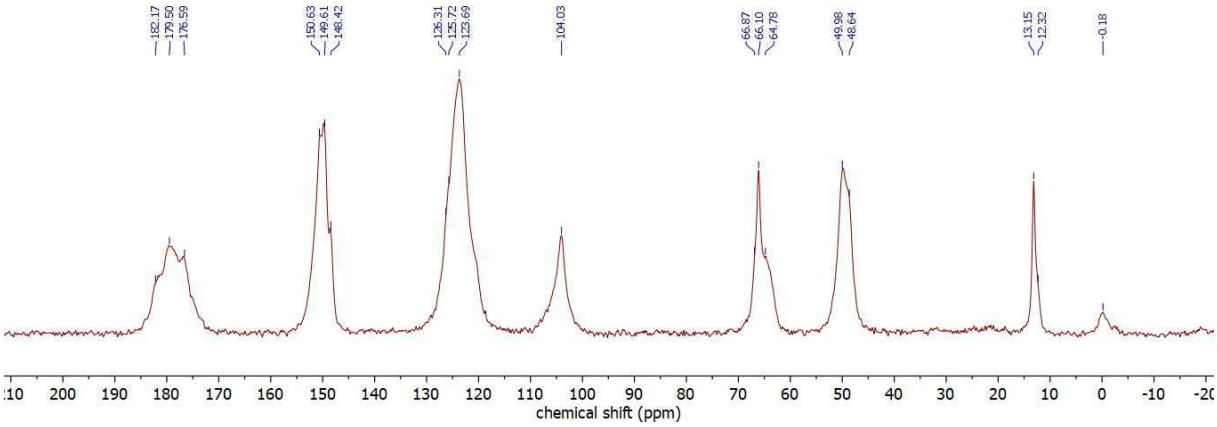

F7S: ^{31}P NMR spectrum of $[Ag_8L^{Me}_2](PF_6)_4$ in solid state:

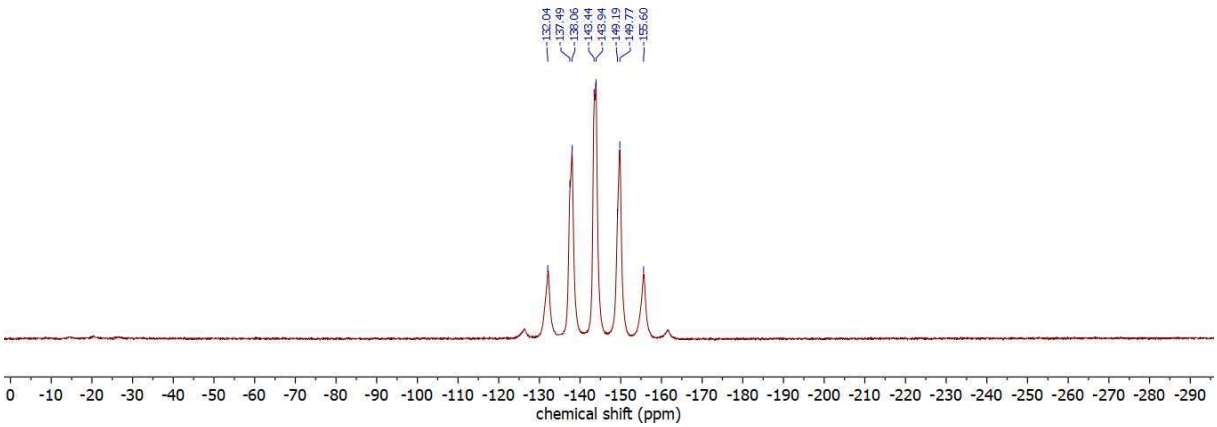

F8S: PXRD pattern of **1** $[Ag_8L^{Me}_2](PF_6)_4$, **2** $[Au_8L^{Me}_2](PF_6)_4$, **3** $[Ag_8L^{Me}_2](OAc)_4$ and **4** $[Au_8L^{Me}_2](OAc)_4$ after the activation by supercritical CO_2:

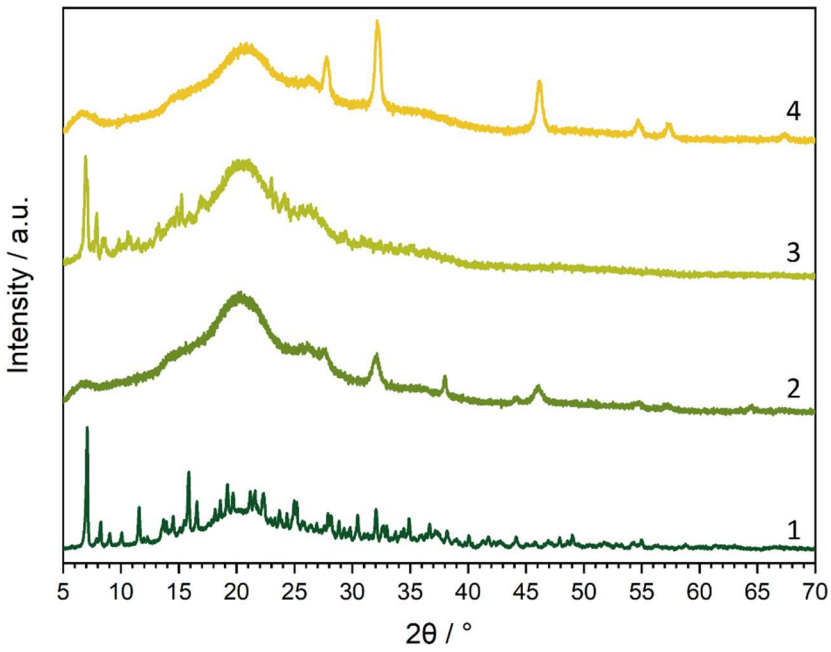

F9S: Comparison of PXRD pattern of **1** $[Ag_8L^{Me}_2](PF_6)_4$, **2** $[Au_8L^{Me}_2](PF_6)_4$, **3** $[Ag_8L^{Me}_2](OAc)_4$ and **4** $[Au_8L^{Me}_2](OAc)_4$; calculated from SC-XRD measurements as synthesized (as) and activated (act):

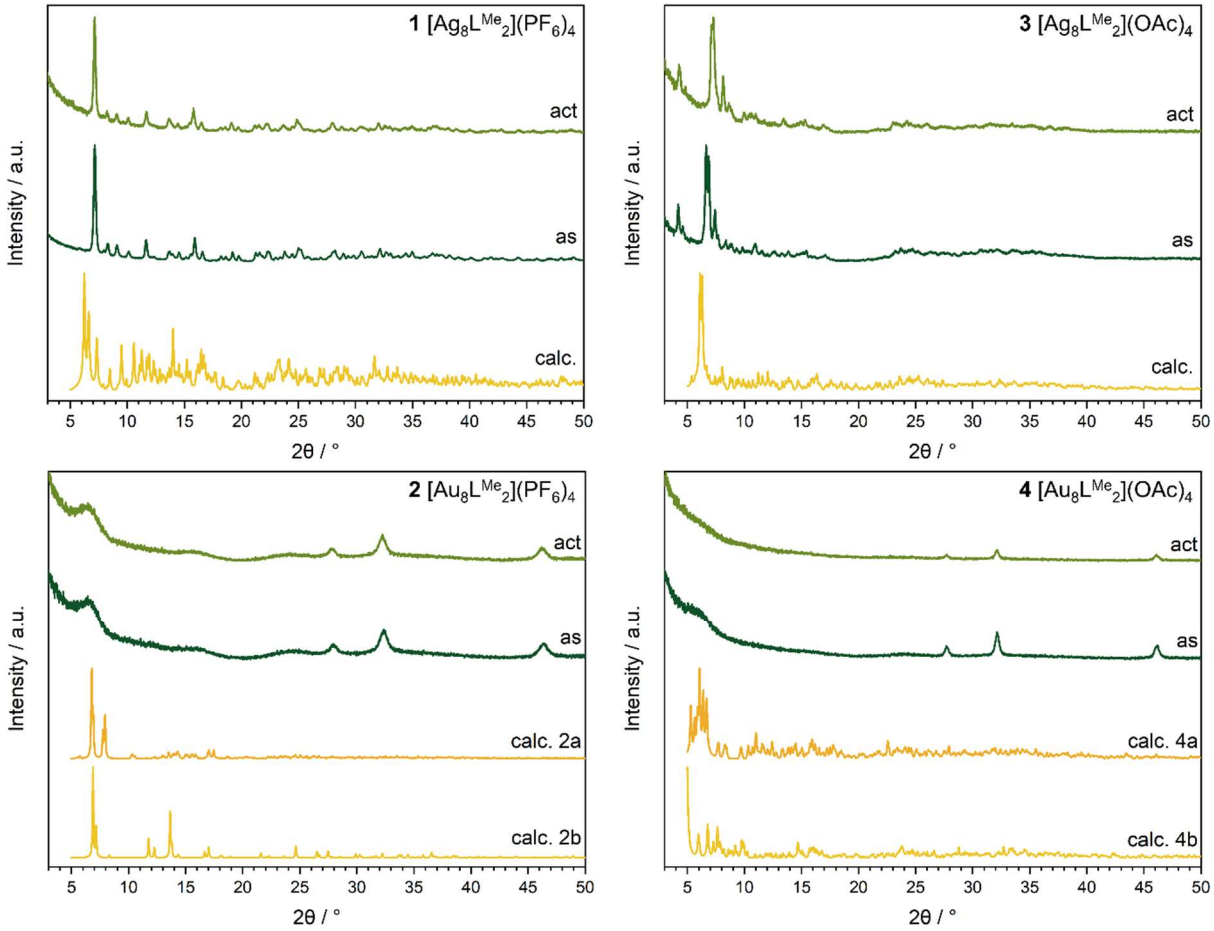

F10S: IR spectra of **1** $[Ag_8L^{Me}_2](PF_6)_4$, **2** $[Au_8L^{Me}_2](PF_6)_4$, **3** $[Ag_8L^{Me}_2](OAc)_4$ and **4** $[Au_8L^{Me}_2](OAc)_4$ as synthesized (as) and activated (act):

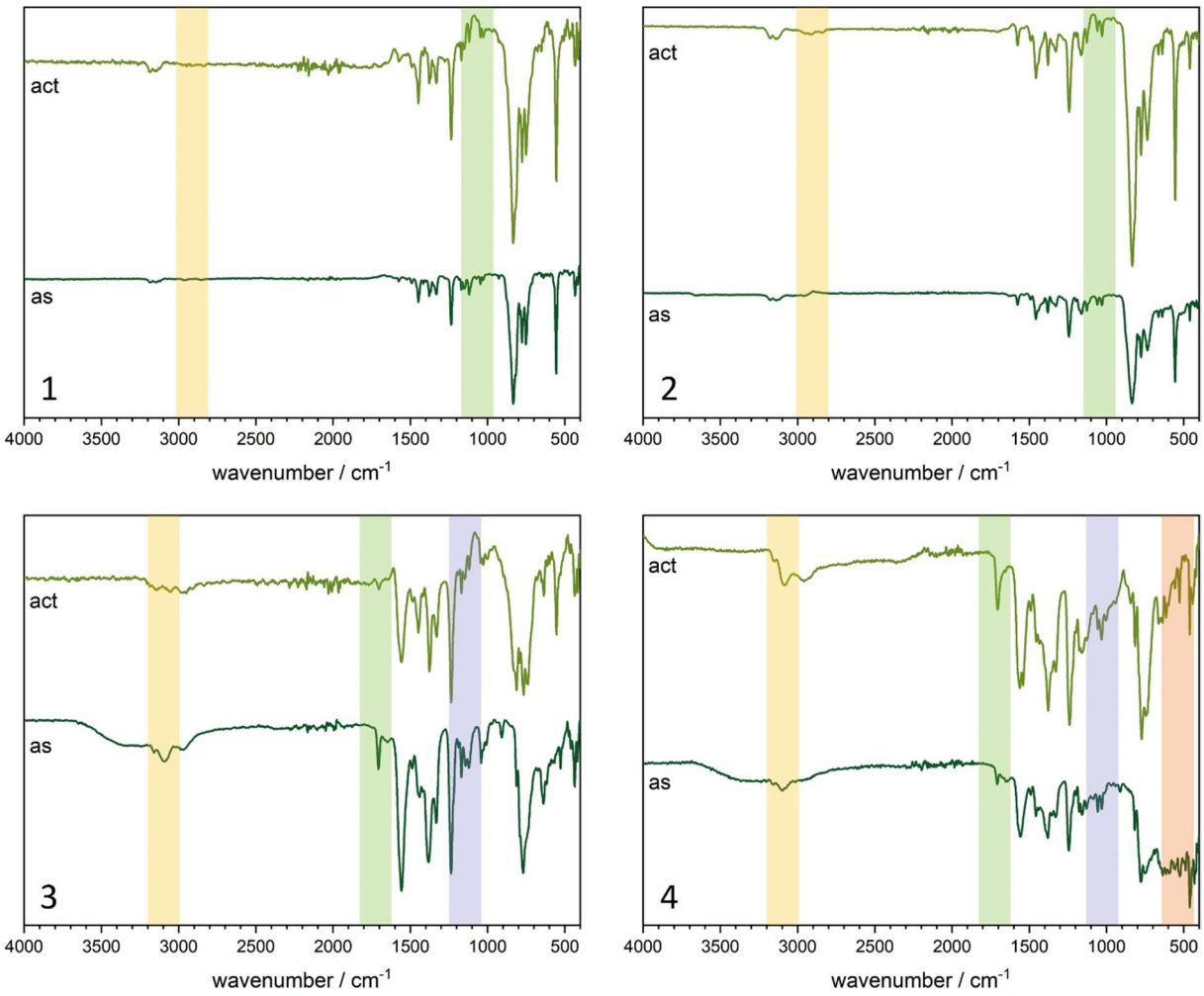

F11S: SEM images of **1** $[Ag_8L^{Me}_2](PF_6)_4$ at various magnifications:

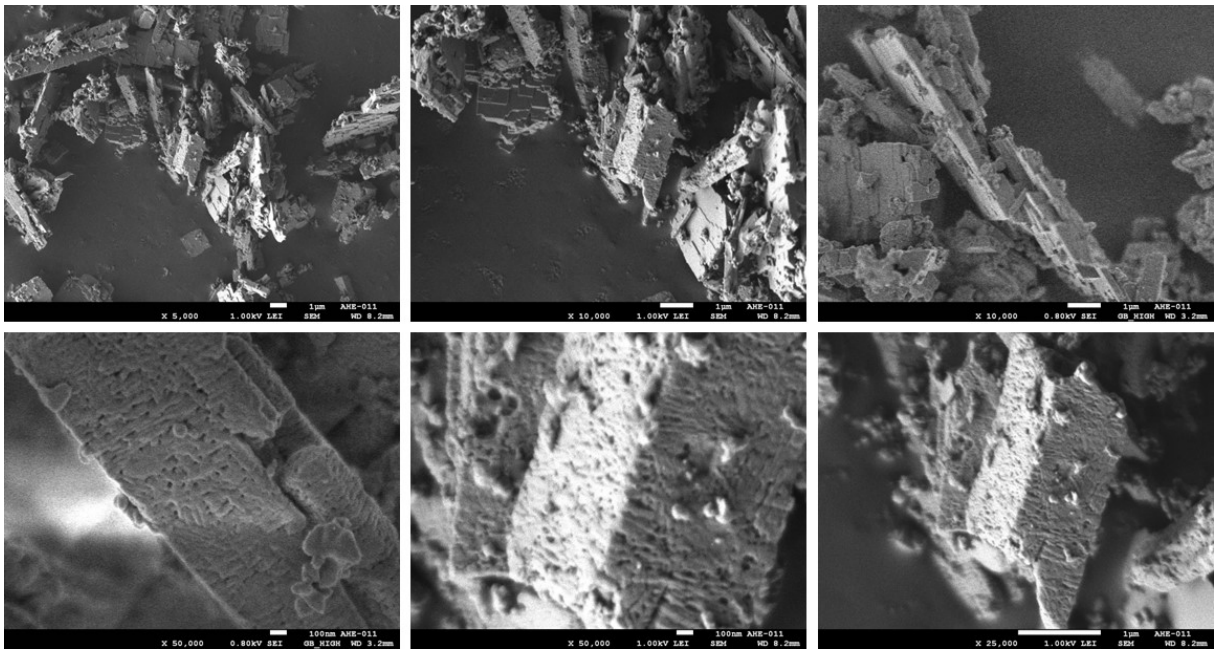

F12S: TGA of **1** $[Ag_8L^{Me}_2](PF_6)_4$ and **2** $[Au_8L^{Me}_2](PF_6)_4$:

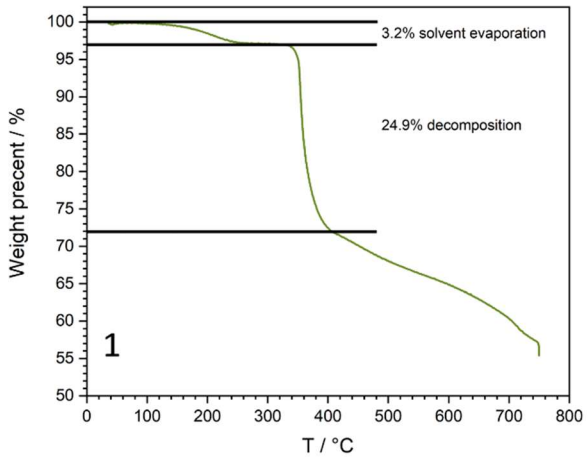

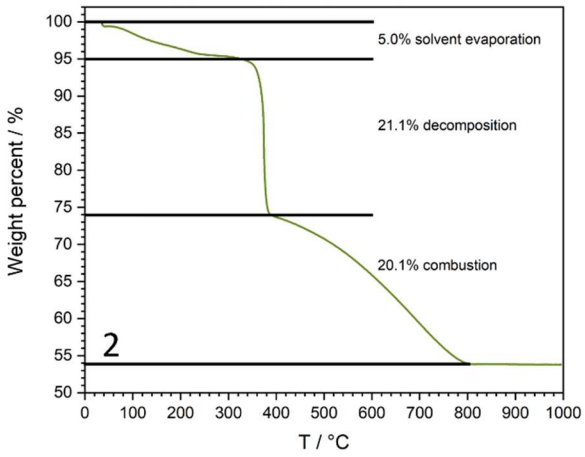

F13S: ESI mass spectra of $[Ag_8L^{Me}_2](OAc)_4$ in water:

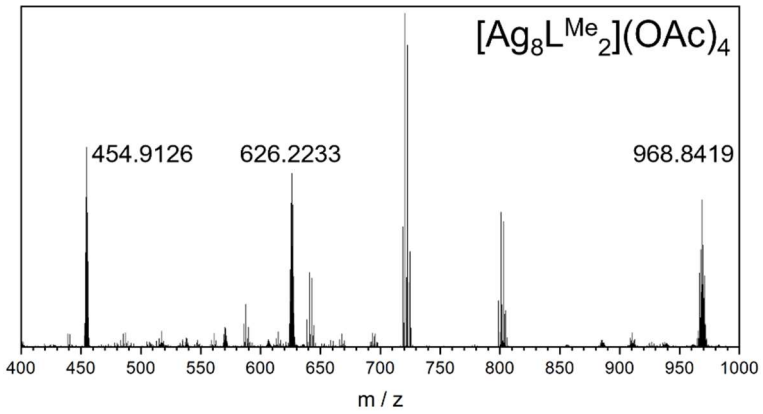

T2S: Overview of the analysed gas uptakes (N_2 at 77 K, CO_2 at 195 K, C_4 hydrocarbons at 298 K):

	$[Ag_8L^{Me}{}_2](PF_6)_4$	$[Au_8L^{Me}{}_2](PF_6)_4$
V_{ads} (N_2) 80 kPa / $cm^3\ g^{-1}$	45.9	16.2
n_{ads} (N_2) 80 kPa / mol mol^{-1}	5.5	2.5
V_{ads} (CO_2) 80 kPa / $cm^3\ g^{-1}$	60.2	20.3
n_{ads} (CO_2) 80 kPa / mol mol^{-1}	7.4	3.1
V_{ads} (C_4H_6) 80 kPa / $cm^3\ g^{-1}$	28.0	28.6
n_{ads} (C_4H_6) 80 kPa / mol mol^{-1}	3.4	4.4
V_{ads} (*i*-C_4H_6) 80 kPa / $cm^3\ g^{-1}$	15.1	10.3
n_{ads} (*i*-C_4H_6) 80 kPa / mol mol^{-1}	1.8	1.6
V_{ads} (*t*2-C_4H_8) 80 kPa / $cm^3\ g^{-1}$	21.0	15.8
n_{ads} (*t*2-C_4H_8) 80 kPa / mol mol^{-1}	2.5	2.4
V_{ads} (C_4H_{10}) 80 kPa / $cm^3\ g^{-1}$	11.6	9.3
n_{ads} (C_4H_{10}) 80 kPa / mol mol^{-1}	1.4	1.4

F14S: Adsorption isotherms for 1,3-C_4H_6 (red circles), *t*2-C_4H_8 (blue triangles), *i*-C_4H_8 (black squares) and C_4H_{10} (green triangles) on $[Ag_8L^{Me}{}_2](OAc)_4$ and $[Au_8L^{Me}{}_2](OAc)_4$ measured at 298 K:

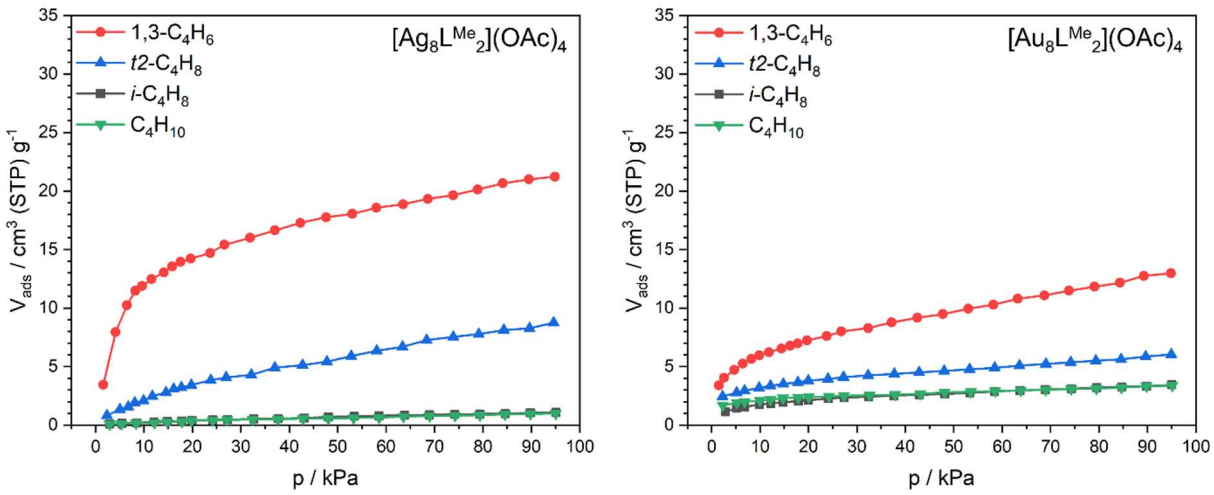

Expanding the Anionic Diversity of Pillarplex Salts:

F15S: NMR analysis of $[Ag_8L^{Me}_2](F)_4$ containing ^1H, COSY and ^{19}F NMR spectra:

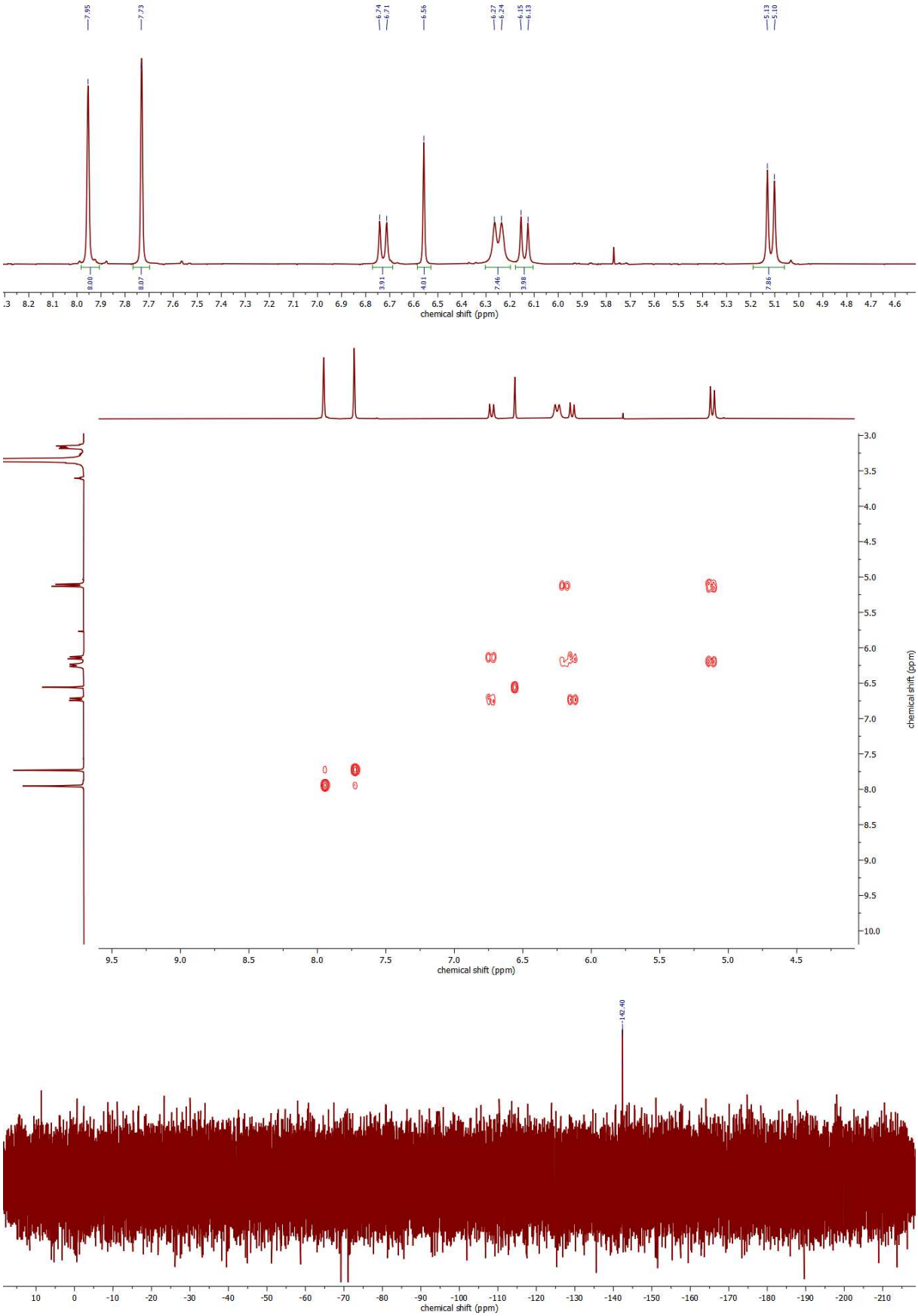

F16S: NMR analysis of $[Ag_8L^{Me}_2](Cl)_4$ containing ^1H, ^{13}C, COSY and DOSY NMR spectra:

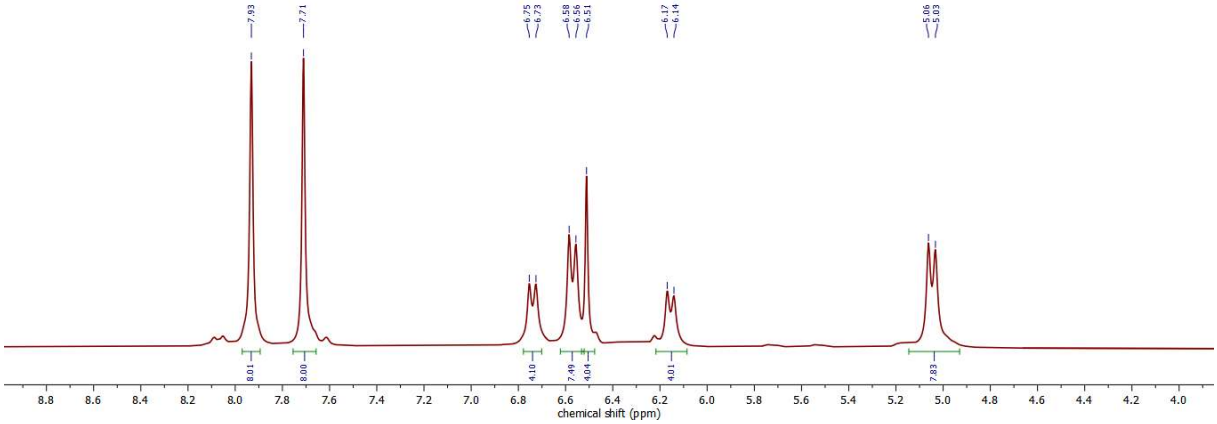

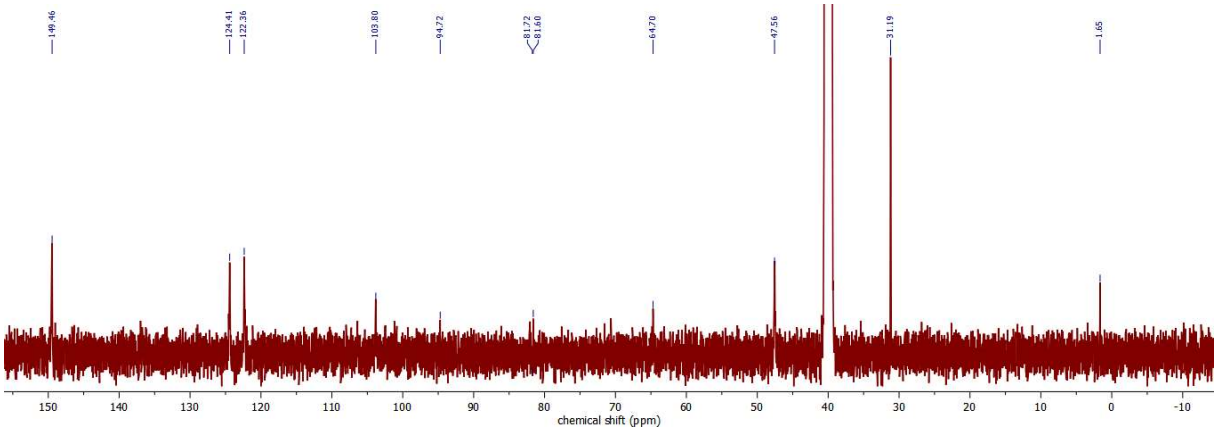

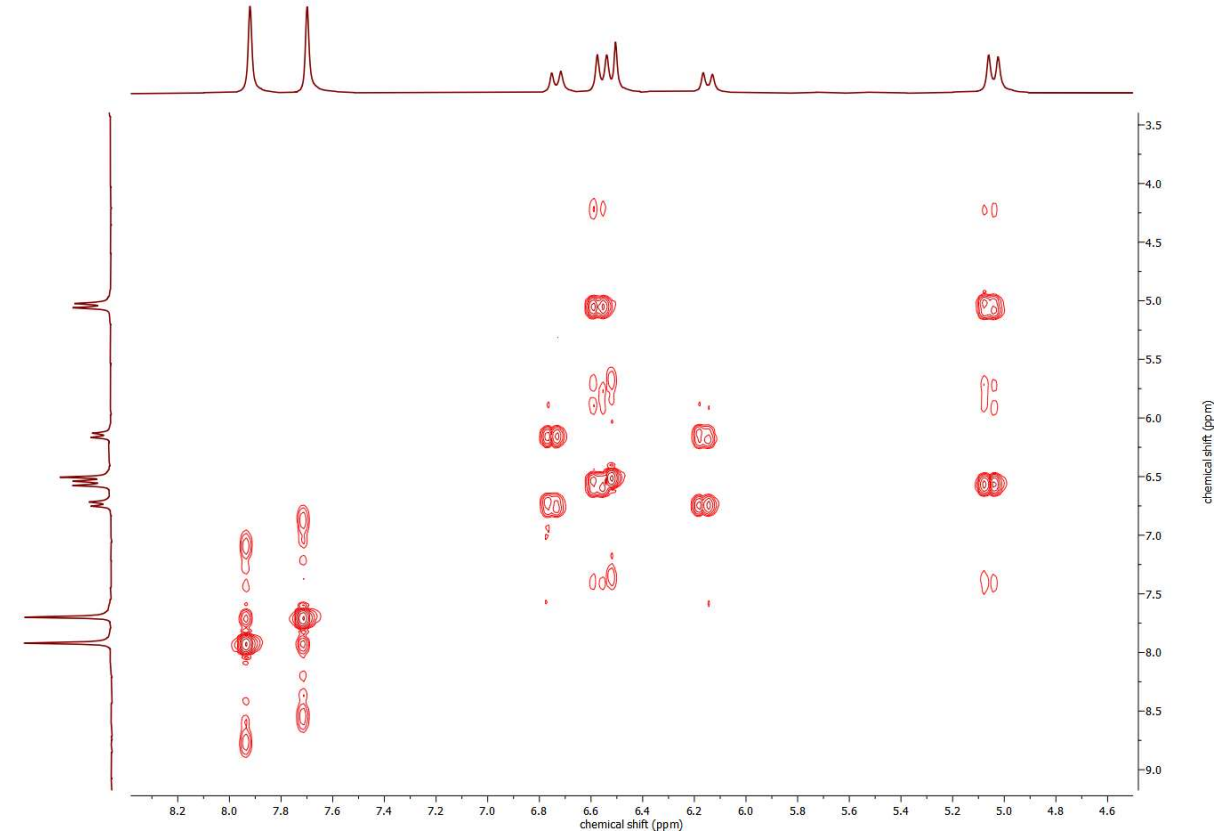

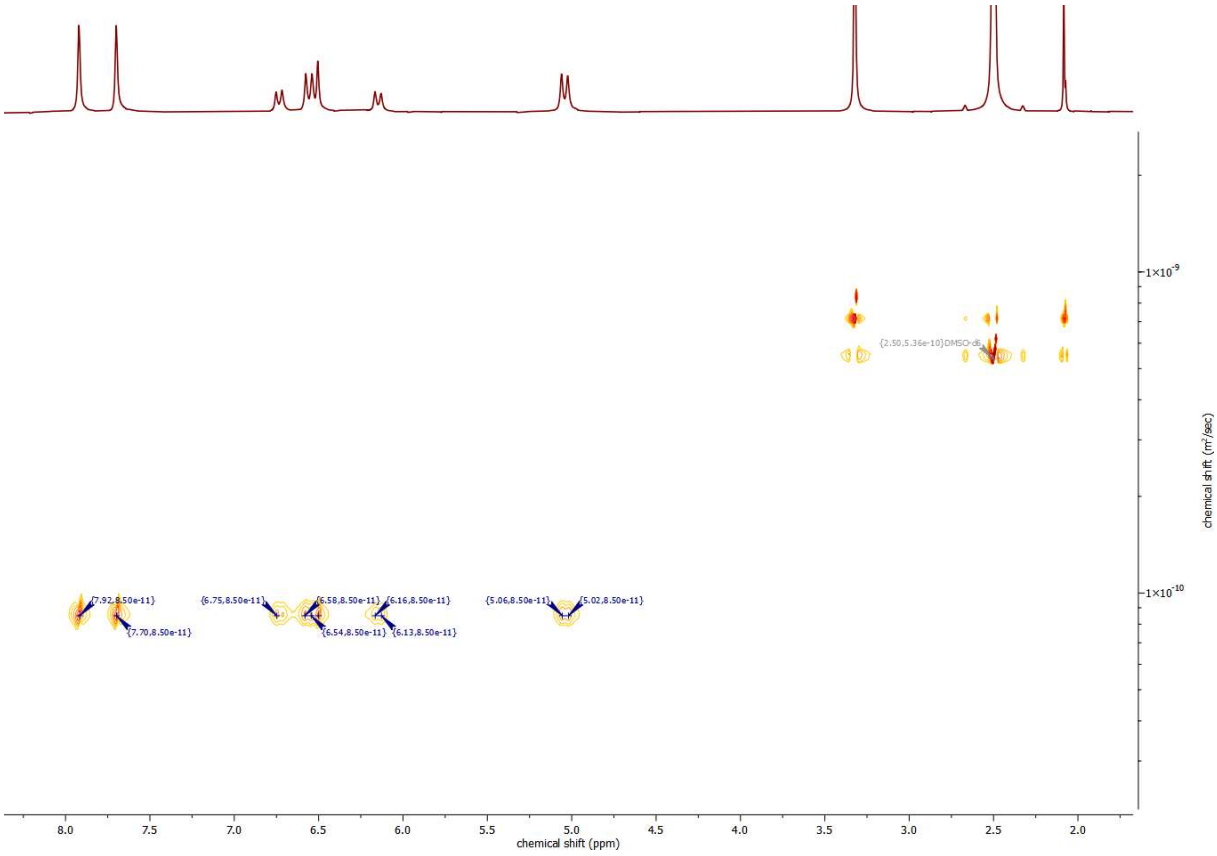

F17S: NMR analysis of $[Ag_8L^{Me}_2](Br)_4$ containing ^1H and COSY NMR spectra:

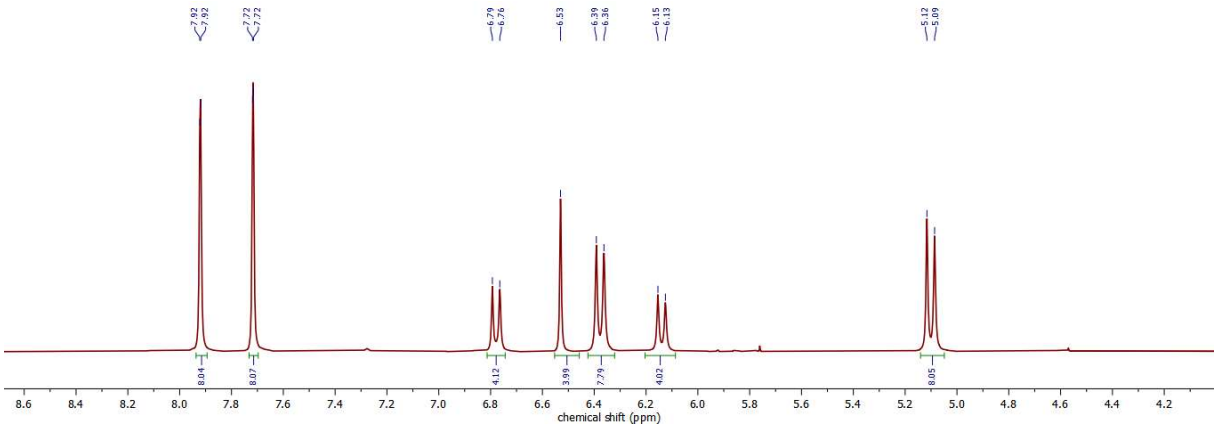

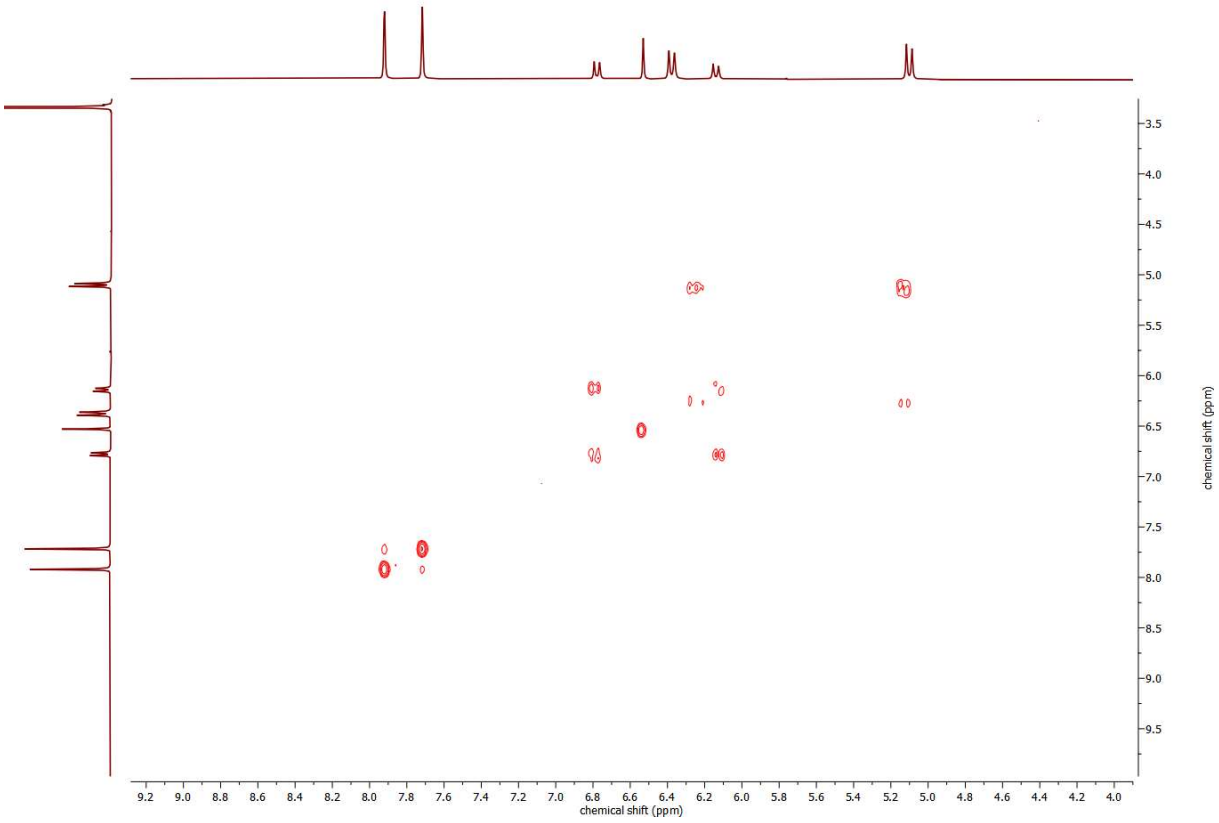

F18S: NMR analysis of $[Ag_8L^{Me}_2](I)_4$ containing ^1H and COSY NMR spectra:

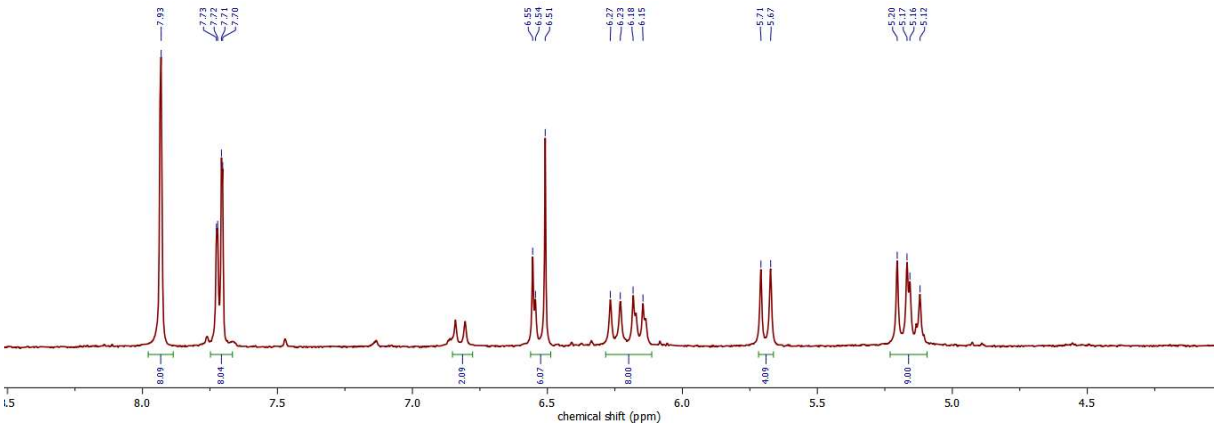

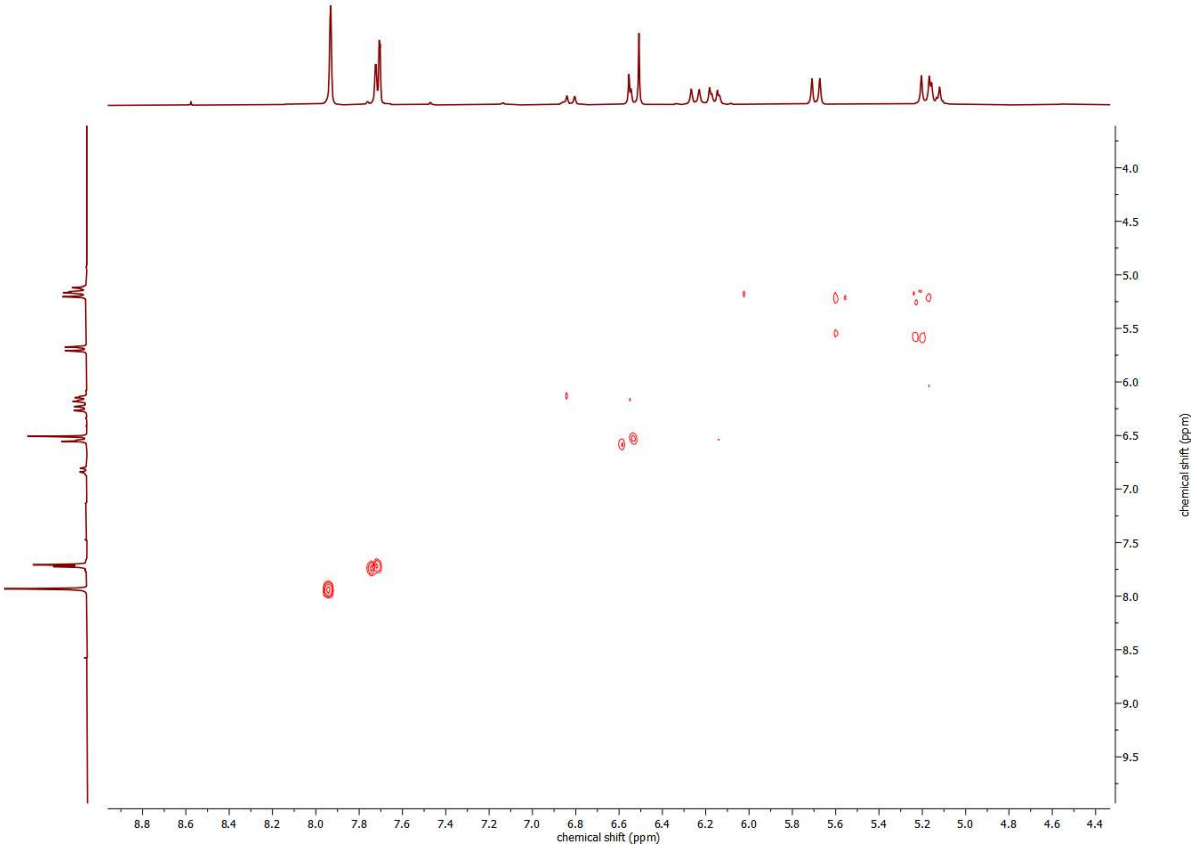

F19S: NMR analysis of $[Au_8L^{Me}_2](Cl)_4$ containing ^1H and COSY NMR spectra:

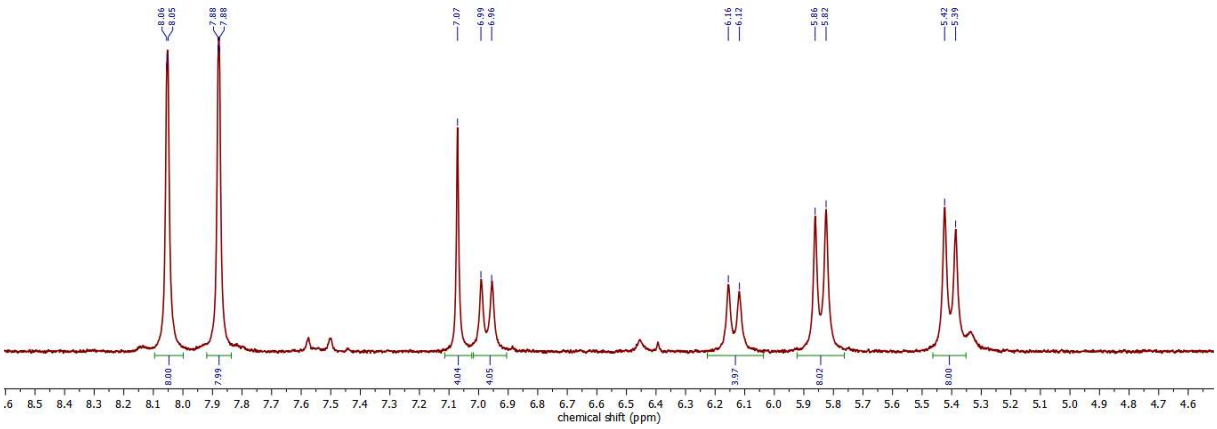

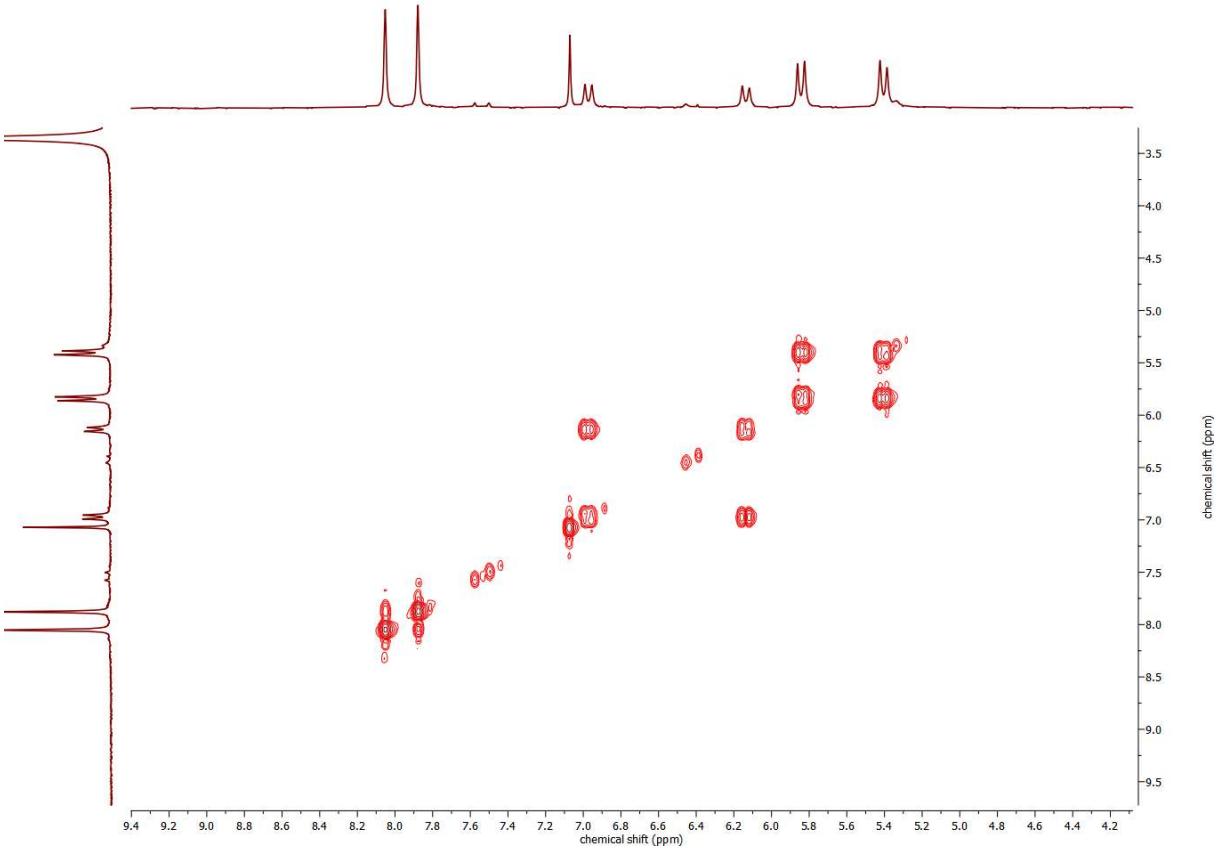

F20S: NMR analysis of $[Au_8L^{Me}_2](Br)_4$ containing ^1H and COSY NMR spectra:

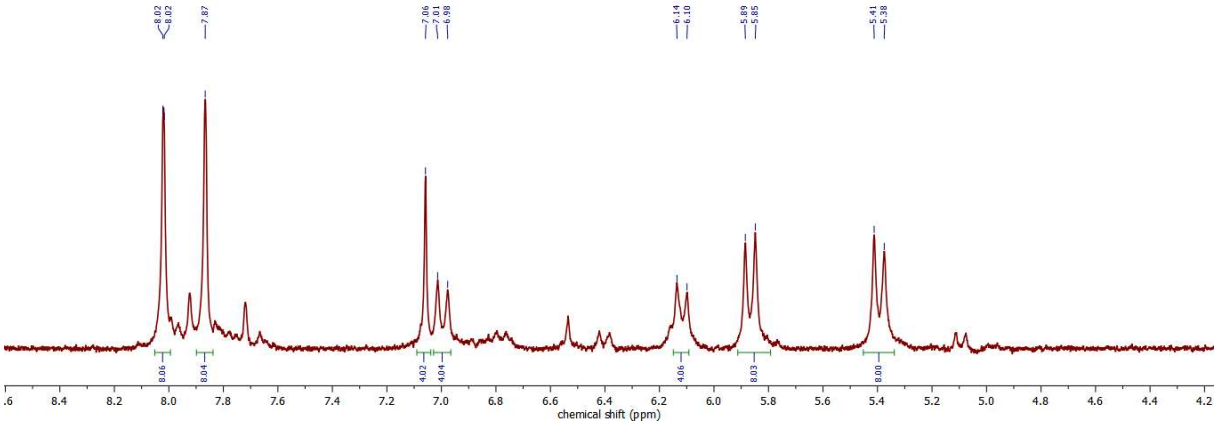

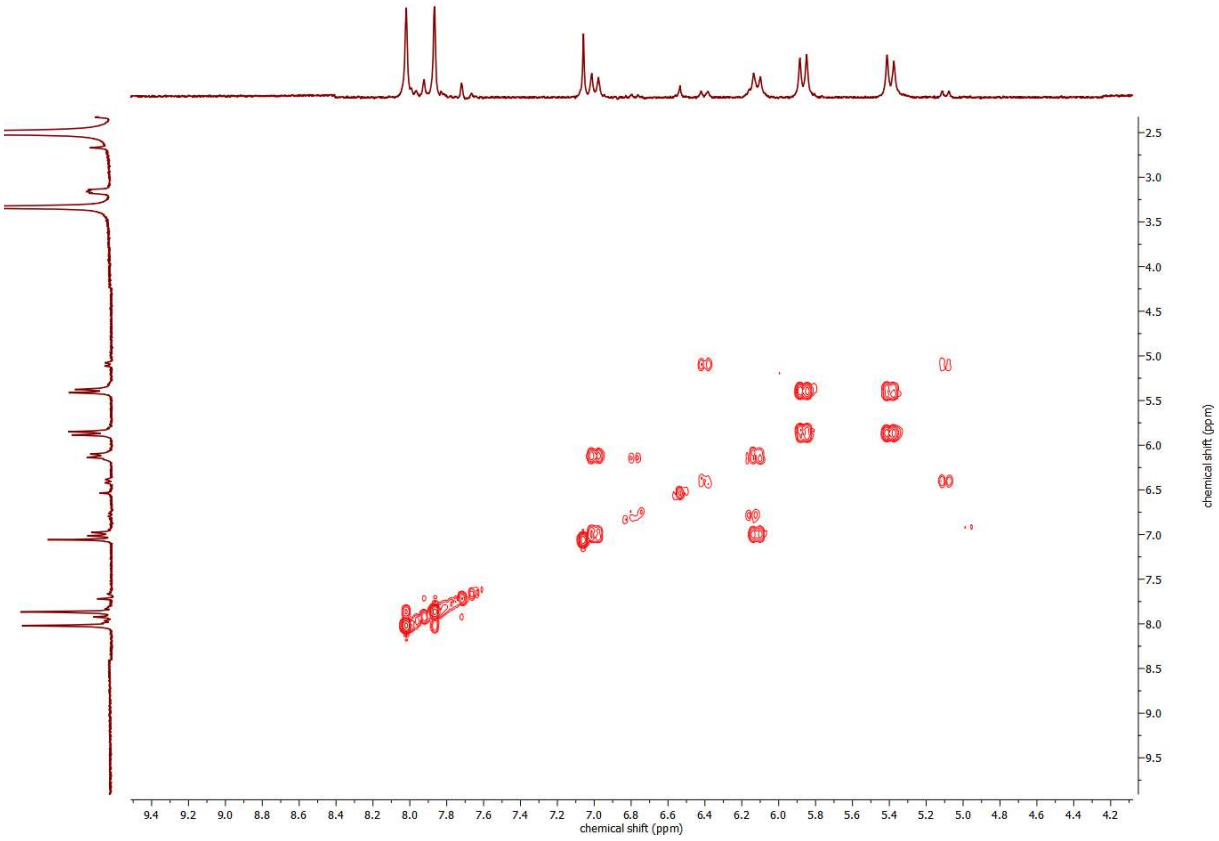

F21S: NMR analysis of $[Ag_8L^{Me}_2](SCN)_4$ containing ^1H, COSY, ^{13}C and DOSY NMR spectra:

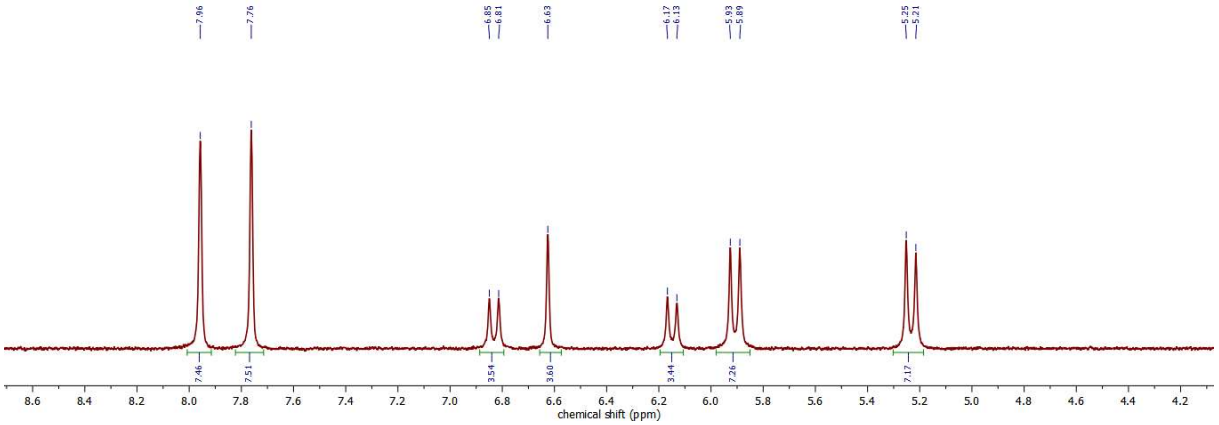

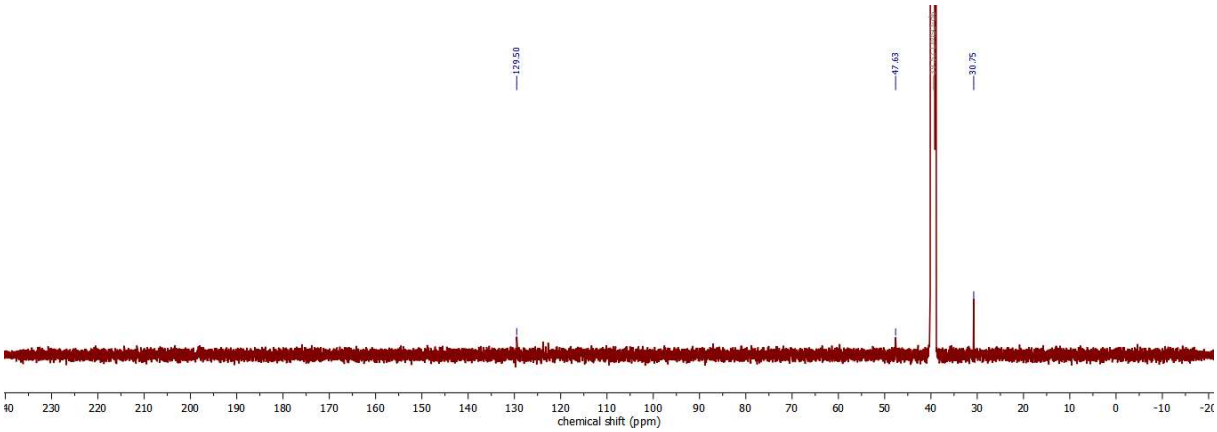
139.50
47.63
30.75
chemical shift (ppm)

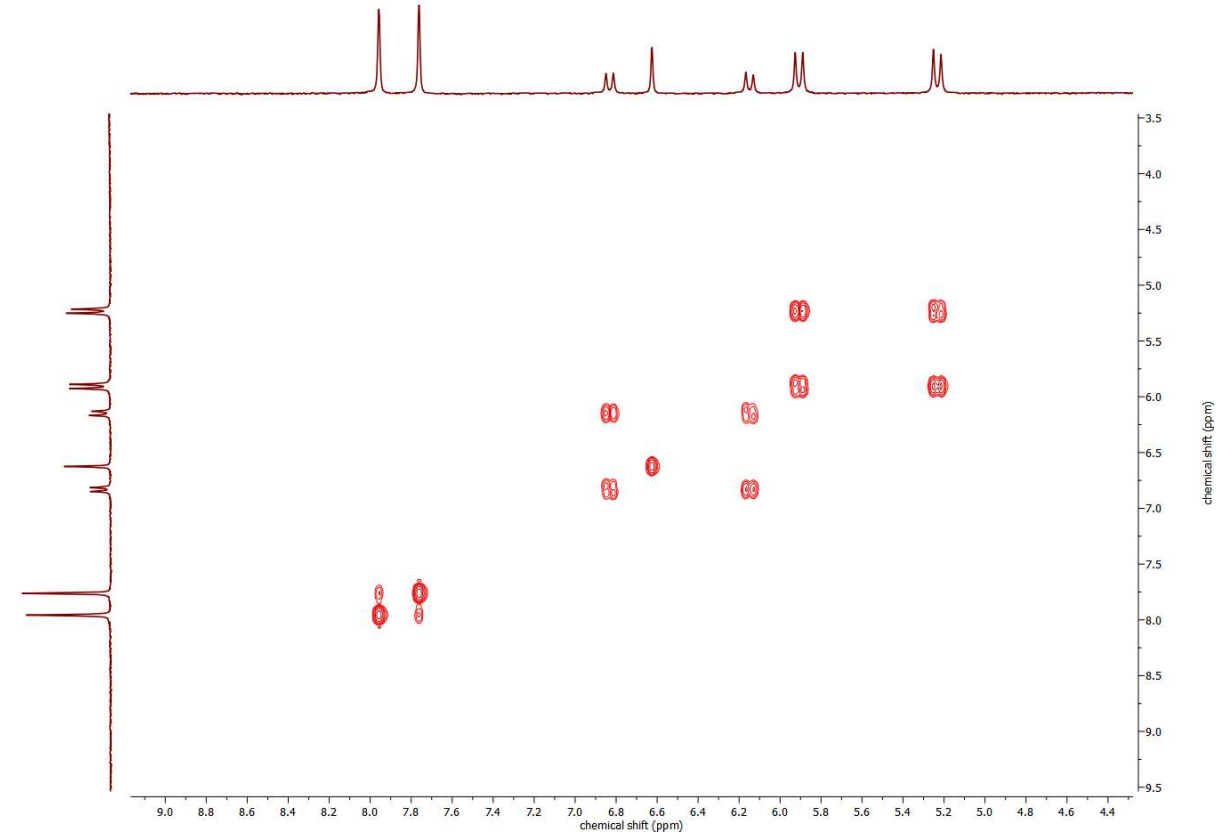
chemical shift (ppm)
chemical shift (ppm)

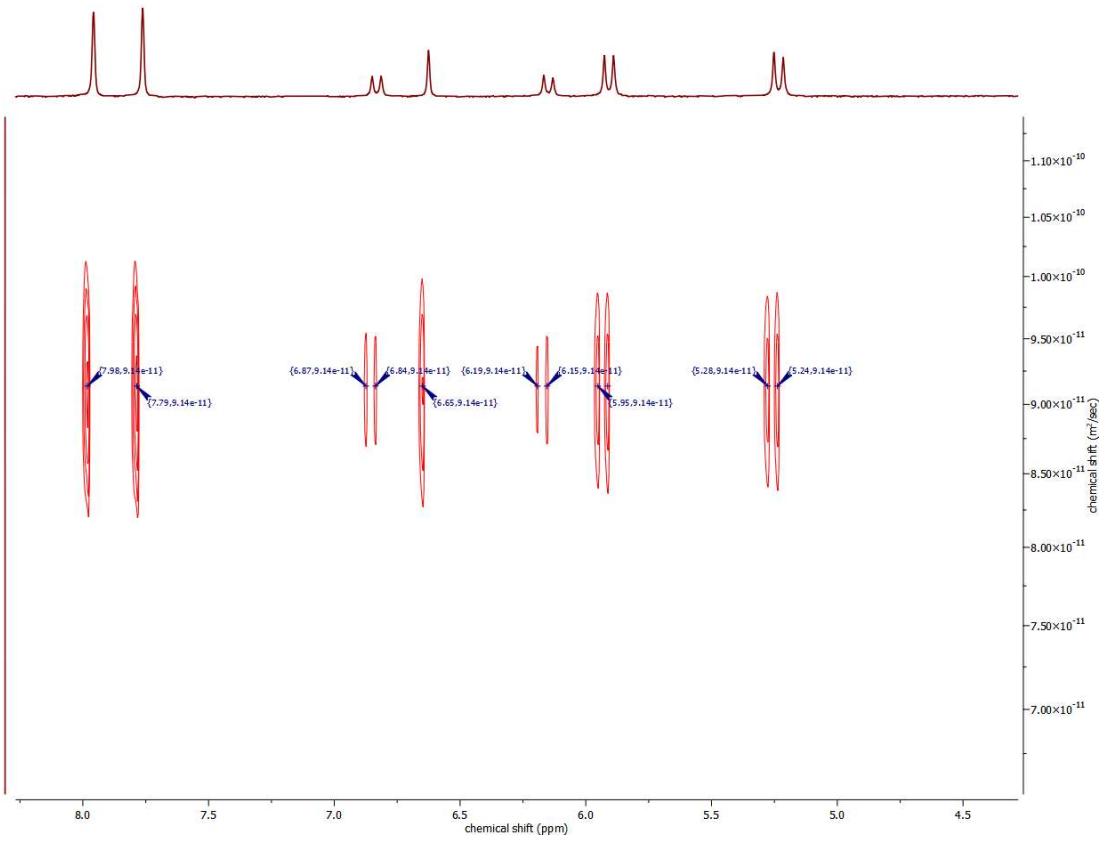

F22S: NMR analysis of $[Ag_8L^{Me}_2](NO_3)_4$ containing ^1H, COSY and DOSY NMR spectra:

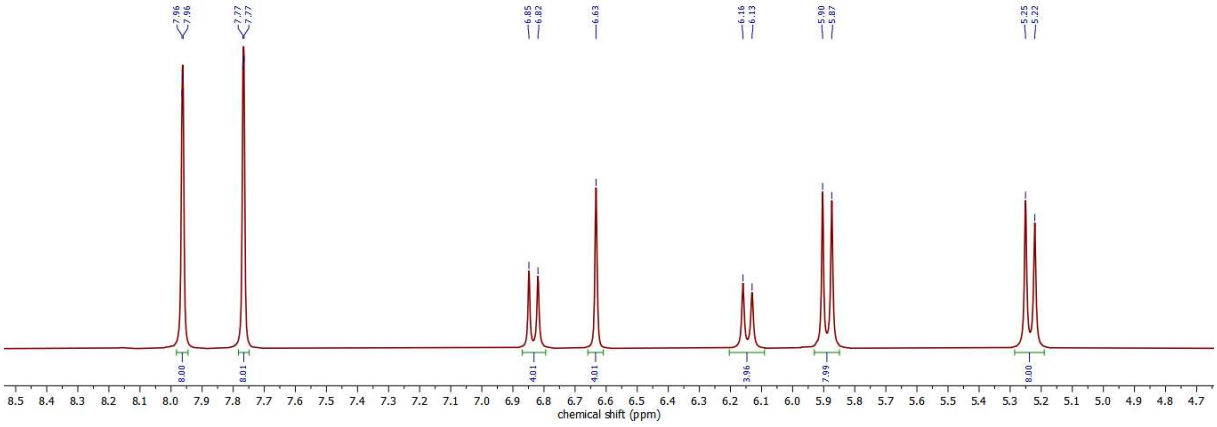

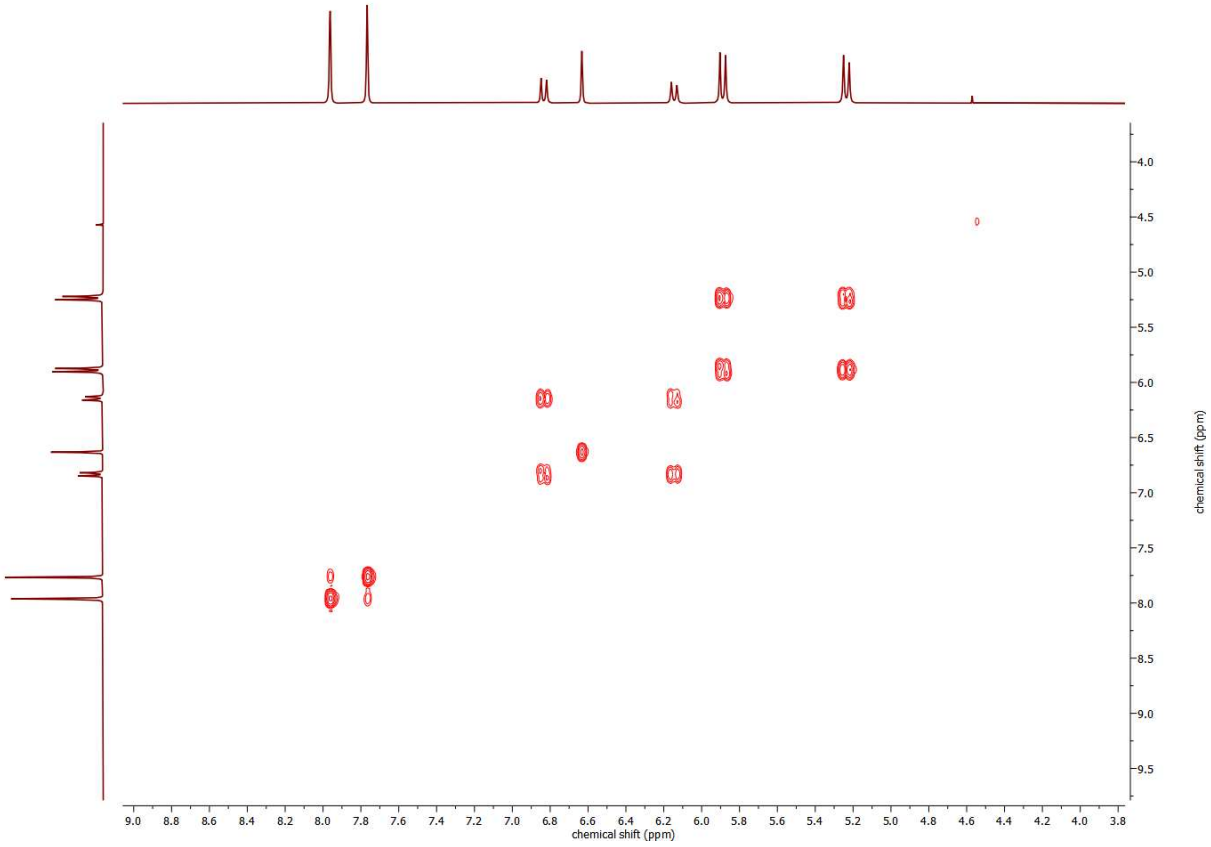
chemical shift (ppm)
chemical shift (ppm)

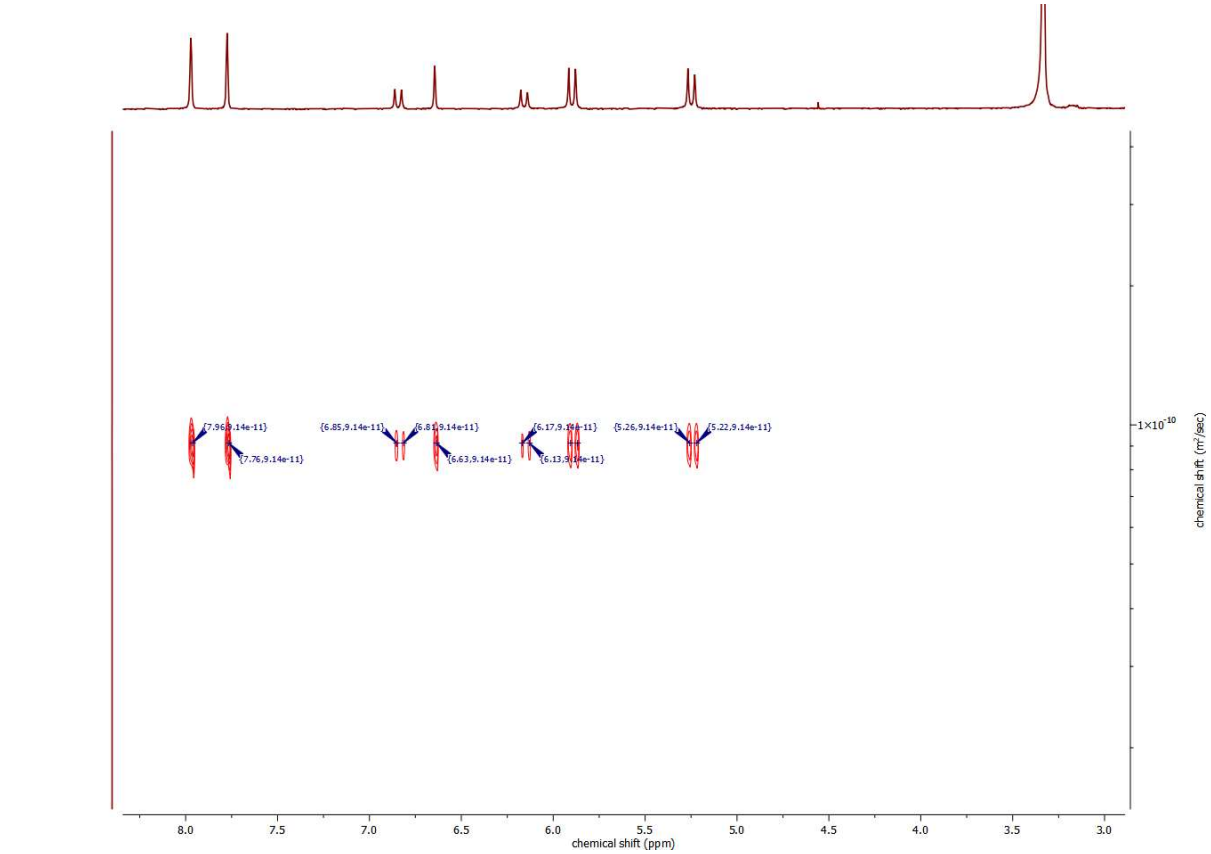
{7.96,9.14e-11}
{7.76,9.14e-11}
{6.85,9.14e-11}
{6.63,9.14e-11}
{6.17,9.14e-11}
{6.13,9.14e-11}
{5.26,9.14e-11}
{5.22,9.14e-11}
chemical shift (ppm)
chemical shift (m²/sec)

F23S: NMR analysis of $[Ag_8L^{Me}_2](ClO_4)_4$ containing ^1H, ^{13}C, COSY and DOSY NMR spectra:

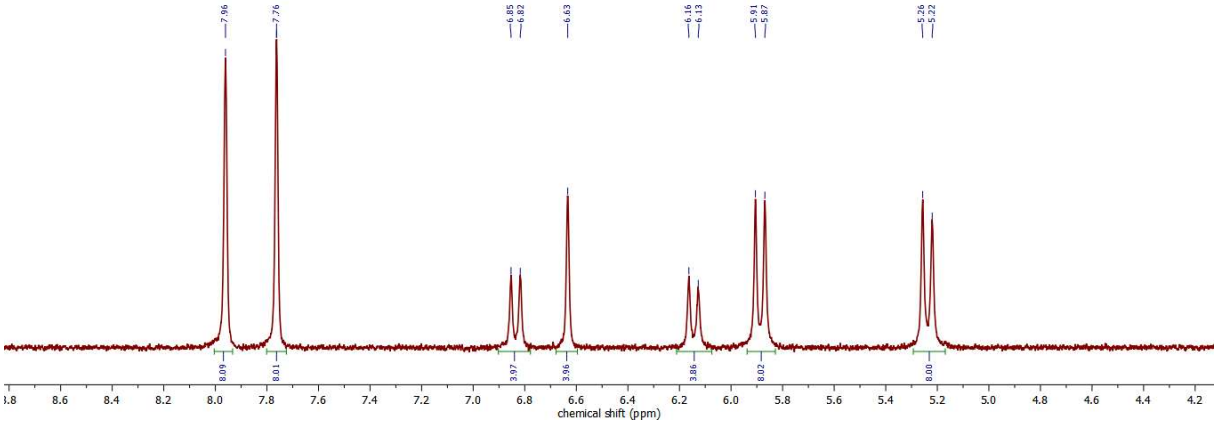

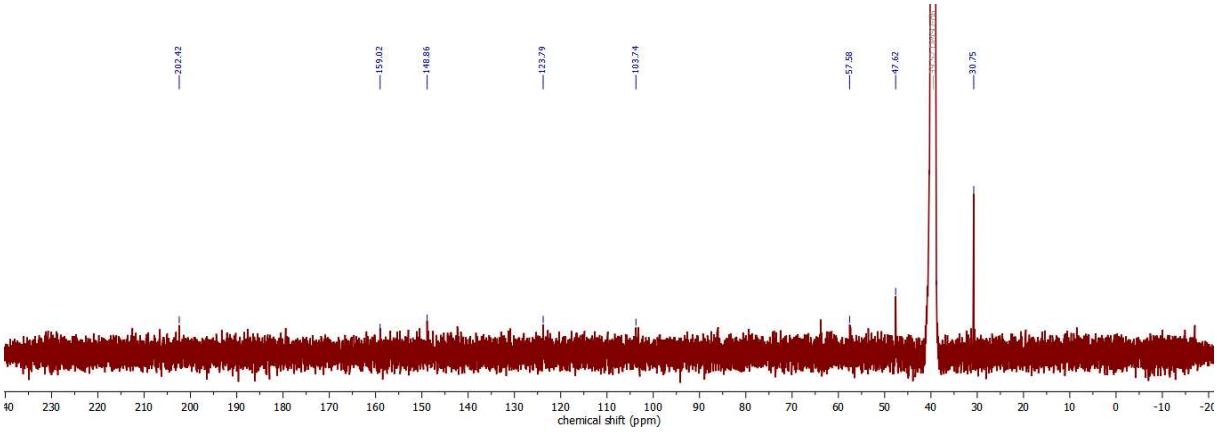

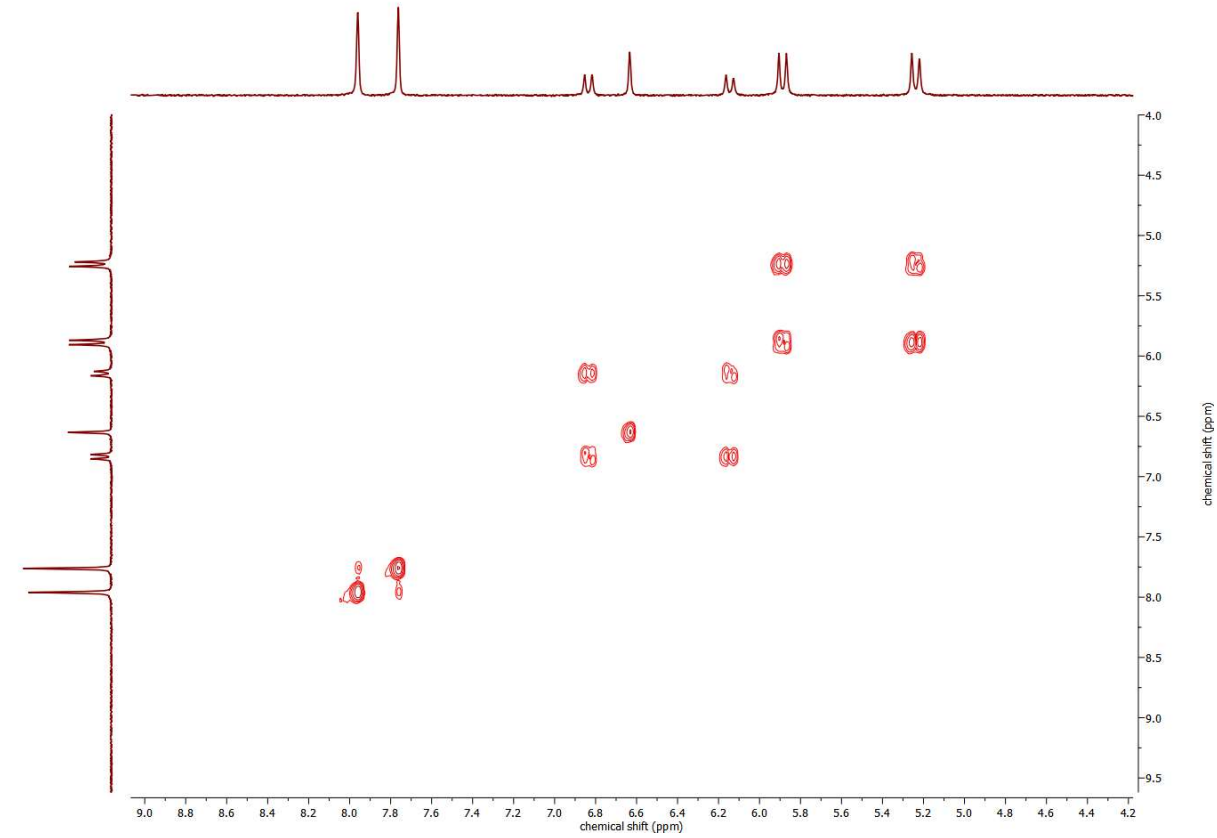

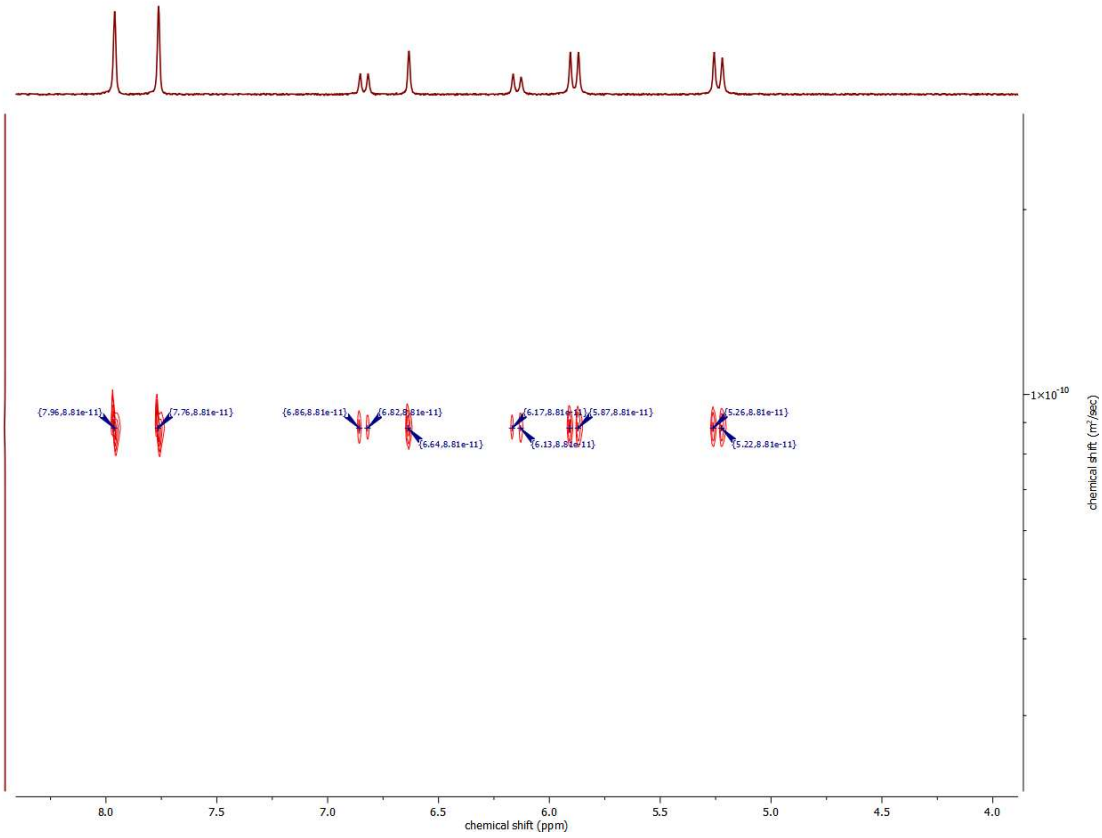

F24S: NMR analysis of $[Ag_8L^{Me}_2](BF_4)_4$ containing ^{1}H, ^{11}B, ^{13}C, ^{19}F and COSY NMR spectra:

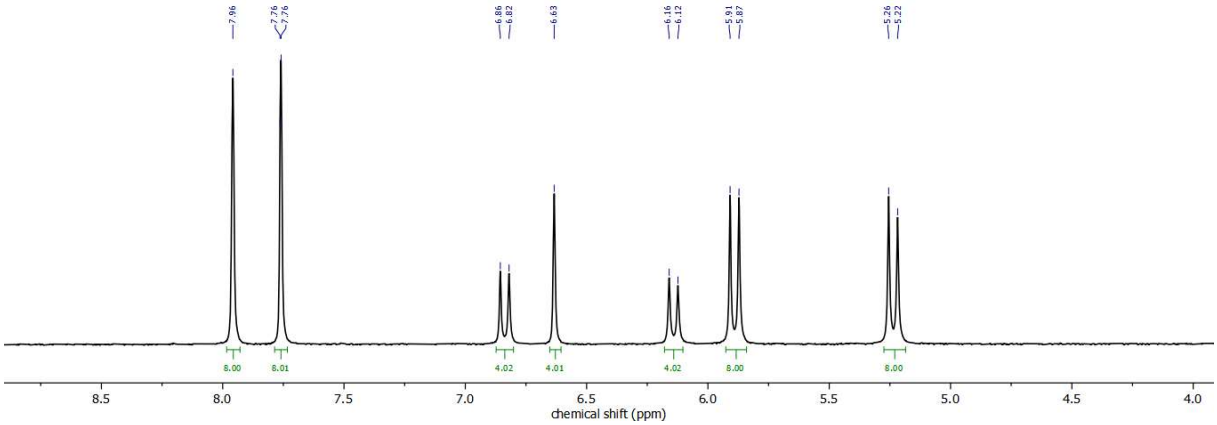

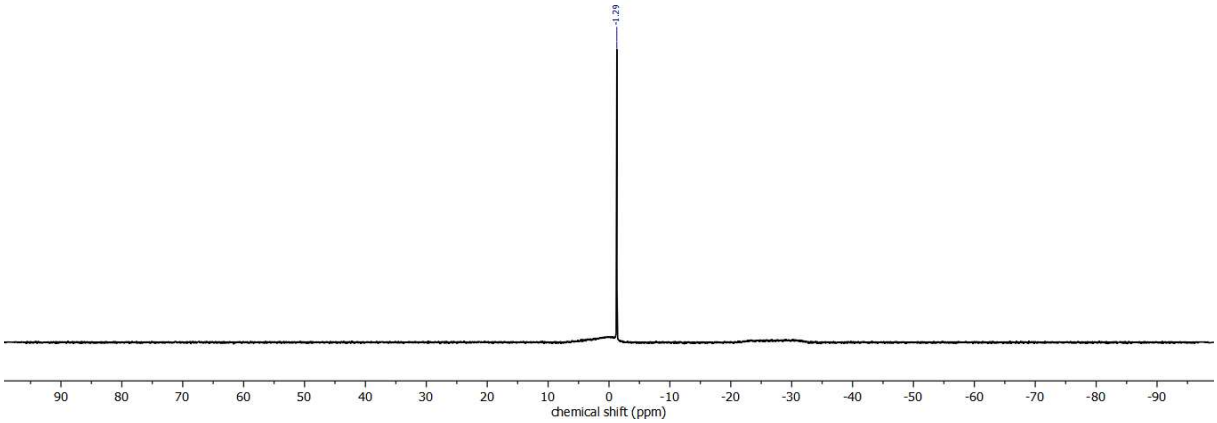

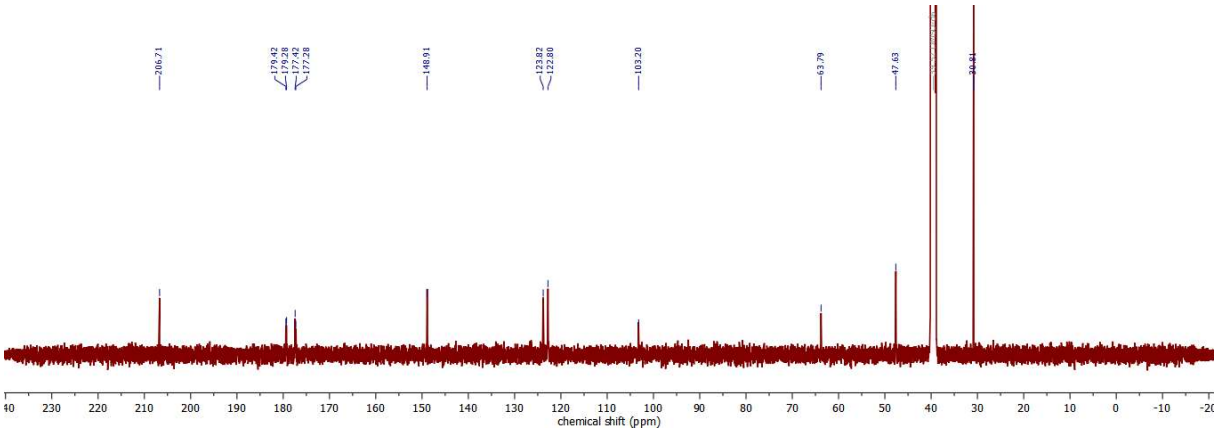
206.71
179.42
179.28
177.42
177.28
148.91
123.82
122.80
103.20
63.79
47.63
30.81
chemical shift (ppm)

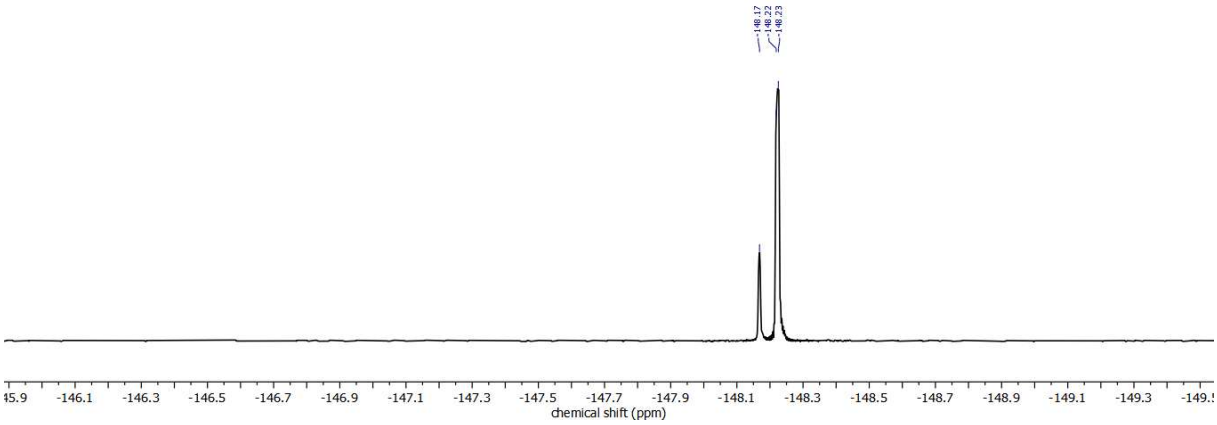
148.17
148.23
148.33
148.39
chemical shift (ppm)

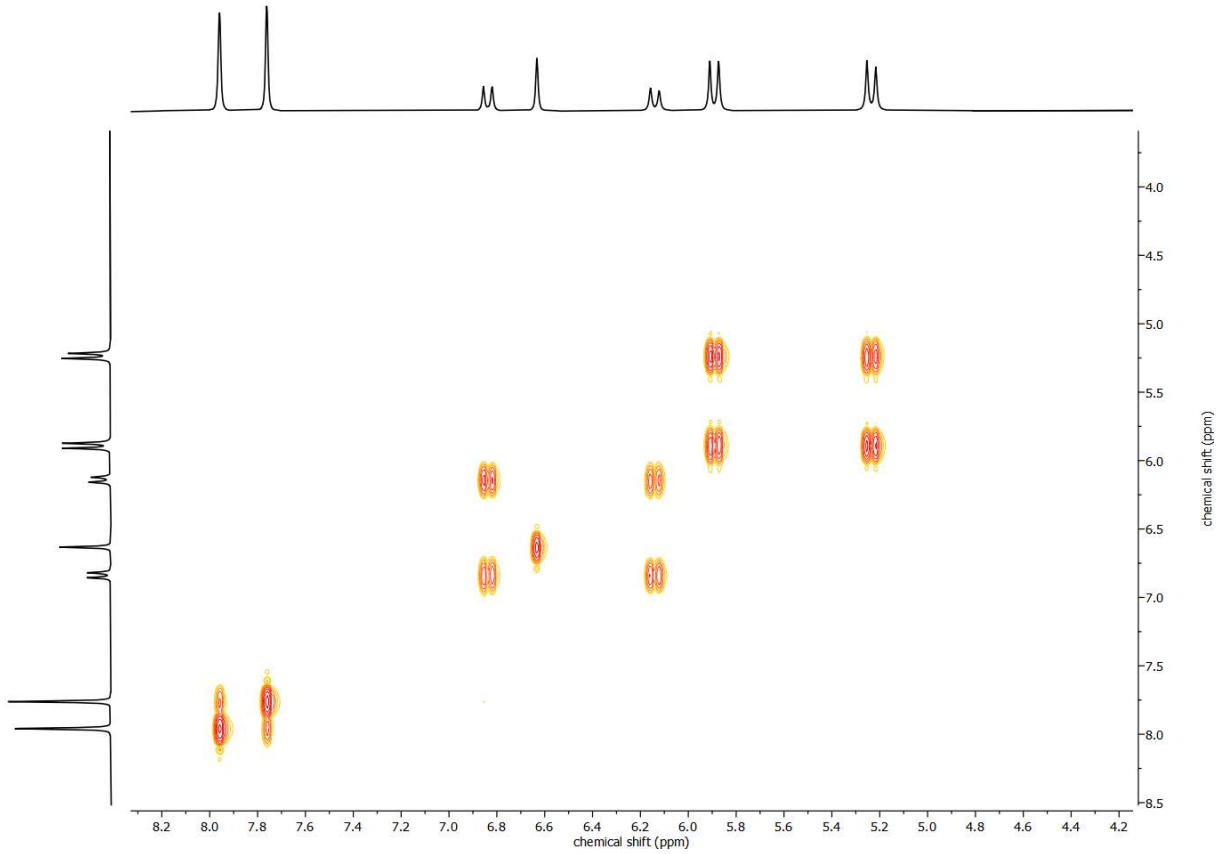
chemical shift (ppm)
chemical shift (ppm)

F25S: ^{1}H NMR spectrum of $[Ag_8L^{Me}_2](F)_4$, $[Ag_8L^{Me}_2](Cl)_4$, $[Ag_8L^{Me}_2](Br)_4$ and $[Ag_8L^{Me}_2](I)_4$ in solid state:

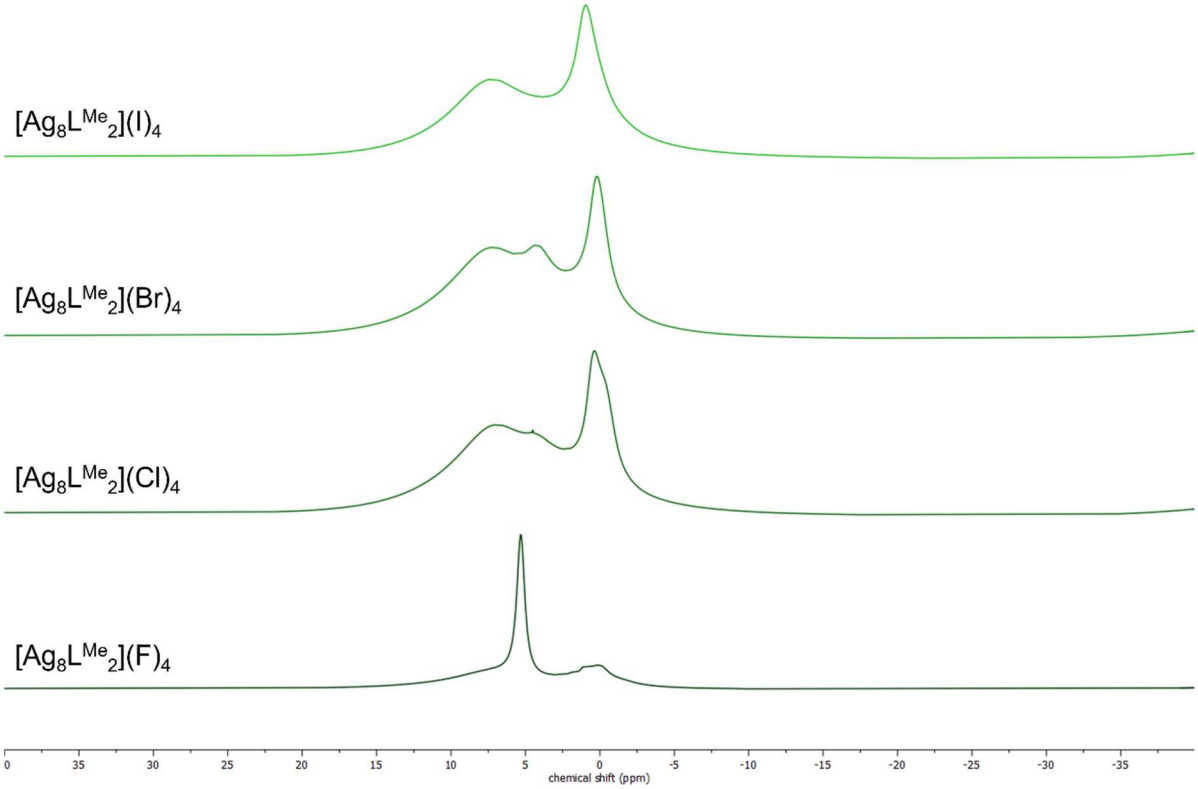

F26S: ^{1}H NMR spectrum of $[Au_8L^{Me}_2](Cl)_4$, $[Au_8L^{Me}_2](Br)_4$ and $[Au_8L^{Me}_2](I)_4$ in solid state:

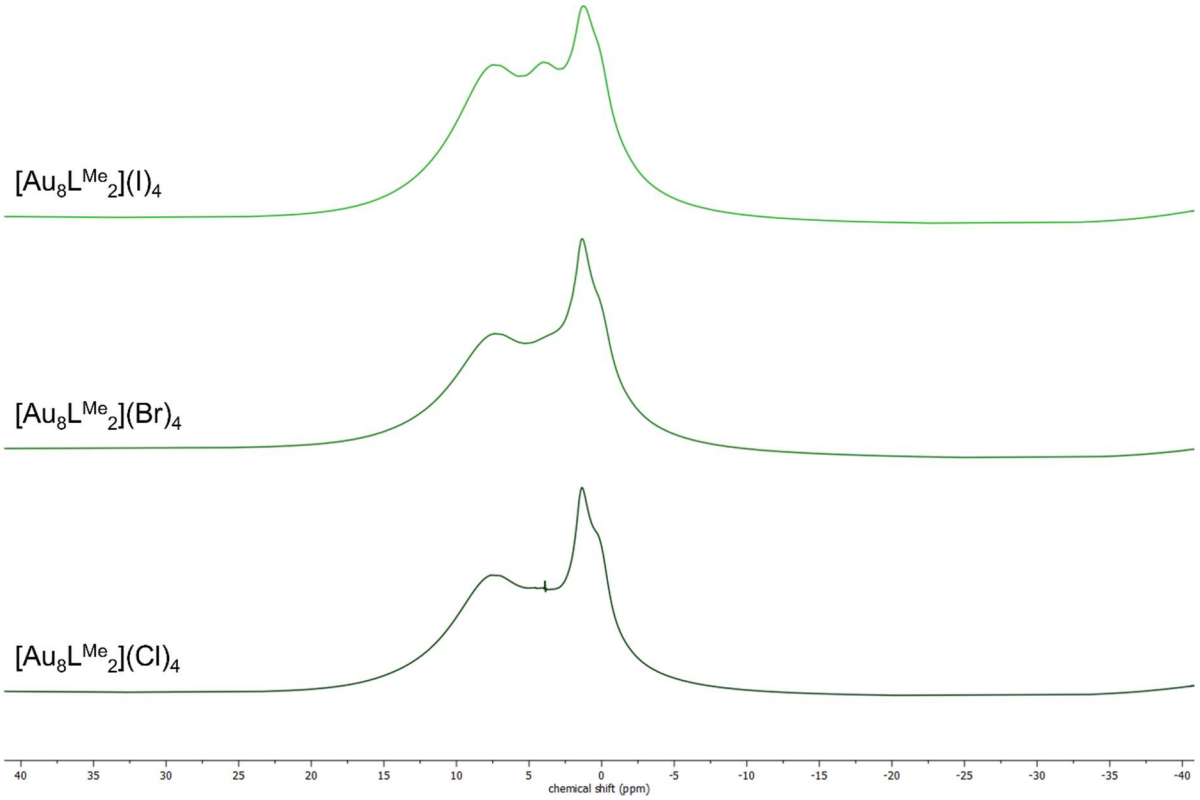

F27S: ^{13}C NMR spectrum of $[Ag_8L^{Me}_2](F)_4$, $[Ag_8L^{Me}_2](Cl)_4$, $[Ag_8L^{Me}_2](Br)_4$ and $[Ag_8L^{Me}_2](I)_4$ in solid state:

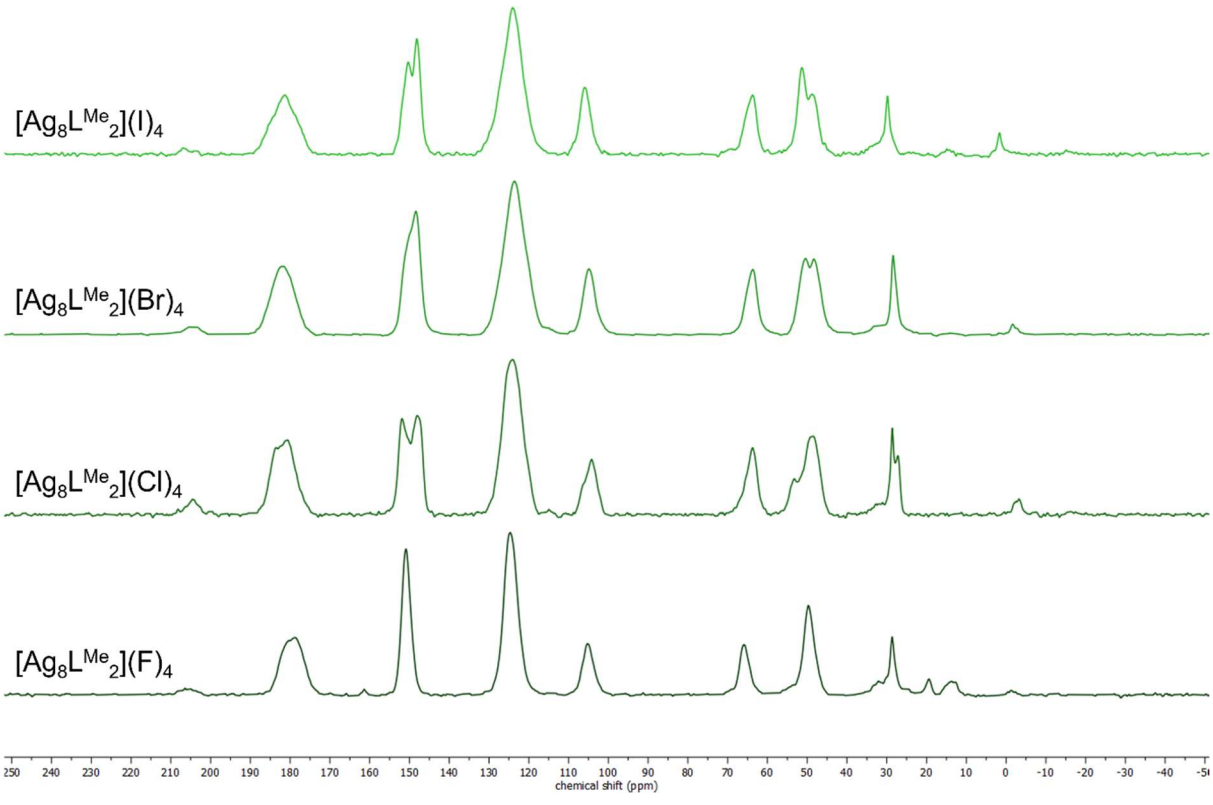

F28S: ^{13}C NMR spectrum of $[Au_8L^{Me}_2](Cl)_4$, $[Au_8L^{Me}_2](Br)_4$ and $[Au_8L^{Me}_2](I)_4$ in solid state:

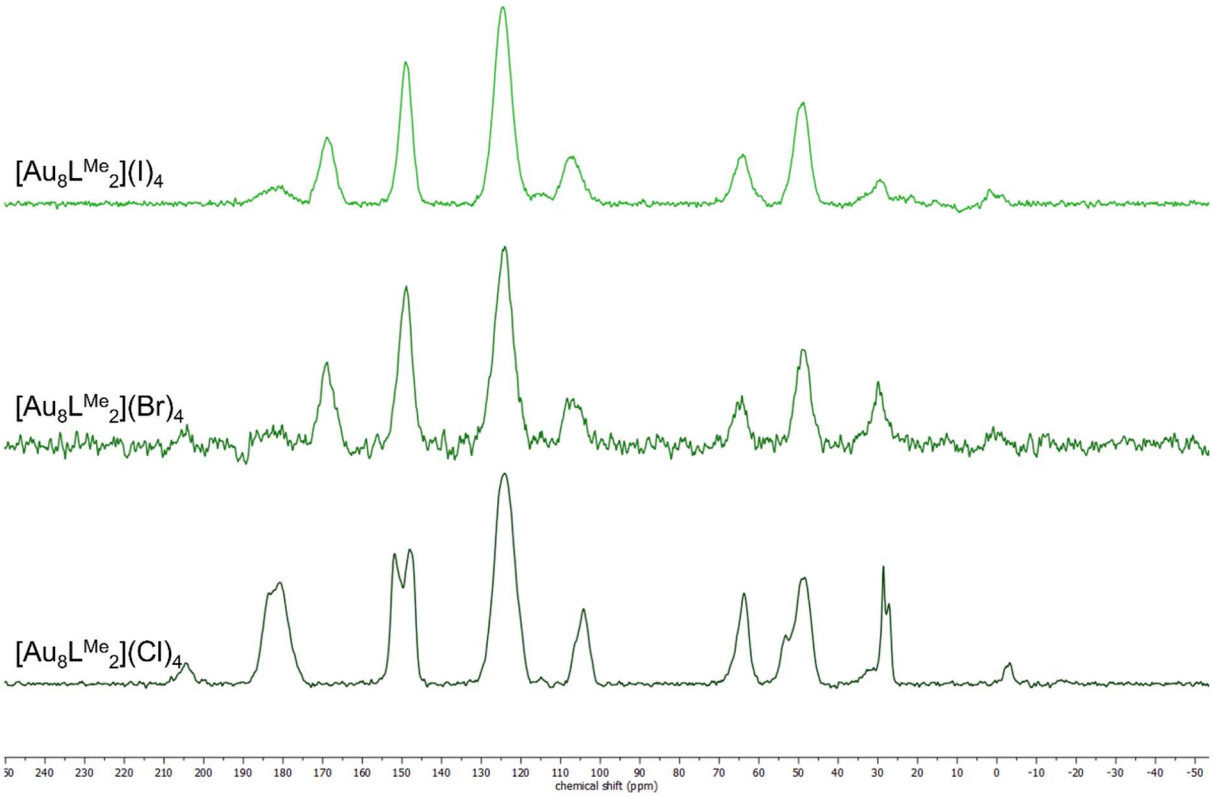

F29S: IR spectrum of $[Au_8L^{Me}_2](Cl)_4$ and $[Au_8L^{Me}_2](Br)_4$ in solid-state:

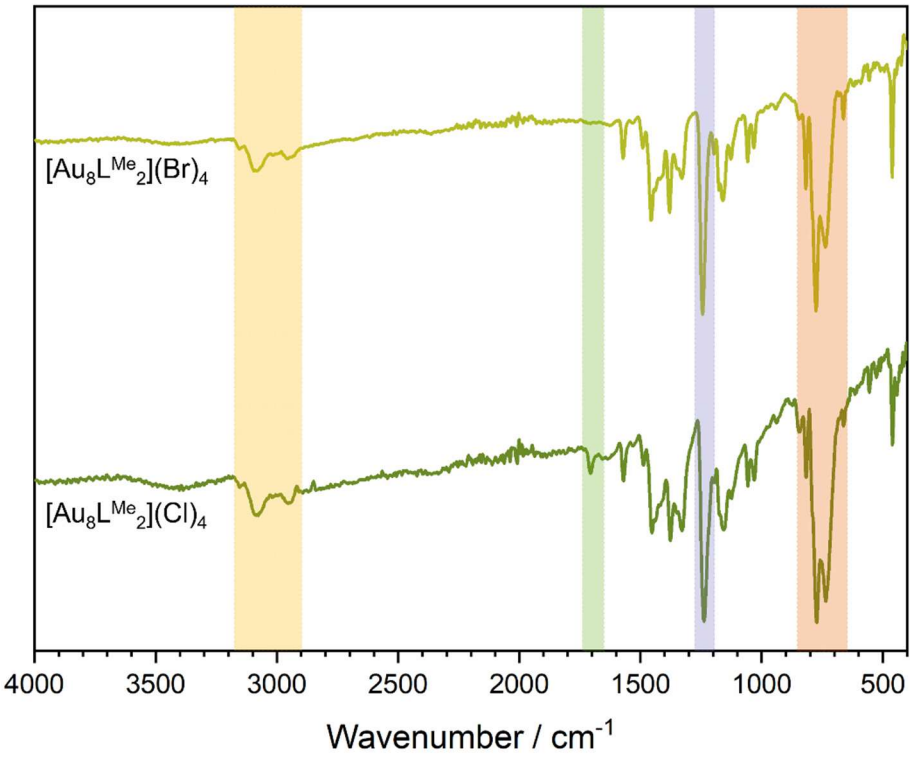

F30S: ESI mass spectra of $[Ag_8L^{Me}_2](Cl)_4$, $[Ag_8L^{Me}_2](Br)_4$, $[Au_8L^{Me}_2](Cl)_4$ and $[Au_8L^{Me}_2](Br)_4$ in water:

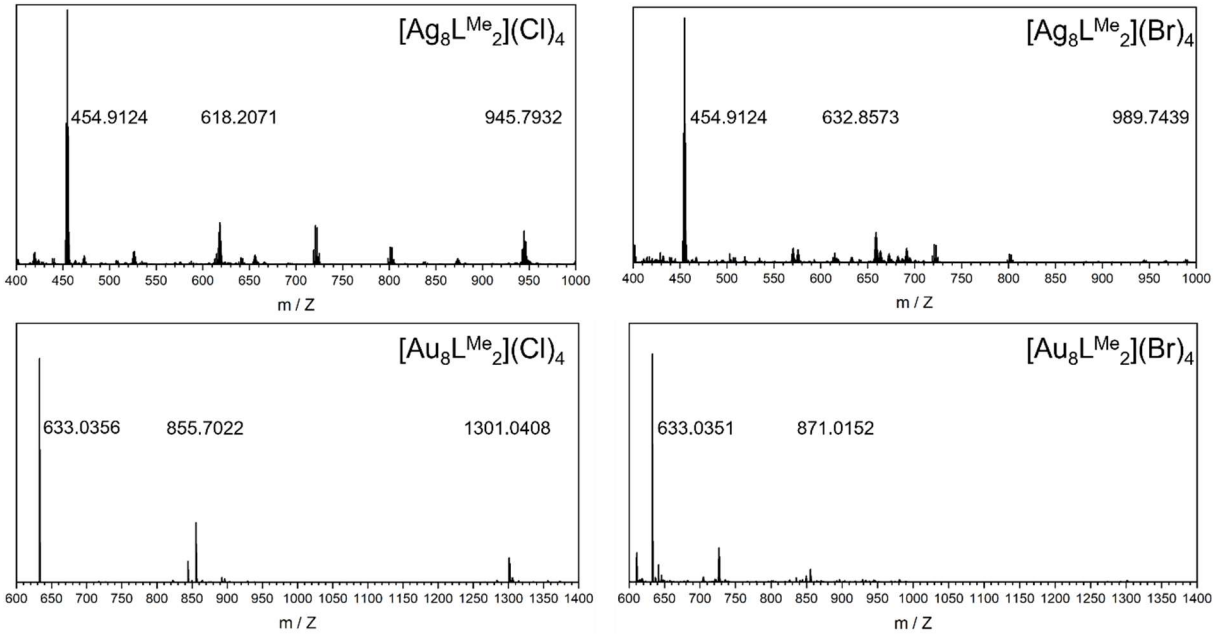

F31S: ESI mass spectra of $[Ag_8L^{Me}_2](SCN)_4$, $[Ag_8L^{Me}_2](NO_3)_4$ and $[Ag_8L^{Me}_2](ClO_4)_4$ in water, $[Ag_8L^{Me}_2](BF_4)_4$ in MeCN:

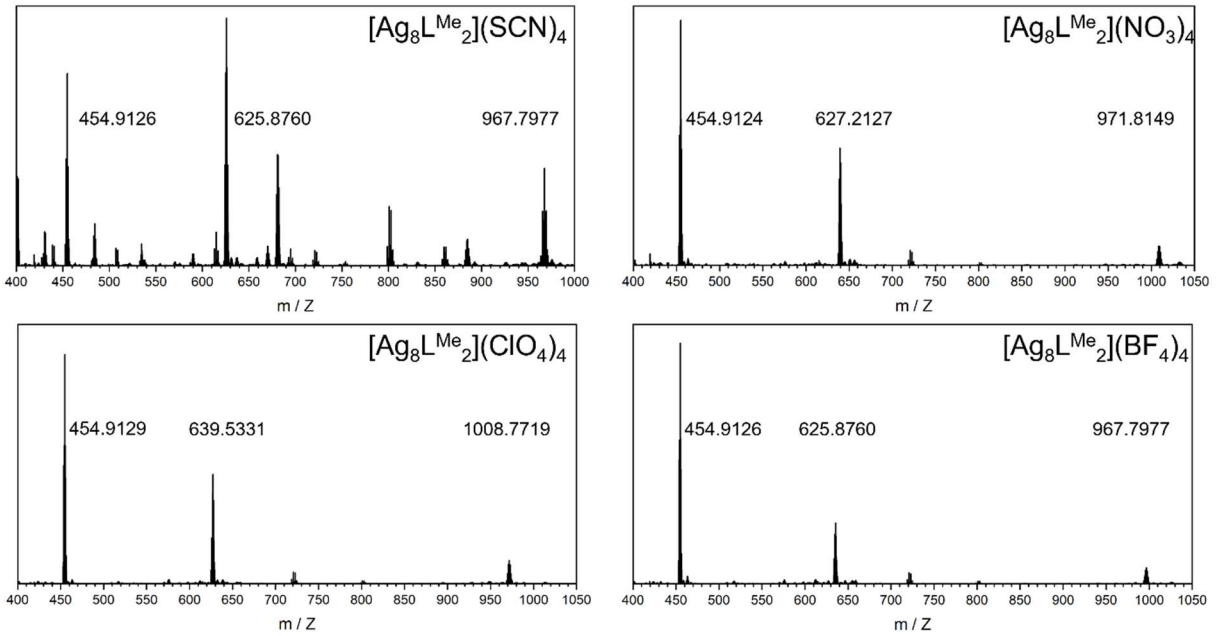

F32S: UV-vis spectrum of $[Ag_8L^{Me}_2](F)_4$, $[Ag_8L^{Me}_2](Cl)_4$, $[Ag_8L^{Me}_2](Br)_4$ and $[Ag_8L^{Me}_2](I)_4$ in water ($c = 1 \cdot 10^{-5}$ mol/L):

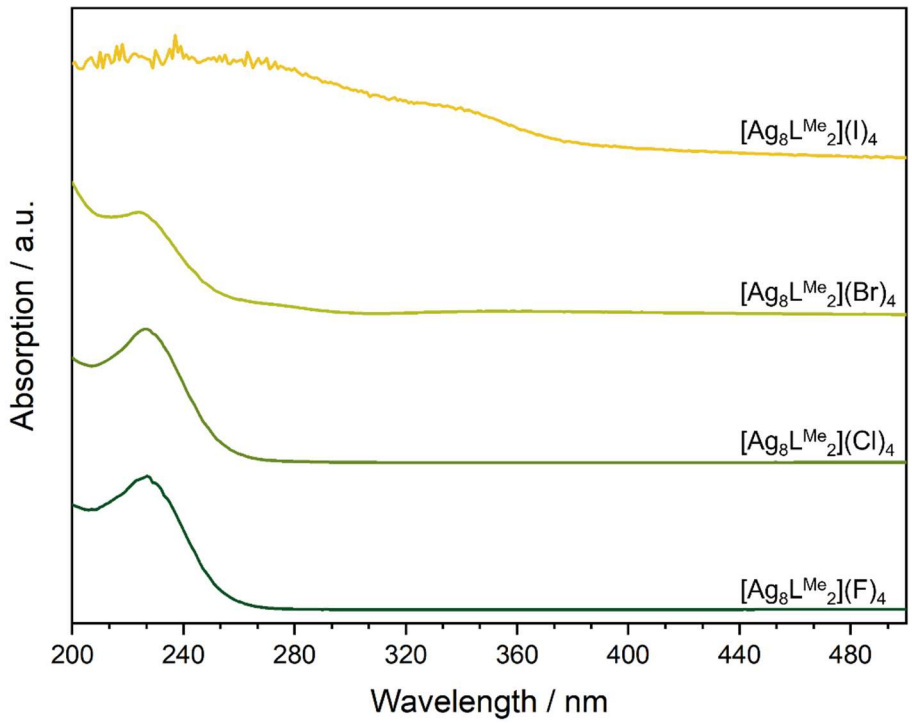

F33S: UV-vis spectrum of $[Au_8L^{Me}_2](Cl)_4$, $[Au_8L^{Me}_2](Br)_4$ and $[Au_8L^{Me}_2](I)_4$ in water ($c = 1 \cdot 10^{-5}$ mol/L):

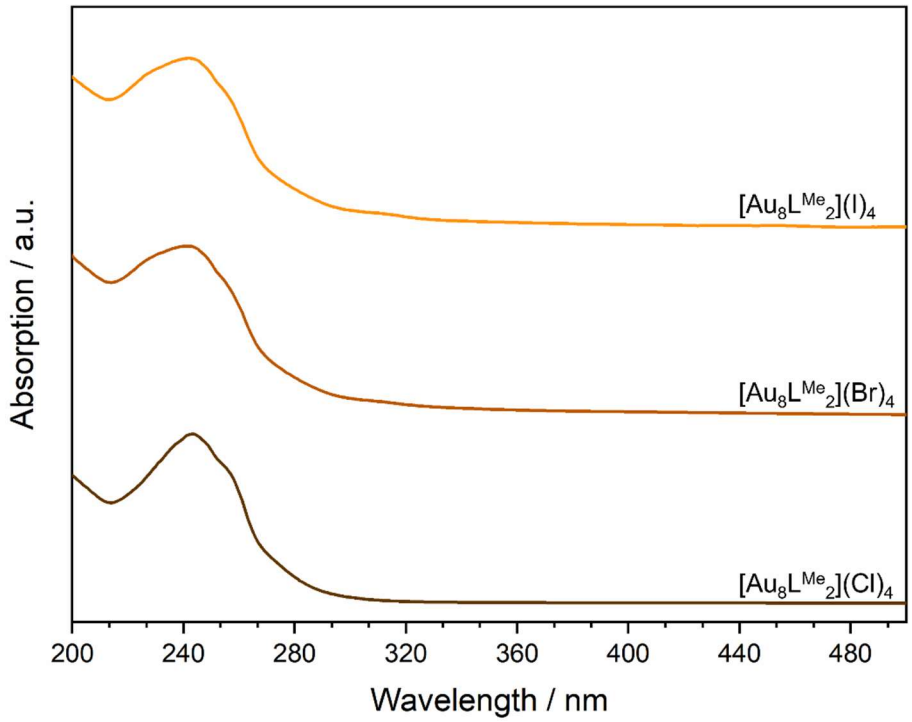

F34S: UV-vis spectrum of $[Ag_8L^{Me}_2](SCN)_4$, $[Ag_8L^{Me}_2](NO_3)_4$, $[Ag_8L^{Me}_2](ClO_4)_4$ in water ($c = 1 \cdot 10^{-5}$ mol/L) and $[Ag_8L^{Me}_2](I)_4$ in MeCN ($c = 1 \cdot 10^{-5}$ mol/L):

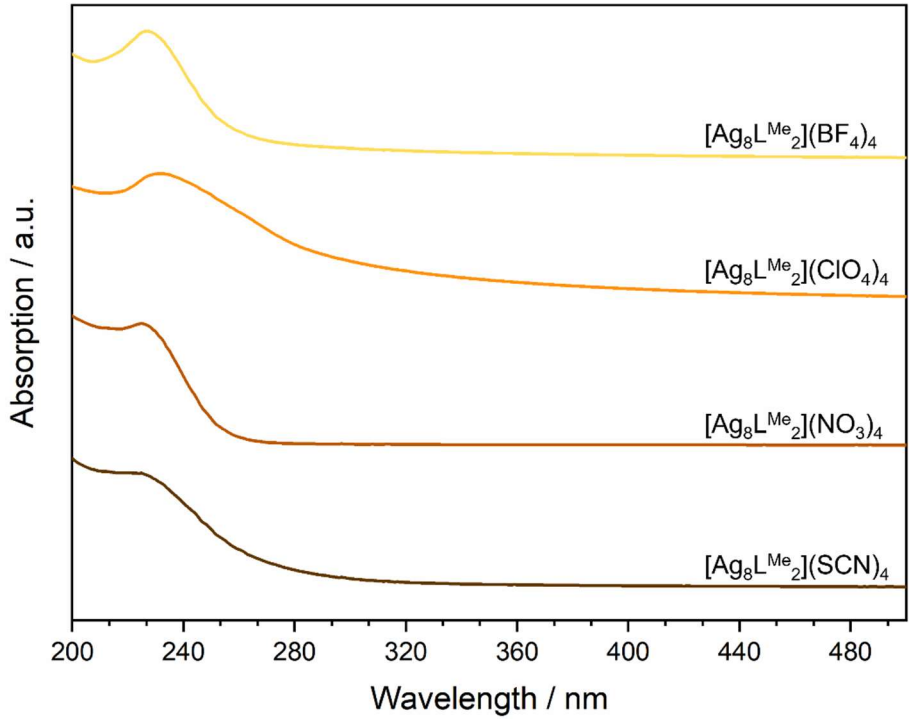

F35S: PXRD pattern of $[Au_8L^{Me}_2](F)_4$, $[Au_8L^{Me}_2](Cl)_4$, $[Au_8L^{Me}_2](Br)_4$ and $[Au_8L^{Me}_2](I)_4$:

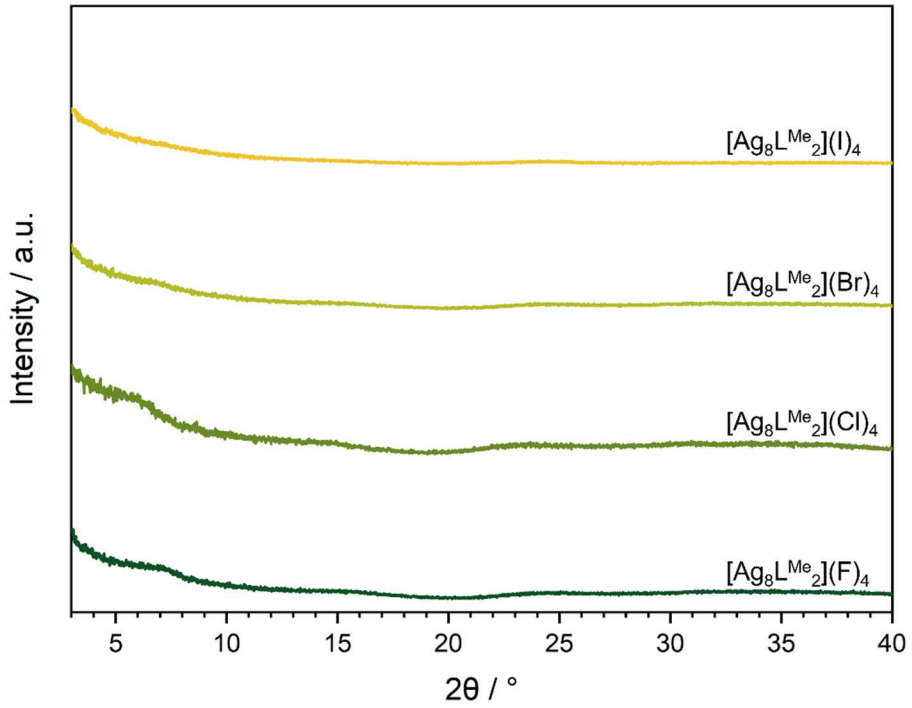

F36S: TGA of $[Ag_8L^{Me}_2](F)_4$, $[Ag_8L^{Me}_2](Cl)_4$, $[Ag_8L^{Me}_2](Br)_4$ and $[Ag_8L^{Me}_2](I)_4$:

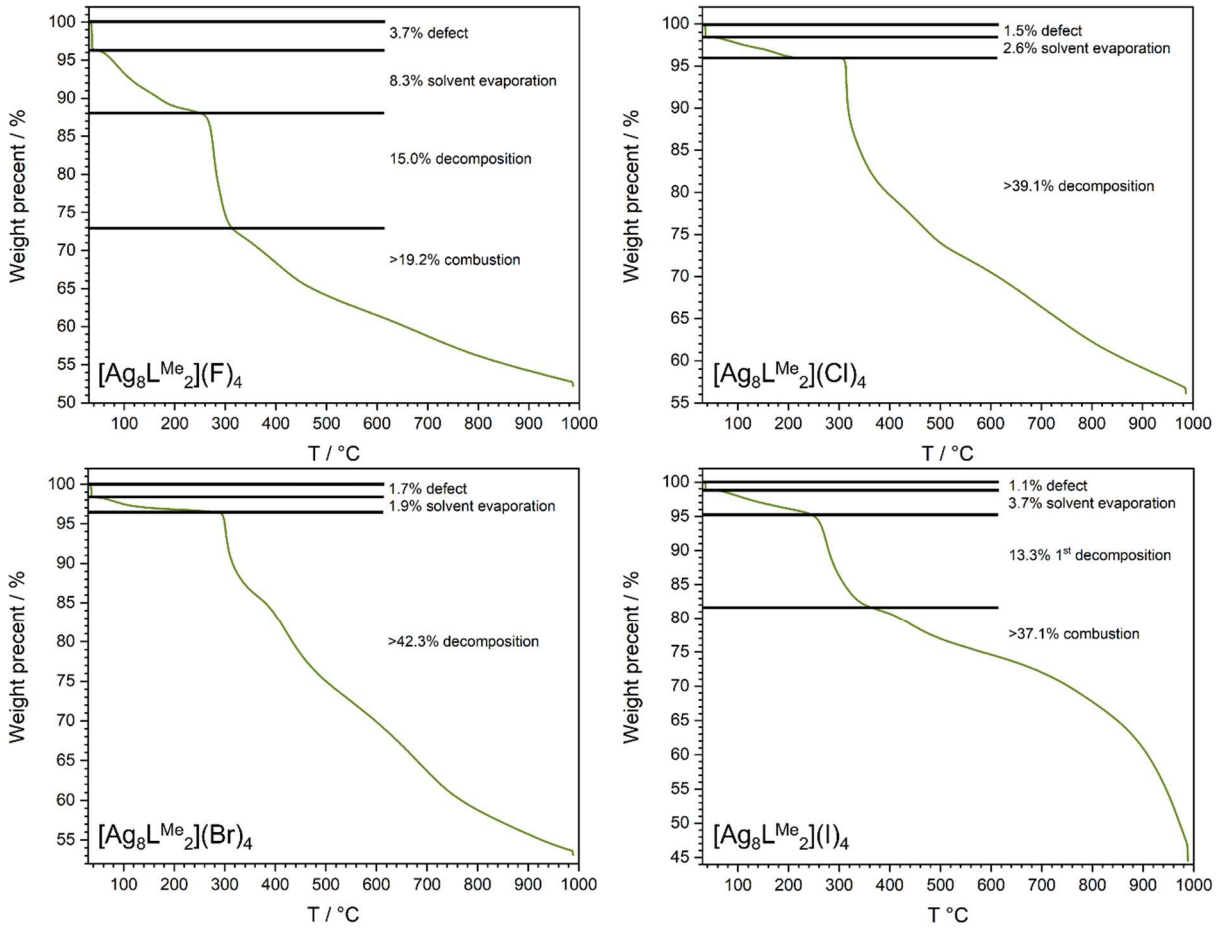

F37S: TGA of $[Au_8L^{Me}_2](Cl)_4$ and $[Au_8L^{Me}_2](Br)_4$:

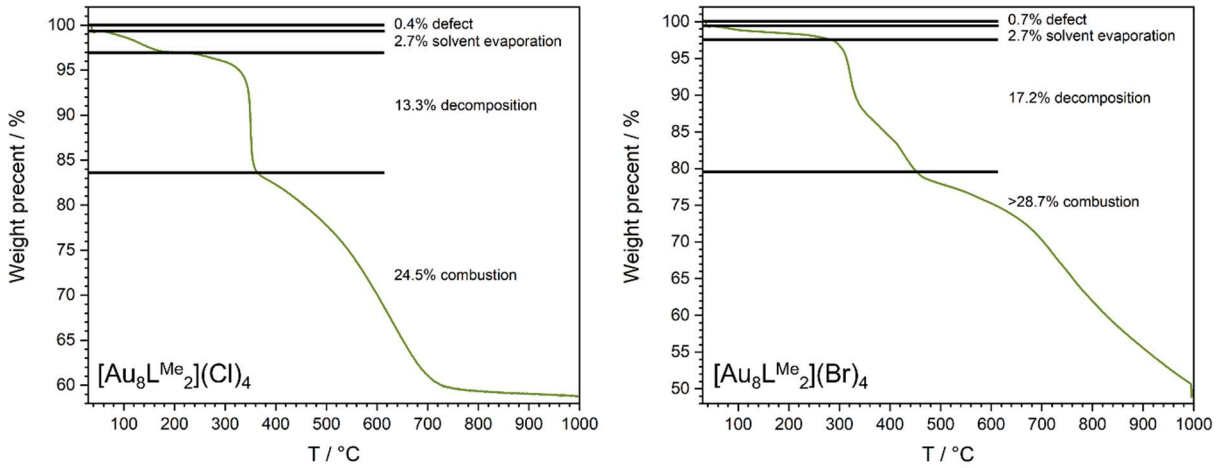

F38S: TGA of $[Ag_8L^{Me}_2](SCN)_4$, $[Ag_8L^{Me}_2](NO_3)_4$, $[Ag_8L^{Me}_2](ClO_4)_4$ and $[Ag_8L^{Me}_2](BF_4)_4$:

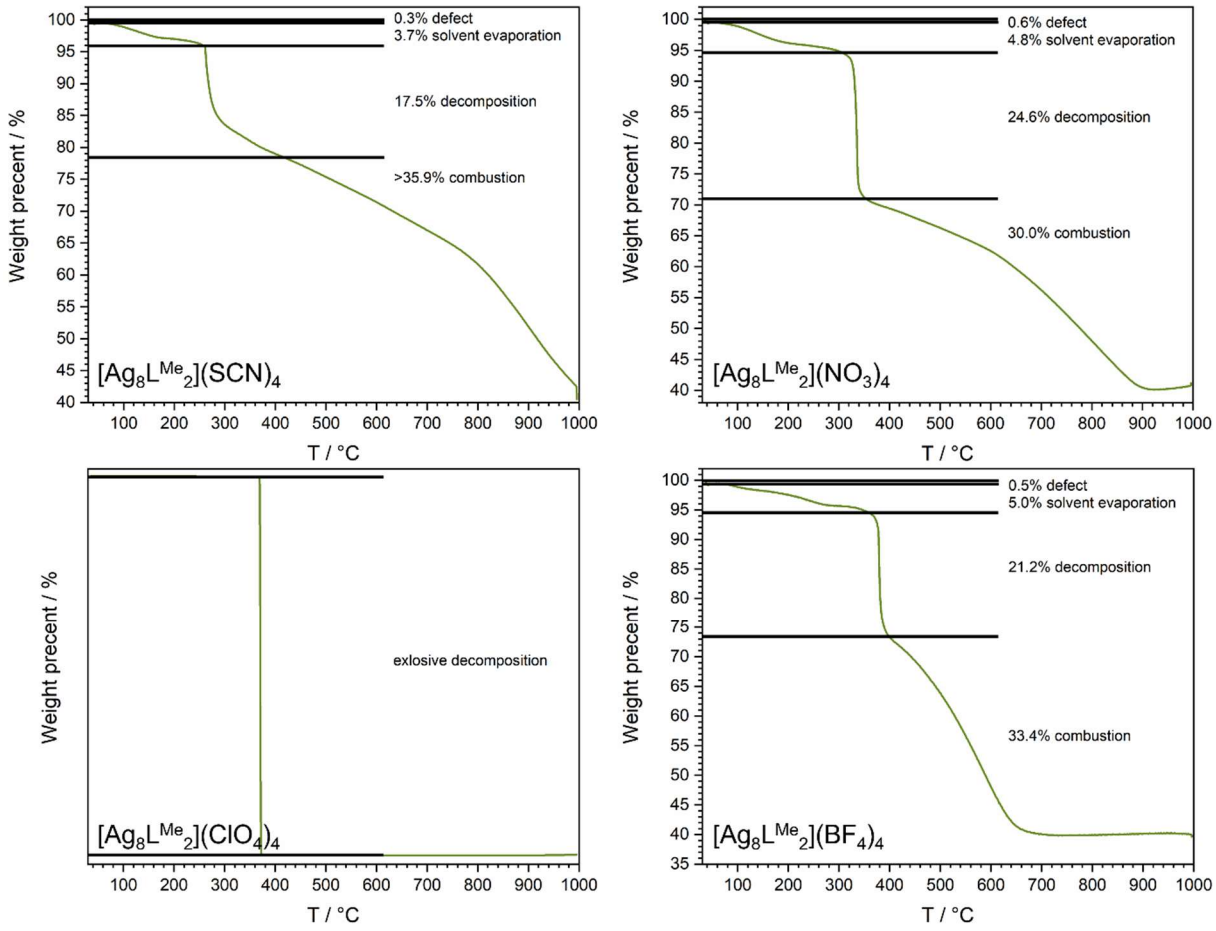

T3S: Table of crystal data, data collection and structure refinement of $[Ag_8L^{Me}_2](BF_4)_4$:

Identification code		AHE_157_4_08
Chemical formula		$C_{48}H_{44}Ag_8B_4F_{16}N_{24}$
Formula weight	[g mol^{-1}]	2167.27
Temperature	[K]	293(2)
Wavelength	[Å]	0.02851
Crystal system		monoclinic
Space group		*P* 1 2/*n* 1
Unit cell dimensions		a = 12.4(4) Å, α = 90° b = 14.1(4) Å, β = 93.18(6)° c = 21.2(6) Å, γ = 90°
Volume	[Å^3]	3700.9
Z		2
Calc. Density	[g cm^{-3}]	1.950
Diffractometer		ELDICO ED-1
Radiation source		LaB_6 source (electron, λ = 0.02851 Å)
Theta range for data collection	[°]	0.07 – 0.75
Index ranges		-11<=h<=11, -12<=k<=12, -19<=l<=19
Reflections collected		15303
Independent reflections		2782 [R_{int} = 0.2013]
Coverage of independent reflections	[%]	93.4
Absorption correction		Multi-Scan
Max., min. transmission		0.7431, 0.2382
Structure solution		direct methods
Refinement method		Full-matrix least-squares on F^2
Refinement program		SHELXL (Sheldrick 2015), ShelXle (Huebschle 2011)
Function minimised		$\sum w(F_o^2 - F_c^2)^2$
Data / restraints / parameters		2782 / 728 / 452
Goodness-of-Fit on F^2		1.188
Δ/σ_{max}		0.001
Final R indices	1866 data; I > 2σ(I)	R1 = 0.2437, wR2 = 0.5763
	All data	R1 = 0.2820, wR2 = 0.6041
Weighting scheme		W = 1 / [$\sum^2$(FO^2) + (0.3641P)^2 + 8.4300P] where P = (FO^2+2FC^2) / 3
Extinction coefficient		205.0000(490000)
Largest diff. peak, hole	[eÅ^{-3}]	0.387, -0.268
R.M.S. deviation from mean	[eÅ^{-3}]	0.078

F39S: Crystal packing along the a- and the c-axis showing highly symmetric chain arrangement with $[Ag_8L^{Me}_2]^{4+}$ cations displayed in cabbed sticks and the BF_4^- counter anions displayed in space fill:

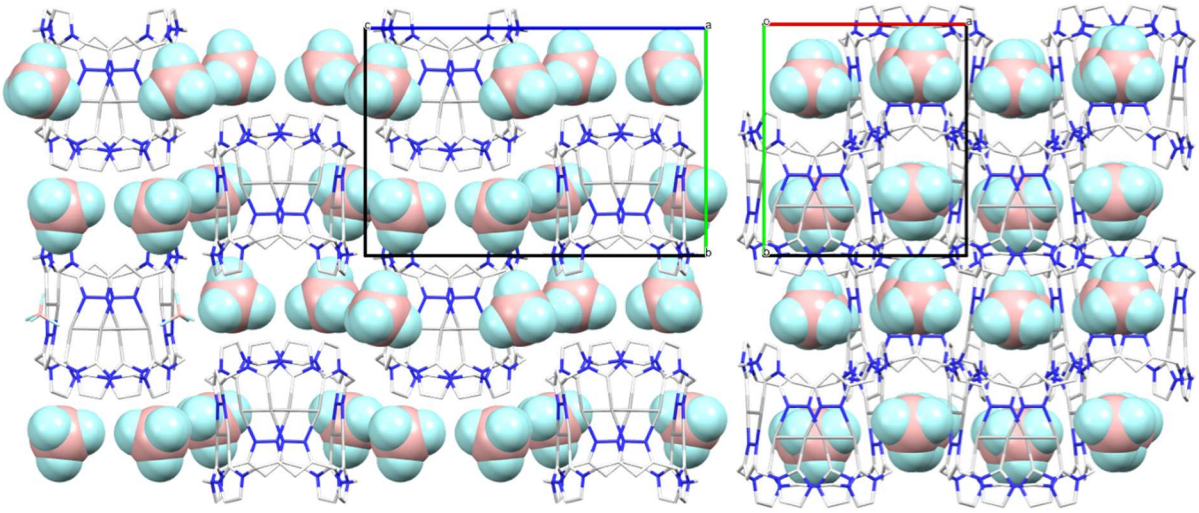

F40S: Comparison of PXRD pattern of $[Ag_8L^{Me}_2](BF_4)_4$; calculated from SC-XRD measurements:

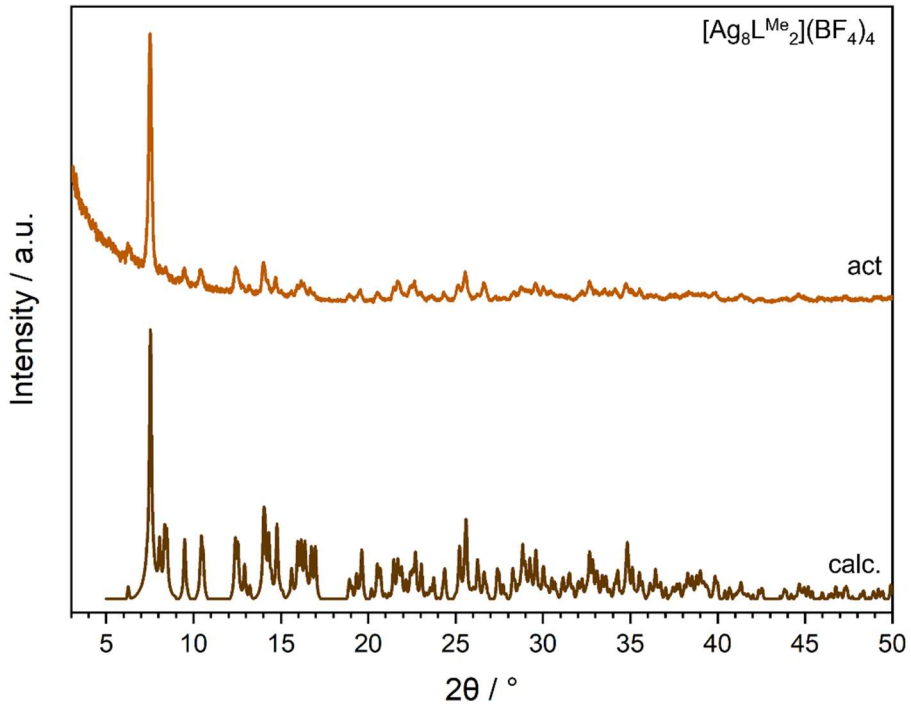

F41S: Physisorption Isotherms of $[Au_8L^{Me}_2](Cl)_4$ and $[Au_8L^{Me}_2](Br)_4$ for N_2 recorded at 77 K. Lines are marked in red and blue represent the ad- and desorption branch:

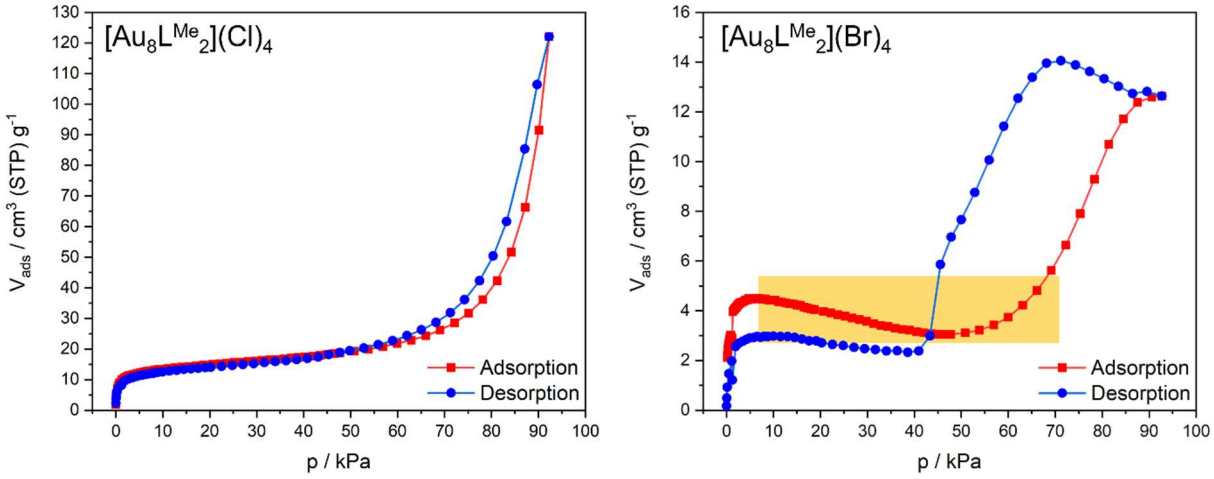

T4S: Overview of the BET surface area calculated for the obtained salts:

Pillarplex salt	BET surface area [m^2 g^{-1}]	Slope [g cm^{-3}]	C	Qm [cm^3 g^{-1}]	Correlation coef.	Molecular cross-sectional area [nm^2]
$[Ag_8L^{Me}_2](F)_4$	27.8825 ± 0.1177	0.155595 ± 0.000659	257.117378	6.40192	0.9999283	0.1620
$[Ag_8L^{Me}_2](Cl)_4$	165.6670 ± 0.0776	0.026240 ± 0.000012	806.441479	38.0618	0.9999985	0.1620
$[Ag_8L^{Me}_2](Br)_4$	124.9686 ± 0.0803	0.034770 ± 0.000022	590.134104	28.7114	0.9999977	0.1620
$[Ag_8L^{Me}_2](I)_4$	11.0425 ± 0.3424	0.378363 ± 0.012201	24.569851	2.53546	0.9958661	0.1620
$[Au_8L^{Me}_2](Cl)_4$	54.2850 ± 0.1008	0.079867 ± 0.000149	256.116734	12.4719	0.9999792	0.1620
$[Au_8L^{Me}_2](Br)_4$	19.2281 ± 0.0801	0.225948 ± 0.000943	542.635769	4.4176	0.9999216	0.1620
$[Ag_8L^{Me}_2](SCN)_4$	33.9741 ± 0.0847	0.127881 ± 0.000319	549.685428	7.8055	0.9999658	0.1620
$[Ag_8L^{Me}_2](NO_3)_4$	156.8829 ± 0.6061	0.027727 ± 0.000107	1659.395028	36.0437	0.9999328	0.1620
$[Ag_8L^{Me}_2](ClO_4)_4$	295.9144 ± 0.6252	0.014700 ± 0.000031	1692.727847	67.9860	0.9999710	0.1620
$[Ag_8L^{Me}_2](BF_4)_4$	138.7983 ± 0.1851	0.031287 ± 0.000042	436.899899	31.8888	0.9999893	0.1620

T5S: Aif-file for $[Ag_8L^{Me}_2](F)_4$ – AHE-084-1, $[Ag_8L^{Me}_2](Cl)_4$ – AHE-084-2, $[Ag_8L^{Me}_2](Br)_4$ – AHE-084-3 and $[Ag_8L^{Me}_2](I)_4$ – AHE-084-4:

AHE-084-1	AHE-084-2	AHE-084-3	AHE-084-4
data_raw2aif	data_raw2aif	data_raw2aif	data_raw2aif
_exptl_operator 'JBG'	_exptl_operator 'JBG'	_exptl_operator 'JBG'	_exptl_operator 'JBG'
_exptl_date 2022-05-01T10:29:31	_exptl_date 2021-02-11T10:54:41	_exptl_date 2021-02-11T10:54:41	_exptl_date 2022-05-01T10:29:31
_exptl_instrument '3Flex 5.01'	_exptl_instrument '3Flex 5.01'	_exptl_instrument '3Flex 5.01'	_exptl_instrument '3Flex 5.01'
_exptl_adsorptive 'N2'	_exptl_adsorptive 'N2'	_exptl_adsorptive 'N2'	_exptl_adsorptive 'N2'
_exptl_temperature 76.904	_exptl_temperature 76.838	_exptl_temperature 76.818	_exptl_temperature 76.941
_adsnt_sample_mass 0.0368	_adsnt_sample_mass 0.0475	_adsnt_sample_mass 0.0544	_adsnt_sample_mass 0.0271

_adsnt_sample_id 'AHE-084-1_N2_77K'	_adsnt_sample_id 'AHE-084-2_N2_77K'	_adsnt_sample_id 'AHE-084-3_N2_77K'	_adsnt_sample_id 'AHE-084-4_N2_77K'
_adsnt_material_id 'unknown'	_adsnt_material_id 'unknown'	_adsnt_material_id 'unknown'	_adsnt_material_id 'unknown'
_units_temperature 'K'	_units_temperature 'K'	_units_temperature 'K'	_units_temperature 'K'
_units_pressure 'kPa'	_units_pressure 'mbar'	_units_pressure 'mbar'	_units_pressure 'kPa'
_units_mass 'g'	_units_mass 'g'	_units_mass 'g'	_units_mass 'g'
_units_loading 'mmol/g'	_units_loading 'cm³/g STP'	_units_loading 'cm³/g STP'	_units_loading 'mmol/g'
_audit_aif_version d546195	_audit_aif_version d546195	_audit_aif_version d546195	_audit_aif_version d546195
loop_	loop_	loop_	loop_
_adsorp_pressure	_adsorp_pressure	_adsorp_pressure	_adsorp_pressure
_adsorp_p0	_adsorp_p0	_adsorp_p0	_adsorp_p0
_adsorp_amount	_adsorp_amount	_adsorp_amount	_adsorp_amount
0.017718095937645437	0.0004058713199445046	0.005143396341975778	0.06656131875357628
95.89653850825195	953.9511067925661	953.9877442757794	95.90061532236328
0.08399907607422002	7.58106940982424	7.403235543953848	0.0026616433248911496
0.07350363356437684	0.0031857007674984633	0.18655109413647653	0.1332174646941662
95.89407289013671	953.9981949309208	953.7681387656252	95.8973359688965
0.11562980671120678	15.094896897956048	14.10599513358534	0.004210467690140138
0.13934550378227234	0.0726947178465128	1.3457331149053573	0.28482380668659213
95.90079434414062	953.9741685158806	954.0889132412109	95.90387840112305
0.13396695369125117	22.370410198419187	18.751019198442215	0.006996361114236573
0.2831029153507233	0.9063780882754325	1.93266389498806	0.47639811934547427
95.91803739624024	953.6694326674804	954.2423023549803	95.9230744180664
0.15716715864189484	27.649690987595168	19.854595039615706	0.009779899446718388
0.4733683855550766	1.4709245504837036	2.8641697971611024	0.6782510220233917
95.92501110820312	953.7814026518555	954.6767556591798	95.92810330253907
0.17570841729664075	28.761224333726744	21.170536405389633	0.0025395034120082225
0.6735237917884827	1.8834394224586486	4.221219078231812	0.8715407587337495
95.92693966098633	953.7454355493163	954.7737529130859	95.92596317856444
0.18156014518504554	29.48324997783629	22.51116153396997	0.0050320660813009425
0.8764522237380982	2.400858608393669	4.762357537136078	0.9568857674171448
95.92285470952147	953.9282818828126	954.6822076860351	95.9299993059082
0.18381965747683385	30.160514901229067	22.81941556129172	0.004108035829089574
0.9759340405357362	3.107507818084717	6.618047948375701	1.324691221961975
95.92137371118166	954.1463629570314	954.831121255371	95.9221386224121
0.18523241493366285	31.044735011158746	23.753654246534637	0.04323433257247469
1.3122553114517213	3.3525813839378356	8.62553878225708	1.7571934685096742
95.93469455888672	954.2672026567383	954.5581130449217	95.92570278325195
0.2310241709597909	31.281535929078355	24.569085666054704	0.04595428850904874
1.7662157592201233	3.8273740288639067	9.608552701789856	2.1092893806541446
95.95423234467773	954.2893362583009	954.4038404105852	95.93378317529297
0.24312665071816625	31.618892045755796	24.870669103782166	0.04991145409418915
2.1234129019958496	4.2584261735858915	13.244913482162476	2.495402354855347
95.96042487070312	954.1923390043944	954.1004682832032	95.95205967128906
0.24932747036538008	31.91429633177579	26.175437499252777	0.051166002441078266
2.4920444250686646	4.7659770701236726	17.645997316703795	2.877988167745972
95.9687982074707	954.4626618881836	953.8909314301757	95.95709669311525
0.25349026476632786	32.25122593391021	26.832614836851203	0.053255429923759076
2.871602125282288	5.723684773818969	21.97112149909973	3.6433273721511843
95.97730987924804	954.5391530112305	953.8325866054687	95.96371236152345
0.25948101708690996	32.756058777970196	27.389480840928453	0.057518211895834975
3.6484991688949586	6.664067225429535	24.845125415130614	4.415022358236695
95.98886492124022	954.5666572661132	953.7320902895507	95.97503955761721
0.26874407903947295	33.154881477942524	27.675563152056412	0.06403014654513019
4.404915256585694	7.602106373519897	28.687802436584473	5.1735493262878425
96.00660435190431	954.5831760937499	953.7206486451936	95.98659459960939
0.2772489921051602	33.50399533297609	28.03389553785753	0.06892795703883932
5.187342140496827	8.570106875816345	36.40151515649414	5.950440266885376
96.00676709897463	954.6853812539063	953.4957815434572	96.00675896162109
0.2832804951144347	33.8813073376746	28.574457423145034	0.0741009937176682
5.949084380355835	9.707871644371032	43.933978498535154	6.716709926806641
96.00653925307617	954.6641427612304	953.26826113916	96.00059084765626
0.28886178306981986	34.11438473493662	29.076990041692138	0.07684163158012029
6.708414403482056	11.490308073509215	52.710510961120605	7.490634293463136
95.99549686435549	954.4922004814453	953.0949355092773	95.99966318935547
0.29197922332094706	34.41739463396127	29.53110090624264	0.08147036841328172
7.4752216373199465	12.998134250724792	59.13635016934204	8.251229675061035
96.00006191967775	954.6682114379882	952.9340600302734	96.0016649783203
0.2967846320151036	35.59523468941176	29.878768656362993	0.08655640743909397
8.245034606112672	15.790829476135254	66.89162950817871	9.016404352349854
95.9806136447754	954.5022094262695	952.9491955078124	95.99764512568359
0.3011376212555434	36.09386919903051	30.234202526388177	0.09038058051890008
9.003792471569824	18.488189247802733	74.52379577416993	9.585158573309327
96.01110430839843	954.5898487236327	952.8770985556642	95.98927992626953
0.30287510500620407	36.50925331177021	30.52638186634639	0.09402734274363364
9.589772452752687	21.019400789680482	82.18130481051635	11.1433376769104
96.00063153442385	954.7456790434571	952.8234733959961	96.00411432172851
0.303215979999508	36.84540365738554	30.857831534073988	0.10154139609540216
11.129157321240235	22.917973782485962	89.82344442041015	12.686672213360596
95.9970185494629	954.6922166308593	953.0051804999999	95.99689648916016
0.30860605214725556	37.091300712302	31.162373164270065	0.10941592624017414
12.663241721081544	24.783088266265867	95.42741600939941	14.186954046697998
96.00997321625977	954.7788794458007	952.9495210019531	95.998898278125
0.313980088672564	37.30095280750545	31.423018028790334	0.11881411974516012
14.20021386425171	26.747796328308105	110.82971737023925	15.732944411901856
96.00916761826171	954.8146024277344	952.9218539999999	96.00391088789063
0.31732729871678317	37.52237776297618	31.853675713086506	0.12697288184458524

15.731529529559326	28.688700088394164	126.15099103344727	17.275711367944336
96.00911879414063	954.7360705399943	952.9194127939453	96.00769475727539
0.3195213425481366	37.72049042951083	32.27712776378439	0.13418508311424932
17.26274449511719	32.41241154437256	141.54106602062987	18.819540248620605
96.02636998359375	954.7330661455078	952.7887268964844	96.01375708564453
0.3236280562856148	38.035810747502104	32.718952009296146	0.14050642871752325
18.805725056689454	36.31729863345337	156.80998598565674	20.753650844274905
96.02972257324218	954.777902963379	952.6499036455077	96.02991786972657
0.3246088438311738	38.34484214549396	33.13966941771885	0.14800775827731122
20.719500405908203	40.03948687857056	172.11672430114746	22.2444526607666
96.0410904561035	954.6979941518554	952.6435565097656	96.02523075410157
0.32563459349668644	38.62075491351325	33.52575151532027	0.15417082265748616
22.258780505969238	44.03285242959595	187.32413604528807	23.79159344432373
96.04709582299805	954.8050003505859	952.5508720532225	96.0485279972168
0.32623742050879057	38.93050250387057	33.932616804520016	0.15875213898336474
23.779554229797366	49.237773288024904	206.34668495507813	25.33665106538086
96.05149813125001	954.8696109375 39.24522188956013	952.2501968408204	96.0444104963379
0.32677344470433783	55.46258934933471	34.406791532153015	0.16529293866647368
25.31992880390625	954.8818983413086	221.57999382678221	26.870731396545413
96.04378392011719	39.60142239331862	952.203651178711	96.04746200390625
0.3294986606517771	59.32743048742675	34.83647906586433	0.1710994707720156
26.86266321053467	954.9307224624023	236.8780760324707	28.416494933020022
96.02795676752932	39.83509162307376	952.1785067563477	96.03645216459962
0.33010020658461514	63.16112590493774	35.20729040924796	0.1770698672166756
28.40058030388184	954.8872689946288	251.02750975927734	29.959931186389163
96.03145582954103	40.07715805513678	952.0847644438476	96.02299298188478
0.3275257114548296	66.93961446469116	35.564553408201455	0.1802774380789215
29.9341195010376	954.9562839164279	266.138188713501	31.49920721777344
96.03572794013672	40.29512012800932	951.9322704389648	96.04017907250977
0.3273807862878143	70.53911176217652	35.910690720054895	0.18363678413439946
31.471525975451662	954.9142850083008	281.31893028149415	33.04531862611084
96.03075601713869	40.458172754623256	951.7059706376953	96.03644402724609
0.32499186904321514	74.61436451879882	36.27160757925099	0.1860681262705986
33.00719512489014	954.8327487260741	296.3433736318359	34.586877185156254
96.05116449975587	40.63717413218512	951.4032610869139	96.03869807416994
0.32316272810182217	81.90757440994263	36.67924487711603	0.18891515515329227
34.55835982976075	954.8520342539063	311.5471845970459	36.132079244238284
96.04246566884765	40.91490341631729	951.3273395786133	96.04484991342775
0.3215718868363851	89.97504331640624	36.99083410516741	0.19151426374702185
36.08247800588379	954.8293310375976	326.7591329157715	37.60790222724609
96.0433689150879	41.24329814567253	951.2879547875976	96.04547648964844
0.32035393964468306	95.70305868804931	37.364493146440076	0.193370045765053
37.62267152387695	954.7980022265625	341.99099740722653	39.143685299633795
96.05596553833007	41.49237665921185	951.3966698305663	96.0527431463379
0.31935736341167625	103.02889428094483	37.72205950202998	0.19685099980485082
39.16900467509766	954.8235535166017	356.90550511157227	40.69336290314941
96.05689319663087	41.71865242580457	951.5415147231445	96.06195463051759
0.3188110097874859	111.10280695422362	38.064995683918006	0.1992000084957245
40.71547616132813	954.8079297978514	372.1984404411621	42.24511960048828
96.04685170239257	41.99269221356302	951.3672126108398	96.04943124345704
0.31557230864685126	118.76448129840088	38.429035183493816	0.2035616004694805
42.25257341630859	954.8181828632812	387.2750849143066	43.78694465786133
96.04737249301758	42.234398097636344	951.327827819824	96.0489430022461
0.31469472725126985	125.88309918402099	38.7717413084711	0.20690738215454887
43.78405589736328	954.8528479892577	404.1034167919922	45.32567345222168
96.04949634228515	42.43872290216186	951.4014708691404	96.04721788330077
0.31527273818118107	134.0343879175415	39.15692543235789	0.20979576769560732
45.32403377548828	954.8760394467772	419.32205808398436	46.86695737558594
96.05242578955077	42.65793466905643	951.3143198129882	96.04899182636719
0.3141011681758708	141.73962761810301	39.53341255676965	0.21291178240887992
46.874097903295905	954.8329928466798	434.660725340332	48.01294493986817
96.04654248295898	42.88164351385706	951.2237510683593	96.05504601738282
0.31100910705477974	149.34015992230223	39.91389647507992	0.21339895637704037
48.02381644416504	954.7455976699217	449.8893755771484	51.08157350002442
96.04622596119198	43.101000144429655	951.0804522729492	96.04999272084962
0.3110725483171364	156.95169799713133	40.34257978854953	0.2197279960839729
51.03520685969239	954.6450199804686	465.0916607885742	54.23699100410157
96.03727403730468	43.328007436870024	951.0344762255859	96.04544394023439
0.30884518065624844	164.6492377269287	40.76727046778251	0.22449863064631617
54.11262783032227	954.5507894267577	478.6510143251953	57.223652002294926
96.04049642929687	43.52053837268363	951.0914377001953	96.04288881123048
0.30898119171223515	172.3383451241455	41.1525598723724	0.22965175101521745
57.19864591494141	954.5236920395506	493.96982643896484	60.305434594409185
96.04493942431641	43.711319155513934	951.0337438637694	96.03806336059571
0.3058755516650503	179.0940980731201	41.58271996083902	0.23306373678395517
60.274492307666016	954.4269389062499	508.97156657299803	63.393564322265625
96.04854427192382	43.86975252381279	950.7162243295899	96.04232854860186
0.30882802047508506	187.546346826416	42.04382906674476	0.23400278773283267
63.353788938281255	954.3607822221678	524.2511159560547	66.47664889094239
96.05568073095704	44.06925320644895	950.6691090527345	96.03850277768555
0.3097359638424788	206.65389039367676	42.512163201231346	0.23448972777015048
66.42428095239258	954.3615145839843	539.3529048515625	69.51220317773438
96.04157869731445	44.43107602794045	950.6082416484375	96.05223863041992
0.31790877573596027	222.11813735815429	43.01650778523672	0.23523182531601877
69.48691228300781	954.3268494580077	554.3431713171386	72.60129718198243
96.05466356176757	44.713263339710196	950.5512801738281	96.04542766552734
0.3247913711206211	236.2761559929199	43.55960905832468	0.2342187543888138
	954.2359552192382		
	44.971577381319705		

72.55950373432617
96.05458218823243
0.3452190109850973
75.6304595775879
96.06075030219728
0.3826887417472054
78.70644430532226
96.05845556850586
0.4439491920101451
81.76509647006836
96.05836605761718
0.547780591802161
84.81891504682618
96.05096920327149
0.7397153012260862
87.84698703706056
96.07756207456057
1.1016086617023753
90.82475390786134
96.06699165234376
1.828574766087406
92.94088082695313
96.07018149492187
2.7738883767966804

loop_
_desorp_pressure
_desorp_p0
_desorp_amount
90.39964228549805
96.06570595048828
2.275513867603549
87.50341983427735
96.05509484150392
1.6110432007243083
83.84584217607423
96.04129388994143
1.0479921226798525
80.97392599980469
96.04056966547851
0.7937115528910169
77.87060790161134
96.04253076767579
0.6221185414363737
74.78415039990234
96.03803894853516
0.5160542264912418
71.69319294169922
96.03528038569337
0.4424814941982927
68.66283435512696
96.04017907250979
0.39319600714905545
65.52148633527833
96.04087888491212
0.3609482340655814
62.52471874401856
96.04853613457031
0.33762434335227987
59.44842886552735
96.0460786538086
0.318102420449811
56.36266303886719
96.04692493857422
0.30582199233767515
53.30789646042481
96.05721869077149
0.2957200488102328
50.219595848144536
96.05621779628908
0.2908836733529247
48.12594836813965
96.05546915976564
0.2887962129484123
45.75939032592774
96.06761822856446
0.2814795088138317
43.42118689204102
96.07294005776369
0.2797975587266565
41.19455064353028
96.07478723701172
0.27752337692319673
38.87696726345215
96.08316057377931
0.2794881206040724
36.538959126049804
96.06863539775391
0.28356656302154415

252.52942109765624
954.1891654365235
45.3104466202494
267.89496196398926
954.1755760561523
45.58536594469064
283.2533623026123
954.0662100249023
45.887408060630285
297.17590627001954
953.9808491865234
46.131139891199936
312.37349215979003
953.8469897211913
46.422523830325886
327.4825436433105
953.8766096879882
46.728493924978245
343.1706288596191
953.9152621171875
47.02267634937636
357.98834274389645
953.8714831552734
47.41032464997219
373.64965606713866
953.8339699555664
47.745907778085275
388.8064941591797
953.7085733378907
48.06390611406563
403.93220687402345
953.7563396030273
48.37790453703758
419.36563361206055
953.7116655322264
48.73128107177425
434.6993777695312
953.5466400029296
49.10138810682986
449.84799713452145
953.4559085112303
49.48615975072644
465.00544552807617
953.2996713237304
49.88422633401369
476.2289310512695
953.1744374531249
50.19777929217272
506.5222638515625
953.0356142021485
51.036915118680504
537.1941870241699
952.9493582548827
51.95578307603574
567.080611461914
952.8733553730468
52.94740626615673
598.4564970871581
952.8863751386717
54.07179507450617
628.7483651638183
952.9181108173827
55.28032621428525
659.141543291748
952.9987519907227
56.56354909612594
689.5764253564453
952.9308864624023
58.04690759933406
719.8975065322265
952.9531828110352
59.65179111413075
750.22 952.8184430194394
61.40207694519572
780.9133361572266
952.691648269043
63.47499674047598
810.6827861381836
952.6488457895508
65.86068287731146
841.3030778027344
952.5681232426758
68.97273734975703
871.4723159619141
952.2297720834961
73.35468712513031
900.8909646328125
952.1883529541017
80.73850552976019

569.598349326416
950.4244188325195
44.11220640157784
592.2953812463379
950.5726814135742
44.990299348310494
615.3808090495605
950.678304262207
45.92867479158238
637.9455276013183
950.5772383315428
47.014031682377066
661.3407444528808
950.5742275107422
48.242937677070906
683.9057478120117
950.5323201401368
49.61210854370078
706.6114053266601
950.5030256674805
51.10810305405747
729.1677424042969
950.3512640244139
52.81627250361393
751.7727408559571
950.3438590327149
54.734310873767036
774.8846964316406
950.2628923652344
56.96255193520676
797.3785386342773
950.2254605390626
59.311196447912415
819.9994862988281
950.1530380927733
61.839577654158276
843.0485401318359
950.3628190664062
64.5138509706619
866.1397454560547
950.2956045263671
67.09122614069986
888.6882706743164
950.2601256650391
69.62253310726526
911.8159313422851
950.2633806064453
71.355496499573
920.7070479140625
950.2460480434571
71.98313863623251

loop_
_desorp_pressure
_desorp_p0
_desorp_amount
887.8759186728515
950.1833904213865
71.30878547906129
857.0951583969726
950.115931760742
70.75415010042303
829.452324383789
949.9473257958983
70.61972043723362
796.1764887729491
949.7777433486326
70.41803032356998
768.6680024663086
949.7581323266601
70.1787789715719
759.2682199262695
949.5504670649412
70.09717783616657
736.0812379511718
949.5608828774414
69.69670933990999
713.3163405029296
949.6707371499023
69.10565986527185
690.666261112793
949.6333053237305
68.160588952381
667.9780582214355
949.568043748535
66.80695604463682
645.1277999348144
949.3964269628906
65.11796963896349

75.67167527314453
96.05948901240234
0.231106476132767
78.76120055712892
96.05708035576174
0.2263340745252478
81.83646919775391
96.05701525693361
0.22634766367965367
84.91832909472657
96.0561282854004
0.2236419289702584
87.9872668743164
96.05912283149414
0.23485237095073183
91.09093487871094
96.04726670742187 0.24009765625
93.16471501010743
96.0677972503418
0.24423101363053273

loop_
_desorp_pressure
_desorp_p0
_desorp_amount
90.13250924428712
96.06067706601564
0.23513533709416107
86.91291650170899
96.0718577897461
0.22388256259462216
83.84565501694337
96.06292297558596
0.2224672487774817
80.7508730025879
96.05968430888673
0.2199369248074779
77.6820084591797
96.04996830878908
0.2201111988199107
74.61512129267578
96.04366999716797
0.2153912293261527
71.53971431704102
96.04505334726564
0.21153100238758976
68.55883083984375
96.04142408759766
0.20697830634333847
65.46725087409668
96.03451547446289
0.20124600117436361
62.36079989479981
96.03176504897463
0.1936904083224073
59.28966096108399
96.03255437226562
0.18770830355192278
56.221073087695316
96.04786073422852
0.17954900594267026
53.15872249577637
96.05256412456055
0.17239985173020458
50.08796601767578 96.05983078125
0.16255051162848166
47.99674753769531
96.0538905131836
0.15749772942520415
45.69110572390137
96.05830909614258
0.15023311965012692
43.38277044609375
96.06168609785155
0.1442756912317012
41.08569726555176
96.06493290190429
0.13898639152975908
38.81196201489258
96.06931893544922
0.13299631261920858
36.548125854785155
96.07140209794922
0.12549190914576835
34.21935361362305
96.07782246987306
0.12027696880116104

34.21496351140137	921.5358373696289	622.3515508784179	31.905560205944827
96.08559364248049	952.1553966723632	949.5356570815429	96.07560097236329
0.2845905779419427	90.3666166170123	63.321306385171795	0.11173453104394547
31.922172613146973		599.4123920046386	29.60432680341797
96.07626009799804	loop_	949.3371056557617	96.07299701923829
0.2834059343842996	_desorp_pressure	61.62455324019165	0.10332331419308444
29.61094857484131	_desorp_p0	576.4432469831543	27.28591341328125
96.08056475800781	_desorp_amount	949.3339320878905	96.07314349160157
0.28178063791675095	893.5369941401367	60.093360444556694	0.09320240733512204
27.316967588635254	952.0439149291992	553.7995554155274	24.993474455566407
96.07639843300781	80.70793871401122	949.1992588872071	96.07290750834962
0.28264860626745064	861.5282258452148	58.771605441395536	0.08255557185690236
25.01729452364502	951.8799472558595	531.0308740979003	22.683249277404787
96.07683785009766	74.16416748696797	948.903466086914	96.07523479145507
0.28236309349254946	831.8652124482421	57.66985706481676	0.07112579770850326
22.68091589128418	951.6995421284179	507.99858321313474	20.368109137719728
96.07547891206053	70.64291892907919	948.8945149980469	96.07584509296875
0.2804895486852507	801.3088803823242	56.592547449236974	0.06108192387345516
20.379627561621096	951.3346631967773	485.2503673395996	19.23771274277344
96.08811622207031	68.09653029174326	948.6549513105468	96.08155751513674
0.2778097294819116	770.2870103217773	55.648366262484096	0.05470845346815242
19.244987536816407	951.3416613208008	462.8902218552246	17.702301954309082
96.09322648007812	66.09225706138625	948.7803479282226	96.0769110862793
0.2797190931468508	739.4438365444336	54.1261216162144	0.045847113675110115
17.704547863879394	951.318876730957	443.7388382958984	16.174136461981202
96.08947516010743	64.44859316824788	948.5660100366209	96.08254213491212
0.2777884563544199	709.108515 951.4130259111328	47.60639385604487	0.03945452976022948
16.1749563003479	63.081207360242026	416.5558461298828	14.620409507922364
96.08984947836915	678.9313429211426	948.4687686621093	96.0802962253418
0.27471919510443227	951.4963524111326	42.978091426709696	0.030987155004044423
14.628942540252686	61.907415155196	395.93505995947265	13.092820750524902
96.07990563237304	665.2607110751953	948.4160386113281	96.08966231923829
0.2728251513582659	951.3972394453126 61.47	41.89666155548726	0.022079623164058856
13.084552182183838	642.57230475 951.3742921083984	370.83942103051754	11.554498823840333
96.08087397744141	60.7333237877189	948.368597840332	96.08845799091799
0.2679375985924258	619.869495309082	41.0883765632367	0.012193176807043153
11.546836488336183	951.3755127114257	349.83215125488283	10.014811856103517
96.08525187363283	60.01107516987205	948.3428024296875	96.07906748496096
0.26333330238878805	596.8958340563964	40.54474014934139	0.002233736756823181
10.01182951604004	951.3205855751952	326.8408726318359	8.863994772509766
96.0839905838379	59.35656642311681	948.159874722656	96.08135408129885 -
0.259290831814192	573.9494329379883	40.03083608070028	0.006627317435610679
8.862643971826172	951.1644297612304	304.06370812316896	8.101697158273316
96.08532510981445	58.7243165507381	948.1793229975585	96.08577266425782 -
0.2540279270488716	550.9267848171387	39.55700425135109	0.010867618184932837
8.092149499676514	951.0886710000001	281.01215205395505	7.331972683200074
96.09086664755861	58.1183369868488	948.1171536166992	96.0828513543457 -
0.2495576760056708	529.8258541025391	39.111544608434386	0.0169973550389996
7.328345457870483	951.056853947754	258.2403581986084	6.564000282055664
96.09599318027344	57.53983416902444	948.135706782715	96.08566687866212 -
0.244810704587182	506.53459194213866	38.67436974475809	0.022500375261823295
6.556981814648438	951.0422067114257	235.45039770153807	5.796108745861817
96.09421923720706	56.95321511108254	948.1174791108397	96.08915780332032 -
0.24149947974319463	483.8422390004883	38.251473879963065	0.027014785212358138
5.78745467039795	951.0567725742187	212.73170007788084	5.027144096173096
96.09854017192384	56.404515449087775	948.1333469501952	96.0826397831543 -
0.23566362658056372	461.1669338144531	37.839917302502144	0.032665847357097814
5.02168596630249	950.7334755190429	189.93348016699218	4.257615171876526
96.09823095249023	55.831477541407295	948.0724795458984	96.09516317021483 -
0.22918720125380035	439.1333810134277	37.438620560635464	0.038361574009473175
4.252140767298889	950.6170299902343	174.7542440093994	3.4903774211791996
96.10225080512694	53.21246184407924	947.9539996787108	96.09816585366214 -
0.22374436913059842	414.5162184711914	37.14106398231152	0.04386673684280019
3.484789856529236	950.5328083813476	159.5624458123169	2.723261730784607
96.10989178007813	50.165238886004396	947.7985762265627	96.09922370961914 -
0.21635144470331702	391.43372011523434	36.8506131612107 24	0.04962261430540241
2.7199579652572634	950.4472847958982	144.44861363360596	1.9608921518280031
96.11836276508791	49.17543201183242	947.4660839619141	96.1000781317383 -
0.20717982380057162	367.73554959228517	36.56423834400311	0.05265949109345407
1.9499480470802308	950.5326456342775	129.2079709720459	1.2328217722320558
96.11668647026367	48.48281716588615	947.6604853374024	96.11447311010743 -
0.1964939521886279	346.1832398781738	36.22496844119661	0.11700533774755938
1.236815814200592	950.6369665063477	113.98243327294922	1.14964047313385
96.11601920727539	47.981962043153885	947.7269675156251	96.12312311689453 -
0.13376308620756708	323.68559346276857	35.89418095964781	0.07777591624002766
1.1454324441970827	950.6150770253907	98.8263377144165	0.4932749587503433
96.11558792753908	47.513025573344926	947.5394828906249	96.1181023697754 -
0.16226444301937606	300.60262720898436	35.54474921093478	0.08586559095059215
0.47466158903331757	950.6136123017577	79.83629753192139	0.2811417495803833
96.12181300297851	47.06654703523914	947.5360652021485	96.11700382705078 -
0.12813857433538828	278.05609564233396	35.04418994032652	0.08859625095311383
0.2827890868692398	950.5303671752929	64.67106779406738	0.16064229296722413
96.12460411523438	46.66344177296444	947.4138421523439	96.12069818554689 -
0.11019481571248907	254.95160608850097	34.58287410014109	0.09042016833289097
0.13544483476667404	950.4983873759766	49.521563491882326	0.09206578722338676
96.12812758930663	46.268821908869164	947.2938975615234	96.11903816542969 -
0.08716793767166252	232.13764039855957	34.058788853300825	0.09172609052620377
	950.452248581543		
	45.89852772332738		

0.04608410569639206	209.27218560424805	34.43158138774109	0.06991472690534592	
96.13153714042969	950.3491483125 45.53755180534677	947.1309063706055	96.13189518398438	-
0.05923373012982071	190.42098901611328	33.33704523482391	0.09224381881956342	
0.014711379573476315	950.2855142080078	19.26440758527374	0.06462921779816151	
96.15090404179688	45.23016558152579	946.9277166533201	96.13369353911133	-
0.03642621423313638	175.13474665979004	32.261902292236734	0.09248478440131776	
	950.2166721972657	5.009672689590454	0.06326312381687164	
	44.9304677430248	946.8041916269532	96.13410854414062	-
	159.98785648242188	28.992315374748767	0.09266831523852191	
	950.1624774228516	4.190200185934066	0.06307046958839893	
	44.663057968278345	946.5972587270506	96.15202699658204	-
	144.79046385479737	28.89833395506245	0.09278264753448373	
	950.3142390659181	0.8521128272151947		
	44.36108492807766	946.6710645234374		
	129.51854324066161	26.142895927655847		
	950.3119606069337	0.05368697951611876		
	44.04207515855882	948.0092720774084		
	114.31977743463135	22.452951032798886		
	950.2711110922851			
	43.702021979409984			
	99.07234008288575			
	950.277295480957			
	43.34619094698548			
	80.05702324603271			
	950.2481637553711			
	42.79891271893864			
	64.8179673684082			
	950.2427117285156			
	42.269447176312404			
	49.64831294458008			
	950.1394487124024			
	41.627118325889136			
	34.49199360882568			
	949.9828860307616			
	40.775420217195474			
	19.27511583391571			
	949.8015857944334			
	39.48094351165012			
	4.999388791219711			
	949.7386026782226			
	35.50265569179965			
	4.182648976163864			
	949.5861086733397			
	35.45956532288608			
	1.1489014997177123			
	949.6875000981444			
	32.643095886239614			
	0.04880501440492272			
	948.765321779216 27.53			

T6S: Aif-file for $[Au_8L^{Me}_2](Cl)_4$ – AHE-085-2 and $[Au_8L^{Me}_2](Br)_4$ – AHE-085-3:

AHE-085-2	AHE-085-3
data_raw2aif	data_raw2aif
_exptl_operator 'JBG'	_exptl_operator 'LSC'
_exptl_date 2021-02-11T10:54:41	_exptl_date 2022-11-16T09:39:01
_exptl_instrument '3Flex 5.01'	_exptl_instrument '3Flex 5.01'
_exptl_adsorptive 'N2'	_exptl_adsorptive 'N2'
_exptl_temperature 76.847	_exptl_temperature 76.869
_adsnt_sample_mass 0.0532	_adsnt_sample_mass 0.0392
_adsnt_sample_id 'AHE-085-2_N2_77K'	_adsnt_sample_id 'AHE-085-3_N2_77K'
_adsnt_material_id 'unknown'	_adsnt_material_id 'unknown'
_units_temperature 'K'	_units_temperature 'K'
_units_pressure 'mbar'	_units_pressure 'mbar'
_units_mass 'g'	_units_mass 'g'
_units_loading 'cm³/g STP'	_units_loading 'cm³/g STP'
_audit_aif_version d546195	_audit_aif_version d546195
loop_	loop_
_adsorp_pressure	_adsorp_pressure
_adsorp_p0	_adsorp_p0
_adsorp_amount	_adsorp_amount
0.009134446899365633 953.9848678968498 1.8670807619487964	1.767111821702957 959.2023448168944 2.1232059864602504
0.13539265915256737 953.9571694877928 3.4724632666063413	1.9599526371488571 959.0022472939453 2.1809371580849715
0.4577720668001175 953.9157503583984 4.652272690585222	2.4158094061517716 959.038539890625 2.294776127987193
0.9347316794314384 953.8641595371095 5.5246258354239925	2.8604062711601257 958.8552866894531 2.389793771604518
2.855371919403076 953.9049276782226 7.145955373128519	3.338549217103958 958.8588671249998 2.4768432040929387
5.038517064880371 953.755037626465 8.084659335924433	3.821856203876495 958.7931986821287 2.5532676818012474
6.969419508911133 953.788970390625 8.63299790121159	4.300382813323974 958.7194742592773 2.6209042277001395
8.605210020275116 953.7355079780274 8.880299422456945	4.779104274244308 958.7224037065429 2.6814874310847294
9.529788205604554 953.7370540751953 9.004457956460218	5.729345320358276 958.7227292006836 2.784931157217986
12.989551885688781 953.7619543769531 10.078677196085764	6.68562358347702 958.7420961020507 2.8723698168707625
17.605652572265626 953.8026411445312 10.585981806841328	7.65678048891449 958.6503881279298 2.9499689011715007
21.26564727875519 953.6702464028319 10.862090576290461	8.615443378051758 958.6362291328126 3.0150832048595624
24.69164984197998 953.8216011782227 11.118435325163539	9.657273834503174 958.5241191576366 2.9813951354385098
28.609007425323487 953.876446940918 11.348521146537099	11.677365487449645 958.5223875571288 2.892170326181832

36.23852905142212 953.8328307260743 11.717021841639157
43.7941126491394 953.9902071430663 12.041878612680247
51.82165257907104 953.8825499560547 12.346133859457128
59.084861064971925 953.9769432568361 12.572431846742816
66.63066966677856 954.0622227216796 12.775305505588104
74.46596970574952 954.0768699580078 12.94882171363687
81.97339034234619 954.16385826709 13.121396468078364
89.49146074035644 954.2609368945313 13.267087428595167
95.27848209667968 954.2705389716797 13.359818144853026
110.56481599822997 954.3118767275391 13.6350148508402
125.70430118389892 954.2961716352538 13.875464451096818
140.97178694036864 954.2971481176758 14.125618663588073
156.24771520111082 954.1643465083007 14.35521011641488
171.50996253625487 954.3550860747071 14.550779121502535
186.79677450732422 954.3616773310547 14.759125680595782
205.67791655639647 954.4277526416015 15.00497809952727
221.21782056518555 954.4208358911133 15.202260483326985
236.29395645373535 954.5085565620117 15.380850023089057
251.57834756213379 954.5024535468751 15.58085239050042
266.9549959160156 954.5364676845701 15.762095731955883
281.9084612003174 954.5174262773438 15.949070912766329
297.1997080290527 954.5787005493163 16.11418642511598
312.39674464746093 954.6070185395507 16.282979631661167
327.68803216296385 954.7070266142578 16.454880307341114
342.85164460180664 954.8019081562501 16.63954283380871
358.38865985009767 954.7073521083985 16.856538735471556
373.6765093337402 954.6468915717772 17.051608015313324
388.73 954.571369475578 17.264574086983846
404.2467155874023 954.5021280527343 17.490755403040946
419.3823151867676 954.5434658085939 17.719641302958326
434.91644167456053 954.6564936489258 17.943697321336224
449.94938855932617 954.5584385390625 18.219861276757193
465.41776523071286 954.5755269814453 18.492463358876748
476.84415566381836 954.6105989750977 18.682868029799728
507.1037998205566 954.7236268154297 19.279927347935306
537.8268255732422 954.691484269043 19.9700390625
568.2545467668457 954.6295590087891 20.79170738970463
599.2828046499023 954.7027138168945 21.797153361377354
629.3040650354004 954.7972698647462 22.90925745593981
659.9974708212891 954.7655341860352 24.348932232168092
690.7948312983398 954.7636625947265 26.196869365563884
721.3101511025391 954.7692773686523 28.563629863629274
751.5163328466797 954.6988892607422 31.73046539874186
781.7491237368164 954.7792863134765 36.10952790838993
812.039689836914 954.8856415239259 42.337750389981
842.2116133227539 954.9270606533203 51.597932287141305
871.9210096347656 954.9306410888672 66.310751109845
901.1463961596679 954.8908494301758 91.5487663965956
922.9060049545898 954.7858775698243 122.06249650254438

loop_
_desorp_pressure
_desorp_p0
_desorp_amount
897.6177955546875 954.7934453085937 106.40316959300776
871.0154849355469 954.796130635254 85.397493421791
832.5079006289062 954.8039424946289 61.67559319406273
803.6712354814453 954.8587068837891 50.383054402039946
774.8349772016601 954.8783992792969 42.34818334769467
742.8597348032226 954.8612294633788 36.11527871783649
712.4781930908202 954.8468263476562 31.855899920820924
681.7724999011231 954.7567458442384 28.686696475673543
650.9392536950684 954.6119823251953 26.261748543626386
620.3940698034668 954.5171821567382 24.345895120710065
589.7579102995605 954.5167752890626 22.744279809289175
558.8585887829589 954.4048866782226 21.44187669715095
528.4170747751465 954.3334407143554 20.33813939724235
497.89117641137693 954.3872286210938 19.434778013675857
476.88113993554686 954.3073198095703 18.847075761813514
453.6542035546875 954.2713527070314 18.161432443409563
431.02401999389645 954.1768780327147 17.389867830043343
408.0891739174805 954.1722397412109 16.927218886520713
385.31699353784177 954.0316262724608 16.56411879333164
362.64628595654295 953.9255965561523 16.22805352110025
339.51130167041015 953.8641595371093 15.91205990573868
316.59378815698244 953.854557459961 15.588455337734057
293.6518218962402 953.9048463046875 15.270586677564705
270.8821437528076 953.8563476777344 14.977519432981882
247.98572632836914 953.7778211141107 14.68804910833686
225.00394806555175 953.745679669922 14.368743526882819
202.03 953.7187062404121 14.083699092657595
190.70540986486816 953.6524255986328 13.936562309463408
175.35809667041016 953.5280054633789 13.712793222171443
160.10673304559324 953.3971568188476 13.525540641591698
144.88706441271972 953.2757475043946 13.328384594511741
129.303147493103 953.0776029462891 13.072717926602461
114.07082527551269 952.9264109179686 12.811237412838971
99.02854077758789 952.870263178711 12.525149895225336
87.59268049932861 952.8416196943359 12.285520237087233
13.13596449028015 958.4013851103515 3.9598107899362636
15.751423070274353 958.4506974726562 4.046022617723262
17.326949485816954 958.3700562993163 4.073270427032153
19.100673860847472 958.2947044057615 4.129238372998952
21.055619641593932 958.2315585424803 4.153824634634512
23.07570620869456 958.2341624956053 4.22691900955348
24.90654463371277 958.142210400879 4.2387785877472695
26.913043091903685 958.0311355253906 4.2869274929722065
28.739255940032958 957.9240393381092 4.323270843284256
32.520569687210084 957.9710004829102 4.340591961854979
36.48171640415954 957.9296627270506 4.375325815437427
40.19278190419006 957.808985774414 4.423357811238678
43.983199315612794 957.7385976665039 4.4421131577130515
47.94890803637695 957.7097097569747 4.48757579956886
51.63413743899536 957.7565812177733 4.472268908966579
55.58727394857788 957.7238690566406 4.467531872098247
59.42120840848386 957.7610567622069 4.493754501980227
63.42333686444092 957.7433987050782 4.506350101973221
66.91263913778687 957.7283446010742 4.4991932474164384
70.74968104193115 957.664710496582 4.49182787578343
74.72802808987427 957.8177741162111 4.469997206589895
82.33945936193848 957.7561743500977 4.479771780209514
89.87690683300781 957.8084975332031 4.427009368868951
95.60157571801757 957.8093112685547 4.4221700455326935
103.44396034039306 957.7364005810546 4.428672225023595
110.86295845935058 957.6865186040039 4.362728214592907
118.53673711688232 957.7398996430663 4.345410869176954
126.40511041204833 957.6866813510742 4.312191378979782
134.03528302642823 957.5280029575196 4.281110865189327
141.96732094116211 957.5360589375 4.275279698870135
149.65406850585939 957.5142508300781 4.231389163644978
157.28068102807617 957.3967474453126 4.216345402631867
164.8981390275879 957.5044046323242 4.152545345512631
172.14780899157714 957.4421538779296 4.113997088582596
179.78630204992675 957.4097672109373 4.073930727938013
187.54827944787598 957.2461250317384 4.053416091884121
206.4346700899658 957.2256189008788 3.973241838530593
221.8333503284912 957.0902947119141 3.9152101329529874
237.12596016394042 957.0430166879883 3.8416001110412084
252.5294821278076 956.8486153124999 3.7798302542162645
267.47977384423825 956.8089864008788 3.709609638180948
282.73228687023925 956.7930371879881 3.645055229067933
298.02906709936525 956.5498116914063 3.5711523372358926
313.11742936157225 956.5918818090819 3.4859262923457988
328.65025387280275 956.5957877387696 3.4135096596985197
343.8651926689453 956.6718719941408 3.370797605617894
359.1984892719726 956.4376789599609 3.2969033566723334
374.4437803967285 956.399677519043 3.2499762795089717
389.5218489067383 956.2202488740234 3.2199385577892423
405.0482042219238 956.1685766791992 3.1534949792560987
420.06996224560544 956.2056016376953 3.116063230094223
435.40468288549806 956.2275724921875 3.072740654966275
450.805722956543 956.1164162431642 3.056286107865673
466.1942315031738 955.9713272299805 3.052968875016498
477.30786275390625 955.9904500107422 3.0489140756796513
507.96212786938474 956.0636861923826 3.1144614108302133
538.4436369697265 956.1501862602539 3.2173556751259813
569.1999038115234 956.1001415361328 3.4269322273763
599.7520044536133 956.1558010341796 3.7387940366407126
630.6308198393555 956.0885051206053 4.228224821676081
660.9145505624999 956.4146502495115 4.813158121563686
691.7291622290039 956.4082217402345 5.6179552297153545
722.28 956.613227067503 6.6375497856565095
753.1149973183593 956.4884560458983 7.900122456793854
783.4561777573242 956.6158870019532 9.295910890816826
814.2130142138672 956.6225596631836 10.691478152031046
845.1185201191406 956.6083192631835 11.714840216936189
875.6217966401367 956.3135843188476 12.383345144156902
905.7960799584961 955.9831263925781 12.591272634407632
926.988596586914 955.9782439804686 12.637222346472887

loop_
_desorp_pressure
_desorp_p0
_desorp_amount
895.4731960356445 956.0401692407225 12.817123145785391
865.0233819272461 956.1422930273438 12.733584527009256
834.690908456543 956.1311448530273 13.024826270440318
803.8806909609375 956.1518951044924 13.334222049371563
773.3883184936524 956.0947708828127 13.61651383015348
743.118746765625 955.903380328125 13.88389459461903
712.3393698398437 955.8616357045897 14.05718291725085
681.4077430297851 955.8944292392578 13.953958507302685
651.4681003000488 955.8214371782227 13.389586172004567
620.8198975129394 955.772694430664 12.539749220515878
590.7191351835937 955.6066924189453 11.418025781732272
559.3054515512695 955.5770724521484 10.057907947817277
528.9267172258301 955.5270277280274 8.762768769020049
499.83409162353513 955.5280042104491 7.664228241383193

79.97672791021728 952.9089969814453 12.111394550751406	478.68531327026363 955.4795869570313 6.967128417392335
72.37228459048461 953.0221875688475 11.90405550839817	455.53206062548827 955.3908084301758 5.86470116159875
64.75053413699341 952.9406512866211 11.70189456246638	433.2391703679199 955.317572248535 2.991437462848847
57.142083170654296 952.9404885395508 11.482538815657154	409.34375039575195 955.1472574394531 2.3858650300870767
49.5528617878418 952.9120891757813 11.238065397880368	386.1848422902832 955.0653142895508 2.3327942366029704
41.95017054203796 952.7356713515624 10.964900192648026	363.3377168847656 954.9745827978516 2.3939303994879553
34.843809545150755 952.6227248847656 10.64356715351789	340.6266480300293 955.074753619629 2.380103092191052
26.81464214451599 952.5330512490234 10.220962477646406	317.28877917736816 955.1698792822265 2.436571900788742
19.10495995751953 952.3271945601412 9.680693886440578	294.3202241140137 955.201289466797 2.476186757349812
12.299144483963012 952.1366807592773 8.1959944518241	271.5997566159668 955.1644272553712 2.5264841050149465
11.105970695274353 952.1939677280274 8.545943751294043	248.62574952575682 955.1869677246093 2.5982777043438006
4.551939879163742 952.0920066884764 7.058587345262689	225.68899117126463 955.0939577739256 2.6471862976575795
2.8857820995140075 951.9199830351562 6.335532302126891	202.73998609973145 955.1113717104492 2.712122382495129
1.5673647453260422 951.6976705371094 5.426331204184549	191.29209270996094 955.1103952280273 2.7956238494978436
0.525877623209238 951.348089830078 4.021842967047901	176.0071319868164 955.1443279921875 2.791974378459374
0.08234921794804931 951.3167430223434 2.3116129590203607	160.71196905670166 955.1346445415038 2.865931843403068
	145.45611971575929 954.9551345229492 2.9225887908580965
	130.1683109188843 955.0448081586916 2.959154540390164
	114.9078029430542 955.0260922456055 2.9592049516904377
	99.64874951916504 954.9600983085937 2.9784642404710593
	88.1527440267334 954.8860483916014 2.9643546640791727
	80.54140938574218 955.0042027646483 2.9693034437791606
	72.93559288760376 954.9666895649415 2.9378897285701977
	65.25810156253051 954.9997272202148 2.966623649720367
	57.65974091455078 954.9556227641601 2.9148536767607176
	50.010226828033446 954.7962933823242 2.912792650912633
	42.364550012283324 954.6944137163085 2.8476547009328823
	34.731620869400025 954.6156441342773 2.7756826588825523
	27.149438297378538 954.6420905332031 2.7021930347347243
	19.52833756070709 954.5143340830076 2.564962028644728
	12.466489159011841 954.2774557221679 1.213760389854167
	11.396020304031373 953.9904512636721 1.9723924325665632
	4.752791378774643 953.8211129370118 1.4653654237618934
	1.7695862446889876 953.8344581967774 0.9301577167520593
	0.7202405767207145 953.7317647954101 0.4940536823647475
	0.3306265141160488 953.8007695532226 0.17060660645784873
	0.20120609829962252 953.6197948110351 -0.009509145578214966
	0.13218755307662486 953.4604654291992 -0.14763416862375683
	0.10400159617102146 953.4482593989258 -0.22219874119364277
	0.09993959458601474 953.4113971874999 -0.23248629406359841

T7S: Aif-file for $[Ag_8L^{Me}_2](SCN)_4$ – AHE-148-2, $[Ag_8L^{Me}_2](NO_3)_4$ – AHE-148-4, $[Ag_8L^{Me}_2](ClO_4)_4$ – AHE-148-3 and $[Ag_8L^{Me}_2](BF_4)_4$ – AHE-157-4:

AHE-148-2	AHE-148-4	AHE-148-3	AHE-157-4
data_raw2aif	data_raw2aif	data_raw2aif	data_raw2aif
_exptl_operator 'LSC'	_exptl_operator 'LSC'	_exptl_operator 'LSC'	_exptl_operator 'LSC'
_exptl_date 2022-03-08T11:11:20	_exptl_date 2022-03-08T11:11:20	_exptl_date 2022-03-08T11:11:20	_exptl_date 2022-11-16T09:39:01
_exptl_instrument '3Flex 5.01'	_exptl_instrument '3Flex 5.01'	_exptl_instrument '3Flex 5.01'	_exptl_instrument '3Flex 5.01'
_exptl_adsorptive 'N2'	_exptl_adsorptive 'N2'	_exptl_adsorptive 'N2'	_exptl_adsorptive 'N2'
_exptl_temperature 76.963	_exptl_temperature 76.965	_exptl_temperature 76.964	_exptl_temperature 76.859
_adsnt_sample_mass 0.0322	_adsnt_sample_mass 0.0316	_adsnt_sample_mass 0.0273	_adsnt_sample_mass 0.0209
_adsnt_sample_id 'AHE-148-2neu_N2_77K'	_adsnt_sample_id 'AHE-148-4_N2_77K'	_adsnt_sample_id 'AHE-148-3_N2_77K'	_adsnt_sample_id 'AHE-157-4_N2_77K'
_adsnt_material_id 'unknown'	_adsnt_material_id 'unknown'	_adsnt_material_id 'unknown'	_adsnt_material_id 'unknown'
_units_temperature 'K'	_units_temperature 'K'	_units_temperature 'K'	_units_temperature 'K'
_units_pressure 'mbar'	_units_pressure 'mbar'	_units_pressure 'mbar'	_units_pressure 'mbar'
_units_mass 'g'	_units_mass 'g'	_units_mass 'g'	_units_mass 'g'
_units_loading 'cm³/g STP'	_units_loading 'cm³/g STP'	_units_loading 'cm³/g STP'	_units_loading 'cm³/g STP'
_audit_aif_version d546195	_audit_aif_version d546195	_audit_aif_version d546195	_audit_aif_version d546195
loop_	loop_	loop_	loop_
_adsorp_pressure	_adsorp_pressure	_adsorp_pressure	_adsorp_pressure
_adsorp_p0	_adsorp_p0	_adsorp_p0	_adsorp_p0
_adsorp_amount	_adsorp_amount	_adsorp_amount	_adsorp_amount
0.001709614999724552	0.0079139674173519	0.00011896392849984113	0.01855574494678527
968.399845043691	968.3895537471349	968.3852943529438	959.1536636291261
1.7892765980512406	1.4840812447755194	1.8209450112656302	7.400339572877761
0.024888515905827285	0.009027859562762081	0.0002142747465900611	0.2567723227264881
968.4393033231322	967.9645654215395	968.4453555025527	958.7056407583008
3.421974966818477	2.985954942203665	3.6358860832746602	13.26792876647026
0.2603431229792833	0.010957167027890681	0.00031490267010207755	0.8590072476611137
968.2756567338865	967.7043884662639	968.5065298125976	958.4994402202148
4.379641371473732	4.49500301406125	5.452489362484374	17.062649040118863
0.665313202091217	0.015293821677312254	0.00044042544323578476	1.7564990916051864
968.0966349565429	967.4214295590035	968.3799026249467	958.0726360283203
4.778710650763385	5.994088028731821	7.268904040195658	19.422144311943033
1.1114099943223 967.998254352539	0.014386152141764759	0.000549477557355024	2.0893990185928346
5.0495944566099995	967.2367834592445	968.3616527964916	957.9557022583008
2.8954118309497834	7.50352404681688	9.096409895019685	19.952754479001477
967.8463299624024	0.0183129355359748	0.0006547380993068219	2.6226604557209012
5.580966999683957	967.0398291097293	968.2581027580769	957.6596653374023
4.968448729534149	8.99340751920305	10.910562480135724	20.881449422760024
967.7901008496093			
5.927571446383932			

6.862332572376251	0.02419382858593762	0.0007806854237057268	2.8909054535751344
967.7319187719727	966.8385895574769	968.1164449684087	957.7724490571288
5.936357647339032	10.485822150356643	12.735927264027842	21.183859151052786
8.910327719112397	0.03569644514170289	0.0009386351015833206	3.304783014398575
967.7280128422852	967.0190260563126	968.022916889811	957.748036996582
5.908648160721059	11.958000196374787	14.581173510017305	21.693166373785775
9.894038399539948	0.03742205429501831	0.0011436376237082295	3.81661937187767
967.5751119697267	967.1977213897187	967.8891477795745	957.7414457402343
5.878701521391015	13.461778433972293	16.392650000345164	22.309141173944862
13.360510946159362	0.052109155410736796	0.0012336875021634623	4.312344405126572
967.5096062739257	967.2708026246693	967.8447354805182	957.6797646005859
7.0491444675782535	14.927884931766563	18.21992957069678	22.758756970746827
17.763714306999205	0.05599661414015293	0.0013564965268475936	4.736589462913513
967.4922737109373	967.3367927082327	967.7644327966966	957.5730838959961
7.236809587518397	16.417967650814568	20.043570150554434	23.211161605462237
21.47888281324768	0.060354801685184235	0.0015702675080420448	5.744269099559784
967.4168404438476	967.4155519603512	967.7648790781532	957.3988631572265
7.37073705571117	17.903175895237645	21.87165263513562	23.756521658450712
25.08469927432251	0.07925804177463054	0.0018427163126869127	6.609635323448181
967.318541213379	967.3066793412063	967.6773564221068	957.4952094228515
7.460761361839952	19.358697895201175	23.710738401258077	24.17583417077998
29.09753344363403	0.11457004364919662	0.0020721191926980393	7.603520874423981
967.3298120882243	967.2156036914063	967.5475919633082	957.2097510615234
7.552138973791494	20.761773953179144	25.531486399924393	24.774518163595783
36.857761310577395	0.1357010680294633	0.002553270515852608	8.66106723058319
967.2610914975586	967.1587235903322	967.4727890606066	957.0369136728515
7.730305065790203	22.203445417250457	27.3518261209086	25.13381416719637
44.469853742614745	0.17695301017177104	0.0031172970086708663	9.564849391834258
967.3240746137695	967.3799782324218	967.4978457540687	956.6140967841795
7.8947585181812014	23.59990263883147	29.17350951256869	25.632708323943074
52.31809725952148	0.2506573081719875	0.0038332285378463566	11.702846847106933
967.2557208442382	967.3903940449218	967.4044478936439	956.6254077055664
8.024827581286115	24.887017015969725	31.00430894762478	25.757873031301965
59.85418172387695	0.35736729610919954	0.004665029134562239	13.430445142318725
967.227484227539	967.2843643286134	967.3135806756927	956.4093609697264
8.140579178968155	26.0828002232214	32.83141848406638	28.156152381745894
67.84266744277954	0.47981217621016503	0.005624540215160697	15.860900990135193
967.1255231879884	967.3580887514648	967.3018999062317	956.2177262944335
8.241858918697444	27.224033236855096	34.66670802933316	28.66846555158767
75.33357433758545	0.6336551222641468	0.007258093818504363	17.698878671401978
967.104610189453	967.2579179296876	967.2524077121044	956.2502757084961
8.296866356517487	28.29455253317786	36.48259190450661	28.990802440554432
83.0729705795288	0.8730384608988762	0.009046491316024214	19.142316767463683
967.1252790673828	967.3388032236328	967.2217132547818	956.0654734731281
8.350495064840985	29.121973487973953	38.30895190531855	29.297060099693347
90.94757912182617	1.1368044972667695	0.012195085026361048	21.126588807403564
967.108678866211	967.4340916333009	967.1215788980878	956.0183611333007
8.439440638432472	29.873843862777505	40.13224011963127	29.585039260155252
96.51631597009278	2.954417497764587	0.01699887760602683	22.95987352432251
967.0418711938476	967.559244130371	967.1301663323046	956.0572576831055
8.499947050778074	31.681713248039017	41.936710089720265	29.86862170288283
112.01699793493653	5.242365399215698	0.024276245116844772	24.926567609207154
966.9836891162109	967.6865123393554	967.1266174583282	956.1456293422851
8.585489951822366	32.629395228884974	43.735263269618	30.137967774484395
127.83588093731689	7.454829810848236	0.03597566503751278	26.82 956.0182912076629
966.8951547099609	967.7785458076171	967.0864588382769	30.42711316732791
8.673544157563251	33.24866068784274	45.51999722769968	28.755357728302002
143.04681208685304	8.67521160389328	0.05697259493073821	956.153249522814
966.971238965332	967.6582757226562	966.9978916751505	30.633462739100697
8.773618307517848	33.58703713975481	47.26173601745296	32.57572314358521
158.54138086486816	9.750972281581879	0.0960696134853959	956.0719862929689
966.8903536713867	967.5456594810553	966.9339296390095	30.93897667879647
8.87401443657488	33.74035146196893	48.928809380311684	36.41936393284607
173.8188755661621	13.16476436441803	0.16014770636880396	956.3834028120116
966.8557699189452	967.3837214150391	966.9380385629881	31.291181738298825
8.938526707025932	35.28070973545915	50.50244032928729	40.303633002456664
189.42092861242676	17.824513052375792	0.2550339964749813	956.3487376860351
966.8038536035157	967.2966517324219	966.8285911582032	31.61919031835672
9.040694587665561	35.72875751720527	51.94183682856057	44.12846633340454
208.66463044738768	22.03752993255615	0.38481020297527313	956.5031846557617
966.8587807397461	967.2798074106445	966.8393324648438	31.87563067147192
9.094701547852923	36.10929326819135	53.23128664334158	48.412498152008055
224.7527683059082	25.145294585861205	0.5474234519662857	956.5291428134766
966.9164745761718	967.2991743120116	966.8883193330078	32.215428765757245
9.108423137385468	36.31591934939312	54.38391964641351	51.724212856567384
240.41037913330078	28.963946071060178	0.7362416016669273	956.5831748408203
966.9756331362304	967.3294452670897	966.9516279433593	32.48892819581127
9.13462044513836	36.523645151965766	55.42802162651102	55.596692935272216
255.07926082177732	36.6953702494812	0.9627136065015792	956.6603169521484
966.9907686137693	967.2757387338868	966.9648918295899	32.78538349325728
9.179185187977078	36.75166937313165	56.31669935242053	59.47361804333496
270.258598696289	45.277618311035155	2.9925829572143554	956.6482736689453
966.9373062011717	967.2579993032227	967.1649893525391	33.08700800272378
9.185843526727444	36.979885903456804	60.03305808536662	63.31327407229614
286.90294501098634	53.02840684790039	5.158532539678573	956.4530585581053
966.9552897524416	967.2681709951172	967.1164093520507	33.36124705597091
9.192272732174272	37.21965392968499	61.704400356754036	67.08863992263794
			956.2714328276367
			33.666516822098934

302.19402909265136	59.90339745510864	7.545528244548797	70.96375446954346
966.9938608081055	967.2231714301759	967.1997358520507	955.9139588876953
9.184477541301863	37.4288001397834	62.80449740851499	33.8989455441062
317.5493168935547	67.6151622960205	8.681964335849761	78.63504614840699
967.0454516293946	967.1841121333006	967.3053587006835	955.94178863671 88
9.168158096020518	37.62957063718565	63.241319153099795	34.20162246795087
332.4348149326172	75.32281268756104	9.731024958045959	86.34871309570312
967.1409841596679	967.1658030878907	967.3165447920458	956.0666156396483
9.18782037616474	37.81977869531898	63.51088268806007	34.532640699469226
347.662651434082	83.04845680206299	13.15096137851715	93.968469897583
967.1486332719725	967.1984338754883	967.3755840615235	956.1462803305665
9.213406284502195	38.028951238813185	65.80507539276616	34.79298376721586
363.1007978371582	90.79818748297119	17.949036176010132	103.61039973486328
967.2068967231445	967.1164907255859	967.3379081147461	956.1732963442383
9.181140214537251	38.203442916919705	66.91082421834774	35.11874552500351
378.59322038818357	96.56320746972656	22.580301583740233	111.20902993267822
967.224392033203	967.1866347128906	967.3371757529296	956.163775640625
9.225485891418781	38.364202410901605	67.71796994375897	35.37582616478059
393.9927550488281	111.92153660650635	25.1403282572937	118.95402060516358
967.1969691518553	966.9387709248047	967.3516602421874	955.9638408647461
9.222547977558198	38.59526635817431	68.2360906391941	35.60558518452668
409.47614513745117	127.45524605493164	29.10955638345337	126.5617849822998
967.137322350586	966.8873428505858	967.3786416433619	955.8377118852538
9.241860684252583	38.85252179606702	68.81515798588279	35.83792305658396
425.04111219506837	143.79804239172364	36.881812276062014	134.1324023406372
967.1771140092774	966.8770897851562	967.3633780312501	955.8342128232423
9.255777177495592	39.09841470359736	69.77688688980457	36.07048453794501
440.4696158342285	159.14924117248535	44.608610877593996	141.87450425262452
967.1391939418945	966.7939260322265	967.395032336426	955.8381187529296
9.308905986577008	39.36181660704603	70.56381254571137	36.29036261489175
455.86862156689455	174.59707102624512	53.81764367953491	149.5052261383667
967.1815895537111	966.7425793315431	967.4330337773437	955.7773327221681
9.33286800092983	39.581670363791794	71.31904459912646	36.52228290004953
471.3184450722656	190.09988904638672	60.169219365234376	157.227076211792
967.2497805761717	966.7683747421876	967.3846165239258	955.680986456543
9.329417043176822	39.81626745085724	71.83069224323265	36.71532057050766
483.7861726347656	209.3401528494873	67.60533135580444	164.8440154550171
967.2653229213867	966.718655512207	967.4406015161132	955.5563222006836
9.318510187865488	40.03746284246958	72.24542800579901	36.89123439650336
514.1462317338867	224.76302137133789	75.66833997537232	172.39 955.5736901183736
967.2930712968749	966.7425793315431	967.4190375292969	37.01660907659107
9.38598497630654	40.248987163251435	72.68614841770821	180.13970731311034
545.0627637531738	240.13488903002929	83.23719763101197	955.5268649809569
967.351334748047	966.7093789291991	967.3650868754884	37.20026760239264
9.402253683881062	40.447238910297855	73.06576122284415	187.443734798584
576.161857298584	255.5562521414795	91.01768242236328	955.5480221000977
967.3265158198242	966.6724353442382	967.3922656362305	37.368894532825706
9.485266050542625	40.648654397364	73.47030512137718	206.817817380249
606.923413420166	271.10400869641114	96.87770601141357	955.3621649458008
967.3498700244139	966.6680411733399	967.3841282827148	37.446813112013565
9.615671997873626	40.84610936192091	73.70900080228304	222.01064291821288
637.842752826416	286.5083443956299	112.38091055584717	955.3081329184571
967.3528808452148	966.6271102851563	967.3357110292967	37.54597676560042
9.779299906674385	41.0072121138634	74.27231543633705	237.12569569995117
668.6268494172363	301.7748943564453	128.0886373092041	955.1928266191405
967.3251324697266	966.5677076044923	967.2863986669921	37.65265577431585
9.999769635692958	41.1737134114539	74.71569164159017	252.58503990893553
699.809310149414	317.48932425476073	143.39121540270995	955.0744281254883
967.3663074785155	966.5649409042968	967.2784240605466	37.74549033166017
10.342093143064984	41.309296380088	75.09687025411579	268.19535236901856
730.5647632558594	332.6979362585449	158.69247117626952	955.0485513413087
967.362889790039	966.5589192626952	967.2719141777343	37.8961101636984
10.89226792785074	41.469494588023196	75.4401667894242	283.4549855793457
761.3697728452148	348.23153381835937	174.46089241516114	955.0429365673829
967.3788390029296	966.5729155107421	967.2631258359374	37.956385364682504
11.732322128428406	41.656376748152 73	75.7119306128807	297.2532925019531
792.479282203125	363.9668156850586	189.70229795361328	955.1051873217773
967.3739565908204 13.2500390625	966.5899225795898	967.1880994365234	38.00604550986497
823.3401140375977	41.80403073734352	75.9616139254344	312.46043978210446
967.409191331543	379.51436880615233	209.2253754781494	955.2306653129881
15.89606796973729	966.6530684428709	967.1625481464844	38.035921422163334
853.9704146469726	41.951782349959096	76.20150539670063	327.97222923449704
967.42587290625	394.52778604248044	224.39667771606446	955.1553134194336
20.532482130800908	966.6195425463867	967.1775208769532	38.04956971923695
884.9521675546874	42.08478462079404	76.35598054451137	343.9317562207031
967.4353936098632	409.92463537646483	239.7847793950195	955.1392786542907
28.20655558954736	966.6637283759766	967.1934700898437	38.075079276667395
917.2012318989258	42.235477412488855	76.44540685785839	358.62789804345704
967.3776183999024	425.5117360356445	255.90748066259766	955.1304944912109
34.60040237801335	966.6278426469727	967.1900524013672	38.123633153077556
938.213180652832	42.364445632665614	76.58905848345714	373.7038101547852
967.3927538774414	440.84836895361326	270.8533578647461	955.1020951274415
35.19979583051789	966.6153111225586	967.1415746248717	38.20072446491351
	42.50676506810756	76.66488311839696	388.99178169873045
loop_	456.5595642539062	286.3141261105957	955.1663802202148
_desorp_pressure	966.6696686440429	967.1934700898437	38.19109445525807
_desorp_p0	42.64687004219045	76.7401716951972	404.9536074873047
_desorp_amount			955.1345631679687
			38.19959401986049

905.8059261562499	471.98204625146485	302.25898551708985	419.6089811689453
967.3453944799804	966.6653558466797	967.1542480458985	955.1478270541993
35.28481036514841	42.79042263773799	76.73817619850762	38.1913307437792
874.9758535180664	483.4865552783203	317.4804545394287	435.5317476606445
967.3662261049805	966.7152378237304	967.1953416811524	955.0594553950194
35.335341268811284	42.89748564178616	76.73880152910264	38.215377655460074
844.3507608149414	514.58145808667	334.69824015637204	450.1333741223144
967.4022745810546	966.6500576220704	967.1687325351562	955.0155950595703
34.467266320509744	43.06667800568791	76.77227346687162	38.283295666080654
815.8083423706055	545.3702743425292	349.02228114624023	465.32593519628904
967.3266785668945	966.5850401674804	967.1901337749023	955.0312187783202
26.83444320241051	43.19238129688293	76.74392039083028	38.273966224412
782.4097140952148	576.387628171875	364.4784111005859	478.1621628127441
967.2584061708984	966.5940726298828	967.1767885151366	955.0046910058592
18.69402940480824	43.37075303537498	76.74514026544668	38.333588927909986
751.3823106342774	607.1305090671386	379.9563491623535	507.3924724365234
967.2976282148438	966.5304385253905	967.1513999721678	955.0054233676757
14.302061339746329	43.49799387218015	76.70453156749025	38.332312244533036
721.6035026967774	638.0760100649414	396.7549390129394	538.4706122966309
967.2545002412108	966.2312280366211	967.2034790346679	954.867006984375
11.926986962503019	43.67602424577793	76.65240498553257	38.324415263586662
690.5571392021484	668.828533724121	412.0106459501953	568.9652225361328
967.264997427246	966.2103150380858	967.1854954833983	954.9486246401367
10.498113640770805	43.800121814689746	76.60992027036248	38.46749874887838
659.3330559067383	699.6429826435547	426.6625612565918	599.0208632402343
967.1641756171875	966.078652658203	967.2157664384766	954.9989134848632
9.627164366978002	43.899223293819254	76.5199524290901	38.556562506069646
628.0454605671387	730.6507750825195	442.03707355517577	629.5680000966797
967.1816709272462	965.9928849521484	967.24880409375	954.9817436689455
9.13270977221772	43.97947784001288	76.42611706969238	38.79281863420931
597.1035806916503	761.3764454750976	457.631741953125	659.9991389787598
967.1588863374022	965.9981742319335	967.2998253002929	954.9480550253907
8.829900872467253	44.046054956706663	76.39740775905281	39.19303748654724
566.6790737526856	792.4151598574218	472.99372272729494	690.4930982299804
967.1741031884765	966.0187617363281	967.3035684829101	954.8183456103515
8.580509823965984	44.15410695258131	76.28606483300011	39.76298284444458
535.0389275720215	823.6516933037109	484.6010065290527	721.0430017866211
967.1777649975587	966.0194127246094	967.2815162548828	954.6459150893554
8.448676717483302	44.2227944161059	76.24058815266868	40.54575592895209
504.1840360056152	853.9267170585937	515.6810586672364	751.3786488251953
967.1977015136719	966.0136352036134	967.2993370590822	954.5302832958986
8.323061821637333	44.22818138300395	76.0943943435342	41.73486486505902
482.812741720459	884.8906491621093	546.5107244377441	781.9580096015625
967.1831356508789	966.0556239477538	967.3487307949218	954.6339531796875
8.246474281510597	44.3726714239348	75.89792209874547	43.43450620967649
459.5878396779785	915.837899690918	578.4720519616699	812.4231219345703
967.2089310615233	966.0251902456055	967.3546710629882	954.4824356572266
8.1806512055392	44.45468517300031	75.73500775588033	45.989016825238046
436.5426510878906	937.1746102236328	609.262821182373	842.7458305810546
967.1861464716795	965.9727043154298	967.3104852333985	954.2012087197264
8.145990475768473	44.577396221323546	75.55300997711717	50.07440750209043
414.29260399658205		640.601885282959	872.774780765625
967.1885876777344	loop_	967.2071408437499	953.8899549477538
8.13391183828574	_desorp_pressure	75.43182983200028	57.38723670561392
390.9928383017578	_desorp_p0	670.6301031057129	902.75 953.7998486465807
967.1547362871094	_desorp_amount	967.2779358193359	71.30185791621888
8.12663393015911	905.42 966.0499527821061	75.46819884837723	923.1490677041015
367.6118211320801	44.6486114956668	699.6612916889649	953.8603349809568
967.117060340332	874.7577724438477	967.2999880473634	90.83807100708515
8.087481430007085	966.0911841826172	75.36446611944235	
344.29976803344726	44.68568015404435	732.2435806596679	loop_
967.1510744780272	843.8529989003906	967.3626456694337	_desorp_pressure
8.039337914107914	966.0067998266601	75.37609236724428	_desorp_p0
321.2946559094238	44.68014678518265	763.0249919238281	_desorp_amount
967.1385429536132	812.7763644506836	967.2461187670898	895.9123690048827
8.004625435260596	966.0919165444334	75.59610362206644	953.8396661030273
297.8771020224609	44.71630286260039	792.2461470249024	72.54908668333456
967.1879366894532	781.8507592822266	967.3971480483399	864.7234390766602
7.923443205883213	966.1331729267579	75.91149851701658	953.736891328125
274.66064248425295	44.74169155729466	823.27 967.2948010946143	59.5405076195959
967.2549884824219	750.9267002109375	76.64166021751235	833.2598734672852
7.84567542050039	966.145216209961	854.3644253041992	953.6234566201172
251.87420139257813	44.760898324591224	967.2660552832033	52.9351385559905
967.2265891186523	720.47 966.2344149490923	77.86755435991441	802.1185470571289
7.759681940369729	44.73026718882983	884.949319480957	953.5140905888671
228.36156252978515	689.7156554750976	967.315937260254	48.9942479024465
967.3279805434569	966.2075483378906	80.3952881349014	771.7511643398437
7.709675005584755	44.68453390234132	916.006668402832	953.4390641894531
205.12819763964842	658.5123631179199	967.2715073100586	46.42267973779435
967.3239118666991	966.0948459916991	85.39678474904493	741.172047684082
7.628033115216809	44.63699492179108	936.550312461914	953.392599900879
193.8068604404297	627.3444682485351	967.252954144043	44.75654967413876
967.2457932729493	966.0221794248047	92.97185811438884	711.1746704311523
7.562138705179989	44.58978602169413		953.3663976225586
178.05782644628906	596.5905612392578	loop_	43.70195676758422
967.3426277797851	965.9822250190431	_desorp_pressure	680.6798974445801
7.507413528676247	44.49319070148563	_desorp_p0	953.4258816767579
		_desorp_amount	42.938644546631785

162.63767376617432
967.3011272768554
7.459873311144243
147.07672452685546
967.2488854672852
7.430420849427618
131.73238146643067
967.2927458027344
7.314111899242753
116.22322648223877
967.2057574936524
7.241002991952037
100.75929484020996
967.3528808452148
7.096556003398006
89.17733855126953
967.4052040283203
7.018760258444484
81.4506213232727
967.3192735751953
6.897503433263772
73.72441776571655
967.4329524038086
6.831328604714596
66.00475460604858
967.4082962226561
6.7404419662891
58.20248713650513
967.3171578632813
6.6279987396219235
50.46654418395996
967.2531982646485
6.5129365839587114
42.75318238742065
967.2518962880858
6.408998814702818
35.05041186506653
967.2432706933592
6.323101949813783
27.335633660430908
967.252465902832
6.214485120965896
19.6261777935791
967.1742659355468
6.069546514308503
12.519598105316161
967.2521404086914
4.5413242195601
11.472197376091003
967.2450609111328
5.53627129723599
5.0401658325634004
967.2363539428712
5.046739611057122
3.8527829152164457
967.3479170595702
4.893054384887246
2.274170503712654
967.3420581650389
4.61277276127571
1.0673924744467735
967.3418954179688
4.251314201577701
0.20151242118501664
967.3696437934572
3.597985404934749
565.4308850969238
966.0278755722657
44.388893748461086
534.6953685065918
966.0185989892577
44.270498329132515
503.66117035546876
966.103552959961
44.15136260088266
482.96950783593746
966.1422053891602
44.06181244032491
459.20143744628905
966.1691400292967
43.92996121413963
436.12203128466797
966.2804590253905
43.80850177129166
412.8750770141601
966.3333518232421
43.70444428393871
389.659980482666
966.4482512548828
43.6110727454382
366.44988842358396
966.5014695468749
43.50157844748575
343.2614417248535
966.6169385932617
43.390494635645105
320.2031113088379
966.616043484375
43.26123745615835
296.9727775828857
966.7145868354492
43.10651037801876
273.99160962158203
966.7766748427733
42.95412578623099
250.7175376204834
966.8796123647461
42.7984627195772
227.337741053833
966.8447031181641
42.62821667962932
204.14018051916503
966.9329120302734
42.43883223254582
192.774026845459
966.9302267036132
42.32064268538304
177.17791406726073
966.9971157495116
42.16135525612924
161.72324883654784
967.1476567895506
42.0150929288531
146.21897626446534
967.0847550468751
41.87394174103245
130.74986723126221
966.9146843583985
41.6955577700827
115.28573215539551
969.7221526948242
41.424525060490964
100.17056748504639
970.0947621123048
41.17955609337692
88.54103819311523
970.1959094165038
41.00581657968918
80.8167621711731
970.2494532026368
40.81068891299359
74.11541251629639
970.5462224853514
40.65164630873118
65.32023534246827
970.241722716797
40.48347894244792
57.54871181167602
970.3784302558593
40.33454569727369
49.8080390223999
970.4125257670898
40.170647630319486
906.6579884428711
967.1903778955077
84.83652015297129
874.5979548208007
967.200956455078
80.7050585246249
843.6114008745117
967.2453050317382
78.69885667370828
812.4795137944336
967.2494550820312
77.47361929998924
783.0148890761718
967.2545002412108
76.732951809408
752.412825083496
967.2848525698242
76.21147770665281
720.9162218188476
967.3873832241211
75.84518625475611
690.03 967.3881949386918
75.65136083772177
657.4963331579589
967.2712631894531
75.58207282365937
626.3248578530273
967.2746808779297
75.57474556146487
595.5320949807128
967.2146272089843
75.6570438218784
565.5487953493653
967.310647980469
75.62544400880121
534.6979317729492
967.1866347128907
75.6899469032439
503.80788683935543
967.088905097168
75.77812713340045
482.192227828125
967.0870335058594
75.89302841602947
459.060539170166
967.2067339760741
75.82650969768551
436.02922476782226
967.2686592363282
75.70953505450989
412.66672007739254
967.3366061381834
75.74661930361847
389.50297024658204
967.1996544785156
75.79182080135085
366.2024721899414
967.3022665063476
75.85753288400406
342.93440148706054
967.2594640268554
75.94864167295981
319.8742198231201
967.3273295551758
75.90274941270299
296.06768009472654
967.4309180654295
75.87419121769285
273.4740739379883
967.2837947138673
75.84962852753192
249.98194120605467
967.321226540039 75.786395715097
226.8789163758545
967.3731428554687
75.64285020733136
205.40875324548338
967.272809286621
75.44735771388882
193.77248012182616
967.2646719331053
75.39428851197663
176.59108881848144
967.3453944799805
75.22473869590843
162.9874172202759
967.2765524692384
75.05856029029094
649.5941491589356
953.3721751435547
42.423118962035645
619.0920118674317
953.407165763672
42.19139397168006
587.7599458908692
953.1121866987304
42.08875202625681
557.5324849672851
953.0789049228514
41.94068061935125
527.2881390351563
953.0385436494141
41.90993106899782
496.59436706835936
953.2388039194335 41.86
476.00177682788086
953.6228870053711
41.70251974882308
453.6686880439453
953.5370379257812
41.691917417592656
430.02157941430664
953.7870174257813
41.33019099133779
408.10223436987303
954.2128451352538
41.156163791095814
384.4991488227539
954.299345203125
41.09046193035735
361.4880150571289
954.2173206796874
41.1243245995118
338.74875027246094
954.1870497246094
41.1972962642958
315.8027560217285
954.0788229228515
41.162020778068445
292.9815480871582
954.2287943481447
41.120331569447664
270.8710362652588
954.2170765590821
41.13522811918107
247.32505459643554
954.0427744467773
41.17436860513465
224.50010347924805
953.8501632890626
41.15634414713974
201.60173308996582
953.7019007080078
41.150800726429445
190.14075890441893
953.6962045605468
41.068424539257705
175.57906650512695
953.8924775273437
40.925237330223716
160.36877617218016
954.0295105605468
40.86463122084835
144.48139699658202
954.2356297250976
40.75995619201909
129.97587267993163
954.2733056718749
40.631941539343785
114.75796374975586
954.3712794082031
40.4709488558831
99.53049342919921
954.4820287895507
40.28164473140746
88.11990980529785
954.3720931435548
40.12364351563234
80.51342197549438
954.383810932617
39.97208593452072
72.83028027557373
954.6509602485352
39.72325492026109
65.26329929708862
954.4679511679687
39.5423647116926

42.07606811553955	147.5022369138794	57.67776006674194
970.649648248535	967.3361178969726	954.5988811860351
39.96991512303597	74.84061648624474	39.30573412716716
35.36215896409607	131.8714081512451	50.14117210363769
970.7683722363281	967.405122654785	954.5480227265624
39.755411066247795	74.54550844878571	39.04547797642862
27.66105914213562	116.505684194458	42.50582972685242
971.4777867158205	967.4738832919921	954.7162218237306
39.411038484760496	74.19501124399306	38.701834988667244
19.981312244384764	101.03995216296387	34.85561887944031
971.5144048066404	967.5379242641602	954.9765357626953
38.85236904697678	73.78961727897135	38.34437590948483
12.53526251083374	89.40903952093505	27.253146325012207
971.811011342285	967.5447596411133	955.1088491308594
37.241411490167714	73.3914712691003	37.88924693130376
10.718344046173096	81.67796880880736	19.634746172538758
972.0477269560547	967.4365328393554	954.8475587094727
38.14517155963881	73.04858537879142	37.31953886285619
4.732164459074021	73.93193045205689	12.468534940544128
972.1499321162111	967.4538654023438	954.6136097958985
37.601077435132595	72.68016688700612	34.38539980542803
3.880152077316284	66.09894955883789	10.885164879089356
971.850640253906	967.4469486518553	954.6119009516601
36.690814761409335	72.24676292332693	35.81158857175197
2.395070756772995	58.428288524871824	4.920264471433639
972.2115318823242	967.4480878813475	954.6610505668945
36.12455872637792	71.81887220252149	34.20063417993533
1.2896188309779166	50.7309674864502	2.9833400679359436
971.4048760283202	967.4724185683593	954.439389057129
35.33566633141689	71.31169330034061	33.15122374641285
0.5454812945451736	42.996219707702636	1.2402720597467423
971.0775916699217	967.4311621860353	954.4546059082031
34.31197034906406	70.72182192574861	31.246718444504776
0.11961422936618328	35.236937808105466	0.18127502563083173
971.1800409506835	967.5385752524414	954.8507322773438
32.500462294372234	69.95936562199998	27.79195546300966
	27.562785340896607	0.026367503747195004
	967.578936525879	955.175910252526
	69.07407867621336	24.155295891028086
	19.811255541984558	
	967.5729148842773	
	67.86796684928592	
	12.555162154563904	
	967.547770461914	
	64.78468876364516	
	10.273900233341216	
	967.4799049335936	
	65.13999426047884	
	4.8860319602279665	
	967.6321548178711	
	62.64614563491455	
	3.876046528175354	
	967.5476077148438	
	61.895892663927164	
	3.1043387003288268	
	967.6201929082031	
	61.19249809959098	
	2.0506830163192746	
	967.6528236958006	
	59.91902133419876	
	1.4151661963062285	
	967.6437912333985	
	58.80549142006061	
	0.8794660960464478	
	967.7032752875976	
	57.409282550034625	
	0.47969361242651937	
	967.7398120048827	
	55.665473659298314	
	0.22156899107587336	
	967.6825250361327	
	53.47254562957513	

Pillarplex Salts with Mixed Anions:

T8S: Table of crystal data, data collection and structure refinement of $[Ag_8L^{Me}_2](PF_6)_2(OTf)_2$ and $[Au_8L^{Me}_2](PF_6)_2(AuCl_2)_2$:

Identification code		CalTo4	HeiAl55
Chemical formula		$C_{24.25}H_{22.25}Ag_4F_{9.75}N_{14.75}O_{2.25}P_{1.25}S_{0.75}$	$C_{50.70}H_{47.56}Au_{9.50}Cl_3F_{15}N_{25.85}P_{2.50}$
Formula weight	[g mol^{-1}]	4943.23	3371.04
Temperature	[K]	100	100(2)
Wavelength	[Å]	0.71073	0.71073
Crystal system		triclinic	triclinic
Space group		*P* -1	*P* -1
Unit cell dimensions		a = 21.296(8) Å, α = 118.657(10)° b = 23.072(9) Å, β = 90.594(12)° c = 23.305(9) Å, γ = 98.005(12)°	a = 12.2674(7) Å, α = 98.263(2)° b = 14.9679(9) Å, β = 91.045(2)° c = 23.1156(15) Å, γ = 90.821(2)°
Volume	[Å^3]	9911(7)	4199.0(4)
Z		2	2
Calc. Density	[g cm^{-3}]	1.656	2.666
Absorption coefficient	[mm^{-1}]	1.704	16.752
F(000)		4764	3025
Diffractometer		TXS rotating anode	TXS rotating anode
Radiation source		Mo K_α	Mo K_α
Theta range for data collection	[°]	1.74 – 25.35	0.89 – 26.02
Index ranges		-25<=h<=25, -27<=k<=27, -28<=l<=28	-15<=h<=15, -18<=k<=18, -28<=l<=28
Reflections collected		230546	197600
Independent reflections		36022 [R_{int} = 0.0888]	16435 [R_{int} = 0.0670]
Coverage of independent reflections	[%]	99.2	99.2
Absorption correction		Multi-Scan	Multi-Scan
Max., min. transmission		0.5279, 0.7453	0.3058, 0.7454
Structure solution		direct methods	direct methods
Refinement method		Full-matrix least-squares on F^2	Full-matrix least-squares on F^2
Refinement program		SHELXL (Sheldrick 2018), ShelXle (Huebschle 2011)	SHELXL (Sheldrick 2018), ShelXle (Huebschle 2011)
Function minimised		$\sum w(F_o^2 - F_c^2)^2$	$\sum w(F_o^2 - F_c^2)^2$
Data / restraints / parameters		36022 / 2877 / 1361	16435 / 69 / 979
Goodness-of-Fit on F^2		1.976	1.10088
Δ/σ_{max}		0.104	0.002
Final R indices	I > 2σ(I)	21165 data, R1 = 0.1729, wR2 = 0.4385	15838 data, R1 = 0.0369, wR2 = 0.1083
	All data	R1 = 0.2491, wR2 = 0.5180	R1 = 0.0383, wR2 = 0.1117
Weighting scheme		W = 1 / [$\sum^2$(FO^2) + (0.2000P)^2] where P = (FO^2+2FC^2) / 3	W = 1 / [$\sum^2$(FO^2) + (0.0583P)^2 + 57.0311P] where P = (FO^2+2FC^2) / 3
Largest diff. peak, hole	[eÅ^{-3}]	9.952, -2.963	3.319, -2.772
R.M.S. deviation from mean	[eÅ^{-3}]	0.484	0.310

F42S: Representation of non-covalent interactions of $[Au_8L^t_2](PF_6)_4$: (A) Non-classical hydrogen bonding between H_{rim} and F_{PF6}; (B) Aurophilic chain alignment; Representation of non-covalent interactions of $[Ag_8L^t_2](OTf)_4$: (C) Hydrogen bonding between H_{rim} and O_{OTf}; (D) Tilted $[Ag_8L^t_2]^{4+}$ cation:[38]

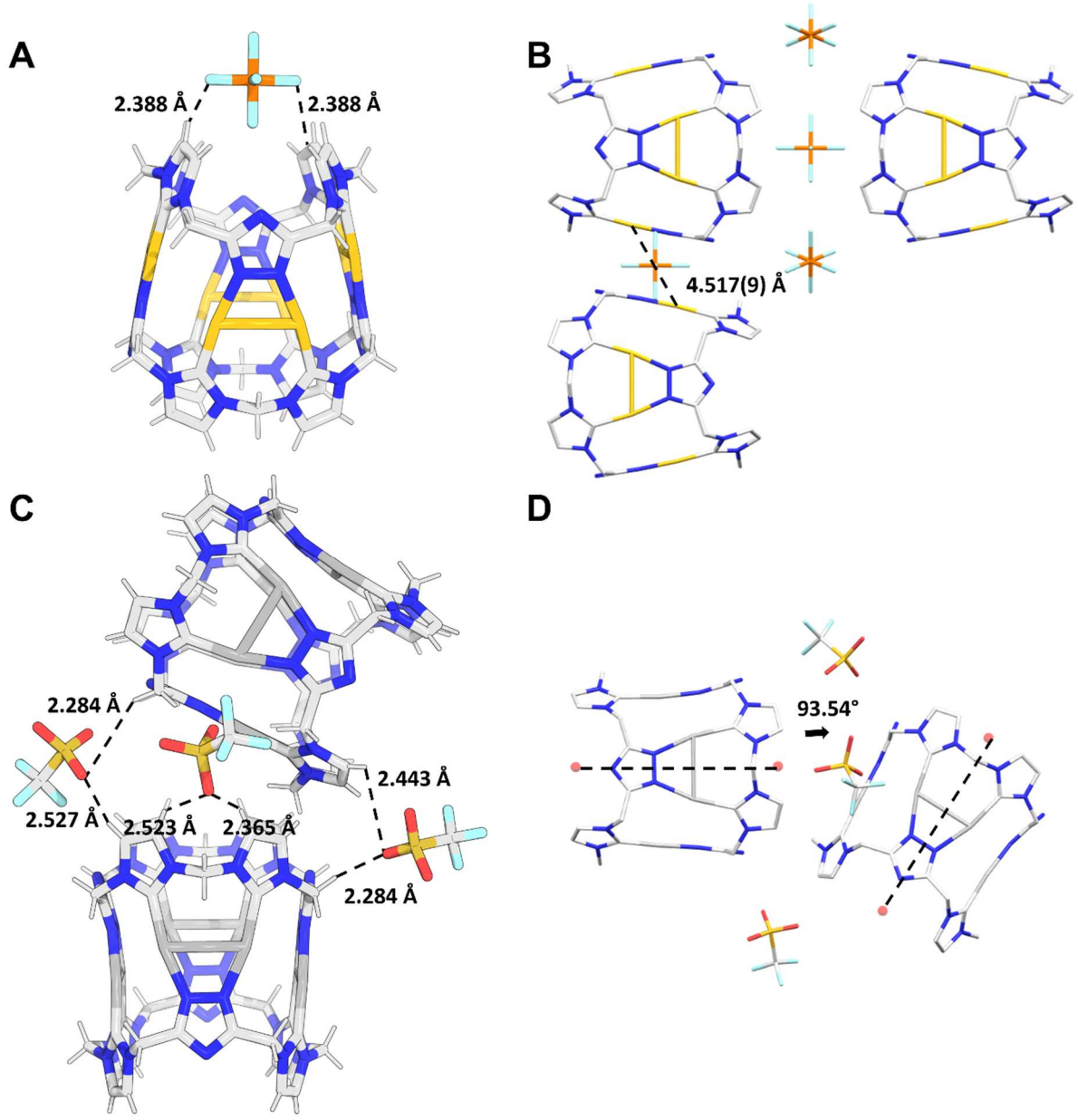

Crystal Structure of a Hexacationic Ag(I)-Pillarplex-Dodecyl-Diammonium Pseudorotaxane as Terephthalate Salt:

F43S: Representation of the centra group assignment of the pillarplex cation by IsoStar:[15,39]

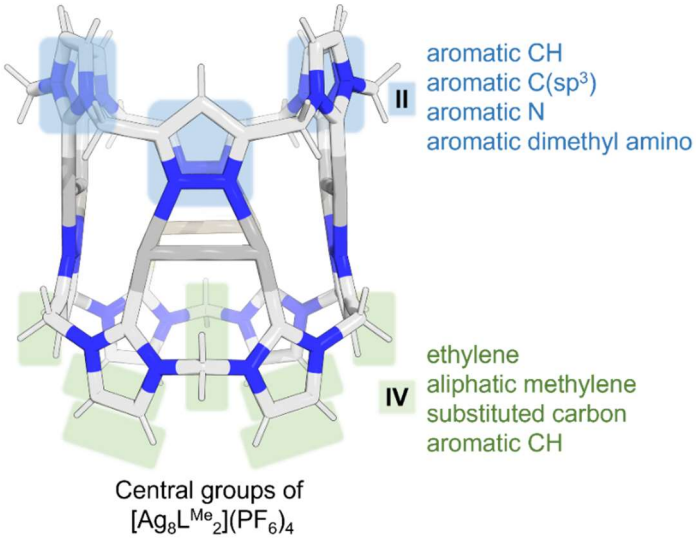

F44S: Crystal packing of $[Ag_8L^{Me}_2]^{4+}$ and guest diammonium dodecyl: (A) along the a-axis, (B) along the b-axis and (C) along the c-axis:

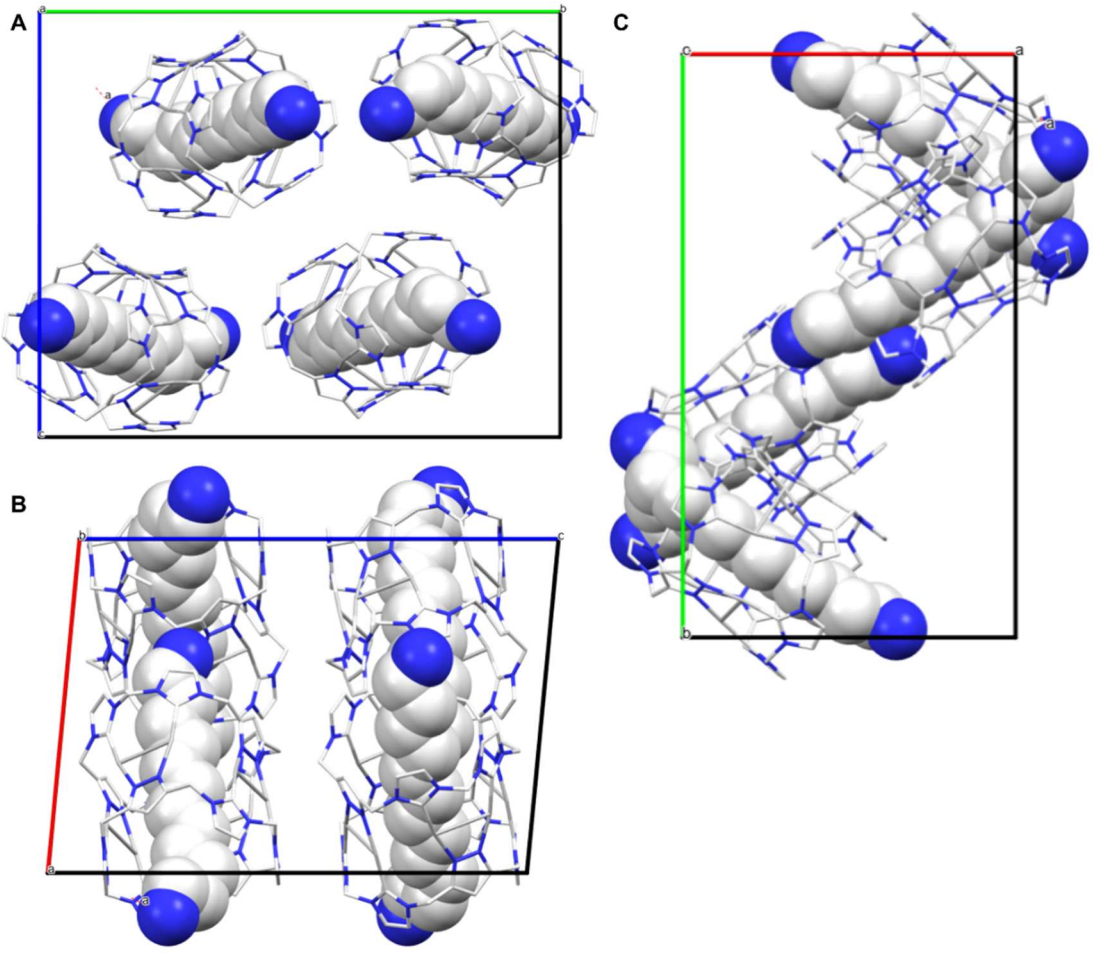

Rim-Functionalisation of Pillarplex:

F45S: NMR analysis of $L^{Br}(PF_6)_4$ containing ^{13}C, ^{19}F, ^{31}P and COSY NMR spectra:

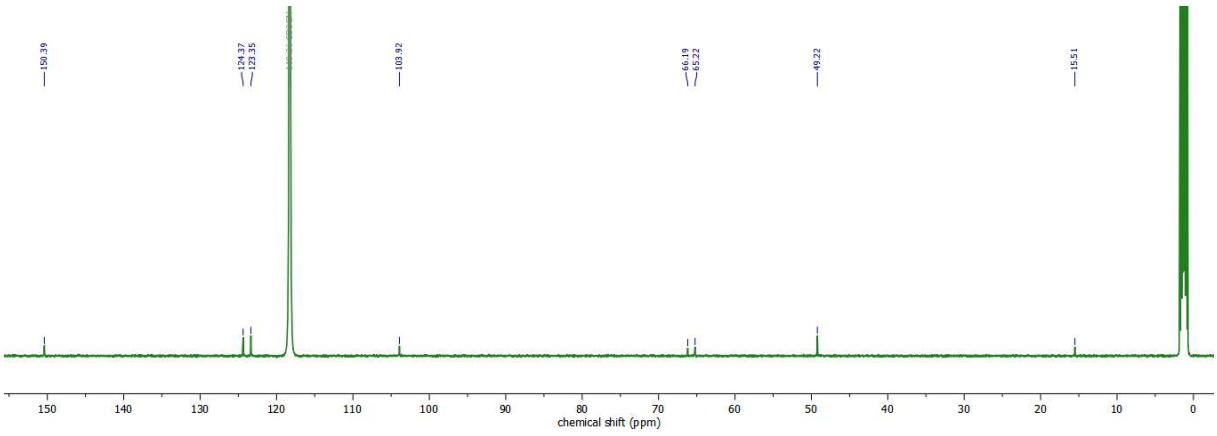

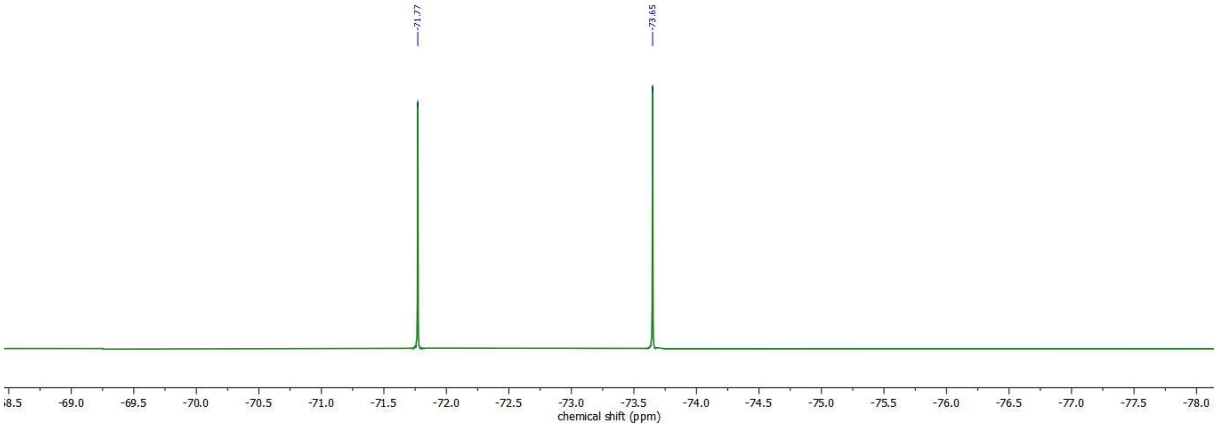

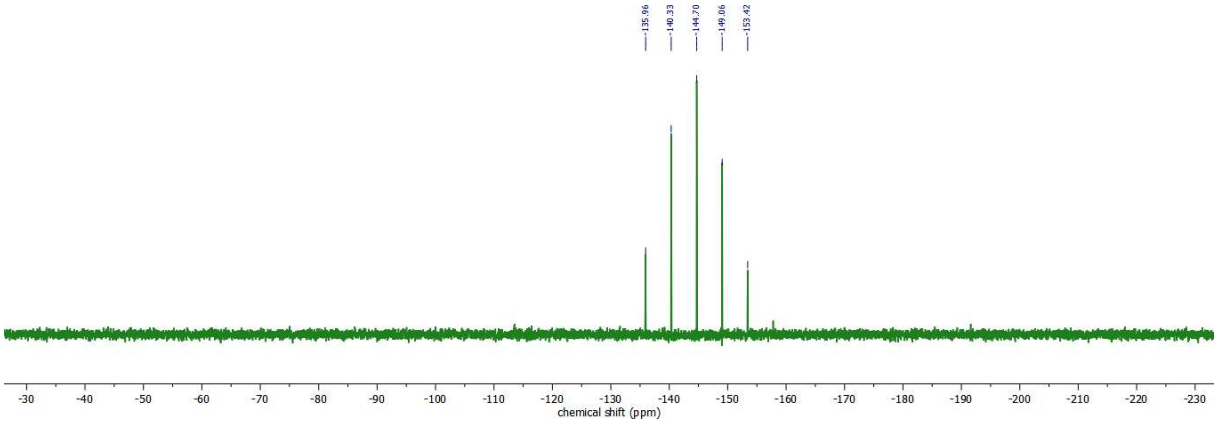

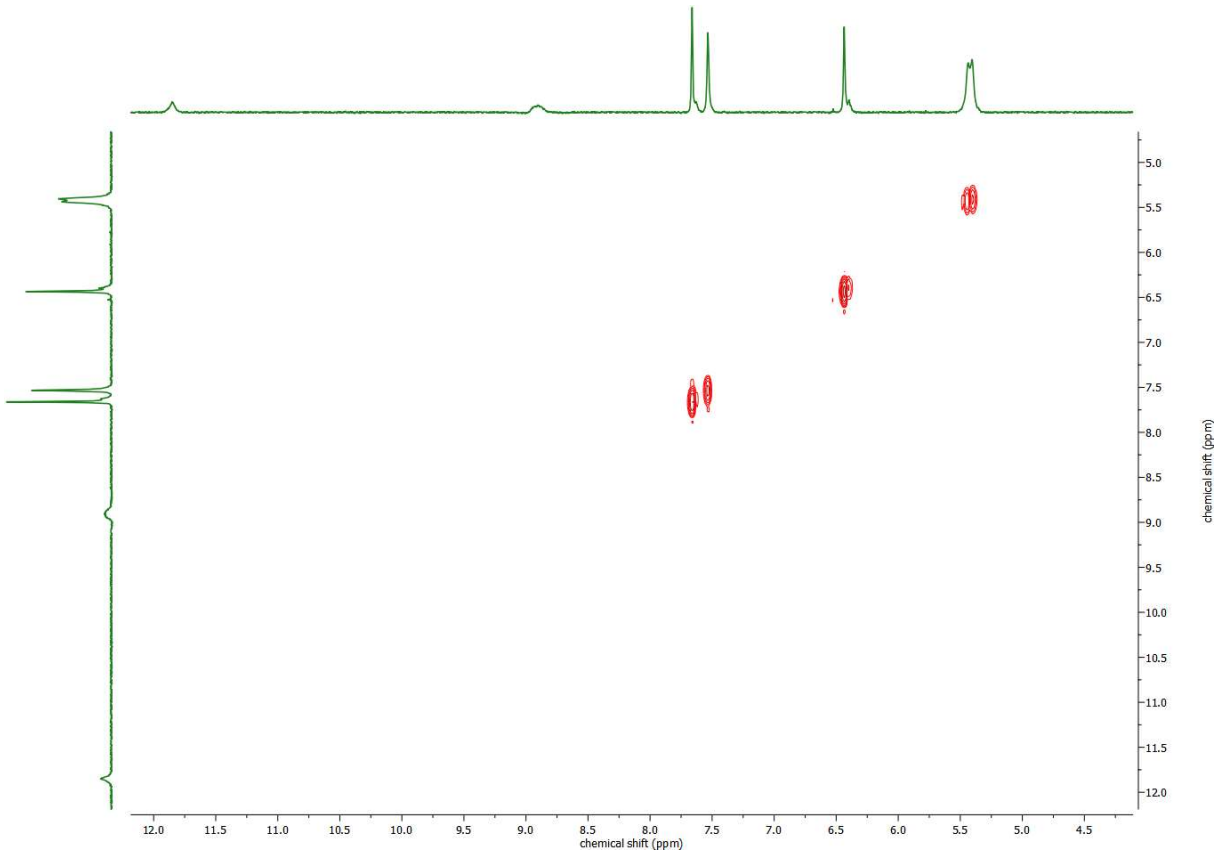

F46S: NMR analysis of $[Ag_8L^{Br}_2](PF_6)_4$ containing ^{13}C, ^{19}F, ^{31}P, COSY and HMBC NMR spectra:

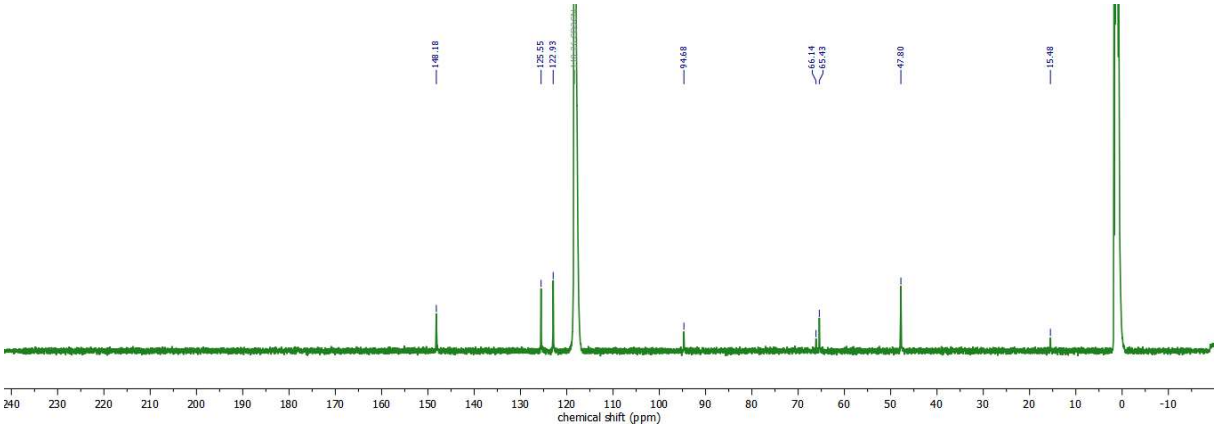

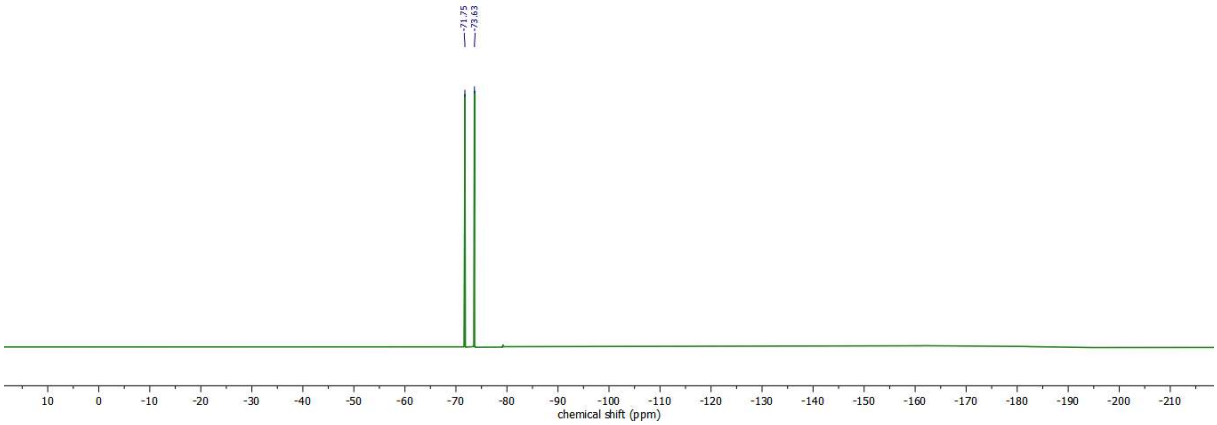
-71.75
-73.63
chemical shift (ppm)

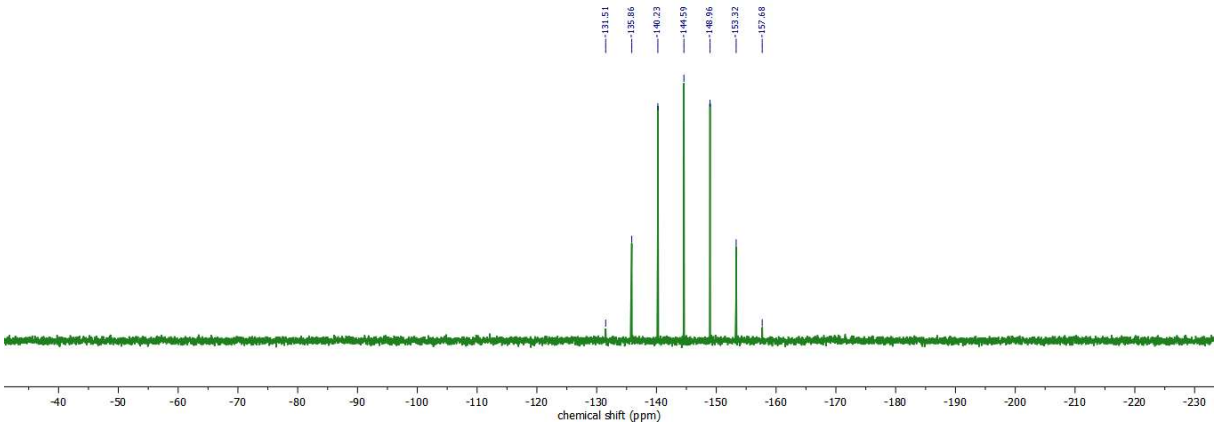
131.51
135.86
140.23
144.59
146.96
153.32
157.68
chemical shift (ppm)

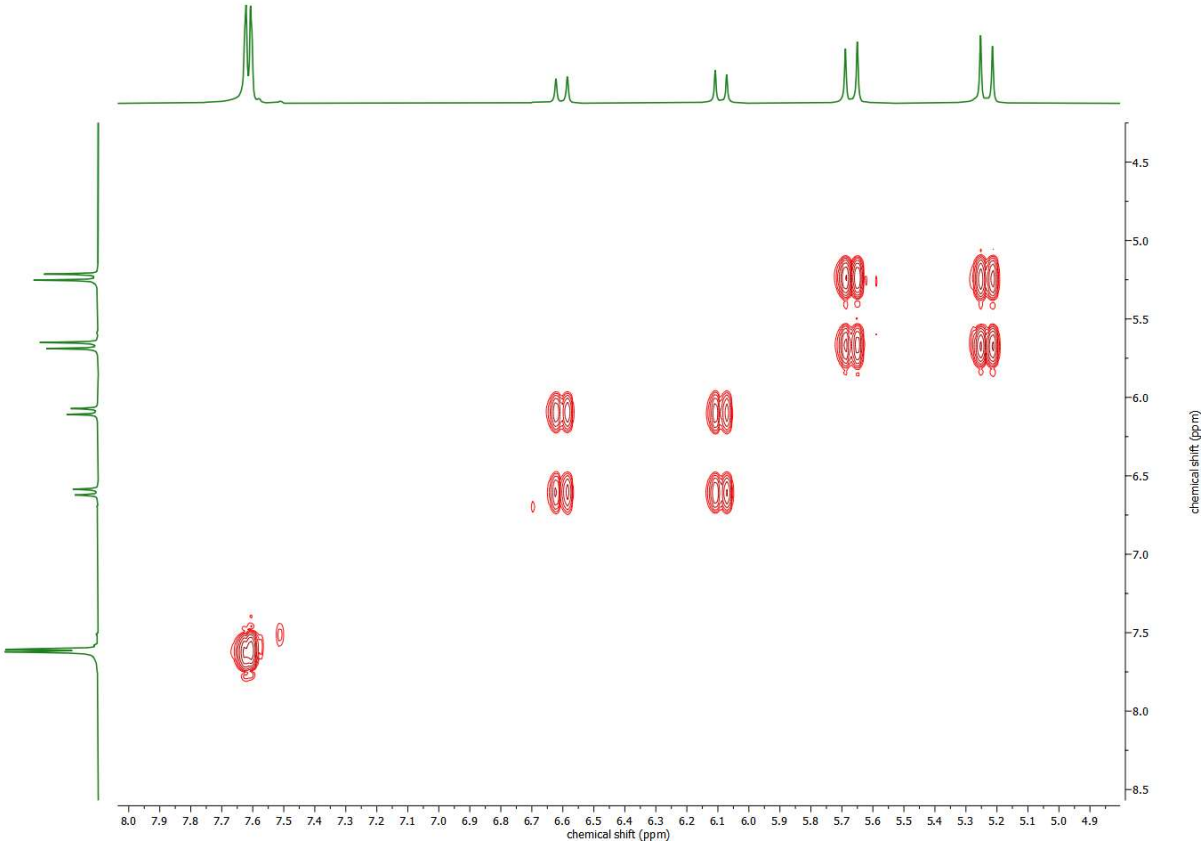
chemical shift (ppm)
chemical shift (ppm)

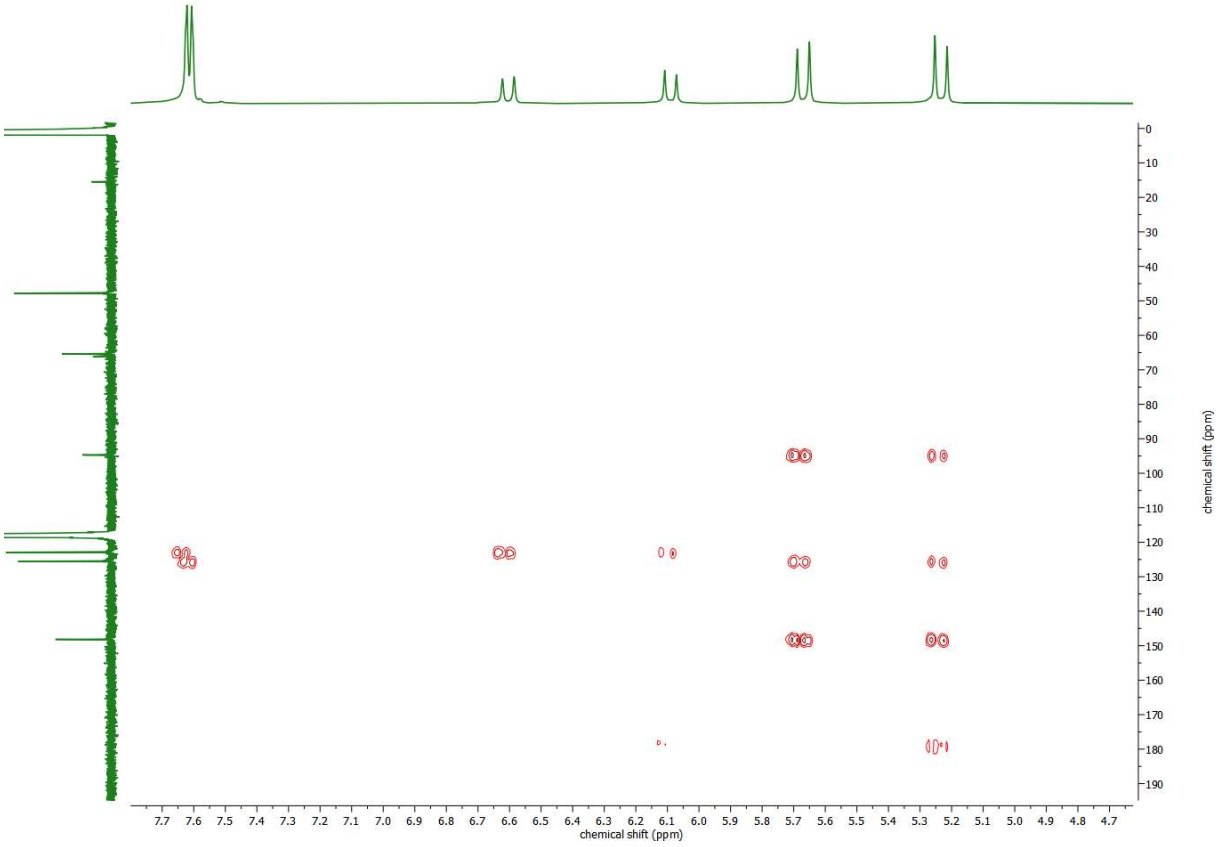

F47S: NMR analysis of $[Au_8L^{Br}_2](PF_6)_4$ containing ^{13}C, ^{19}F, ^{31}P, COSY and HMBC NMR spectra:

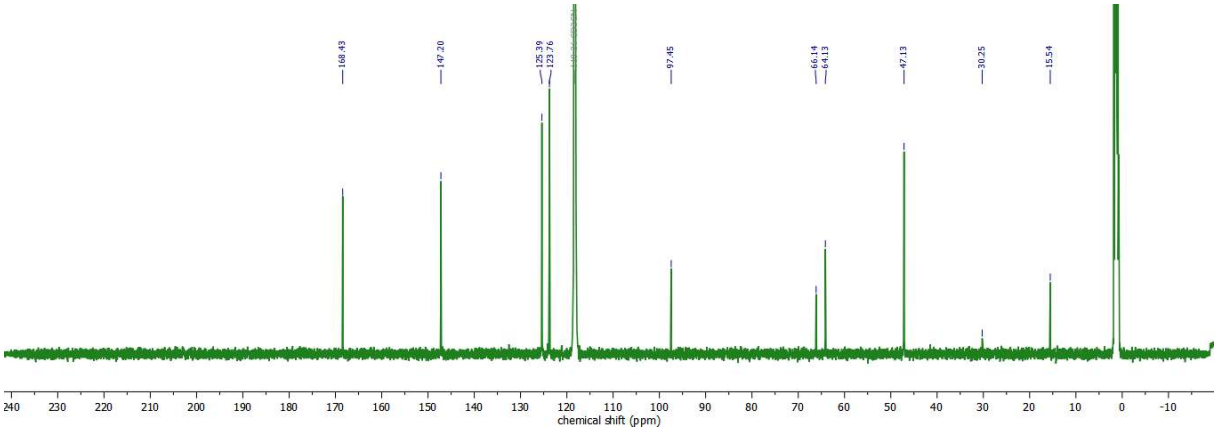

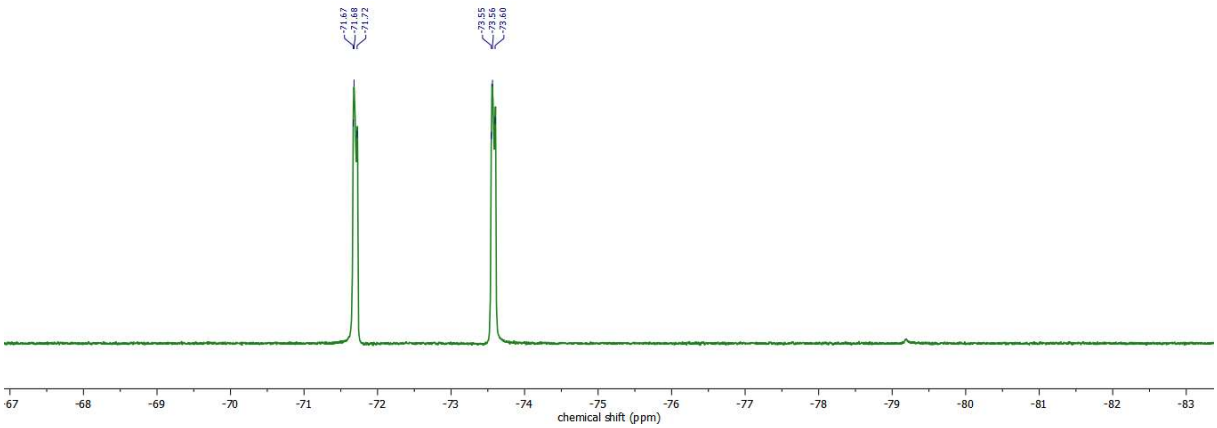
-71.67
-71.68
-71.72
-73.55
-73.56
-73.60
chemical shift (ppm)

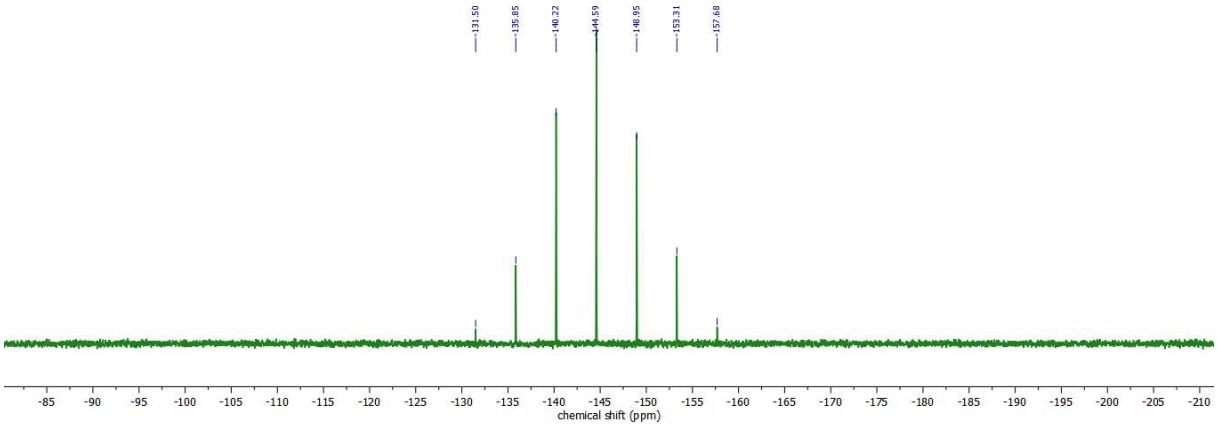
-131.50
-135.65
-140.22
-144.59
-148.95
-153.31
-157.68
chemical shift (ppm)

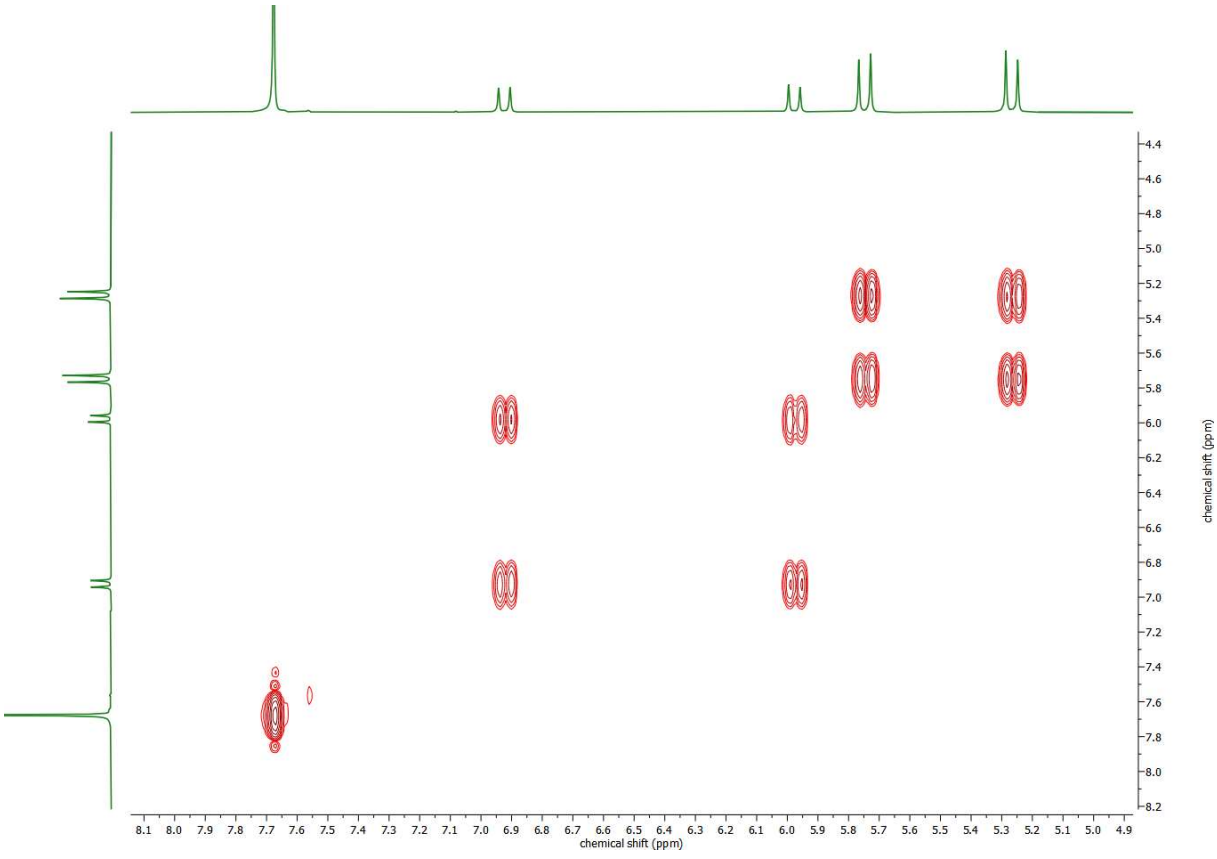
chemical shift (ppm)
chemical shift (ppm)

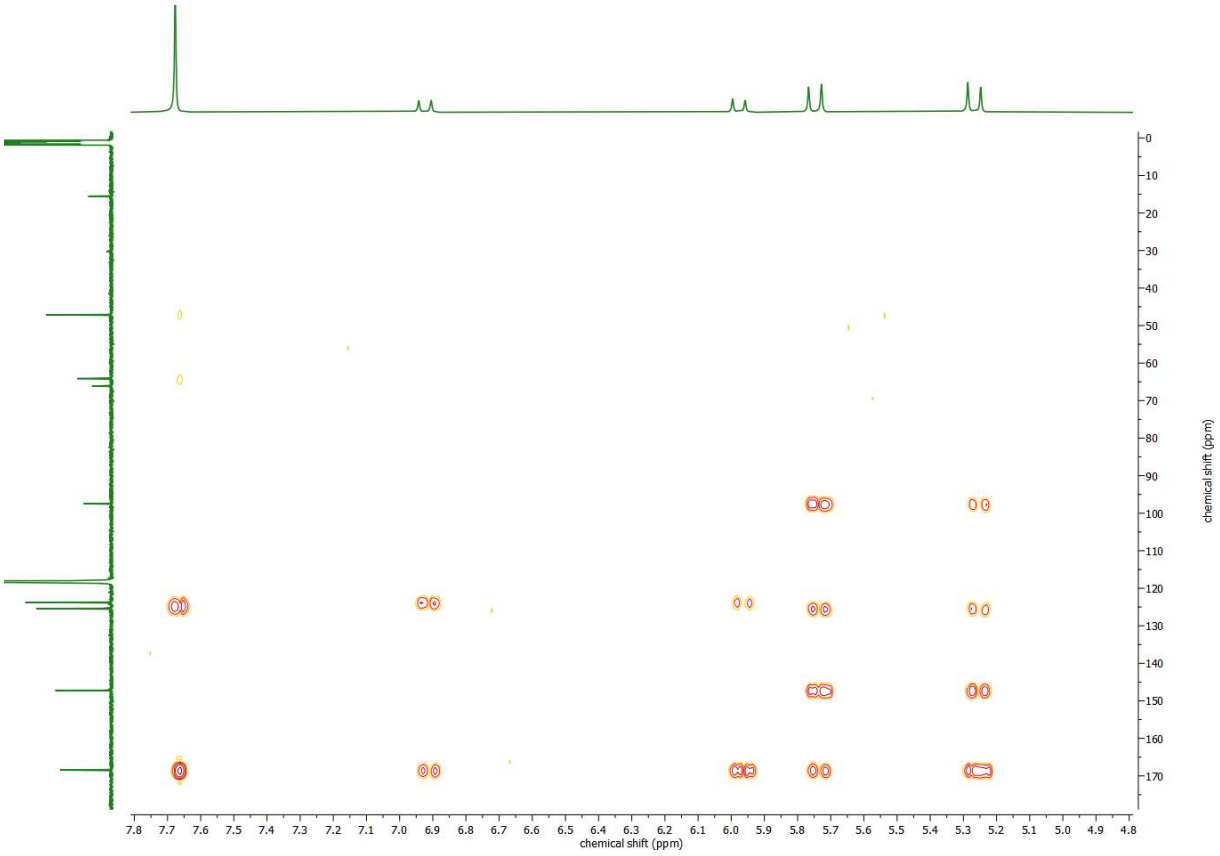

F48S: IR spectrum of $L^{Br}(PF_6)_4$ compared to $L^{Me}(PF_6)_4$ in the solid-state:

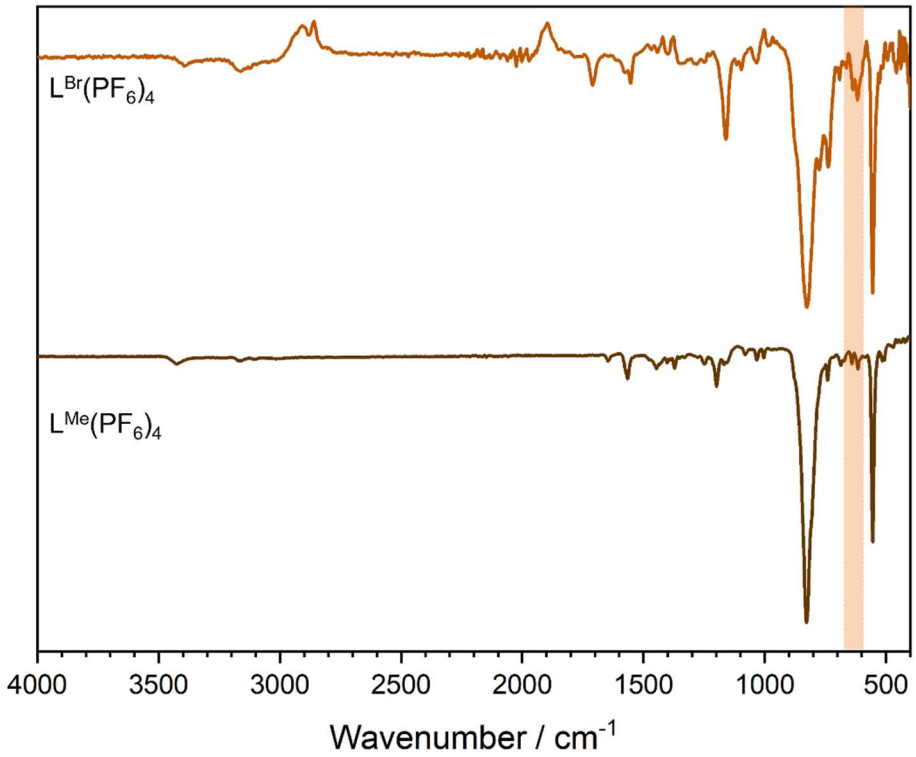

F49S: IR spectrum of $[Ag_8L^{Br}_2](PF_6)_4$ compared to $[Ag_8L^{Me}_2](PF_6)_4$ in the solid-state:

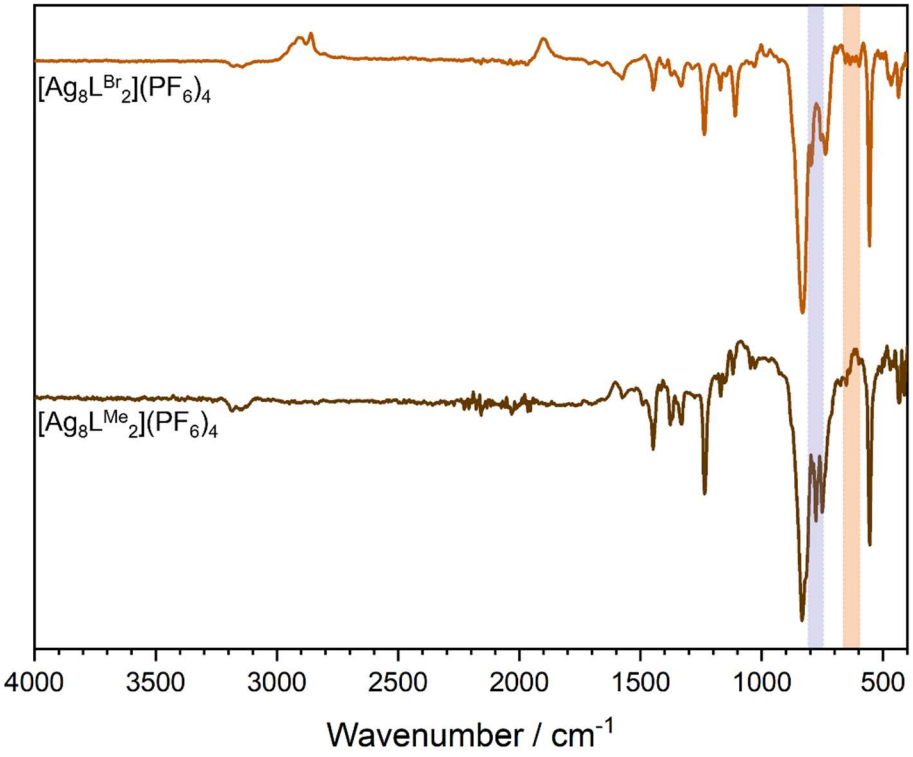

F50S: IR spectrum of $[Au_8L^{Br}_2](PF_6)_4$ compared to $[Au_8L^{Me}_2](PF_6)_4$ in the solid-state:

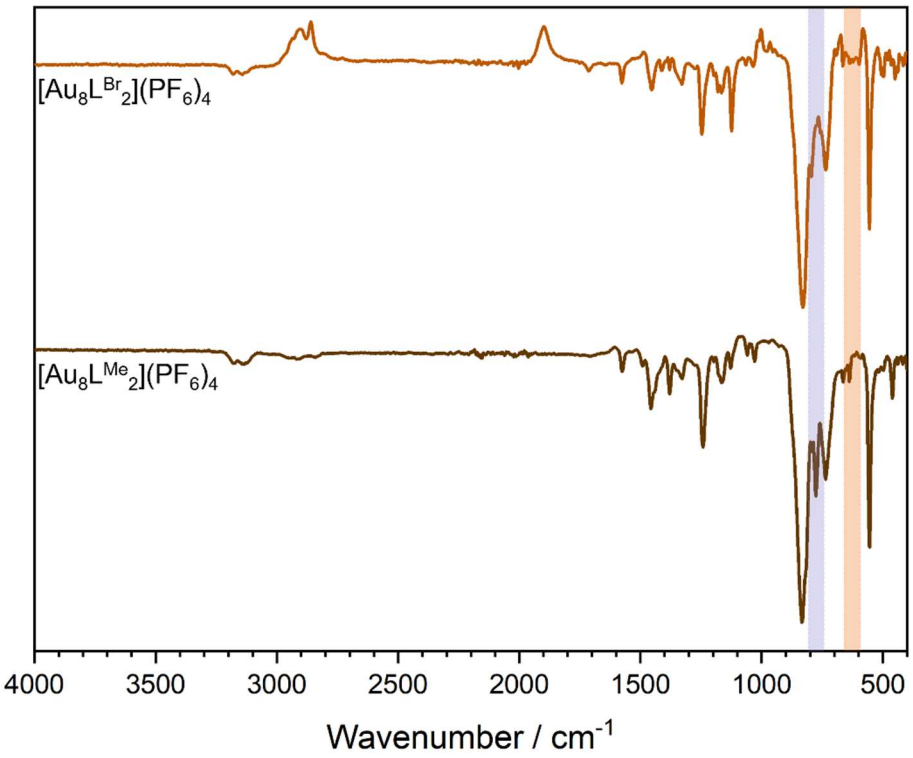

F51S: ESI mass spectra of $L^{Me}(PF_6)_4$, $[Ag_8L^{Me}_2](PF_6)_4$ and $[Au_8L^{Me}_2](PF_6)_4$ in MeCN:

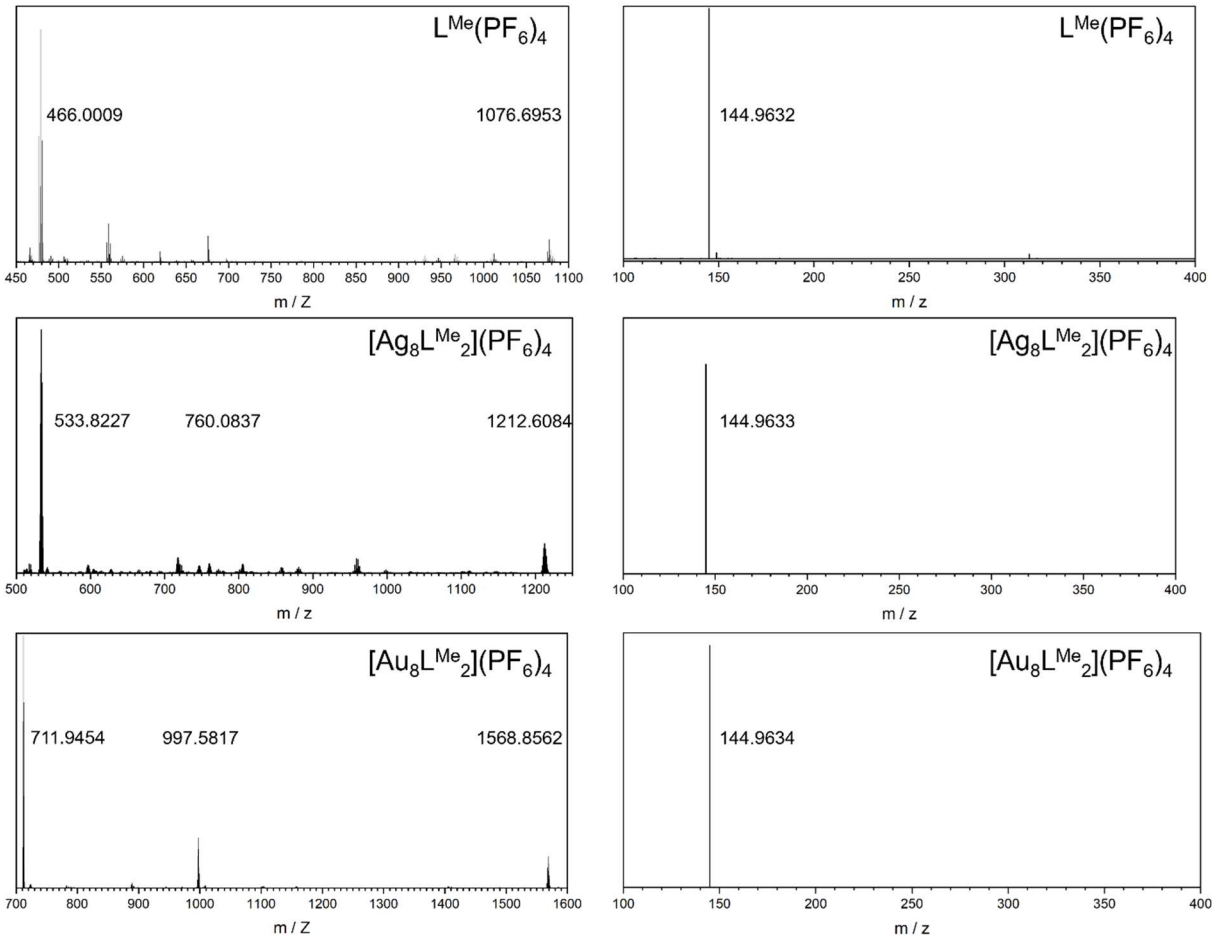

F52S: DLS measurement evaluated towards size distribution of $L^{Br}(PF_6)_4$:

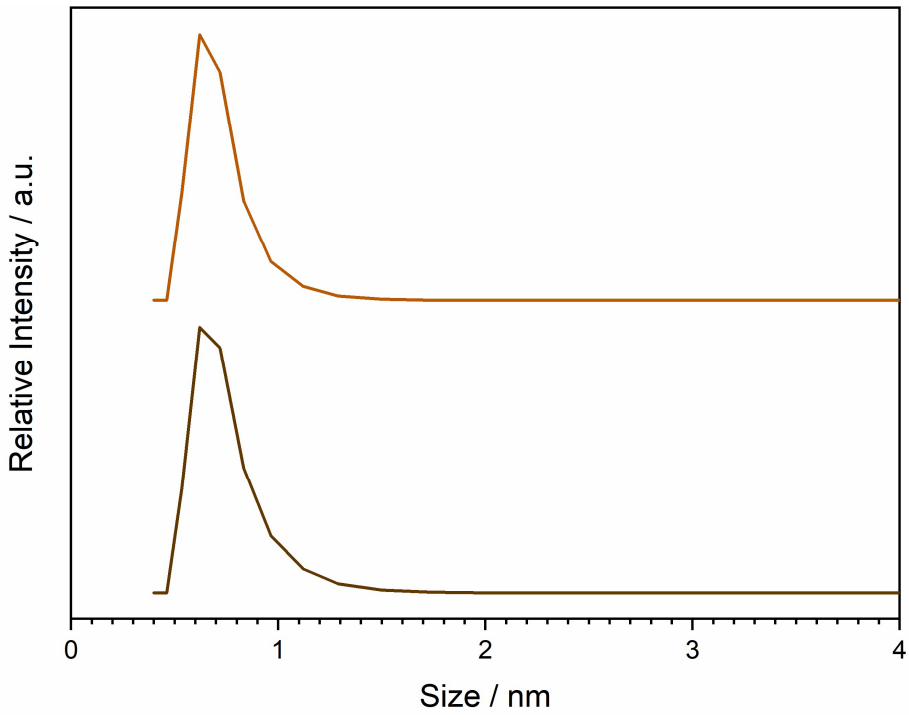

F53S: DLS measurement evaluated towards size distribution of $[Ag_8L^{Br}_2](PF_6)_4$:

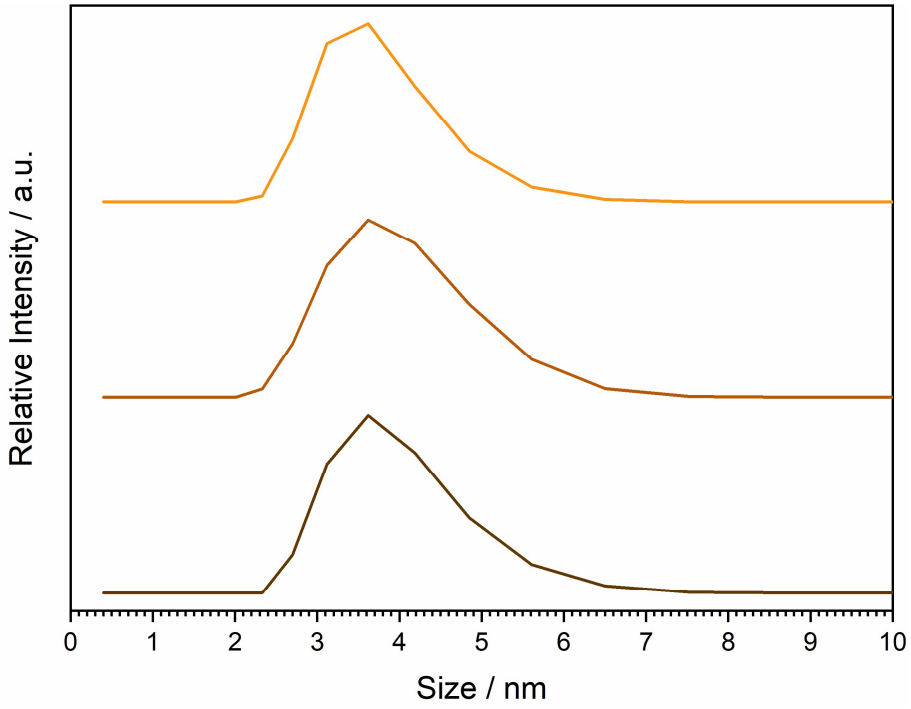

F54S: DLS measurement evaluated towards size distribution of $[Au_8L^{Br}_2](PF_6)_4$:

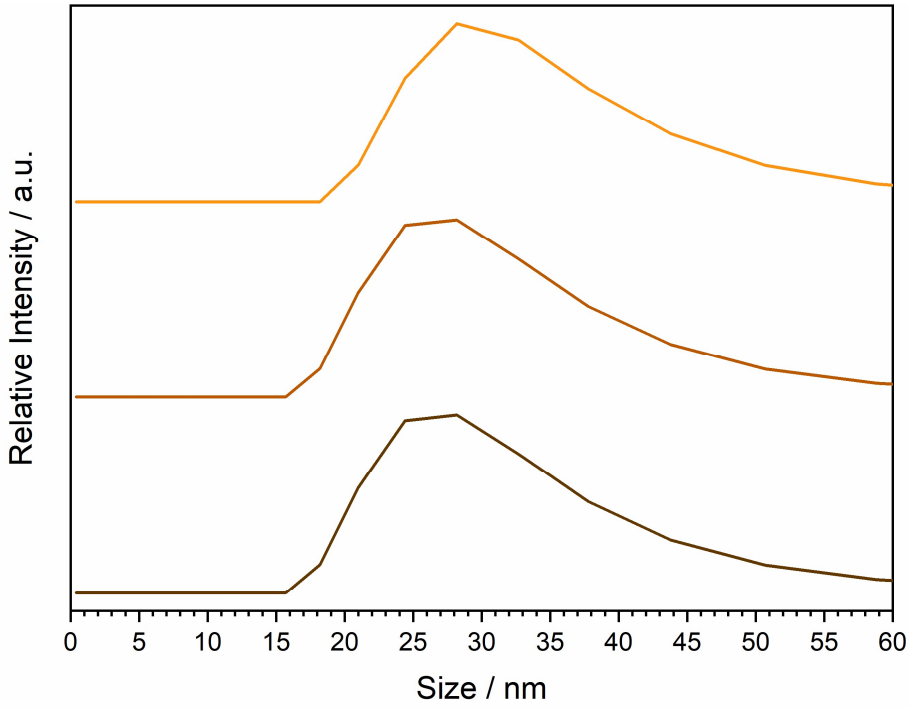

T9S: Table of crystal data, data collection and structure refinement of $[Ag_8L^{Br}_2](PF_6)_4$ and $[Au_8L^{Br}_2](PF_6)_4$:

Identification code		HeiAl12	HeiAl14
Chemical formula		$C_{48}H_{40}Ag_8Br_4N_{24}P_4F_{24}$	$C_{48}H_{44}Au_8Br_4N_{24P4}F_{24}$ + 2 C_2H_3N
Formula weight	[g mol^{-1}]	1835.68	3510.39
Temperature	[K]	100(2)	100(2)
Wavelength	[Å]	0.71073	0.71073
Crystal system		orthorhombic	tetragonal
Space group		*P n m a*	*P* 4_1 2_1 2
Unit cell dimensions		a = 24.1945(15) Å, α = 90° b = 24.0406(15) Å, β = 90° c = 20.9494(13) Å, γ = 90°	a = 14.3499(8) Å, α = 90° b = 14.3499(8) Å, β = 90° c = 51.556(4) Å, γ = 90°
Volume	[Å^3]	12185.2(13)	10616.4(14)
Z		6	4
Calc. Density	[g cm^{-3}]	1.501	2.196
Absorption coefficient	[mm^{-1}]	2.695	12.660
F(000)		5224	6352
Diffractometer		IMS microsource	TXS rotating anode
Radiation source		Mo K_α	Mo K_α
Theta range for data collection	[°]	1.94 – 26.02	2.01 – 25.76
Index ranges		-29<=h<=29, -29<=k<=29, -25<=l<=25	-17<=h<=17, -17<=k<=17, -62<=l<=62
Reflections collected		270042	231404
Independent reflections		12303 [R_{int} = 0.0517]	10144 [R_{int} = 0.0666]
Coverage of independent reflections	[%]	99.9	99.9
Absorption correction		Multi-Scan	Multi-Scan
Max., min. transmission		0.6425, 0.7454	0.3840, 0.7452
Structure solution		direct methods	direct methods
Refinement method		Full-matrix least-squares on F^2	Full-matrix least-squares on F^2
Refinement program		SHELXL (Sheldrick 2018), ShelXle (Huebschle 2011)	SHELXL (Sheldrick 2018), ShelXle (Huebschle 2011)
Function minimised		$\sum w(F_o^2 - F_c^2)^2$	$\sum w(F_o^2 - F_c^2)^2$
Data / restraints / parameters		12303 / 792 / 532	10144 / 1091 / 533
Goodness-of-Fit on F^2		1.033	1.165
Δ/σ_{max}		0.001	0.001
Final R indices	I > 2σ(I)	9028 data, R1 = 0.0961, wR2 = 0.2675	9304 data, R1 = 0.0515, wR2 = 0.1160
	All data	R1 = 0.1282, wR2 = 0.3139	R1 = 0.0584, wR2 = 0.1199
Weighting scheme		W = 1 / [$\sum^2$(FO^2) + (0.1643P)^2 + 229.5295P] where P = (FO^2+2FC^2) / 3	W = 1 / [$\sum^2$(FO^2) + (0.0167P)^2 + 403.8635P] where P = (FO^2+2FC^2) / 3
Largest diff. peak, hole	[eÅ^{-3}]	5.591, -3.442	2.268, -2.146
R.M.S. deviation from mean	[eÅ^{-3}]	0.263	0.284

Pillarplex Pseudorotaxanes with α,ω-Dicarboxylic Acids:

F55S: Theoretical Investigation of the dicarboxylic acids with the average distances of O-H, O-C, C-C and the van der Waals radii of hydrogen (1.09 Å[40]) with ConQuest search for the defined distances. Exemplary shown at CCDC. No. CIWGIA (983628), CIWHIB (983633) and JOHPOL (1188368):[41]

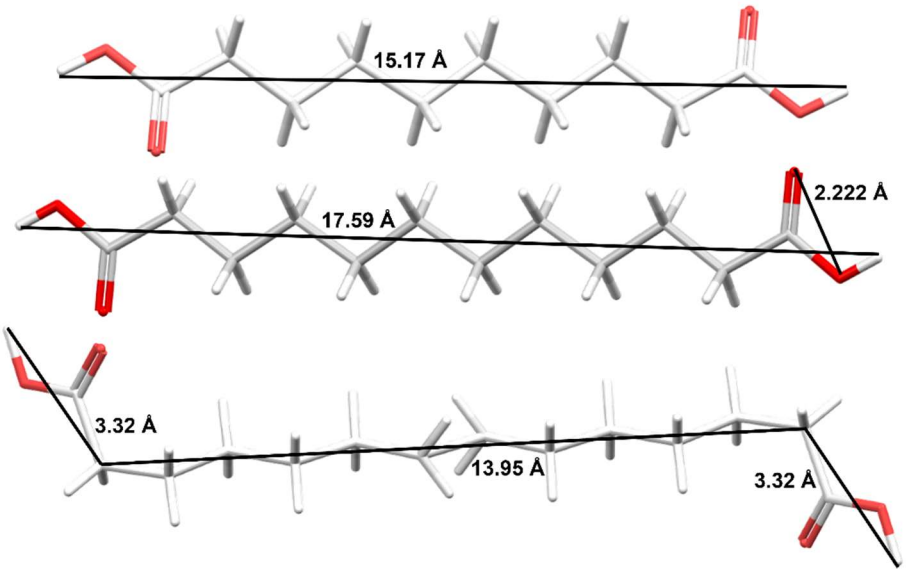

F56S: Crystal packing of $[Ag_8L^{Me}_2](C_{10}H_{18}O_4)(PF_6)_4$ (A) along the b-axis, (B) along the c-axis and (C) zigzag formation of the 1D chains pillarplex cations:

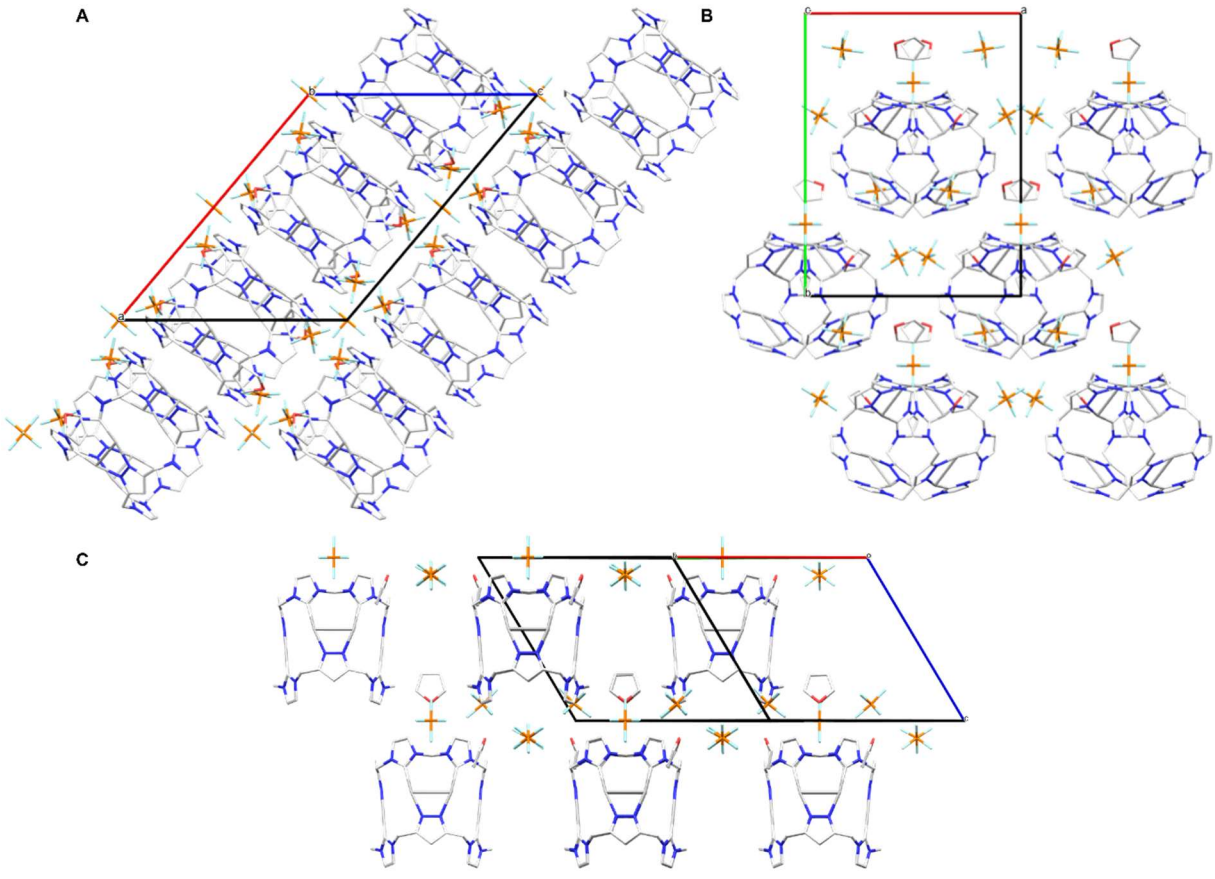

F57S: Crystal packing of $[Ag_8L^{Me}_2](C_{12}H_{22}O_4)(PF_6)_4$ (A) along the b-axis and (B) along the c-axis:

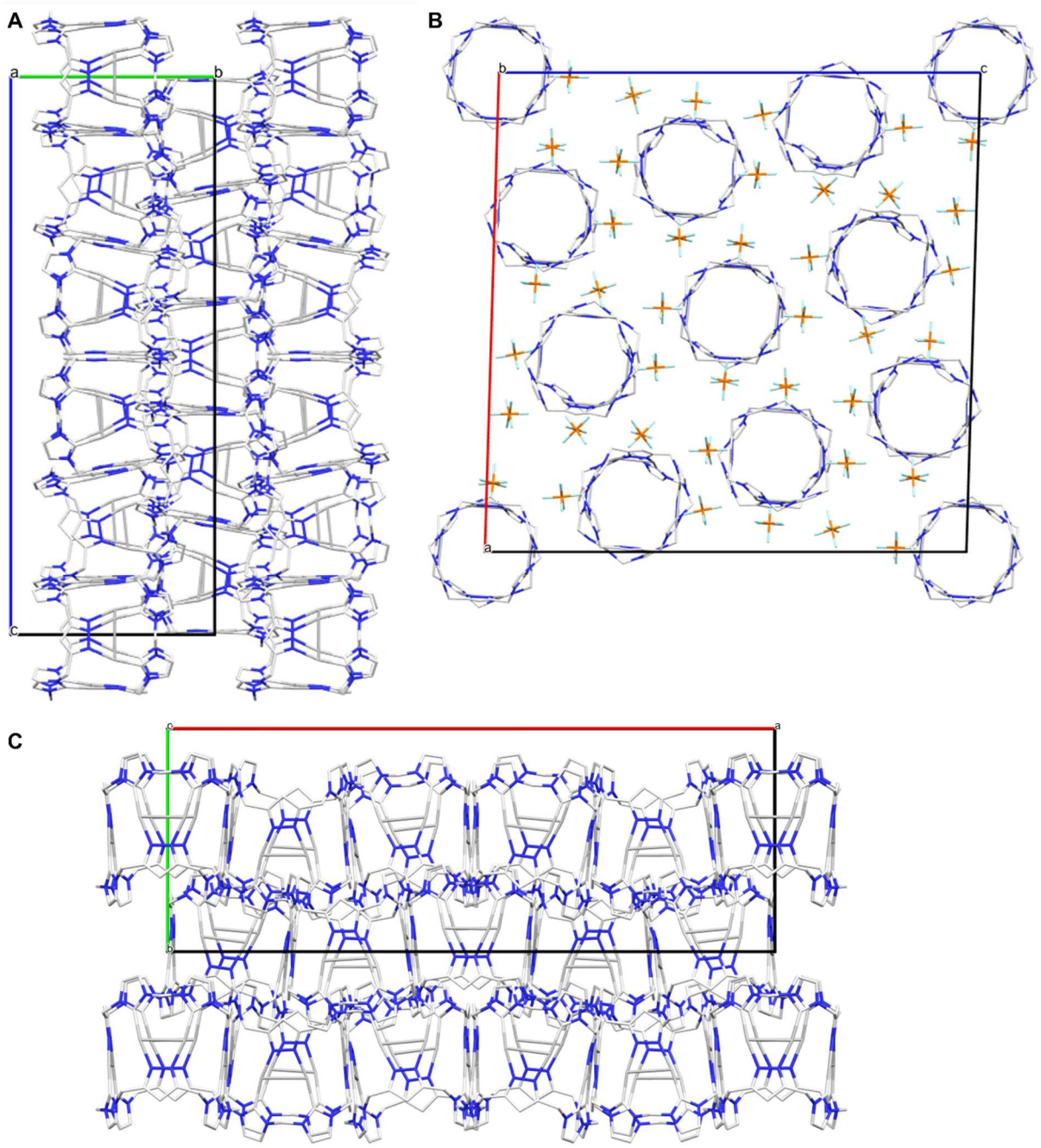

F58S: Crystal packing of $[Ag_8L^{Me}_2](C_{14}H_{26}O_4)(PF_6)_4$ (A) along the b-axis and (B) along the c-axis:

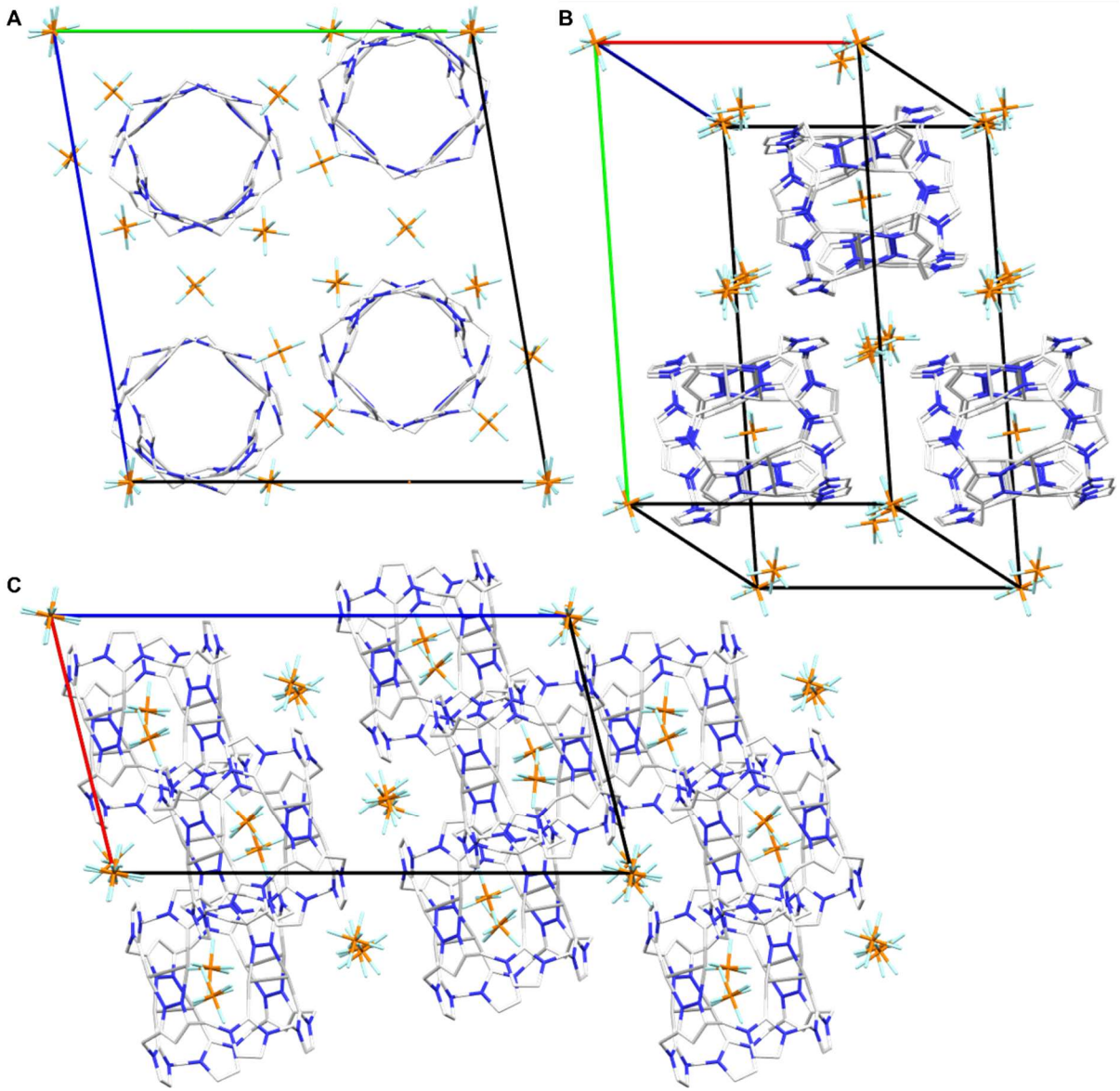

Utilising $[M_8L^{Me}_2](\alpha,\omega\text{-Dicarboxylic Acid})(X)_4$ as Building Blocks:

F59S: ^{1}H NMR spectrum of $C_{12}H_{20}O_4K_2$ in D_2O:

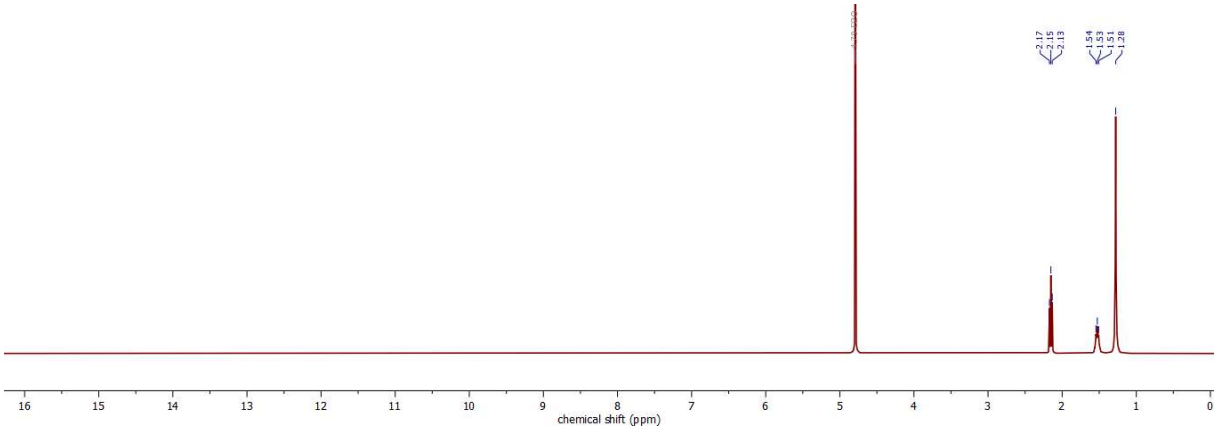

F60S: ^{1}H NMR spectra of $[Ag_8L^{Me}_2](C_{12}H_{20}O_4K_2)(PF_6)_4$ in D_2O (4.79 ppm) with solvent impurities (MeCN at 2.06 ppm, $C_{12}H_{20}O_4K_2$ at 1.27, 1.51, 2.14 ppm, Et_2O at 3.75, 1.89 ppm), acidic proton signal at 8.44 ppm is marked with a yellow box:

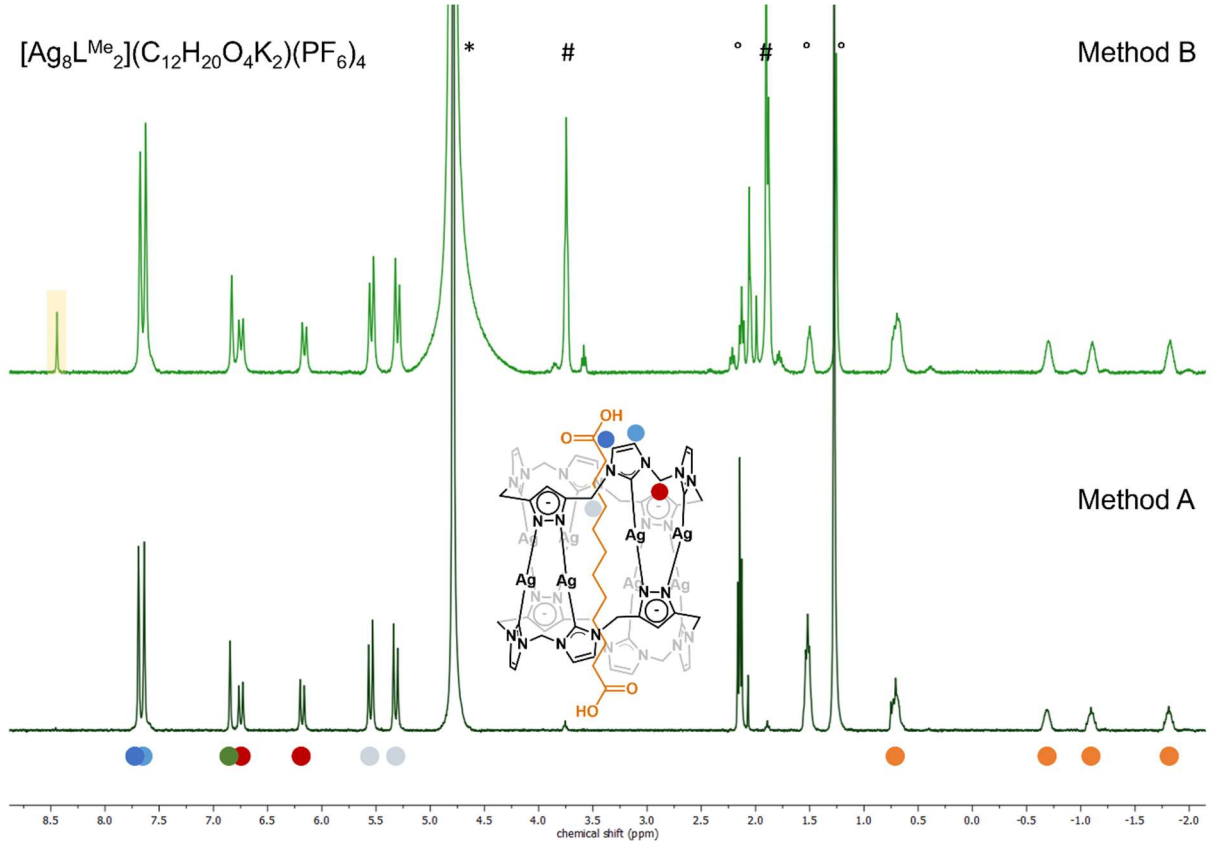

F61S: ^{1}H NMR spectra of $[Ag_8L^{Me}_2](C_{12}H_{22}O_4)(PF_6)_4$, $[Mo_2(DaniF)_3(OAc)]$ and after coordination attempt following synthesis route 1:

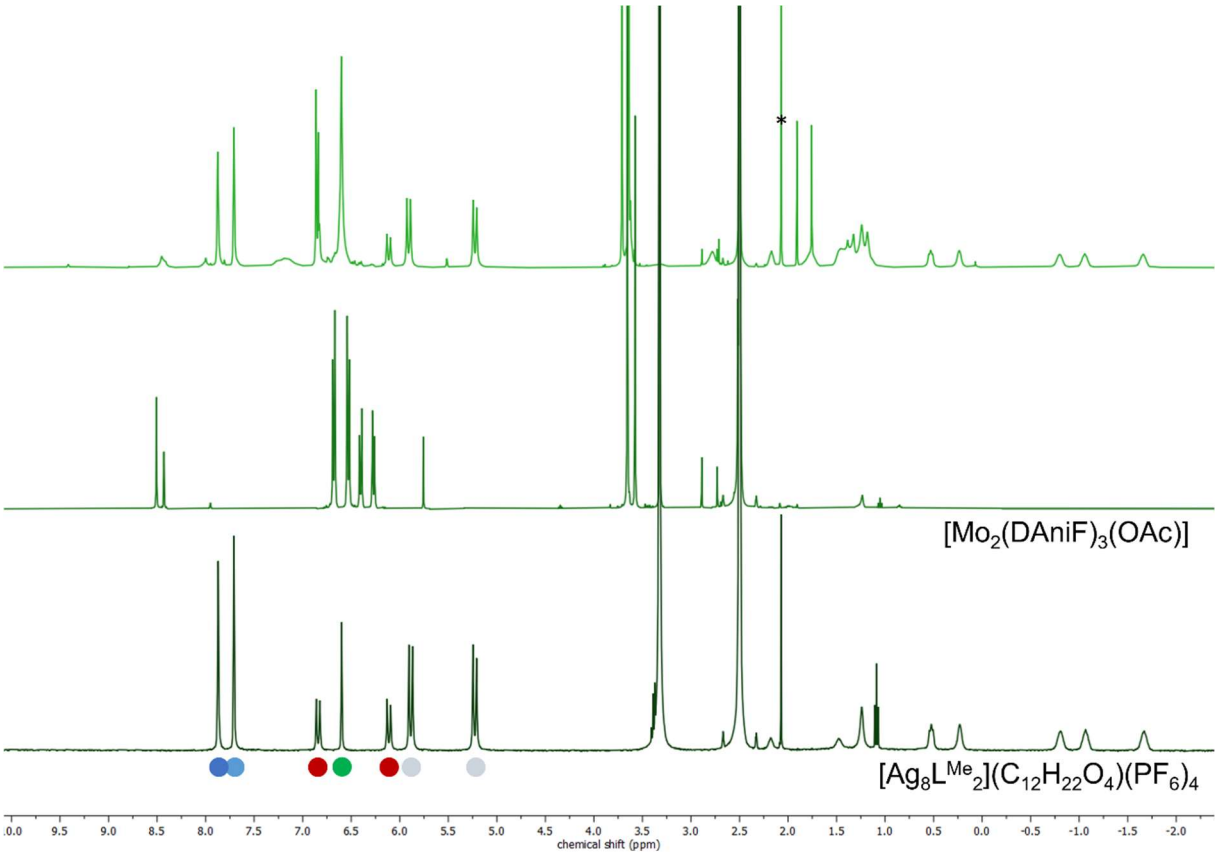

F62S: ^{1}H NMR spectrum of the coordination attempt of $[Ag_8L^{Me}_2](C_{12}H_{22}O_4)(PF_6)_4$ and $[Zn(OAc)_2]$ following synthesis route 4 in MeCN-d_3 with solvent impurities DMF (2.77, 2.89 and 7.92 ppm):

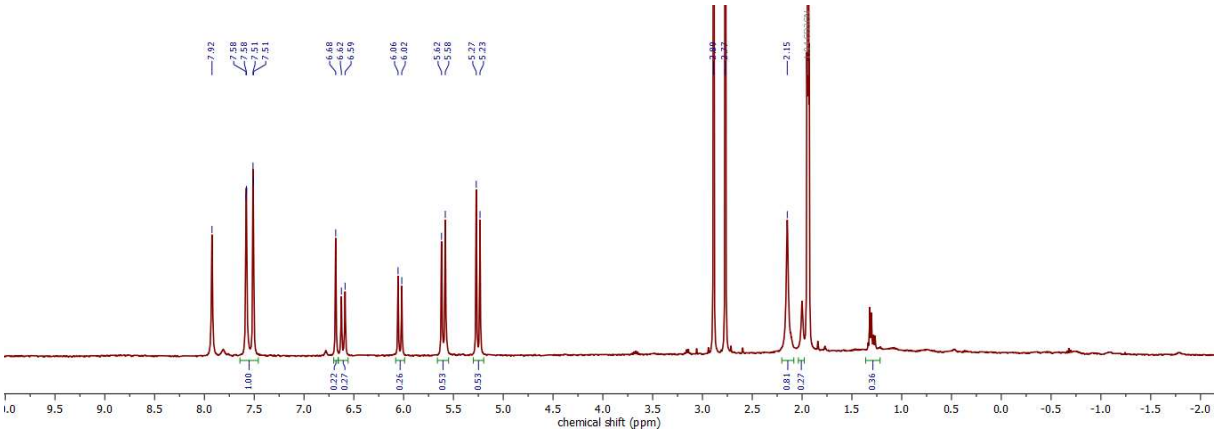

F63S: ^{1}H NMR spectrum of the pseudorotaxane $[Ag_8L^{Me}_2](C_{12}H_{22}O_4)(OAc)_4$ and in D_2O:

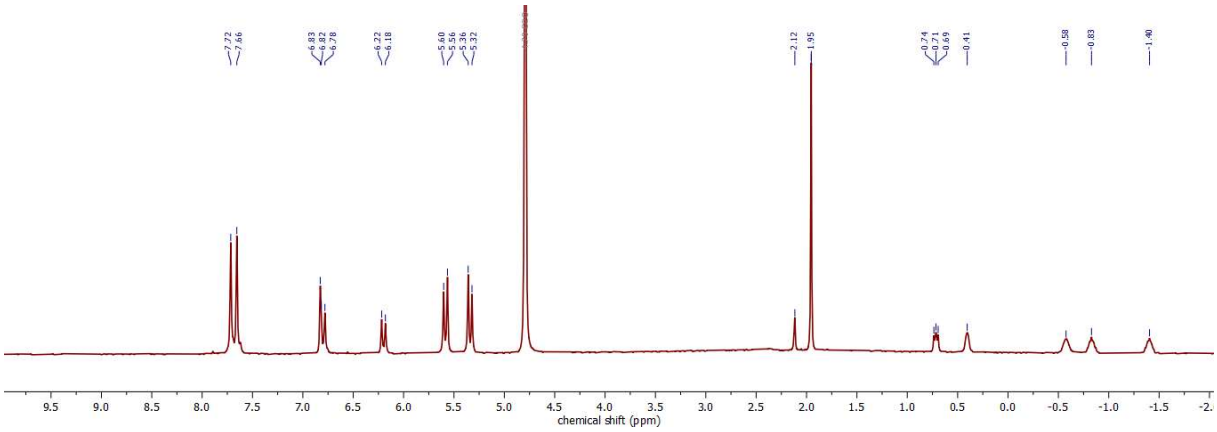

T10S: Table of crystal data, data collection and structure refinement of CP attempts with $[Ag_8L^{Me}_2](NO_3)_2(O)_3$:

Identification code		HeiAl56
Chemical formula		$C_{42.67}H_{39.11}Ag_{7.11}N_{23.48}O_{7.79}$
Formula weight	[g mol^{-1}]	1772.51
Temperature	[K]	100(2)
Wavelength	[Å]	0.71073
Crystal system		orthorhombic
Space group		*P b c a*
Unit cell dimensions		a = 23.521(3) Å, α = 90° b = 31.152(4) Å, β = 90° c = 46.027(5) Å, γ = 90°
Volume	[Å^3]	33725.(7)
Z		18
Calc. Density	[g cm^{-3}]	1.571
Absorption coefficient	[mm^{-1}]	1.872
F(000)		15408
Diffractometer		TXS rotating anode
Radiation source		MoK$_\alpha$
Theta range for data collection	[°]	1.85 – 25.42
Index ranges		-28<=h<=29, -37<=k<=37, -55<=l<=55
Reflections collected		756029
Independent reflections		31012 [R_{int} = 0.2118]
Coverage of independent reflections	[%]	99.6
Absorption correction		Multi-scan
Max., min. transmission		0.8260, 0.6920
Structure solution		Direct methods
Refinement method		Full-matrix least-squares on F^2
Refinement program		SHELXL (Sheldrick 2018), ShelXle (Huebschle 2011)
Function minimised		$\Sigma\, w(F_o^2 - F_c^2)^2$
Data / restraints / parameters		31012 / 1985 / 1657
Goodness-of-Fit on F^2		1.032
Δ/σ_{max}		0.016
Final R indices	I > 2σ(I)	22190 data, R1 = 0.0789, wR2 = 0.2063
	All data	R1 = 0.1072, wR2 = 0.2212
Weighting scheme		W = 1 / [$\sum^2$(FO^2) + (0.0930P)^2 + 539.9154P] where P = (FO^2+2FC^2) / 3
Largest diff. peak, hole	[eÅ^{-3}]	3.441, -1.442
R.M.S. deviation from mean	[eÅ^{-3}]	0.182

F64S: Representation of the electron density of HeiAl56 inside the cavity in ShelXle:

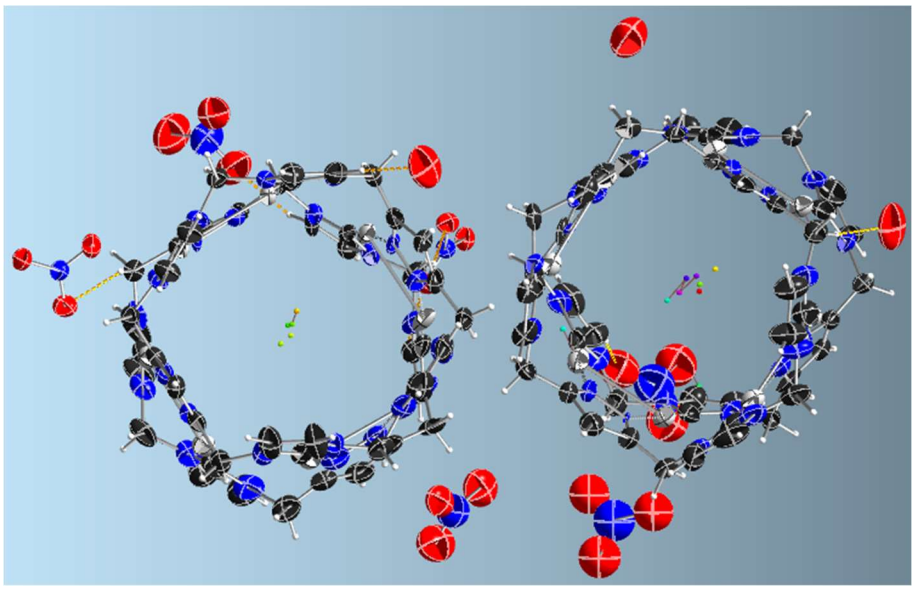

F65S: Crystal packing of $[Ag_8L^{Me}_2](NO_3)_2(O)_3$ (A) along the b-axis and (B) along the c-axis:

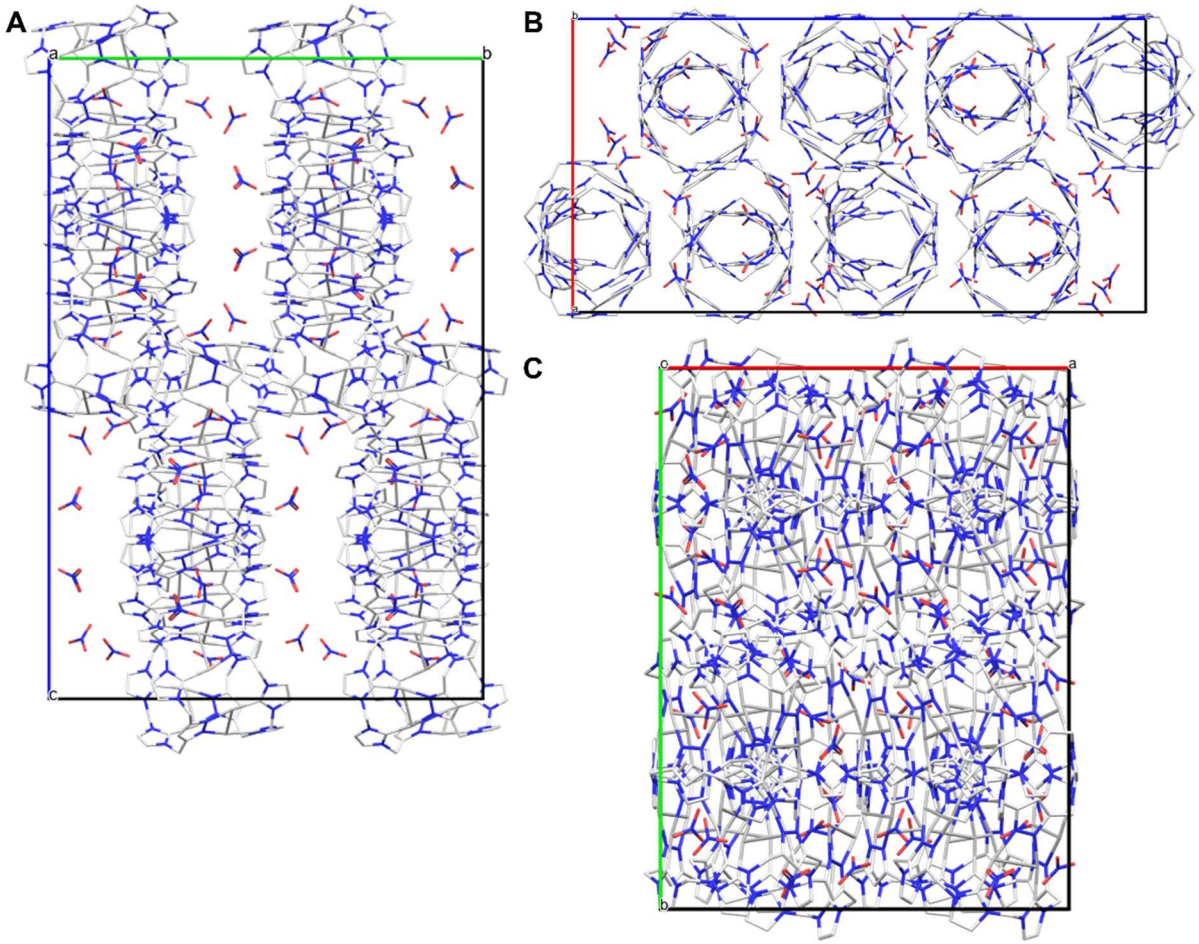

F66S: NMR analysis of $[Ag_8L^{Me}_2](C_{12}H_{28}N_2)(PF_6)_4$ containing ^1H and DOSY NMR spectra:

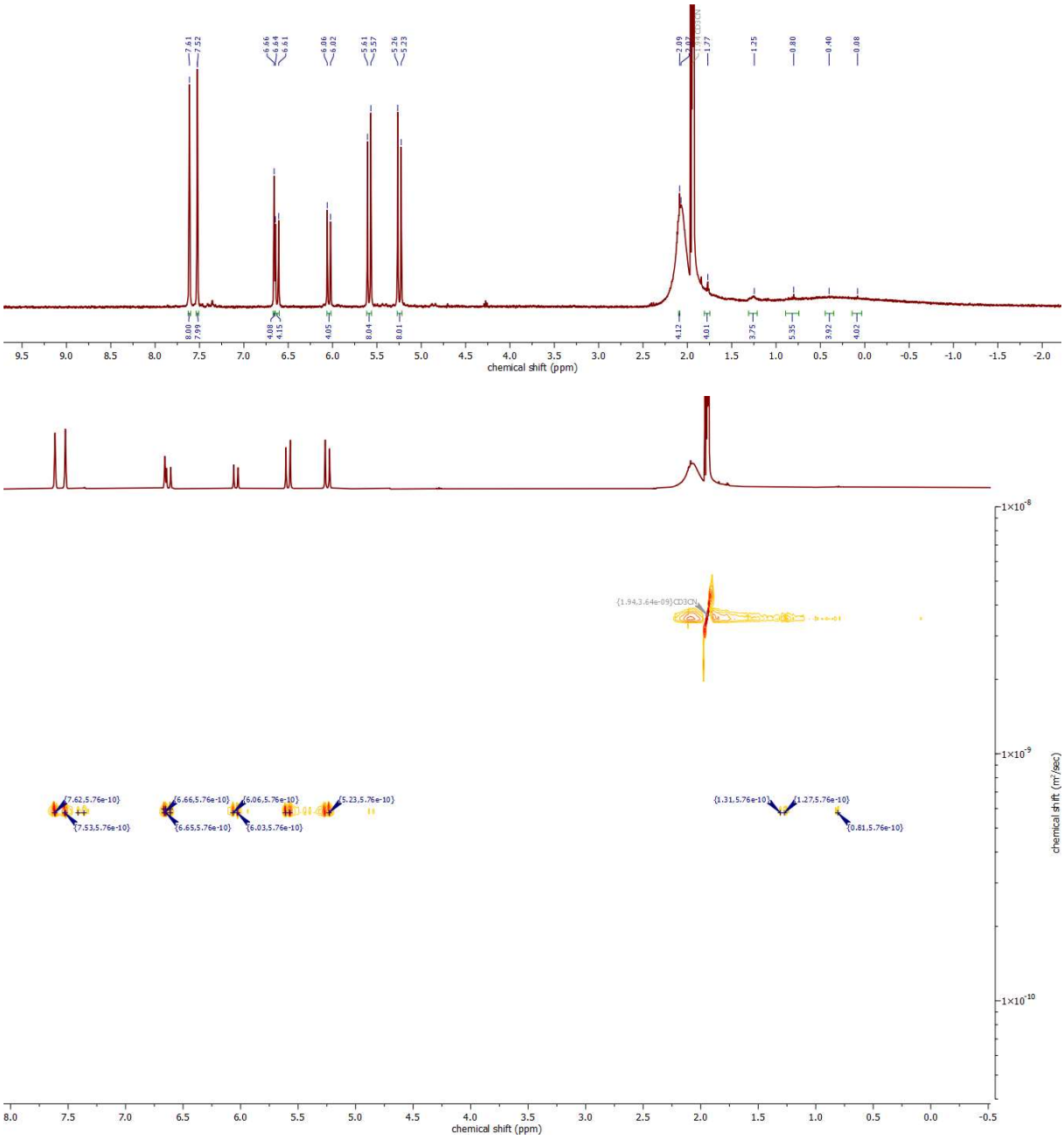

F67S: NMR analysis of $[Ag_8L^{Me}_2](C_{12}H_{22}O_4)(PF_6)_4$ containing ^1H and DOSY NMR spectra:

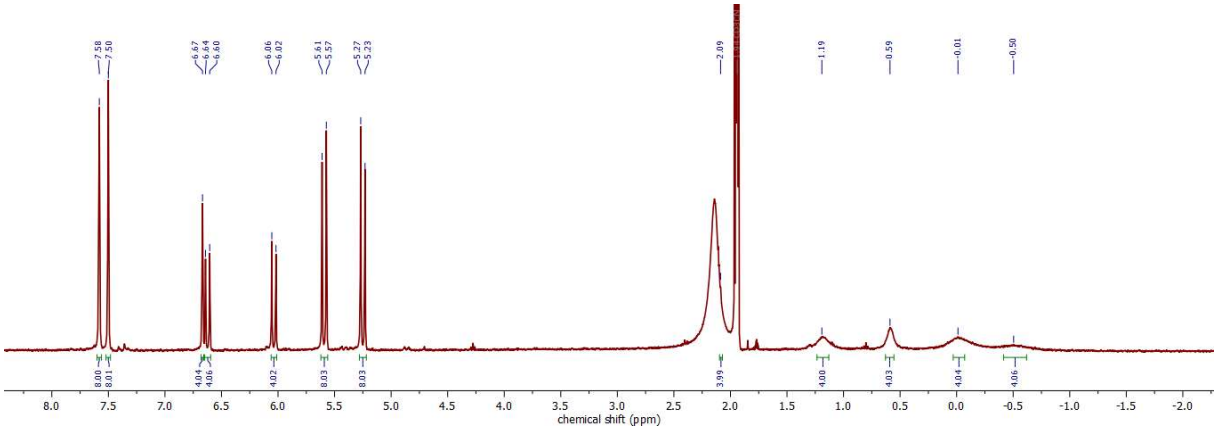

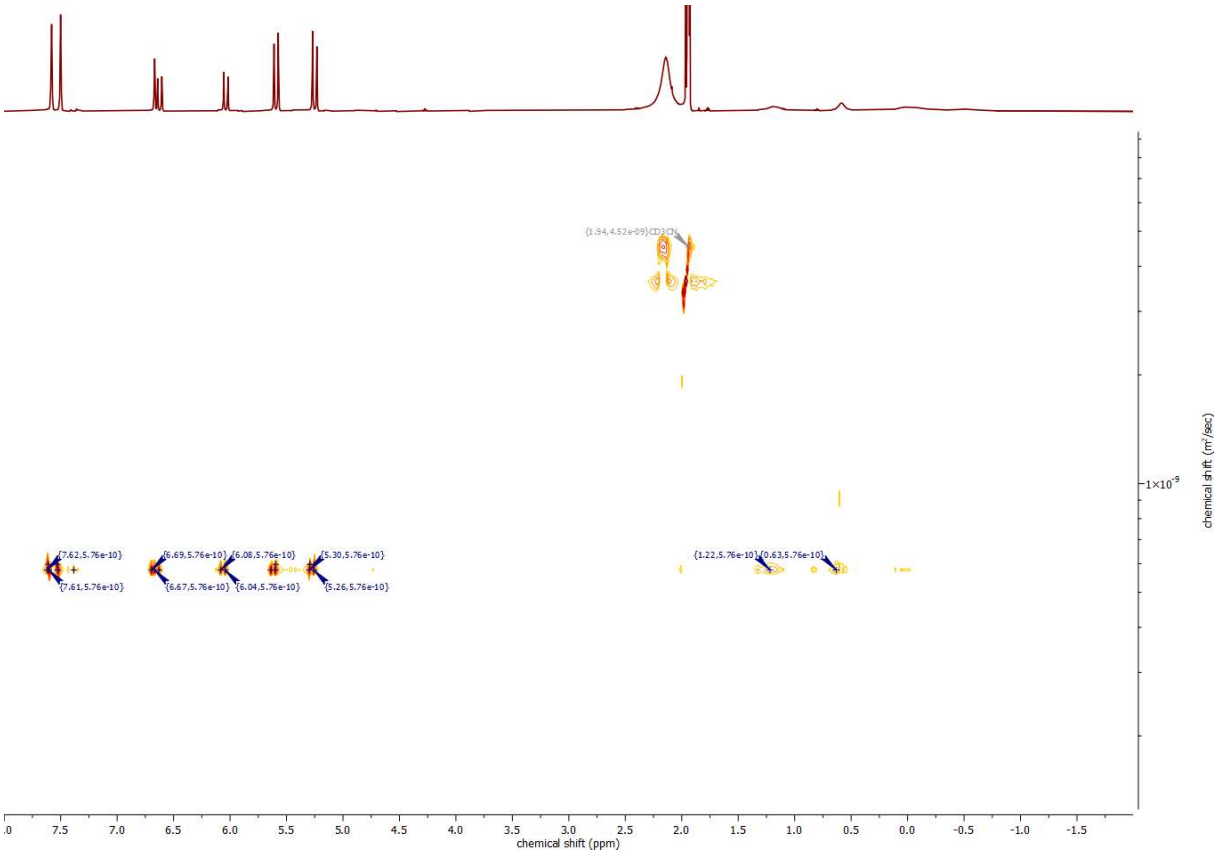

F68S: NMR analysis of $[Ag_8L^{Me}_2](C_{12}H_{22}O_4)(PF_6)_4$ and $[Ag_8L^{Me}_2](C_{12}H_{28}N_2)(PF_6)_4$ containing ^1H and DOSY NMR spectra:

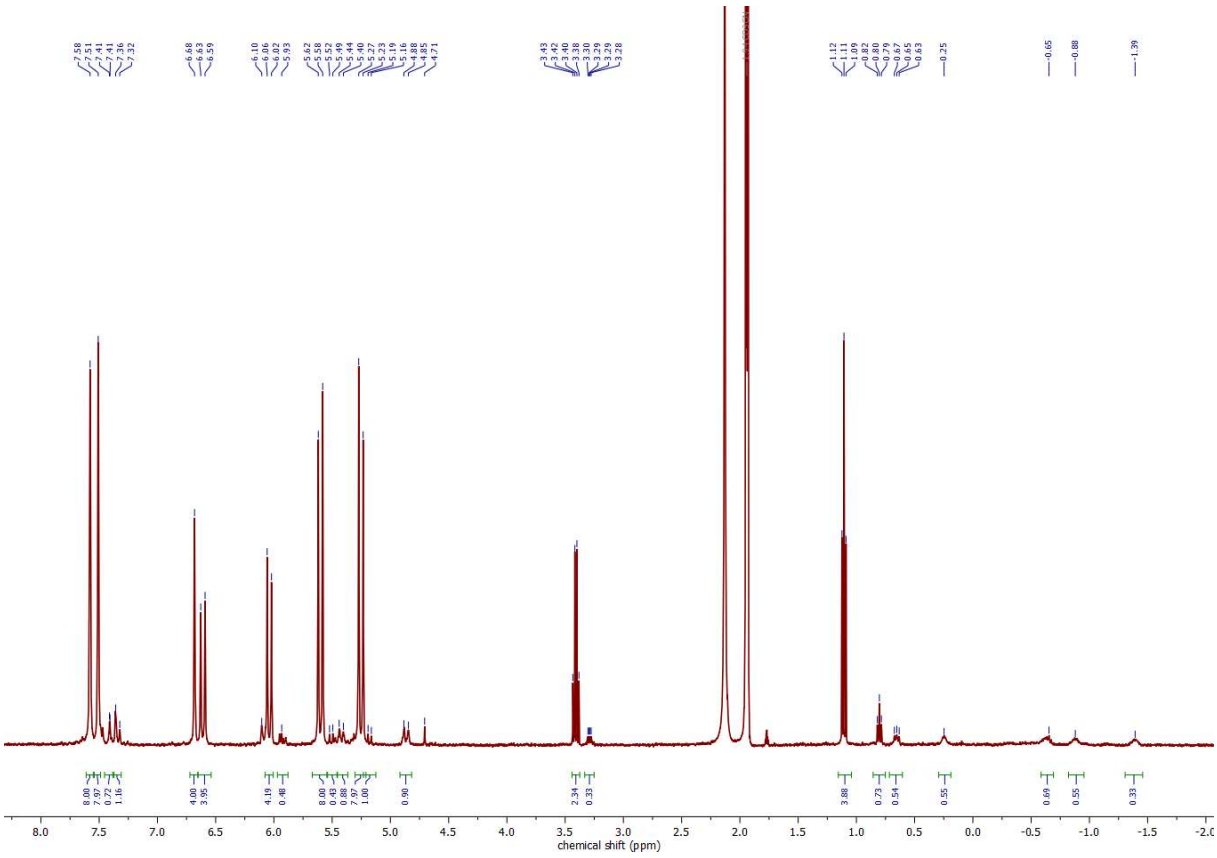

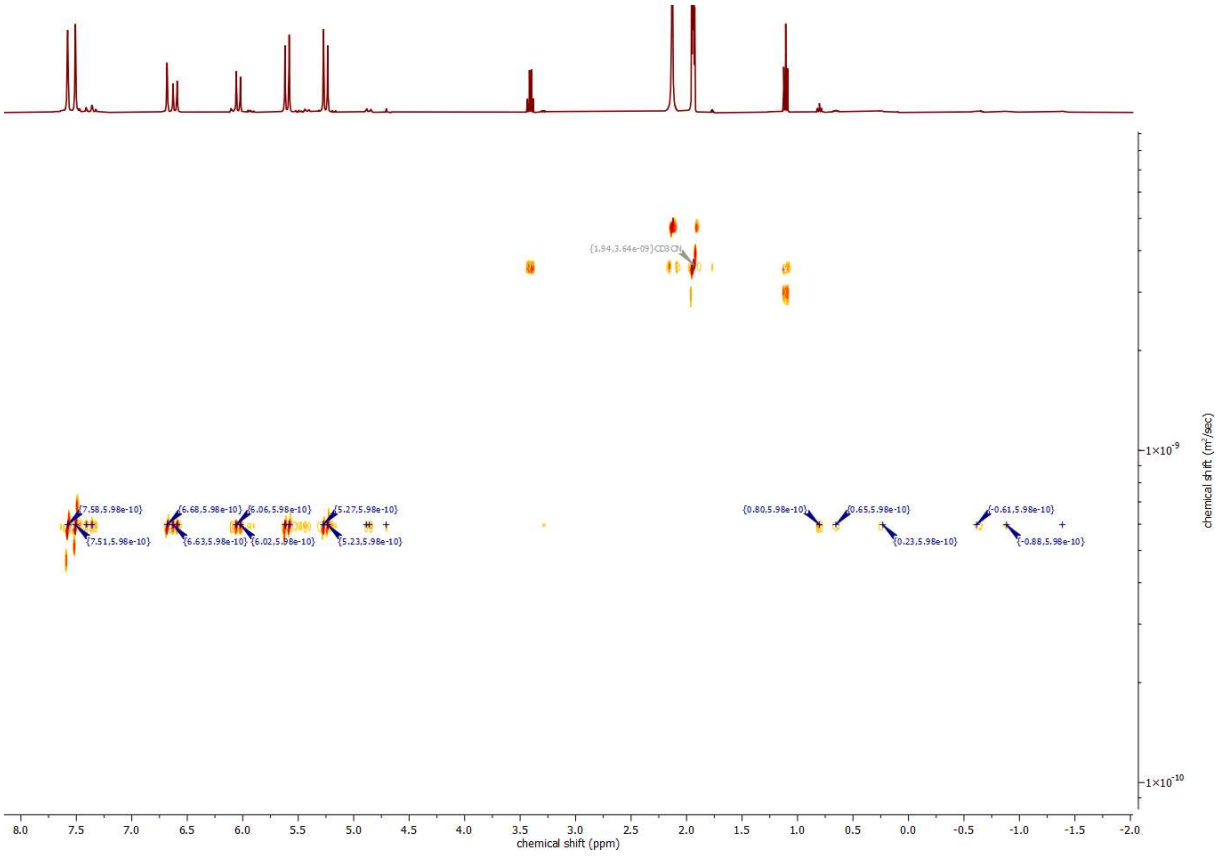

F69S: NMR analysis of $[Ag_8L^{Me}{}_2](C_{12}H_{22}O_4)(PF_6)_4$ and $[Ag_8L^{Me}{}_2](C_{12}H_{28}N_2)(PF_6)_4$ + DCC containing ^1H and DOSY NMR spectra:

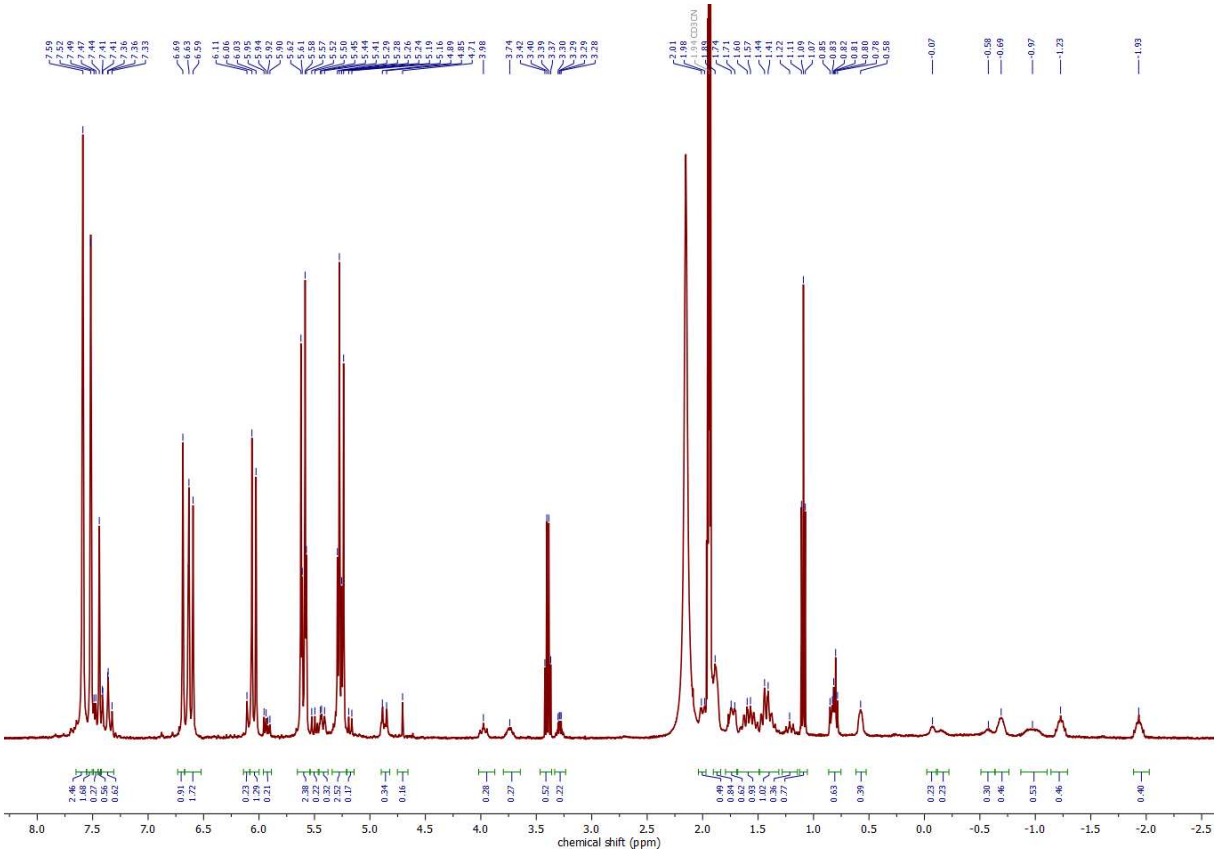

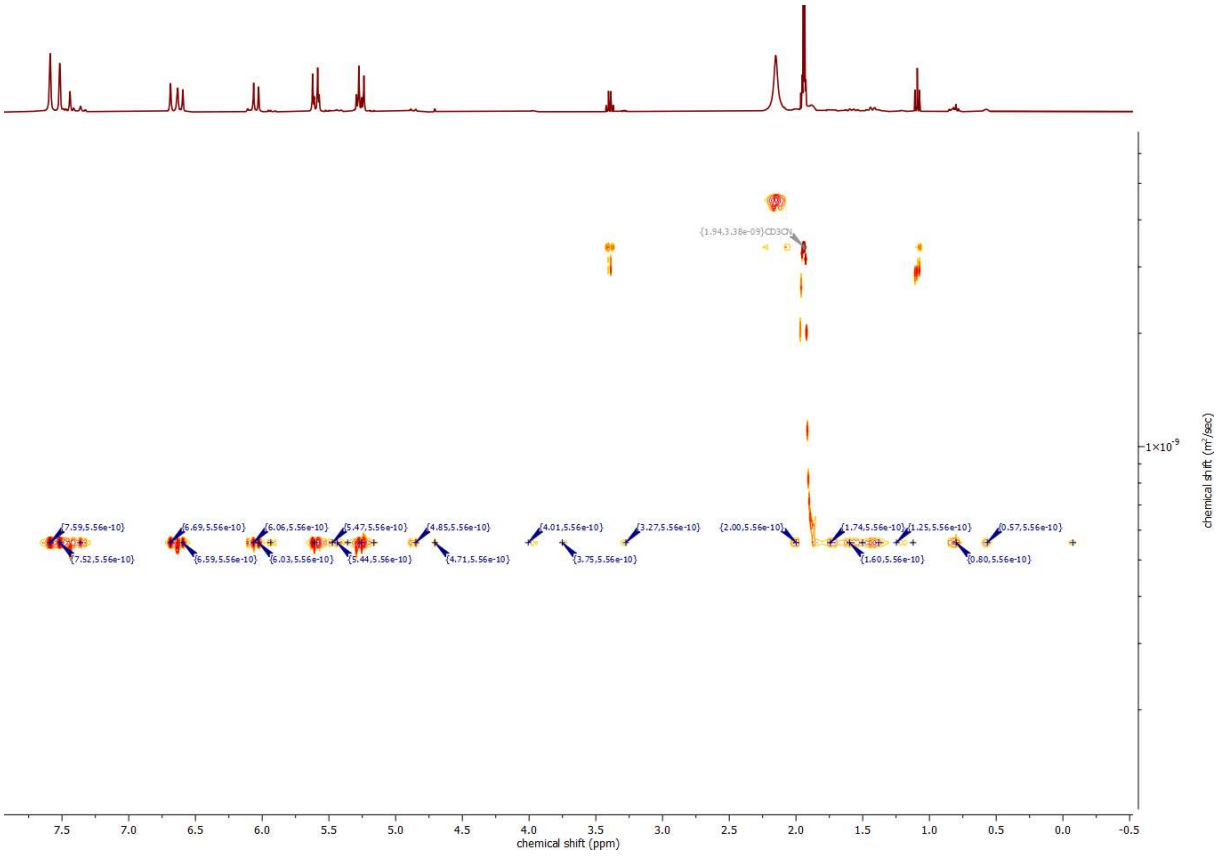

F70S: Size distribution of $[Ag_8L^{Me}_2](PF_6)_4$ in MeCN (1 mg mL^{-1}) measured by DLS experiments with the average size of 28.2 nm calculated based on n = 3 measurements:

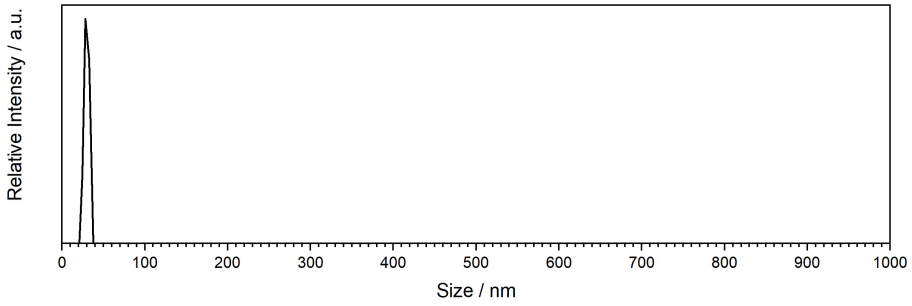

T11S: Table of crystal data, data collection and structure refinement of $[Zn_2L^{Me}(NO_3)_6(OH)_2]$:

Identification code		HeiAl22
Chemical formula		$C_4H_{4.67}N_3O_{3.33}Zn_{0.33}$
Formula weight	[g mol^{-1}]	169.90
Temperature	[K]	100(2)
Wavelength	[Å]	0.71073
Crystal system		triclinic
Space group		*P* -1
Unit cell dimensions		a = 7.6797(10) Å, α = 73.402(6)° b = 11.0464(15) Å, β = 77.973(7)° c = 11.8391(18) Å, γ = 79.306(7)°
Volume	[Å^3]	932.8(2)
Z		6
Calc. Density	[g cm^{-3}]	1.815
Absorption coefficient	[mm^{-1}]	1.395
F(000)		518
Diffractometer		TXS rotating anode
Radiation source		MoK_α
Theta range for data collection	[°]	2.29 – 25.03
Index ranges		-9<=h<=9, -13<=k<=13, -14<=l<=14
Reflections collected		22031
Independent reflections		3293 [R_{int} = 0.0992]
Coverage of independent reflections	[%]	98.9
Absorption correction		Multi-Scan
Max., min. transmission		0.6539, 0.7452
Structure solution		direct methods
Refinement method		Full-matrix least-squares on F^2
Refinement program		SHELXL (Sheldrick 2018), ShelXle (Huebschle 2011)
Function minimised		$\sum w(F_o^2 - F_c^2)^2$
Data / restraints / parameters		3293 / 0 / 201
Goodness-of-Fit on F^2		1.076
Δ/σ_{max}		0.000
Final R indices	I > 2σ(I)	2628 data, R1 = 0.0550, wR2 = 0.1467
	All data	R1 = 0.0751, wR2 = 0.1587
Weighting scheme		W = 1 / [$\sum^2$(FO^2) + (0.0887P)^2 + 2.8697P] where P = (FO^2+2FC^2) / 3
Largest diff. peak, hole	[eÅ^{-3}]	1.718, -0.913
R.M.S. deviation from mean	[eÅ^{-3}]	0.148

F71S: Crystal packing of $[Zn_2L^{Me}(NO_3)_6(OH)_2]$ (A) along the a-axis, (B) along the c-axis and (C) along the b-axis:

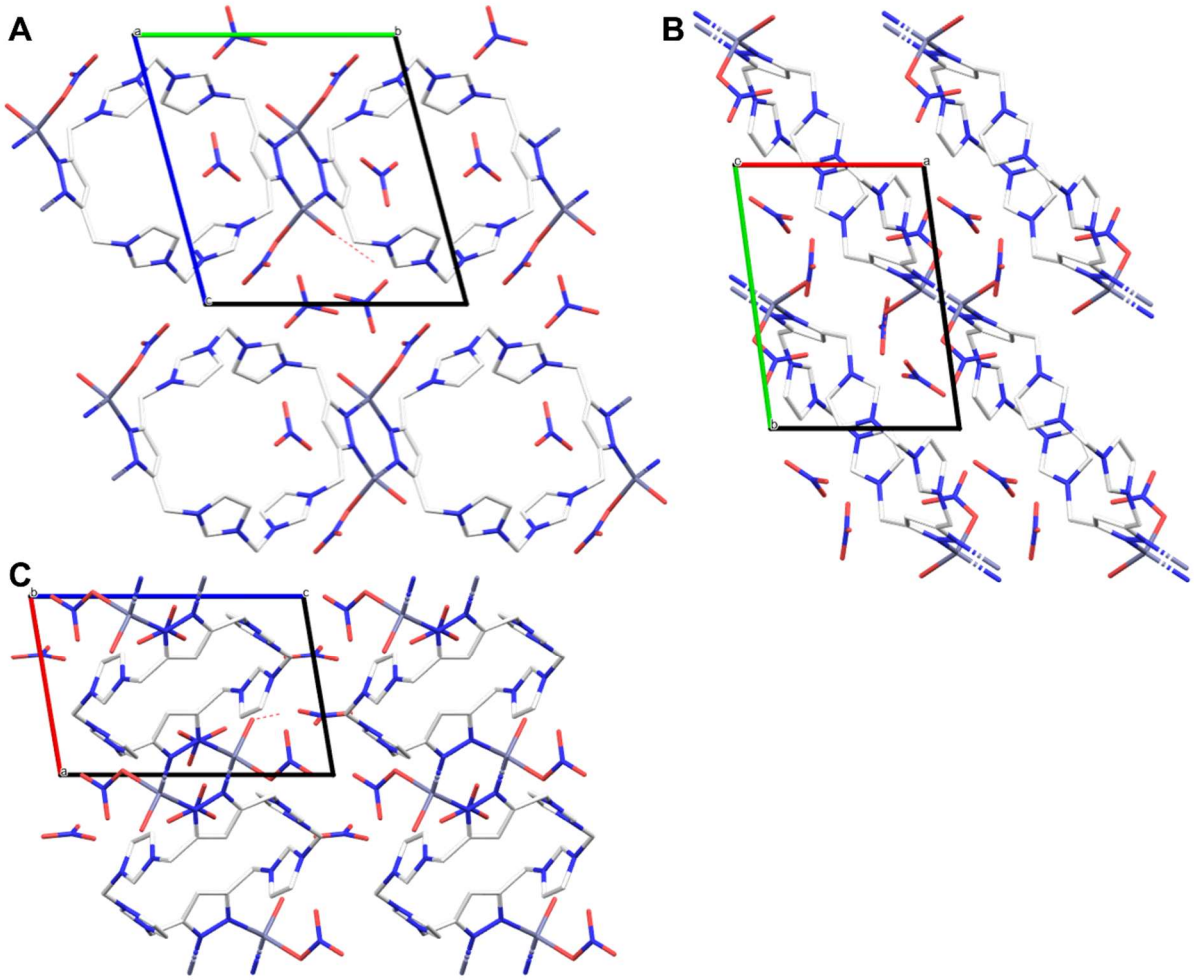

Pillarplex Rotaxanes with Pyridine as Functionality:

F72S: NMR analysis of $[Ag_8L^{Me}_2][Py](PF_6)_4$ containing ^{1}H, ^{13}C, ^{31}P, COSY and DOSY NMR spectra in MeCN-d_3:

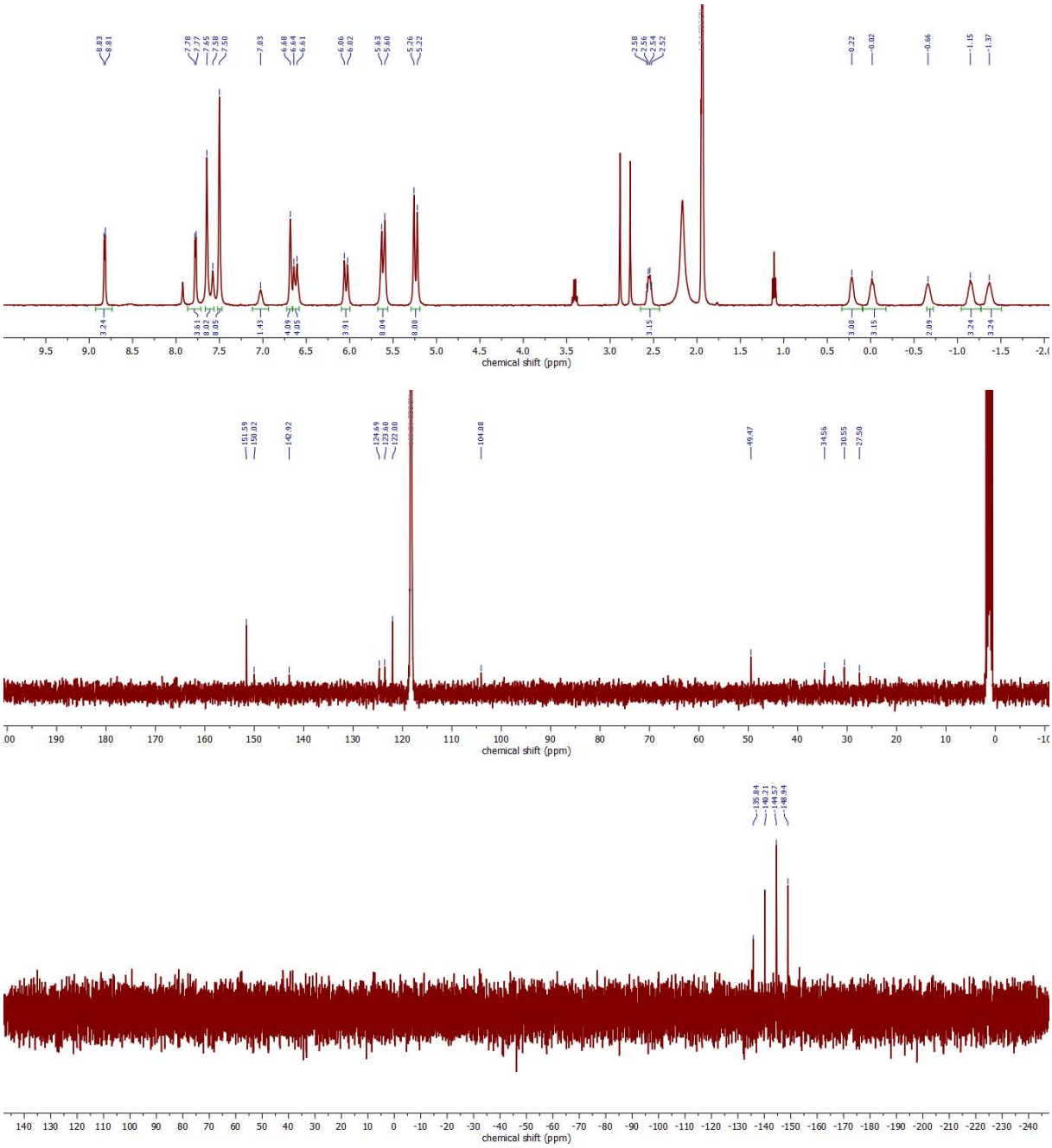

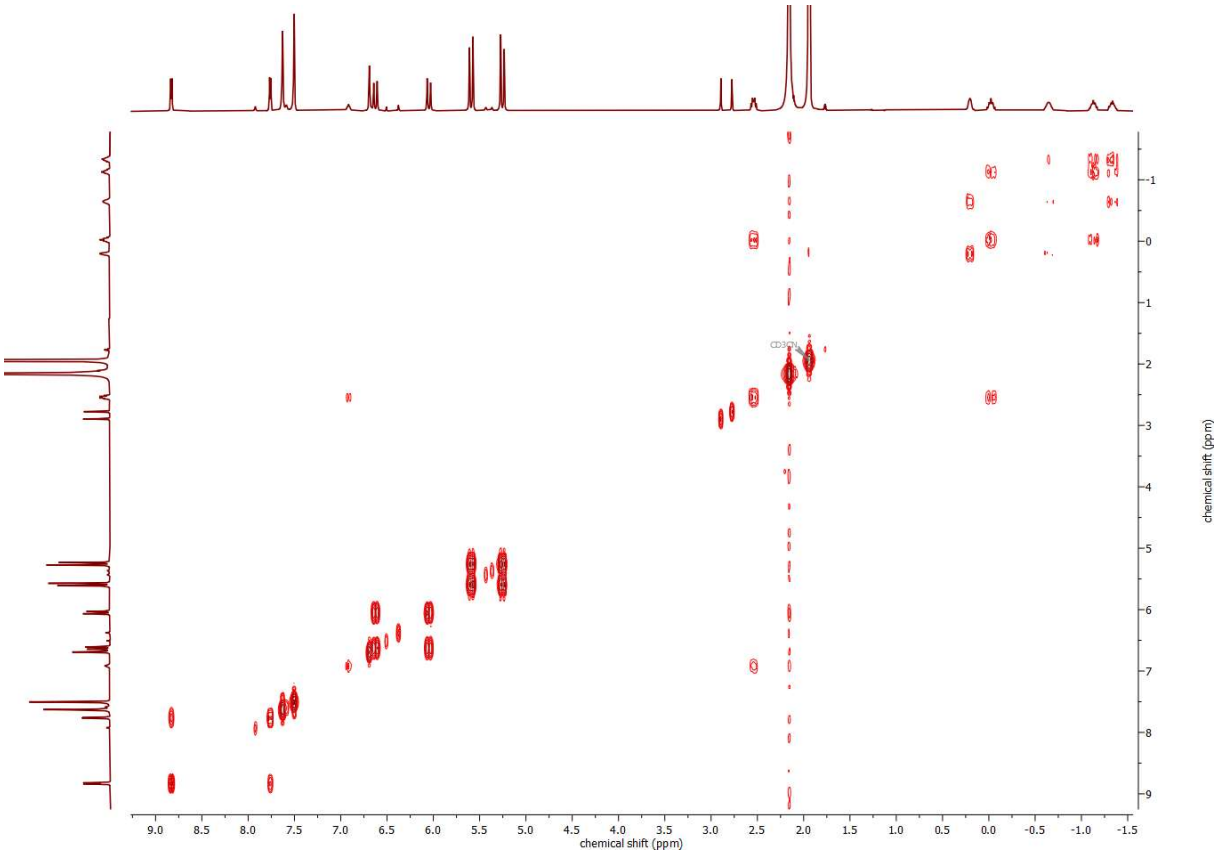
chemical shift (ppm)
chemical shift (ppm)

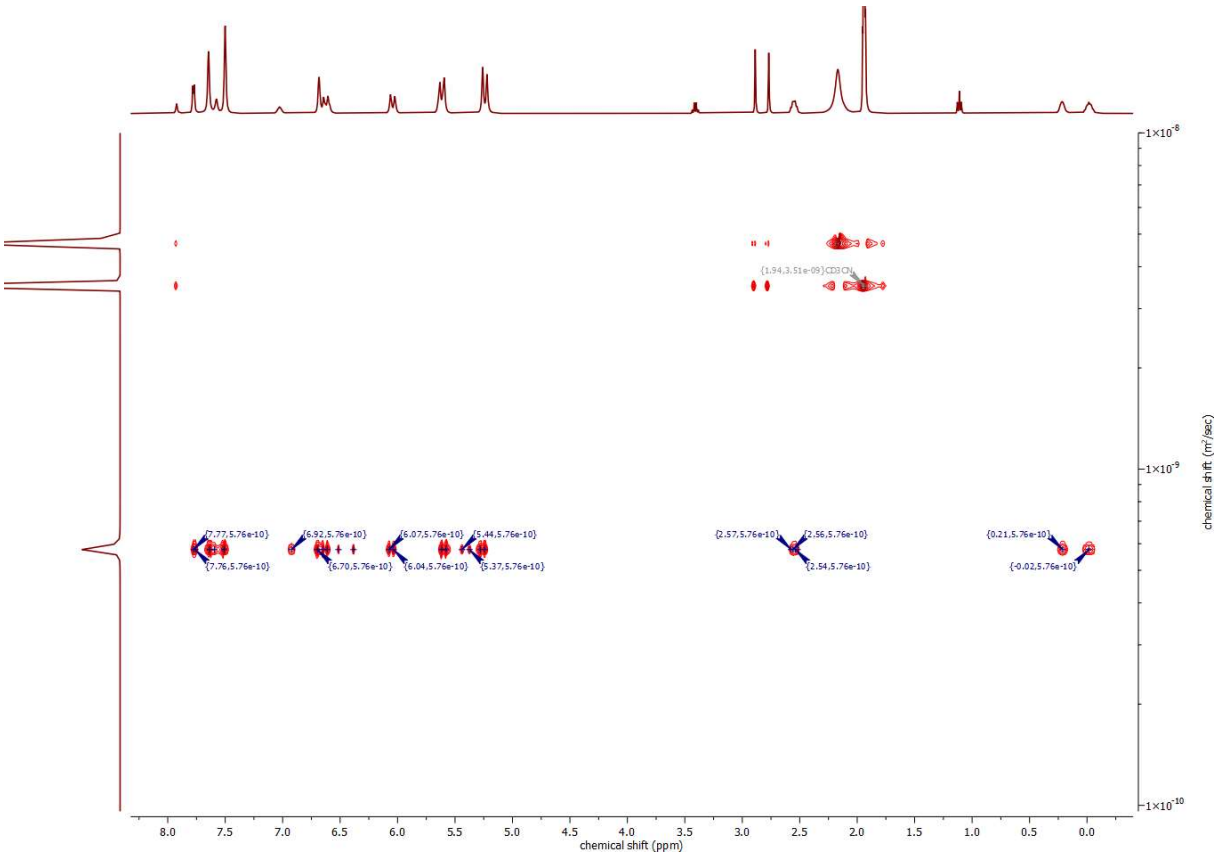
{1.94,3.51e-09}CD3CN
{7.77,5.76e-10}
{7.76,5.76e-10}
{6.92,5.76e-10}
{6.70,5.76e-10}
{6.07,5.76e-10}
{6.04,5.76e-10}
{5.44,5.76e-10}
{5.37,5.76e-10}
{2.57,5.76e-10}
{2.56,5.76e-10}
{2.54,5.76e-10}
{0.21,5.76e-10}
{-0.02,5.76e-10}
chemical shift (ppm)
chemical shift (m²/sec)

F73S: NMR analysis of $[Au_8L^{Me}_2][Py](PF_6)_4$ containing ^1H NMR spectrum in MeCN-d_3:

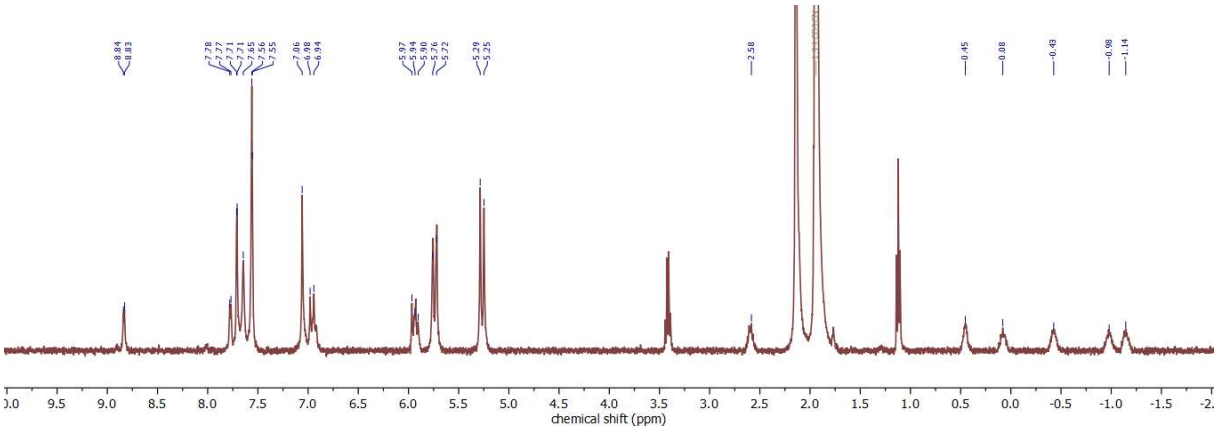

F74S: ESI mass spectra of $[Ag_8L^{Me}_2][Py](PF_6)_4$ and $[Au_8L^{Me}_2][Py](PF_6)_4$ in DMF:

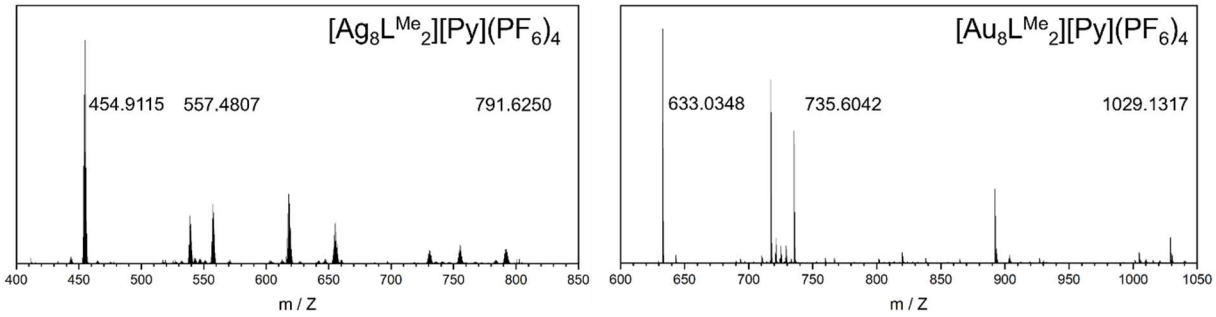

F750S: PXRD pattern of $[Ag_8L^{Me}_2][Py](PF_6)_4$ and $[Au_8L^{Me}_2][Py](PF_6)_4$:

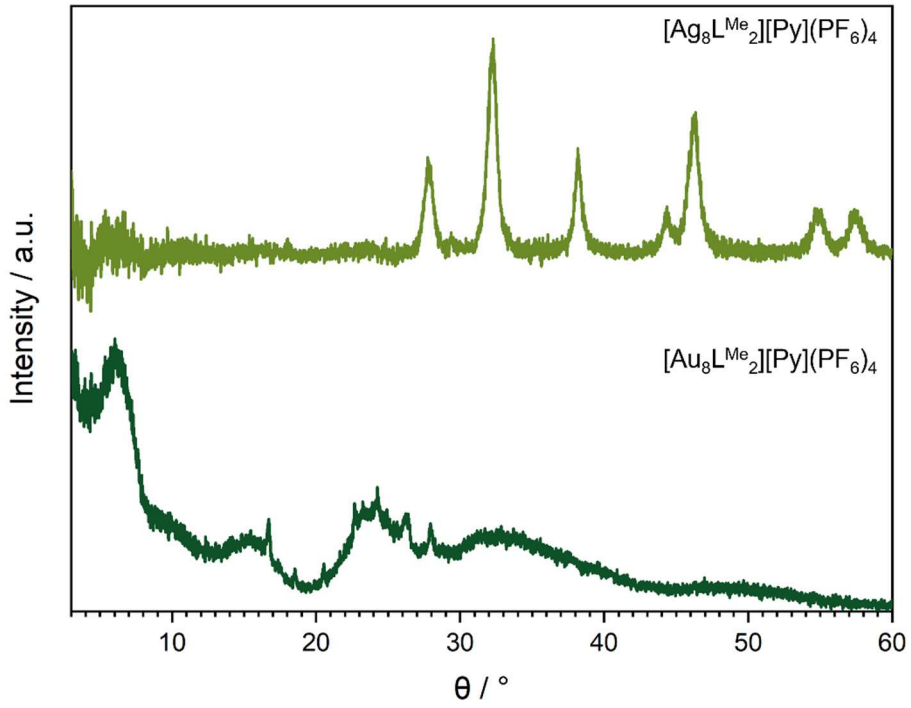

F76S: Schematic representation of a network material containing the pillarplex rotaxane $[Ag_8L^{Me}_2][Py](PF_6)_4$ as organic linker and terephthalic acid as pillar molecule to compensate the high steric demand of the rotaxane linker:

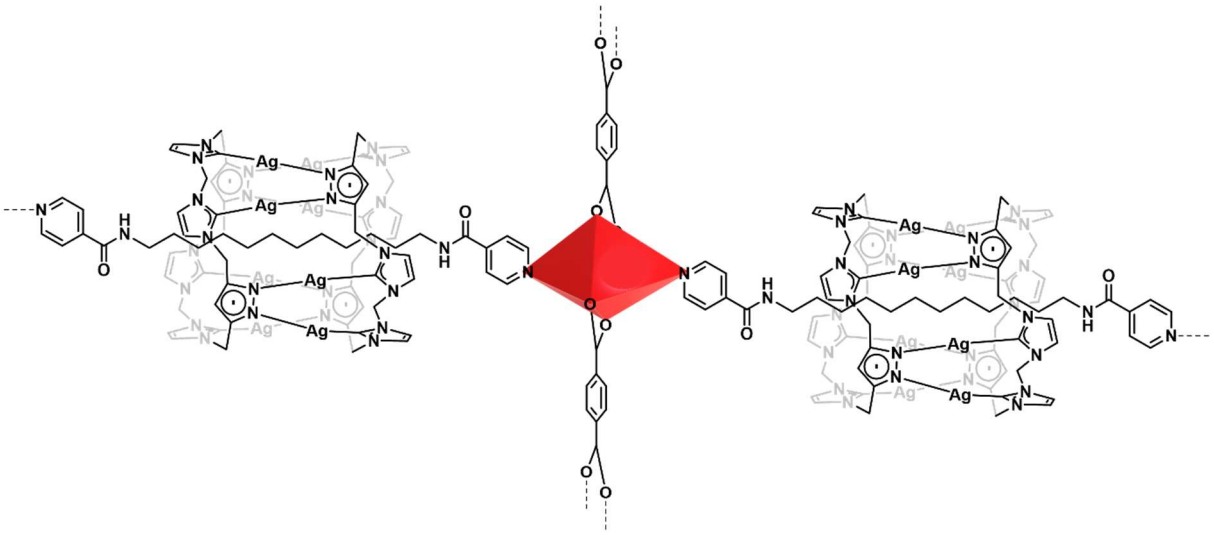

Photochemistry of Au(I)-Pillarplexes and Pillarplex Rotaxanes Containing *N*-naphthalimide as (Photo-)Active Unit:

F77S: UV-vis absorption spectra of $[Au_8L^{Me}_2](PF_6)_4$ in MeCN:Et_2O (c = 6.425 · 10^{-6} M):

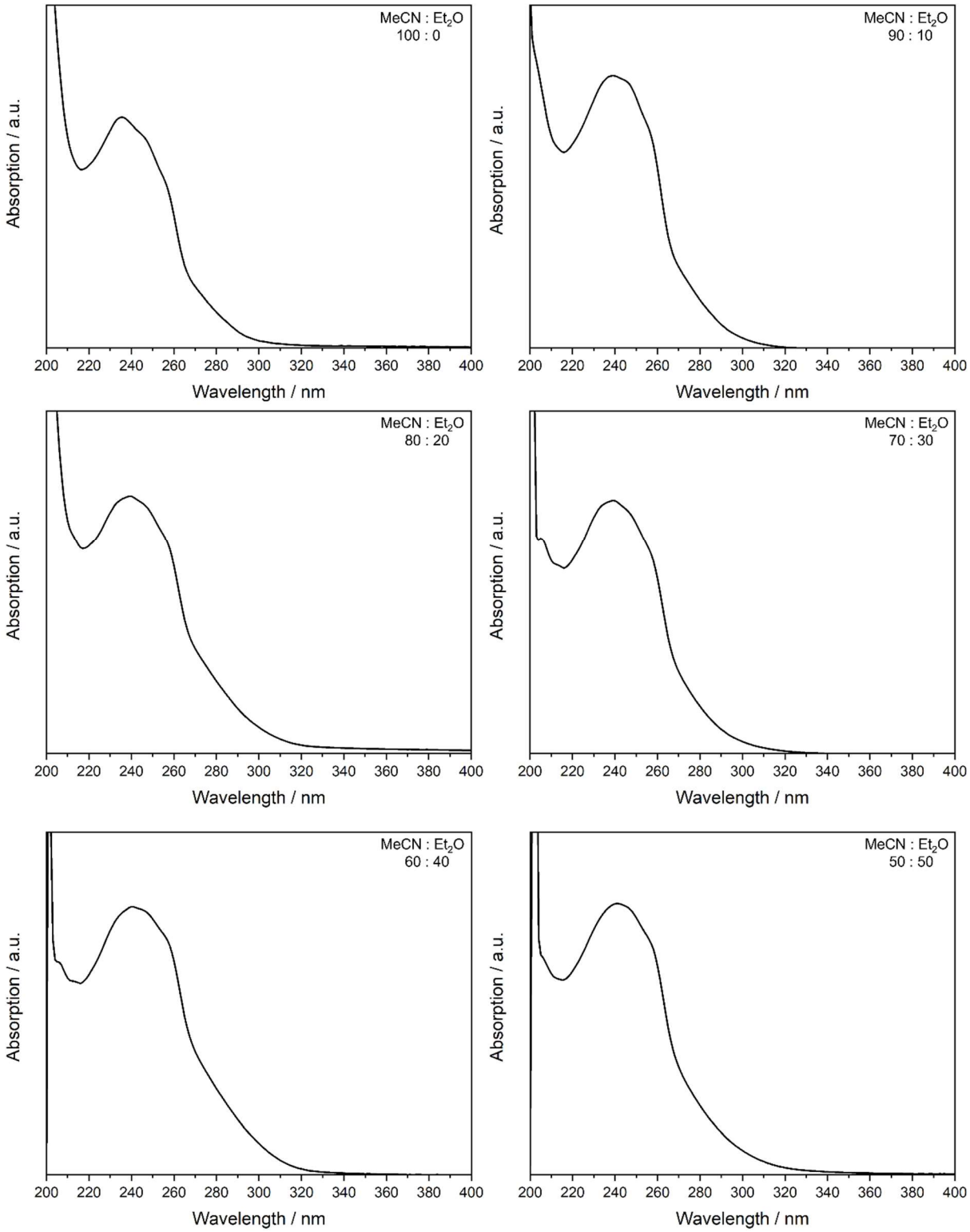

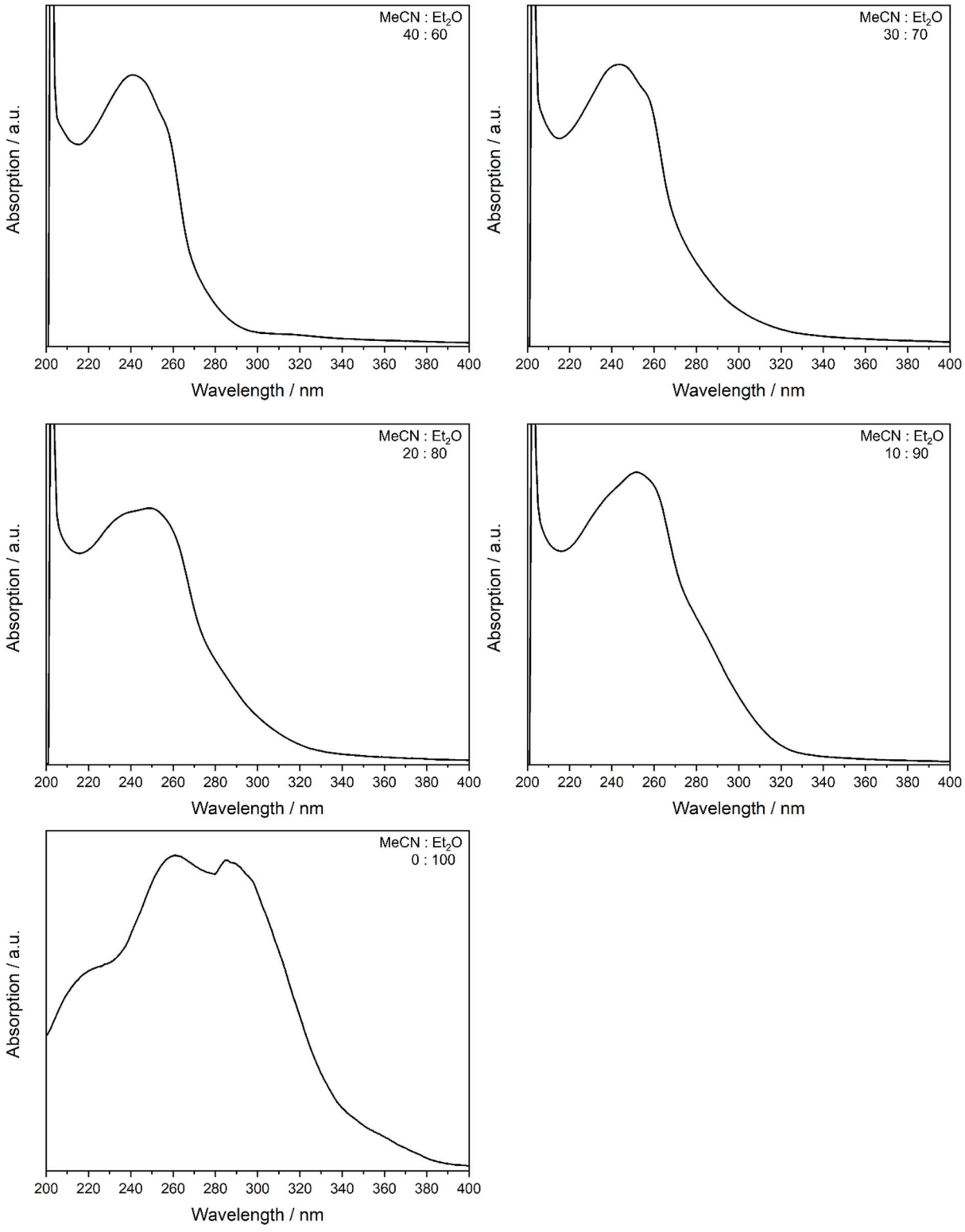
MeCN : Et2O
40 : 60
Absorption / a.u.
Wavelength / nm
MeCN : Et2O
30 : 70
Absorption / a.u.
Wavelength / nm
MeCN : Et2O
20 : 80
Absorption / a.u.
Wavelength / nm
MeCN : Et2O
10 : 90
Absorption / a.u.
Wavelength / nm
MeCN : Et2O
0 : 100
Absorption / a.u.
Wavelength / nm
200 220 240 260 280 300 320 340 360 380 400

F78S: Excitation spectra of $[Au_8L^{Me}_2](PF_6)_4$ in MeCN:Et_2O (c = 6.425 · 10^{-6} M):

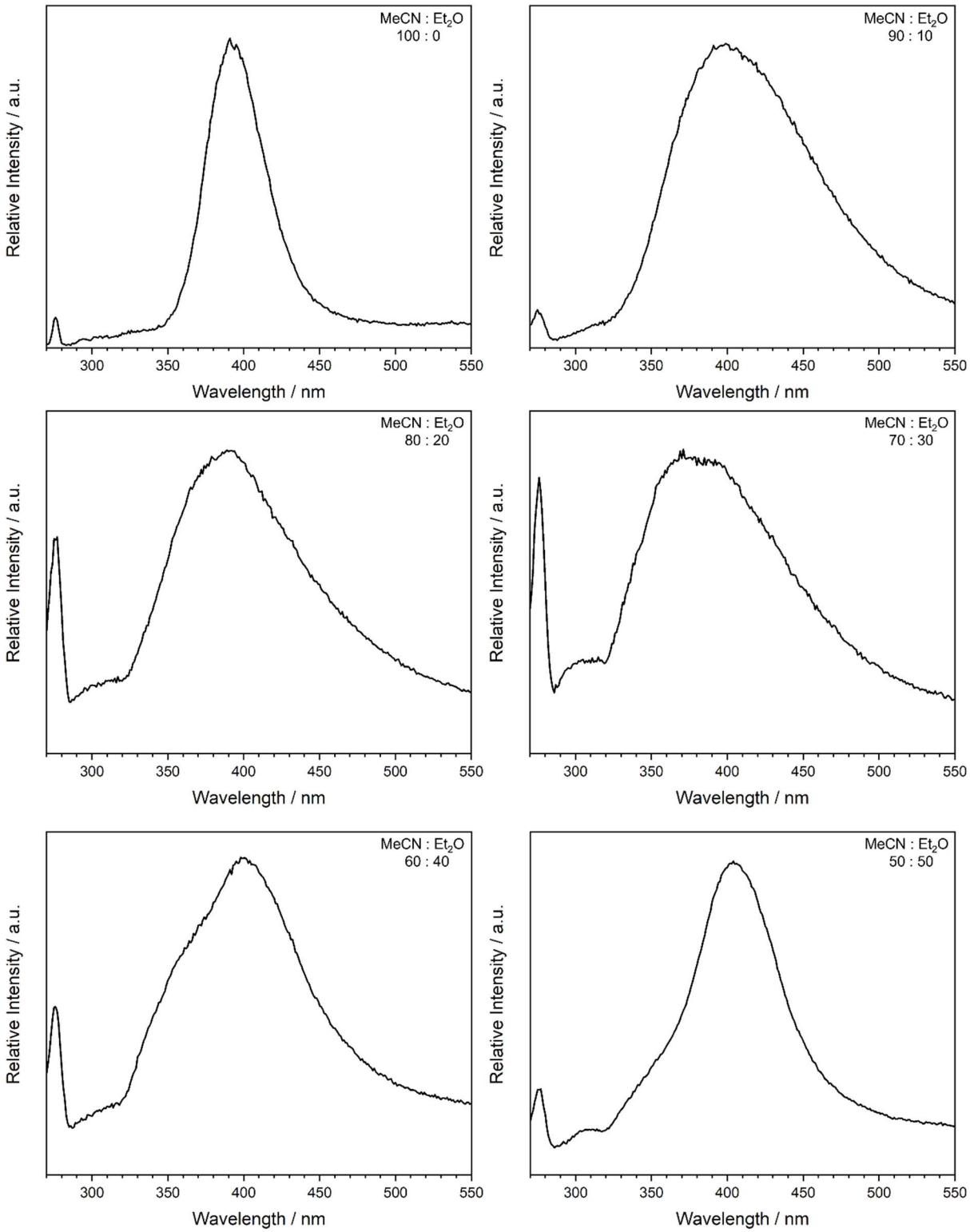

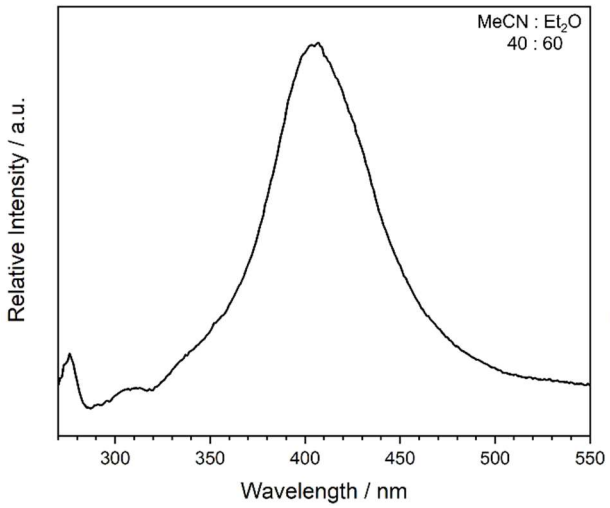
MeCN : Et2O
40 : 60
Relative Intensity / a.u.
300
350
400
450
500
550
Wavelength / nm

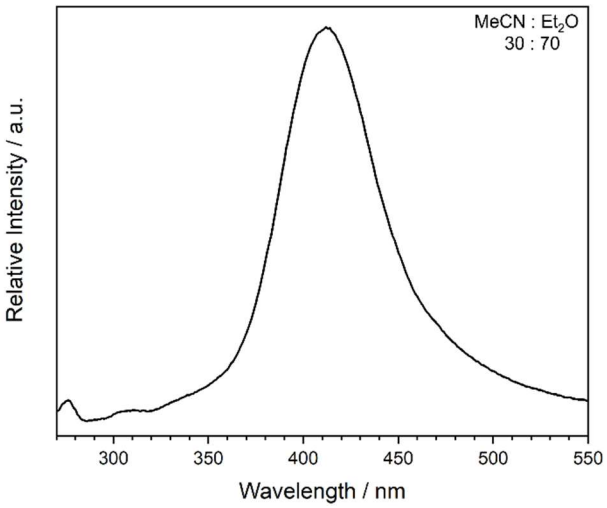
MeCN : Et2O
30 : 70
Relative Intensity / a.u.
300
350
400
450
500
550
Wavelength / nm

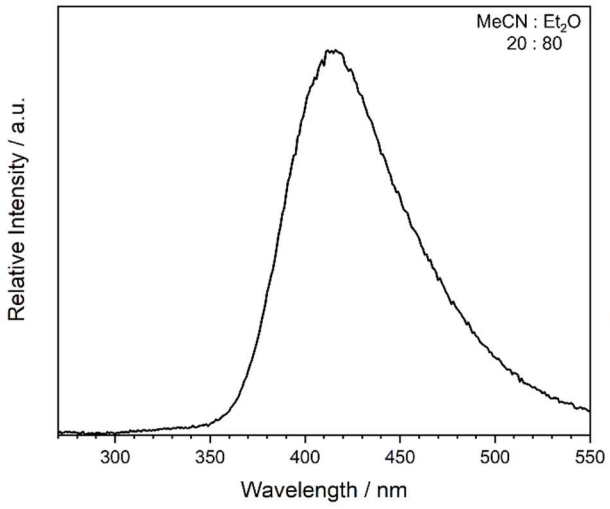
MeCN : Et2O
20 : 80
Relative Intensity / a.u.
300
350
400
450
500
550
Wavelength / nm

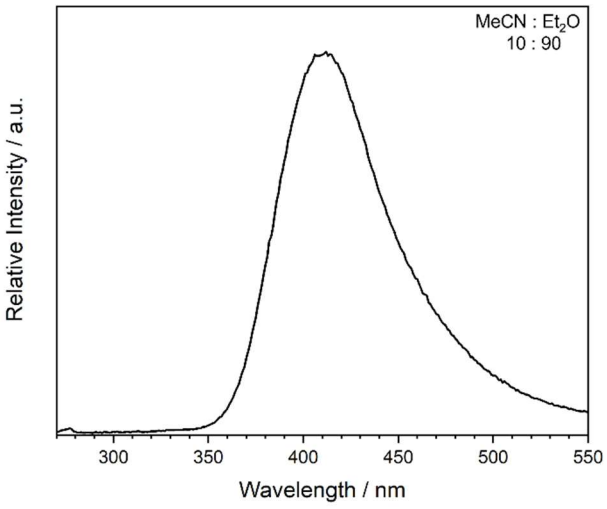
MeCN : Et2O
10 : 90
Relative Intensity / a.u.
300
350
400
450
500
550
Wavelength / nm

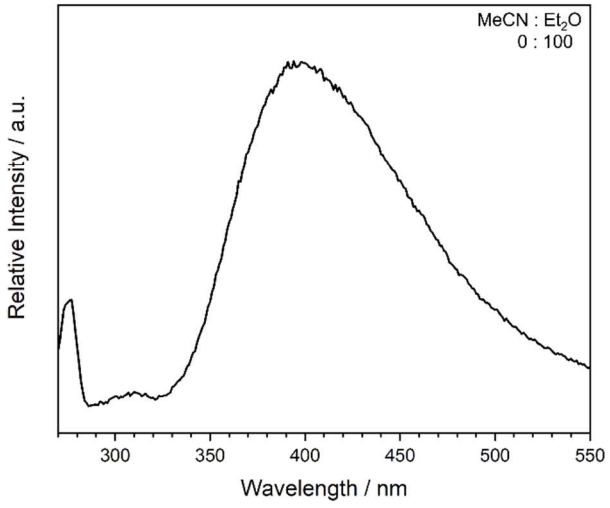
MeCN : Et2O
0 : 100
Relative Intensity / a.u.
300
350
400
450
500
550
Wavelength / nm

F79S: DLS measurement evaluated towards size distribution of $[Au_8L^{Me}_2](PF_6)_4$ ($c = 6.425 \cdot 10^{-6}$ M):

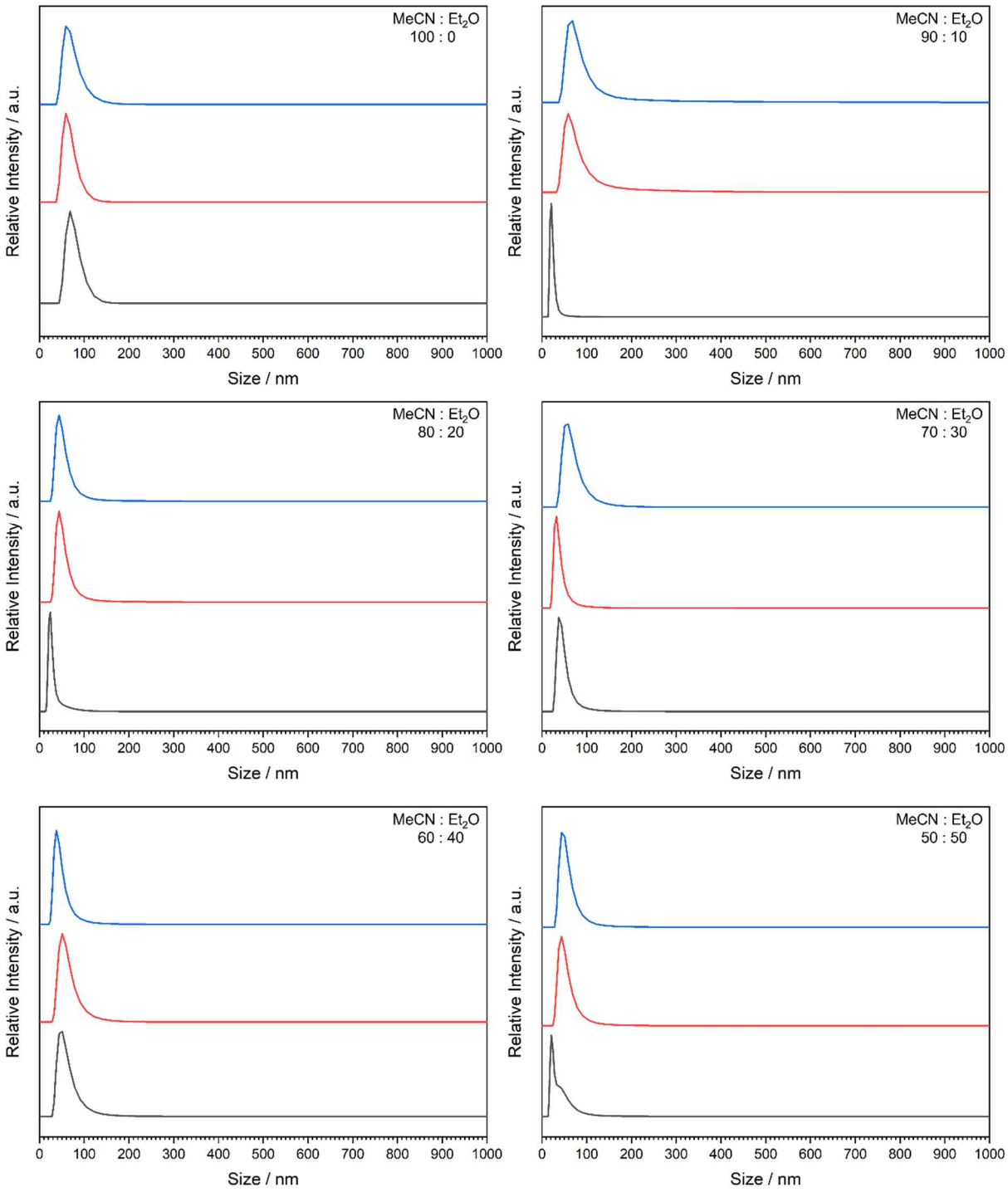

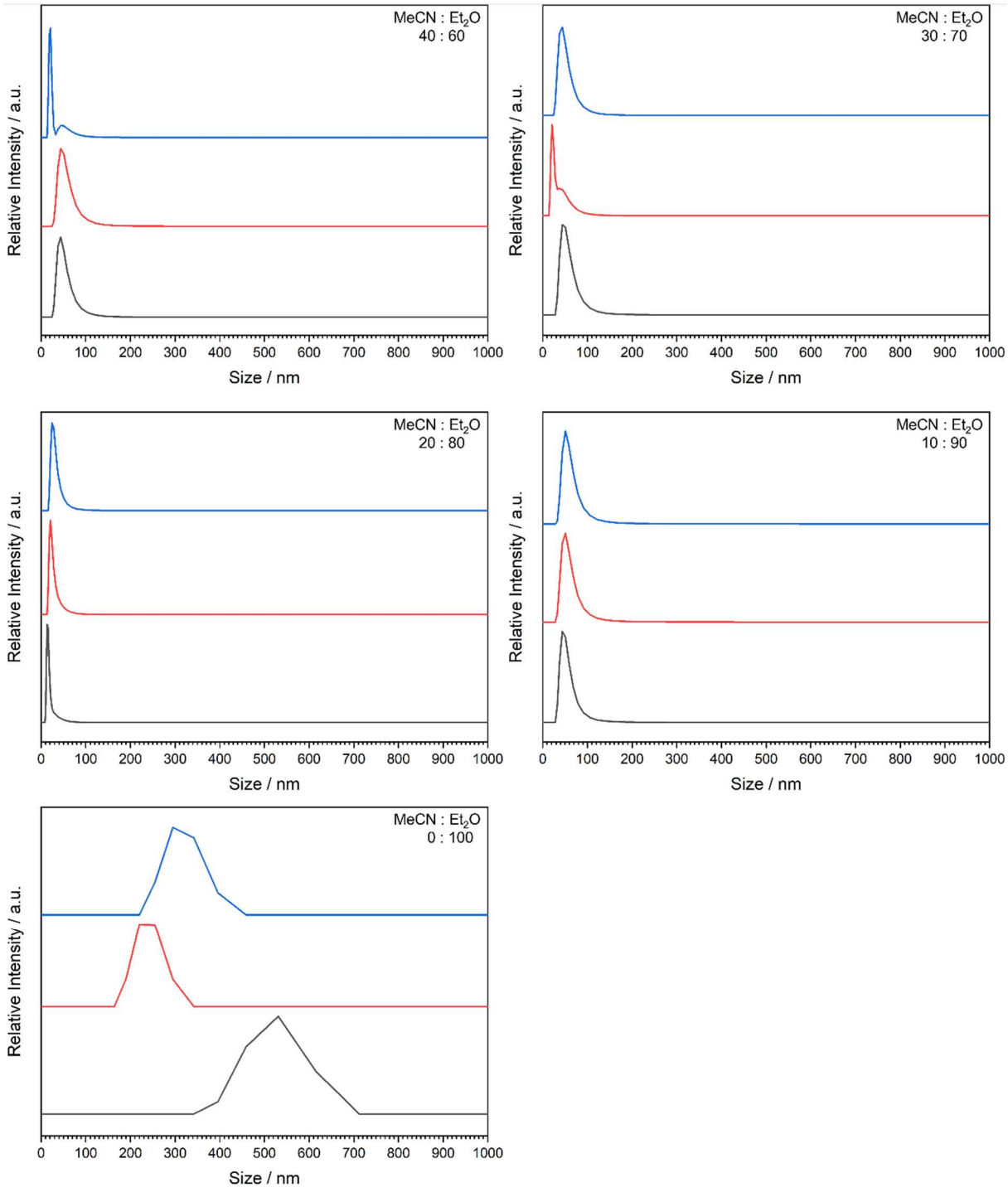
MeCN : Et2O
40 : 60
Relative Intensity / a.u.
0 100 200 300 400 500 600 700 800 900 1000
Size / nm
MeCN : Et2O
30 : 70
Relative Intensity / a.u.
0 100 200 300 400 500 600 700 800 900 1000
Size / nm
MeCN : Et2O
20 : 80
Relative Intensity / a.u.
0 100 200 300 400 500 600 700 800 900 1000
Size / nm
MeCN : Et2O
10 : 90
Relative Intensity / a.u.
0 100 200 300 400 500 600 700 800 900 1000
Size / nm
MeCN : Et2O
0 : 100
Relative Intensity / a.u.
0 100 200 300 400 500 600 700 800 900 1000
Size / nm

F80S: NMR analysis of $[Ag_8L^{Me}_2][NMI\text{-}\mathbf{C_{12}}](PF_6)_4$ containing ^{31}P, COSY and DOSY NMR spectra in MeCN-d_3:

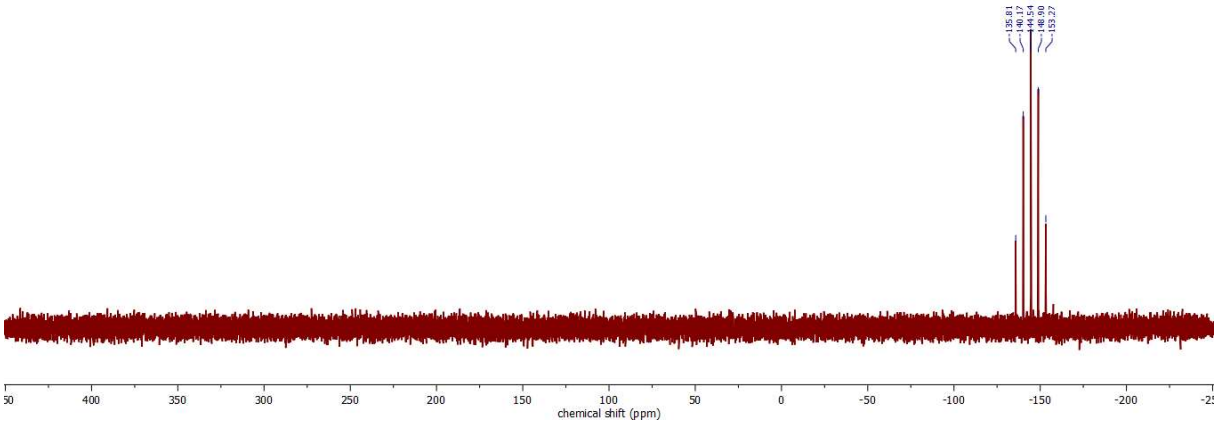

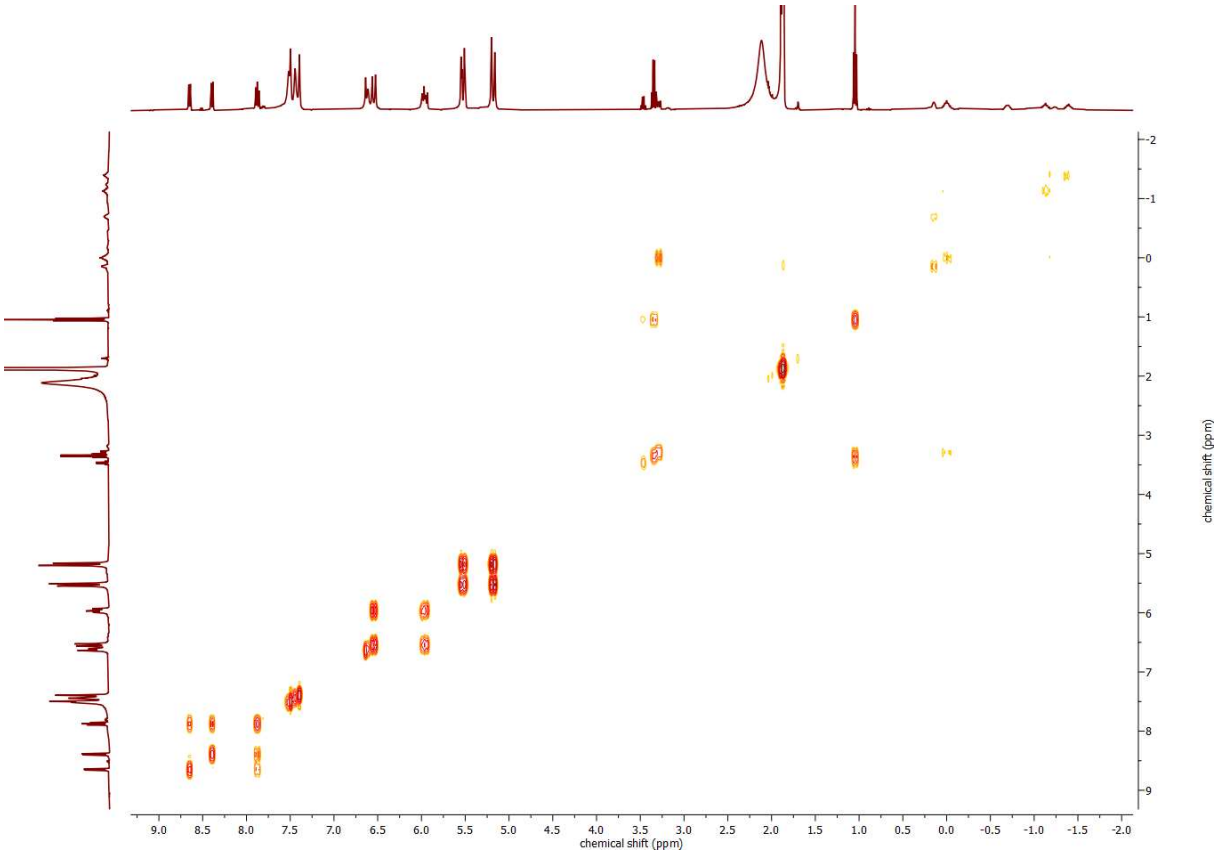

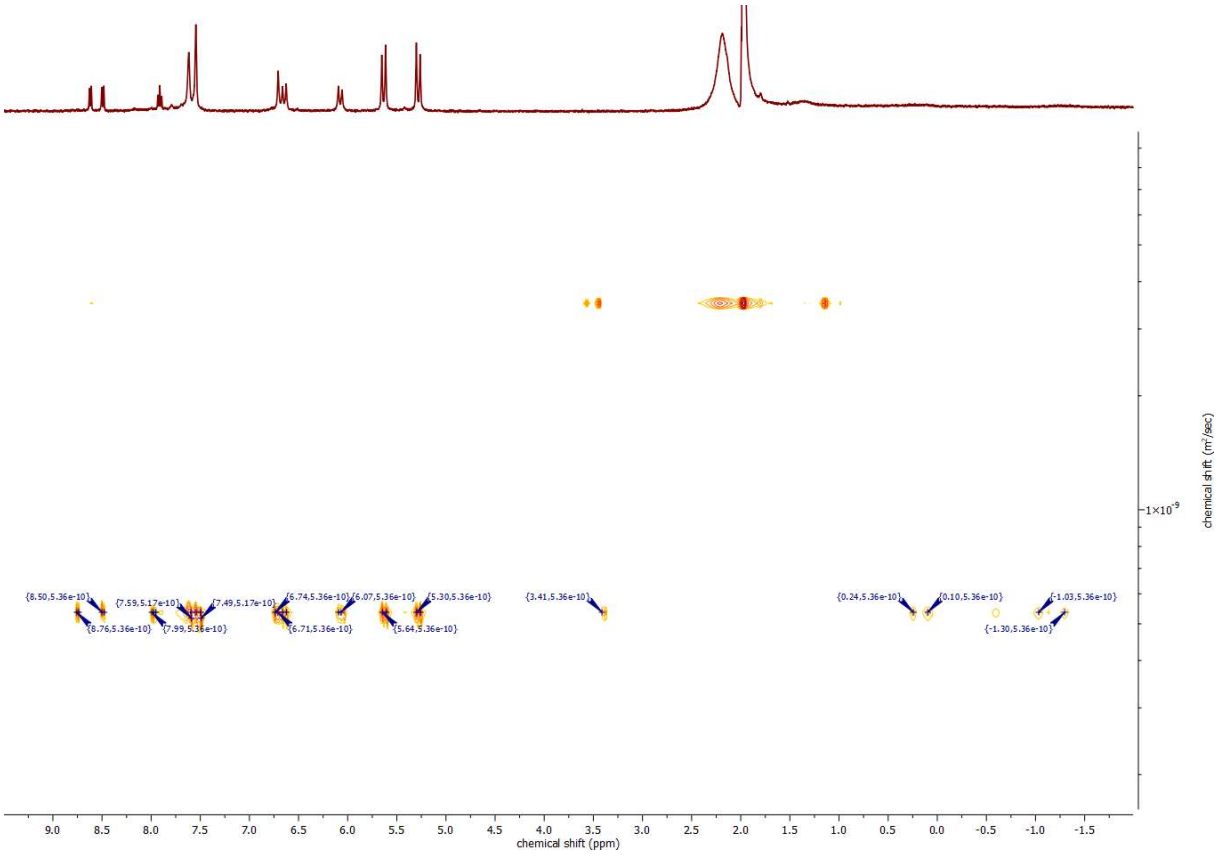
{8.50,5.36e-10}
{8.76,5.36e-10}
{7.59,5.17e-10}
{7.99,5.36e-10}
{7.49,5.17e-10}
{6.74,5.36e-10}
{6.71,5.36e-10}
{6.07,5.36e-10}
{5.64,5.36e-10}
{5.30,5.36e-10}
{3.41,5.36e-10}
{0.24,5.36e-10}
{0.10,5.36e-10}
{-1.30,5.36e-10}
{-1.03,5.36e-10}
1×10-9
chemical shift (m²/sec)
9.0
8.5
8.0
7.5
7.0
6.5
6.0
5.5
5.0
4.5
4.0
3.5
3.0
2.5
2.0
1.5
1.0
0.5
0.0
-0.5
-1.0
-1.5
chemical shift (ppm)

F81S: IR spectra of 1,8-naphthalic anhydride, $[Ag_8L^{Me}{}_2](PF_6)_4$ and $[Ag_8L^{Me}{}_2][NMI\text{-}\mathbf{C_{12}}](PF_6)_4$ in solid state:

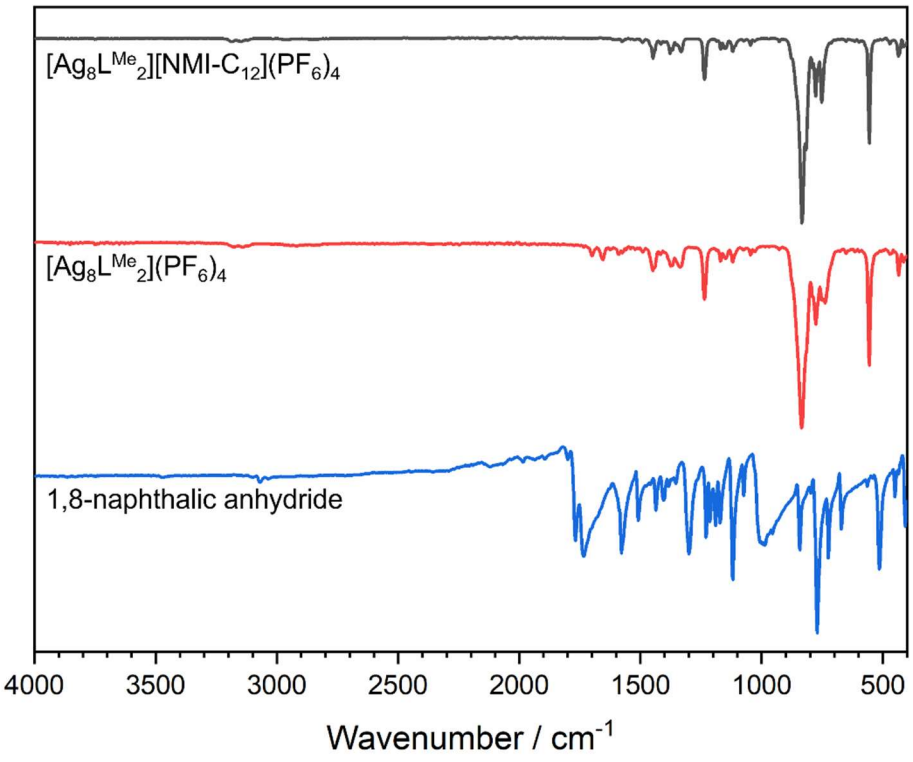

F82S: UV-vis spectra of 1,8-naphthalic anhydride, $[Ag_8L^{Me}{}_2](PF_6)_4$ and $[Ag_8L^{Me}{}_2][NMI\text{-}\mathbf{C_{12}}](PF_6)_4$ in MeCN:

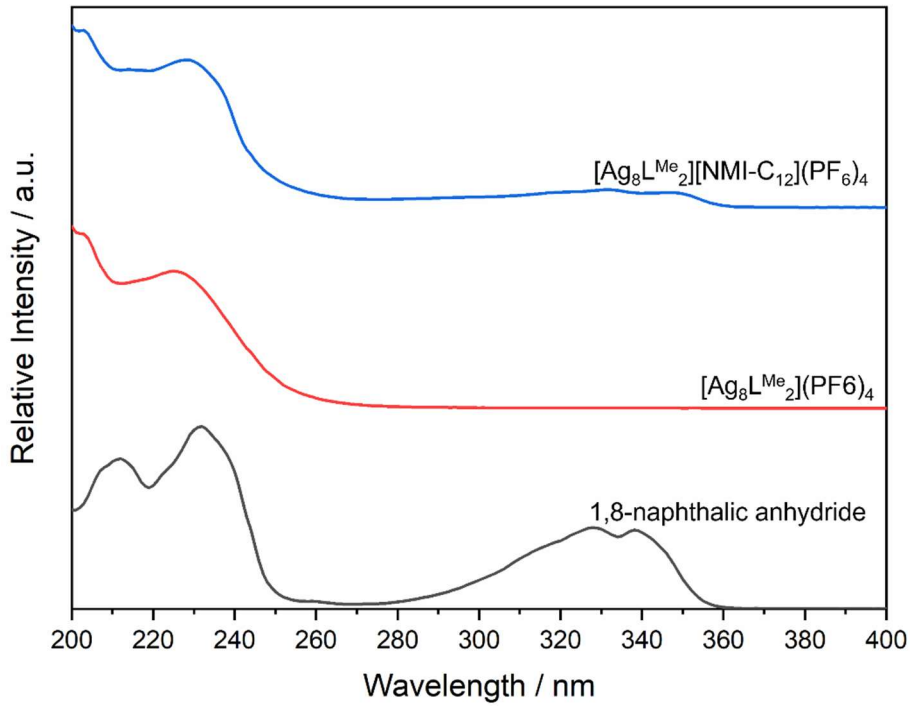

F83S: NMR analysis of $[Ag_8L^{Me}{}_2]NMI\text{-}\mathbf{C_{12}}](OTf)_4$ containing ^1H, ^{19}F and COSY NMR spectra in MeCN-d_3:

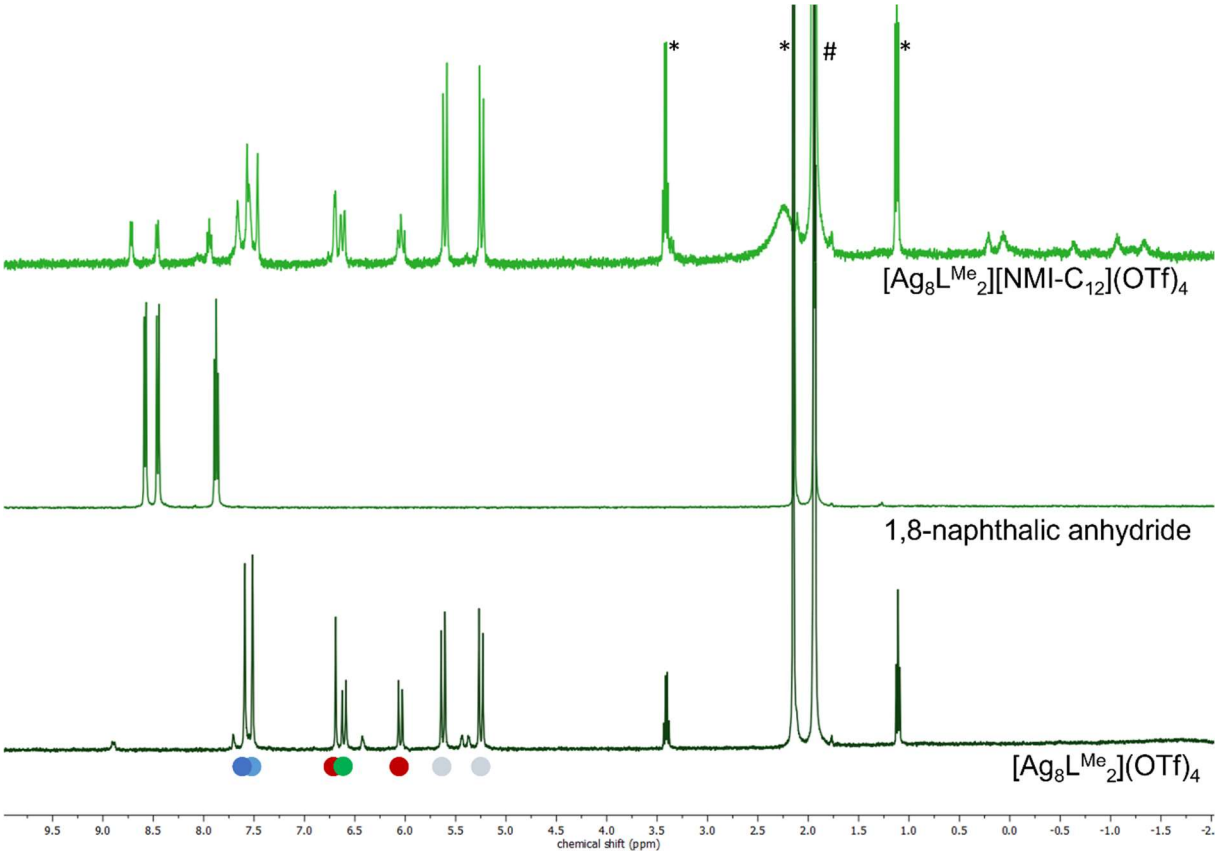

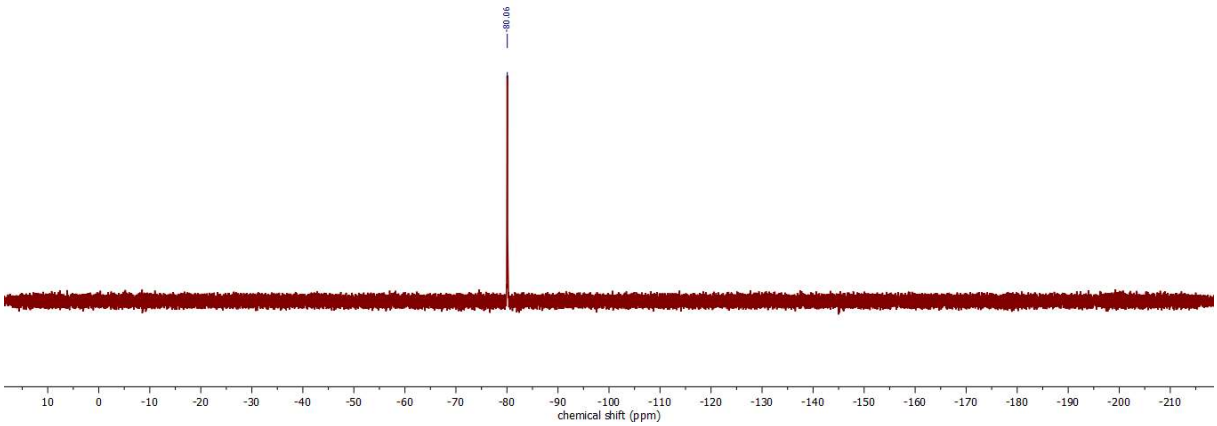

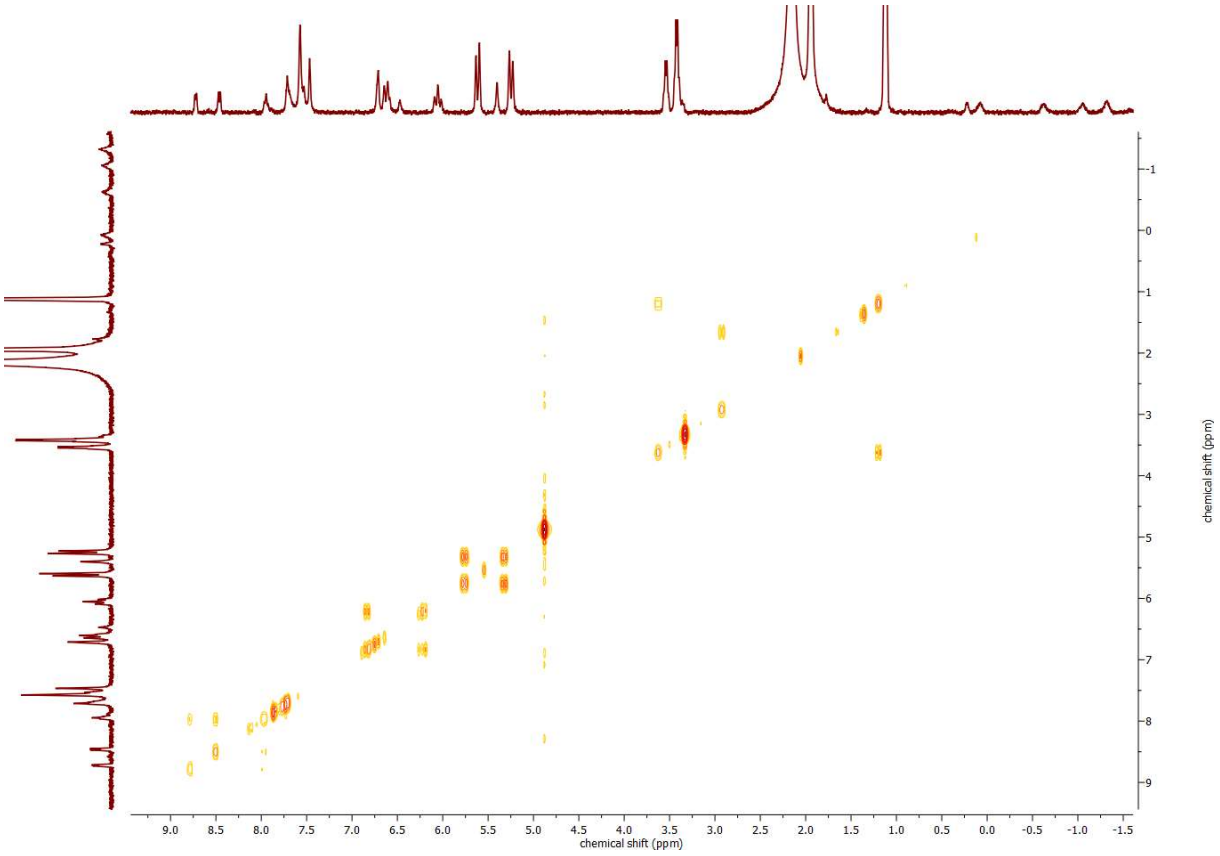

F84S: IR spectra of 1,8-naphthalic anhydride, $[Ag_8L^{Me}{}_2](OTf)_4$ and $[Ag_8L^{Me}{}_2][NMI\text{-}\mathbf{C_{12}}](OTf)_4$ in solid state:

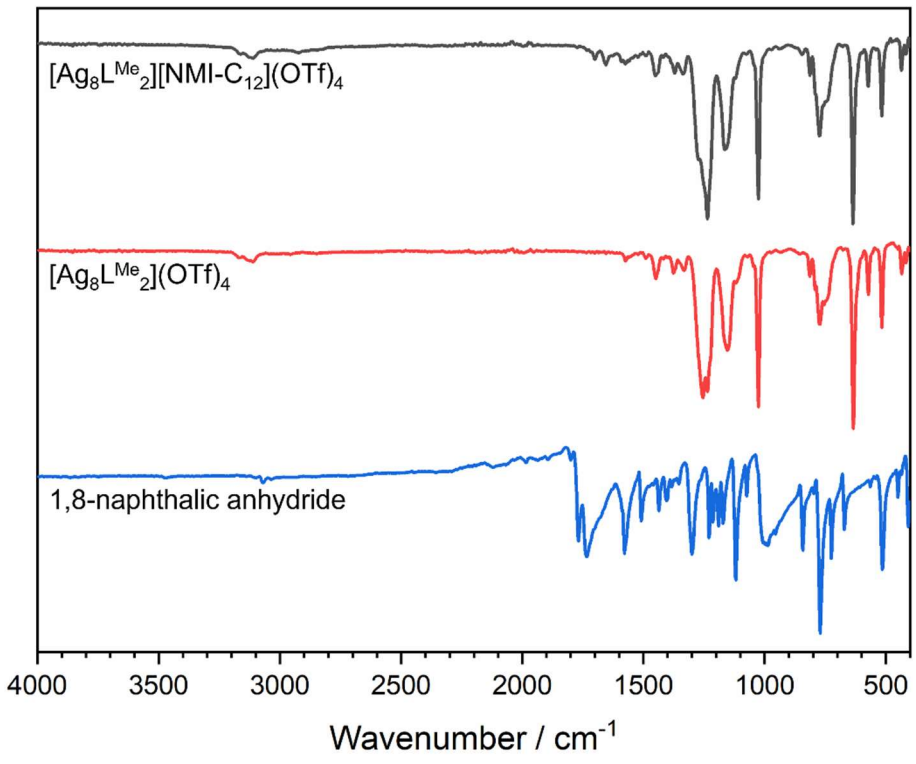

F85S: UV-vis spectra of 1,8-naphthalic anhydride, $[Ag_8L^{Me}_2](OTf)_4$ and $[Ag_8L^{Me}_2][NMI\text{-}\mathbf{C_{12}}](OTf)_4$ in MeCN:

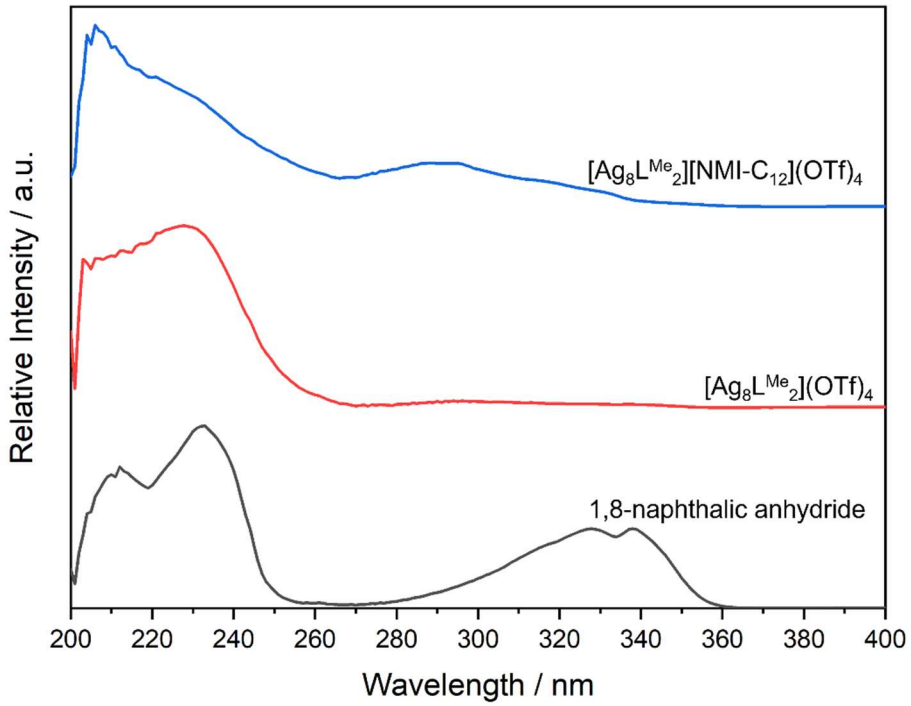

F86S: ESI mass spectra of $[Ag_8L^{Me}_2][NMI\text{-}\mathbf{C_{12}}](OTf)_4$ in DMF:

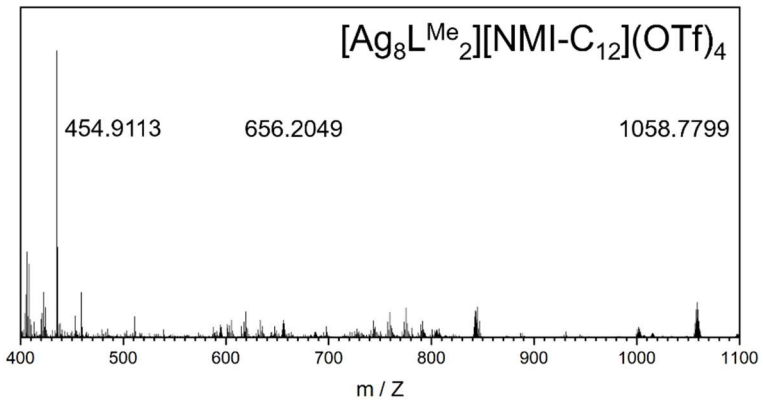

F87S: ^{1}H NMR spectrum of $[Ag_8L^{Me}{}_2]_2[NDI\text{-}C_{12}](OTf)_4$ in MeCN-d_3:

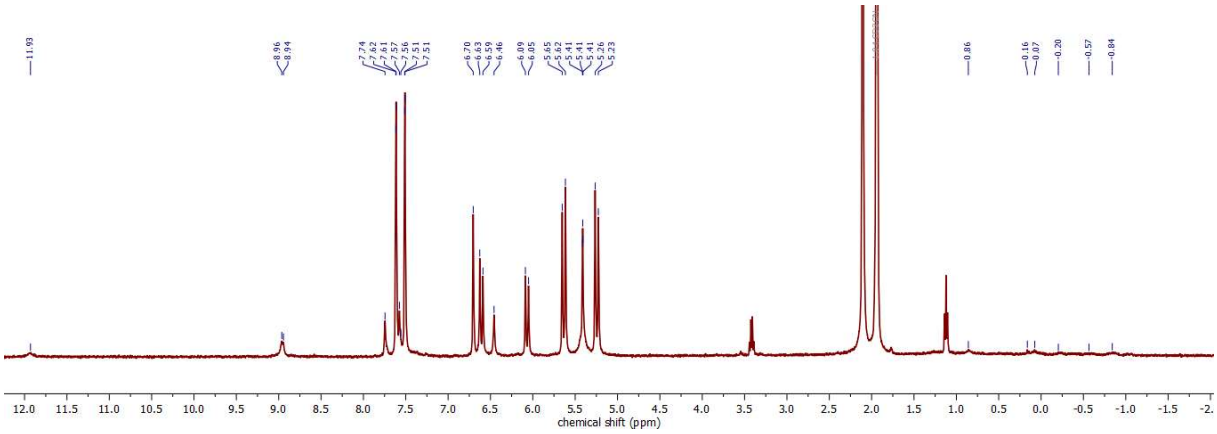

F88S: NMR analysis of $[Ag_8L^{Me}{}_2]_2[NDI\text{-}C_{12}NH_2](OTf)_4$ containing ^{1}H and COSY NMR spectra in MeOH-d_4:

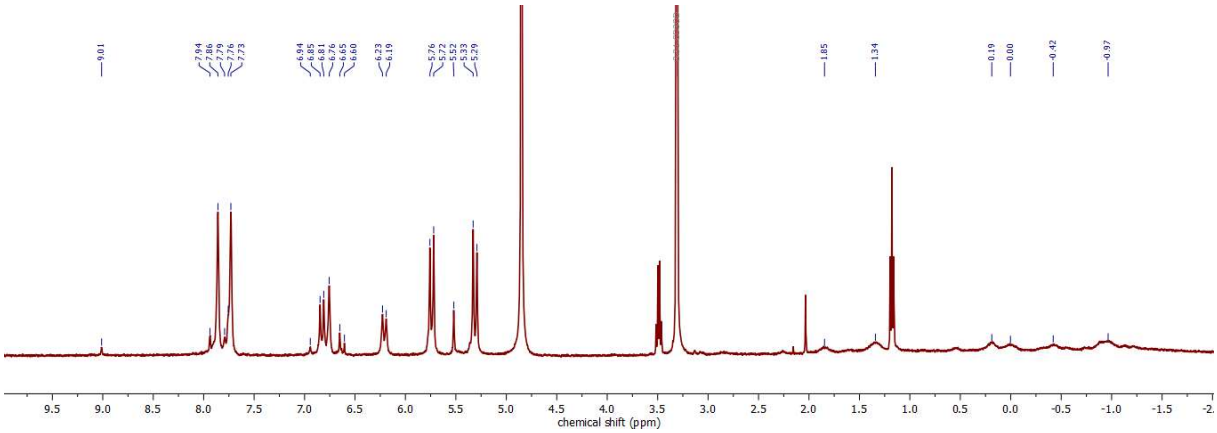

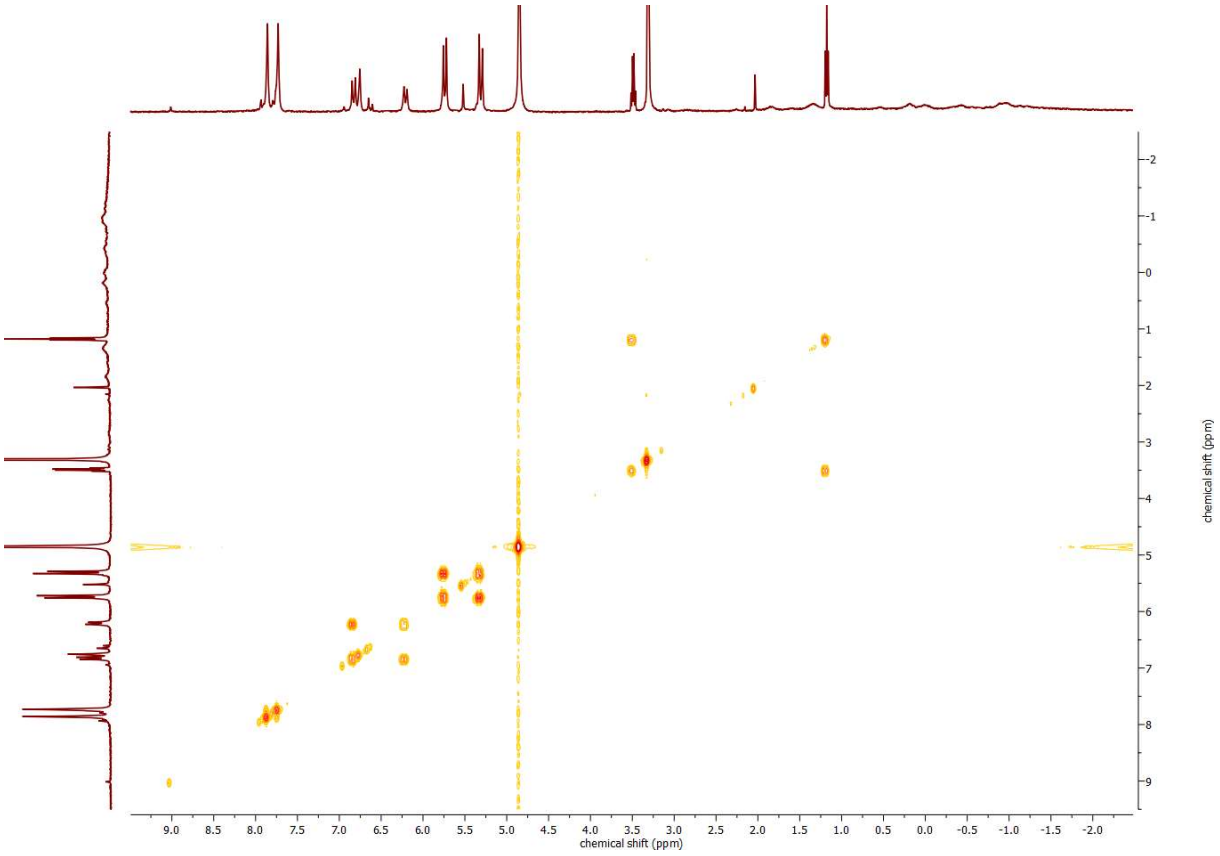

F89S: UV-vis spectra of $[Ag_8L^{Me}_2](OTf)_4$, *N*,*N'*-(12-aminododecyl)-1,4,5,8-naphthalenetetracarboxydiamide and $[Ag_8L^{Me}_2]_2[NDI\text{-}C_{12}NH_2](OTf)_4$ in MeCN:

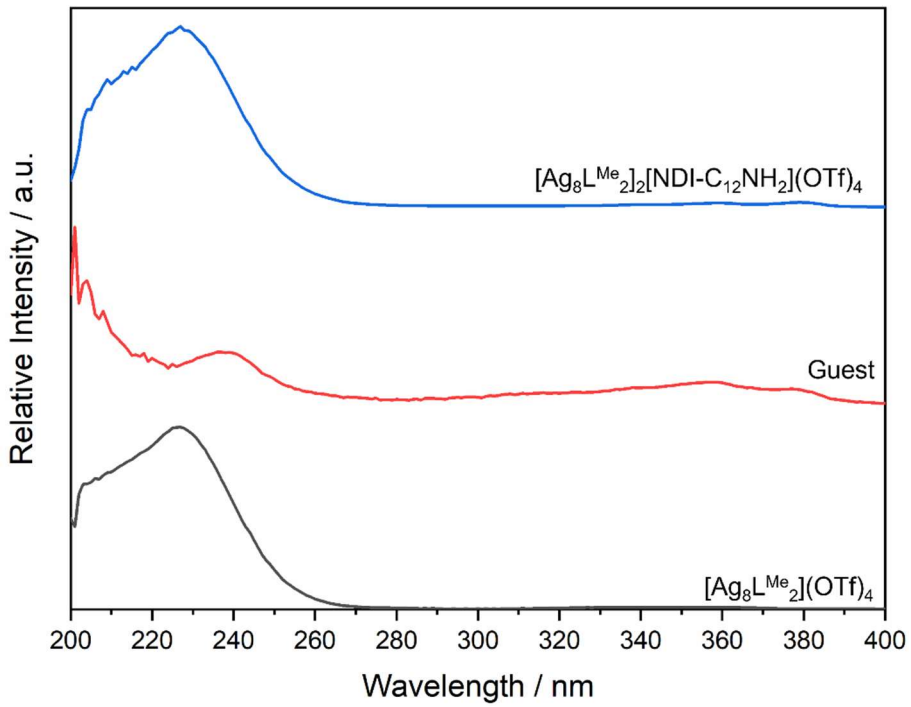

F90S: ^{1}H NMR spectrum of $[Ag_8L^{Me}{}_2]_2$[NDI-NHCO-*t*BuPh](OTf)$_4$ in MeCN-d_3:

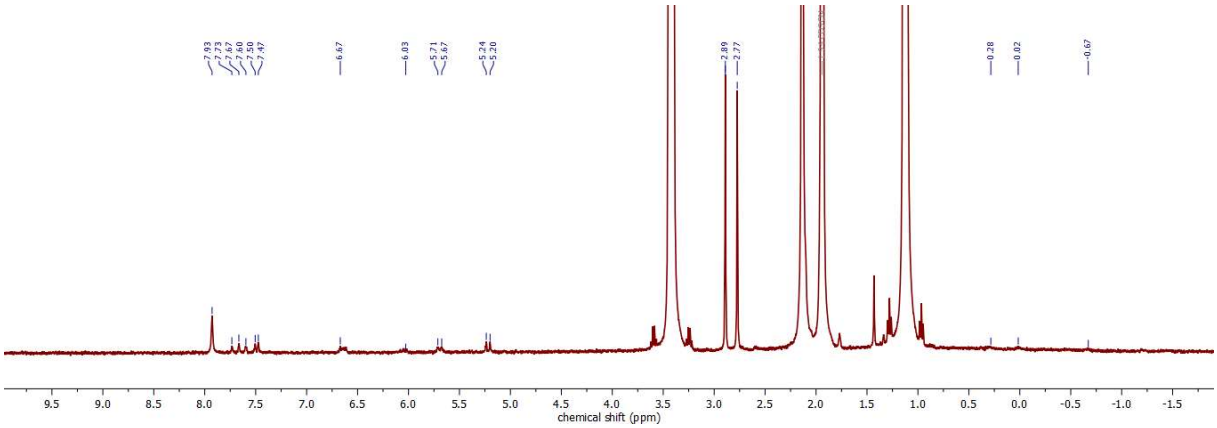

Supramolecular Re-Arrangements:

F91S: NMR analysis of $[Ag_{12}L^{Me}{}_3][TE1](PF_6)_6$ containing ^{1}H, ^{13}C and ^{31}P NMR spectra in MeCN-d_3:

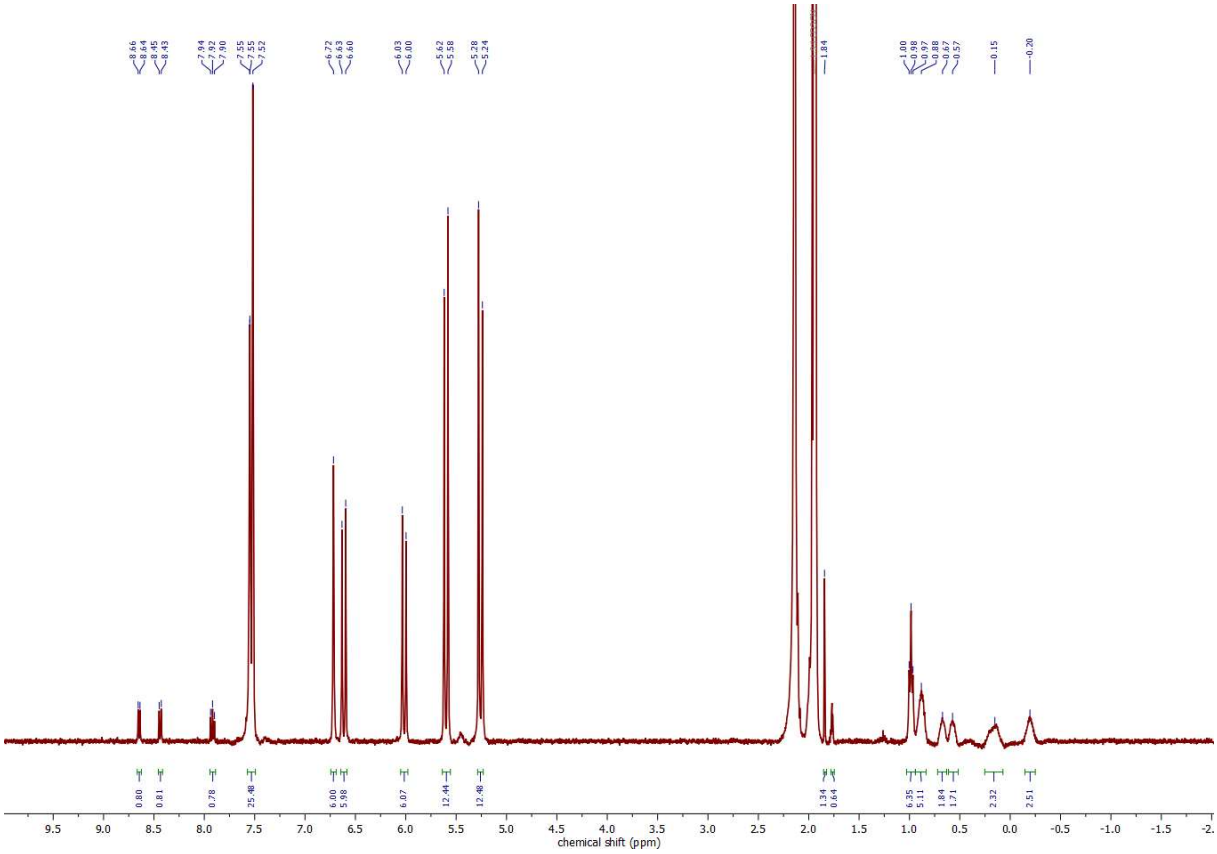

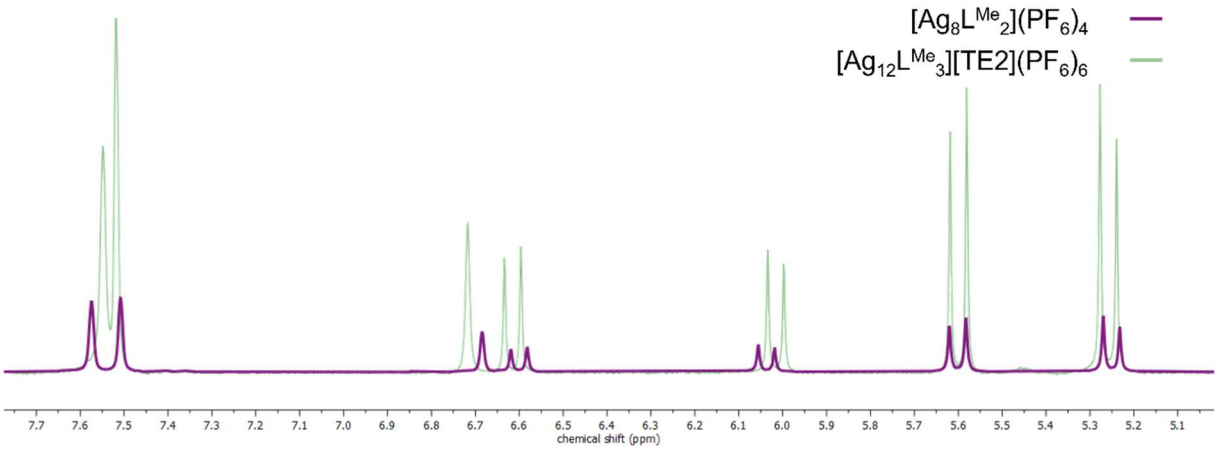

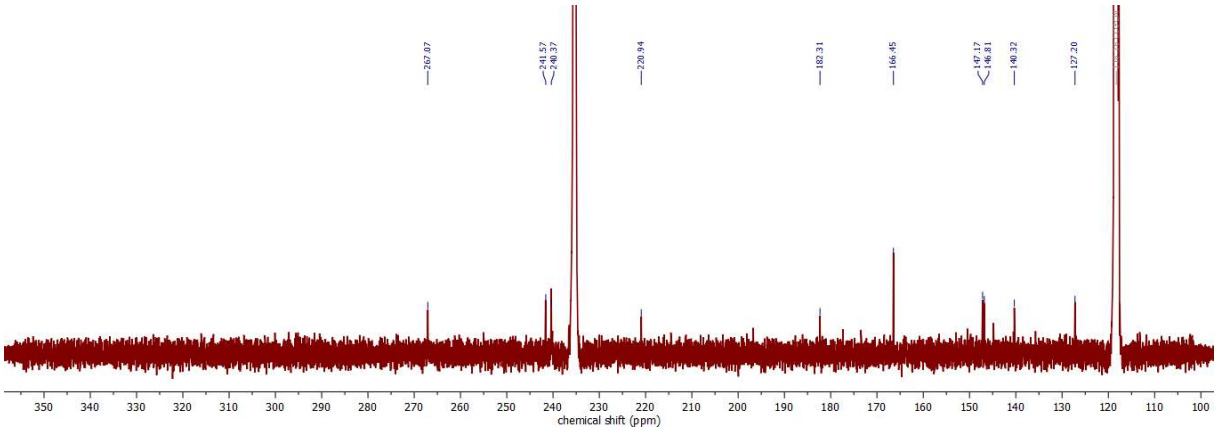
267.07
241.57
240.37
220.94
182.31
166.45
147.17
146.81
140.32
127.20
chemical shift (ppm)

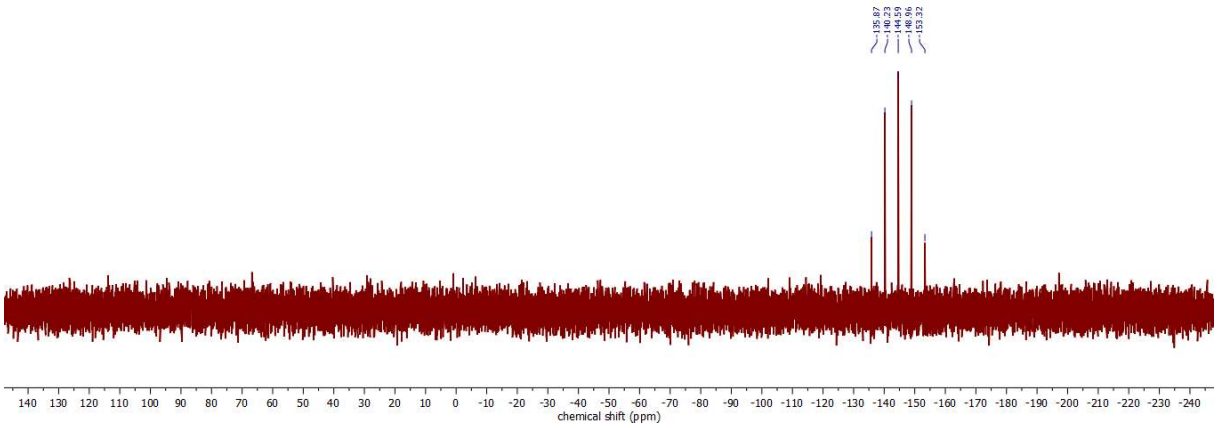
135.87
140.23
144.59
148.96
153.32
chemical shift (ppm)

T12S: Table of crystal data, data collection and structure refinement of Trillarplex $[Ag_{12}L^{Me}_3](PF_6)_6$ and S-shaped complex $[Ag_6(HL^{Me})_2](PF_6)_3$:

Identification code		CalTo7	HeiAl49
Chemical formula		$C_{72}H_{66}Ag_{12}F_{18}N_{36}P_3$	$C_{32}H_{25}Ag_3F_{12}N_{13}O_2P_2$
Formula weight	[g mol^{-1}]	3164.95	1237.20
Temperature	[K]	100(2)	100(2)
Wavelength	[Å]	0.71073	0.71073
Crystal system		monoclinic	orthorhombic
Space group		*P* 2_1 / *m*	*C m m a*
Unit cell dimensions		a = 20.710(2) Å, α = 90°	a = 23.9846(19) Å, α = 90°
		b = 14.3430(16) Å, β = 96.735(3)°	b = 29.650"2) Å, β = 90°
		c = 22.738(2) Å, γ = 90°	c = 14.7846(12) Å, γ = 90°
Volume	[Å^3]	6707.5(13)	10514.01(14)
Z		2	8
Calc. Density	[g cm^{-3}]	1.567	1.563
Absorption coefficient	[mm^{-1}]	1.814	1.249
F(000)		3042	4824
Diffractometer		TXS rotating anode	TXS rotating anode
Radiation source		Mo K_α	Mo K_α
Theta range for data collection	[°]	1.95 – 25.35	1.95 – 26.02
Index ranges		-24<=h<=24, -17<=k<=17, -27<=l<=27	-29<=h<=29, -36<=k<=36, -18<=l<=18
Reflections collected		92449	118985
Independent reflections		12802 [R_{int} = 0.0668]	5430 [R_{int} = 0.0329]
Coverage of independent reflections	[%]	99.9	99.9
Absorption correction		Multi-Scan	Multi-Scan
Max., min. transmission		0.6673, 0.7453	0.9180, 0.8230
Structure solution		direct methods	direct methods
Refinement method		Full-matrix least-squares on F^2	Full-matrix least-squares on F^2
Refinement program		SHELXL (Sheldrick 2018), ShelXle (Huebschle 2011)	SHELXL (Sheldrick 2018), ShelXle (Huebschle 2011)
Function minimised		$\sum w(F_o^2 - F_c^2)^2$	$\sum w(F_o^2 - F_c^2)^2$
Data / restraints / parameters		12802 / 0 / 650	5430 / 18 / 285
Goodness-of-Fit on F^2		1.023	1.064
Δ/σ_{max}		0.001	0.001
Final R indices	I > 2σ(I)	8665 data, R1 = 0.0574, wR2 = 0.1358	4998 data, R1 = 0.0579, wR2 = 0.1619
	All data	R1 = 0.0930, wR2 = 0.1626	R1 = 0.0625, wR2 = 0.1688
Weighting scheme		W = 1 / [$\sum^2$(FO^2) + (0.0678P)^2 + 66.5191P] where P = (FO^2+2FC^2) / 3	W = 1 / [$\sum^2$(FO^2) + (0.0916P)^2 + 141.4596P] where P = (FO^2+2FC^2) / 3
Largest diff. peak, hole	[eÅ^{-3}]	3.741, -1.300	2.755, -1.360
R.M.S. deviation from mean	[eÅ^{-3}]	0.161	0.171

F92S: Crystal packing of $[Ag_{12}L^{Me}{}_3][TE](PF_6)_6$ (A) along the a-axis, (B) along the b-axis and (C) along the c-axis:

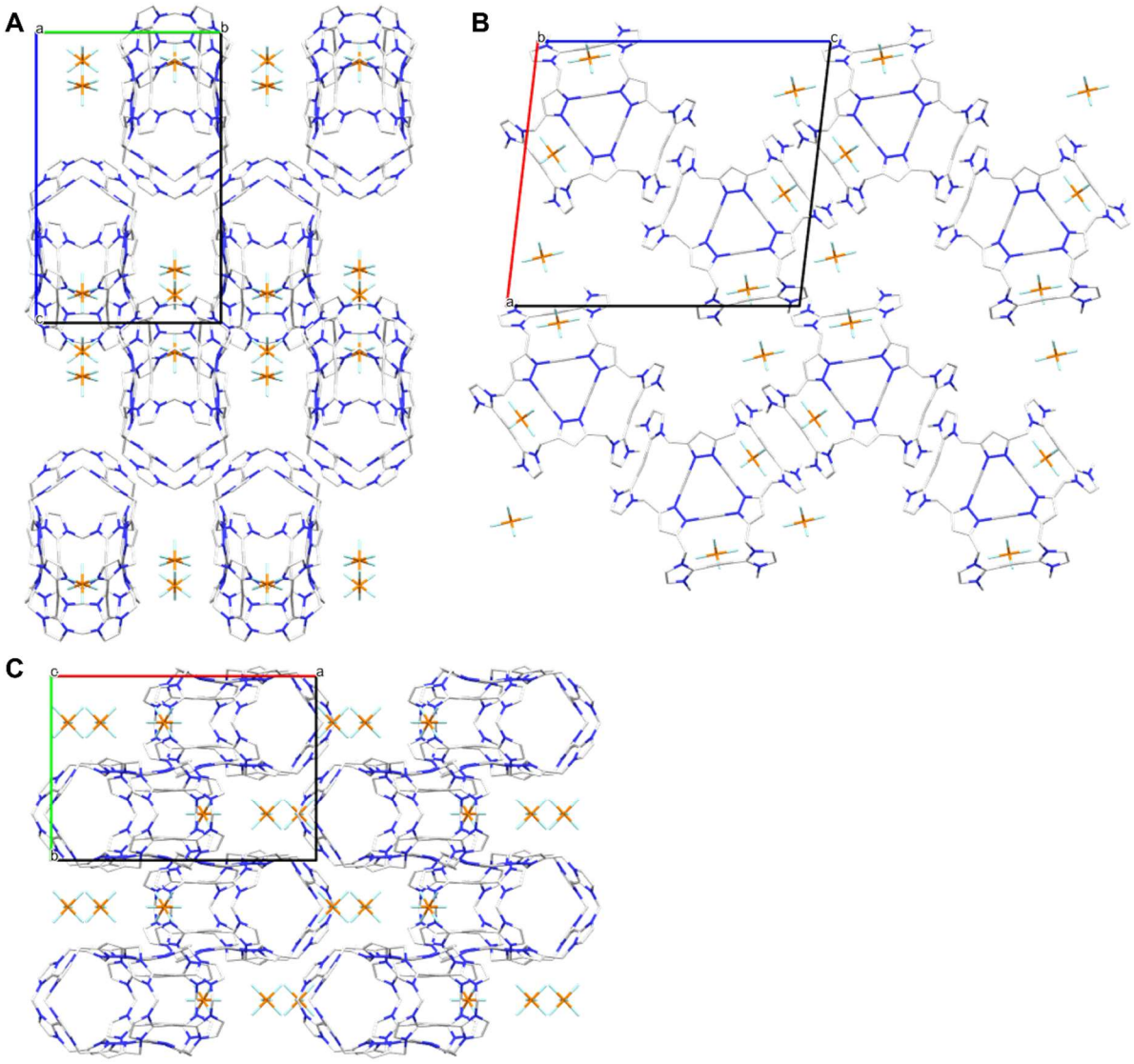

F93S: Crystal packing of $[Ag_6(HL^{Me})_2](PF_6)_4 \cdot$ TE1 (A) along the a-axis, (B) along the b-axis and (C) along the c-axis:

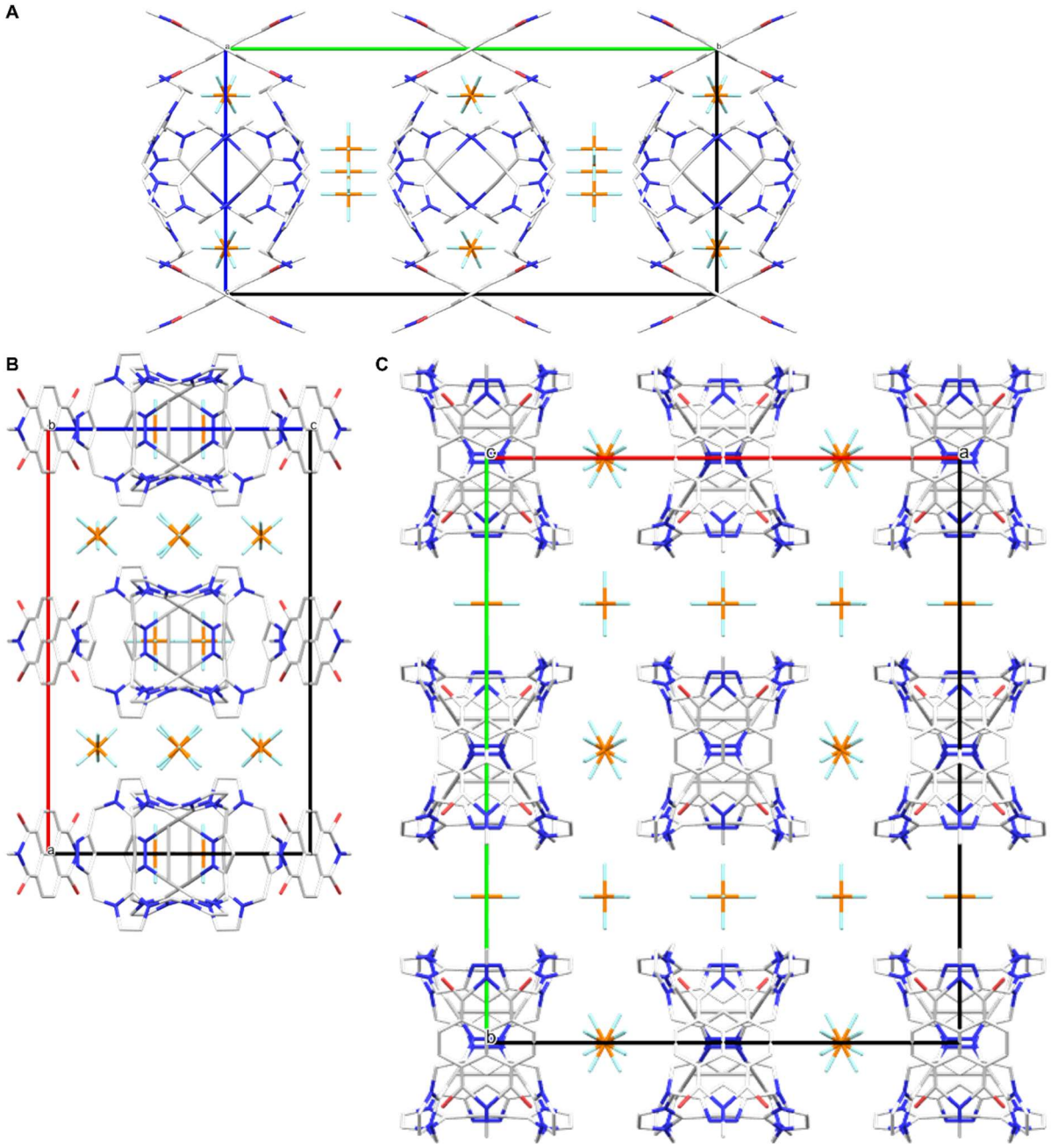

Encapsulation Studies of Perfluorinated Guest Molecules:

F94S: ^{1}H NMR spectra of $[Ag_8L^{Me}_2](PF_6)_4$ (green) and PFOA (grey) displayed at the bottom in comparison with a solution containing 1 eq. $[Ag_8L^{Me}_2](PF_6)_4$ and 1 eq. PFOA after stirring at rt for 15 min. Spectra were measured in MeCN-d_3 (1.94 ppm) and the residual solvent signals are marked with # with water at 2.13 ppm:

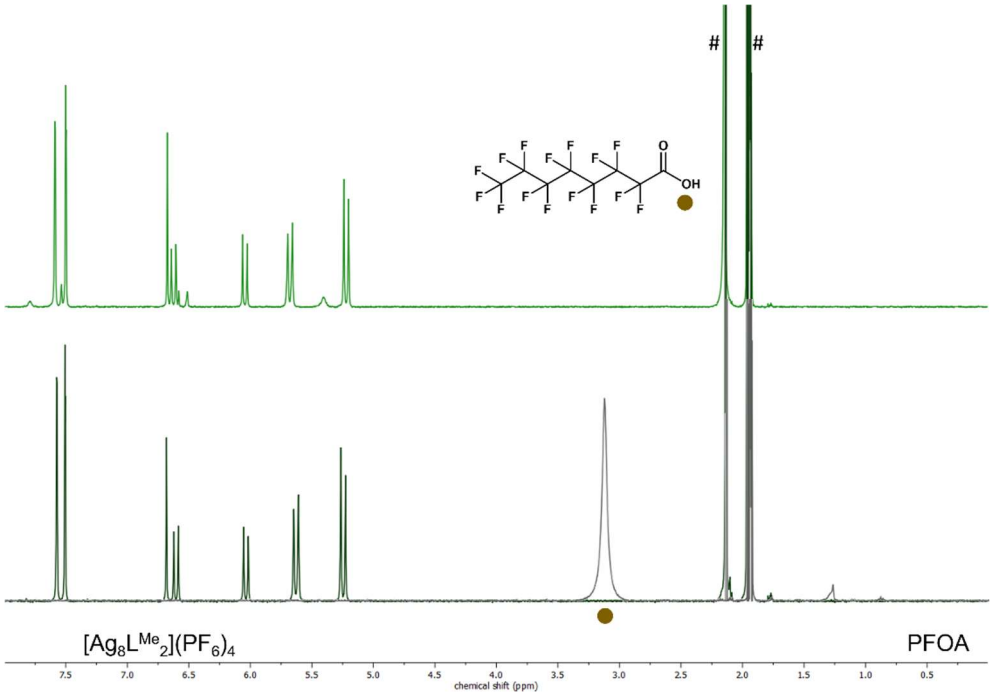

Encapsulation of Heterocyclic Guest Molecules:

T13S: Table of crystal data, data collection and structure refinement of $[Ag_8L^{Me}_2](PF_6)_4 \cdot THF$:

Identification code		HeiAl67
Chemical formula		$C_{33.07}H_{40.65}Ag_4F_{12}N_{12.50}O_{2.39}P_2$
Formula weight	[g mol^{-1}]	2745.35
Temperature	[K]	100(2)
Wavelength	[Å]	0.71073
Crystal system		triclinic
Space group		*P* -1
Unit cell dimensions		a = 14.7482(8) Å, α = 79.231(3)° b = 16.0408(12) Å, β = 76.639(2)° c = 22.9771(16) Å, γ = 78.791(2)°
Volume	[Å^3]	5130.1(6)
Z		2
Calc. Density	[g cm^{-3}]	1.777
Absorption coefficient	[mm^{-1}]	1.653
F(000)		2686
Diffractometer		TXS rotating anode
Radiation source		Mo K_α
Theta range for data collection	[°]	1.77 – 25.35
Index ranges		-17<=h<=17, -19<=k<=19, -27<=l<=27
Reflections collected		216646
Independent reflections		18347 [R_{int} = 0.0471]
Coverage of independent reflections	[%]	97.8
Absorption correction		Multi-Scan
Max., min. transmission		0.6673, 0.7453
Structure solution		direct methods
Refinement method		Full-matrix least-squares on F^2
Refinement program		SHELXL (Sheldrick 2018), ShelXle (Huebschle 2011)
Function minimised		$\sum w(F_o^2 - F_c^2)^2$
Data / restraints / parameters		18347 / 4502 / 1439
Goodness-of-Fit on F^2		1.041
Δ/σ_{max}		0.001
Final R indices	I > 2σ(I)	16340 data, R1 = 0.0440, wR2 = 0.1339
	All data	R1 = 0.0496, wR2 = 0.1398
Weighting scheme		W = 1 / [$\sum^2$(FO^2) + (0.0758P)^2 + 28.7626P] where P = (FO^2+2FC^2) / 3
Largest diff. peak, hole	[eÅ^{-3}]	1.330, -1.223
R.M.S. deviation from mean	[eÅ^{-3}]	0.146

F95S: Crystal packing of $[Ag_8L^{Me}_2](PF_6)_4 \cdot THF$ (A) along the a-axis, (B) along the b-axis and (C) along the c-axis:

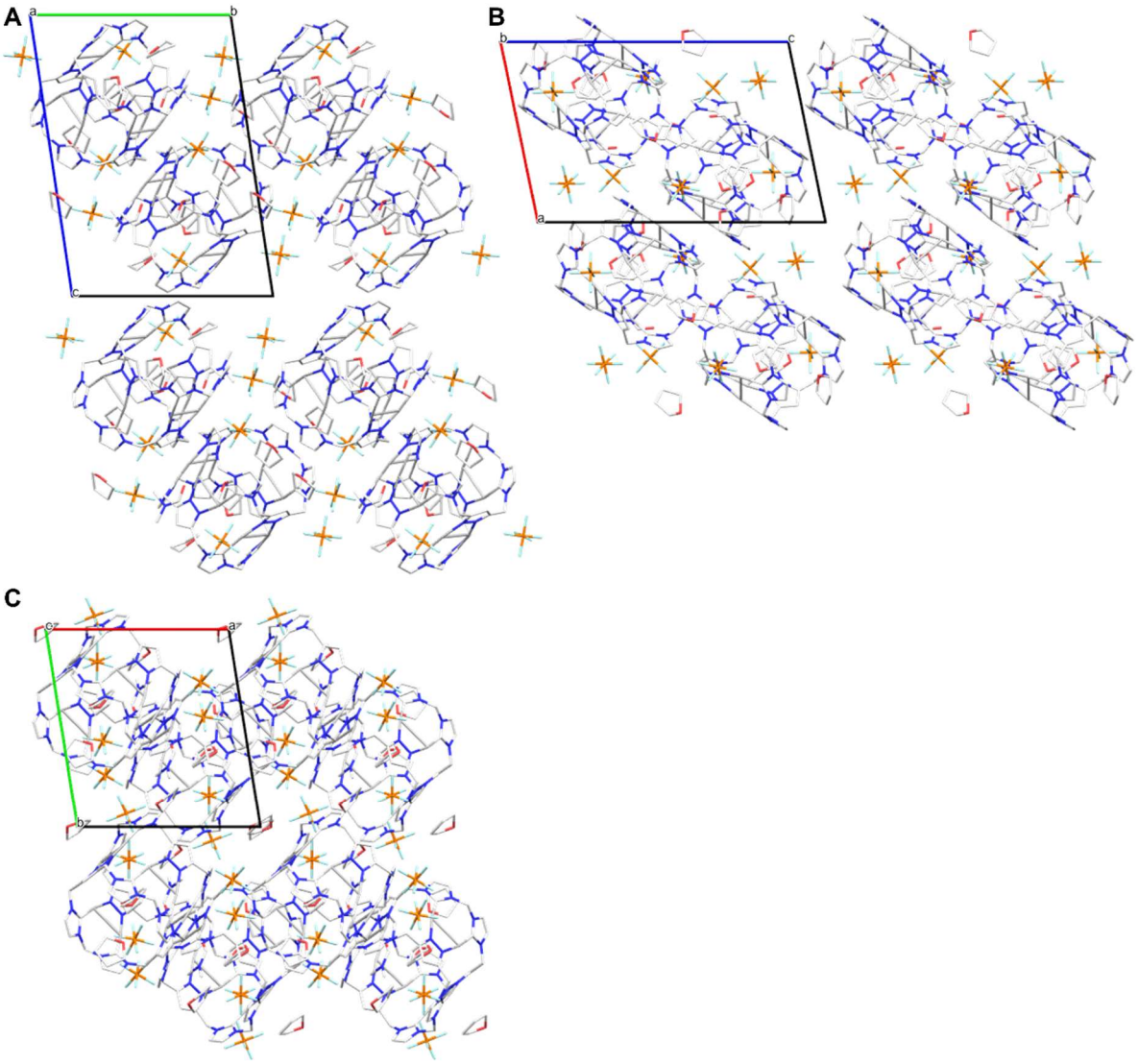

Additional Crystal Structures:

T14S: Table of crystal data, data collection and structure refinement of Ligand Step 3 (3,5-bis(hydroxymethyl)-1*H*-pyrazole-2-ium chloride):

Identification code		HeiAl31
Chemical formula		$C_5H_9ClN_2O_2$
Formula weight	[g mol^{-1}]	164.59
Temperature	[K]	100(2)
Wavelength	[Å]	0.71073
Crystal system		monoclinic
Space group		$P\ 1\ 2_1\ 1$
Unit cell dimensions		a = 4.3636(2) Å, α = 90° b = 10.8523(4) Å, β = 91.5150(10)° c = 7.5634(3) Å, γ = 90°
Volume	[Å^3]	358.04(3)
Z		2
Calc. Density	[g cm^{-3}]	1.527
Absorption coefficient	[mm^{-1}]	0.472
F(000)		172
Diffractometer		IMS microsource
Radiation source		Mo K_α
Theta range for data collection	[°]	2.69 – 30.02
Index ranges		-6<=h<=6, -15<=k<=15, -10<=l<=10
Reflections collected		23287
Independent reflections		2085 [R_{int} = 0.0292]
Coverage of independent reflections	[%]	99.6
Absorption correction		Multi-Scan
Max., min. transmission		
Structure solution		direct methods
Refinement method		Full-matrix least-squares on F^2
Refinement program		SHELXL (Sheldrick 2018), ShelXle (Huebschle 2011)
Function minimised		$\sum w(F_o^2 - F_c^2)^2$
Data / restraints / parameters		2085 / 1 / 97
Goodness-of-Fit on F^2		1.130
Δ/σ_{max}		5.038
Final R indices	I > 2σ(I)	2039 data, R1 = 0.0190, wR2 = 0.0487
	All data	R1 = 0.0201, wR2 = 0.0502
Weighting scheme		W = 1 / [$\sum^2$(FO^2) + (0.0272P)^2 + 0.0478P] where P = (FO^2+2FC^2) / 3
Largest diff. peak, hole	[eÅ^{-3}]	0.225, -0.260
R.M.S. deviation from mean	[eÅ^{-3}]	0.064

F96S: Crystal packing of Ligand Step 3 (3,5-bis(hydroxymethyl)-1*H*-pyrazole-2-ium chloride) (A) along the a-axis, (B) along the b-axis and (C) along the c-axis:

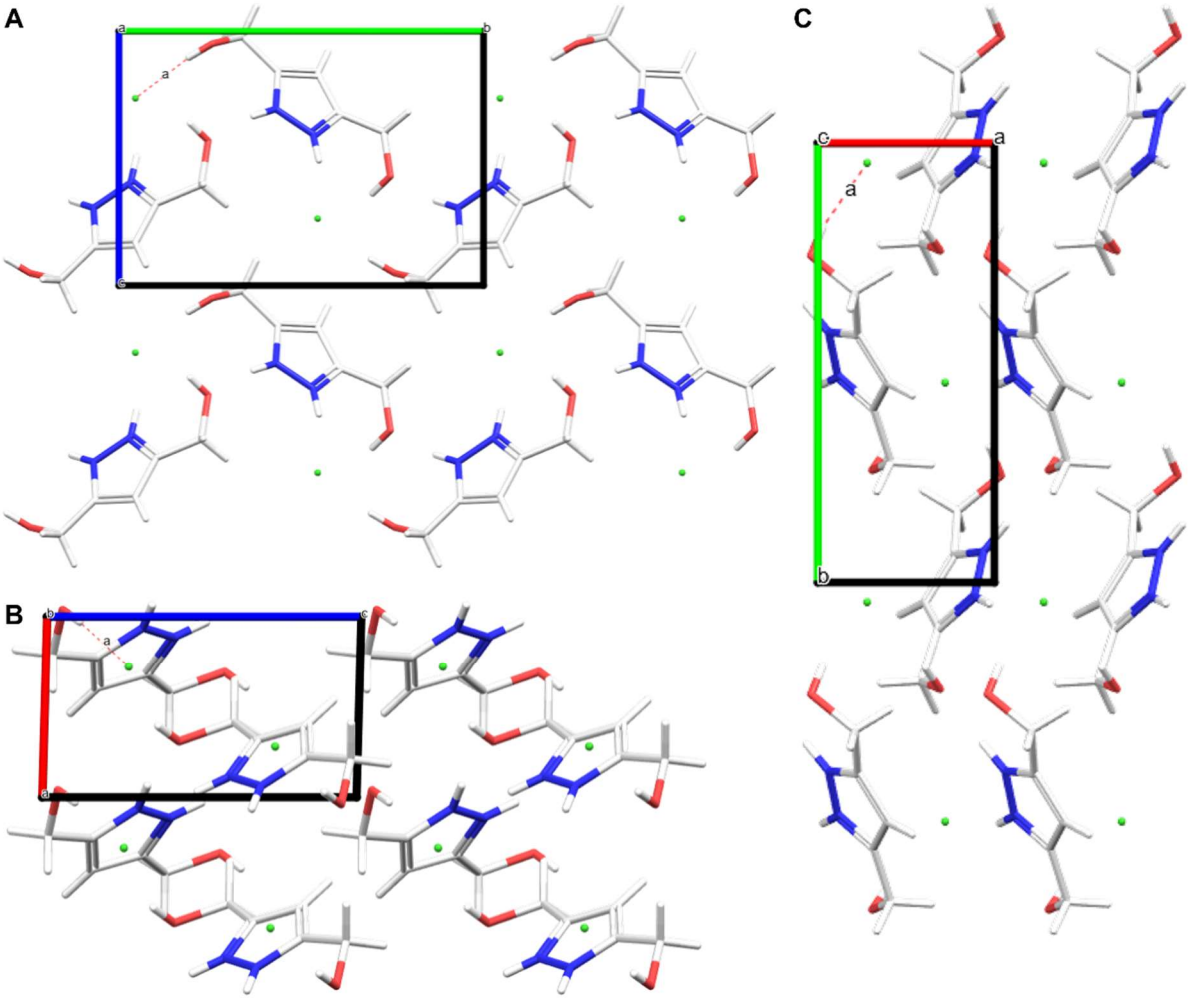

6.2 Supplementary Information of the Computational Part

F97S: Optimised structures of (A) $[Au_8L^{Me}_2](PF_6)_4$ in gas phase; (B) $[Au_8L^{Me}_2](PF_6)_4$ in solution (MeCN); (C) $[Au_8L^{Me}_2](OAc)_4$ in gas phase and (D) $[Au_8L^{Me}_2](OAc)_4$ in solution (H_2O):

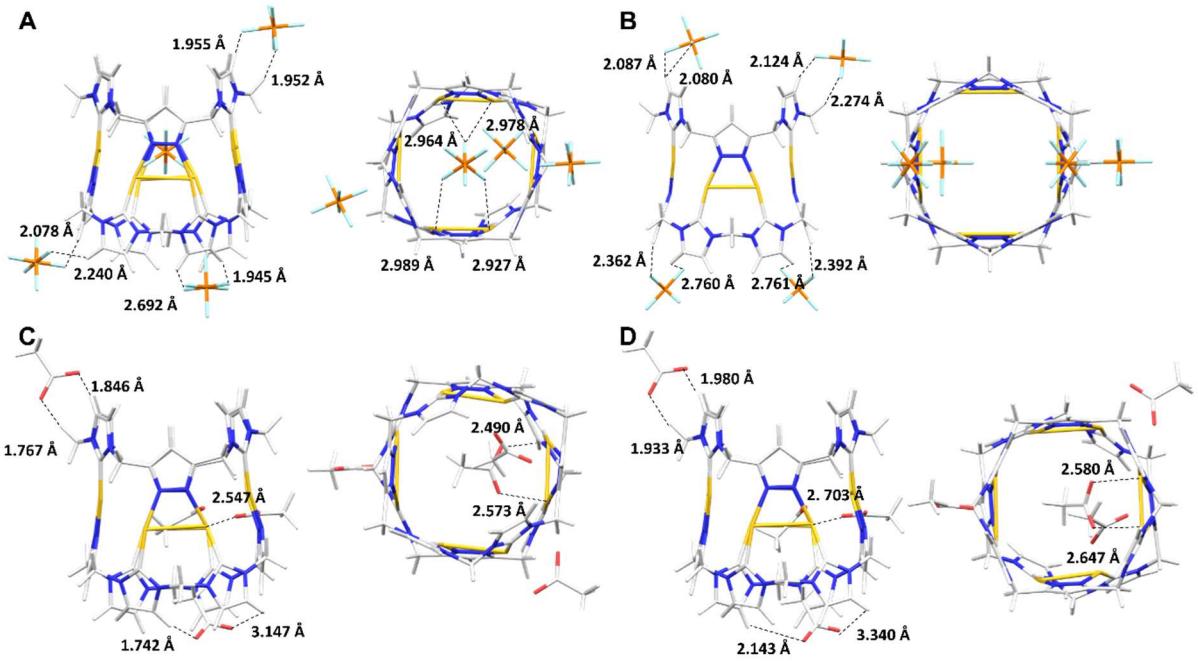

F98S: Optimised structures of (A) $[Ag_8L^{Me}_2](Cl)_4$ in gas phase and (B) $[Ag_8L^{Me}_2](Br)_4$ in gas phase:

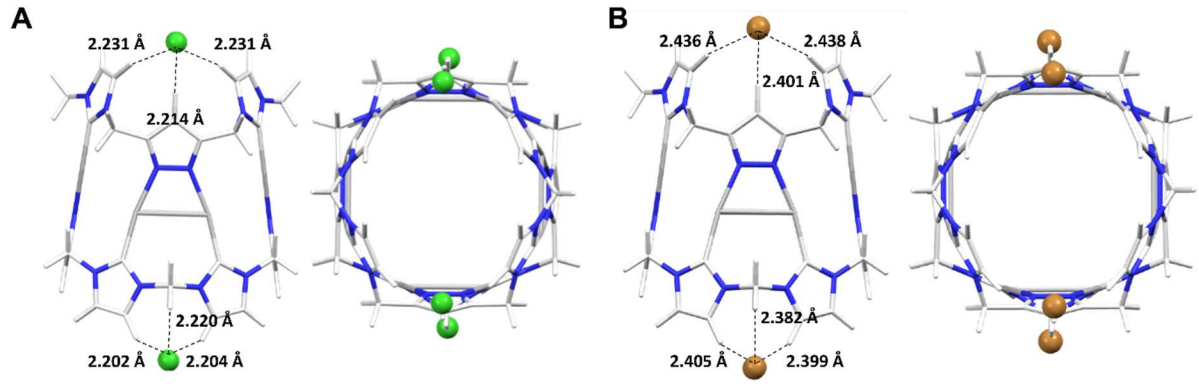

F99S: Optimised structure of $[Ag_8L^{Me}{}_2]^{4+}$(NMI-C_{12}) in gas phase:

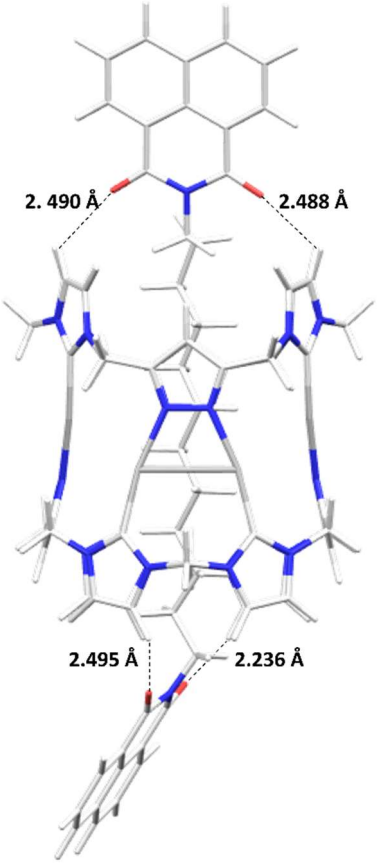

6.3 List of Publications

6.3.1 Journal Contributions

First Author:

Crystal structure of a hexacationic Ag(I)-pillarplex-dodecyl-diammonium pseudo-rotaxane as terephthalate salt

A. A. Heidecker*, M. Bohn and A. Pöthig*

Zeitschrift für Kristallographie - Crystalline Materials **2022**, 237 (4-5), 167-177 (DOI: 10.1515/zkri-2021-2076).

Silver and Gold Pillarplex Pseudorotaxanes with α,ω-dicarboxylic acids

A. A. Heidecker, M. Stasi, A. Spears, J. Boekhoven and A. Pöthig*

ChemPlusChem **2023**, e202300234 (DOI: 10.1002/cplu.202300234).

Other Publications:

Highly-fluorescent BODIPY-functionalised metallacages as drug delivery systems: synthesis, characterisation and cellular accumulation studies

B. Aikman, R. Bonsignore, B. Woods, D. Doellerer, R. Scotti, C. Schmidt, **A. A. Heidecker**, A. Pöthig, E. J. Sayers, A. T. Jones and A. Casini

Dalton Trans. **2022**, *51*, 7476-7490 (DOI: 10.1039/D2DT00337F).

Organometallic Pillarplex that bind DNA 4-way Holliday Junctions and Forks

J. S. Craig, L. Melidis, H. D. Williams, S. J. Dettmer, **A. A. Heidecker**, P. J. Altmann, S. Guan, C. Campbell, D. F. Browning, R. K. O. Sigel, S. Johannsen, R. T. Egan, B. Aikman, A. Casini, A. Pöthig and M. Hannon

JACS **2023**, 145, 25, 13570-13580 (DOI: 10.1101/2023.01.04.522759).

Photochemical Deracemization of 3-substituted Oxindoles

J. Großkopf, **A. A. Heidecker**, T. Bach*

Angew. Chem. - In. Ed. **2023**, e202305274 (DOI: 10.1002/anie.202305274).

Interplay between coordination sphere engineering and properties of nickel diketonate-diamine complexes as vapor phase precursors for the growth of NiO thin films

M. Benedet, D. Barreca*, E. Fois, R. Seraglia, G. Tabacchi*, M. Roverso, G. Pagot, C. Invernizzi, A. Gasparotto, **A. A. Heidecker**, A. Pöthig, E. Callone, S. Dire, S. Bogialli, V. Di Noto, C. Maccato

Dalton Trans. **2023**, *51*, 10677-10688. (DOI 10.1039/D3DT01282D).

Diastereoselective, Lewis acid-mediated Diels-Alder reactions of allenoic acid derivatives and 1,3-cyclopentadienes

F. Harvey, **A. A. Heidecker**, T. Bach*

Organic & Biomolecular Chemistry **2023**, *21*, 4422-4428. (DOI: 10.1039/d3ob00598d).

Exploring the Anticancer Activity of Tamoxifen-Based Metal Complexes Targeting Mitochondria

V. Scalcon, R. Bonsignore, J. Aupic, S. R. Thomas, A. Folda, **A. A. Heidecker**, A. Pöthig, A. Magistrato, A. Casini, M. P. Rigobello

J Med Chem. **2023**, *66* (14), 9823-9841 (DOI: 10.1021/acs.jmedchem.3c00617).

Cyclometalated C^N Diphosphine Ruthenium Catalysts for *Oppenauer*-Type Oxidation / Transfer Hydrogenation Reactions and Cytotoxic Activity

D. Alessi, P. del Mestre, E. Aneggi, M. Ballico, A. P. Betrami, M. Busato, D. Cesselli, **A. A. Heidecker**, D. Zuccaccia, W. Baratta

Catal. Sci. Technol. **2023**, *13*, 5367-5279 (DOI: 10.1039/D3CY00676J).

6.3.2 Conference Contributions

03.2021 Poster presentation at 29th Annual Meeting of the German Crystallographic Society (DGK), online.

07.2021 Poster presentation at 16th International Symposium of Macrocyclic and Supramolecular Chemistry (ISMSC), online (Twitter).

07.2021 Poster presentation at 6th European Crystallographic School, online.

09.2021 Poster presentation and Oral Talk at 1st Women in Supramolecular Chemistry Workshop (WISC), Cagliari, Italy.

03.2022 Poster presentation at 30th Annual Meeting of the German Crystallographic Society (DGK), online.

06.2022 Poster presentation and Oral Talk at 17th International Symposium of Macrocyclic and Supramolecular Chemistry (ISMSC), Eugene, Oregon, USA.

03.2023 Poster presentation at 31st Annual Meeting of the German Crystallographic Society (DGK), Frankfurt a. Main, Germany.

06.2023 Poster presentation at 18th International Symposium of Macrocyclic and Supramolecular Chemistry ISMSC 2023, Reykjavik, Iceland.

6.4 List of Contributions

Chapter	Header	Author	Contribution
3.1	Adsorption Studies of $[M_8L^{Me}_2](PF_6)_4$ and $[M_8L^{Me}_2](OAc)_4$	-	Syntheses, characterisation, SC-XRD measurements, evaluation, theoretical evaluation, DFT-calculations
3.2	Expanding the Anionic Diversity of Pillarplex Salts	-	Syntheses, characterisation, theoretical evaluation, DFT-calculations, Crystallisation attempts, crystal structure evaluation, evaluation of gas adsorption experiments, supervision of research internship
3.3	Pillarplex Salts with Mixed Anions	-	SC-XRD measurements, evaluation, supervision of master thesis
3.4	Crystal Structure of a Hexacationic Ag(I)-Pillarplex-Dodecyl-Diammonium Pseudorotaxane as Terephthalate Salt	First + corresponding author	Syntheses, characterisation, SC-XRD measurements, evaluation, supervision of research internship
3.5	Rim-Functionalisation of Pillarplex	-	Syntheses, characterisation, SC-XRD measurements, evaluation, supervision of master thesis
3.6	Pillarplex Pseudorotaxanes with α,ω-Dicarboxylic Acids	First author	Syntheses, characterisation, SC-XRD measurements, evaluation, Performance and evaluation of NMR-titrations, supervision of internship
3.7	Utilising $[M_8L^{Me}_2]$(α,ω-Dicarboxylic Acid)$(X)_4$ as Building Blocks	-	Syntheses, characterisation, SC-XRD measurements, evaluation, supervision of research internship
3.8	Pillarplex Rotaxanes with Pyridine as Functionality	-	Syntheses, characterisation, DFT-calculations
3.9	Photochemistry of Au(I)-Pillarplexes and Pillarplex Rotaxanes Containing *N*-naphthalimide as (Photo-)Active Unit	-	Syntheses, characterisation, supervision of bachelor thesis and research internship
3.10	Supramolecular Re-Arrangements	-	Crystallisation attempts, SC-XRD measurements, evaluation, supervision of master thesis and research internship
3.11	Encapsulation Studies of Perfluorinated Guest Molecules	-	Performance and characterisation of encapsulation studies
3.12	Encapsulation of Heterocyclic Guest Molecules	-	SC-XRD measurement, evaluation

6.5 Reprint Permissions

AW: Anfrage für Reprint Permission eines Artikels

DeGruyter, Rechte <rights@degruyter.com>

Do 17.08.2023 10:01

An:Alexandra Heidecker <alexandra.heidecker@tum.de>;

Liebe Frau Heidecker,

das ist dann völlig in Ordnung!

Herzlich,
Ashleen Sauerborn

Von: Alexandra Heidecker <alexandra.heidecker@tum.de>
Gesendet: Donnerstag, 17. August 2023 09:34
An: DeGruyter, Rechte <rights@degruyter.com>
Betreff: AW: Anfrage für Reprint Permission eines Artikels

Sie erhalten nicht oft eine E-Mail von alexandra.heidecker@tum.de. Erfahren Sie, warum dies wichtig ist

Sehr geehrte Frau Sauerborn,

Vielen Dank für Ihre Nachricht.

Genau, ich möchte gerne Teile des Artikels in meiner Promotionsarbeit nutzen.

Diese wird nur auf das Universitätrepositorium gestellt und nicht bei anderen Verlagen oder sonstig wertschöpfend veröffentlicht.

Mit freundlichen Grüßen,

Alexandra Heidecker

Von: DeGruyter, Rechte <rights@degruyter.com>
Gesendet: Mittwoch, 16. August 2023 08:37:02
An: Alexandra Heidecker

Betreff: AW: Anfrage für Reprint Permission eines Artikels

Sehr geehrte Frau Heidecker,

haben Sie vielen Dank für Ihre Nachricht.
Wenn ich Sie richtig verstehe, geht es darum, den Artikel in Ihrer Promotionsarbeit zu nutzen?
Das können wir gerne und ohne anfallende Lizenzgebühr genehmigen.

Sollte die Promotionsarbeit bei einem anderen Verlag oder sonstig wertschöpfend veröffentlicht werden, würde eine Lizenzgebühr für die wiederabgedruckten Seiten anfallen.
Die Stellung auf z.B. das Universitätsrepositorium ist aber in Ordnung.

Herzlich,
Ashleen Sauerborn

Team Legal & Licenses

DE GRUYTER
Genthiner Straße 13
10785 Berlin, Germany
www.degruyter.com

Walter de Gruyter GmbH. Genthiner Str. 13. 10785 Berlin.

Domicile Berlin. District Court Charlottenburg HRB 143490 B. Legal Form: GmbH
Managing Director: Carsten Buhr
Chairman of the Supervisory Board: Rüdiger Gebauer

Newsletter and Alerts: www.degruyter.com/newsletter

Diese Nachricht ist vertraulich und es kann gesetzlicher oder anderweitiger Schutz gegen die Weitergabe dieser bestehen. Sollten Sie nicht der beabsichtigte Empfänger sein, bitten wir Sie, den Absender darüber zu informieren und diese Nachricht und ggf. anhängende Dokumente von Ihrem System zu löschen. Zudem dürfen Sie die Inhalte derartiger Nachrichten oder ggf. anhängender Dokumente nicht kopieren oder an andere Personen weitergeben.
Informationen über den Datenschutz bei De Gruyter finden Sie in unserer Datenschutz-Erklärung auf unserer Webseite hier https://www.degruyter.com/cms/pages/privacy-policy

-

This message is confidential and may be legally privileged or otherwise protected from disclosure. If you are not the intended recipient, please inform the sender and delete this message and any attachment from your system; you must not copy or disclose the contents of this message or any attachment to any other person.
For information about data protection at De Gruyter, please see our Privacy Statement on our website here https://www.degruyter.com/cms/pages/privacy-policy

---

Von: Alexandra Heidecker <alexandra.heidecker@tum.de>
Gesendet: Dienstag, 15. August 2023 23:01
An: DeGruyter, Rechte <rights@degruyter.com>
Betreff: Anfrage für Reprint Permission eines Artikels

Sie erhalten nicht oft eine E-Mail von alexandra.heidecker@tum.de. Erfahren Sie, warum dies wichtig ist

Sehr geehrte Damen und Herren,

Ich bin einer der Autoren dieser Publikation und möchte höflich um Ihre Unterstützung und Erlaubnis bitten, einen Reprint dieser Arbeit zu erstellen. Der Reprint wird für die Zusammenschrift meiner Promotion verwendet werden.

Hier sind die Details der Publikation:

Titel:

Crystal structure of a hexacationic Ag(I)-pillarplex-dodecyl-diammonium pseudo-rotaxane as terephthalate salt

Autoren:

Alexandra A. Heidecker, Moritz Bohn und Alexander Pöthig

Erscheinungsdatum:

23.02.2022

Publikationsquelle:

Zeitschrift für Kristallographie - Crystalline Materials, vol. 237, no. 4 - 5, 2022, 167 - 177.

https://doi.org/10.1515/zkri-2021-2076

Ich möchte sicherstellen, dass alle notwendigen Schritte unternommen sind, um die Copyright-Richtlinien zu respektieren, und bitten daher um Ihre offizielle Erlaubnis für die Erstellung und Verwendung dieses Reprints.

Bitte lassen Sie mich wissen, welche Informationen Sie von uns benötigen, um den Prozess zu starten, und ob etwaige Gebühren oder Lizenzbedingungen anfallen.

Vielen Dank im Voraus für Ihre Zeit und Ihre Unterstützung. Ich freue mich auf eine positive Rückmeldung.

Mit freundlichen Grüßen,

Alexandra Heidecker

M. Sc. / PhD Student

Chair of Inorganic and Metal-Organic Chemistry (AMC)
Prof. Dr. Roland A. Fischer
Technical University of Munich
Catalysis Research Center
Ernst-Otto-Fischer-Straße 1
85748 Garching

Tel.: +49 89 289 54134
Room: CRC 4040
Mail: alexandra.heidecker@tum.de

RightsLink

Help | Live Chat

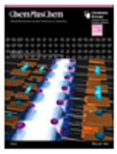

Silver and Gold Pillarplex Pseudorotaxanes from α,ω-Dicarboxylic Acids

Author: Alexandra A. Heidecker, Michele Stasi, Alexander Spears, et al
Publication: CHEMPLUSCHEM
Publisher: John Wiley and Sons
Date: Jul 19, 2023

© 2023 The Authors. ChemPlusChem published by Wiley-VCH GmbH

Open Access Article

This is an open access article distributed under the terms of the Creative Commons CC BY license, which permits unrestricted use, distribution, and reproduction in any medium, provided the original work is properly cited.

You are not required to obtain permission to reuse this article.

For an understanding of what is meant by the terms of the Creative Commons License, please refer to Wiley's Open Access Terms and Conditions.

Permission is not required for this type of reuse.

Wiley offers a professional reprint service for high quality reproduction of articles from over 1400 scientific and medical journals. Wiley's reprint service offers:

- Peer reviewed research or reviews
- Tailored collections of articles
- A professional high quality finish
- Glossy journal style color covers
- Company or brand customisation
- Language translations
- Prompt turnaround times and delivery directly to your office, warehouse or congress.

Please contact our Reprints department for a quotation. Email corporatesaleseurope@wiley.com or corporatesalesusa@wiley.com or corporatesalesDE@wiley.com.

© 2023 Copyright - All Rights Reserved | Copyright Clearance Center, Inc. | Privacy statement | Data Security and Privacy | For California Residents | Terms and ConditionsComments? We would like to hear from you. E-mail us at customercare@copyright.com

6.6 Eidesstattliche Erklärung

Ich, Alexandra Annabella Heidecker, erkläre an Eides statt, dass ich die bei der promotionsführenden Einrichtung TUM School of Natural Sciences der TUM zur Promotionsprüfung vorgelegte Arbeit mit dem Titel:

Organometallic Pillarplexes as Building Blocks for Supramolecular and Porous Solid-State Materials

unter der Anleitung und Betreuung durch: Priv.-Doz. Dr. Alexander Pöthig

ohne sonstige Hilfe erstellt und bei der Abfassung nur die gemäß § 7 Abs. 6 und 7 angegebenen Hilfsmittel benutzt habe.

☒ Ich habe keine Organisation eingeschaltet, die gegen Entgelt Betreuer*innen für die Anfertigung von Dissertationen sucht, oder die mir obliegenden Pflichten hinsichtlich der Prüfungsleistungen für mich ganz oder teilweise erledigt.

☒ Ich habe die Dissertation in dieser oder ähnlicher Form in keinem anderen Prüfungsverfahren als Prüfungsleistung vorgelegt.

☒ Teile der Dissertation wurden in Zeitschrift für Kristallographie – Crystalline Materials, ChemPlusChem veröffentlicht.

☒ Ich habe den angestrebten Doktorgrad noch nicht erworben und bin nicht in einem früheren Promotionsverfahren für den angestrebten Doktorgrad endgültig gescheitert.

☐ Ich habe bereits am _____ bei der promotionsführenden Einrichtung _____ der Hochschule _____ unter Vorlage einer Dissertation mit dem Thema_____ die Zulassung zur Promotion beantragt mit dem Ergebnis:

☒ Ich habe keine Kenntnis über ein strafrechtliches Ermittlungsverfahren in Bezug auf wissenschaftsbezogene Straftaten gegen mich oder eine rechtskräftige strafrechtliche Verurteilung mit Wissenschaftsbezug.

Die öffentlich zugängliche Promotionsordnung sowie die Richtlinien zur Sicherung guter wissenschaftlicher Praxis und für den Umgang mit wissenschaftlichem Fehlverhalten der TUM sind mir bekannt, insbesondere habe ich die Bedeutung von § 27 PromO (Nichtigkeit der Promotion) und § 28 PromO (Entzug des Doktorgrades) zur Kenntnis genommen. Ich bin mir der Konsequenzen einer falschen Eidesstattlichen Erklärung bewusst.

Mit der Aufnahme meiner personenbezogenen Daten in die Alumni-Datei bei der TUM bin ich

☒ einverstanden, ☐ nicht einverstanden.

Neufahrn b. Freising, 27.09.2023

Ort, Datum, Unterschrift